# fractography in failure analysis

STRAUSS/CULLEN, editors

ASTM STP 645

AMERICAN SOCIETY FOR TESTING AND MATERIALS

# FRACTOGRAPHY IN FAILURE ANALYSIS

A symposium
presented at
May Committee Week
AMERICAN SOCIETY FOR
TESTING AND MATERIALS
1-6 May 1977, Toronto, Canada

ASTM SPECIAL TECHNICAL PUBLICATION 645
B. M. Strauss, Gulf Research and
Development Company, and
W. H. Cullen, Jr., U.S. Naval
Research Laboratory, editors

List price $36.50
04-645000-30

AMERICAN SOCIETY FOR TESTING AND MATERIALS
1916 Race Street, Philadelphia, Pa. 19103

Library of Congress Catalog Card Number: 77-91648



Printed In Baltimore, Md.
May 1978

# Foreword

The symposium on "A Fractographic Approach to Failure Analysis" was held at the American Society for Testing and Materials' Committee Week, 3-4 May 1977, in Toronto, Canada. ASTM Committee E-24 on Fracture Testing of Materials sponsored the symposium. B. M. Strauss, Gulf Science and Technology Company, presided as symposium chairman and W. H. Cullen, Naval Research Laboratory, D. E. Passoja, Union Carbide Corporation, and W. R. Warke, Illinois Institute of Technology, served as co-chairmen.

# Related ASTM Publications

Fracture Toughness Testing and Its Applications, STP 381 (1965), $19.50, 04-381000-30

Mechanics of Crack Growth, STP 590 (1976), $45.25, 04-590000-30

Fractography—Microscopic Cracking Process, STP 600 (1976), $27.50, 04-600000-30

Properties Related to Fracture Toughness, STP 605 (1976), $15.00 04-605000-30

# A Note of Appreciation to Reviewers

This publication is made possible by the authors and, also, the unheralded efforts of the reviewers. This body of technical experts whose dedication, sacrifice of time and effort, and collective wisdom in reviewing the papers must be acknowledged. The quality level of ASTM publications is a direct function of their respected opinions. On behalf of ASTM we acknowledge their contribution with appreciation.

*ASTM Committee on Publications*

# Editorial Staff

# Contents

STRESS AND NONMETALS



SUMMARY

# Introduction

The utilization of fractography as a means of determining crack origins and mechanisms is a field of continuing development in research and for diagnosing material failures. This symposium volume deals primarily with the application of state-of-the-art fractographic techniques and interpretations to material failures.

This symposium was organized into four broad areas: techniques, environmental effects, fatigue, and stress and nonmetals. The papers discussed in the techniques portion offer general fractographic procedures used in the pursuit of everyday material failures. The papers in the other three sections discuss specific cases where the results can be applied to a broader class of materials and failure mechanisms.

This volume will serve as a ready background reference for investigators in its discussions of failures encountered in service and also as a fractographic atlas of typical fracture morphologies. It is interesting to note the preponderance of scanning electron fractographs used in these studies where, in the past, symposium volumes contained mainly transmission electron fractographs. It appears that the relative ease of specimen preparation for scanning microscopy as well as its three-dimensional images is making this the primary electron-optical tool in failure investigations while the transmission electron microscope with its improved resolution is used for corroborating fractographic interpretations.

We feel that this symposium volume is a benchmark in the development of fractography in failure analysis and provides a sound basis for continued progress in this area.

The collection of papers demonstrates the diversity with which fractography is being used as an analytical diagnostic tool and the increasing sophistication in the level of interpretation of these fractographs. We believe that the techniques and methods presented here will continue to be refined and serve as powerful tools in performing material failure analyses.

*B. M. Strauss*

Gulf Research and Development Company, Pittsburgh, Pa. 15230, editor

*W. H. Cullen, Jr.*

U.S. Naval Research Laboratory, Washington, D.C. 20375, editor

# Techniques

*J. H. Steele, Jr.*[1] *and D. F. Lentz*[2]

# Application of Fractographic-Microstructural Correlations in Evaluating Failure Mechanisms in Two Types of Steels

**REFERENCE:** Steele, J. H., Jr. and Lentz, D. F., **"The Application of Fractographic-Microstructural Correlations in Evaluating Failure Mechanisms in Two Types of Steels,"** *Fractography in Failure Analysis, ASTM STP 645,* B. M. Strauss and W. H. Cullen, Jr., Eds., American Society for Testing and Materials, 1978, pp. 5-31.

**ABSTRACT:** Steel alloys exhibit a variety of fracture mechanisms depending upon their composition, heat treatment, degree of cold working, and environmental and stress conditions. Determination of the operative mechanisms from fractographic features requires that comparisons be made between observed features and those which are characteristic of cleavage, ductile rupture, or intergranular or hydrogen embrittlement. In most cases this involves generating controlled laboratory fractures under conditions which will produce each type individually. In addition, a correlation of microstructural and fractographic features must be obtained to characterize these different mechanisms. Illustrations of these two important aspects of fractographic analyses will be presented for fracture processes occurring in drawn cup walls of low carbon sheet steel and in bending tests of a quenched and tempered plate steel.

**KEY WORDS:** fractography, steels, microstructure, scanning electron microscopy, fracture mechanisms, cleavage, intergranular, ductile rupture, hydrogen embrittlement, drawing steel, quenched and tempered steel, plate steel, quasicleavage

One of the most important aspects of fractographic analysis is an understanding of the relationship between the microtopography of the fracture surface and the underlying microstructure. This type of correlation between the size, shape, and spatial distribution of fractographic and microstructural features can be obtained by a variety of techniques [*1,2*].[3] One of the most useful of these is to electroplate a hard metallic coating over the fracture

[1] Research metallurgist, Research and Technology, Armco Steel Corporation, Research Center, Middletown, Ohio 45043.

[2] Formerly senior research metallurgist, Armco Steel Corporation, Research Center, Middletown, Ohio. Now deceased.

[3] The italic numbers in brackets refer to the list of references appended to this paper.

surface and then observe metallographic sections perpendicular to the fracture plane [*3*]. An excellent discussion of the utility of this and other sectioning techniques has been presented by Van Stone and Cox [*4*].

The importance of the concept of microstructure-fractographic correlations is emphasized in this paper using two practical failure analysis problems in steels. Briefly, these may be described as:

1. Splitting in cold-drawn steel cups
2. Failure during 90-deg bend tests in a quenched and tempered plate steel (0.3 percent carbon)

The problem of identifying the specific fracture mechanisms for these steels (and many other ferritic alloys) is complicated by the interaction of composition, heat treatment, cold working, and environmental and applied stress conditions. For example, given a selected ferritic alloy composition, microstructure (determined by the heat treatment, and cold worked state) and environment, the fracture mechanism may change from ductile, to intergranular, and to cleavage (including mixtures) depending upon stress conditions. Thus, it is essential to have or obtain background information on the fractographic features which are characteristic of these three mechanisms for the particular alloy composition and microstructure when fractured under controlled laboratory conditions. This information on the microfractographic features which are characteristic of cleavage, intergranular separation, or ductile rupture then can form a comparative basis for identifying the fracture mode or mixture of modes occurring under field or test conditions, which may be either uncontrolled or unknown.

Several alloy compositions, heat treatments, test conditions, sectioning techniques, and observations are involved in characterizing the fracture morphology in relation to the microstructure for the two examples which are described. Although complete solutions to each of these problems have not been developed at this point, the general observations and the relationships between fractographic and microstructural features are sufficiently definitive to illustrate the importance of the concept.

## Fracture Morphology of Splits in Drawn Low Carbon Sheet Steel

In drawing quality low carbon steels, there is sometimes a tendency for delayed cracking or splitting to occur in severely cold drawn cups. An example of this type of fracture is illustrated in Fig. 1. The fracture initiates at the top and crack propagation occurs in an apparently brittle[4] manner down the cup wall terminating or blunting in some cases with a ductile appearance. Examples of the type of fractographic features which are characteristic of these splits are shown in Fig. 2.

[4] Apparently brittle is used to imply macroscopic absence of plastic flow or necking. Also, ductile here implies that some indication of deformation occurs macroscopically.

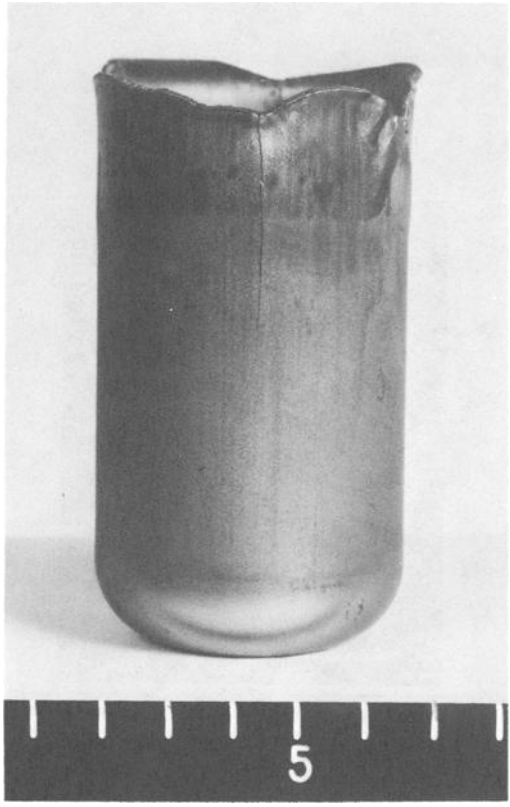


FIG. 1—*Photomacrograph showing splitting type fracture in a drawn steel cup. The scale shows the size in centimetres.*

These scanning electron microscope (SEM) fractographs are quite difficult to interpret in terms of a ductile rupture, cleavage, or a brittle intergranular mechanism (or mixture thereof) without additional information relating the observed features to the microstructure. In order to develop a consistent interpretation of the fractographic features illustrated in Fig. 2, which could then be used to describe the fracture mode, several sectioning and controlled laboratory fracturing experiments were conducted and will be described later.

Typical fracture surfaces were nickel plated to provide edge retention and to minimize seepage during metallographic preparation. Three orthogonal sections were cut from cup samples as indicated in Fig. 3 to provide perpendicular views relative to the fracture surface. Conventional metallographic techniques were used to prepare the sections which were examined optically as well as with the SEM. Typical SEM micrographs from these sections are presented in Fig. 4.

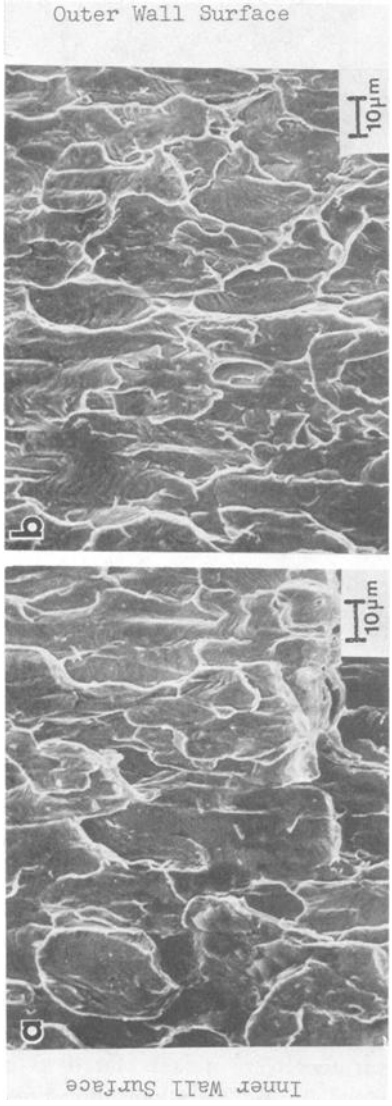
Outer Wall Surface
10 μm
b
10 μm
a
Inner Wall Surface

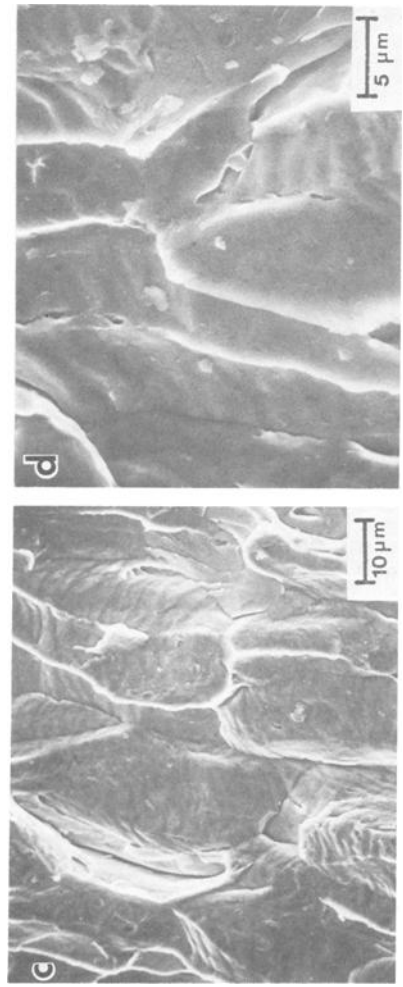


FIG. 2—*Scanning electron micrographs illustrating perpendicular views of the morphology of the split fractures. Micrographs* (a) *and* (b) *show areas near the inner and outer wall, respectively, and* (c) *and* (d) *are higher magnification micrographs of typical features.*

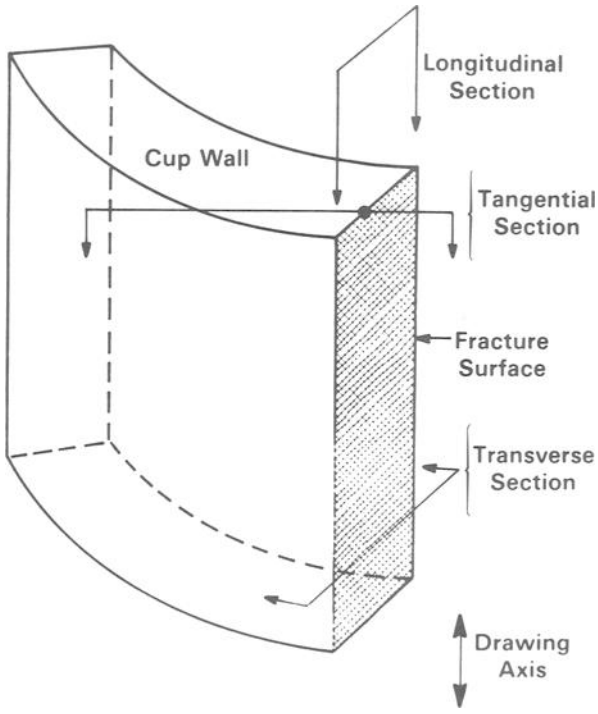


FIG. 3—*Diagram indicating orientation of metallographic sections obtained from drawn cup walls relative to the split fracture surfaces.*

The tangential and transverse sections show that the fracture path is primarily along grain boundaries. They also reveal that features which have the appearance of curled-up knife-edges or lips are present on the fracture surface. These features which are marked with arrows in Fig. 4(*a*) and (*b*) are very difficult to identify in the fractographs presented in Fig. 2. The reason for this difficulty lies in the fact that the high secondary electron intensity produced by the knife-edges also is produced by vertical steps and the curled-up knife-edges, in most cases, are associated with vertical steps. This type of SEM image contrast is not unusual since ductile rupture also tends to produce a knife-edge topography between microvoids.

Careful examination of the metallographic sections also indicated that there is a significant tendency for grain boundary rupture (as opposed to brittle separation) at both the inner and outer skins of drawn cup walls. This was verified by electropolishing the outer surface of a 5-cm-diameter 10-cm-deep drawn cup which had exhibited splitting failure. Micrographs indicating the occurrence of this ductile-type intergranular separation are presented in Fig. 5. The occurrence of such a ductile intergranular fracture mechanism has been reported recently by Meuris and Hornbogen [*5*] in

aluminum alloys exhibiting precipitate free zones along the grain boundaries and by Hecker [6] in high strength low alloy (HSLA) steels. This grain boundary rupture, which is currently under investigation, is thought to have a ductile origin and to initiate splitting when external die constraints are removed. Tension tests on cup walls indicate that the drawn material will exhibit ductile behavior[5] even with a significant amount of grain boundary rupture present in the outer and inner skins. This suggests that residual hoop stresses coupled with the grain boundary voids may cause crack propagation from the outer surface into, as well as down, the wall when the cup is removed from the die.

Sheet specimens were also cut from drawn cup walls and charged with hydrogen in an attempt to produce intergranular fracture surfaces using notched slow bend tests. Fractographs from various positions in a cup with a flat top flanged region are presented in Fig. 6(*a*) through (*d*). The intergranular nature of these fracture surfaces is apparent, as are the elongated grain shapes which are present in the drawn cup wall when compared to the bottom (Fig. 6(*d*)) and top flange (Fig. 6(*a*)).

These micrographs also show some similarities to the morphology exhibited by the split fractures as can be observed by comparison of Fig. 6(*b*) and (*c*) with Fig. 2. However, there are two notable differences; first, the knife-edge lips do not occur as frequently, and, second, extensive strain markings are present on the intergranular facets of the hydrogen-charged specimens. Although these strain markings could occur during the brittle intergranular fracture of the hydrogen-charged specimens, they may in fact reflect the grain boundary topography which existed within the cold drawn microstructure.

Figure 5(*b*) provides evidence on how this type of serrated grain boundary topography could be formed during drawing. It shows heavy deformation banding within a single grain and cavities formed at the tip (that is, triple junction) and also where the bands intersect the grain boundary.

The micrographs presented in Figs. 4 and 5 also suggest how the knife-edge lips are formed. If before final failure a majority of the triple junctions are ruptured in a manner such as shown in Fig. 5(*b*), then overlap between grains which are being carried with the separate fracture surfaces will cause their grain edges to be fretted. This will cause the grain edges or triple junctions to be curled up without being blunted or rounded by rubbing.

Sheet Charpy specimens were prepared from drawn cup wall material so that the crack path would have the same longitudinal orientation as the split fractures. Specimens broken at −196 °C had fractographic features which were very similar to the splits as illustrated in Fig. 7(*a*), (*b*), and (*c*). These micrographs were taken to illustrate the appearance of cleavage facets side by side with the serrated grain boundary facets. The only difference

[5] Ductile failure in this case occurs by necking at approximately 45 deg to the tensile axis.

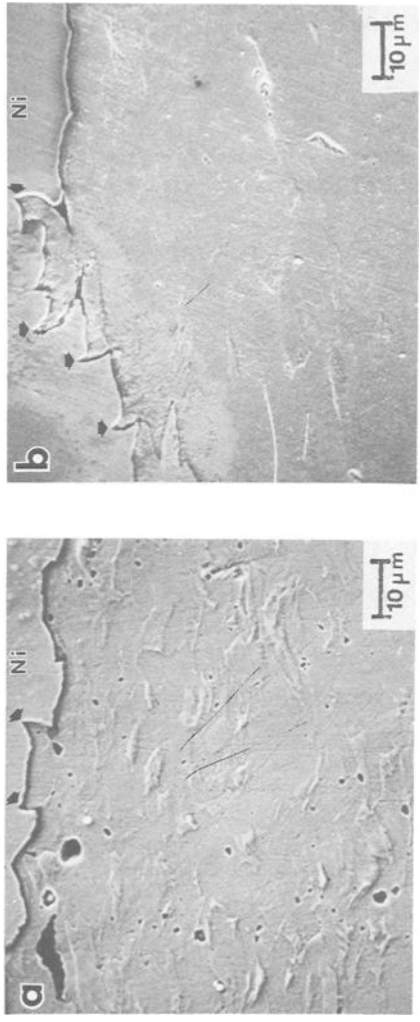
a
Ni
10 μm
b
Ni
10 μm

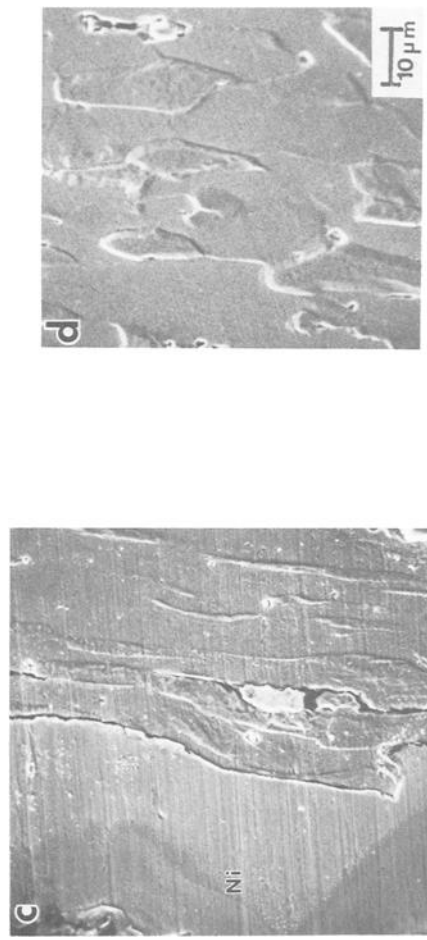


FIG. 4—*Scanning electron micrographs of metallographic sections illustrating fracture surface profiles (as retained by nickel plating) and the underlying microstructure. Nital etch:* (a) *and* (b) *transverse,* (c) *tangential, and* (d) *longitudinal.*

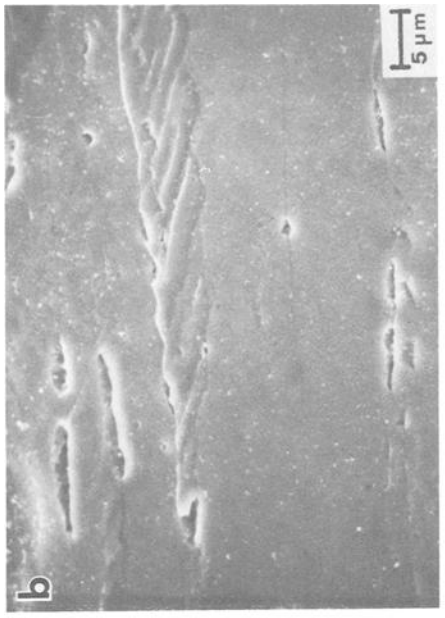
5 μm
b

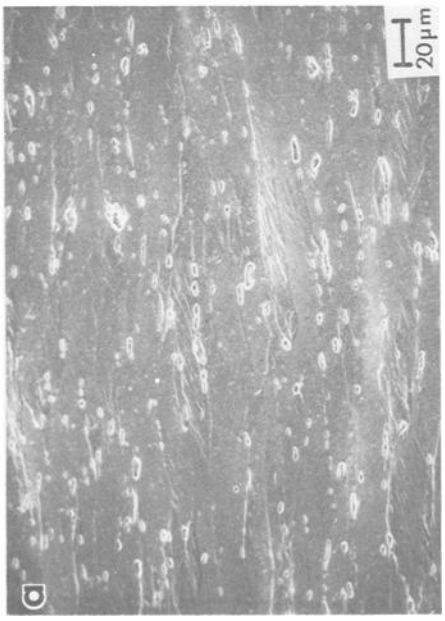
20 μm
a

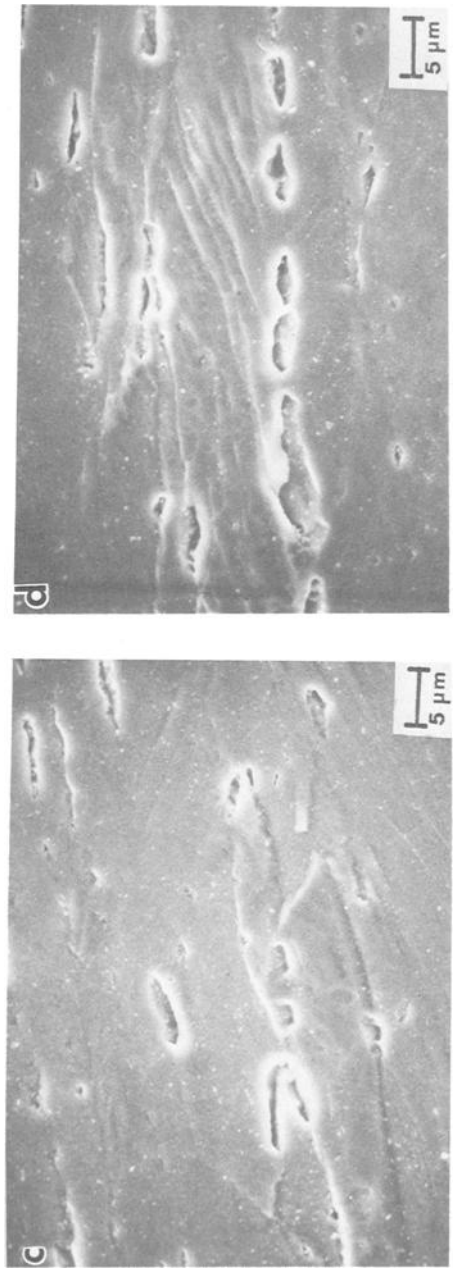


FIG. 5—*Scanning electron micrographs illustrating grain boundary rupture which occurs in the inner and outer skins of drawn cup walls. These were obtained by electropolishing the outer surface and etching with 3 percent nital. Note cavities at grain tips and deformation bands.*

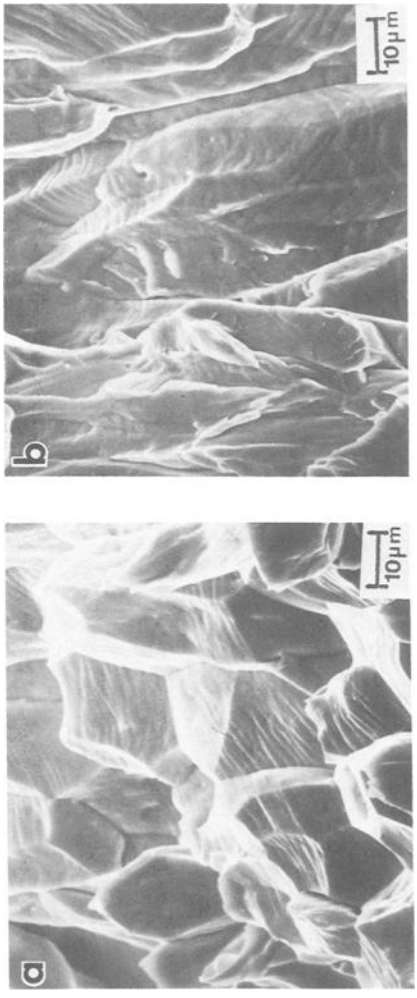
a
10μm
b
10μm

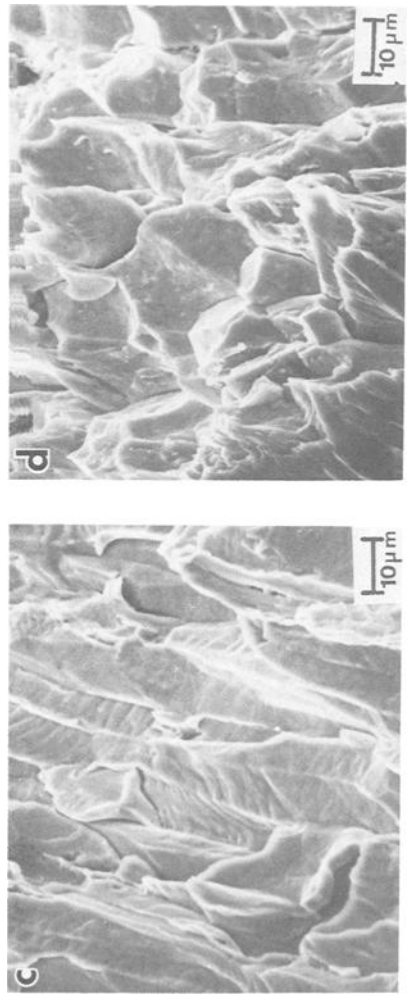


FIG. 6—*Fracture surfaces from hydrogen charged bend fractures from various positions in drawn cup:* (a) *top flange,* (b) *and* (c) *wall areas, and* (d) *bottom. These illustrate the elongated grain morphology in the cup wall and the strain markings on the facets.*


2 μm

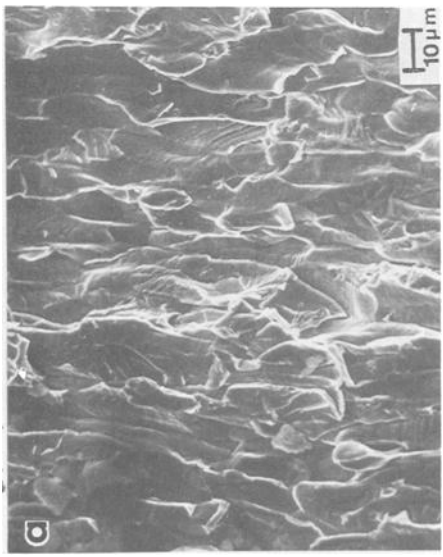
10 μm

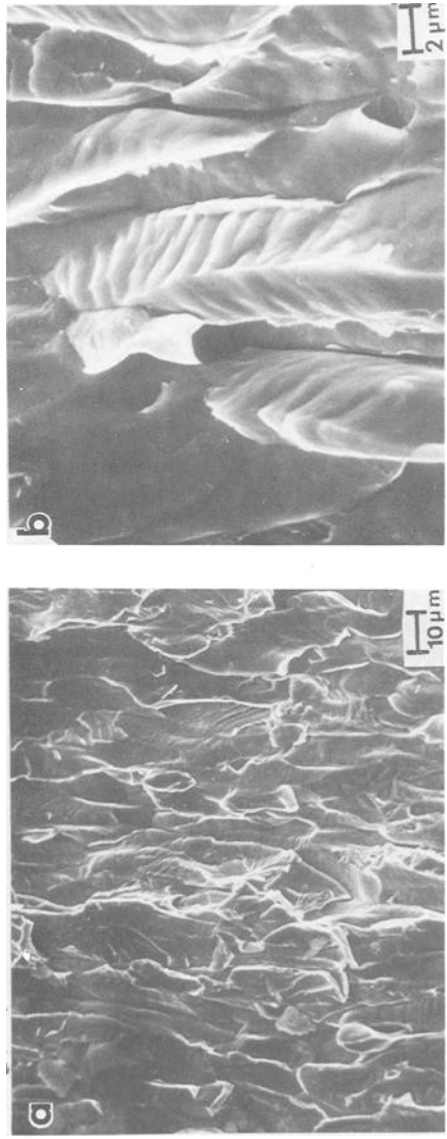


FIG. 7—*Scanning electron micrographs of sheet Charpy fracture surfaces;* (a), (b), *and* (c) *are from liquid nitrogen specimens and* (d) *is a room temperature specimen.*

between the fracture morphology in these specimens and those formed in the cup walls is a slight increase in the amount of cleavage. Figure 7(*b*) and (*c*) also illustrate the fractographic appearance of the serrated grain boundaries such as the one indicated in the cross section in Fig. 5(*b*). Room temperature sheet Charpy specimens had typically full oblique fractures (ASTM Test for Plane-Strain Fracture Toughness of Metallic Materials E 399-74). There were some very small flat regions where manganese-sulfide stringers were apparently elongated along triple junctions as indicated in Fig. 7(*d*).

If one excludes brittle intergranular fracture modes such as might be caused by hydrogen [*7*] or solute segregation [*8*], then there are at least three mechanisms which could account for the intergranular fracture appearance.

1. Localized plastic flow in a thin layer on either side of a grain boundary as described by Meuris and Hornbogen [*5*] where precipitate free zones exist. These zones are not observed in the steels which exhibit the splitting failures even though the material contains some extremely fine precipitates.
2. Grain boundary rupture at triple junctions and faces where sufficient plastic flow occurs. This type of ductile fracture mode, in fact, may be quite general in polycrystals where nonhomogeneity of plastic strain caused by orientation differences must be accommodated at boundaries.
3. Microvoid formation at noncontinuous grain boundary precipitates. This fracture mode, which cannot be completely excluded, may contribute locally in initiating cavities at boundaries. It can be concluded, however, from the absence of observable precipitates on the split and on the hydrogen-charged fracture surfaces that it is extremely unlikely that this mechanism can explain the failures.

Even though a complete understanding of the cause and the mechanism of splitting failures has not been obtained as yet, the fractographic-microstructural observations which are presented provide consistent evidence that some type of ductile grain boundary fracture is occurring during the drawing process particularly in the skin regions where die interaction occurs. They further demonstrate quite conclusively that the split fractures occur by an almost completely intergranular mode. However, additional work, which is presently underway, is needed to establish the cause of the intergranular fracture mode.

## Fracture Morphology in Quenched and Tempered Armor Plate Steel (0.3 percent Carbon)

A problem of occasional insufficient 90-deg bend ductility in an armor plate steel was investigated in an attempt to determine if it could be attributed to hydrogen embrittlement. The steel, which was rare earth treated for inclusion shape control, had the following ladle chemistry.

| C | Mn | P | S | Si | Cr | Mo |
|---|---|---|---|---|---|---|
| 0.30 | 0.61 | 0.010 | 0.010 | 0.33 | 1.10 | 0.19 |

The plate used in this study was 5-mm-thick material which had been quenched and tempered at 205 °C to a hardness of 49 HRC. This steel had a fine-grained tempered martensitic microstructure with no retained austenite.

Figure 8 illustrates the fracture morphology observed on the low ductility 90-deg bend specimens consisting of large dimples formed primarily by rare earth sulfides[6] and titanium carbonitrides together with extremely fine, shallow dimples in which second-phase particles are either absent or below the resolution limit of the SEM. A few cleavage facets also could be found as shown in the enlargement (Fig. 8(*d*)).

The problem of identifying features in the fracture morphology that could be linked with hydrogen embrittlement in this complicated microstructure, which contains inclusions, prior $\alpha$ austenite grain boundaries, lath and possibly plate martensite boundaries, as well as fine carbide particles and some proeutectoid ferrite near the plat surface, was investigated by generating controlled laboratory fractures. These were produced by three-point notched slow bend and Charpy impact tests at room and liquid nitrogen ( − 196 °C) temperatures and also by a slow bend testing after cathodically charging with hydrogen. These specimens were notched to produce transverse fracture surfaces relative to the rolling direction.

The liquid nitrogen ( − 196 °C) fracture surfaces exhibited morphologies as illustrated in Fig. 9. The SEM micrographs indicate that the surface consists of a multiply faceted blocky texture with some extremely fine river markings which are variable in orientation relative to the macroscopic failure direction. The morphology of these flat blocky regions is controlled by the martensitic lath structure as demonstrated by the cross-section profiles presented in Fig. 10. The fracture and microstructural-feature correlation suggest that crack propagation occurs by the formation and linking of very small clevage cracks ahead of the main front. This is referred to as satellite nucleation by Beacham [*9*]. Some ductile shear steps also can be observed linking the cleavage cracks in Fig. 9(*a*).

The features characteristic of this type of fracture have led to it being called "quasicleavage" [*1, 9*] because it resembles cleavage with the apparent exception that the facet size extends over much larger regions than the tempered martensite features. In this microstructure, however, the facets tend to coincide with the martensitic packets as indicated by the nickel-plated cross sections presented in Fig. 10.

In addition there are blocky features which appear to be caused by sub-

[6] Possibly oxysulfides.

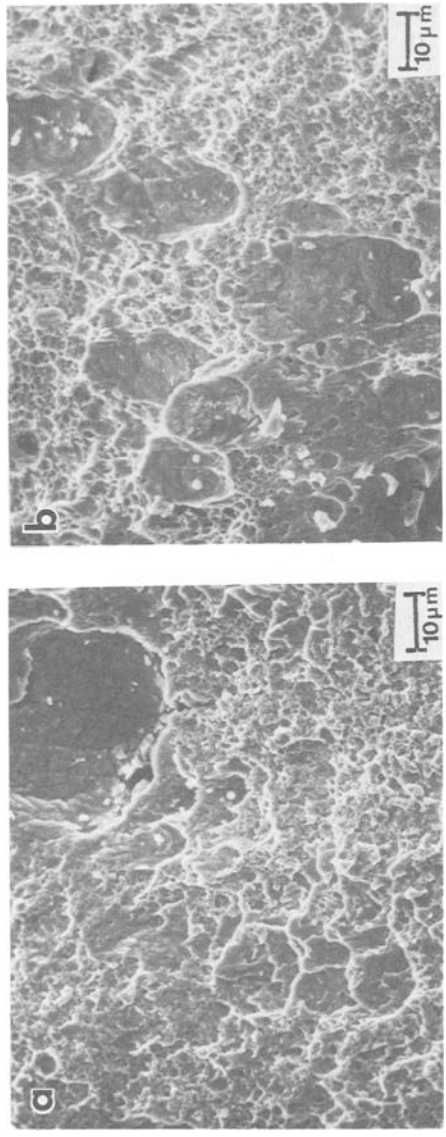
b
10 μm
a
10 μm

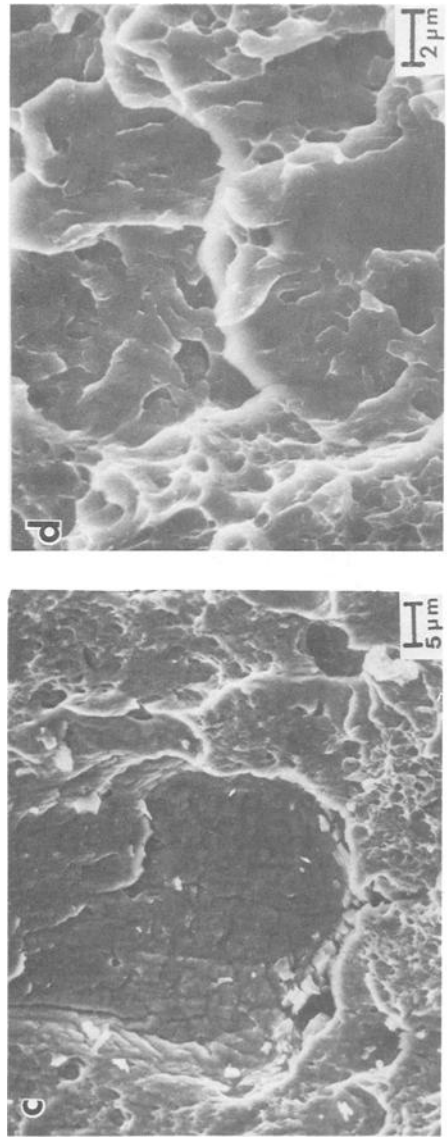


FIG. 8—*Scanning electron micrographs of bend test fracture specimen of quenched and tempered plate:* (a) *and* (b) *illustrate large microvoids formed by rare earth sulfides and titanium carbonitrides, and* (c) *and* (d) *provide enlargements from areas shown in* (a). *Area* (d) *illustrates cleavage facets.*

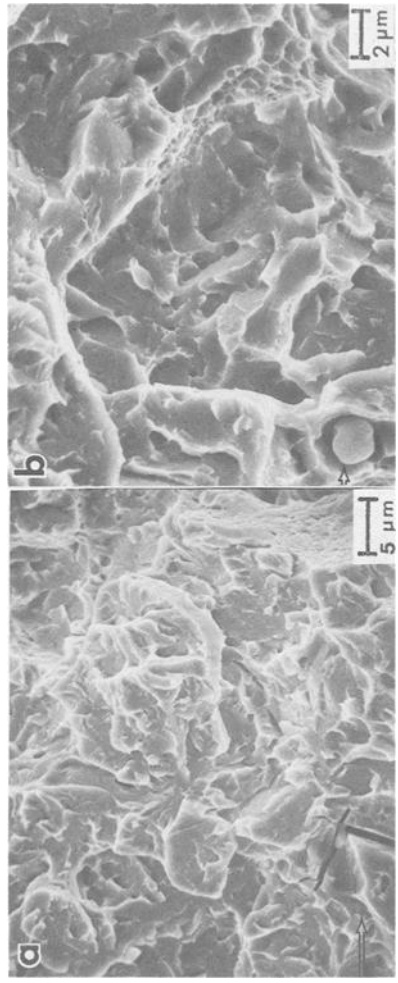
a
5 μm
b
2 μm

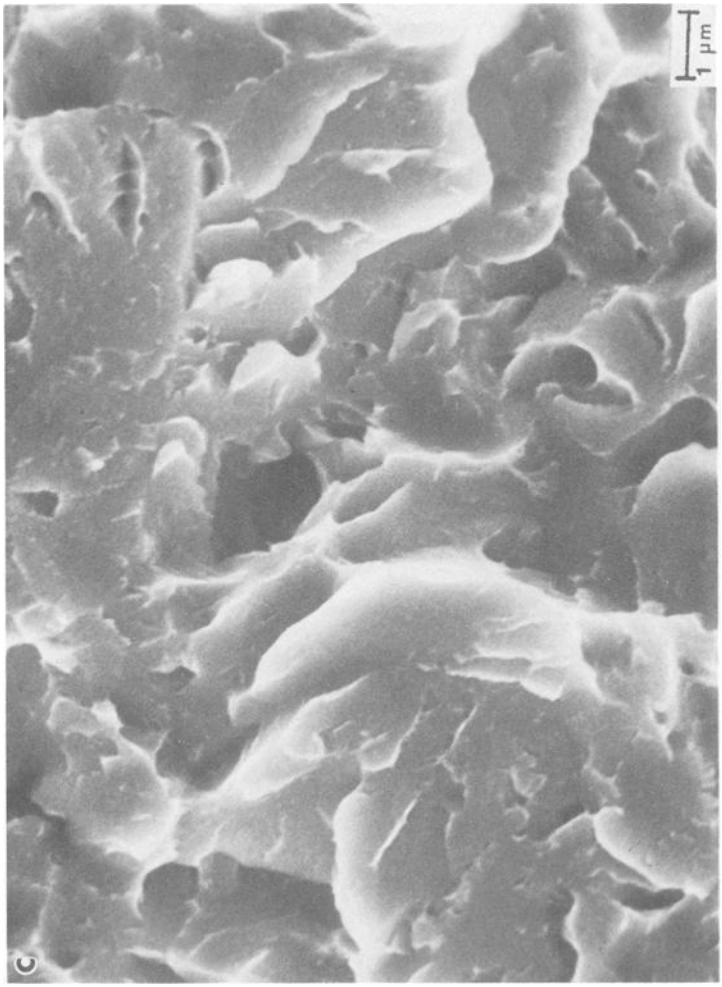


FIG. 9—*Fractographs indicating the morphology of Charpy V-notch and three-point bend specimens fractured at liquid nitrogen temperatures. A titanium carbonitride particle can be observed in* (a) *and a rare earth sulfide in* (b) *as marked by arrows.*

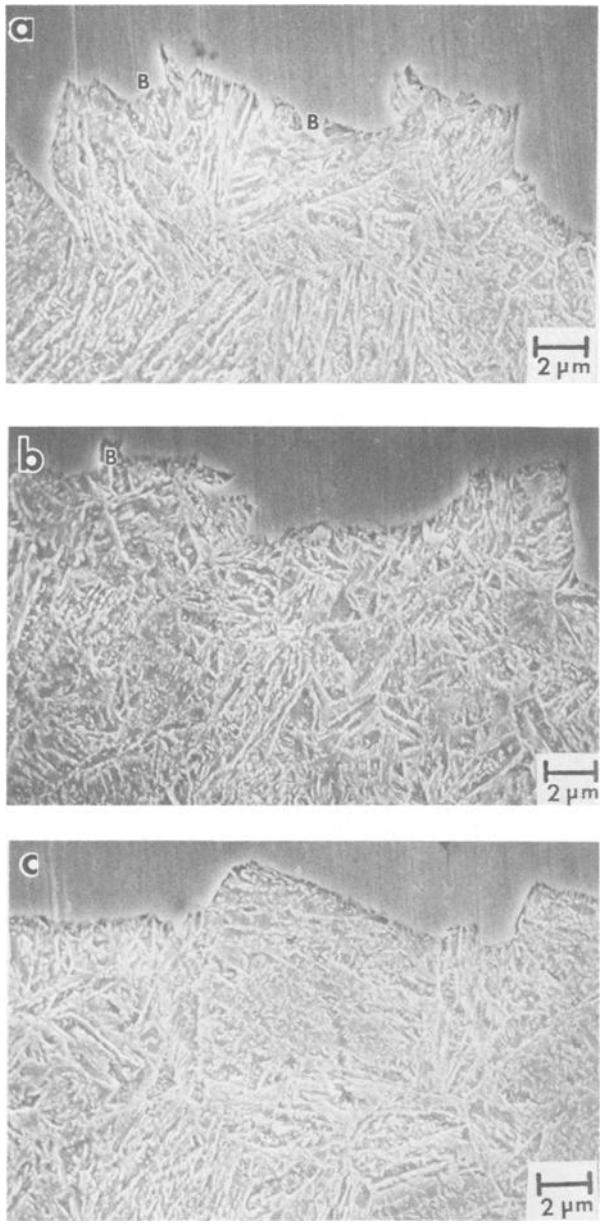


FIG. 10—*Metallographic cross sections of liquid nitrogen fracture surfaces showing profiles and their relationship to the microstructure.*

structure within the tempered martensitic packets. These regions have a tendency to exhibit one or more planar sides combined with fine knife-edges. Examples are marked with the letter B in Fig. 10. These do not appear to be "tongues" such as are formed by mechanical twinning [*10*]. Tear ridges between martensite packets also can be seen in Fig. 9(*b*) along with the fine dimples and shear surfaces.

Two examples of inclusions also are indicated in Figs. 9(*a*) and (*b*). A rare earth sulfide is shown in Fig. 9(*b*) in a rounded crater which is not much larger than the particle itself, whereas the titanium carbonitride shown in Fig. 9(*a*) (also see Fig. 11(*c*)) contains distinct internal crystallographic cracking. This is probably cleavage parallel to the faces of the cubical-shaped particles which have a sodium chloride (NaCl) type crystal structure.

Figure 11 provides illustrations of the ductile fracture appearance formed in room temperature three-point bend and Charpy V-notch specimens. Large dimples are formed at rare earth sulfides and titanium carbonitrides. These have a characteristic roughened appearance which is probably a result of extensive plastic deformation during void growth [*2*]. The ductile Charpy and three-point bend specimens exhibited only a small central flat fracture area with average width of about 1.4 mm and thus a 70 percent oblique fracture (ASTM Test E 399-74). The fractographs shown were taken from the central flat part of the ductile fracture surface.

The large dimples are surrounded by fine microvoids which in most cases do not appear to contain particles. These regions may be examples of microvoid sheet formation [*2*] although cross sections (Fig. 11(*e*)) do not seem to provide confirmation of this observation. An example of a microvoid formed several millimetres away from the fracture surface is shown in Fig. 11(*f*).

Figure 12 shows the slow bend fracture morphology generated by cathodically charging 5-mm-thick specimens for 48 h with hydrogen. The heterogeneous nature of crack propagation is evident from the low magnification micrograph (Fig. 12(*a*)). The smooth areas with rounded edges which occur along the specimen edges appear to have been formed by cracks propagating along the tempered martensite lath boundaries as indicated by the unusual feathery appearance illustrated in Fig. 12(*b*)). Nickel-plated cross sections also suggest that the crack propagation mechanism is associated with lath boundaries as indicated in Fig. 12(*c*).

The central region of the specimens exhibited the same type of inter-lath boundary morphology in small circular regions such as observed in Fig. 12(*d*). These appear to have been formed by crack nucleation at titanium carbonitride particles. A metallographic section showing this type of crack initiation is presented in Fig. 12(*e*). In addition, the central part of the fracture contains microvoid regions (dimple rupture) which appear to link the inter-lath cracks. Their morphology is illustrated in Fig. 12(*f*).

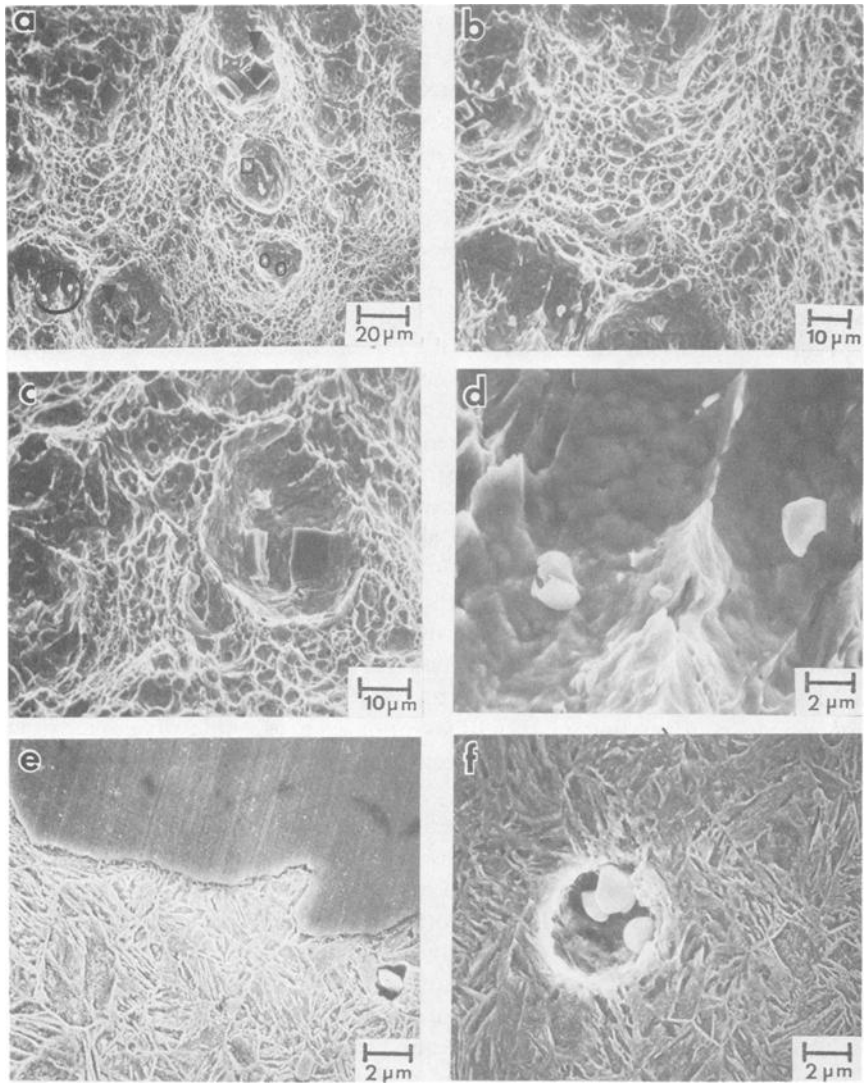


FIG. 11—*Scanning micrographs illustrating fracture surface morphology and profiles from room temperature notched three-point bend specimens. Circles in* (a) *indicate rare earth sulfides, arrows titanium carbonitride, and squares iron rich particles.* (c) *and* (d) *are higher magnification micrographs of microvoids containing a titanium carbonitride particle and rare earth sulfide particles, respectively.* (e) *and* (f) *show the fracture surface profile, and a microvoid formed away from the main fracture path.*

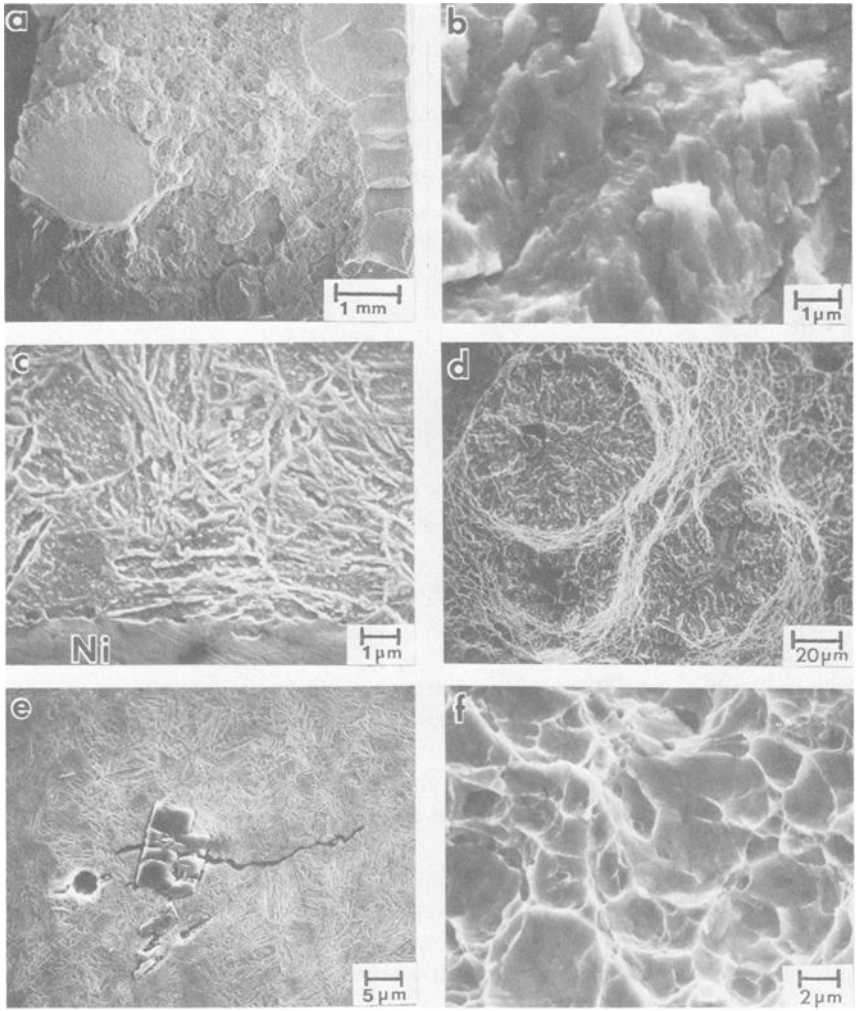


FIG. 12—*Scanning micrographs illustrating hydrogen charged three-point notched bend fracture morphology.* (a) *Low magnification showing macroscopic appearance,* (b) *lath boundary topography on flat regions.* (c) *nickel plated cross-section of lath boundary fracture,* (d) *lath boundary cracks formed by cleavage of titanium carbonitride particles,* (e) *cross section illustrating same effect as shown in* (d), *and* (f) *dimple rupture observed in central region.*

These fractographic-microstructure observations, although not conclusive, suggest that hydrogen embrittlement may not be the cause of the low bend ductility in this plate of steel. Additional studies are currently being conducted to determine whether lower hydrogen concentrations can affect microvoid formation and growth during ductile rupture in this steel. These observations also indicate the following conclusions: (*a*) quasicleavage in this plate steel exhibits a distinct relationship to microstructure in the size of the facets and in the size and spatial arrangements of the smaller blocky regions relative to substructure occurring within the tempered martensite packets. (*b*) Hydrogen charging can embrittle martensite lath boundaries producing a distinctive fractographic appearance. (*c*) Cleavage of titanium carbonitride particles can nucleate lath boundary crack propogation in hydrogen charged specimens and large microvoids during ductile rupture.

## Discussion

It is important after discussing these two examples to emphasize several factors which are important in making fractographic analyses with the SEM.

1. The SEM fractographs alone can be misleading without knowledge or background of the microstructure involved.
2. Controlled laboratory fractures, such as liquid nitrogen, Charpy impact, or cathodically charged hydrogen-induced embrittlement can provide meaningful comparisons or guide lines in interpreting scanning microscope fractographs.
3. Sectioning of fracture surfaces after plating to provide edge retention is essential in interpreting and understanding the origin of fractographic features.
4. The identification of hydrogen embrittlement as a cause of fracture can be extremely difficult based upon fractography alone since it may not produce a unique fracture mode.

In addition, the observations and interpretations discussed indicate that SEM fractographs which in general are relatively easy to obtain may be quite difficult to interpret unambiguously. This is emphasized by the need for sectioning and for comparison with controlled laboratory fracture surfaces as pointed out for these two examples.

## Summary and Conclusions

The importance of obtaining fractographic-microstructure correlations in interpreting observed features and describing fracture mechanisms has been illustrated by the two examples described. Also the observations, discussions, and results presented indicate that controlled laboratory fracture

experiments and the application of sectioning techniques can provide important supportive information in characterizing failure mechanisms.

The specific fractographic conclusions for the steels described have been presented at the end of each section. The major conclusions can be summarized as follows.

1. In deep drawing of low carbon steel there is a skin effect which can cause a ductile grain boundary rupture.

2. The identification of an intergranular fracture morphology in heavily deformed materials does not necessarily imply a brittle fracture mode.

3. Quasicleavage in a tempered martensitic microstructure can be correlated with packet size and substructure.

4. Heavy hydrogen concentrations such as can be obtained by cathodic charging can cause martensitic lath boundary embrittlement.

*Acknowledgments*

The authors would like to express their appreciation to P. J. Erfort and A. G. Golembiewski for their assistance with the laboratory work, and to D. A. Sarno, W. G. Granzow, and A. J. Heckler for their helpful and stimulating discussions during the course of the investigations reported here.

## References

[1] Beachem, C. D. and Pelloux, R. M. N. in *Fracture Toughness Testing and Its Applications, ASTM STP 381*, American Society for Testing and Materials, 1964, pp. 210-244.
[2] Cox, T. B. and Low, J. R. Jr., *Metallurgical Transactions*, Vol. 5, 1974, pp. 1457-1470.
[3] Turkalo, A. M., *Transactions*, American Institute of Mining, Metallurgical, and Petroleum Engineers, Vol. 218, 1960, pp. 24-30.
[4] Van Stone, R. H. and Cox, T. B. in *Fractography–Microscopic Cracking Process, ASTM STP 600*, American Society for Testing and Materials, 1976, pp. 5-28.
[5] Meuris, M. and Hornbogen, E., *Praktische Metallographic*, Vol. 13, 1976, pp. 160-171.
[6] Hecker, S. S., *Metallurgical Transactions*, Vol. 5, 1974, pp. 2107-2110.
[7] Bernstein, I. M., *Metallurgical Transactions*, Vol. 1, 1970, pp. 3143-3150.
[8] Rellick, J. R. and McMahon, C. J., Jr., *Metallurgical Transactions*, Vol. 5, 1974, pp. 2439-2450.
[9] Beacham, C. D. in *Fracture*, Vol. 1, H. Liebowitz, Ed, Academic Press, New York, 1969, Chapter 4, pp. 243-349.
[10] Broek, D., *International Journal of Fracture Mechanics*, Vol. 7, 1971, pp. 483-486.

*J. D. Young*[1] *and Arun Kumar*[1]

# Use of Laboratory Failure Simulation Exemplars to Study Intergranular Fracture Modes in 9Ni-4Co-0.20C Steel

**REFERENCE:** Young, J. D. and Kumar, Arun, **"Use of Laboratory Failure Simulation Exemplars to Study Intergranular Fracture Modes in 9Ni-4Co-0.20C Steel,"** *Fractography in Failure Analysis, ASTM STP 645,* B. M. Strauss and W. H. Cullen, Jr., Eds., American Society for Testing and Materials, 1978, pp. 32–48.

**ABSTRACT:** During structural spectrum load testing of the aft-fuselage structure of the B-1 aircraft, a 124-mm-long crack was detected in the 9Ni-4Co-0.20C steel primary structure. Review of the fracture location revealed that the crack path was adjunct to a production weld used in the fabrication of the 727-kg (1600-lb) forged and welded horizontal-vertical stabilizer support assembly. Upon removal and examination of the fracture on a scanning electron microscope, two distinct fracture modes were observed: (*a*) at the origin, a 0.5 to 1-mm intergranular fracture mode was observed, followed by (*b*) 123 mm of transgranular high-stress low-cycle fatigue crack propagation.

Fatigue crack growth rate analysis on the scanning electron microscope showed that the fatigue crack started propagation at the onset of testing, strongly suggesting a preexisting crack which was corroborated by the observation of an intergranular fracture mode at the origin, which exhibited no evidence of cyclic growth.

A laboratory failure exemplar study program was conducted to establish standards for intergranular fracture mechanisms possible in 9Ni-4Co-0.20C steel, fabricated using the same environmental conditions as present during manufacturing. The salient features of the fractographs of known failure mechanisms were used to establish the cause of service failure intergranular cracking to be hydrogen embrittlement.

**KEY WORDS:** fractography, intergranular fracture, hydrogen embrittlement, weldments

One of the significant innovations on the U.S. Air Force B-1 advanced strategic aircraft is the use of fracture control in the design of all structures. Fracture control is applied to all single load path primary structures. This involves five phases of evolution to the final production design, namely: (*a*) analytical design and selection of materials, (*b*) material control (fracture mechanics), (*c*) design development test (structural elements), (*d*) design verification test (full scale structure) and (*e*) proof and flight test of prototype aircraft.

[1] Supervisor and member of technical staff, respectively, Metallurgy Unit of Materials and Producibility, Los Angeles Division, Rockwell International, Los Angeles, Calif. 90009.

It was during the spectrum fatigue design verification test of the aft-fuselage (empennage) after 991 flights of testing, that a 124-mm (4.875-in.) long crack was detected in the 727-kg (1600-lb) cruciform shaped 9Ni-4Co-0.20C welded steel structure member. This member supports the vertical and both horizontal stabilizers and ties the empennage to the fuselage. Detailed examination of the test structure revealed that the crack path was adjunct to the main production weld which joins the two steel forgings which comprise the primary structure. Since 991 flights represent only 75 percent of an aircraft life (defined), the fracture surfaces were removed, and a failure analysis was performed.

Subsequent to completion of the failure analysis and corrective action implementation, subject test structure was repair welded on site, put back into test, and completed 2.3 lifetimes of testing without recurrence of cracking at this location.

The chemistry and mechanical properties of the 9Ni-4Co-0.20C steel used in the structure are listed in the following table.

*Chemical Composition*

| C | Mn | P | S | Si | Cr | Ni | Co | Mo | V |
|---|---|---|---|---|---|---|---|---|---|
| 0.16/0.23 | 0.20/0.40 | 0.010 max | 0.010 max | 0.2 max | 0.65/0.85 | 8.5/9.5 | 4.25/4.75 | 0.9/1.1 | 0.06/0.12 |

*Mechanical Properties*

| Ultimate Strength | Yield Strength | % Elongation | % Reduction in Area | Fracture Toughness, $K_{Ic}$ |
|---|---|---|---|---|
| 924 to 1020 MPa (190 to 210 ksi) | 875 to 972 MPa (180 to 200 ksi) | 14 to 19 | 55 to 65 | 121 to 143 MPa$\sqrt{m}$ (110 to 130 ksi$\sqrt{in.}$ ) |

## Procedures

### *Visual and Macroscopic*

The location of the horizontal-vertical stabilizer spindle support fitting in the aft-fuselage section of the aircraft and the crack path in the R/H side plate are shown in Fig. 1. The thickness of the side plate is 27.2 mm (1.07 in.) and the crack traces on both the internal and external surface were approximately 124 mm (4.875 in.) long. As will be seen later in the text, the crack initiated at the toe of the weld and broke through the outer surface at a repair weld on the side plate.

Specimens containing the fracture surface were removed from the structure. Figures 2 and 3 are micrographs of the specimen near the origin. The load spectrum proved to be very helpful to determine the crack propaga-

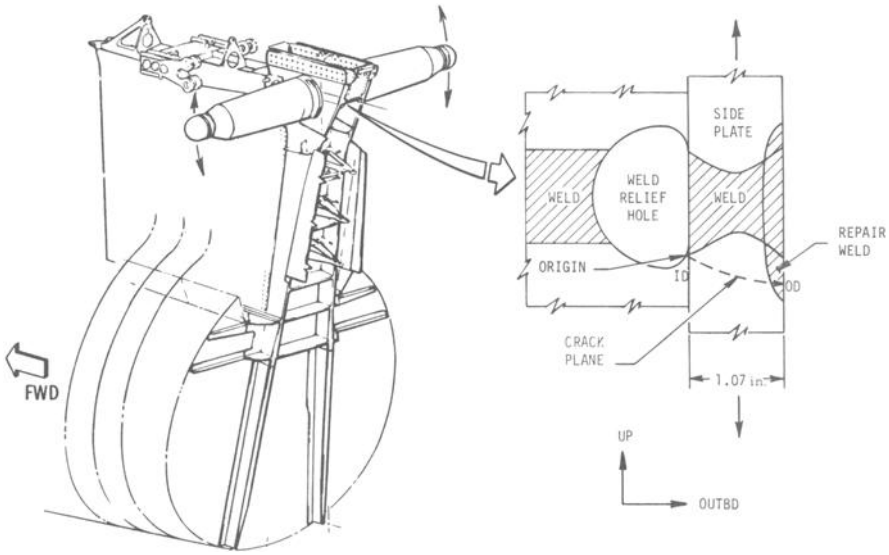


FIG. 1—*Location of horizontal stabilizer spindle support fitting in the aft-fuselage section, and a schematic drawing showing the crack location and the origin.*

tion rate, direction, etc., since the fracture surface was marked accordingly. A total of 991 flights could be accounted for from the fractographs in the fatigue fracture area, verifying immediate crack propagation upon start of the test.

### *Scanning Electron Microscopy*

The origin was examined by scanning electron microscope and the fractographs are shown in Figs. 4 and 5. An intergranular fracture mode was observed at the origin. The intergranular area at the origin was roughly semicircular, about 0.5 mm (0.02 in.) deep and 1.0 mm (0.04 in.) wide. A fatigue crack had initiated at the intergranular crack, which subsequently propagated by conventional transgranular fatigue.

The grains in the intergranular area at the origin were equiaxed. No fine structure or tear was observed on the grain facets. Electron microprobe analysis did not reveal the presence of any corrosion products or other foreign elements at the origin.

### *Metallography*

Following fractographic analysis, the fracture specimen was carefully sectioned adjacent to the origin and perpendicular to the side plate. The specimen was mounted and polished to examine metallographically the section (see Fig. 6). The orientation of the specimen and the different structures also are identified. It can be seen that the intergranular portion of the

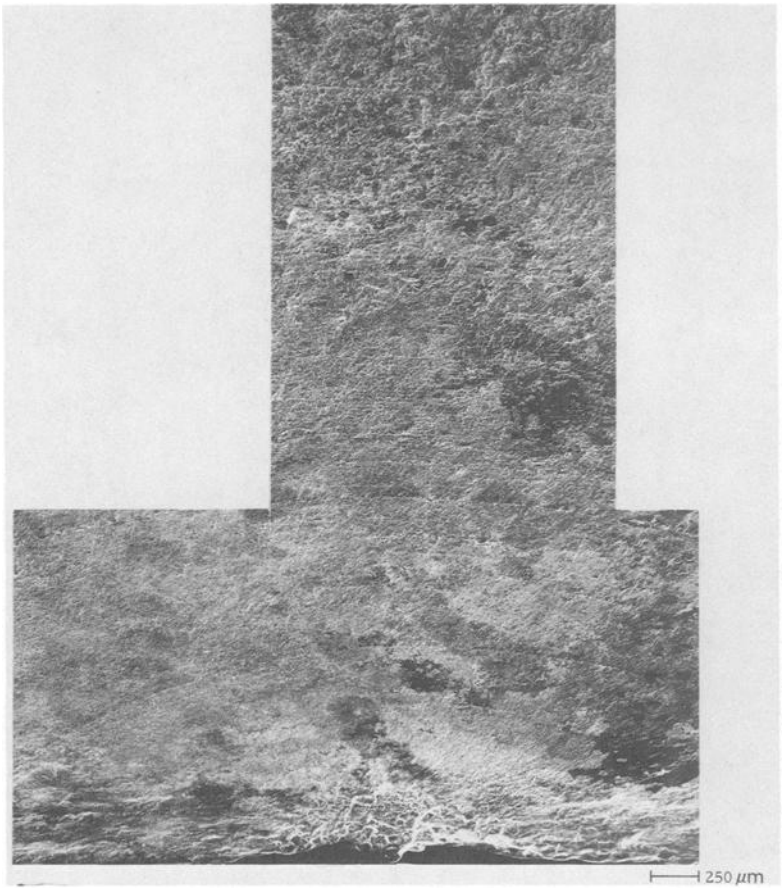


FIG. 2—*Scanning electron micrograph showing the intergranular fracture mode at the origin and fatigue striations originating from the intergranular area (origin).*

crack was at the toe of the weld. The parent metal reveals a normal forged structure. Another cast weld metal structure and heat-affected zone can be seen away from the origin. Both heat-affected zones show the so-called weld "eye-brows," which are created by the heat produced by individual weld passes during welding.

### *Laboratory Failure Simulation*

After establishing that the crack initiated from an origin with intergranular cracking, the direction of this failure analysis was diverted to determine the cause of the intergranular crack in the 9Ni-4Co-0.20C steel structure.

From fractography and other studies, the cause of intergranular crack-

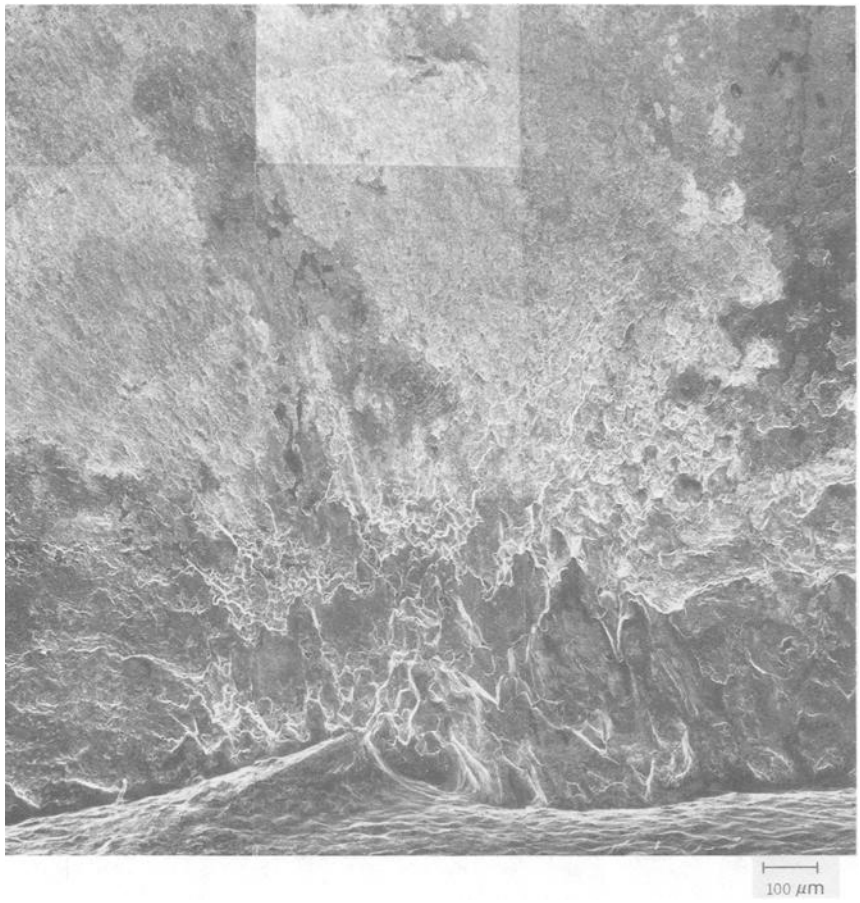


FIG. 3—*Scanning electron fractograph showing the origin.*

ing at the origin was not evident. Therefore, it was decided to study the various possible intergranular cracking mechanisms in 9Ni-4Co-0.20C steel. Since the intergranular crack was formed sometime prior to the start of test, and most probably during the manufacturing or processing of the structure, or both, the complete manufacturing and processing history for the part was reviewed. The following possibilities existed which could have produced intergranular cracking: (*a*) crater cracking, (*b*) stress corrosion cracking, (*c*) hydrogen embrittlement, (*d*) elevated temperature fracture, and (*e*) weld defect.

Laboratory failure exemplars were prepared for these mechanisms using different variables. Attempt was made to duplicate the actual processing conditions that the part underwent during manufacture. The fracture surfaces produced by these known failure mechanisms were examined on

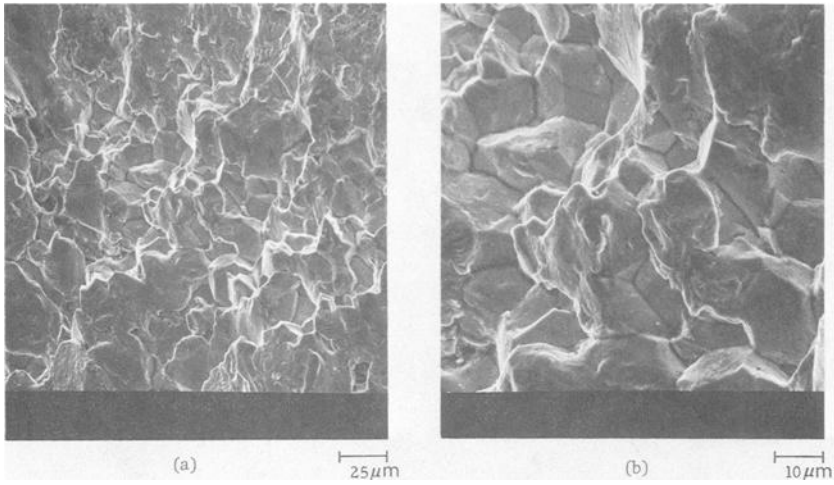


FIG. 4—*Intergranular fracture at the origin showing equiaxed grains.*

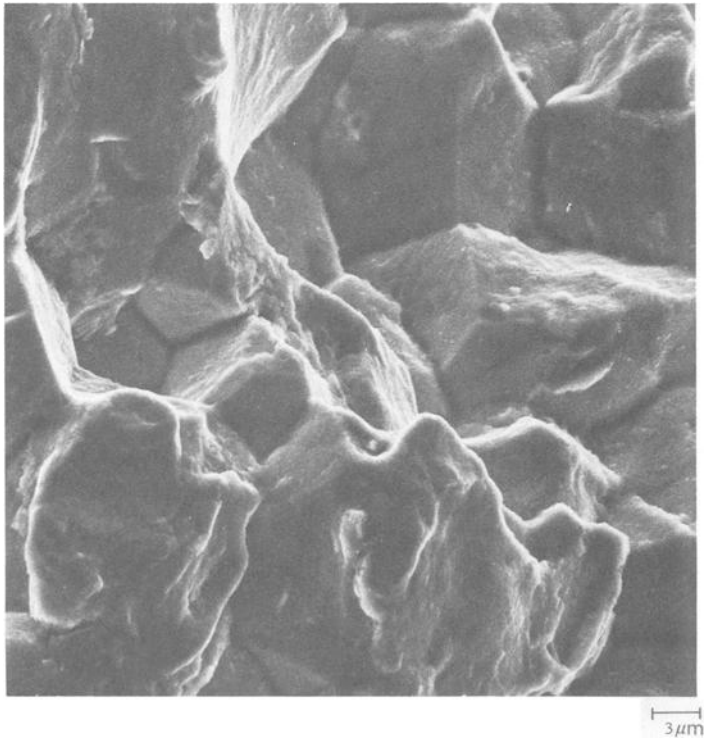


FIG. 5—*Detail scanning electron fractograph of the intergranular fracture at the origin.*

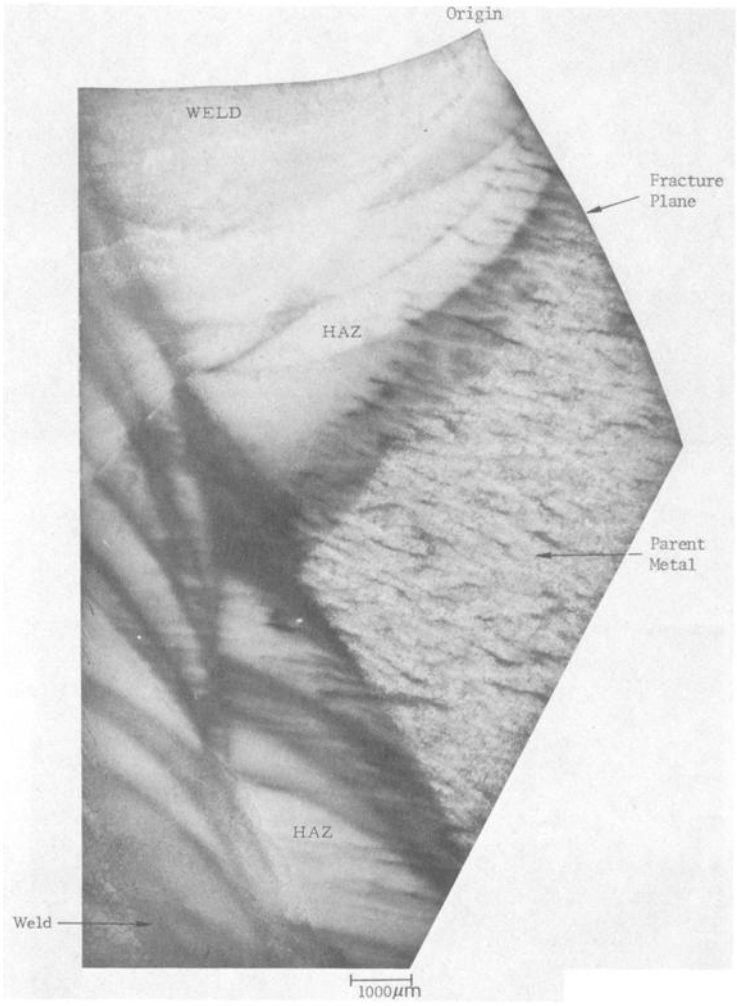


FIG. 6—*Metallographic microsection through the origin showing the orientation of the specimen and different areas.*

the scanning electron microscope. The fracture mode, grain size and orientation, and grain facet morphology were the features under consideration to match the exemplars to the service failure.

## Results and Discussion

### *Crater Cracking*

Since the origin was determined to be at the toe of the weld, it was considered that crater cracking might have caused the intergranular crack.

Crater cracking is caused by sudden termination of the welding process such as pulling the weld torch away or suddenly cutting off the power supply. Due to excessively rapid solidification and high residual stresses generated above the equicohesive temperature, the cracks developed are intergranular in nature. Crater cracking is a type of hot tear.

Attempts to produce crater cracks in 9Ni-4Co-0.20C steel specimens during welding by cutting off the power supply or by pulling away the welding torch, practically, were quite difficult. This would be expected because of the high toughness and alloy composition of 9Ni-4Co.-0.20C steel.

The weld crater fracture surface might be either unoxidized or oxidized depending on whether the solidification occurred in an argon atmosphere or in air. Since tungsten inert gas (TIG) welding was used, the power supply may be cut off during welding with the torch still in place and the crater crack would solidify under argon atmosphere. The other case could be when the welding torch is suddenly pulled away and the crater crack solidifies under a nonprotective atmosphere producing oxidation of the fracture surface.

Crater cracks produced during welding (in argon) were broken open for fractographic examination. The scanning electron fractographs are shown in Figs. 7 and 8. The fracture mode is intergranular, exhibiting both equiaxed and columnar grains. The columnar grains are near the surface of the crater, revealing rapid solidification with a high rate of heat transfer. Althouth the crack produced by crater cracking was intergranular in nature, fractography revealed the following morphological differences from the fracture surface of the service failure: (*a*) the grain separation was very sharp and well defined, and (*b*) the grain facets exhibited a fine tear structure not observed on the service failure.

The crater crack produced by suddenly pulling away the welding torch loses the beneficial effect of the argon protective atmosphere, resulting in oxidation of the surfaces exposed to air. Such a crater crack is shown in Fig. 9. The solidified free surface is shown revealing oxidized dendrites. Since no elevated temperature oxidation was observed on the fracture surface in the service failure, this mechanism can be discounted totally as a cause of failure.

### *Stress Corrosion Cracking*

Stress corrosion cracking is a mechanical-environmental failure which occurs in the combined presence of a sustained load and a corrosive environment. Since the crack was at the toe of the weld, where higher localized residual stresses are produced by the solidifying weld metal, coupled with restraint imposed by the adjacent metal and the part weight during welding, one can account for the residual stresses produced during welding.

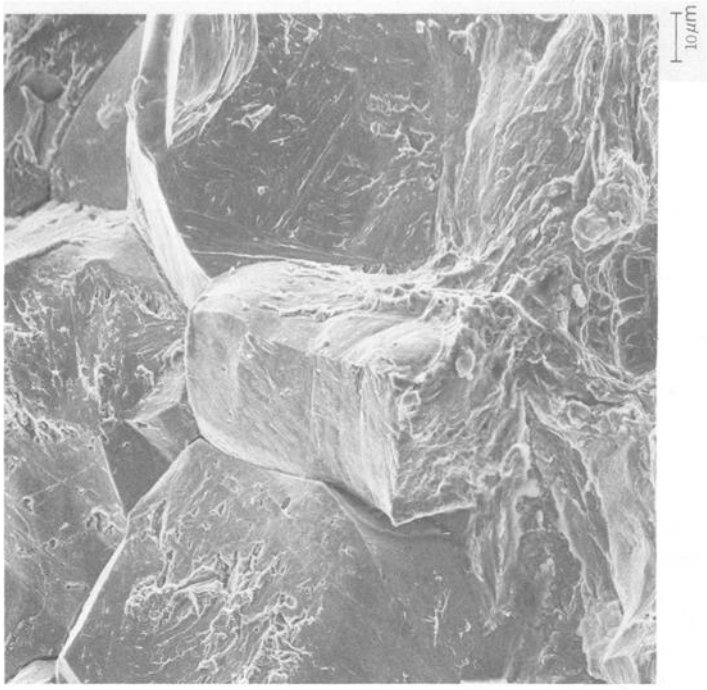


FIG. 8—*Scanning electron fractograph showing equiaxed intergranular cracking in weld crater.*

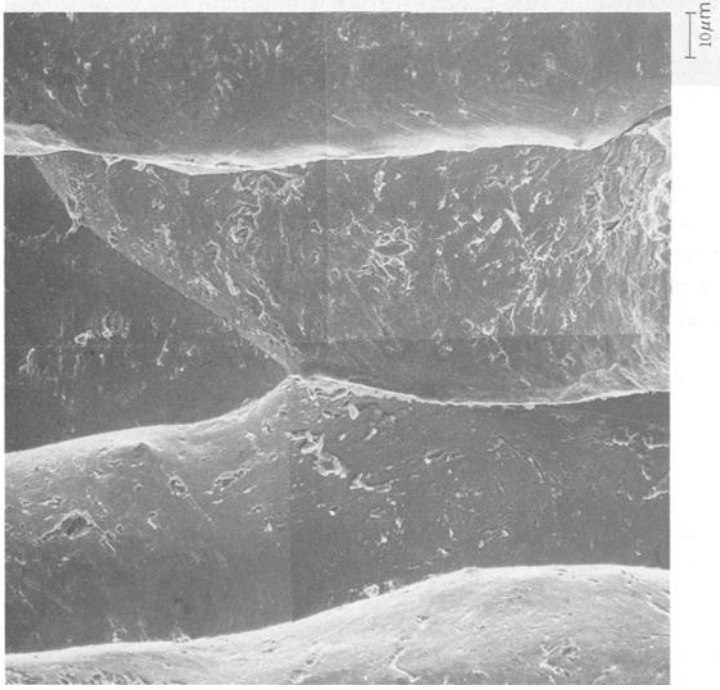


FIG. 7—*Scanning electron fractograph showing columnar intergranular cracking in weld crater.*

The simultaneous presence of unrelieved welding stresses along with a humid noncontrolled atmosphere can produce stress corrosion cracking.

Three laboratory specimens of 9Ni-4Co.-0.20C steel in the as-welded condition were subjected to stress corrosion cracking environments by intermittent immersion in 5 percent sodium chloride (NaCl) solution in water, with the specimens loaded in tension. All three specimens were standard 6-mm (0.25-in.) diameter round-bar tension specimens and were subjected to the same corrosive media, but were tested under sustained loads of 75, 80, and 85 percent of the ultimate tensile strength, respectively. Scanning electron fractographs of typical stress corrosion cracking fractures are shown in Figs. 10, 11, and 12. Figure 10 reveals intergranular cracking, however, the fracture surface is covered with corrosion products. Another typical fractograph (Fig. 11) exhibits "mud-cracking" and recrystallized salt crystallites on the fracture surface. A similar area was observed on the specimen shown in Fig. 11 near the origin and is shown in Fig. 12.

*Hydrogen Embrittlement*

Hydrogen embrittlement is a mechanical-environmental failure which occurs in the presence of hydrogen in metals and alloys in dissolved or absorbed form, along with residual or static stresses. High strength steels are very susceptible to hydrogen embrittlement and 9Ni-4Co-0.20C steel falls in this category. Weld metal is generally more prone to hydrogen cracking than the parent metal. Also, the heat-affected zone with higher hardness than the parent metal is generally more susceptible to hydrogen embrittlement than the parent metal, as has been evidenced for some steels.

The presence of residual stresses in the part developed during the welding operation already has been described. Moisture can condense from the atmosphere on the part prior to welding. Also, a very small leak of the cooling-water line in the welding torch could act as a source of water and consequently hydrogen. If the weld wire is stored unprotected in a humid atmosphere, some moisture can be picked up by the wire. The use of non-hydrogen controlled weld wire also can contribute to hydrogen embrittlement. Hydrogen also may be produced by a corrosion reaction at the surface which can diffuse into the steel. Thus, under these conditions, hydrogen embrittlement could very well be the cause of intergranular crack in the present service failure.

Standard round bar tension specimens of 9Ni-4Co-0.20C steel 6 mm (0.25 in.) in diameter, in the as-welded condition, were cathodically charged with hydrogen in an acid solution. Within 1 h after hydrogen charging, the specimens were loaded at a constant load of 70 and 75 percent of the ultimate tensile strength of 9Ni-4Co-0.20C steel, respectively. Both the specimens failed in a totally brittle manner and no ductility was observed.

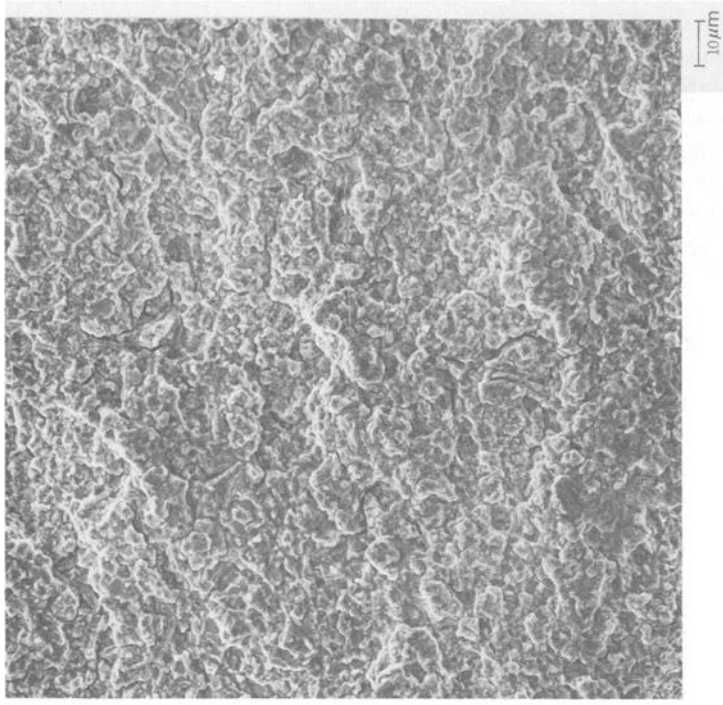


FIG. 10—*Scanning electron fractograph of 9Ni-4Co-0.20C steel specimen failed by stress corrosion cracking.*

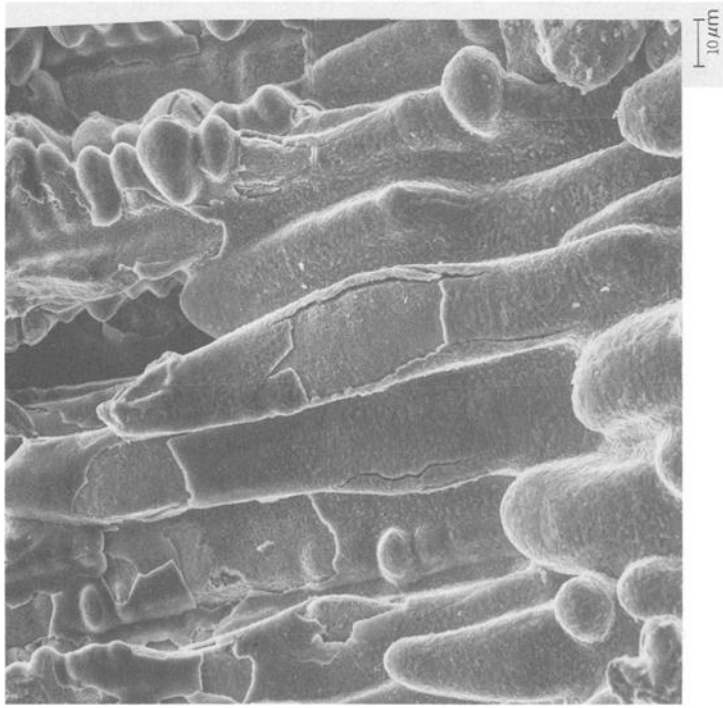


FIG. 9—*Scanning electron fractograph of a crater crack formed in air. Oxidized dendritic structure and oxide scale spalling are clearly visible.*

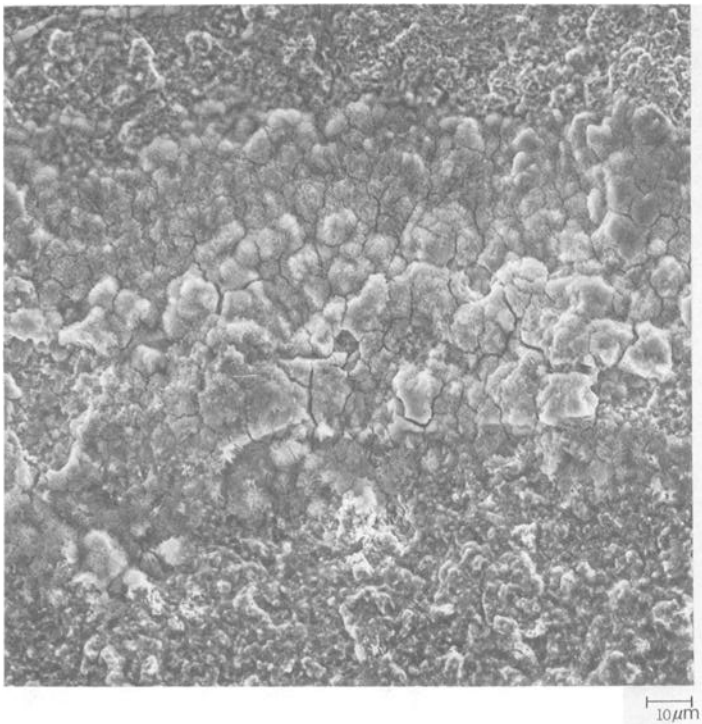


FIG. 11—*Scanning electron fractograph of another area from stress corrosion cracking specimen revealing mud-cracking and salt crystallites on the fracture surface.*

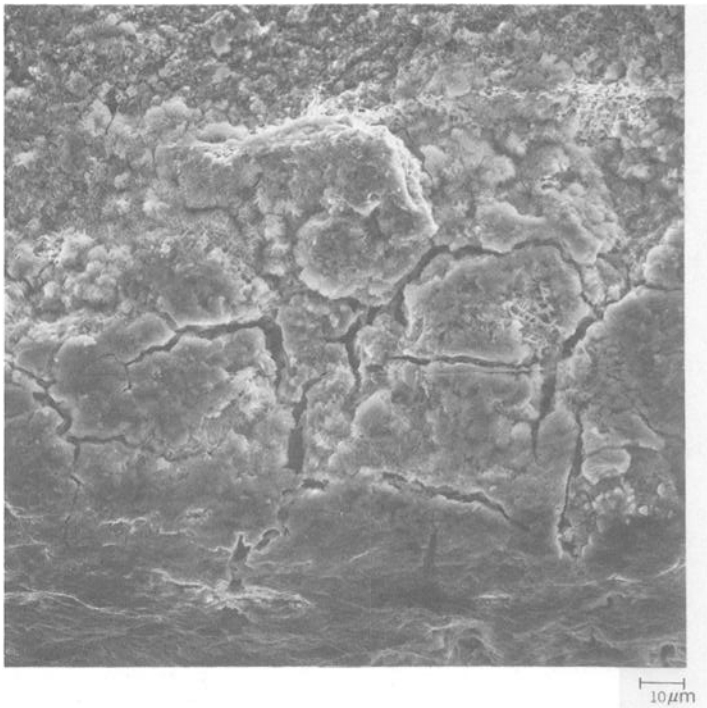


FIG. 12—*Scanning electron fractograph of area at the origin of the stress corrosion cracking specimen.*

The scanning electron fractographs are shown in Figs. 13 and 14. The intergranular topography and grain facet morphology very closely resemble the intergranular area of the service failure, that is, no perceivable differences existed between these fractographs (Figs. 13 and 14) and the service failure (Fig. 4) when viewed at a wide range of magnifications.

*Elevated Temperature Fracture*

Grain boundaries are weaker than the grains at elevated temperatures ($T > Tm/2$) and fractures are generally intergranular. At low temperatures, however, grain boundary areas have higher strength than the grains, and the fractures are generally transgranular (excluding environmental failures). The temperature at which the transition occurs from transgranular to intergranular fracture is called the "equicohesive temperature." Since the origin area in the present service failure had been heated several times above the equicohesive temperature during the welding passes, a possibility for elevated temperature fracture exists.

Gleeble (hot tension) testing of 9Ni-4Co-0.20C steel weldments as 6-mm (0.25-in.) diameter round specimens (with water cooled ends for gripping) was performed at various temperatures under argon and air atmospheres. Localized temperature adjacent to the fracture was measured by a thermocouple which was welded to the specimen. The temperature control was within ± 10°C (± 50°F). Very high strain rates were applied and a continuous temperature recording was made during the test.

A weld specimen of 9Ni-4Co-0.20C steel was fractured in an argon atmosphere at 1260°C (2300°F). The intergranular fracture area is shown in Fig. 15. The grain facets exhibit deformation bands and twins (probably revealed by thermal etching).

Gleeble testing of a 9Ni-4Co-0.20C steel weldment at 1260°C (2300°F) in air produced an oxidized intergranular fracture as shown in Fig. 16. Wavelength dispersive microprobe analysis revealed that the oxidation product on the fracture surface was iron oxide.

The 9Ni-4Co-0.20C steel weldment which fractured at 1315°C (2400°F) in argon is shown in Fig. 17. The onset of grain boundary melting and "tendril" formation is evident in this fractograph.

In summary, none of the fractographs produced by elevated temperature fracture match the service fracture.

*Weld Defect*

The possibility of a weld defect at the origin causing intergranular cracking was ruled out after examining the fracture surface of a 9Ni-4Co-0.20C steel weldment that failed in a fatigue test, in which the crack initiated at a lack of fusion. The scanning electron fractograph of the weld defect is

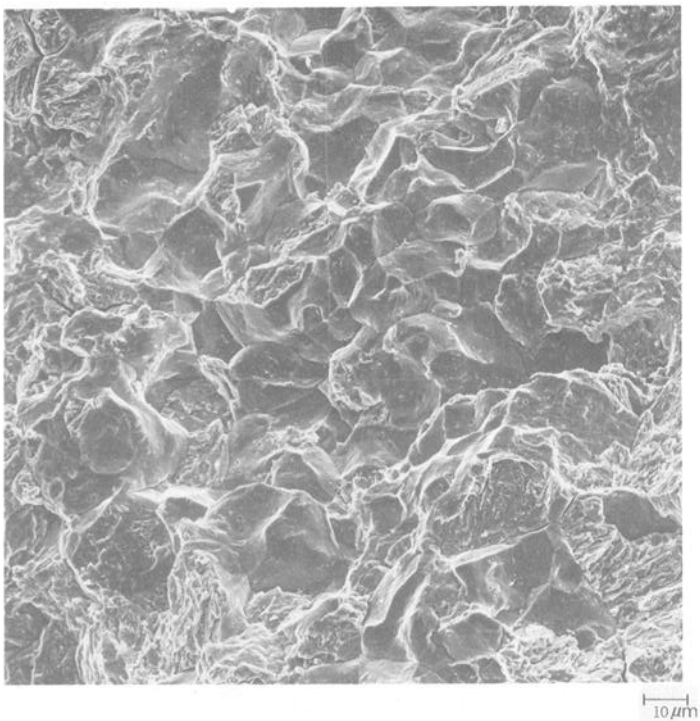


FIG. 13—*Scanning electron fractograph of the fracture caused by hydrogen embrittlement.*


FIG. 14—*Scanning electron fractograph of another specimen failed due to hydrogen embrittlement.*

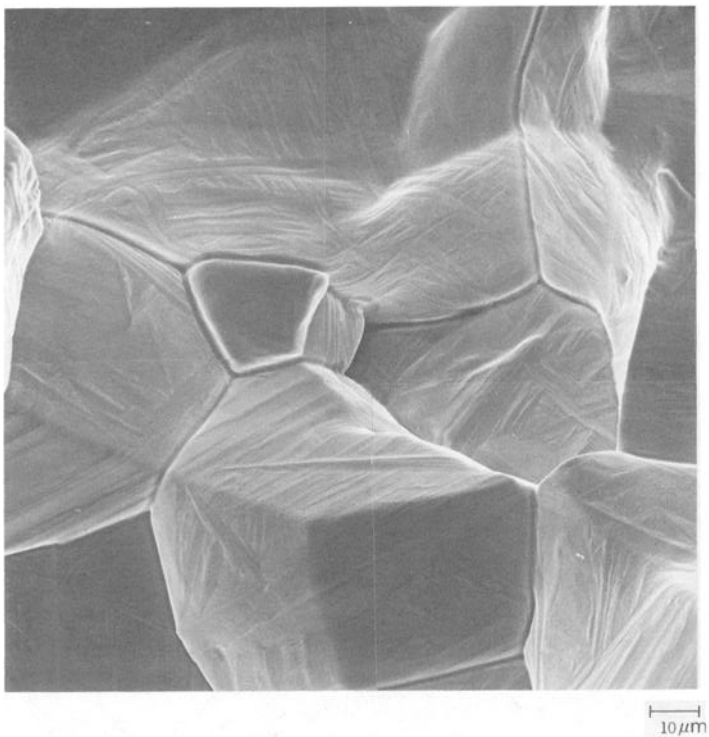


FIG. 15—*Scanning electron fractograph of an elevated temperature fracture produced at 1260°C (2300°F) in argon.*

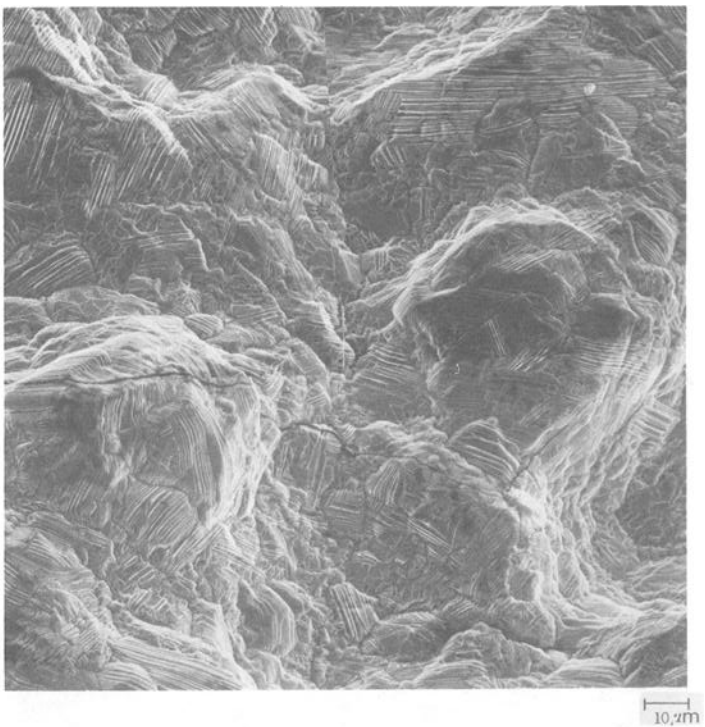


FIG. 16—*Scanning electron fractograph of an elevated temperature fracture produced at 1260°C (2300°F) in air. Intergranular crack and oxidized grain facets are evident.*

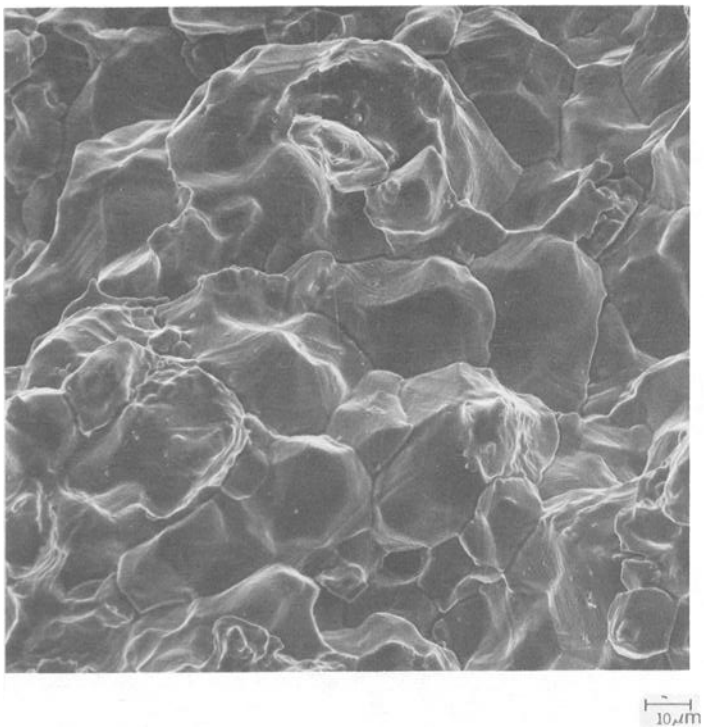


FIG. 17—*Scanning electron fractograph of an elevated temperature fracture produced at 1315°C (2400°F) in argon. Grain boundary melting and tendril formation is evident.*

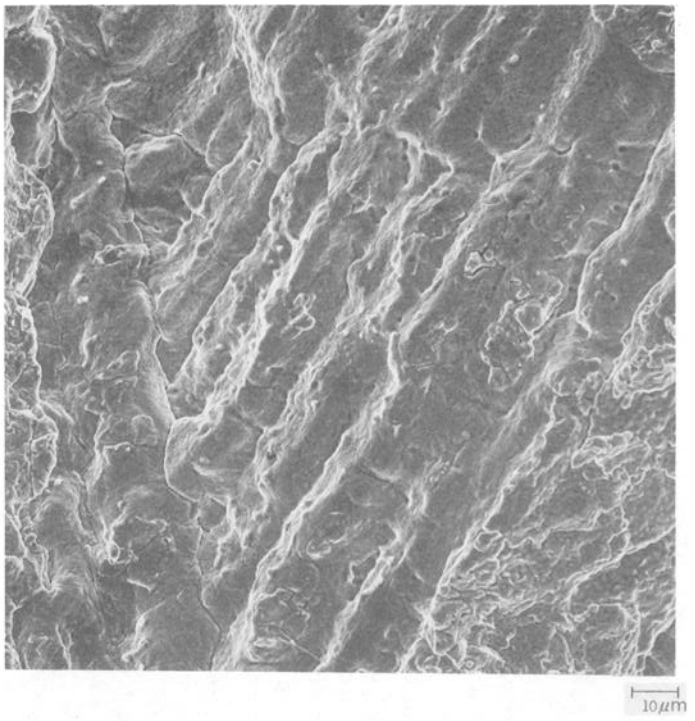


FIG. 18—*Scanning electron fractograph of an intergranular crack at a lack of fusion in the weld.*

shown in Fig. 18, which reveals a dendritic, rounded intergranular fracture with strong evidence of thermal exposure.

## Conclusions

An intergranular crack, roughly semicircular and about 0.5 mm deep and 1.0 mm wide, was produced on the interior surface of the right-hand side plate/weld relief hole of the horizontal stabilizer spindle support fitting prior to the test, probably during manufacturing. The intergranular crack most probably was caused by hydrogen embrittlement during the period between the welding operation and the stress relieving as determined by comparative fractography. This intergranular crack was present in the part prior to the aft-fuselage fatigue test. Upon beginning of the test, a fatigue crack initiated at this preexisting crack and propagated through the side plate for 991 flights of testing, until a 124-mm-long crescent shape crack was observed on the exterior surface of the side plate. Corrective actions have been implemented in the welding process to preclude recurrence of delayed environmental failure of the type observed in this study.

*D. A. Meyn*[1]

# Case Histories Illustrating Fractographic Analysis Techniques

**REFERENCE:** Meyn, D. A., **"Case Histories Illustrating Fractographic Analysis Techniques,"** *Fractography in Failure Analysis, ASTM STP 645,* B. M. Strauss and W. H. Cullen, Jr., Eds., American Society for Testing and Materials, 1978, pp. 49-72.

**ABSTRACT:** The Naval Research Laboratory receives cracked and fractured parts ranging from the exotic to the mundane: for example, titanium alloy jet engine components, ultrahigh strength steel landing gear parts, aluminum alloy airframe sections, and galvanized mild steel radio antenna support frames. Failure analysis involving so many materials over such a wide range of applications demands great adaptability in the use of fractographic techniques. The use of all techniques from the unaided eye through low-power magnifiers to high-powered light microscopes and transmission and scanning microscopes, will be discussed, using actual case histories for illustration. The application of surface chemical analysis to failure analysis also will be mentioned.

**KEY WORDS:** failure, fractures (materials), fractography

The Engineering Materials Division of the Naval Research Laboratory (NRL) receives many failure analysis requests every year, mostly from Navy activities, but occasionally from other sources. Usually, we get specimens which already have undergone examination or preliminary treatment by other organizations, and thus are seldom in virgin condition. Nevertheless, it is usually possible to obtain considerable information even from severely damaged fractures. Typically, the submitter wishes to know as much as possible of the history of the fractured part from the time of manufacture and hopes that we can reconstruct the events leading to failure; but more often the investigation will end in some uncertainty as to the fracture mechanism itself. The honest failure investigator must admit that it is not always possible to distinguish between corrosion fatigue and stress corrosion cracking (SCC), for example, or even between fast fracture and SCC in some instances. Therefore, a knowledge of the circumstances of failure and the operating stresses and environment can be of great help in diagnosing a failure mechanism.

[1] Metallurgist, Naval Research Laboratory, Washington, D.C. 20375.

## NRL Failure Analysis Techniques

Specimens are examined first and photographed as completely as possible without initial cleaning or other treatment, to an extent judged desirable in light of the history of the failure and the type of information likely to be required. For example, if the composition of surface contaminations is desired, ultrasonic cleaning and replica stripping would defeat analysis. After such preliminary analysis, the whole fracture, or cut sections thereof as necessary, is cleaned ultrasonically and examined in the light microscope and scanning electron microscope (SEM). Then replicas are stripped, either to remove further surface coatings or for transmission electron microscope (TEM) examination. At times it is found necessary to resort to rather vigorous cleaning methods, such as chemical cleaning and mechanical removal of dirt and surface layers. Some background on such methods have been provided elsewhere [*1*].[2]

The usual techniques employed by others are used at NRL, including low-power stereomicroscopy, light and electron microscopy, and metallography. In addition, specialized surface analysis techniques such as electron microprobe and Auger spectrometry are available.

## Illustrative Examples

Fractography was not well developed in the early 1960s and most failure analyses involved considerable analytical work and laboratory simulation of fracture to identify causes of fracture. An example of the pioneering nature of failure analysis of the time is the cracking and failure by ejection of some sintered tungsten rocket nozzle liners [*2,3*]. One of these, ejected from the nozzle after 30 s of a planned 1-min test firing, was intact when recovered from a pool of water some distance away, but contained numerous circumferential cracks on the outside which penetrated about 75 percent of the thickness. At first it was thought that the cracks occurred upon quenching from operating temperature (about 4700 K after 20 s) when the liner hit the water. However, further study, which included exhaustive metallography, X-ray diffraction, X-ray fluorescence spectroscopy, and fractographic examination, led to the conclusion that the cracks were caused by thermal stresses and occurred early in the test firing: (*a*) many cracks were partly coated with a thin layer of fused aluminum oxide ($Al_2O_3$), indicating they were there during firing. The $Al_2O_3$ originated from the solid rocket propellant; (*b*) the tungsten matrix contained various contaminants in greater quantities on one side of a crack than on the other, again ruling out the possibility of cracking after ejection; (*c*) the cracks initiated on the outside surface of the liner, where tensile stresses are highest during rapid initial heating in the early stages of firing; (*d*) they stopped after

[2]The italic numbers in brackets refer to the list of references appended to this paper.

penetrating 75 percent of the thickness, near the expected point of transition from tensile to compressive thermal gradient-induced stress; and (*e*) they initiated and grew at a fairly high temperature above the brittle-to-ductile transition temperature. Figure 1 shows fractographs comparing the service crack surface, Fig. 1(*a*), with the room temperature fracture surface, Fig. 1(*b*). The room temperature fracture shows well defined intergranular fracture mixed with cleavage, whereas the service fracture surface consists of pointed, drawn-out hillocks. Figure 2 shows a service crack in cross section, suggesting the intergranular nature of the cracking and showing considerable distortion of the grains. The entire length of all cracks had the same appearance, which is evidently a type of plastic intergranular decohesion occurring at high temperature. The possibility that the cracks might have existed before firing was ruled out because of careful inspection before assembly, the large size of the cracks, and the likelihood that the surfaces would have been smoothed thermally rather than made more jagged by high temperature exposure.

The following failure analysis provided a particularly classic example of the progression of hydrogen embrittlement cracking (HEC)/SCC propagation mechanism as the stress intensity factor increases with crack growth, and changes after the onset of fast fracture in very high strength alloy steels. The broken part was a jet fighter-bomber catapult socket lug which broke during test after 617 simulated launches. The lug was made of AMS6407 (4330Si) steel, heat treated to about 180-ksi yield strength. The fracture, Fig. 3, bisected a threaded lube fitting hole which was filled with grease during testing. No corrosion was evident and although the lug had been cadmium plated, the threaded hole where cracking initiated was not. The cracking mechanism was intergranular at the origin, Fig. 4(*a*), became mixed with cleavage and dimples further along, Fig. 4(*b*), and ultimately changed to 100 percent microvoid coalescence at the end of the slow crack area, Fig. 4(*c*). Some evidence of fatigue was noted in a narrow band near this point, but did not comprise a significant part of the slow crack zone. The remainder of the fracture surface contained a mixture of cleavage, microvoid coalescence, and intergranular cracking which is typical of fast fracture in this steel at this strength level. In the absence of obvious corrosion, the crack initiation and slow growth was attributed to HEC. The hydrogen was probably induced during cadmium plating of the exterior parts of the lug, and diffused into the unplated regions during storage. The initial low stress intergranular cracking may have been caused by overtightening of the grease plug, the remainder of crack propagation and final fracture occurring in increments during simulated launch testing.

The progression of fracture mechanisms from pure intergranular at the origin through quasicleavage to microvoid coalescence as the crack lengthens and crack tip stress increases is very diagnostic of HEC and SCC failures in low alloy steels of this strength level. The reversion from *pure*

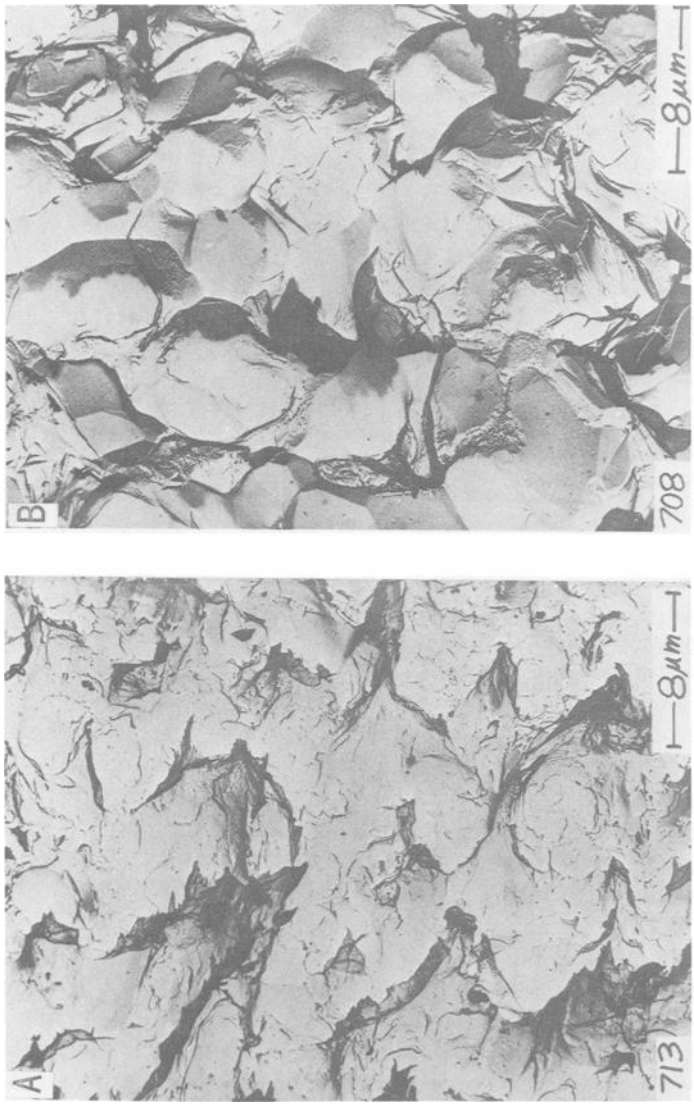


FIG. 1—*Tungsten rocket nozzle insert fracture surfaces (two stage replica TEMs).* (a) *In-Service failure near origin.* (b) *Room temperature laboratory fast fracture.*

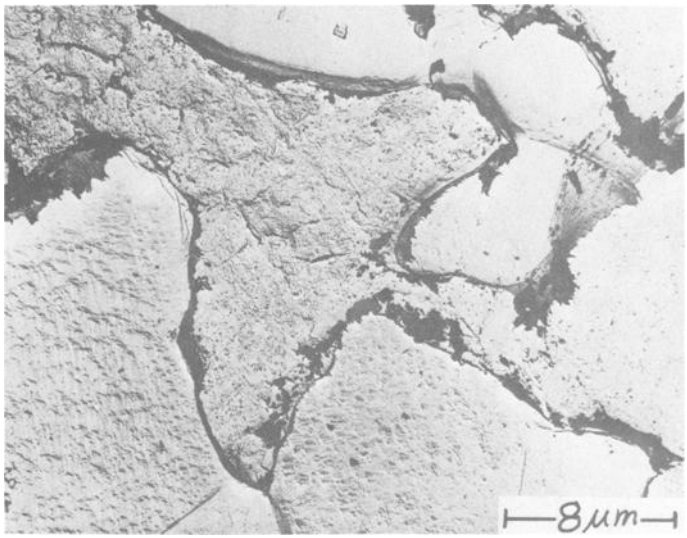


FIG. 2—*Metallographic cross section of in-service crack in tungsten rocket nozzle insert. The crack is filled with epoxy resin which appears somewhat darker than the tungsten and runs from upper left to middle right.*

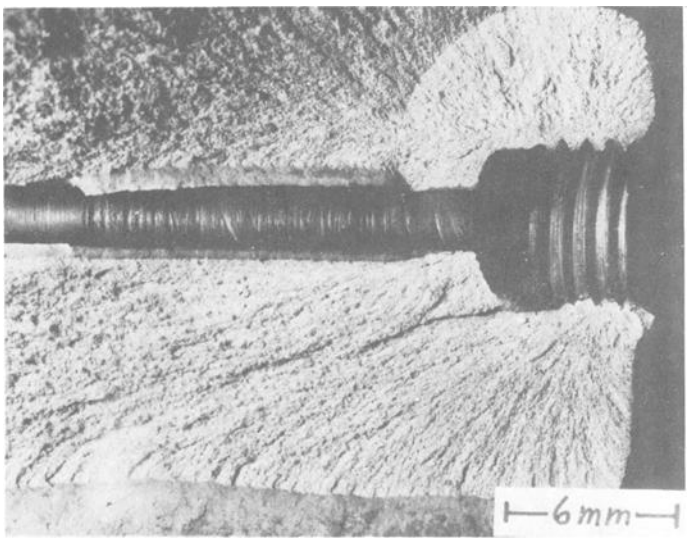


FIG. 3—*Fracture surface of aircraft landing gear catapult lug which failed after 617 simulated launch load cycles. Slow crack growth area at upper right.*

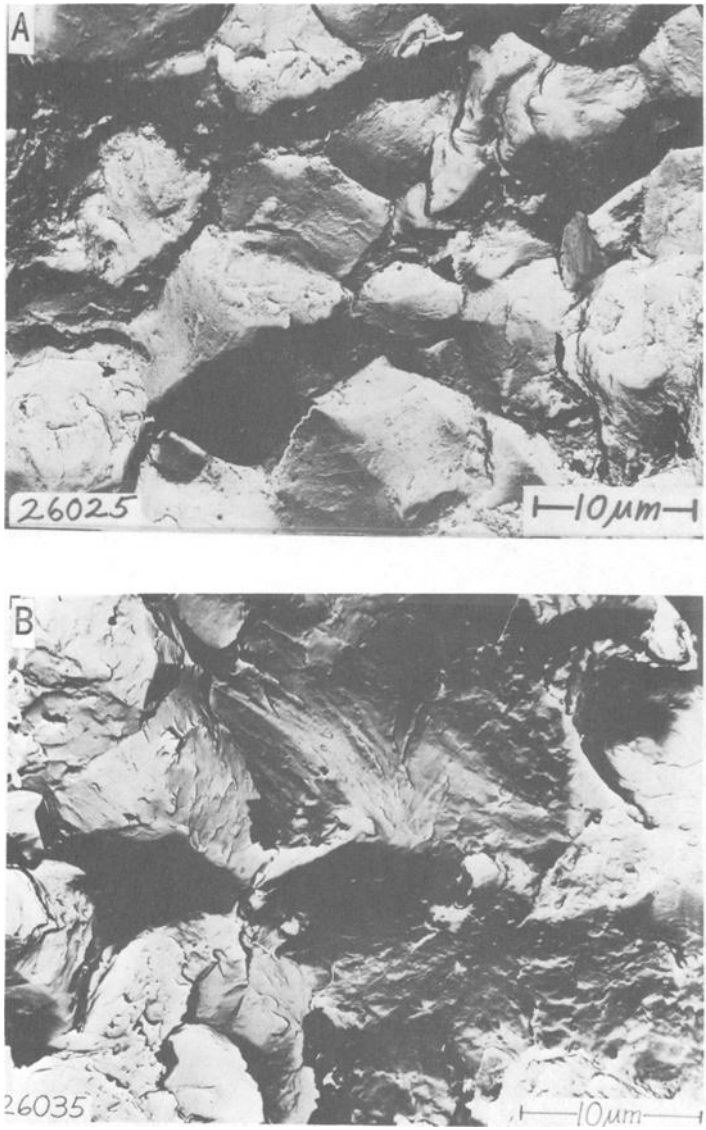


FIG. 4—*Catapult lug fracture surface (two stage replica, TEMs).* (a) *Nearly 100 percent intergranular at origin of slow crack region.* (b) *Mixed intergranular with transgranular cleavage and dimples midway through slow crack area.* (c) *100 percent dimples within slow crack area near onset of fast fracture.*

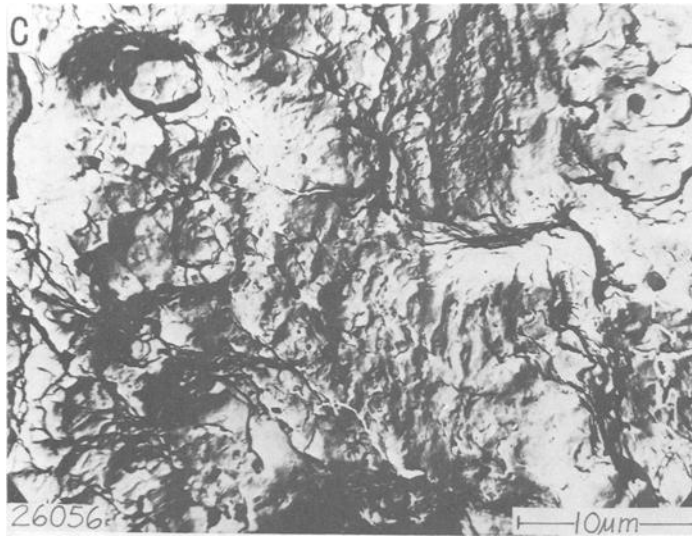


FIG. 4—(*Continued.*)

microvoid coalescence to a mixture of mechanisms indicates the onset of final overload (fast) fracture. HEC and SCC cannot be differentiated except where obvious association of a corrosion pit with the origin is seen, since in most cases both types of cracking result from hydrogen activity. The main distinction occurs in that HEC results from hydrogen already in the metal before cracking starts whereas the hydrogen is produced by the local corrosion processes during SCC.

An early fractographic failure analysis that still has something to teach involved a study of an aircraft skin assembly comprising two 7075-T6 aluminum sheets overlapped and spot welded [*4*]. A through-thickness crack traversed the skin assembly following a line of spot welds. Fractographs of two areas of spot-weld fracture are shown in Fig. 5. Although effects of corrosion are evident, both dimples and striation-like markings can be seen. The investigators were able to prove fatigue was not the cause by breaking other spot welds in the skin assembly by fatigue and fast fracture, respectively, showing that the spot weld fatigue striations, Fig. 6(*a*), were quite different from the service fracture markings, which were also observed in the laboratory-produced spot weld fast fractures, Fig. 6(*b*). Such distinctions between other parallel markings and true fatigue striations were not then as obvious as they might seem today and evidently still cause some confusion.

One of the most surprising recent developments in SCC was the demonstration that titanium alloys are subject to this phenomenon in ordinary water if precracked. However, it was still widely believed that titanium

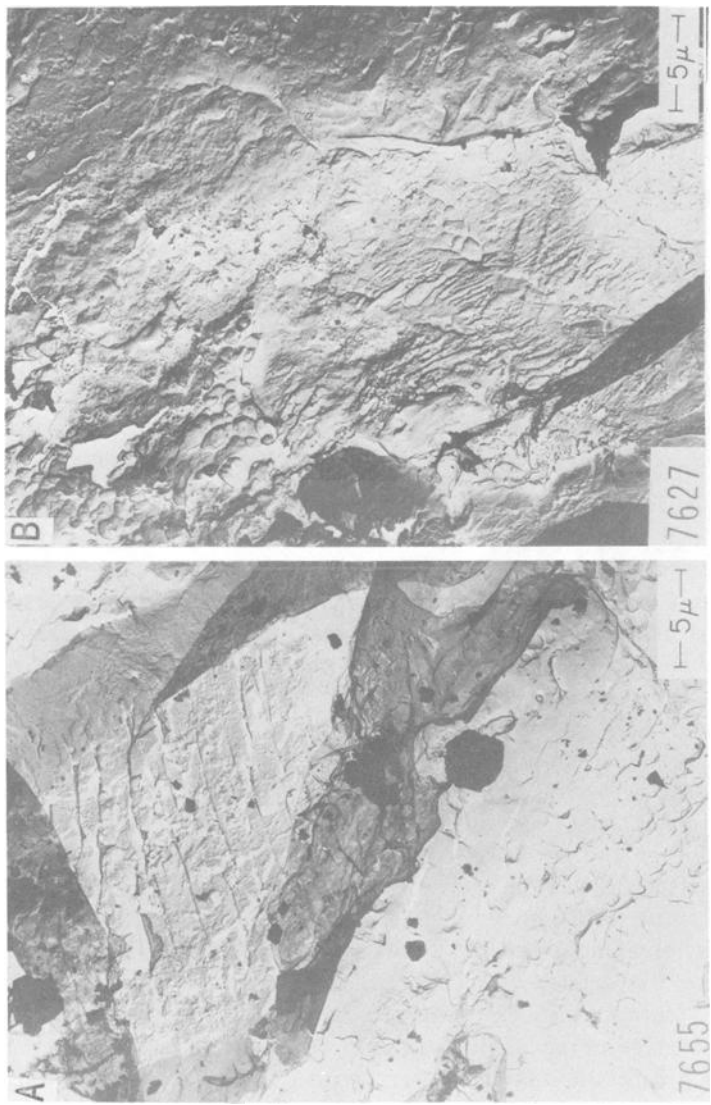


FIG. 5—*7075-T6 aircraft skin sheet spot weld fracture surface (two-stage replicas, TEMs).* (a) *In-service fracture.* (b) *Same.*

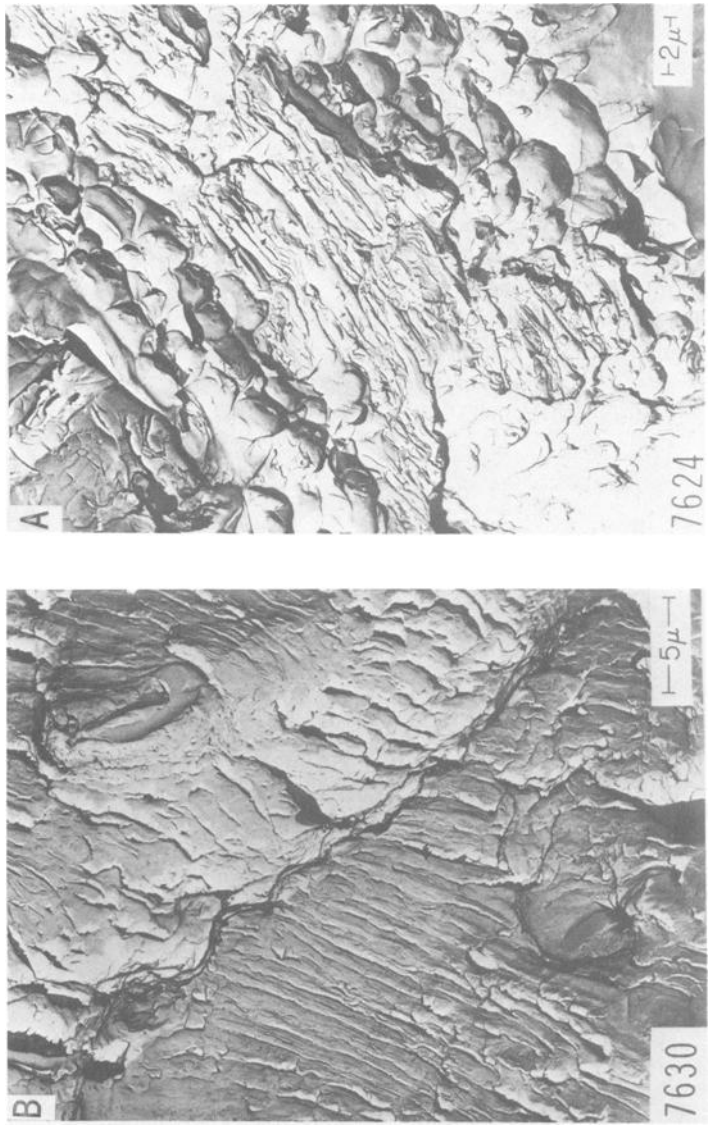


FIG. 6—*7075-T6 aircraft skin sheet spot weld fracture (two-stage replicas, TEMs).* (a) *Laboratory-produced fatigue fracture.* (b) *Laboratory-produced fast fracture.*

alloys would not be subject to SCC if not precracked, especially in media which did not cause severe pitting. Real shock waves radiated through the titanium metallurgical fraternity when rocket motor tankage made of Ti-6Al-4V (160-ksi yield) filled with reagent quality methanol began fracturing at unexpectedly low stresses. NRL scientists were asked to verify the failure mechanism, which was announced to be SCC in methanol. The original service fractures were found to be a mixture of quasicleavage and microplastic cracking at their origins, typical of aqueous SCC in precracked alpha-beta titanium alloys. Strips of tankage material, carefully screened for flaws, were immersed in reagent grade methanol, stressed to 65 percent of their yield strengths, whereupon they failed within minutes. The fracture surface origin area, Fig. 7, was identical with the service fractures, confirming that the service failures were caused by the same mechanism, SCC.

The following analysis may well seem of self-evident outcome to many but it caused considerable concern to the analyst under pressure to supply the correct answers. Some pieces of a fractured turbojet engine compressor blade, made of Ti-8Al-1Mo-1V alloy, were submitted for our analysis after

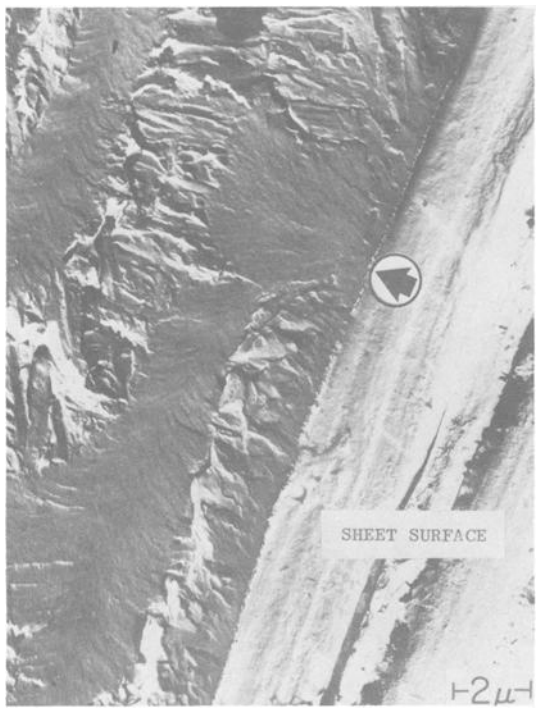


FIG. 7—*Ti-6Al-4V rocket fuel tank stress corrosion failure in methanol, initiating from as-machined unnotched surface (arrow). Two-stage replica, TEM.*

having already undergone examination by another agency. One of four cut pieces comprising the mating fracture surfaces at the apparent failure origin was selected for analysis. It appeared to be in the best condition, one piece looking corroded, the other two having been heavily dented right at the origin edge. The fracture surface of the selected piece showed what appeared to be cleavage facets pocked with round cavities, Fig. 8(*a*), and extensive areas of unusually well-shaped dimples, Fig. 8(*b*). It appeared necessary to examine the mating fracture surface to see if such features appeared there. None were found, the typical appearance being shown in Fig. 9(*a*), and a brief precision matching study (not illustrated to save space) proved that the "dimples" appeared only on one of the mating surfaces. The cause of the dimples was undoubtedly etch pitting from the inspection procedure used to look for small cracks, which comprises a blue anodizing treatment. The major fracture mode near the origin was cleavage with no visible striations, even when examined by TEM. Some isolated, very coarse striations were found near the terminal end of the slow crack zone, Fig. 9(*b*). The cause of crack initiation and failure was thought to be high mean stress, low amplitude (striationless) fatigue, although this is difficult to distinguish objectively from SCC in the absence of striations near the origin.

Occasionally it is necessary to convince someone that a particular crack is not only (*a*) a fatigue crack, but can further be classified, (*b*) as a normal fatigue crack or a shear fatigue crack, as the case may be. Normal fatigue is caused by stresses applied perpendicular to the crack plane; shear fatigue is caused by stresses parallel to the crack plane, either parallel to the crack front (transverse shear) or as in this case parallel to the crack propagation direction (forward shear). Two examples serve to demonstrate how we have approached this kind of problem. The first example is a pretty obvious normal fatigue crack, which the submitter had circumstantial reason to believe might have been caused by shear fatigue. The crack, whose fracture surface appears in Fig. 10, was found in the main bulkhead of a late model Navy jet. The material is 2024-T4. Note the fatigue striations in an area near the origin, Fig. 10(*a*), and the striations with tire tracks, Fig. 10(*b*). Tire tracks are caused by small hard particles, retained by one crack surface, periodically denting the opposite surface. The dent or tire-track spacing is an indication of the relative shear displacement of the opposing crack surfaces with each successive cycle. If shear stress components are high, tire tracks will be absent or very widely spaced. Their existence proves that the crack opened and closed with very little permanent shear displacement per cycle, thus that stresses were mostly normal to the crack plane.

An example of a probable shear fatigue crack was found in the flap torque tube fitting, of Ti-4Al-4Mn, from yet another late model Navy aircraft. The fracture, Fig. 11, shows no striations, but abundant evidence of

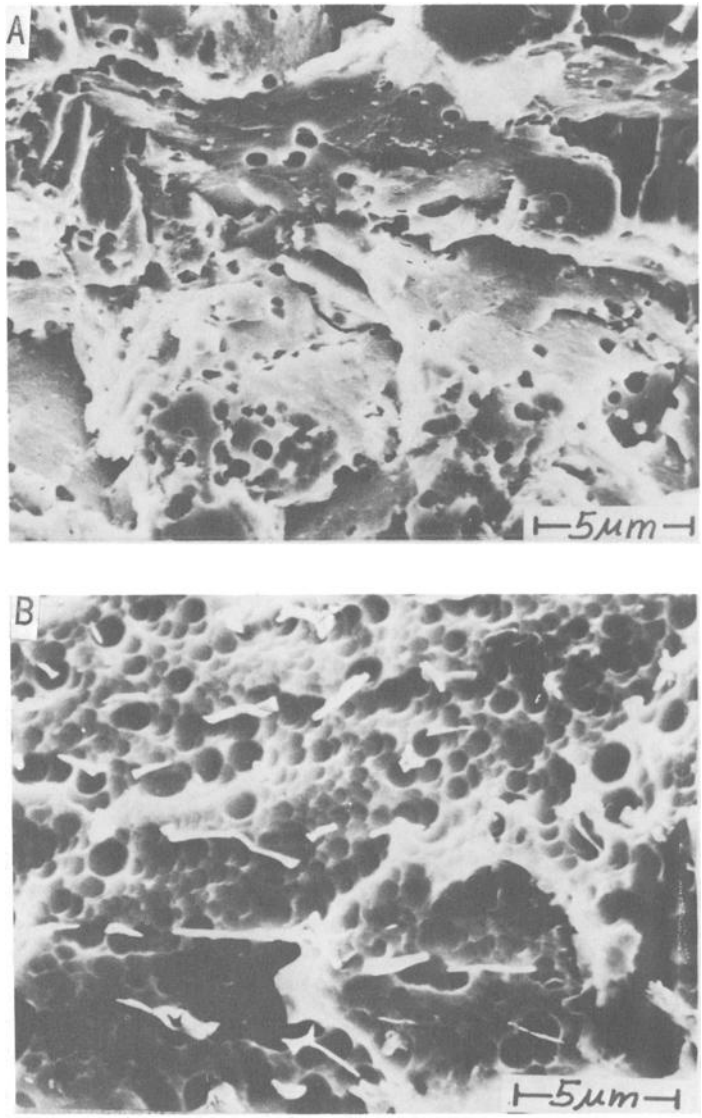


FIG. 8—*Turbojet engine compressor blade (Ti-8Al-1Mo-1V) fracture (SEMs).* (a) *Cleavage with pits or voids near origin of fracture half A.* (b) *Apparent dimples, same area as* (a).

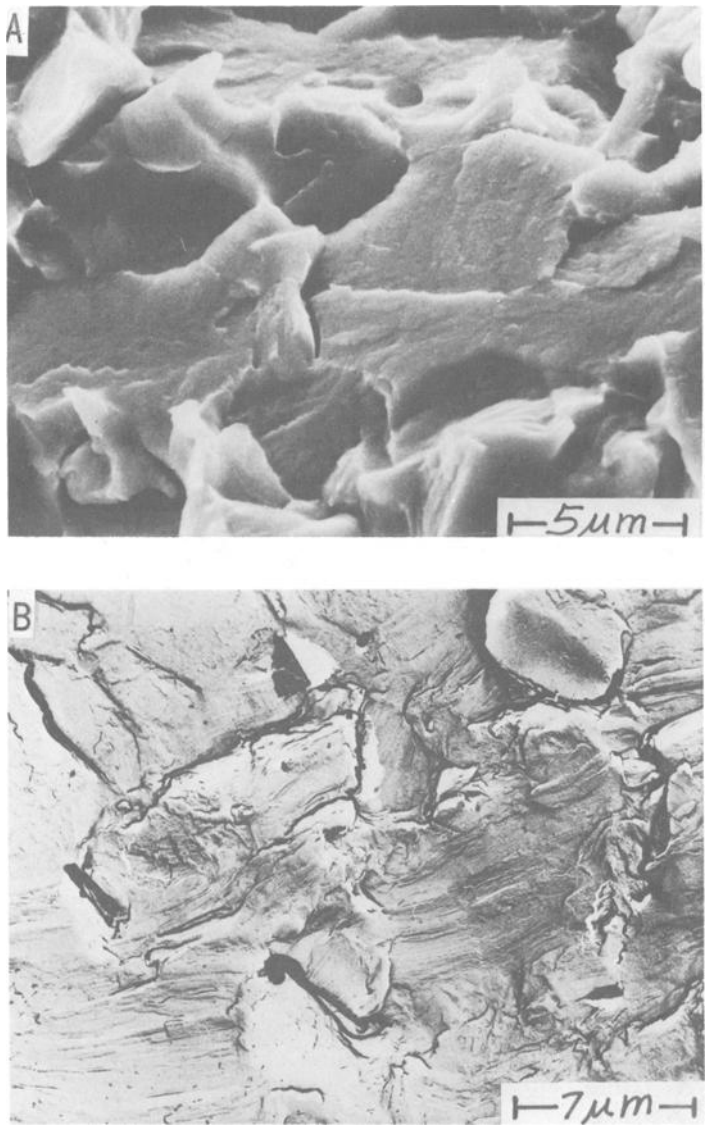


FIG. 9—*Turbojet engine compressor blade (Ti-8Al-1Mo-1V).* (a) *Demonstrating clean, pit-free cleavage near origin of fracture half B (SEM).* (b) *Coarse striations near end of slow crack area (two-stage replica, TEM).*

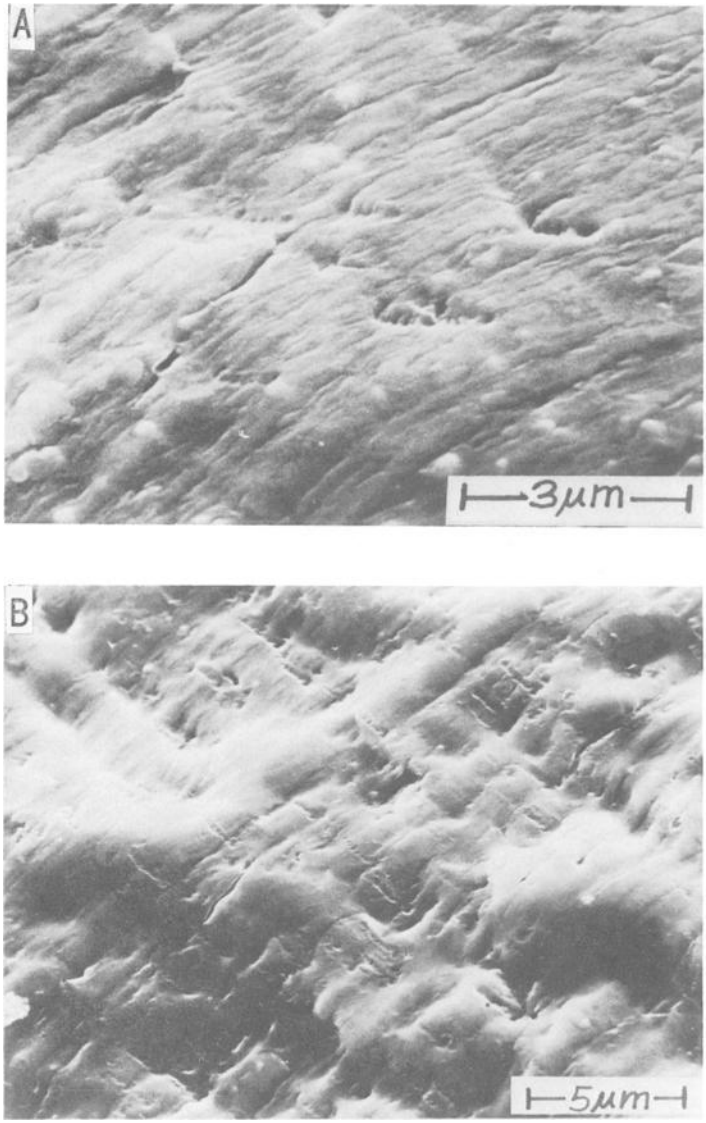


FIG. 10—*Jet aircraft bulkhead (2024-T3) crack fracture surface (SEMs).* (a) *Fatigue striations near origin.* (b) *Coarse fatigue striations with "tire tracks" near end of slow crack area.*

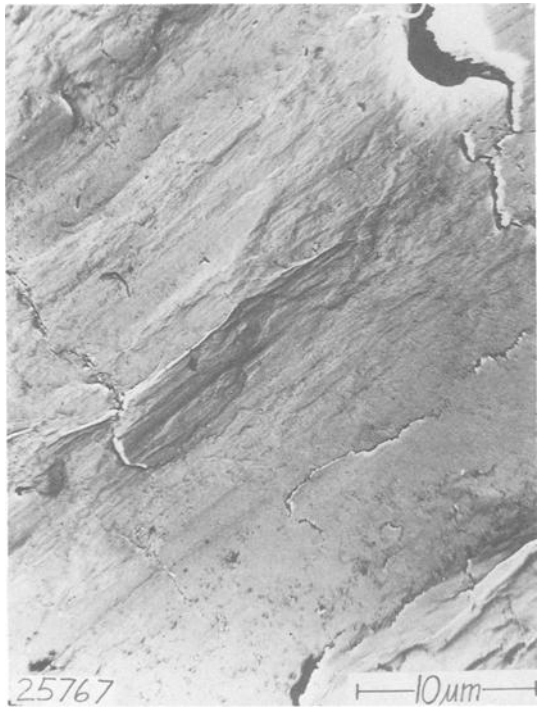


FIG. 11—*Aircraft wing flap actuator fitting (Ti-4Mn-4Al) crack surface (two-stage replica, TEM).*

rubbing and burnishing, and evidence of considerable mutual shearing motion of the surfaces. How does one prove fatigue? Well, one thing is the very tightness of the crack; it is unlikely to have resulted from overload in shear. Furthermore, the broken-open fracture was examined metallographically in cross section. Figure 12(*b*) shows that the part created by laboratory overloading (to open the crack) shows only somewhat distorted grains at the fracture edge, whereas the service crack, Fig. 12(*a*), has indications of twinning substructure formation and microcracking underlying the fracture surface. These findings, though not conclusive for lack of laboratory verification of shear fatigue-induced subsurface microstructural changes, pointed to fatigue as the possible cause of cracking.

The fractographic analysis of an aircraft arresting gear trunnion which failed during programmed fatigue testing created a mystery which has not yet been solved. The part, made of 300M steel of 220-ksi yield, showed alternate smooth (light) and rough (dark) bands on the fracture surface, Fig. 13, attributable to regular changes in loading conditions during the test. Although fatigue was known to have caused cracking, no striations could be found, Fig. 13(*b*), a distressingly common circumstance with high

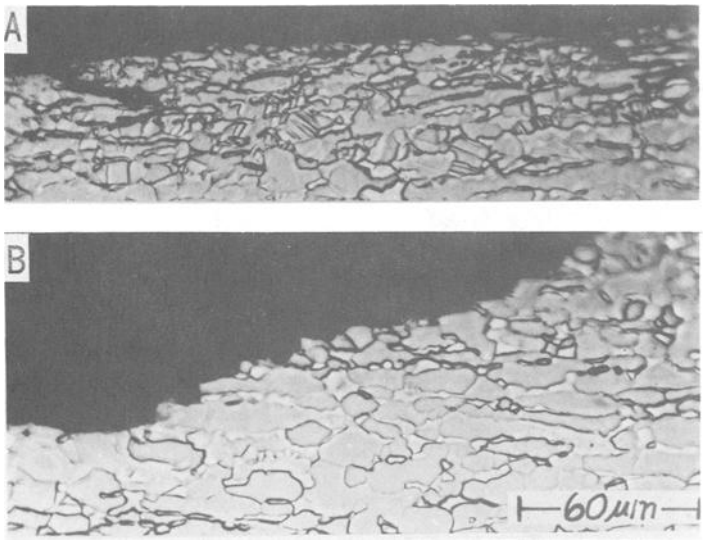


FIG. 12—*Aircraft wing flap actuator fitting (Ti-4Mn-4Al) crack cross-sections (polished and etched, light optical micrographs).* (a) *In-service crack.* (b) *Laboratory-produced fast fracture.*

strength steels—no mysteries yet. The trouble began when surface chemical analysis, using both electron microprobe and Auger spectrometry, showed that copper and cadmium were present on the fracture surface and were especially concentrated in the rough, dark bands. No significant difference in microscopic cracking mechanism could be detected between the two types of zones, except for greater roughness on the dark ones. We could only speculate that the copper and cadmium were mechanically dragged in by the continual relative motion of the crack faces and that they were preferentially retained in the dark bands because they were rougher and hence acted as better debris traps. The copper came from copper-alloy bushings in the trunnion, while the whole steel part was cadmium-plated. No active role in crack initiation or propagation was suspected of either element.

Although we have specialized in aircraft component failures, other kinds of components also come our way. The following problem [*6*] is mostly straightforward, but has an unusual twist. Large cracks were noted traversing the 5456 aluminum alloy deck plates of an experimental hydroplane, and repair welding proved fruitless, somewhat like chopping off Hydra's heads one at a time. The cracks were examined and found to be typical of SCC, being both long transverse and short transverse intergranular cracking with typical "mud-crack" deposits, Fig. 14. The 5456 alloy processed to H321 is supposed to be immune to SCC, and this was proven with stock material to be true. However, a specimen of the actual

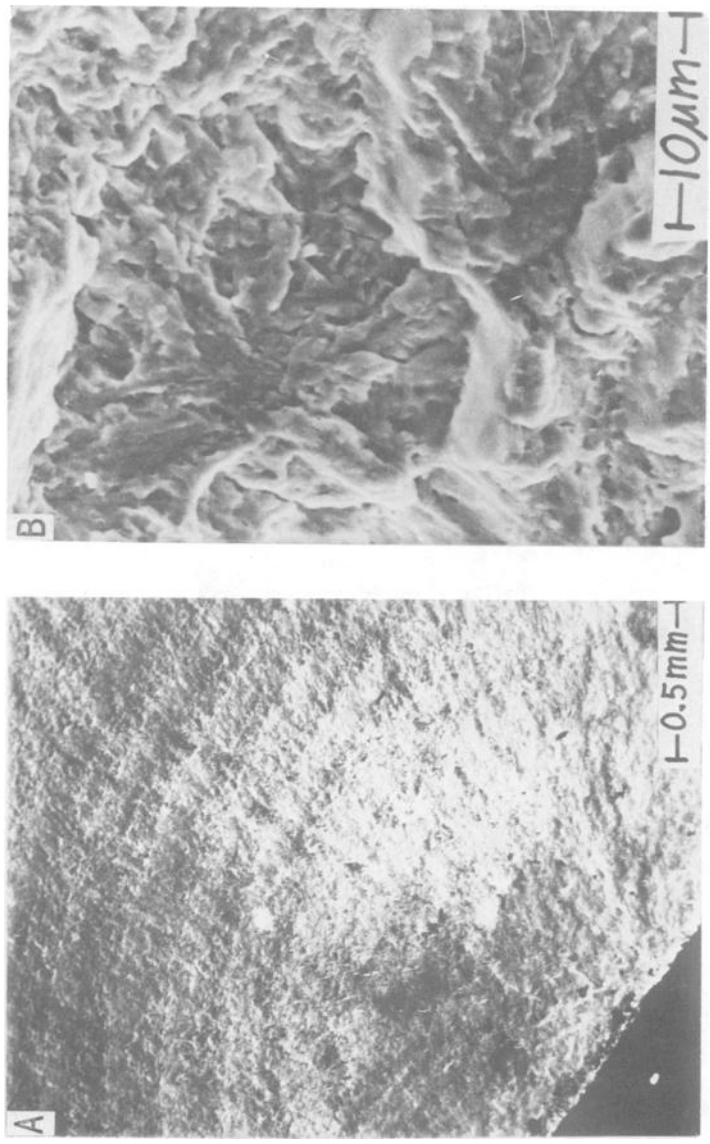


FIG. 13—*Carrier aircraft arresting hook trunnion bearing (300M steel) fracture surface (SEMs). (a) General view of slow crack zone showing concentric bands from programmed fatigue load variations. (b) Typical striationless rough cleavage in slow crack zone.*

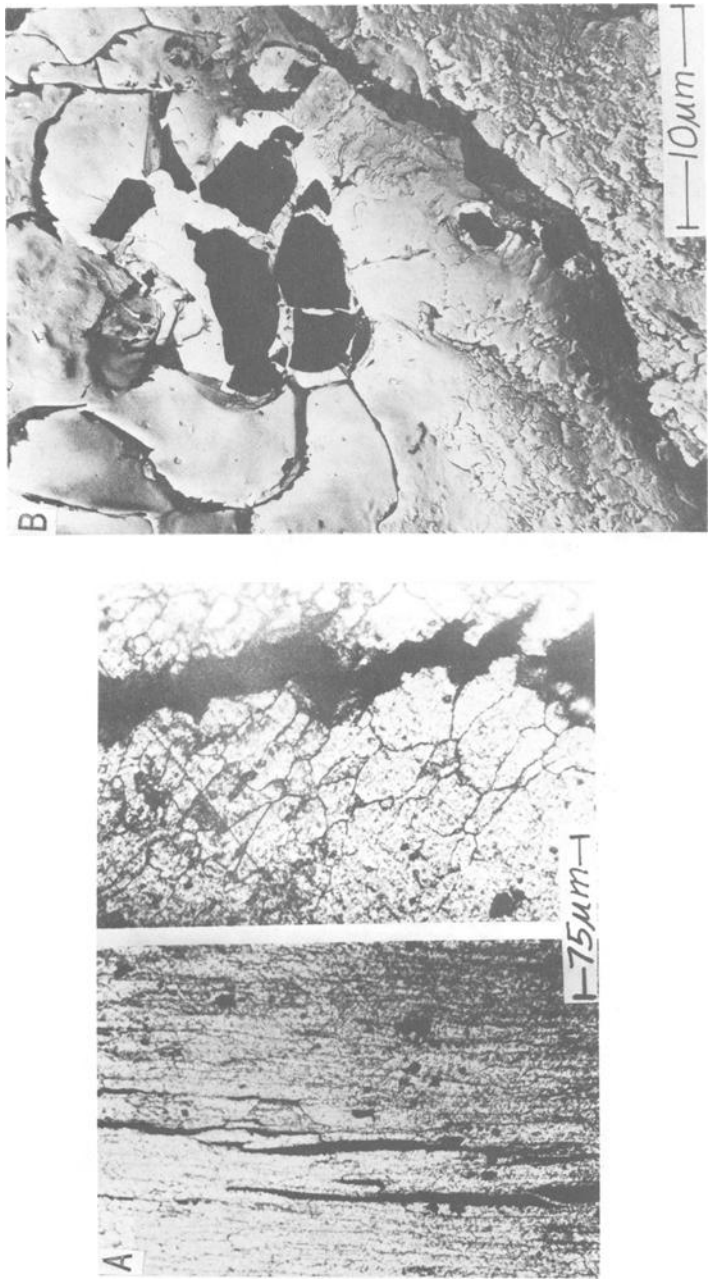


FIG. 14—*Small high speed ship deck plate (5456-H321) cracks.* (a) *Cross sections (polished and etched, light optical micrographs).* (b) *Mud crack appearance of fracture surfaces (two-stage replica, TEMs).*

deck plate, which had seen service, cracked readily. The reason became evident on comparing the microstructure of stock 5456-H321 plate with the "used" deck plate, Fig. 15. The deck plate had become further aged and thus "sensitized" to SCC by tropical sun exposure. The obvious moral to be drawn from all this is to avoid using materials which literally change from good to bad under one's feet.

Those who work with advanced structural materials tend to forget that more ordinary materials also cause expensive problems. Many Navy structural applications make use of plain hot rolled galvanized steel tubing, probably the same material used for backyard fences, certainly not exotic, but indispensable for such things as antenna frameworks and mounting supports. The state of the art in producing welded structures of this steel is well established, it is tolerant of error, yet look what can happen. Figure 16 shows the corner section of an antenna support framework, with a fracture surface where a sound weld should have been. A large proportion of this and up to 75 percent of other fractures on the assembly were perfectly coated with zinc, which was applied after welding by hot dipping. The zinc-free areas showed fatigue striations, Fig. 17(*a*), and the zinc-coated areas, after inhibited acid stripping, showed a rather corroded looking appearance, Fig. 17(*b*). It is evident that final in-service failure was caused by fatigue, but the original cracks which weakened the structure obviously formed after welding, either before hot zinc coating or during coating. The

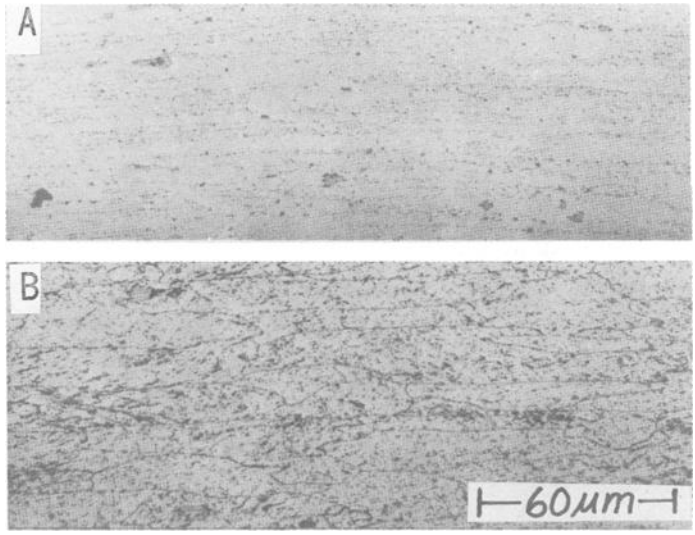


FIG. 15—*Small high speed ship deck plate (5456-H321) material (polished and etched, light optical micrographs).* (a) *Piece of plate from stock.* (b) *Piece from deck of ship showing over-aging.*

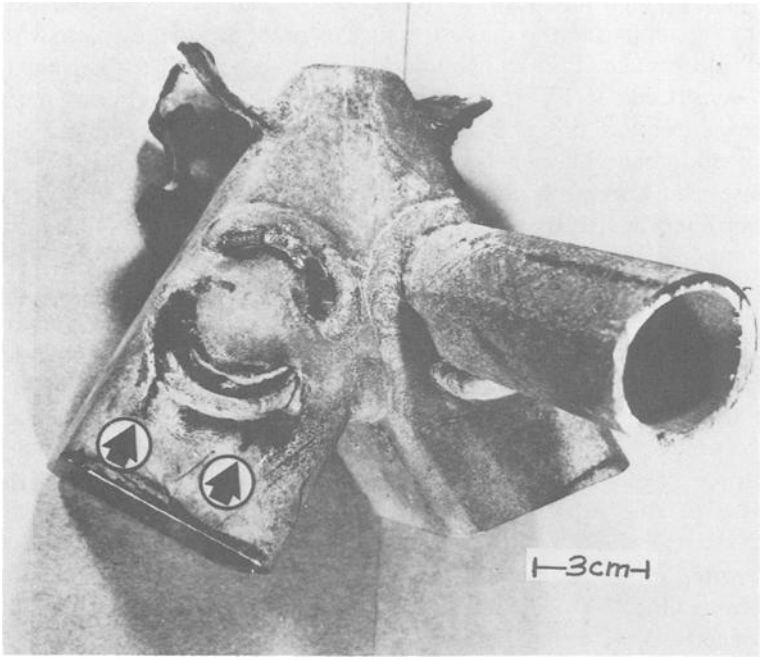


FIG. 16—*Radio antenna support frame (galvanized hot-rolled low-carbon steel). Arrows point to cracks in box section emanating from weld area.*

latter seems quite possible, since liquid zinc cracking is a very well known phenomenon and could be expected to occur if the residual stresses caused by welding were not relieved before dipping. Further, the zinc-coated fracture surface areas showed no signs of dimples to be expected of residual stress cracks.

The final example of failure analysis is rather unusual. High power radio transmission generates considerable induced radio frequency (RF) current flow in nearby metal structures, including the supporting structures of the antennas. Damage often occurs at points of intermittent or poor electrical contact between such things as elevator cables and their pulleys, couplings, joints, etc. In two cases antenna tower elevator cables, which are made of cold-drawn high carbon steels, were severely damaged by what are very similar to welding arc strikes, Fig. 18. The damage consists of brittle, untempered martensite formation, pits, extensive metal removal, and cracks, Fig. 19(*a*). The fractured ends of individual strands exhibited brittle cleavage and intergranular cracking, Fig. 19(*b*). Very little can be done about such damage except to keep all affected parts clean, and frequently inspect and remove damaged components.

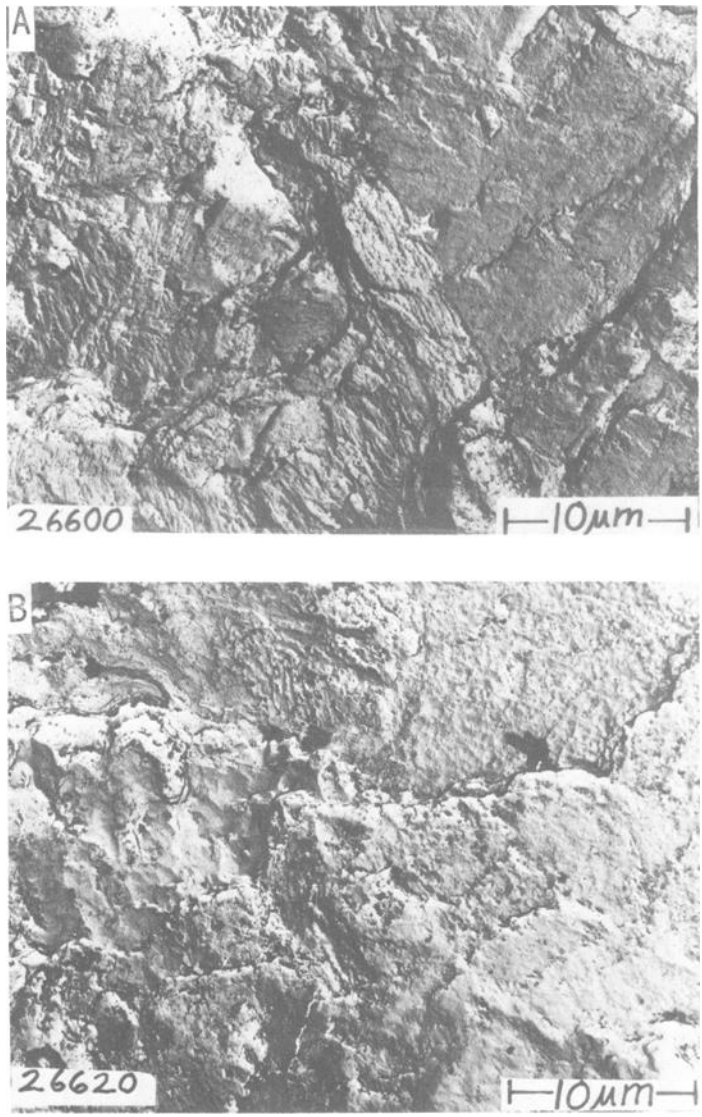


FIG. 17—*Radio antenna support frame (galvanized hot-rolled low carbon steel) fracture surfaces (two-stage replicas, TEMs).* (a) *Fatigue striations in slow crack zone not coated by zinc.* (b) *Corroded surface with possible grain boundary fracture in originally zinc-coated area stripped with inhibited acid.*

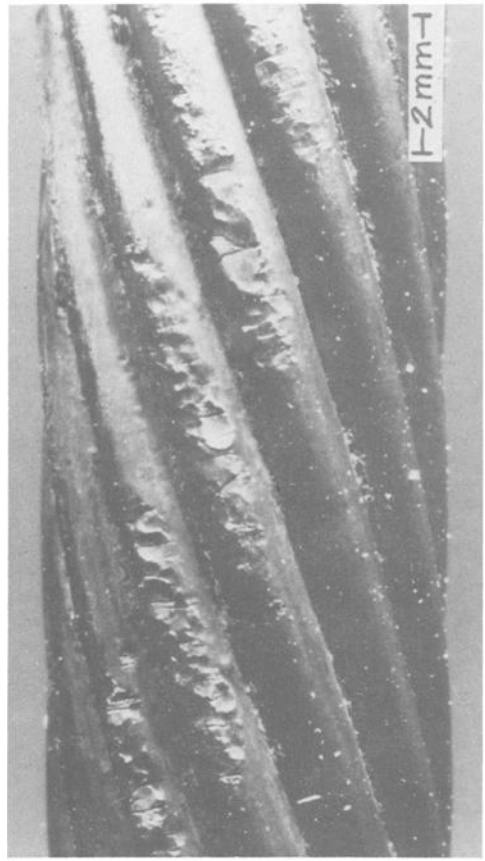


FIG. 18—*Radio transmission tower elevator cable RF arc damage.*

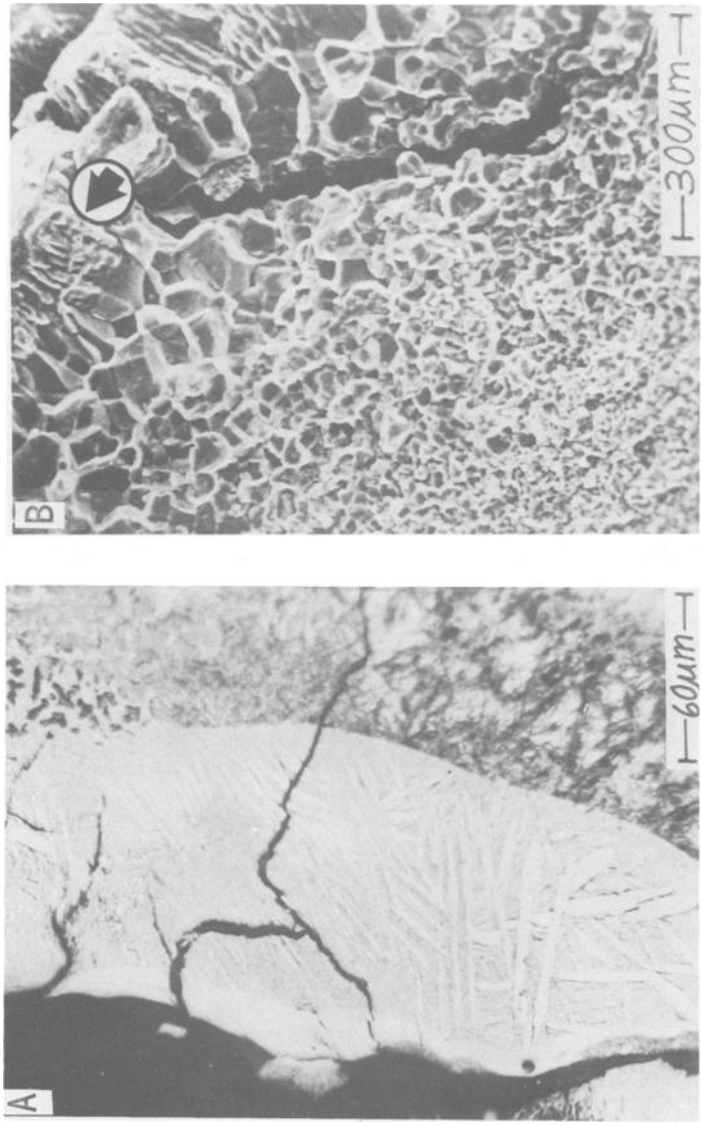


FIG. 19—*Radio transmission tower elevator cable RF arc damage.* (a) *Polished and etched cross-section showing untempered martensite formation and cracks (light optical micrograph).* (b) *Fracture surface of broken cable wire. Note cleavage in untempered martensite at arrow, decrease in grain size with distance from surface.*

*Acknowledgments*

The material used in this paper is the product of many others, and it is with gratitude that the author thanks the following for their contributions: C. D. Beachem, E. P. Dahlberg, and B. F. Brown, who showed the way; T. C. Lupton, J. E. Flint (deceased), and W. S. Kenton, who paved the road; J. DeVault and H. C. Wade, the current bricklayers; C. T. Fujii, a silent co-author; and our sponsors through many years, the Office of Naval Research, Naval Air Systems Command, and Naval Facilities Engineering Command.

## References

[1] "Fractography and Atlas of Fractographs," *Metals Handbook,* 8th ed., American Society for Metals, Vol. 9, 1974.

[2] Dahlberg, E. P., "An Electron Microscope Study of Crack Surfaces in A Tungsten Rocket Nozzle Insert," U.S. Naval Research Laboratory Memorandum Report 1217, Sept. 1961.

[3] Meussner, R. A. and Goode, R. J., "An Examination of Three Tungsten Rocket Nozzle Insert Failures," U.S. Naval Research Laboratory Memorandum Report 1204, Aug. 1961.

[4] Beachem, C. D. and Kenton, W. S., "The Fractographic Study of Fatigue and Monotonic Fracture Surfaces in Spot Welds in 7075-T6 Aluminum Alloy," U.S. Naval Research Laboratory Memorandum Report 1545, July 1964.

[5] Meyn, D. A., Dahlberg, E. P., and Beachem, C. D., "Analysis of Stress Corrosion Cracking of Ti-6Al-4V Fuel Tank Material in Methyl Alcohol," U.S. Naval Research Laboratory Memorandum Report 1744, Jan. 1967.

[6] Fujii, C. T., Beachem, C. D., Meyn, D. A., and Brown, B. F., "Study of the Fracture Mechanism of 5456-H321 Aluminum Alloy," U.S. Naval Research Laboratory Memorandum Report 2422, April 1972.

*A. Madeyski*[1] *and L. Albertin*[1]

# Fractographic Method of Evaluation of the Cyclic Stress Amplitude in Fatigue Failure Analysis*

**REFERENCE:** Madeyski, A. and Albertin, L., **"Fractographic Method of Evaluation of the Cyclic Stress Amplitude in Fatigue Failure Analysis,"** *Fractography in Failure Analysis, ASTM STP 645,* B. M. Strauss and W. H. Cullen, Jr., Eds., American Society for Testing and Materials, 1978, pp. 73-83.

**ABSTRACT:** The first part of this paper describes laboratory work results substantiating the correlation of fatigue striation spacings with crack growth rate and with cyclic stress intensity amplitude, $\Delta K$. The results were obtained by transmission electron microscope (TEM) replica fractography of a fracture mechanics type wedge-opening-loading (WOL) steel specimen previously tested in fatigue.

In the second part of this paper, an illustration of a practical application of this fractographic approach is described in detail. The laboratory test results from the first part are applied successfully to the service failure analysis of a crankshaft. Cyclic stresses calculated using a combined fractographic-fracture mechanics method were in good agreement with the values obtained from a theoretical and experimental stress analysis.

**KEY WORDS:** metal surface, fractures (materials), fractography, failure, transmission electron microscopes, fatigue (materials), striations, crack growth rate, stress intensity, stresses, stress analysis

As our knowledge and understanding of fracture phenomena improves, so does the amount of information which we can obtain from a failure analysis of metallic components. In the past, an investigator usually was satisfied with identifying the type of failure (for example, fatigue), locating the fracture origin, determining the material composition, microstructure, and properties, and providing a general explanation for the failure.

More recently, however, it was realized that there is a definite relation between fatigue striation spacings, $S$, and the cyclic stress intensity amplitude, $\Delta K$. This relationship, in turn, makes possible the calculation of the

* Original experimental data were measured in U.S. customary units.

[1] Senior engineers, Materials Evaluation and Application Department, Westinghouse Research and Development Center, Pittsburgh, Pa. 15235.

cyclic stress amplitude $\Delta\sigma$ responsible for the crack advance. The great practical importance of knowing the fracture stress amplitude in the component failure is obvious.

The following is a contribution towards a better knowledge of the correlation between the fatigue striation spacings, $S$, the crack growth rate, $da/dN$, and the stress intensity amplitude, $\Delta K$. The equation relating $S$ to $\Delta K$ then is applied successfully to a case of a broken crankshaft.

## Correlation of Fatigue Striation Spacing $S$ With Crack Growth Rate $da/dN$ and Cyclic Stress Intensity Factor Amplitude, $\Delta K$

The experimental part of this investigation involved fatigue testing of a 2T (that is, 50.8 mm (2 in.) thick) wedge-opening-loading (WOL) specimen, followed by fractography. The specimen configuration and dimensions are shown in Fig. 1. The material was a 3.5Ni-1.5Cr-0.5Mo-0.1V steel. The specimen was tested at 10 Hz, in 24°C (75°F) air, with a constant load range $\Delta P$ = 62.3 kN (14 000 lb), that is, with $P_{min}$ = 4.45 kN (1000 lb) and $P_{max}$ = 66.7 kN (15 000 lb).

The arrangement of the transmission electron microscope (TEM) replica grids on plastic tape on the fracture surface of the specimen is shown in Fig. 2. Replicas B to M were examined in the TEM. The location of the replicas in terms of the crack depth, $a$, and stress intensity factor amplitude, $\Delta K$, is shown in Fig. 3. About 15 fatigue striation areas from each replica were photographed and analyzed. Examples of striations near the beginning of the fracture (Replica B) and close to the overload fracture area (Replica M) are shown in Figs. 4 and 5, respectively. The striation spacings in Fig. 4 are 0.1 $\mu$m (4.7 $\mu$in.), whereas those in Fig. 5 are 1.8 $\mu$m (71.5 $\mu$in.), although the average spacing for the Replica M was 1.5 $\mu$m (57.4 $\mu$in.). It is interesting to note that despite a fast crack propagation in the region of the Replica M, the striations were still very distinct and uniform; however, between the fatigue striation islands there were large areas of dimpled rupture. This duplex mode of the fracture propagation is well indicated both in Fig. 2 and in Fig. 6. Figure 2 shows the roughness of the fracture which starts beyond the Replica K, whereas Fig. 6 clearly displays the large disparity between the fatigue striation spacing and the measured crack growth rate per cycle $da/dN$ for Replicas L and M. In contrast, Replicas B to K show an excellent agreement between the fatigue striation spacings and $da/dN$. The fracture appearance, as seen in the TEM, also indicated that striated fatigue was the only mode of the crack propagation in Replicas B to K.

Figure 7 shows the striation spacings $S$ versus $\Delta K$ plotted on double logarithmic paper, so that the data could be compared with the Bates-Clark relation[2]

[2]Bates, R. C. and Clark, W. G., *ASM Transactions Quarterly*, Vol. 62, June 1969.

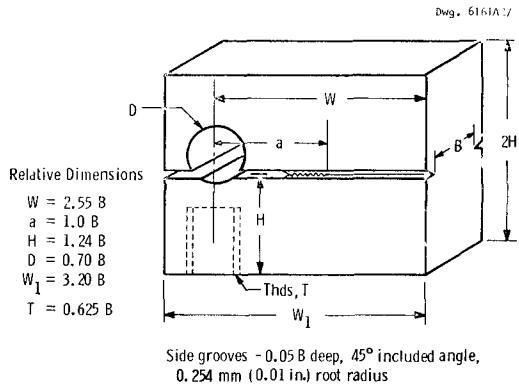


FIG. 1—*WOL type compact fracture toughness specimen (relative dimensions in terms of thickness B).*

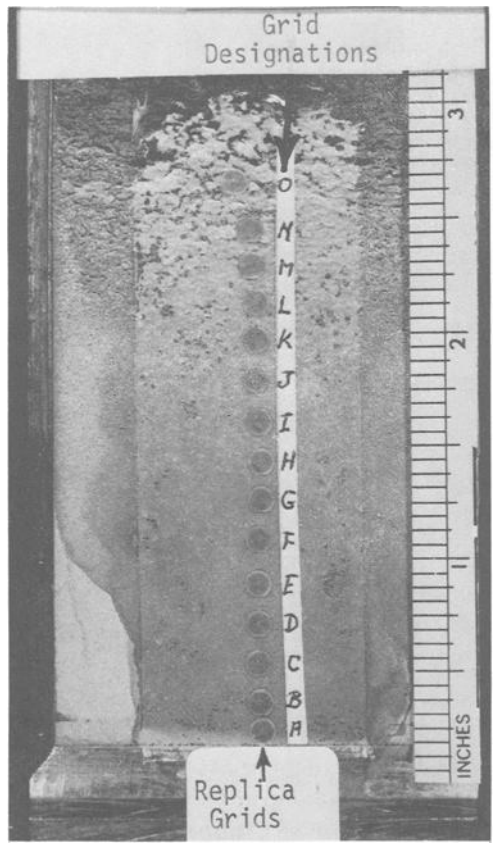


FIG. 2—*Location of replica grids on tape on the specimen fracture.*

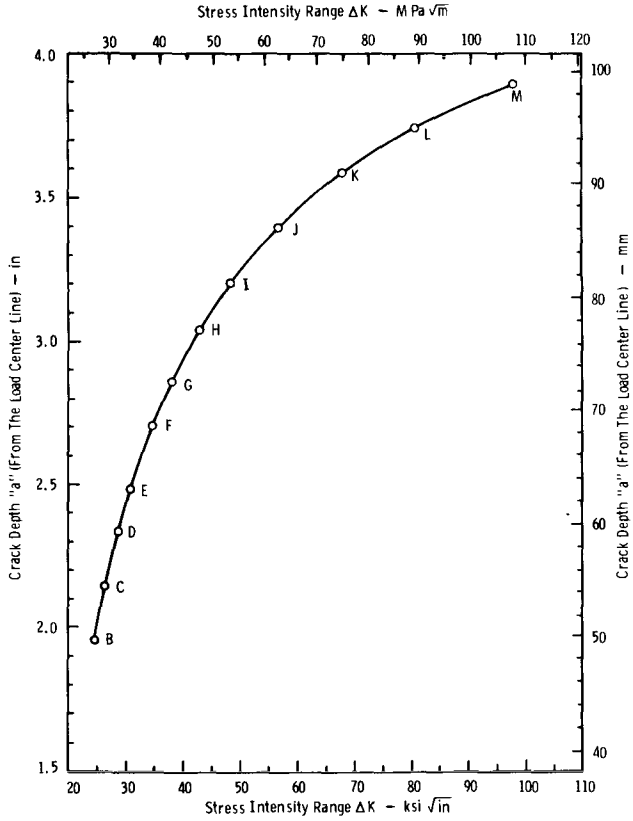


FIG. 3—*Replica locations with respect to crack depth and stress intensity range.*

$$S = 6\left(\frac{\Delta K}{E}\right)^2 \tag{1}$$

where

$S$ = fatigue striation spacing,
$\Delta K$ = stress intensity factor peak-to-peak amplitude $K_{max} - K_{min}$ in the given cycle, and
$E$ = Young's modulus of the metal.

Each vertical bar represents the total range of the averages of striations spacings from each small group of parallel striations, that is, the range from $S_{min}$ to $S_{max}$ observed for the given replica. The average value of $S$ for a complete replica (marked by an open point in Fig. 7) was calculated from the average spacings of at least 15 groups, randomly distributed over the whole area of the replica.

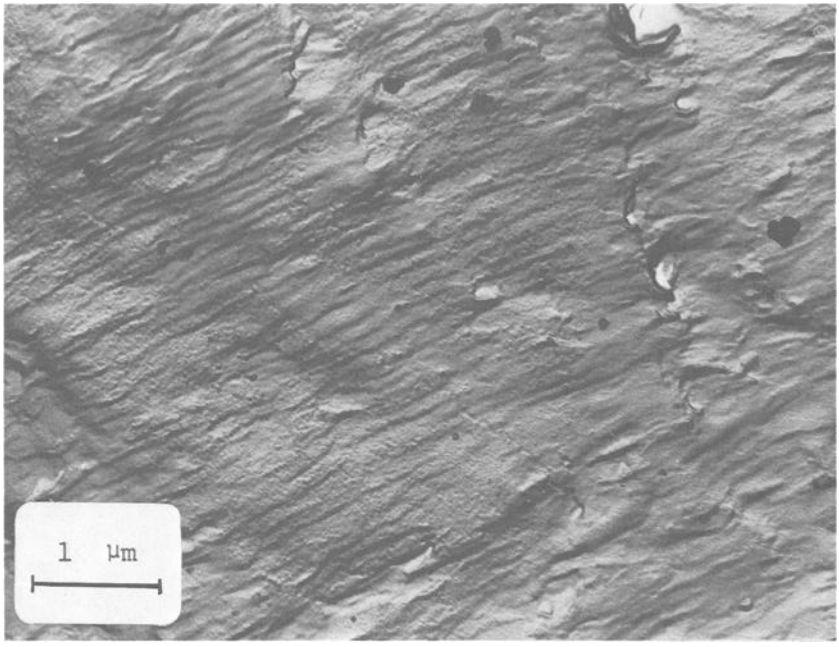


FIG. 4—*Replica B fatigue striations.*

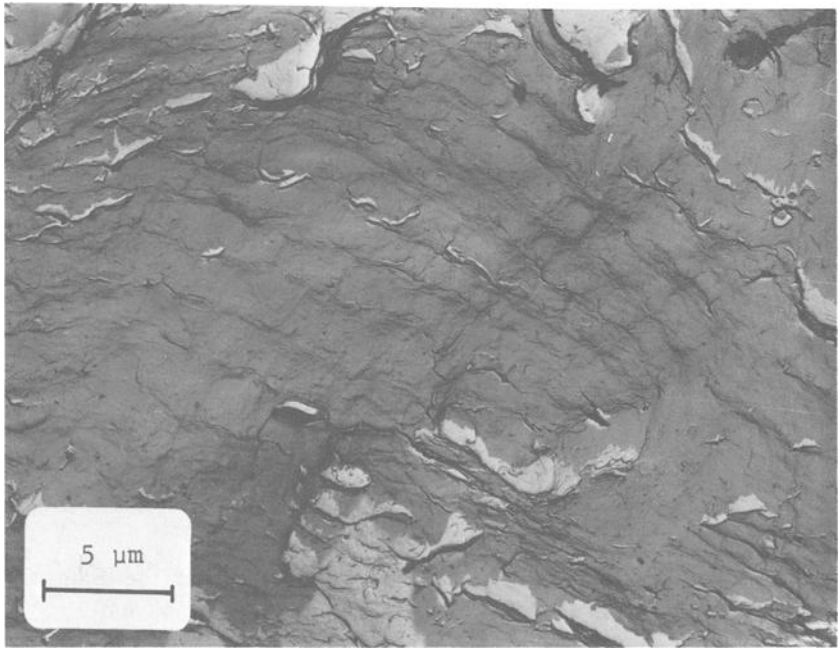


FIG. 5—*Replica M fatigue striations.*

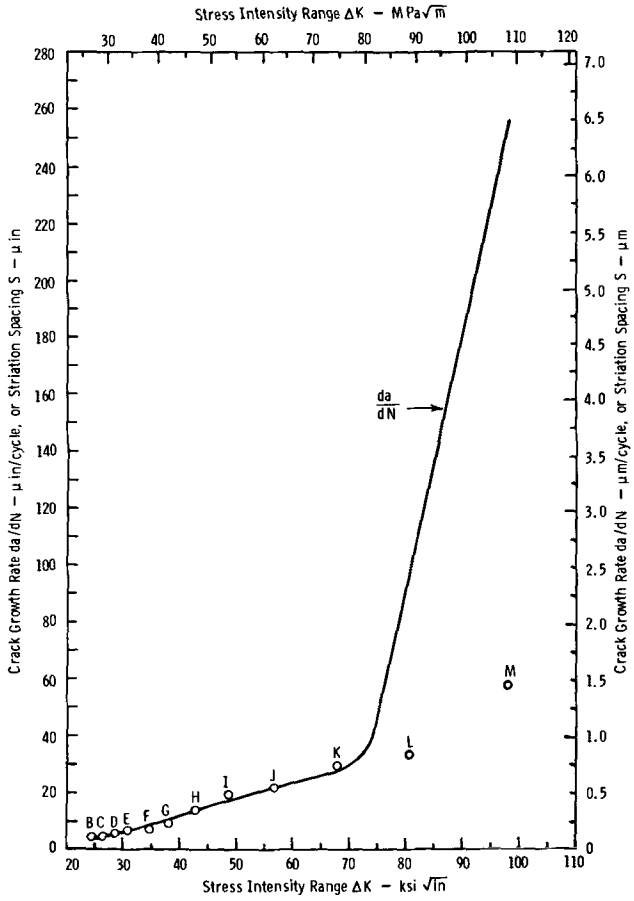


FIG. 6—*Comparison of fatigue striation spacings (points on the diagram) with crack growth rate (continuous line).*

The statistical distribution of the group averages for each replica was found to be close to normal. Good correlation between the experimental data and Eq 1, particularly in the early part of the crack propagation, is clearly visible in Fig. 7. Thus, this laboratory work provided additional supporting evidence for the validity of the Bates-Clark equation.

## Application of the Bates-Clark Equation to Failure Analysis

The following example illustrates the application of the Bates-Clark equation to the stress analysis of a broken ductile iron crankshaft.

The average chemical composition of the crankshaft was 3.5C, 0.40Mn, 2.40Si, 1.15Ni, and 0.06Mg. The crankshaft had been heat treated by aus-

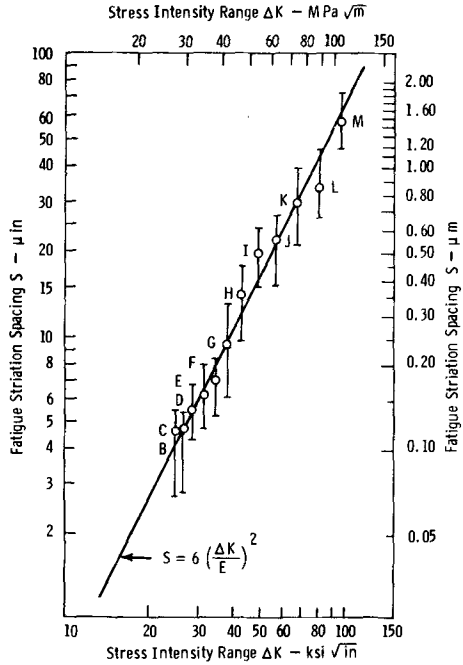


FIG. 7—*Comparison of fatigue striation spacings from fractography (points on the diagram) with the Bates-Clark equation (continuous line).*

tenitizing at 885°C (1625°F), quenching in oil, and tempering to produce the following average mechanical properties:

brinell hardness = 250,
tensile strength = 827 MPa (120 ksi),
yield strength (0.2 percent offset) = 655 MPa (95 ksi),
endurance limit (estimated as 35 percent of the tensile strength) = 283 MPa (41 ksi), and
elongation in 50.8 mm (2 in.) = 5 percent.

The crankshaft broke through a crank, next to a pin journal, as shown in Fig. 8. The origin of the fracture was in the transition zone between a straight and a filleted section of the crank, where two surface machining operations formed a junction resulting in a step. Scanning electron microscope examination of the origin revealed no material defects which could have been responsible for the initiation of the crack.

The general topography of the fracture was typical of low stress-high cycle fatigue. In order to determine the fatigue striation spacings, a two-stage plastic-carbon (platinum shadowed) replica technique was used. The average striation spacing near the origin was 0.1 μm (4.7 μin.), with a

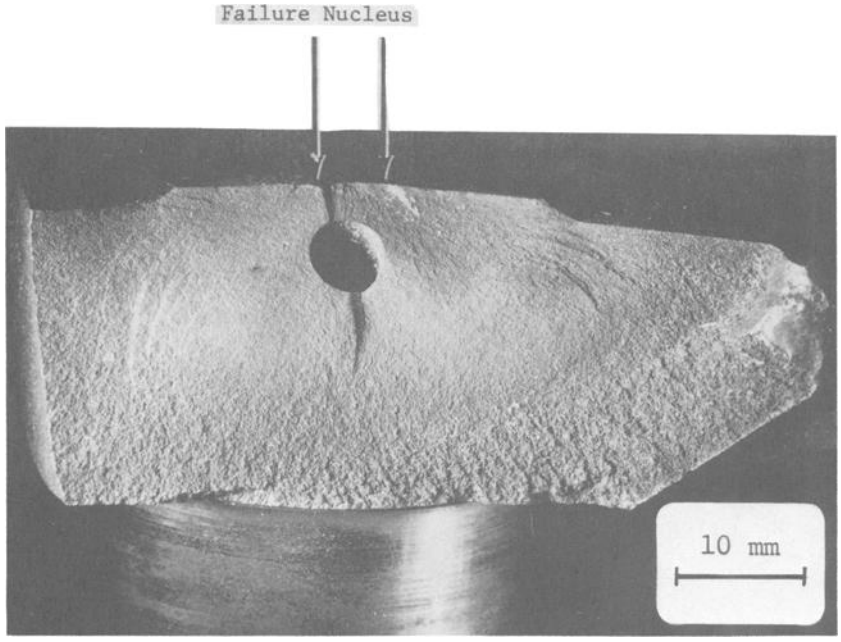


FIG. 8—*Crankshaft fracture.*

range of 0.08 to 0.18 $\mu$m (3.2 to 7.2 $\mu$in.). Further along the fracture the spacings reached 0.76 $\mu$m (30 $\mu$in.).

This information was used to calculate the stress intensity factor amplitude $\Delta K$ from the Bates-Clark Eq 1

$$\Delta K = \left(\frac{S}{6}\right)^{1/2} E \tag{2}$$

Substituting the value of $S = 4.7 \times 0.1$ $\mu$m ($10^{-6}$ in.), and the Young's modulus $E = 165.5 \times 10^3$ MPa ($24 \times 10^3$ ksi) for ductile iron, we obtained $\Delta K = 23.3$ MPa $\sqrt{\text{m}}$ (21 ksi $\sqrt{\text{in.}}$) near the origin of the fracture.

In order to apply the linear fracture mechanics methods to the calculation of the stress amplitude which caused the cracking, the following simplifying assumptions were made: (*a*) the shape of the initial crack was semielliptical, (*b*) the applied load was in bending only, and (*c*) the stress was essentially alternating, that is, the mean stress was practically zero.

The stress intensity factor $K$ for a surface crack in a plate subjected to bending may be estimated using the results presented by Smith.[3]

$$K = M_B \sigma \sqrt{\pi} \sqrt{a/Q} \tag{3}$$

[3] Smith, F. W., "Stress Intensity Factors for a Semi-Elliptical Surface Flaw," Structural Development Research Memorandum No. 17, The Boeing Company, Aug. 1966.

where

$M_B$ = crack depth factor,
$\sigma$ = stress, MPa,
$a$ = crack depth, millimetres, and
$Q$ = crack shape parameter.

The semielliptical surface crack at the fracture origin was well marked by an arrest line at $a = 2.5$ mm (0.1 in.), so that the ratio of the crack depth $a$ to its length $2C$ could be easily determined. This ratio was found to be equal to 0.2, for which $Q = 1.3$ (Fig. 9). The factor $M_B$ depends both on $a/2C$ and on $a/t$, where $t$ is the total thickness of the plate (crank).

In this particular case there was $M_B = 0.94$ (Fig. 10).

Since the stress intensity amplitude $\Delta K = K_{max} - K_{min}$, and the nominal stress amplitude

$$\Delta\sigma = \sigma_{max} - \sigma_{min}$$

then from Eq 3

$$\Delta K = M_B \Delta\sigma \sqrt{\pi} \sqrt{a/Q}$$

so that

$$\Delta\sigma = \frac{\Delta K}{M_B \sqrt{\pi} \sqrt{a/Q}}$$

Substituting the previously found numerical values of the parameters, the stress peak-to-peak amplitude was found to be $\Delta\sigma = 317$ MPa (46 ksi), that is, 159 MPa ($\pm 23$ ksi).

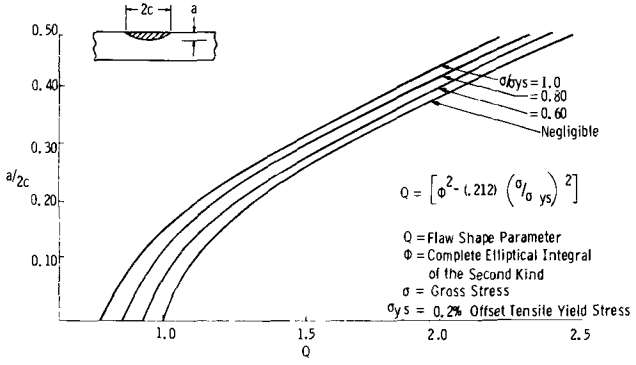


FIG. 9—*Crack shape parameter curves (after Tiffany and Masters*[4]).

[4]Tiffany, C. F. and Masters, J. N. in *Fracture Toughness Testing and its Application, ASTM STP 381,* American Society for Testing and Materials, 1965, pp. 249-277.

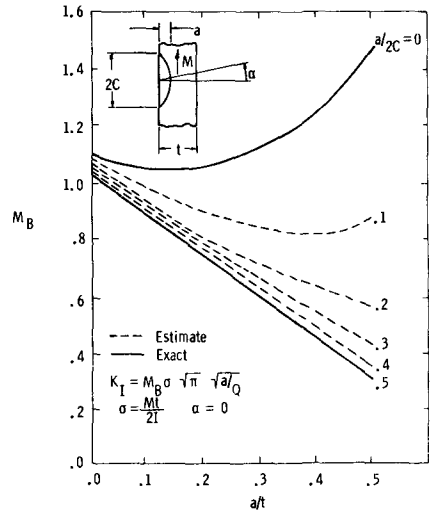


FIG. 10—*Approximate stress intensity factors for semielliptical surface cracks in bending at* $\alpha = 0$ *(after Smith (see footnote 3)).*

Finite element stress analysis indicated an alternating stress of 193 MPa (±28 ksi). Actual stress measurements using strain gages were also performed on a similar crankshaft tested under simulated service conditions. The stress measured at a location corresponding to the crack origin gave an alternating stress 103 MPa (15 ksi) in tension and 138 MPa (20 ksi) in compression.

Thus, a good agreement was found between the stress amplitude calculated from fractography using the Bates-Clark equation, and the stresses determined both experimentally with strain gates, and analytically using the finite element technique.

# DISCUSSION

---

*Susumu Hioki*[1] *(written discussion)*—I quantitatively analyzed fatigue machine parts using fatigue striations and fracture mechanics and compared the calculated value with finite element method (FEM) results or measured stresses actually. I found approximately ±10 percent errors between the value from fracture surface and FEM or measuring results. My question is what is your opinion and your data on that problem?

[1]Doctor of Engineering, Merl, Hitachi, Ltd., Hitachi-Tsuchiura, Japan.

*A. Madeyski and L. Albertin (authors' closure)*—A discrepancy between the measured striation spacings and the calculated crack growth rate or the cyclic stress amplitude may result from many causes. For example, the crack extension is often measured microscopically on the sides of the specimen, whereas the crack tip may be in form of an arc, so that most of the crack front is actually further ahead than the reported length. Unless this is taken into account, which is not always possible, most of the corresponding fatigue striations, in fact, will be located further along the specimen than considered in the calculations. When other methods of crack length measurement are applied, utilizing, for instance, ultrasonics or electric resistance changes, the results are usually *average* values over the whole crack front. Furthermore, there are limitations to the spatial resolutions shown by these methods. The measured values of the crack length are subsequently used to calculate the crack growth rates, which again usually involves some averaging and "smoothing" errors. Thus, the reported crack growth rates are inherently of somewhat limited accuracy.

Similarly, fatigue striation spacings may also vary widely from point to point, even within a small area of the fracture. Their individual values are governed by the local properties of the material and by the microstress intensities at each specific spot, rather than by the calculated macrostress of that region.

Despite these variations, the average values of the striation spacings and the corresponding crack growth rates or the macrostress intensities in any region of a specimen fracture are usually in reasonably good agreement, as shown in Figs. 5 and 6. However, in view of the variations just discussed, the errors of $\pm 10$ percent found by Hioki should be considered quite reasonable and not excessive.

# Environmental Effects

*R. P. Gangloff*[1] *and R. P. Wei*[2]

# Fractographic Analysis of Gaseous Hydrogen Induced Cracking in 18Ni Maraging Steel

**REFERENCE:** Gangloff, R. P. and Wei, R. P., **"Fractographic Analysis of Gaseous Hydrogen Induced Cracking in 18Ni Maraging Steel,"** *Fractography in Failure Analysis, ASTM STP 645,* B. M. Strauss and W. H. Cullen, Jr., Eds., American Society for Testing and Materials, 1978, pp. 87-106.

**ABSTRACT:** Fracture surfaces, produced by sustained load gaseous hydrogen assisted cracking of 18Ni maraging steel, were examined by scanning electron microscopy. Cracking developed along boundaries associated with the maraging steel microstructure. The specific crack path depended on test temperature and correlated with the influence of this variable on crack growth rates. At low temperatures, crack growth proceeded predominantly along prior austenite grain boundaries. Increasing temperature produced a continuously increasing amount of transgranular quasicleavage associated with lath martensite boundaries. The proportions of quasicleavage fracture correlated with temperature induced reductions in the crack rate over those predicted from low temperature Arrhenius behavior. Both reduced hydrogen pressure and yield strength decreased the temperature for the onset of the transition to transgranular fracture but had no influence on the crack path. The lower strength steel fracture morphology contained an increased proportion of features typical of ductile rupture. The crack path through the microstructure was independent of the applied stress intensity factor, and hence crack growth rate, from very low values to those beyond the Stage I and Stage II transition for all temperature conditions. Comparison between fractographic observations and known sites for hydrogen segregation suggested that microstructural features play a significant role in the mechanism for gaseous hydrogen embrittlement.

**KEY WORDS:** fractography, crack propagation, hydrogen embrittlement, alloy steels, fractures (materials)

High-strength steels can be severely embrittled by hydrogen dissolved in the microstructure (internal hydrogen embrittlement), by exposure to external hydrogen producing environments (hydrogen environment embrittle-

[1] Metallurgist, General Electric Corporate Research and Development Center, Schenectady, N.Y. 12301.

[2] Professor of Mechanics, Department of Mechanical Engineering and Mechanics, Lehigh University, Bethlehem, Pa. 18015.

ment), and by exposure to gaseous hydrogen over a wide range of pressures [*1-11*].[3] Aside from generic or phenomenological distinctions, there may not be any fundamental differences between these forms of embrittlement. Embrittlement is typically manifested by changes in the fracture surface morphology as compared to that produced in an inert environment. As such, fractographic characterization of surfaces produced by well documented laboratory experiments can be used to aid in identification of causes for service failures and can provide insight into the mechanisms of embrittlement. Systematic fractographic analyses of hydrogen embrittled high strength steels are few and do not document the dependence of crack path on interactive effects between critical variables for gaseous hydrogen embrittlement.

Gaseous hydrogen and hydrogen producing environments generally produce an intergranular[4] (along prior austenite grain boundaries) crack path in both 18Ni maraging [*13-15*] and quenched and tempered alloy steels [*6,8,16*]. A small percentage of transgranular cleavage or quasicleavage typically accompanies intergranular separation [*6,13*]. An increase in the stress intensity factor was alternately reported to: (*a*) increase the amount of ductile tearing that coexisted with intergranular fracture [*8,16,17*], (*b*) produce a transition in fracture morphology from intergranular separation to a "rough, ductile" mode [*7*], or (*c*) produce a transition from intergranular separation to transgranular cleavage (or quasicleavage) and subsequently to microvoid coalescence [*18,19*]. Composition [*20*] and tempering temperature [*13,21*] were observed to alter the fracture morphology from intergranular separation to transgranular cleavage (or quasicleavage) for high strength quenched and tempered alloy steels. A correlation [*21*] was established between increasing yield strength and a transition in crack path from transgranular cleavage to intergranular separation. This correlation, however, does not appear to apply to maraging steel. These steels were embrittled along transgranular boundaries in the optimally aged condition, while intergranular separation was observed for a lower strength, underaged form of the alloy [*5*].

A recent study [*4,22*] established that temperature, hydrogen pressure, stress intensity factor, and material yield strength interact to establish the kinetics for sustained load gaseous hydrogen assisted crack propagation in 18Ni maraging steel. Results from the complementary fractographic analysis are reported here. The objective of this analysis was to define fracture surface characteristics associated with gaseous hydrogen embrittlement as influenced by a range of chemical, mechanical, and material variables.

[3] The italic numbers in brackets refer to the list of references appended to this paper.

[4] Fracture mechanisms are characterized as cleavage, quasicleavage, intergranular separation, or microvoid coalescence [*12*]. Cleavage is defined as bond separation along a crystallographic plane. Quasicleavage is assumed to describe separation along interfaces associated with transgranular microstructural features.

## Experimental Procedure

### *Material, Specimen, and Test Procedure*

A 0.60-cm-thick plate of 18Ni(200) maraging steel and a 0.47-cm-thick plate of 18Ni(250) maraging steel were selected for study. Chemical composition, heat treatment, and mechanical properties for each steel are given in Table 1. Prior austenite grain size equaled 15 $\mu$m for the 18Ni(200) maraging steel, and 20 $\mu$m for the higher strength 250-grade material. The reverted austenite content of each steel was less than 5 volume percent [*23*].

Fatigue precracked wedge-opening-load (WOL) specimens, machined in the longitudinal (LT) orientation, were tested in purified hydrogen gas under sustained load to develop data on crack growth kinetics. This test method provided increasing stress intensity with increasing crack length. A range of known $K$ levels and crack speeds was obtained from a single specimen. Experimental procedures and test data are given elsewhere [*4,22*].

### *Fractographic Procedure*

Fracture surfaces were examined with a scanning electron microscope (SEM) in the secondary mode at 20 kV. Working distance was 11 mm, and all specimens were tilted 20 deg about an axis parallel to the direction of crack growth. Morphological features normal to this axis were either foreshortened or lengthened due to specimen tilt. Features parallel to the direction of cracking were undistorted. The complete fractured specimen half was examined, thus eliminating artifacts associated with sample sectioning. All fractographs were obtained from areas near the midthickness region of each specimen. Distances from the fatigue crack tip to areas of interest were measured with a micrometer stage; corresponding $K$ and crack speed values were determined from growth rate data.

## Results and Discussions

### *Crack Growth Kinetics Summary*

Crack growth in gaseous hydrogen was strongly affected by test temperature and stress intensity level for both 18Ni(200) and 18Ni(250) maraging steels [*22*]. The crack speed increased rapidly with increasing $K$ over a low stress intensity range defined as Stage I. Above a critical $K$ level, the crack speed was independent of $K$ for a wide range of values (Stage II). The mean Stage II growth rate increased with increasing test temperature for a low temperature regime defined as Region A. Within an intermediate

TABLE 1—*Composition, heat treatment, and mechanical properties.*

| Maraging Steels | Chemical Composition, weight % | | | | | | | | | Heat Treatment[a] |
|---|---|---|---|---|---|---|---|---|---|---|
| | C | P | S | N | Ni | Co | Mo | Ti | Fe | |
| 18Ni(200) | 0.002 | 0.003 | 0.007 | 0.004 | 17.9 | 7.5 | 2.8 | 0.18 | balance | 900°C, ½ h, AC + 815°C, ½ h, WQ + 482°C, 16 h, WQ |
| | $\sigma_{ys}$ = 1270 MN/m$^2$; $\sigma_{uts}$ = 1330 MN/m$^2$; elongation = 12.8% of 5.08 cm | | | | | | | | | |
| 18Ni(250) | 0.004 | 0.001 | 0.001 | 0.002 | 17.9 | 7.2 | 4.8 | 0.40 | balance | 927°C, 1 h, AC + 482°C, 3 h, AC |
| | $\sigma_{ys}$ = 1650 MN/m$^2$; $\sigma_{uts}$ = 1720 MN/m$^2$; elongation = 10.0% of 2.54 cm | | | | | | | | | |

[a] AC = air cooled and WQ = water quenched.

temperature range, Region B, Stage II growth rates increased at slower rates, passed through a maximum, and decreased with increasing temperature. The crack growth rate decreased with decreasing hydrogen pressure and material yield strength; however; these variables did not alter the two stage $K$ and Region A/B temperature dependencies.

Stress intensity and temperature dependencies of the hydrogen embrittled crack growth rate are presented in ensuing sections with corresponding fractographic results. Two yield strength levels and several hydrogen pressures are discussed.

### *Fractographic Observations*

Fracture surfaces produced by gaseous hydrogen embrittlement were macroscopically flat without shear walls for all $K$ range and material strength levels investigated as illustrated in Fig. 1. Fractures produced by Stage II cracking in Region A were characterized as the baseline condition for each steel. The effect of stress intensity was defined, and the potential for a fracture morphology change corresponding to the Stage I to II transition was evaluated. The effect of temperature on the Stage II growth rate suggests that there may be a corresponding effect on the crack path; this possibility was investigated.

*Fracture Morphology for Stage II Cracking in Region A*—Stage II cracking in both 18Ni(200) and 18Ni(250) maraging steels was predominantly intergranular along prior austenite grain boundaries for all Region A temperature and hydrogen pressure conditions. The crack morphology was defined by five components, Figs. 2 and 3:

1. A predominant component of intergranular separation along prior austenite grain boundaries
2. Grain facet markings and boundary phase cracking
3. Microcracks along prior austenite grain boundaries out of the macroscopic plane of fracture (that is, secondary cracks)
4. A small component of transgranular quasicleavage within prior austenite grains
5. A small amount of ductile tearing

Comparison of Components 1 through 4 with the characteristics of maraging steel fracture surfaces produced in an inert environment indicates that hydrogen embrittlement produced a fracture mode transition. The 18Ni maraging steels fail by microvoid nucleation, growth, and coalescence when stressed in a nonaggressive environment [*24*]. Transgranular cleavage was not observed for these materials impact loaded in inert environment for the temperature range under study [*25*].

The 18Ni maraging steels fractured in hydrogen producing environments exhibited a predominantly intergranular fracture morphology with a small

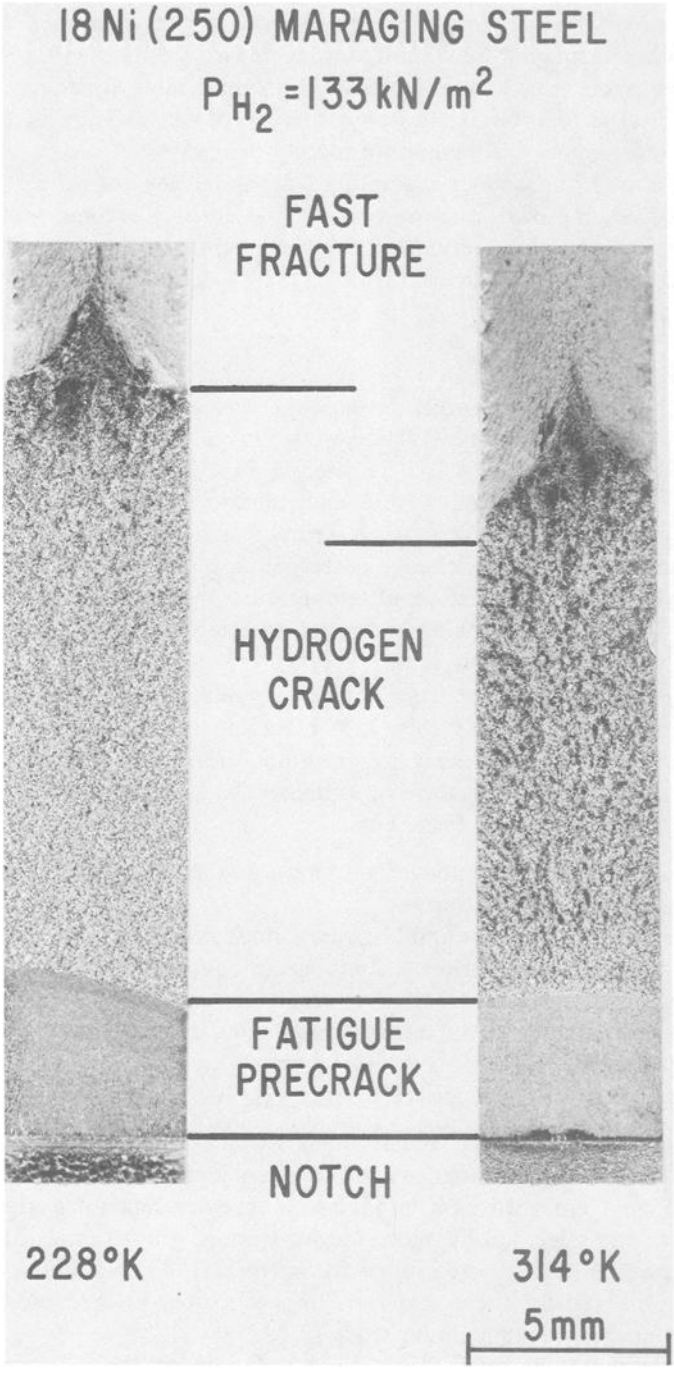


FIG. 1—*Macrophotographs of 18Ni(250) maraging steel fracture surfaces produced by sustained load cracking in gaseous hydrogen.*

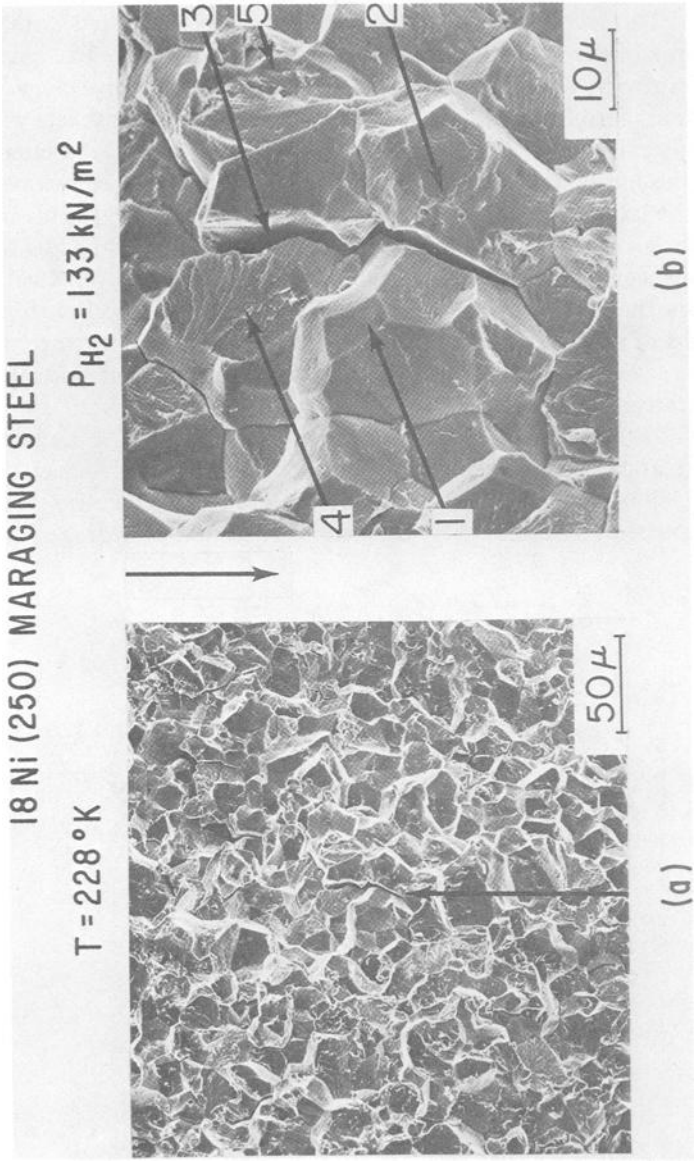


FIG. 2—*Scanning electron fractographs of Stage II, Region A hydrogen cracking in 18Ni(250) maraging steel.* ($P_{H_2}$ = *133 kN/m*$^2$, T = *228 K*, K = *23 MN/m*$^{3/2}$.) (*The arrow indicates the macroscopic direction of crack growth in each figure.*)

amount of transgranular quasicleavage and microcracking [*5,13-15,26*]. The susceptibility of prior austenite boundaries to hydrogen embrittlement is well documented [*27-30*]. The component defined as "quasicleavage" was correlated [*5*] with hydrogen induced cracking along lath martensite boundaries. This separation process, while clearly associated with the microstructure of the iron-nickel martensite, may be complex. The martensitic transformation for maraging steels produces a lath morphology with individual units forming on $\{111\}_A$ habit planes in multiple packets within a parent austenite grain [*31*]. While either the low angle lath interface [*31,32*] or the incoherent packet boundary [*31,32*] could be embrittled by hydrogen, the latter boundary is probably most susceptible [*29*]. This interface provides an obstacle to dislocation motion and was identified as a site for hydrogen segregation through a trapping mechanism [*33,34*]. Evidence [*32*] suggests that inert environment transpacket cleavage occurs through parallel laths of an iron-nickel martensite packet. Since this fracture mode was not observed for maraging steel [*24,25*], it is unlikely that this mechanism is operative during hydrogen assisted cracking.

The 18Ni(200) maraging steel fracture surface included a sixth morphological feature that was not observed for the 250-grade steel. This component, illustrated by Feature A in Fig. 3, was indicative of mechanical rupture over several grain diameters. Apparently, hydrogen is less

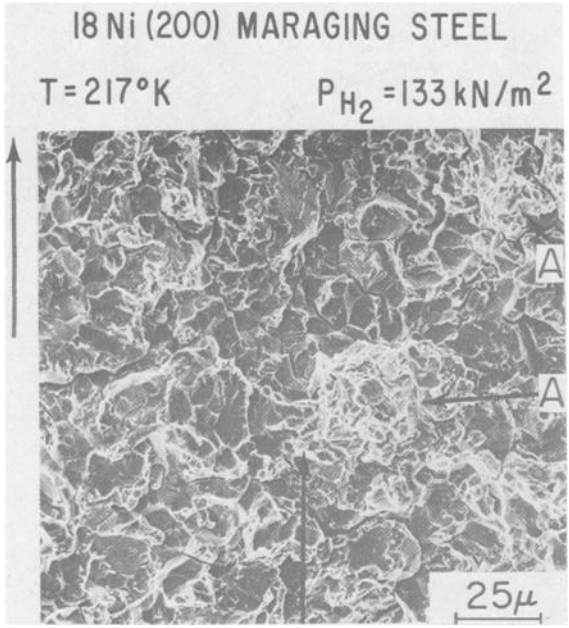


FIG. 3—*Fractograph of Stage II, Region A gaseous hydrogen cracking in 18Ni(200) maraging steel.* ($P_{H_2}$ = *133 kN/m*$^2$, T = *217 K*, K = *44 MN/m*$^{3/2}$.)

effective in embrittling prior austenite and lath martensite boundaries in the lower strength maraging steel.

*Effect of Stress Intensity Factor for Cracking in Region A*—Fractographic results for each grade of 18Ni maraging steel, cracked in Region A at several hydrogen pressures, indicate that increasing stress intensity within Stages I and II had no influence on the hydrogen assisted intergranular crack path. Fractographs supporting this conclusion are contained in Figs. 4 and 5 in conjunction with corresponding crack growth rate data [*22*]. The intergranular fracture surface morphology was unaffected by increasing stress intensity from the fatigue precrack tip, through the Stage I to II growth rate transition, to $K$ levels well within the growth rate plateau for 18Ni(250) maraging steel, Fig. 4. Similar fractographs characterizing crack growth in 18Ni(200) maraging steel are presented in Fig. 5. These results describe a limited $K$ range. Additional observations were made and indicated that the fracture morphology was similar for stress intensity values between 33 and 67 MN/m$^{3/2}$.

Results presented in Figs. 4 and 5 are not consistent with those studies

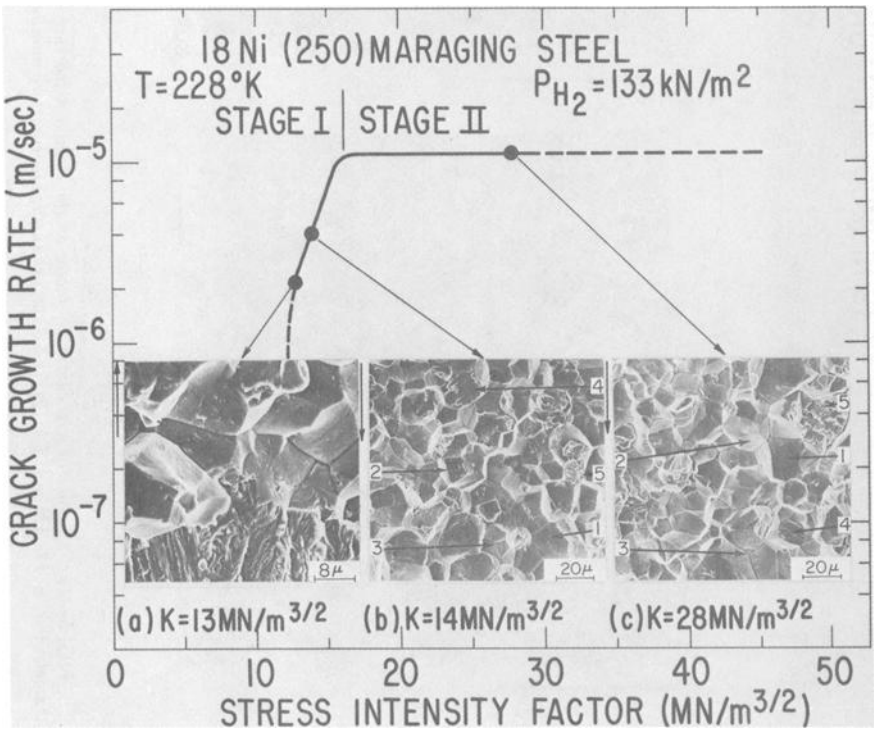


FIG. 4—*The influence of stress intensity factor on the Region A fracture surface morphology produced by gaseous hydrogen embrittlement* ($P_{H_2}$ = *133 kN/m*$^2$, T = *228 K*) *of 18 Ni(250) maraging steel. Fracture surface features are numbered as described for Fig. 2.*

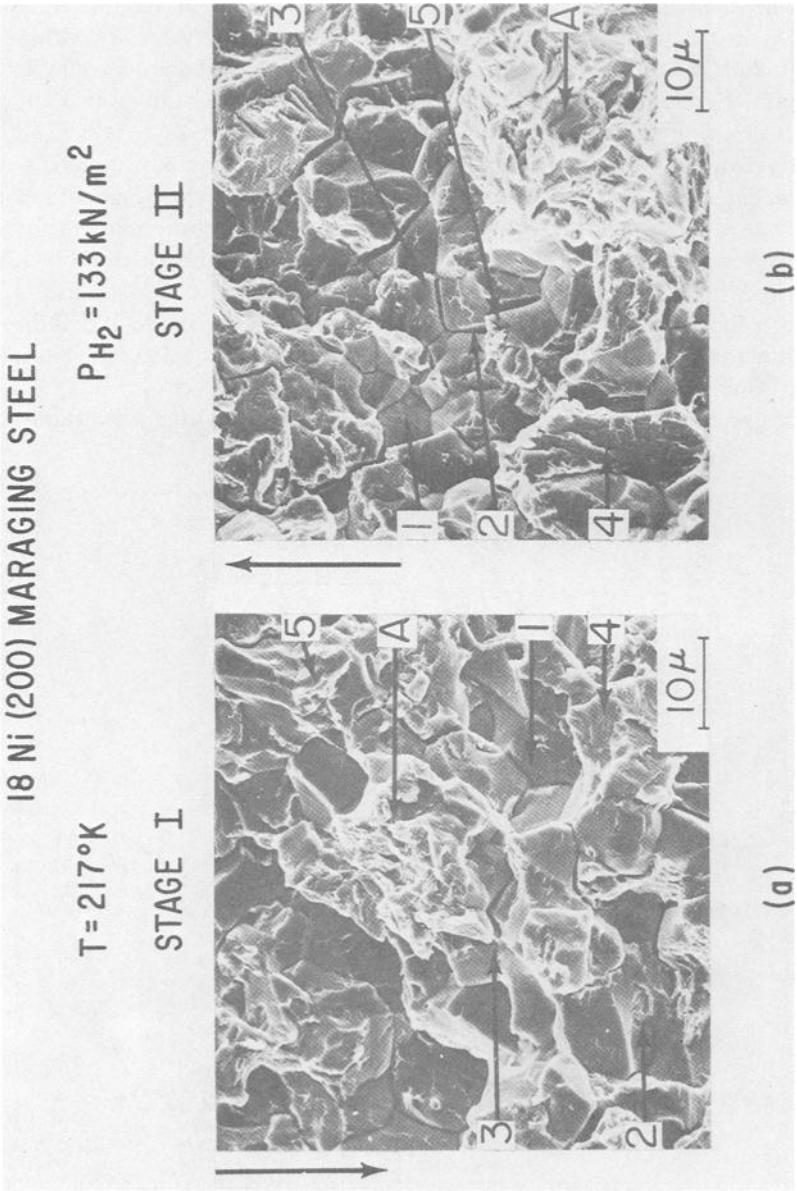


FIG. 5—*The influence of stress intensity factor on the Region A fracture surface morphology produced in 18Ni(200) maraging steel.* ($P_{H_2}$ = 133 kN/m$^2$, T = 217 K). *Fracture surface features are numbered as described for Fig. 2.*

that reported a fracture mode transition at the Stage I to II growth rate transition [*7,18,19*]. The maximum $K$ level investigated for Region A cracking was equal to about 40 percent of the estimated critical stress intensity value for fast fracture. Increased ductile tearing would be expected for higher $K$ levels [*8,16,17*].

Examination of the interface between the fatigue precrack and the initial portion of the hydrogen assisted crack revealed the absence of a resolvable "stretch" zone [*20*]. A typical fractograph that supports this conclusion is contained in Fig. 4. While a micron size stretch zone may be a prerequisite to initiate hydrogen embrittlement in lower strength steels [*20*], there is no evidence to suggest that this process was essential for cracking of high strength steels such as the 18Ni maraging variety.

*Effect of Test Temperature for Stage II Cracking*—Test temperature influenced the fracture surface morphology for hydrogen assisted Stage II cracking in 18Ni maraging steel, consistent with the influence of this variable on the Stage II growth rate [*22*]. Comparison between fracture surfaces of 18Ni(250) maraging steel, produced by cracking in 133 kN/m$^2$ hydrogen ($H_2$) at the temperature extremes of Regions A and B, indicates that a predominantly transgranular fracture morphology with respect to prior austenite grains was produced at Region B temperatures as illustrated in Fig. 6. The Region B fracture morphology is, in contrast to Region A results, defined by four components:

1. A small amount of intergranular separation, with attendant grain surface markings
2. A predominant component of transgranular quasicleavage associated with lath martensite platelet or packet interfaces
3. A component of mechanically ruptured material
4. Microcracks of both intergranular and transgranular orientation out of the macroscopic fracture plane (that is, secondary cracks)

The transition from intergranular to transgranular cracking with increasing temperature was confirmed by metallographic sections of fractured specimens characterized in Figs. 6(*a*) and (*b*). These results are shown in Fig. 7. The cross section through the crack produced in Region A revealed extensive hydrogen assisted separation of prior austenite boundaries adjacent to the macroscopic crack plane. Cross sections of the specimen embrittled at Region B temperatures revealed extensive transpacket lath martensite cracking along the main crack surface and through adjacent grains, Fig. 7. A small proportion of prior austenite boundary separation was noted.

Fractographic results indicate that the transition from intergranular to transgranular cracking was continuous with increasing temperature above the Region A/B boundary. A qualitative correlation was established be-

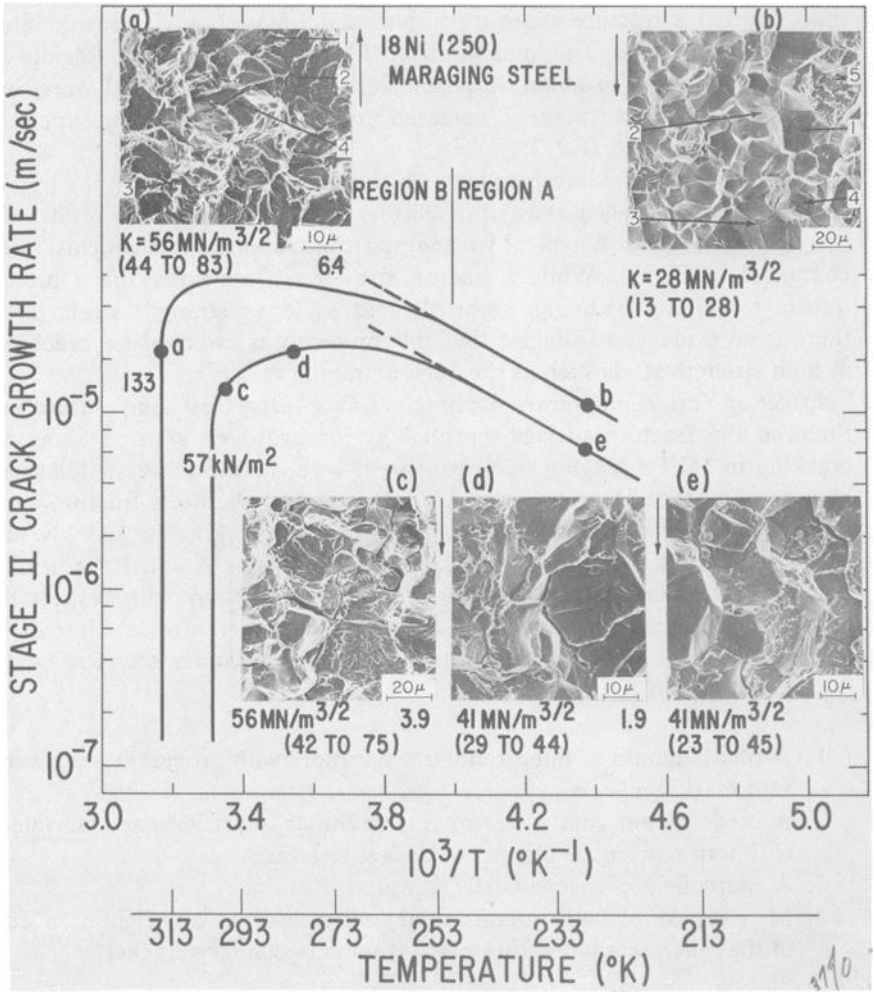


FIG. 6—*The influence of test temperature on the Stage II fracture surface morphology produced in 18Ni(250) maraging steel at two hydrogen pressures. Features in fractograph* (b) *are numbered as described in Fig. 2.*

tween the reduction factor[5] [22] and the amount of transgranular quasi-cleavage. The fracture morphology transition is complete at the temperature where reduction factor (RF) = 6.4, Figs. 6(*a*) and (*b*). The fracture path was predominantly intergranular at the Region B temperature where RF = 1.9 at 57 kN/m², Figs. 6(*d*) and (*e*). A clear transgranular character developed at the higher temperature where the reduction factor equaled 3.9,

[5]The reduction factor is defined as the ratio between the Stage II growth rate that would be realized if Region A cracking persisted to the indicated temperature and the actual Stage II, Region B growth rate.

Fig. 6(*c*). Analogous results were obtained for the 18Ni(200) maraging steel as illustrated in Fig. 8. The proportion of transgranular lath martensite boundary failure increased with increasing temperature as the RF increased from 1.8 to 3.2.

Temperature was the critical variable that defined the crack path for hydrogen embrittlement of the 18Ni maraging steels. Degree of crack tip constraint, magnitude of the crack growth rate, hydrogen pressure, and stress intensity level had no influence on the crack path transition illustrated in Figs. 6 and 8 as shown by the following considerations. While yield strength decreased by about 10 percent with increasing temperature from 213 to 336 K, the information contained in Figs. 6 and 8 could be presented for comparable values of the parameter $1/B(K/\sigma_{ys})^2$ [*22*]. As such, it is concluded that the Region A to B transitions in growth rate and fracture surface morphology were not related to decreasing crack tip constraint. While Region B cracking typically required higher stress intensity levels [*22*], data indicate that *K per se* had no effect on the crack path for either Region A or Region B embrittlement. Fractographs contained in Figs. 6 and 8, while obtained at specific $K$ levels, also described the fracture morphology over the complete $K$ range studied and parenthetically noted. Intergranular cracking was produced at relatively high stress intensity levels for 18Ni(200) maraging steel, Fig. 8. Fractographs contained in Fig. 9 indicate that the Region B transgranular fracture surface was unaffected by increasing $K$ through the Stage I to II growth rate transition analogous to Region A results. Comparison of Fig. 9(*a*) with Figs. 6(*c*) through (*e*) confirms the existence of the intergranular to transgranular crack path transition at a constant $K$ level of 41 $MN/m^{3/2}$. While cracking in Region B was associated with higher crack speeds, crack growth rate had no influence on the crack morphology. Comparison between Figs. 6(*b*) and (*c*) indicates that the fracture path transition was observed at near constant crack growth rate. The Region B transgranular crack morphology shown in Fig. 9(*a*) was produced at a *slower* crack growth rate ($4 \times 10^{-6}$ m/s) than the speeds for Region A cracking at 133 $kN/m^2$ (Fig. 6(*a*)) and at 57 $kN/m^2$ (Fig. 6(*e*)). Region B transgranular cracking in 18Ni(200) maraging steel was produced at slower growth rates than Region A intergranular cracking in the 250-grade steel, as illustrated by comparison between Figs. 6 and 8. McIntyre [*20*] reported that the crack path for hydrogen embrittlement of an alloy steel was unaffected by changing crack growth rate over four orders of magnitude. This observation is in agreement with current findings.

### *Mechanistic Implications*

Fundamental understanding of hydrogen embrittlement of high strength steels remains elusive [*4*]. Fractographic results, correlated to quantitative

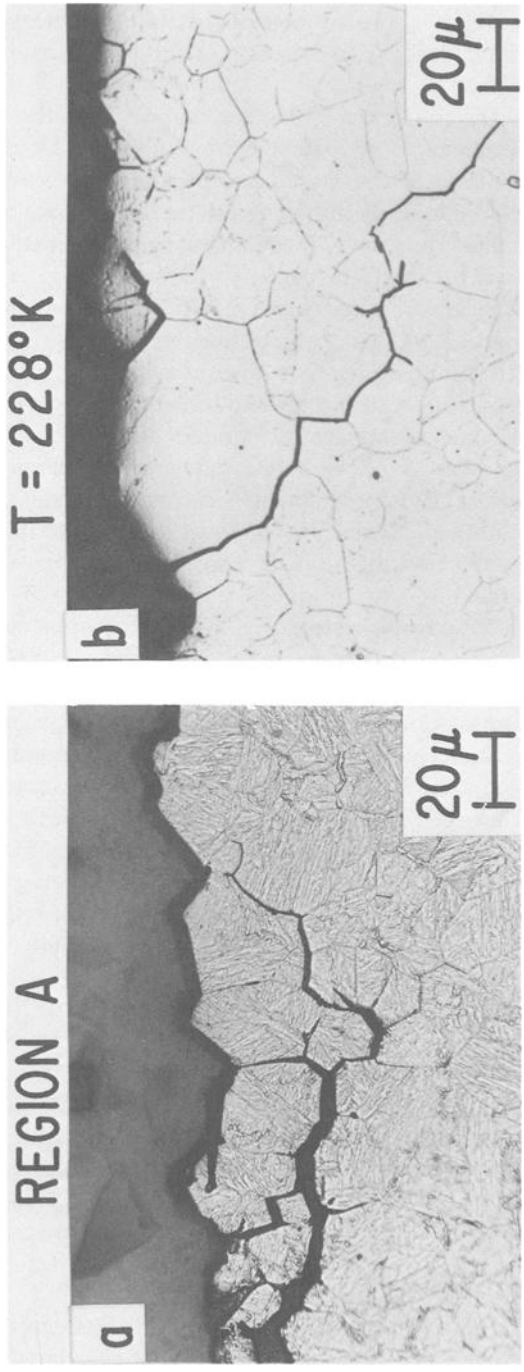
a
REGION A
20μ
b
T = 228°K
20μ

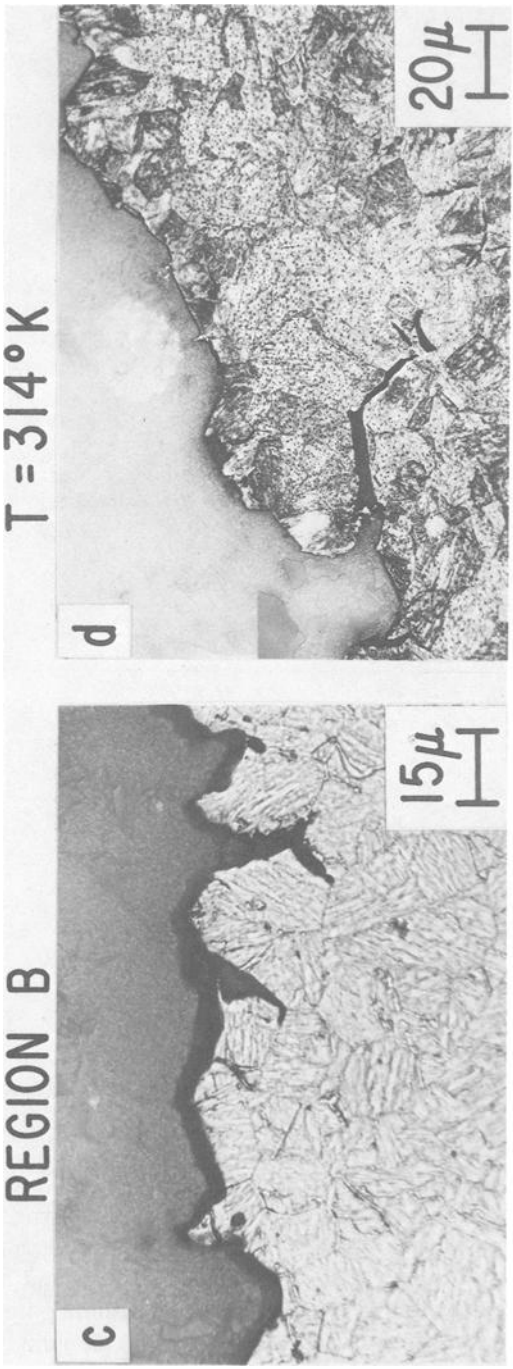


FIG. 7—*Metallographic cross sections through cracks produced by gaseous hydrogen embrittlement of 18Ni (250) maraging steel at temperatures in Regions A and B. Etchants:* (a) *and* (c) *10 ml acetic acid + 10 ml nitric acid ($HNO_3$) + 15 ml hydrochloric acid (HCl) + glycerine,* (b) *10 g chromic acid ($CrO_3$) + 100 ml water ($H_2O$) at 6 V, 5s,* (d) *95 ml aqueous ferric chloride ($FeCl_2$) + 5 ml HCl.*

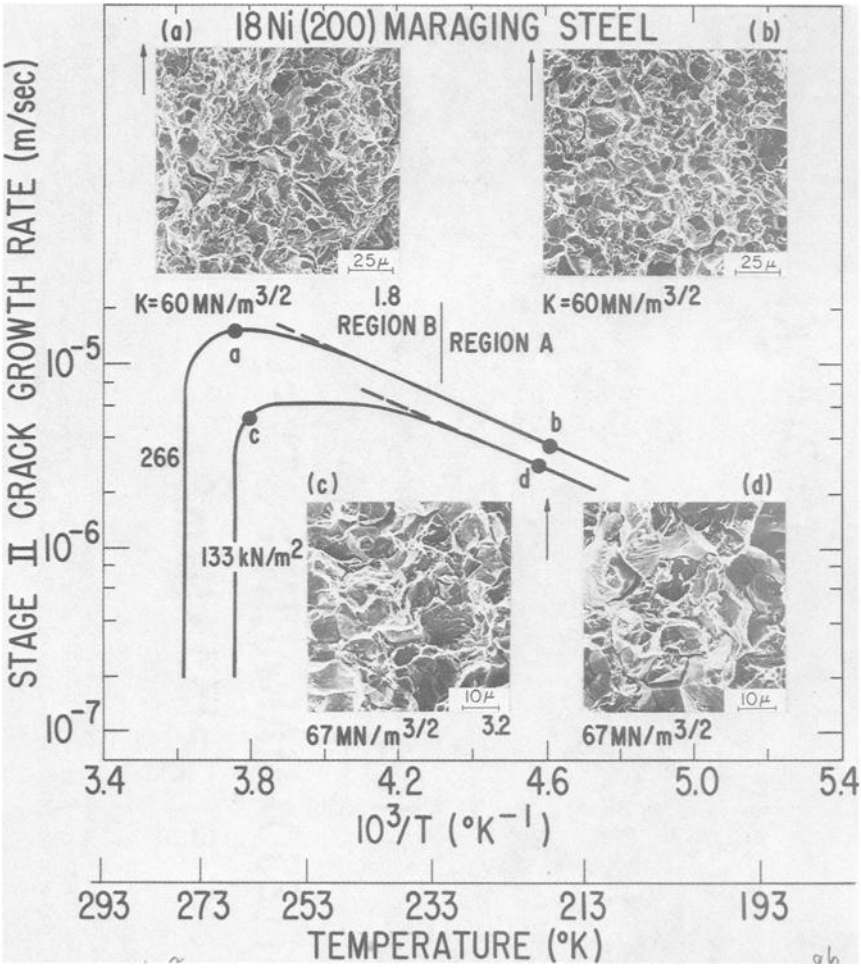


FIG. 8—*The influence of test temperature on the Stage II fracture surface morphology produced in 18Ni(200) maraging steel at two hydrogen pressures.*

crack growth kinetics data, provide some qualitative insight into this problem.

*Microstructural Aspects of Cracking*—There is, at present, no evidence that unequivocally identifies the location of the fracture site for external hydrogen embrittlement. Hydrogen assisted failure is probably governed by a critical combination of local tensile stress and hydrogen concentration [*17*]. Several models [*10*] are based on the hypothesized dominant role of the crack tip stress state, however, current fractographic findings indicate that microstructural features play a significant role in defining the fracture site. Microautoradiographic studies [*33,34*] of 18Ni(250) maraging

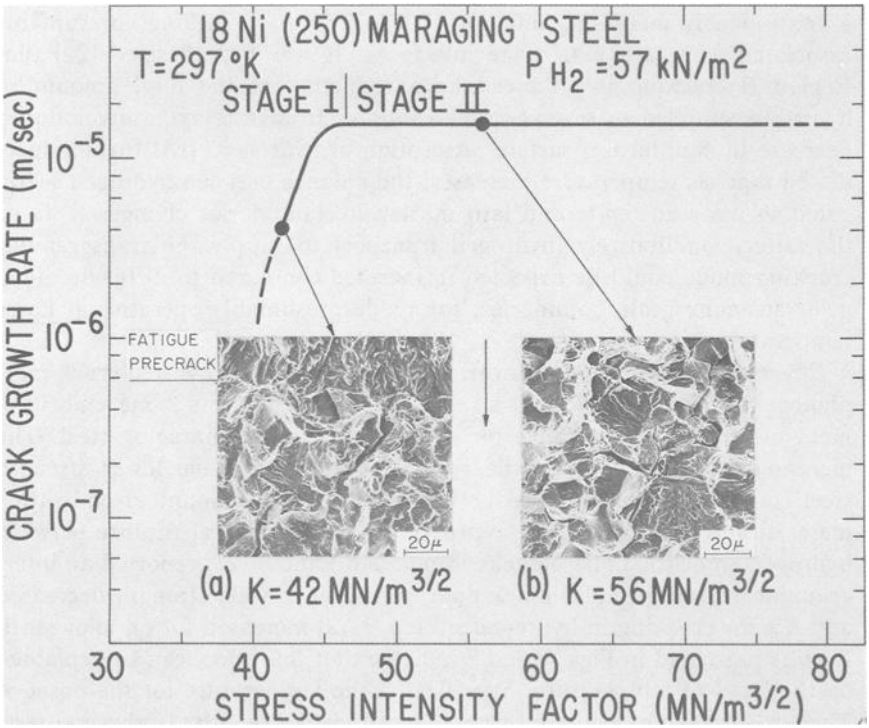


FIG. 9—*The influence of stress intensity factor on the Region B fracture surface morphology produced by gaseous hydrogen embrittlement* ($P_{H_2}$ = *57 kN/m*$^2$, T = *297 K*) *of 18Ni(250) maraging steel.*

steel showed significant segregation of hydrogen at prior austenite grain boundaries and detectable segregation at interfaces associated with the lath martensite structure. Hydrogen was segregated to these microstructural features far in excess of that estimated lattice hydrogen concentration produced by hydrostatic stress effects [*10,17*]. Microstructural sites for hydrogen segregation correlate with the preferred path for cracking in Region A.

*Effects of Stress Intensity*—The continuity of the fracture surface morphology through the Stage I to II growth rate transition is consistent with the hypothesis [*22*] that a single embrittlement mechanism is operative over the complete stress intensity range. Stage I reflects mechanical control of the crack speed, while the Stage II $K$-independent plateau region is established by the rate limiting kinetics of the chemical sequence for embrittlement. This result impacts models for the temperature-hydrogen pressure dependency of Stage II cracking [*4*].

*Effect of Temperature*—Fractographic results indicated that increasing temperature through the Region A to B growth rate transition produced

a continuously increasing amount of transgranular cracking, presumably associated with lath martensite interfaces. It was hypothesized [*22*] that Region B cracking is produced by a reduction in the total amount of hydrogen supplied to fracture sites resulting from a temperature induced decrease in equilibrium surface adsorption of hydrogen. It is further speculated that, as temperature increases, the balance between hydrogen segregated to prior austenite and lath martensite boundaries changes to favor the latter. Qualitatively, hydrogen transport to supply the transgranular cracking mode could be expected to increase compared to diffusion along prior austenite grain boundaries, the mode presumably operative at lower temperatures.

*Effect of Yield Strength*—Invariance of the hydrogen assisted crack morphology with increasing yield strength indicates that the same embrittlement mechanism is operative for each grade of 18Ni maraging steel. The increased proportion of ductile rupture observed for the lower strength steel could be related to a reduction in the overall amount of embrittled material and an increase in the proportion of mechanical rupture between hydrogen embrittled microcracks. Moon and Landes [*21*] reported an intergranular to transgranular crack path transition as yield strength decreased and $K_{th}$ for cracking in hydrogen sulfide ($H_2S$) increased for an alloy steel. Results presented in Figs. 6 and 8 indicate that this effect can be explained on the basis of temperature. Specifically, the temperature for the onset of Region B cracking decreased with reduced yield strength. Isothermal tests can intersect different *regions* of cracking to produce an intergranular, Region A type crack path in the high strength steel, and a transgranular, Region B morphology in the lower yield strength material.

## Conclusions

Fractographic analysis supplemented an extensive study of the kinetics of gaseous hydrogen assisted cracking in 18Ni maraging steel. The following conclusions were drawn.

1. Temperature determined the crack path morphology in each steel which, in turn, was directly related to the temperature dependence of the crack growth rate. (*a*) Crack growth in the low temperature (Region A) regime proceeded along prior austenite grain boundaries. (*b*) Increased temperature above the Region A/B transition value produced a continuously increasing proportion of transgranular quasicleavage associated with lath martensite boundaries. The amount of transgranular cracking was qualitatively correlated to the degree of temperature induced deviation from Arrhenius behavior.

2. Fracture morphologies were independent of stress intensity factor and crack growth rate through the Stage I to II transition for all temperature and hydrogen pressure conditions investigated.

3. Each grade of 18Ni maraging steel exhibited identical fracture morphologies for comparable regions and stages of cracking.

Fractographic observations were interpreted in terms of hypothesized mechanisms for gaseous hydrogen embrittlement. It was concluded that hydrogen segregation to prior austenite and lath martensite boundaries must be considered as a significant factor in developing mechanisms for gaseous hydrogen embrittlement of high strength steels.

*Acknowledgments*

The authors gratefully acknowledge informative discussions with G. W. Simmons, K. Klier, and P. S. Pao. Support of this research by the National Aeronautics and Space Administration (Lewis Research Center) under NASA Grant NGR 39-007-067, the American Iron and Steel Institute under Project No. 62-259, and the National Science Foundation under Grant DMR 74-10489 is acknowledged.

## References

[1] Jewett, R. P., Walter, R. J., Chandler, W. T., and Frohmberg, R. P., "Hydrogen Environment Embrittlement of Metals," NASA Report CR-2163, National Aeronautics and Space Administration, Washington, D.C., 1973.

[2] Walter, R. J. and Chandler, W. T., "Influence of Gaseous Hydrogen on Metals," NASA Report CR-124410, National Aeronautics and Space Administration, Washington, D.C., 1973.

[3] Hudak, S. J., Jr., Masters thesis, Lehigh University, 1972.

[4] Gangloff, R. P., Ph.D. thesis, Lehigh University, 1974.

[5] Dautovich, D. P. and Floreen, S. in *Proceedings, International Conference on Stress Corrosion Cracking and Hydrogen Embrittlement of Iron Based Alloys,* J. Hochmann, J. Slater, and R. W. Staehle, Eds., National Association of Corrosion Engineers, Houston, Tex. 1974, in press.

[6] Sawicki, V. R., Jr., Ph.D. thesis, Cornell University, 1971.

[7] Kerns, G. E., Ph.D. thesis, Ohio State University, 1973.

[8] Nelson, H. G. and Williams, D. P. in *Proceedings, International Conference on Stress Corrosion Cracking and Hydrogen Embrittlement of Iron Based Alloys,* J. Hochmann, J. Slater, and R. W. Staehle, Eds., National Association of Corrosion Engineers, Houston, Tex., 1974, in press.

[9] Troiano, A. R. and Fidelle, J. P. in *Proceedings, Conference L'Hydrogene Dans Les M'etaux,* Paris, 1972, p. 31.

[10] Gerberich, W. W., Chen, Y. T., and St. John, C., *Metallurgical Transactions,* Vol. 6A, 1975, p. 1485.

[11] Johnson, H. H. in *Proceedings, International Conference on Stress Corrosion Cracking and Hydrogen Embrittlement of Iron Based Alloys,* J. Hochmann, J. Slater, and R. W. Staehle, Eds., National Association of Corrosion Engineers, Houston, Tex., 1974, in press.

[12] Beachem, C. D. and Pelloux, R. M. N. in *Fracture Toughness Testing and Its Applications, ASTM STP 381,* American Society for Testing and Materials, 1965, p. 210.

[13] Fidelle, J. P., Legrand, J., and Couderc, C., "A Fractographic Study of Hydrogen Gas Embrittlement in Steels," Paper No. F71-8, The Metallurgical Society of the American Institute of Mining, Metallurgical, and Petroleum Engineers, 1971.

[14] Wei, R. P. and Landes, J. D., *Materials Research and Standards,* Vol. 9, 1969, p. 25.

[15] Stavros, A. J. and Paxton, H. W., *Metallurgical Transactions,* Vol. 1, 1970, p. 3049.

[16] Nelson, H. G., Williams, D. P., and Tetelman, A. S., *Metallurgical Transactions,* Vol. 2, 1971, p. 953.
[17] Oriani, R. A. and Josephic, P. H., *Acta Metallurgica*, Vol. 22, 1974, p. 1065.
[18] Dautovich, D. P. and Floreen, S., *Metallurgical Transactions,* Vol. 4, 1973, p. 2627.
[19] Beachem, C. D., *Metallurgical Transactions,* Vol. 3, 1972, p. 437.
[20] McIntyre, P. in *Proceedings, International Conference on Stress Corrosion Cracking and Hydrogen Embrittlement of Iron Based Alloys,* J. Hochmann, J. Slater, and R. W. Staehle, Eds., National Association of Corrosion Engineers, Houston, Tex., 1974, in press.
[21] Moon, D. M. and Landes, J. D., *Scripta Metallurgia*, Vol. 10, 1976, p. 121.
[22] Gangloff, R. P. and Wei, R. P., *Metallurgical Transactions,* Vol. 8A, 1977, p. 1043.
[23] Pampillo, C. A. and Paxton, H. W., *Metallurgical Transactions,* Vol. 3, 1972, p. 2895.
[24] Cox, T. B. and Low, J. R., *Metallurgical Transactions,* Vol. 5, 1974, p. 1457.
[25] Spaeder, G. J., *Metallurgical Transactions,* Vol. 1, 1970, p. 2011.
[26] Carter, C. S., *Metallurgical Transactions,* Vol. 1, 1970, p. 1551.
[27] Wayman, M. L. and Smith, G. C., *Metallurgical Transactions,* Vol. 1, 1970, p. 1189.
[28] Bernstein, I. M., *Metallurgical Transactions,* Vol. 1, 1970, p. 3143.
[29] Rath, B. B. and Bernstein, I. M., *Metallurgical Transactions,* Vol. 2, 1971, p. 2845.
[30] Bernstein, I. M., *Materials Science and Engineering*, Vol. 6, 1970, p. 1.
[31] Krauss, G. and Marder, A. R., *Metallurgical Transactions,* Vol. 2, 1971, p. 2357.
[32] Roberts, M. J., *Metallurgical Transactions,* Vol. 1, 1970, p. 3287.
[33] Lapasset, G., Laurent, J. P., Avcouturer, M., and Lacombe, P. in *Proceedings, Conference L'Hydrogene Dans Les M'etaux,* Paris, 1972, p. 108.
[34] Laurent, J. P., Lapasset, G., Avcouturer, M., and Lacombe, P. in *Hydrogen in Metals,* I. M. Bernstein and A. W. Thompson, Eds., American Society for Metals, Metals Park, Ohio, 1974, p. 559.

*Yoneo Kikuta,[1] Takao Araki,[1] and Toshio Kuroda[2]*

# Analysis of Fracture Morphology of Hydrogen-Assisted Cracking in Steel and Its Welds

**REFERENCE:** Kikuta, Yoneo, Araki, Takao, and Kuroda, Toshio, **"Analysis of Fracture Morphology of Hydrogen-Assisted Cracking in Steel and Its Welds,"** *Fractography in Failure Analysis, ASTM STP 645,* B. M. Strauss and W. H. Cullen Eds., American Society for Testing and Materials, 1978, pp. 107-127.

**ABSTRACT:** The relationships between fracture morphology of hydrogen-assisted cracking, microstructure, and crystallographic orientation were investigated using the scanning electron microscope.

In the fracture morphology of hydrogen-assisted cracking, quasicleavage fracture, intergranular fracture, and dimple rupture were observed. In the quasicleavage fracture caused by hydrogen, subcracks often were observed along the boundary of martensite lath or ferrite lath, or both, and at the interface between the matrix and carbides.

The unit fracture facet for hydrogen-assisted cracking, therefore, was defined as the region between subcracks. The unit fracture facet for hydrogen-assisted cracking was smaller than that for cleavage fracture of martensite, upper bainite, and bainitic ferrite. Using the etch pit method the crystallographic orientation of the fracture morphology of hydrogen-assisted cracking was found to be the {110} plane.

The fracture morphologies of hydrogen-assisted cracking can be categorized as one of four types, each of which can be explained by the microscopic diffusion behavior of hydrogen.

**KEY WORDS:** hydrogen embrittlement, fractography, crystallography, orientation, three-point bending test, implant weld cold cracking test, cleavage, fractures (materials), subcrack, unit fracture facet, hydrogen cold-work-peak height

It is generally said that steel can absorb hydrogen from production, processing, and use under natural environment, and thus have its properties impaired due to hydrogen-assisted cracking. Hydrogen-assisted cracking is recognized as hydrogen embrittlement, delayed cracking, weld cold cracking, lamellar tearing adjacent to inclusions elongated in the rolling direc-

[1] Professor and associate professor, respectively, and Drs. of Engineering, Department of Welding Engineering, Osaka University, Osaka, Japan.

[2] Research instructor and Dr. of Engineering, Welding Research Institute of Osaka University, Osaka, Japan.

tion, and environmental embrittlement occurring in use under natural environments or a hydrogen sulfide ($H_2S$) atmosphere.

Recently, electron fractography has been used to investigate the causes of various fracture morphologies. Although complex, the characteristic fracture morphology has been related to stress level and microstructure. Therefore, causes and mechanisms of fracture can be suggested approximately by observations of fracture morphology. The morphology of hydrogen-assisted cracking includes dimple rupture (DR), quasicleavage fracture (QC), and intergranular fracture (IG). However, these fracture morphologies do not necessarily exhibit characteristics of fracture induced by only hydrogen but also are observed in the case of other cracking processes. It is difficult to isolate uniquely the characteristics of fracture morphology induced by hydrogen. However, it is important to establish the characteristics of the fracture morphology which are relevant to investigations of causes of premature failure.

## Experimental Procedure

Present work was carried out for commercial HT-80A and B steels (80 kg/mm$^2$ class high strength steel). In the implant weld cold-cracking test, the steels were compared on the basis of variations in sulfur content. These chemical compositions are given in Table 1.

Ordinary V-notch specimens were used for the three-point bending test and delayed cracking test as shown in Fig. 1(*a*). The specimen used for the implant weld cold-cracking test is shown in Fig. 1(*b*). This specimen was prepared from sections in the longitudinal (X – ) and short transverse (Z – ) direction of plate.

Specimens were hydrogenated by cathodically charging for the three-point bending test by a high-temperature hydrogenation treatment for the delayed cracking test and by manual bead-on-plate welding for the implant test. These hydrogenating conditions are given in Table 2.

The three-point bending test was carried out with a bending rate of 1 mm/min by an Instron-type tension machine. For the delayed cracking test and the implant weld cold-cracking test, the applied gross stress was maintained at a constant until complete failure occurred. Details of the apparatus used are given in Fig. 2.

Fracture surfaces obtained by the tests were observed by scanning electron microscopy and two-stage replica method. Inclusions on the fracture surfaces were analyzed by the electron probe. Crystallographic orientation on the fracture surfaces was measured using the etch pit method [*1*].[3] In body-centered-cubic iron and steel, pits were observed on {110} and {100} planes and exhibited shapes as shown in Fig. 3.

[3] The italic numbers in brackets refer to the list of references appended to this paper.

TABLE 1—*Chemical compositions of materials used, weight percent.*

| Materials | C | Si | Mn | P | S | Al | Mo | Ni | Cr | Cu | V | B | Ti |
|---|---|---|---|---|---|---|---|---|---|---|---|---|---|
| HT-80A | 0.17 | 0.35 | 1.31 | 0.021 | 0.023 | 0.03 | 0.42 | 0.32 | 0.49 | 0.26 | 0.04 | 0.003 | 0.015 |
| HT-80B | 0.10 | 0.24 | 0.79 | 0.009 | 0.004 | 0.06 | 0.50 | 1.05 | 0.41 | 0.23 | 0.03 | 0.002 | ... |

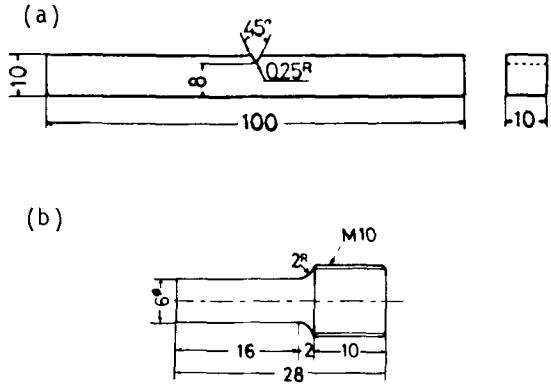


FIG. 1—*Specimen geometries.* (a) *45-deg V-notched specimen for three-point bending test.* (b) *Specimen prepared from longitudinal rolling (X) and short transverse (Z) direction of plate for implant weld cold-cracking test.*

## Results and Discussion

### *Fracture Morphology of Hydrogen Embrittlement and Others*

The fracture strength of material ordinarily depends on prior austenite grain size or lath width and length [*2,3*]. The fracture morphology was divided between intercrystalline cracking along austenitic grain boundaries and transgranular cracking across the austenite grain. Moreover, the cracking could be classified into such groups as ductile fracture with considerable plastic deformation, brittle fracture with little plastic deformation, and fatigue cracking with gradual development of fracture by the cyclic stress.

First, typical ductile and brittle fractures are shown in Fig. 4. Figure 4(*a*) was produced, for example, by the three-point bending test performed with a crosshead speed of 1 mm/min at 25°C. This fracture appeared at failure after plastic deformation. The fracture surface was caused by microvoid nucleation and coalescence at inclusions resulting in dimple rupture pattern.

Next, typical brittle fracture is shown in Fig. 4(*b*). This fracture was found, for example, in impact tests at low temperatures of large heat input welded weld-bonds in high strength steel [*4*]. The characteristic of this fracture is a cleavage step or a river pattern (CF).

The fracture resulting from an impact test of the synthetic weld heat affected zone (HAZ) with a bainitic structure is shown in Fig. 4(*c*) in which cleavage facets enclosed by tear ridges are recognized. It is difficult in this region to identify whether any characteristics of cleavage fracture exist or not. For this reason, this fracture is named a quasicleavage fracture (QC).

TABLE 2—*Methods of hydrogenation and hydrogen contents.*

| Methods of Hydrogenation | Conditions of Hydrogenation | Hydrogen Contents, ppm | Remark |
|---|---|---|---|
| Cathodic charging | current density: 80 mA/cm$^2$ for 3 h at 20°C<br>electrolyte: 5% $H_2SO_4$ in Poison P (20 mg/litre) | 8 | three-point bending test |
| High temperature method | hydrogen atmosphere (1 atm) at 950°C for 2 h and water quenching. | 4 | three-point bending delayed cracking test |
| Shielded metal arc welding | used electrode: E11016 (4 mm) as received<br>welding conditions: 25 V, 180 A and 150 mm/min speed | 12 | implant weld cold-cracking test |

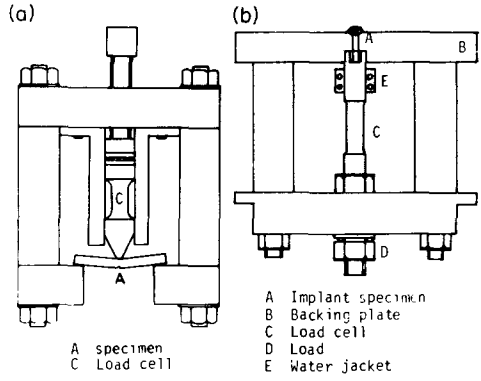


FIG. 2—*Schematic diagrams of experimental apparatus.* (a) *Three-point bending test for delayed cracking test.* (b) *Implant weld cold-cracking test.*

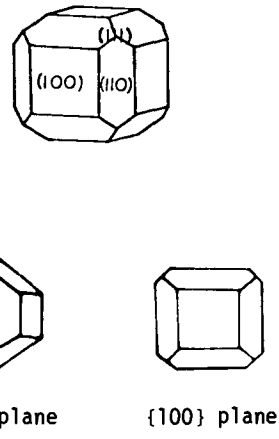


FIG. 3—*Schematic illustration of faceted etch pits.*

Fracture of hydrogen-charged specimens of HT-80A steel with various microstructures tested by the three-point bending test with a crosshead speed of 1 mm/min is shown in Fig. 5. In Fig. 5(*a*), (*b*), and (*c*), equidistant subcracks are oriented approximately vertical to the main crack surfaces. These fracture morphologies clearly differed from those of ductile fracture or brittle fracture shown in Fig. 4. Moreover, in Fig. 5(*d*) and (*e*), a striation-like or ripple pattern was identified between subcracks. This fine surface topography generally is observed by using a replica method as shown in Fig. 5(*e*). Phillips [*5*] and Meyn [*6*] also observed the same pattern in the fractures of a high strength steel with a high hydrogen content and a titanium alloy, respectively. The formation of the pattern

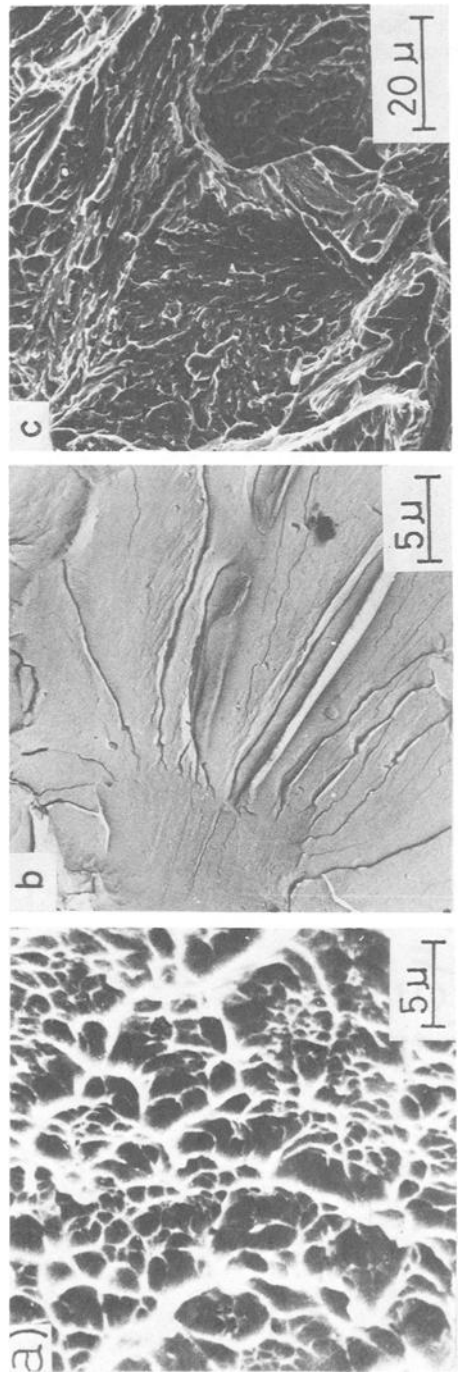


FIG. 4—*Typical fracture modes of hydrogen free materials.* (a) *Ductile fracture (dimple rupture, DR).* (b) *Brittle fracture* (CF) *tested at 0°C.* (c) *Quasicleavage fracture* (QC) *tested at −75°C.*


a Martensite
subcrack
5μ
b Upper Bainite
subcrack
5μ
c Bainitic ferrite
subcrack
5μ

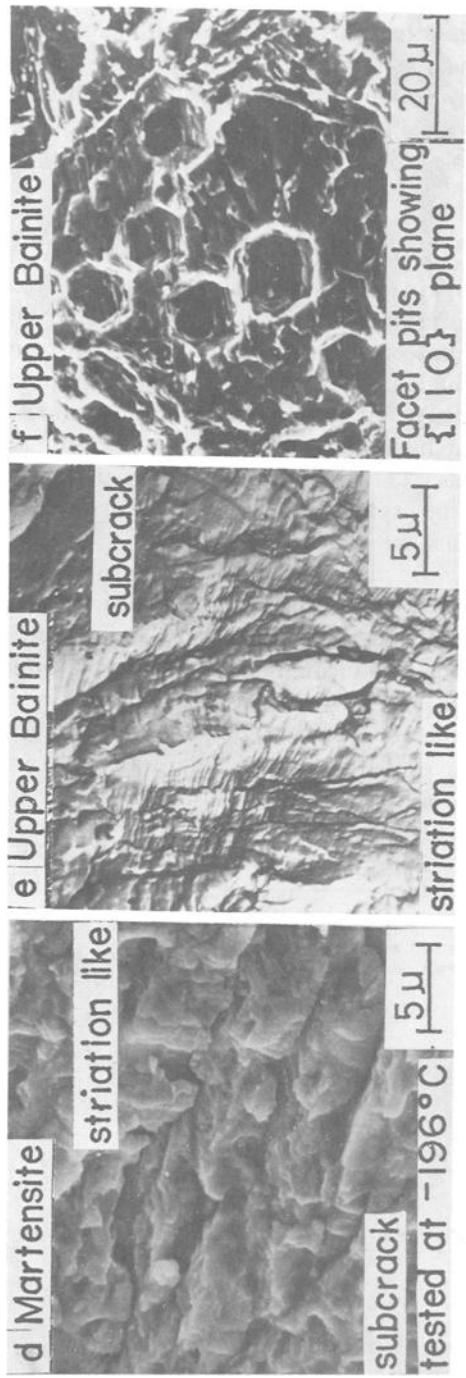


FIG. 5—*Characteristic fracture modes of quasicleavage fracture due to hydrogen embrittlement, $QC_{HE}$ tested at 25°C.*

has not been explained clearly, but it is considered to be due to the collapse of slip planes after considerable plastic deformation without the formation of voids, such as dimples. The pattern is formed because materials deform plastically not only on the slip plane but also on the cross-slip plane within the individual laths. However, for these materials it is not difficult to explain the role of hydrogen in the formation of the pattern.

### *Characteristics of Fracture Morphology for Hydrogen Embrittlement*

It was found that hydrogen embrittlement fracture differed from dimple and cleavage fractures. However, based only on the information from the scanning electron microscope, it was conjecture to determine the characteristics of fracture. Since this was the case, crystallographic orientation of the fracture surface was investigated by the etch pit method. The crystallographic orientation of hydrogen embrittlement fracture, for example, as shown in Fig. 5(*f*), was a {110} plane on which the etch pits are hexagonal. It is well known that the crystallographic orientation of cleavage is a {100} plane on which etch pits are square.

The relation between fracture facet size and prior austenite grain size for martensitic structure is shown in Fig. 6. It was clear that the distance between subcracks corresponded to martensite lath or ferrite lath width. Facet size of the hydrogen embrittlement fracture was a third or a half of that of brittle fracture [*7*]. The schematic representation is shown in Fig. 7. In this figure, the fracture path was classified into one of three types: translath fracture, interlath fracture, or intergranular fracture. Actually, these three types came out as a mixture. From the aforementioned results,

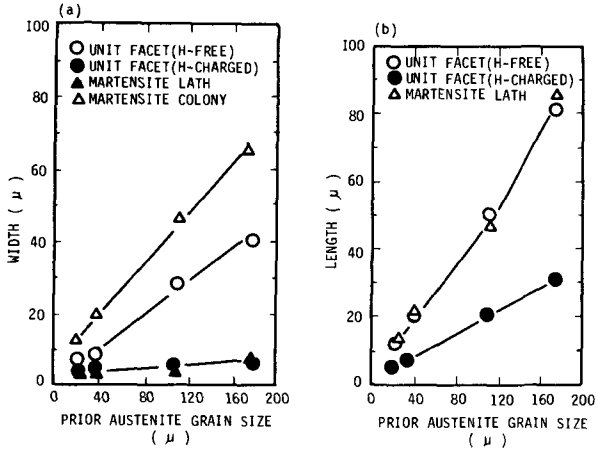


FIG. 6—*Variation of unit facet size, martensite lath width, and colony spacing with prior austenite grain size for martensite structure (HT-80A steel).*

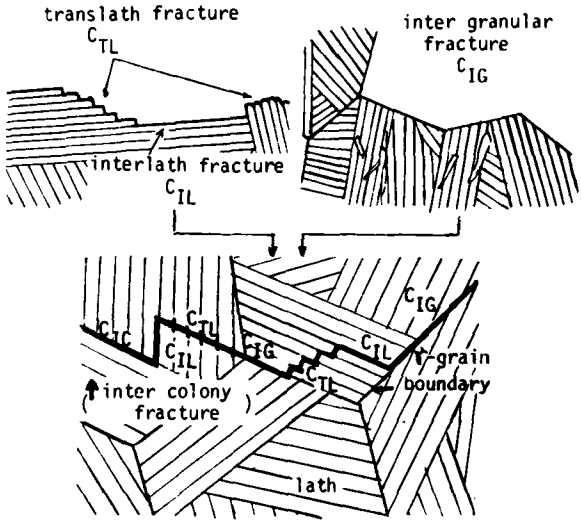


FIG. 7—*Schematic representation of fracture profile of hydrogen embrittlement.*

it was found that fracture morphology of hydrogen embrittlement was different from ductile fracture, brittle fracture, and quasicleavage fracture. Therefore, the authors propose that this fracture be named quasicleavage fracture of hydrogen embrittlement ($QC_{HE}$).[4] Since this fracture occurs on the {110} planes and the striation-like markings are recognized in it, hydrogen embrittlement is considered to be glide-plane decohesion.

### *Fracture Morphology of Delayed Cracking Due to Hydrogen*

There are various types of delayed failure of material, for example, fatigue cracking, stress-corrosion cracking, creep rupture, and so on. In these types, crack initiation occurs after a time lag without variation in external conditions such as stress. This phenomenon is called delayed hydrogen cracking or static fatigue fracture. This time delay is necessary for the accumulation of hydrogen by diffusion at the crack tip. This type of fracture includes season cracking, environment cracking, and weld-cold cracking. It may be said safely that delayed cracking induced by hydrogen is hydrogen embrittlement. However, in this paper the delayed cracking is defined as fracture which arises under constant stress with the passage of time.

[4] The definition of quasicleavage ($QC_{HE}$) used in this paper is not the same as that (QC) proposed by Beachem [*8*], which may be considered to be the crystallographic orientation of the fracture as {100} plane, similar to cleavage fracture. QC is also observed in the case of other cracking processes without hydrogen. $QC_{HE}$ is considered to be cracking by glide-plane decohesion {110} plane in conjunction with hydrogen gathering around a dislocation. It is considered that its cracking process differs from QC, somewhat like brittle fracture.

The delayed cracking fracture of high-temperature hydrogenated specimens and the weld cold-cracking fracture of each HAZ of specimens prepared from longitudinal rolling (X) and short transverse (Z) direction of HT-80A steel plate are shown in Fig. 8. Figure 8(*a*), (*b*), and (*c*) exhibit fractures from the three-point bend, delayed cracking test of specimens hydrogenated at 950°C for 2 h. The fracture morphology of the delayed cracking was a mixture of several modes such as DR, $QC_{HE}$, IG, and CF, but the dominant fracture morphology differs according to applied stress level. Dimple pattern was dominant with an applied stress (three-point bending nominal stress) of 1400 MPa. The hydrogen-free specimen had a fracture stress of 2500 MPa, while failure of the specimen, including hydrogen, occurred under a constant load which was lower than that of the hydrogen-free specimen. The fracture of the hydrogen-free specimen also had the dimple pattern. It was difficult to understand whether the fracture was induced by hydrogen or not. However, dimple size of the delayed cracking appeared as small as that of the hydrogen-free specimen. $QC_{HE}$ fracture was dominant with an applied stress of 1000 MPa, and $QC_{HE}$ and IG were recognized with an applied stress of 750 MPa which was nearly a critical low stress level.

*Fracture Morphology of Weld Cold Cracking*

Figure 8(*d*), (*e*), and (*f*) exhibit weld cold-cracking fractures for the longitudinal rolling direction for HT-80A steel. As in the previous case, fracture morphologies varied with applied stress level.

Figure 8(*g*), (*h*), and (*i*) exhibit weld cold-cracking fracture in the short transverse direction for the same steel. These fractures also varied with applied stress level and had the same general characteristics as the aforementioned morphology. But, in high applied stress, fracture differed slightly from the result. With an applied stress of 530 MPa or on leaving it unloaded as it was for two weeks after welding, terrace and wall-like fractures, namely, lamellar tearing was observed. The terrace consisted of elongated manganese sulfide (MnS) clusters and fine dimples with inclusions. The wall consisted of extended dimples. With an applied stress of 400 MPa, the terrace was the same as before and intergranular failure appeared in the wall. With an applied stress of 300 MPa, which was nearly a critical low stress level, the distinction between terrace and wall was not clear, and $QC_{HE}$ and IG were observed. Inclusion content had no effect on the fracture morphology. The fracture path in this case is shown in Fig. 9 which has the same characteristics as Fig. 7. From Fig. 9 it is deduced that inclusions were not of consequence in the fracture. The steel with low sulfur content had little tendency toward lamellar tearing. The fracture for HT-80B steel, which was left for two weeks after welding, was observed to have the dimple fracture with fine MnS inclusions in the dimple bottoms.

While under constant load after welding, delayed cracking occurred. Its fracture morphology exhibited $QC_{HE}$ as shown in Fig. 10, and the fracture path consisted of translath and interlath cracking. In the short transverse direction of the low sulfur level steel, the terrace and wall-like fracture was not observed.

*Fracture Morphology of Lamellar Tearing*

In steel with a high sulfur content and large elongated MnS clusters, the terrace and wall structure was observed in fracture along the short transverse direction obtained in the weld cold-cracking test. In the tension test of a hydrogen-free specimen, Elliott proposed that the terrace and wall-like fracture morphology of the hydrogen-free specimen was caused by lamellar tearing [*9*]. In Japan, this phenomenon has been investigated [*10*] and it has been stated that lamellar tearing was observed in high sulfur content steel, and close attention should be paid to these inclusions. The authors propose that the terrace and wall-like fracture of hydrogen includes lamellar tearing in the specimen, too. It was difficult to observe lamellar tearing in the fracture morphologies in which the terrace and wall were not clear, and inclusions were not observed in the short transverse direction specimen with high sulfur content and low stress level.

Therefore, this implies that in the weld cold-cracking test lamellar tearing is the fracture morphology of a specimen with a high sulfur level under high applied stress.

*Effect of Hydrogen Diffusion on Fracture Morphology of Hydrogen Assisted Cracking*

It has been proposed that hydrogen embrittlement is diffusion dependent. There is also much discussion in the literature concerning the exact location of hydrogen in the material. Several workers have postulated that hydrogen interacts with a "trap" of some sort. Various defects such as voids [*11*], second phases [*12*], vacancies [*13*], and dislocations [*14*] have been suggested as possible traps. There is, however, no direct evidence that interaction is a necessary part of the embrittlement process.

Recently, the authors carried out a tension test and an internal friction experiment as shown in Fig. 11 [*15*]. When specimens of HT-80A steel were hydrogen charged by the high temperature method, their ductility decreased at an early stage of aging, steadied at 0°C, and then went through a minimum. At a later stage of aging, it recovered the value of the hydrogen-free specimen. Notch tensile strength (NTS) could be regarded as a measure of ductility, and it was used as the most convenient parameter for embrittlement. Hydrogen cold-work-peak height increased with increasing aging time, went through its maximum, and decreased to a vanishing small


a
DR
5μ
b
QC$_{HE}$
subcrack
20 μ
c
QC$_{HE}$+IG
20 μ


FIG. 8—*Typical fracture modes of hydrogen delayed cracking (HT-80A). Three-point bending test (martensite at 950°C charged hydrogen) at 25°C tested:* (a) *fracture time 6 min at applied stress 1400 MPa,* (b) *30 min, 1000 MPa, and* (c) *90 min, 750 MPa. Implant test (HT-80A-HAZ-X):* (d) *3 min, 850 MPa* (e) *8 min, 750 MPa, and* (f) *50 min, 700 MPa. Implant test (HT-80A-HAZ-Z):* (g) *700 MPa (TS)* (h) *15 min, 400 MPa and 100 min, 300 MPa.*

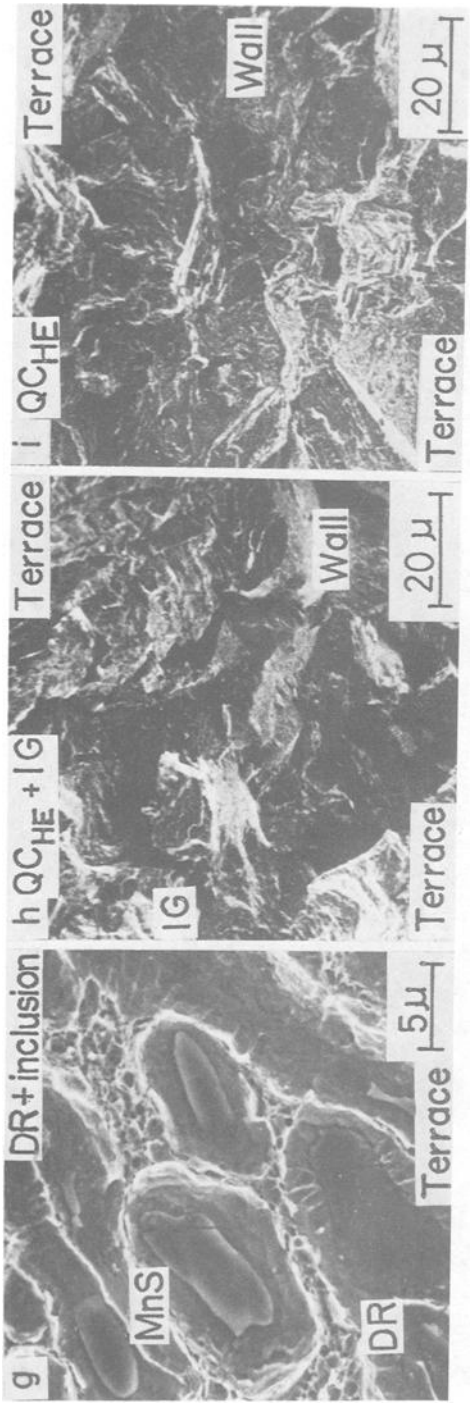


FIG. 8—*Continued.*

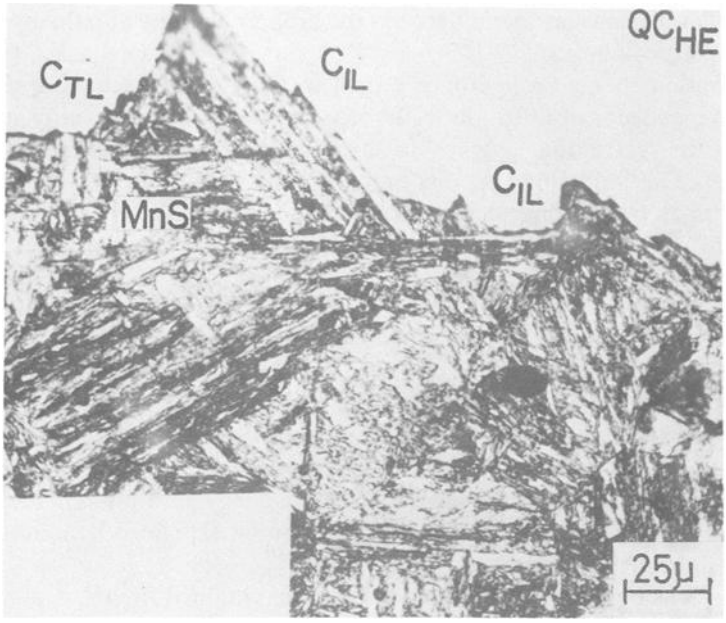


FIG. 9—*Fracture profile of hydrogen delayed fracture for (HT-80A-HAZ-Z) applied stress 300MPa (fracture time: 100 min).*

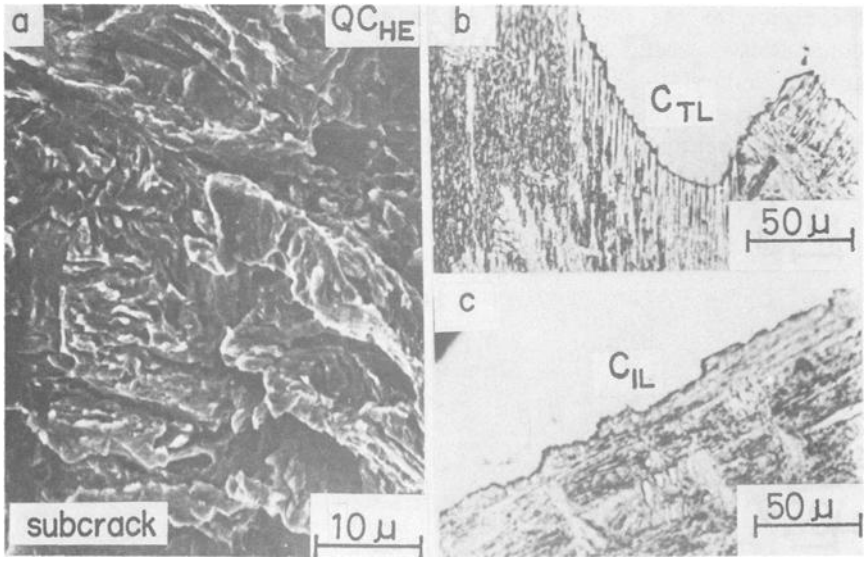


FIG. 10—*Fracture profile of hydrogen delayed fracture for (HT-80B-HAZ-Z) applied stress 700MPa (fracture time: 100 min).*

value. Parallelism was found between the drop in ductility and the hydrogen cold-work-peak height.

Activation energy for hydrogen diffusion, Q, is determined from temperature dependency of diffusion in the tension test [*16*]. In the early stage of aging, the activation energy for hydrogen diffusion was about 3200 cal/mol. This value may express only the lattice diffusion of hydrogen. In the latter stage of aging, it was about 8000 cal/mol. This value may result from diffusion through microscopic defects such as dislocations and vacancies.

From these experimental results, it may be concluded that hydrogen cold-work-peak height can be proportional to hydrogen, $C_D$, in the neighborhood of the dislocation, as shown in Fig. 11 and that hydrogen first diffuses toward dislocations and then away from dislocations.

It seems that the microscopic diffusion behavior of hydrogen affects fracture morphology of hydrogen embrittlement as observed in this study. The fracture morphology of hydrogen-assisted cracking can be summarized into four types as shown in Table 3, and these can be explained by microscopic diffusion behavior of hydrogen.

$QC_{HE}$ was observed on the fracture surface obtained under medium and low constant applied stress within the region in which delayed fracture occurred. Since occurrence of this fracture takes an average or long time, the concentration of hydrogen at dislocations may increase and ductility decrease as shown in Fig. 11. Therefore, it seems that $QC_{HE}$ starts from a region of the highest hydrogen concentration which is generally located in the region of the highest dislocation density such as lath and grain boundaries. It seems that IG is caused by accumulated hydrogen at the grain boundary.

In the case of the continuous slow bending conditions, $QC_{HE}$ also is observed. The reason for this may be that as hydrogen is charged cathodically,

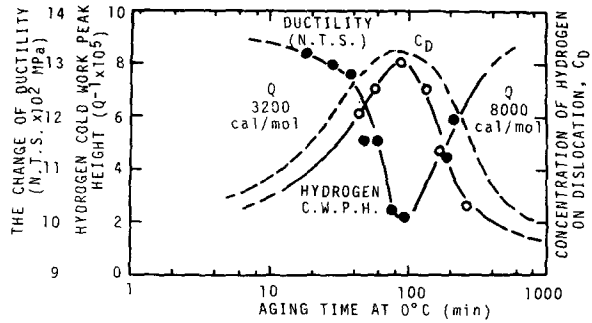


FIG. 11—*Relationship between ductility and hydrogen cold-work-peak height for hydrogenated steel (HT-80).*

TABLE 3—*Schematic representation of factors affecting the fracture morphologies of hydrogen-assisted cracking.*

| Conditions of Applied Loading | Fracture Time | Concentration of Hydrogen on Dislocation, $C_D$, and Ductility | Dominant Fracture Modes | Characteristic Fracture Morphologies | Hydrogen Assisted Cracking |
|---|---|---|---|---|---|
| Average and lower applied stress within the range in which delayed fracture occurred | average and long | high, hydrogen accumulation at lath and grain boundary (low) | $QC_{HE}$ | • subcracks at lath boundary<br>• striation-like pattern in lath<br>• fracture path through trance and interlath<br>• main fracture surface, {110} plane | delayed cracking<br>weld cold cracking<br>hydrogen embrittlement |
| Continuous slower bending and tension | | | IG | • fracture path through grain boundary<br>• subcrack at grain boundary | |
| Higher constant applied stress within the range in which delayed fracture occurred | short | low, hydrogen random distribution (high) | DR | • dimple pattern | transitional state from ductile fracture to HAC fracture |
| Continuous rapid bending and tension | | | DR + Inclusion | • dimple pattern and elongated inclusion on terrace<br>• terrace and wall-like (high sulfur content) | lamellar tearing |

hydrogen accumulates easily at the dislocations as compared with the high temperature charging method. Therefore, $QC_{HE}$ will occur.

While $QC_{HE}$ did not occur in the fracture surface obtained under higher constant applied stress within the range of delayed fracture, DR and DR+ inclusions on the terraces were observed. Since occurrence of fracture takes a short time, Fig. 11 corresponds to an early stage at which the concentration of hydrogen on dislocations may be lower and thus the ductility higher, but still lower than the case of the hydrogen-free specimen. It seems that this fracture, which is similar to ductile fracture, occurs at the transitional state from ductile fracture to hydrogen embrittlement fracture; but it is difficult to distinguish whether this fracture is concerned with hydrogen or not.

In the case of continuous rapid bending or tensile fracture, DR also is observed because dislocations break away from the hydrogen atmosphere, resulting in low hydrogen on dislocations.

## Conclusions

The characteristic morphology of hydrogen embrittlement was quasi-cleavage fracture ($QC_{HE}$) which involved subcracks along martensite lath boundaries, ferrite lath boundaries, and the interfaces between the matrix and carbides. The unit fracture facet for hydrogen embrittlement was defined as the region between subcracks or tear ridges. The unit fracture facet for hydrogen embrittlement was smaller than that of cleavage fracture.

The crystallographic orientation of the fracture morphology of hydrogen embrittlement was {110} planes. So, it seemed that hydrogen embrittlement was caused by slide plane decohesion.

The fracture morphology of hydrogen-assisted cracking could be summarized into four types and they could be explained by microscopic diffusion behavior of hydrogen.

## References

[1] Taoka, T., Furubayashi, F., and Takenouchi, S., *Japan Journal of Applied Physics*, Vol. 4, 1965, p. 120.
[2] Petch, N. J. in *Fracture*. Wiley, New York, 1959, p. 54.
[3] Embury, J. D., Keh, A. S., and Fisher, R. M., *Transactions*, Metallurgical Society of the American Institute of Mining, Metallurgical, and Petroleum Engineers, Vol. 239, 1966, p. 1252.
[4] Kikuta, Y. and Araki, T., *Technology Reports of the Osaka University*, Vol. 26, 1976, p. 53.
[5] Phillips, A. and Bennett, G. V., *Metals Progress*, Vol. 79, No. 5, May 1961, p. 97.
[6] Meyn, D. A., *Metallurgical Transactions*, Vol. 3, 1972, p. 2302.
[7] Terasaki, F. and Otani, H., *Journal of the Iron and Steel Institute of Japan*, Vol. 58, 1972, p. 1067.
[8] Beachem, C. D., *Metallurgical Transactions*, Vol. 3, No. 2, 1972, p. 437.

[9] Elliot, D. N., *Metal Construction and British Welding Journal,* Vol. 2, 1969, p. 50.
[10] Kihara, H., Suzuki, H. and Ogura, N., *Journal of the Japan Welding Society,* Vol. 25, No. 2, 1951, p. 94.
[11] Podgurski, H. H., *Transactions*, Metallurgical Society of the American Institute of Mining, Metallurgical, and Petroleum Engineers, Vol. 221, 1961, p. 389.
[12] Coe, F. R. and Moreton, J., *Journal of the Iron and Steel Institute,* Vol. 207, p. 366.
[13] Heller, W. R. in *Stress Corrosion Crack Embrittlement,* Wiley, New York, 1956, p. 163.
[14] Bastien, P. and Azou, P., *Proceedings,* First World Metal Congress, American Society for Metals, Cleveland, Ohio, 1951, p. 535.
[15] Kikuta, Y., Sugimoto, K., Ochiai, S., and Iwata, K., *Proceedings,* First International Congress, Hydrogen in Metals, Paris, 1972, p. 144.
[16] Kikuta, Y., Araki, T., and Ochiai, S., *Journal of the Japan Welding Society,* Vol. 45, No. 12, 1976, p. 1016.

*E. U. Lee,[1] R. G. Mahorter,[2] and J. D. Wacaser[3]*

# Fracture of Ti-8Al-1Mo-1V Alloy Fan Blade by Stress Corrosion Cracking and Fatigue

**REFERENCE:** Lee, E. U., Mahorter, R. G., and Wacaser, J. D., **"Fracture of Ti-8Al-1Mo-1V Alloy Fan Blade by Stress Corrosion Cracking and Fatigue,"** *Fractography in Failure Analysis, ASTM STP 645,* B. M. Strauss and W. H. Cullen, Jr., Eds., American Society for Testing and Materials, 1978, pp. 128-143.

**ABSTRACT:** Similar fractures occurred in two gas turbine engine fan blades made of Ti-8Al-1Mo-1V alloy. Their analyses and a supplementary test were performed with the aid of scanning electron microscope (SEM) and transmission electron microscope (TEM) fractography to identify the common mechanism(s).

The initial fracture surface of each fan blade exhibited an area of subcritical crack growth. The area in one fan blade contained three blue discolored zones along the crack initiation side, whereas that in the other fan blade was discolored to white-gray. Intergranular separation and transgranular cleavage were evident at the three discolored zones in one fan blade and near the crack initiation site in the other. Cleavage-like facets were predominant in the remaining area of subcritical crack growth. On some of those facets, striations were seen.

A hot salt stress corrosion cracking test of Ti-8Al-1Mo-1V alloy plates resulted in discoloration, intergranular separation, and transgranular cleavage, similar to those observed in one fan blade.

The mechanism of initial crack growth is stress corrosion cracking at an elevated temperature in one fan blade and at ambient temperature in the other. The mechanism of subsequent subcritical crack growth is fatigue at ambient temperature in both fan blades.

**KEY WORDS:** fractography, fractures (materials), crack initiation, subcritical crack growth, intergranular separation, transgranular cleavage, stress corrosion, fatigue (materials), striations, stress intensity factor, microvoid coalescence

The Ti-8Al-1Mo-1V alloy has been used in aircraft gas turbine engines for parts requiring low density and high modulus for optimum performance.

[1] Metallurgist, Materials Engineering Laboratory, Naval Air Rework Facility, Norfolk, Va. 23511.

[2] Metallurgist, Naval Air Development Center, Warminster, Pa. 18974.

[3] Manufacturing research and development technologist, Pratt and Whitney Aircraft, East Hartford, Conn. 06108.

The most critical of these parts are fan blades. Due to the rotational speed (approximately 167 rps or 10 000 rpm), blades are subjected to high steady (centrifugal) stresses and high frequency vibratory stresses along with air pressure loading on the concave surface. In addition, they must operate in salt-laden air and are subject to damage from objects ingested into the engine. Fan blades are manufactured by several forging operations, chemical descaling, heat treatment,[4] chemical milling, straightening operations, machining of the root and midspan shroud, belt blending and sanding of the airfoil surface, and finally a stress relief treatment. A typical fan blade is shown in Fig. 1.

Fan blade fractures often have led to catastrophic failures of engines which have resulted in the loss of the aircraft. On the other hand, they have created interesting fractographic features, characterizing a combination of complex stresses or detrimental environments during manufacture and service. Many times the fractographic features have indicated stress corrosion cracking or fatigue as the fracture mechanism.

The stress corrosion cracking [*1-10*][5] and fatigue [*11-19*] of Ti-8Al-1Mo-1V and other titanium alloys have been studied extensively. Stress corrosion cracking proceeds by intergranular separation at low levels of stress intensity factor, $K$, transgranular cleavage at intermediate levels, and microvoid coalescence at levels close to the critical stress intensity factor, $K_{Ic}$ [*8*]. Fracture is accompanied by crack branching which increases with $K$ [*8*]. The fatigue results in cleavage-like facets at low levels of growth rate, $da/dn$, striations at intermediate levels, and coalesced microvoids at high levels [*13,16*].

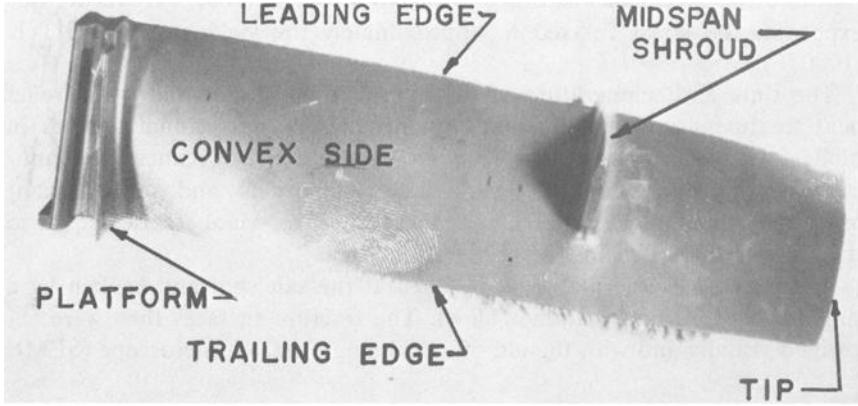


FIG. 1—*Fan blade.*

[4] Heat treating: (*a*) heat at a temperature within the range 1172 to 1200 K (1650 to 1700°F) for 1 h and cool at a rate equivalent to air cool or faster; (*b*) heat at a temperature within the range 839 to 867 K (1050 to 1100°F) for not less than 8 h and cool in air.

[5] The italic numbers in brackets refer to the list of references appended to this paper.

This paper presents the analyses, with fractographic evidences, of two separate Ti-8Al-1Mo-1V alloy fan blade fractures, which occurred during engine operation. An analysis of a hot salt stress corrosion test was made to confirm the failure mode of one of the blades and to relate the failure to the manufacturing process.

## Procedure of Fracture Analysis

The two fractured fan blades were examined visually and with a low magnification ($\times 15$ to $\times 90$) optical microscope to determine the extent of the fracture and the macromorphology of the fracture surface. The micromorphology of the fracture surface, especially that of the subcritical crack growth area, was studied with scanning and transmission electron microscope, operated at 20 and 60 kV, respectively. For the study with a transmission electron microscope (TEM), chromium-shadowed carbon replicas of the fracture surface were prepared by employing the standard two-stage replication technique. For a further examination of fracture path, optical micrographs of sections through the fracture were made. A blue etch anodize inspection [*20*] was performed to detect possible alpha case[6] on a fan blade airfoil surface.

A Ti-8Al-1Mo-1V alloy plate, 20.32 by 2.54 by 0.24 cm (8 by 1 by 3/32 in.), was subjected to a hot salt stress corrosion cracking test. The plate was loaded in a four-point bend fixture in a constant deflection mode. The deflection used gave a nominal outer fiber stress of 75 percent of the room temperature yield stress. Salt slurry was applied to a 0.5-cm-diameter spot and the specimen was exposed for 2 h at 811 K (1000°F). During this exposure, the stress relaxed to approximately the yield stress at 811 K (1000°F).

The time and temperature of the exposure duplicated the stress relief heat treatment used during blade manufacture. The residual stresses in blades prior to heat treatment were not known. However, since the manufacturing process includes straightening operations and a significant amount of machining, it is felt that the induced residual stresses equal to the 811 K (1000°F) yield stress are not unlikely.

After exposure, the plate was notched at the salt spot and broken by a single rapid overload (hammer blow). The fracture surfaces then were examined visually and with the aid of a scanning electron microscope (SEM).

## Results

In order to distinguish the two fractured fan blades, they are referred to as A and B, respectively, in this paper. The results of their fracture analyses and the hot salt stress corrosion cracking test are as follows.

[6] Alpha case: brittle layer of alpha phase, stabilized by segregated interstitials, such as oxygen.

*Fan Blade A*

The airfoil of this fan blade was fractured at 16.51 cm (6½-in.) outboard of the platform. Near the fracture, several cracks were detectable along tool marks, parallel to the fracture, on the concave side of the inboard portion. The outboard portion was missing.

The fracture surface consisted of an area of subcritical crack growth in the mid portion and two separated areas of fast fracture on both sides (Fig. 2). The area of subcritical crack growth was flat, lenticular, about 3.81 cm (1½ in.) long; this area extended through the airfoil cross section in the middle. This area contained three semielliptic zones, discolored to blue, along the concave side, with a beach mark in the rest. The discolored zones were 0.18 cm (0.071 in.) long and 0.04 cm (0.015 in.) deep, 0.24 cm (0.096 in.) long and 0.05 cm (0.021 in.) deep, and 0.49 cm (0.192 in.) long and 0.05 cm (0.021 in.) deep. Both areas of fast fracture were slanted and had a relatively fine texture.

The SEM fractographs of the discolored zones exhibited predominantly intergranular and some interspersed cleavage facets with secondary cracks (Fig. 3). There was a discernible tendency towards more intergranular facets in the immediate vicinity of the concave side or the crack initiation site. Deeper in these zones, secondary cracks extended farther and diverged more. This observation of intergranular crack path and crack branching was confirmed by the optical micrographs of sections through the discolored zones (Fig. 4). Outside of these zones but within the subcritical crack growth area, the SEM and TEM fractographs showed mostly cleavage-like facets, some of which contained striations normal to the river lines (Fig. 5). However, near the transition to fast fracture area, a mixture of cleavage-like facets and dimples were observed (Fig. 6). The slanted area of fast fracture was completely covered with dimples, some of which were elongated (Fig. 7).

The largest of the cracks, detectable near the fracture on the concave side of the airfoil, was about 0.13 cm (0.050 in.) long. Its crack surface was discolored to blue, and the SEM fractograph displayed mostly intergranular and some interspersed cleavage facets with secondary cracks. The optical micrograph of a section through the crack also indicated intergranular and transgranular crack path and crack branching.

*Fan Blade B*

This fan blade airfoil had four fractures, and its tip was missing. One of the fractures was located at 3.81 cm (1½ in.) outboard of the platform, one branched out of the preceding one and off to the leading edge, and the other two at and just outboard of the midspan shroud. Only the fracture at 3.81 cm (1½ in.) outboard of the platform had an indication of subcritical crack growth and was believed to be the initial one. The others

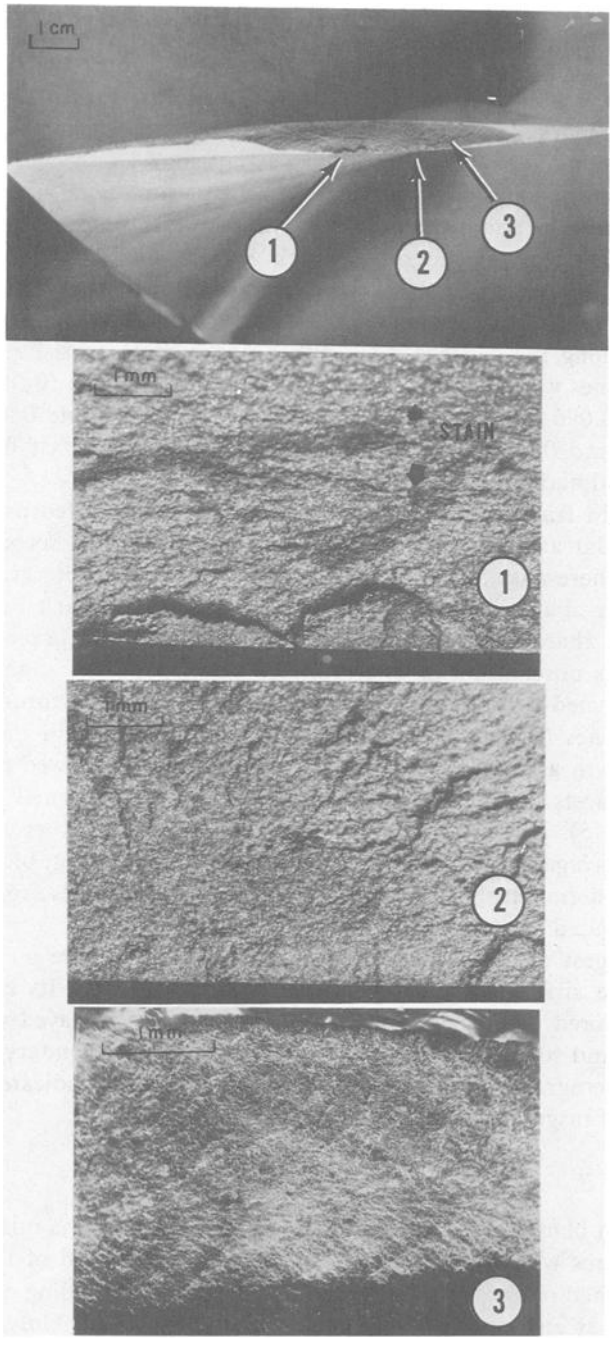


FIG. 2—*Fracture surface of Fan Blade A.*

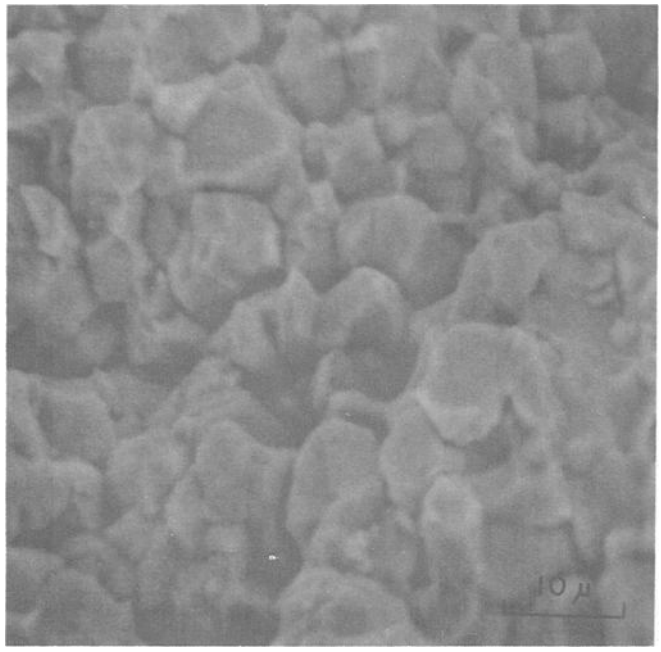


FIG. 3—*SEM fractograph of a discolored zone on the fracture surface of Fan Blade A.*

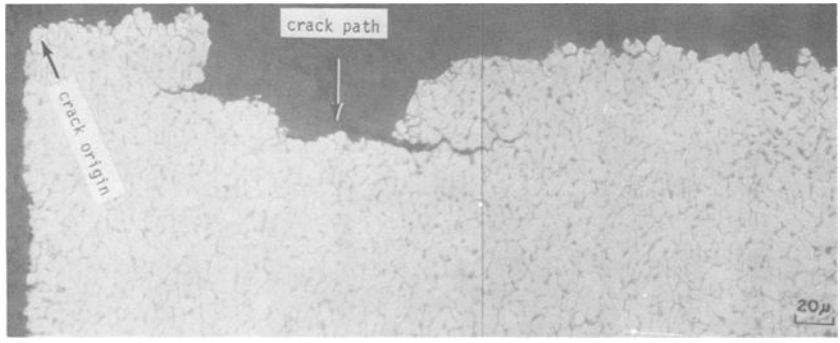


FIG. 4—*Optical micrograph of a section through a discolored zone on the fracture surface of Fan Blade A.*

appeared to have occurred as the outboard portion of the blade burst through the engine case.

The initial fracture surface consisted of a flat and lenticular mid portion and two slanted side portions (Fig. 8). In the flat portion, fracture lines converged to a point, the crack initiation site, 3.56 cm (1.4 in.) from the trailing edge on the concave side. Around the crack initiation site, a thumbnail-

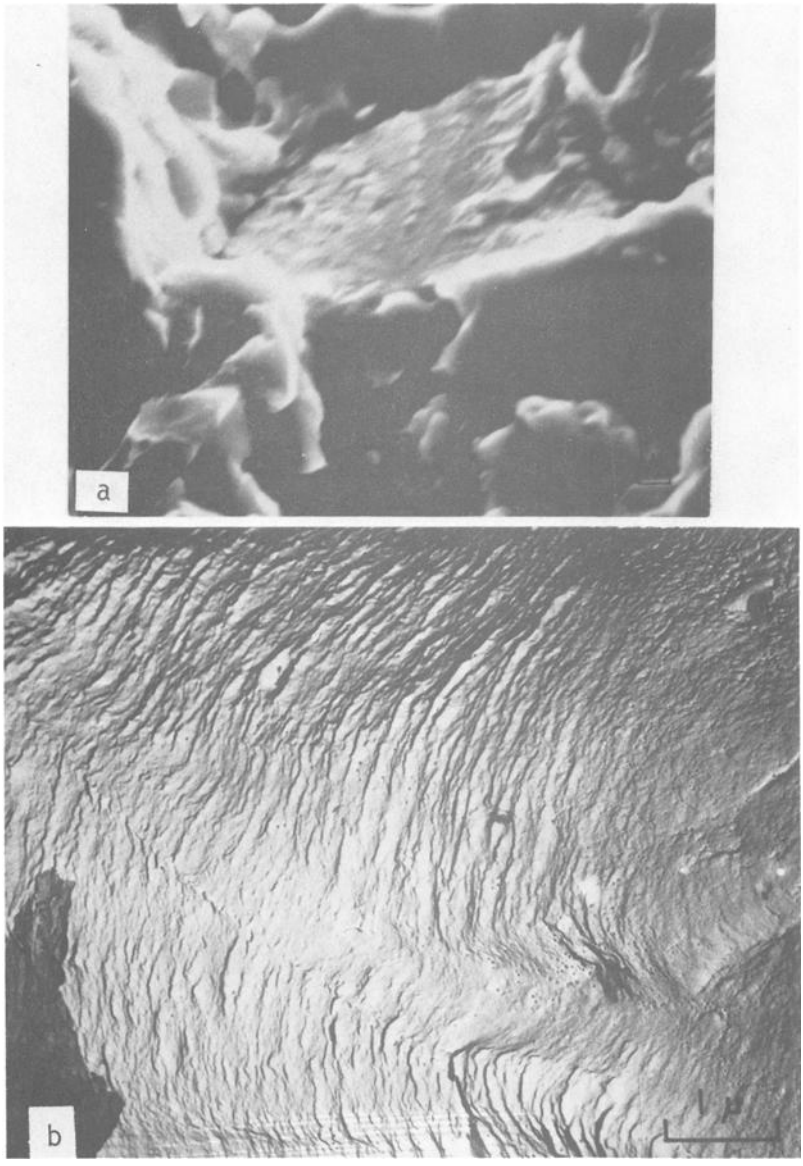


FIG. 5—*SEM and TEM fractographs outside of discolored zones in subcritical crack growth area of Fan Blade A*: (a) *SEM fractograph, and* (b) *TEM fractograph.*

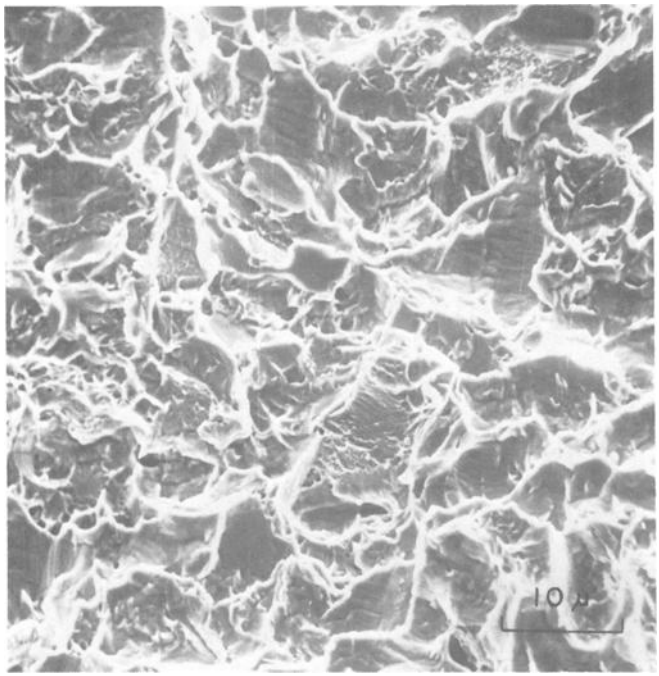


FIG. 6—*SEM fractograph near transition from subcritical crack growth to fast fracture in Fan Blade A.*

shaped area of subcritical crack growth, 1.78 cm (0.7 in.) long on the concave side and 0.38 cm (0.15 in.) deep, was discolored to white-gray. The rest of the flat portion displayed a rough texture, and the slanted side portions were typical shear lips with a relatively fine texture.

In the immediate vicinity of the crack initiation site, a mixture of intergranular and cleavage facets with some secondary cracks was found (Fig. 9). The intergranular and transgranular crack path and crack branching also were evidenced in the optical micrograph of a section through the fracture. In the remaining area of subcritical crack growth, the SEM fractograph exhibited mostly cleavage-like facets, some of which contained faint striations (Fig. 10). The presence of such striations was verified by the TEM fractograph (Fig. 11).

A blue etch anodizing of this blade indicated presence of alpha case by discoloring it to dark blue in an area on the concave side surrounding the main fracture. The alpha case was about 0.008 cm (0.003 in.) thick and had a Rockwell hardness C (HRC) 43, whereas that of the base metal was HRC 35. Within the area of alpha case, tight cracks, mostly parallel to the main fracture, were detectable. They were about 0.005 cm (0.002 in.) deep, and followed an intergranular and transgranular path, as shown in the optical micrograph (Fig. 12).

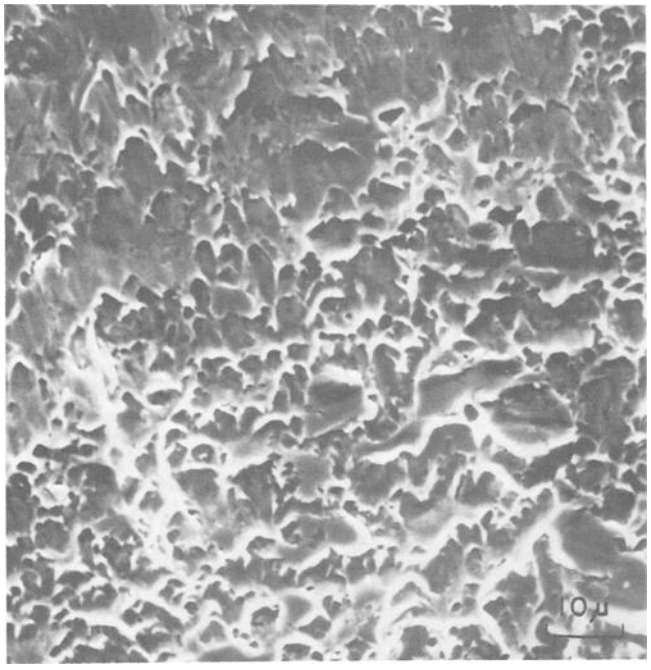


FIG. 7—*SEM fractograph of slanted area in fracture surface of Fan Blade A.*

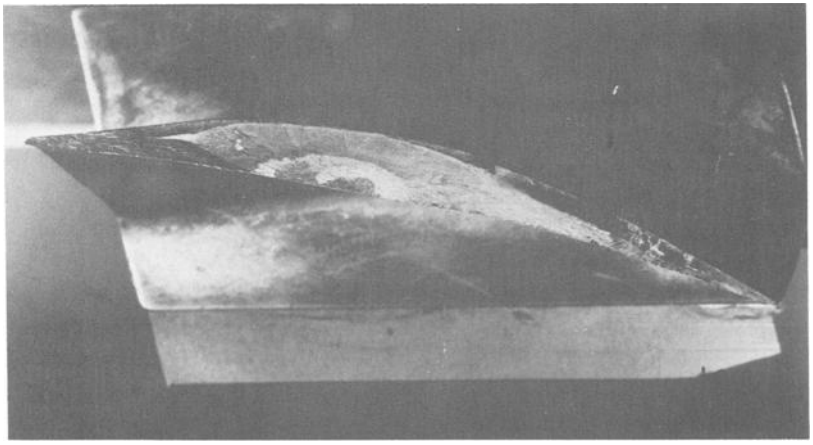

FIG. 8—*Fracture surface of Fan Blade B.*

### *Hot Salt Stress Corrosion Cracking of Ti-8Al-1Mo-1V Alloy Specimen*

Before it was broken, several cracks, 0.06 to 0.33 cm (0.022 to 0.129 in.) long, were visible and detectable with fluorescent penetrant in the area of

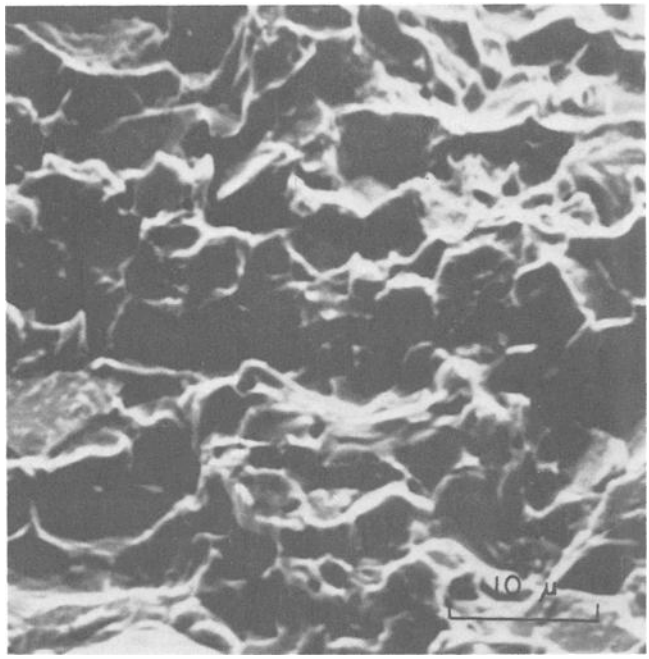


FIG. 9—*SEM fractograph near crack initiation site of Fan Blade B.*

hot salt application on the surface of the specimen. The fracture surface, which was contained in the area of the cracks, had two discolored and interconnected areas along the side exposed to salt (Fig. 13). The discoloration was dark blue in the initially cracked portion and brownish yellow in the rest. One of the areas was crescent-shaped, 0.55 cm (0.216 in.) long, and 0.14 cm (0.054 in.) deep. The other was elliptic, 0.23 cm (0.090 in.) long and 0.11 cm (0.045 in.) deep. The SEM fractographs of both areas show mostly intergranular and some interspersed cleavage facets with secondary cracks (Fig. 14). Those facets, in the dark blue portion, were covered with corrosion and oxidation products.

## Discussion

The area of subcritical crack growth was discolored partly to blue in Fan Blade A and totally to white-gray in Fan Blade B. In both blades, the discoloration was greater near the crack initiation site on the airfoil surface. Such a part or total discoloration of subcritical crack growth area indicates a prior exposure of the initial crack surface to elevated temperatures or a corrosive environment.

The common fractographic features of the subcritical crack growth areas were intergranular and cleavage facets with branched cracks at and near

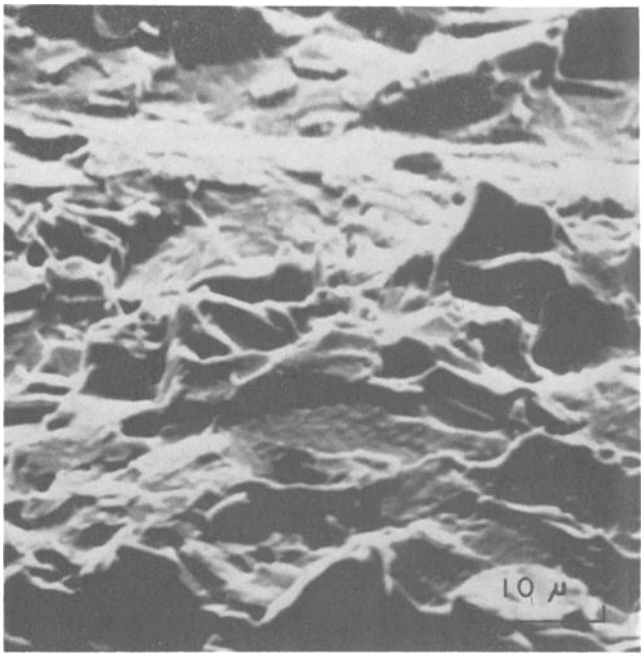


FIG. 10—*SEM fractograph away from crack initiation site in subcritical crack growth area of Fan Blade B.*

the crack initiation site, and cleavage-like facets with occasional striations away from it.

The observed crack initiation from external surface, greater discoloration near the crack initiation site, intergranular separation mixed with transgranular cleavage, and crack branching are typical of stress corrosion cracking in titanium alloys [*8,21*]. Considering the initial crack surface discoloration, the stress corrosion cracking evidently occurred at an elevated temperature in Fan Blade A and at ambient temperature in Fan Blade B. The small cracks, found near the fracture on the airfoil surface of each fan blade, had fractographic features similar to those at and near the fracture initiation site. The small cracks in Fan Blade A had discolored surfaces, intergranular and cleavage facets, and secondary cracks. Those in Fan Blade B followed intergranular and transgranular paths. These evidences suggest that the mechanism of those crackings was identical to the initial stage mechanism of the fracture, stress corrosion cracking at an elevated or ambient temperature.

The temperature of the fan blade does not exceed 389 K (240°F) during the engine operation. Therefore, the elevated temperature stress corrosion cracking of Fan Blade A must have occurred during the heat treatment. Its

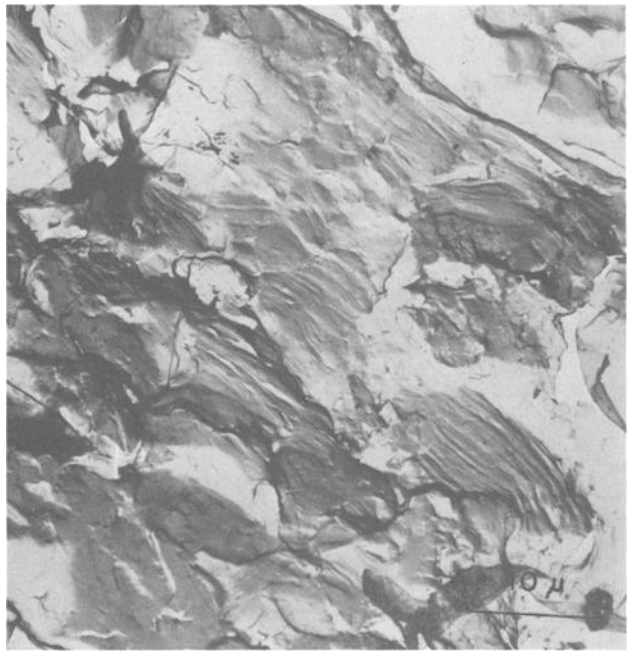

FIG. 11—*TEM fractograph away from crack initiation site in subcritical crack growth area of Fan Blade B.*

initiation site, a spot on the airfoil surface, was presumably contaminated by corrosive media such as moisture and salt from a fingerprint [*8*] and had residual stress induced during the manufacturing process. Similar crackings, discoloration, and fractographic features were reproduced by a hot salt stress corrosion cracking test of Ti-8Al-1Mo-1V alloy specimens.

In Fan Blade B, the origin of the initial fracture and adjacent small cracks were located within a patch of alpha case. The alpha case was confined to a surface layer of limited thickness, 0.008 cm (0.003 in.), and believed to have been formed by oxidation under the heat of excessive airfoil surface blending or sanding. The preferential initiation of stress corrosion cracks in such a patch of alpha case demonstrates its great susceptibility to stress corrosion cracking, arising from high oxygen concentration [*22*].

The mixture of intergranular separation and transgranular cleavage, found in both fan blades, is an evidence for an initial stress corrosion cracking at not very low crack growth velocity, $V$, and stress intensity factor, $K$. The mode of stress corrosion cracking is known to change from intergranular separation to transgranular cleavage with increasing $V$ and $K$, creating their mixture in the transition [*8*].

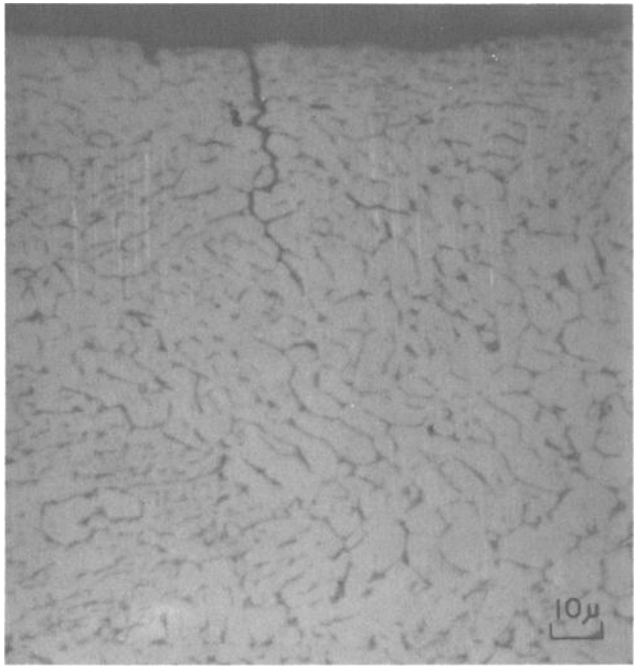


FIG. 12—*Crack in alpha case on Fan Blade B airfoil.*

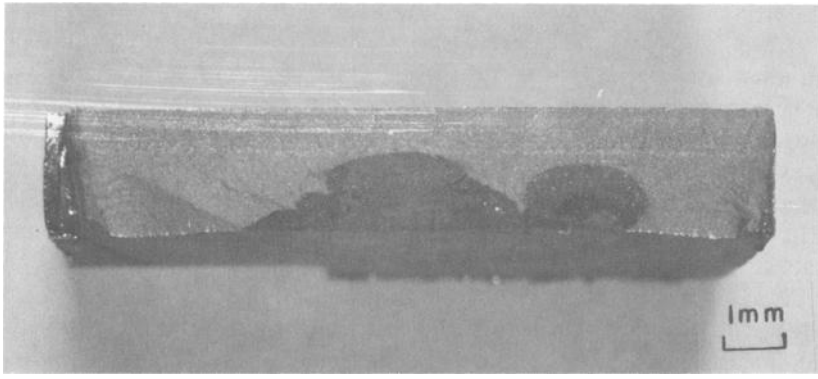


FIG. 13—*Fracture surface of hot salt stress corrosion cracking specimen.*

The observed cleavage-like facets with occasional striations are characteristic of fatigue at low $da/dn$ and small stress intensity factor range $\Delta K$ [*13,16*]. In Fan Blade A, those fractographic features were detectable in the undiscolored portion of the subcritical crack growth area, having a beach mark. This suggests a fatigue crack growth at ambient temperature during the engine operation. In Fan Blade B, those fractographic features were seen within the white-gray discolored area of subcritical crack growth.

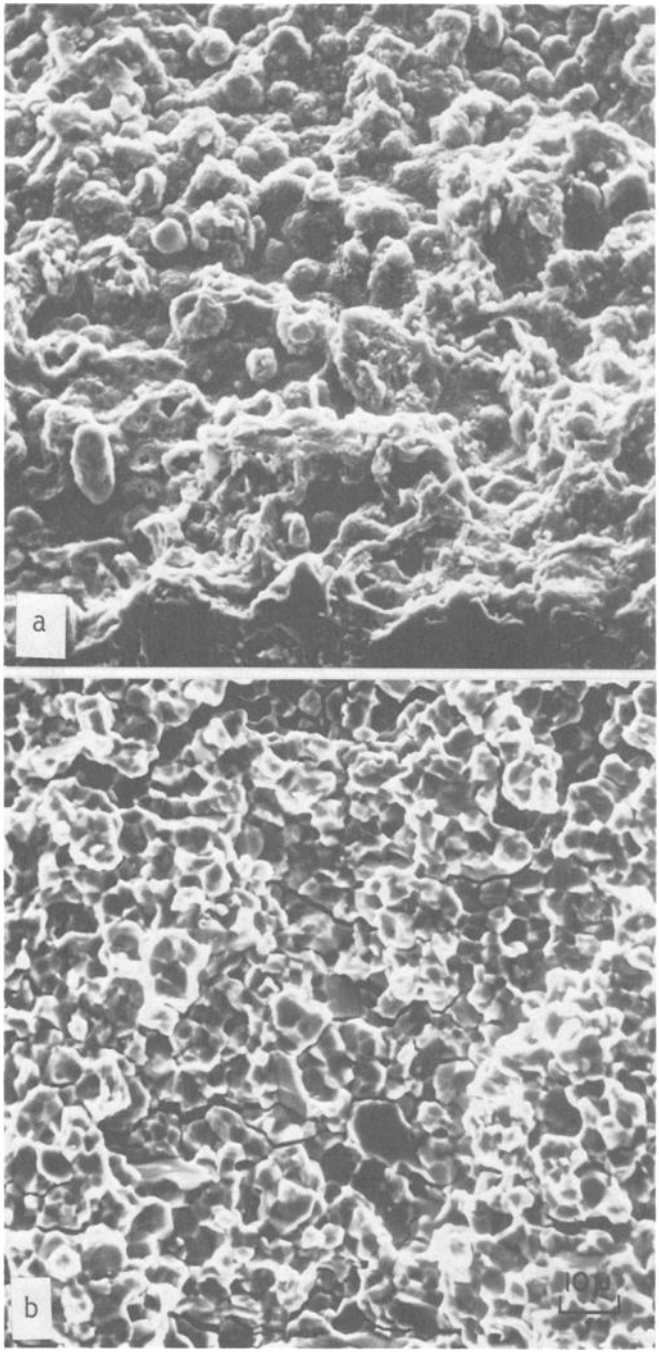


FIG. 14—*SEM fractograph of hot salt stress corrosion cracking specimen*: (a) *near crack initiation site, and* (b) *away from crack initiation site.*

This suggests possible acceleration of the fatigue crack growth by corrosion at ambient temperature during the engine operation.

The partial microvoid coalescence near the transition to fast fracture, seen in Fan Blade A, is similar to Hertzberg's observation of Ti-6Al-4V and other alloys, fatigued at high $da/dn$ and $\Delta K$ [*16*].

## Conclusion

On the basis of the fracture analysis results and discussion, the following conclusions may be drawn.

1. The initial subcritical crack growth was characterized by intergranular separation, transgranular cleavage, and crack branching. Its mechanism was stress corrosion cracking at an elevated temperature in one fan blade and at ambient temperature in the other.

2. The subsequent subcritical crack growth was characterized by cleavage-like faceting. Its mechanism was ambient temperature fatigue, which was possibly accelerated by corrosion in one fan blade.

## References

[*1*] Meyn, D. A. and Sandoz, G., *Transactions,* The Metallurgical Society of the American Institute of Mining, Metallurgical, and Petroleum Engineers, Vol. 245, 1965, p. 1253.

[*2*] Beck, T. R., "Stress-Corrosion Cracking of Titanium Alloys, Preliminary Report on Ti-8Al-1Mo-1V Alloy and Proposed Electrochemical Mechanism," Boeing Document No. DI-82-0554, The Boeing Company, Seattle, Wash., July 1965.

[*3*] MacKay, T. L., Gilpin, C. B., and Tiner, N. A., "Stress-Corrosion Cracking of Titanium Alloys at Ambient Temperatures in Aqueous Solutions," Contract NAS 7-488, Report SM-49105-Fl, McDonnell Douglas Corporation, Santa Monica, Calif., July 1967.

[*4*] Piper, D. E., Smith, S. H., and Carter, R. V., *Metals Engineering Quarterly,* Vol. 8, 1968, p. 50.

[*5*] Fager, D. N. and Spurr, W. F., *Transactions,* American Society for Metals, Vol. 61, 1968, p. 283.

[*6*] Sandoz, G. in *Proceedings of Conference on Fundamental Aspects of Stress Corrosion Cracking,* R. W. Staehle et al, Eds., National Association of Corrosion Engineering, Houston, Tex., 1969, p. 684.

[*7*] Beck, T. R., Blackburn, M. J., Smyrl, W. H., and Speidel, M. O., "Stress Corrosion Cracking of Titanium Alloys: Electrochemical Kinetics, SCC Studies with Ti: 8-1-1, SCC and Polarization Curves in Molten Salts, Liquid Metal Embrittlement, and SCC Studies with Other Titanium Alloys," Contract NAS 7-489, Quarterly Progress Report 14, The Boeing Company, Seattle, Wash., Dec. 1969.

[*8*] Blackburn, M. J., Smyrl, W. H., and Feeney, J. A. in *Stress-Corrosion Cracking in High Strength Steels and in Titanium and Aluminum Alloys,* B. F. Brown, Ed., Naval Research Laboratory, Washington, D.C. 1972, p. 245.

[*9*] Boyd, J. D., *Metallurgical Transactions,* Vol. 4, 1973, p. 1029.

[*10*] Boyd, J. D., *Metallurgical Transactions,* Vol. 4, 1973, p. 1037.

[*11*] Meyn, D. A., *Metallurgical Transactions,* Vol. 2, 1971, p. 853.

[*12*] Irving, P. E. and Beevers, C. J., *Metallurgical Transactions,* Vol. 5, 1974, p. 391.

[*13*] Yuen, A., Hopkins, S. W., Leverant, G. R., and Rau, C. A., *Metallurgical Transactions,* Vol. 5, 1974, p. 1833.

[*14*] Bowen, A. W., *Acta Metallurgica,* Vol. 23, 1975, p. 1401.

[*15*] Neal, D. F. and Blenkinsop, P. A., *Acta Metallurgica,* Vol. 24, 1976, p. 59.

[16] Hertzberg, R. W. and Mills, W. J. in *Fractography—Microscopic Cracking Processes, ASTM STP 600,* American Society for Testing and Materials, 1976, p. 220.

[17] Cullen, W. H. and Stonesifer, F. R., "Fatigue-Crack-Growth Analysis of Titanium Gas-Turbine Fan Blades," NRL Memorandum Report 3378, Naval Research Laboratory, Washington, D.C., Oct. 1976.

[18] Yoder, G. R., Cooley, L. A., and Crooker, T. W., "A Micromechanistic Interpretation of Cyclic Crack-Growth Behavior in a Beta-Annealed Ti-6Al-4V Alloy," NRL Report 8048, Naval Research Laboratory, Washington, D.C., Nov. 1976.

[19] Yoder, G. R., Cooley, L. A., and Crooker, T. W., "Enhancement of Fatigue Crack Growth and Fracture Resistance in Ti-6Al-4V and Ti-6Al-6V-2Sn through Microstructural Modification," NRL Report 8049, Naval Research Laboratory, Washington, D.C., Nov. 1976.

[20] Vicki, F. J. in *Titanium Science and Technology,* R. I. Jaffee and H. M. Burte, Eds., Plenum Press, New York, Vol. 1, 1973, p. 733.

[21] *Metals Handbook,* 8th ed., Vol. 9, American Society for Metals, Metals Park, Ohio, 1974, p. 90.

[22] Seagle, S. R., Seeley, R. R., and Hall, G. S. in *Applications Related Phenomena in Titanium Alloys, ASTM STP 432,* American Society for Testing and Materials, 1968, p. 170.

*Susumu Hioki*[1] *and Yoshihiko Mukai*[2]

# Effect of the Cyclic Rate on Corrosion Fatigue and Fractography of Type 304 Stainless Steel in Boiling 42 Percent Magnesium-Chloride Solution

**REFERENCE:** Hioki, Susumu and Mukai, Yoshihiko, **"Effect of the Cyclic Rate on Corrosion Fatigue and Fractography of Type 304 Stainless Steel in Boiling 42 Percent Magnesium-Chloride Solution,"** *Fractography in Failure Analysis, ASTM STP 645,* B. M. Strauss and W. H. Cullen, Jr., Eds., American Society for Testing and Materials, 1978, pp. 144-163.

**ABSTRACT:** Corrosion fatigue tests of Type 304 stainless steel were conducted at various cyclic rates between 0 and $10^4$ rpm in boiling 42 percent magnesium-chloride ($MgCl_2$) solution in rotating bending. As a result, the following conclusions were obtained: (*a*) the cyclic rate affects the failure life at the cyclic rates less than $10^3$ rpm, (*b*) the rate of crack propagation, $da/dn$, is proportional to the maximum stress intensity factor, $K_{max}$, that is, $da/dn = C \cdot K_{max}^m$, where $C$ and $m$ depend on the cyclic rate, (*c*) the fracture surfaces at higher cyclic rates and static loading were mostly of the transgranular type, that is, step pattern and striation, but the intergranular type was observed partly on the fracture surfaces at lower cyclic rates. Intergranular type fracture surface was observed most frequently at 1 rpm.

**KEY WORDS:** corrosion fatigue, stress corrosion, cyclic rate, Type 304 stainless steel, rotating bending, fractography

The resistance to the environmentally assisted fracture has been discussed as two big independent problems, that is, stress corrosion cracking (SCC) and corrosion fatigue [*1-3*].[3] However, considering the actual environment, stress cycling, and materials used in products, many strength members are simultaneously subjected to SCC and corrosion fatigue. A few works have been devoted to elucidate the general properties and the mechanism of simultaneously occurring SCC and corrosion fatigue [*3*]. The effect of cyclic rate of applied stress seems to be essential for both damages

[1]Doctor of Engineering, Mechanical Engineering Research Laboratory, Hitachi, Ltd., Ibaraki 300, Japan.
[2]Doctor and professor, Faculty of Engineering, Osaka University, Osaka 565, Japan.
[3]The italic numbers in brackets refer to the list of references appended to this paper.

for the combination of a certain material and environment. In this paper, the effect of cyclic rate on corrosion fatigue of Type 304 stainless steel in boiling 42 percent magnesium chloride ($MgCl_2$) solution was reported.

## Experimental Procedure

### *Testing Apparatus and Method*

The testing apparatus used in this study consisted of a rotary-bending fatigue testing machine and a bath containing corrosive media as shown in Fig. 1. The cyclic rate could be varied up to $10^4$ rpm.

The corrosion bath was able to contain a 70-mm-long notched specimen dipped in boiling 42 percent $MgCl_2$ solution. The leakage of the solution through the gap between bath and rotary specimen was prevented by oilless seals. The temperature and concentration of solution were kept constant at 143 °C and 42 percent, respectively, by a heater and a condenser.

Corrosion-fatigue testing and fatigue testing in air at 143 °C were done using the apparatus just mentioned. In the case of the latter, the specimen was covered by a glass tube in order to prevent environmental attack.

### *Material and Specimen*

The specimens shown in Fig. 2 were machined from Type 304 stainless steel sheet and solution heat treated for 2 h at 1100 °C, followed by water

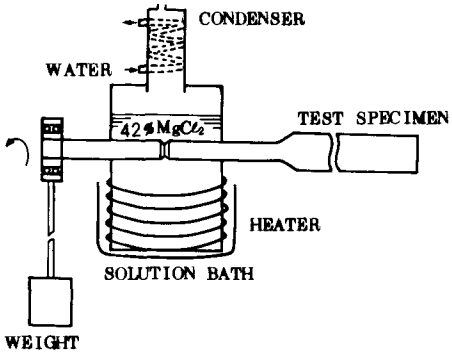


FIG. 1—*Illustration of the testing apparatus.*

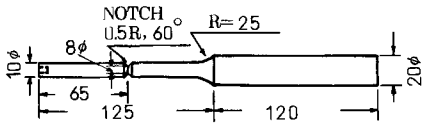


FIG. 2—*Specimen dimensions in millimetres (stress concentration factor of the notch,* $k_t$ = *2.3).*

quenching. The chemical compositions and mechanical properties are given in Table 1.

*Measurement of Crack Length by the Electric Resistance*

In order to measure the crack length at an arbitrary number of cycles during testing, the electric resistance was measured with Type 304 stainless steel rods between both ends of the notch of the specimen at room temperature, removing load and corrosive media, which were given by a current of 5 ± 0.2 A through both ends of the specimen, as shown in Fig. 3. Therefore, no effects of corrosive media were assumed to exist on the measurement of crack length.

The calibration curve for crack length and electric resistance is shown in Fig. 4. It was obtained by measuring the crack length and the resistance of several cracked specimens by rotary-bending fatigue in air and corrosive

TABLE 1—*Mechanical properties and chemical compositions of Type 304 stainless steel tested.*

| | Chemical Composition, weight % | | | | | | |
|---|---|---|---|---|---|---|---|
| Material | C | Si | Mn | P | S | Cr | Ni |
| Type 304 stainless steel | 0.076 | 0.85 | 1.15 | 0.020 | 0.012 | 18.35 | 9.2 |
| | Mechanical Properties (at 143°C) | | | | | | |
| 0.2% Proof Stress | Tensile Strength | | | Elongation, (gage length = 25 mm)% | | | |
| 137.3 N/mm$^2$ | 423.6 N/mm$^2$ | | | 71.0 | | | |

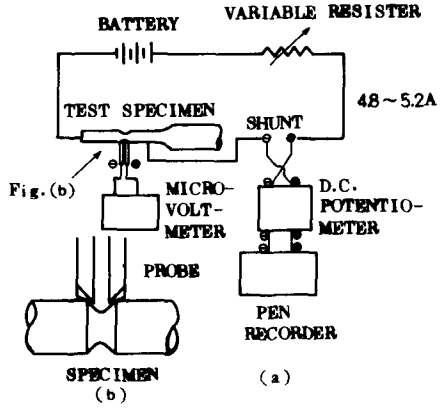


FIG. 3—*Circuit for measurement of crack length electric resistance.*

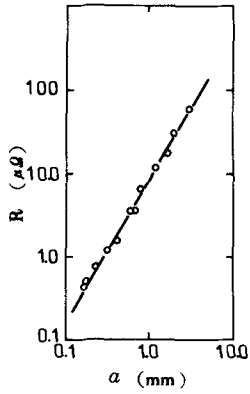


FIG. 4—*Calibration curve for crack length,* a, *and electric resistance,* R.

media, 42 percent $MgCl_2$ solution. The crack length of the specimen was obtained by measuring the temper colored part in 30-min heating at 600°C, during which time the specimen stopped testing at an arbitrary number of cycles, that is, crack length. Considering the measuring method and the results, the error of calibration curve seemed to be just reaching one, only 0.02 mm in this experiment. The contact resistance and the probable existence of $MgCl_2$ solution at the crack tip, etc., had no effect on the data.

### *Stress Intensity Factor* K *of a Circumferentially Cracked Rotating Round Bar*

Some analyses of stress intensity factor, $K$, of a rotating round bar are given [*4*] in the following equation

$$K = \sqrt{\pi r a/(0.8r + 7.1a)} \times \sigma_{net} \tag{1}$$

where

$r$ = the distance between the crack tip and the center of the specimen,
$a$ = crack length, and
$\sigma_{net}$ = net stress for actual cross section.

However, the effect of crack closure in the compression side is not considered in this analysis. So, the authors derived the following equation from Eq 1 on the assumption that the cross section of a circle of $(2r + a)$ diameter would resist to bending moment

$$K = 8 \times \sqrt{\frac{(2r + a)(t + a)}{0.8(2r + a) + 14.2(t + a)}} \times \left(\frac{r + a}{2r + a}\right)^3 \sigma_{gross} \tag{2}$$

where

$t$ = depth of notch, and
$\sigma_{gross}$ = gross stress for the original cross section.

The bending stress, $\sigma_N$, at the notch root has been used to describe the experimental results in this paper.

## Experimental Results

### *Testing Results of Fatigue in Air and of Stress Corrosion Cracking in Static Bending*

Fatigue tests in air were done at room temperature and 143°C for the cyclic rates of 1.5, 10, and $10^3$ rpm. The results are shown in Fig. 5 and fatigue life appears to be shorter at 143°C than at room temperature.

Stress corrosion cracking testing was conducted in static bending using the corrosion fatigue testing apparatus, at a cyclic rate of 0 rpm. The results are shown in Fig. 6 and the threshold stress of SCC was 147 N/mm$^2$.

The testing stresses, 147, 196, and 245 N/mm$^2$, were selected for the corrosion-fatigue testing based on the results just mentioned.

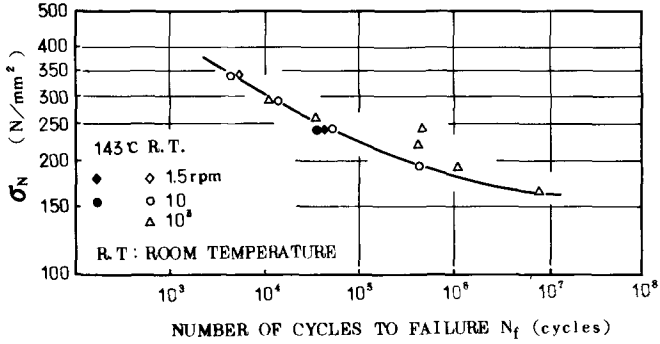


FIG. 5—*Fatigue strength of Type 304 stainless steel in air.*

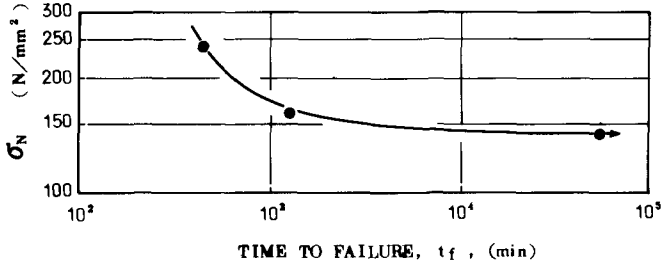


FIG. 6—*Results of SCC of Type 304 stainless steel in 42 percent $MgCl_2$ under static bending.*

*Results of Corrosion-Fatigue Tests*

The results of corrosion fatigue at cyclic rates between $10^{-4}$ and $10^{4}$ rpm are shown as the relation between the number of cycles to fatigue, $N_f$, and the applied stress, $\sigma_N$, in Fig. 7.

The effect of cyclic rate can be demonstrated by plotting the number of cycles against the cyclic rate as shown in Fig. 8. It can be seen that at the cyclic rates lower than $10^{3}$ rpm, the number of cycles to failure decreased as the cyclic rate decreased. This suggests that the cyclic rate is effective on the life of corrosion fatigue at these cyclic rates, which would provide enough time for the material to be subjected to environmental attack. But,

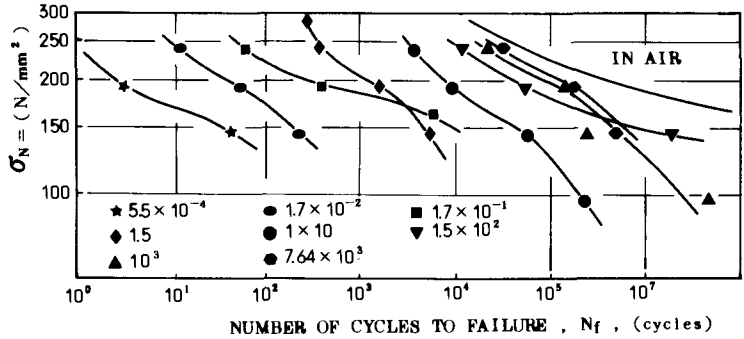


FIG. 7—*Results of corrosion fatigue of Type 304 stainless steel in 42 percent $MgCl_2$ in rotating bending* ($N_f - \sigma_N$ *curve*).

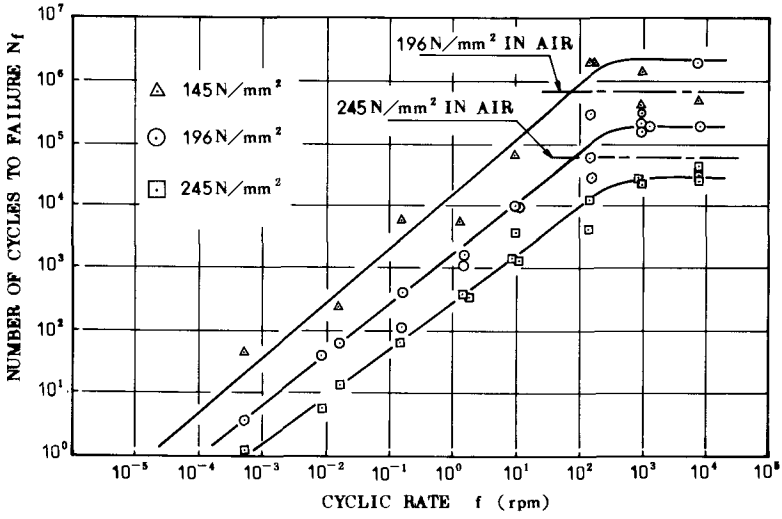


FIG. 8—*Relation between number of cycles to failure, $N_f$, and cyclic rate, f.*

the number of cycles to failure become constant at the cyclic rates higher than $10^3$ rpm, which is slightly less than the life in air, indicating that the reduction of life due to environmental attack becomes constant.

### *Effect of Cyclic Rate on the Crack Initiation Life and Propagation Properties*

The behavior of crack initiation and propagation was studied by the electric-resistance method in order to clarify the effect of cyclic rate. Some of the test results are shown as the relation between number of cycles, $n$, crack length, $a$, and the resistance, $R$, in Fig. 9.

The effect of cyclic rate is shown as the relation between cyclic rate, $f$, and the number of cycles to crack initiation, $N_i$, in Fig. 10 on the assumption that $N_i$ is at the number of cycles when a crack of 0.2 mm long is found, as there is no significant difference between the onset of the first crack and a 0.2-mm-long crack.

As shown in these figures, $N_i$ increased as the cyclic rate increased. However, $N_i$ would saturate to the value of SCC at a very slow cyclic rate. At cyclic rates higher than $1.6 \times 10^{-3}$ rpm, $N_i$ can be expressed as

$$N_i = A \cdot f^{0.73} \tag{3}$$

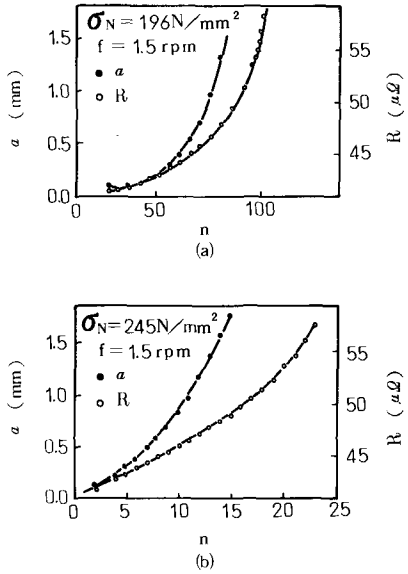


FIG. 9—*Examples of the relation between crack length, electrical resistance, and number of cycles.*

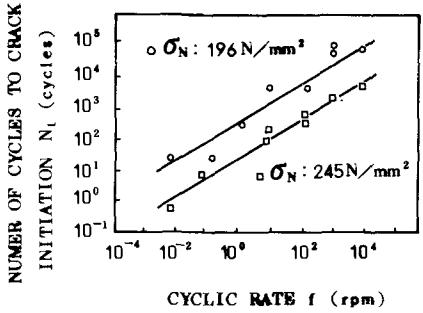


FIG. 10—*Relation between number of cycles to crack initiation,* $N_i$, *and cyclic rate,* f.

where

$N_i$ = number of cycles to initiation of crack,
$f$ = cyclic rate, and
$A$ = constant related to the applied stress, which is 730 for a stress of 196 N/mm² and 52.7 for 245 N/mm².

As the time to initiation of crack $t_i$ is equal to $N_i/f$, $t_i$ can be expressed as follows

$$t_i = A \cdot f^{-0.27} \tag{4}$$

where $t_i$ = time to initiation of crack.

The behavior of crack propagation may be discussed in terms of the relation between the cyclic rate, $f$, the rate of crack propagation, $da/dn$, and stress intensity factor, $K_{max}$, as shown in Fig. 11. In this figure, the rate of crack propagation is determined by the relation

$$(a_s - a_{s-1})/(n_s - n_{s-1})$$

where $a_q$ is crack length at number of cycles, $n_q$, of which data were shown in Fig. 10, for examples. The rate of crack propagation increased abruptly at a small $K_{max}$ value, indicating a rapid crack propagation just after the initiation. This phenomena would be affected by the stress concentration of the notch. After that, the rate of crack propagation would be described as a function of $K_{max}$ in the following equation

$$da/dn = C \cdot K_{max}{}^m \tag{5}$$

where

$da/dn$ = the rate of crack propagation,
$K_{max}$ = stress intensity factor, and

$C$, $m$ = constants affected by the cyclic rate, $f$, where

$$C = 2.6 \times 10^{-8} \times f^{-0.92}$$

and

$$m = 4.8 \times 10^{-2} \times f^{7.0}$$

*Effect of Cyclic Rate on Fractography*

The effect of cyclic rate on the fractography was studied. No distinctive features of the fracture surface of corrosion-fatigued specimens were observed by naked eyes. However, various distinctive features of the fracture surface were clarified by the continuous observation from the notch root to the center of fracture surface by scanning electron microscopy. For ex-

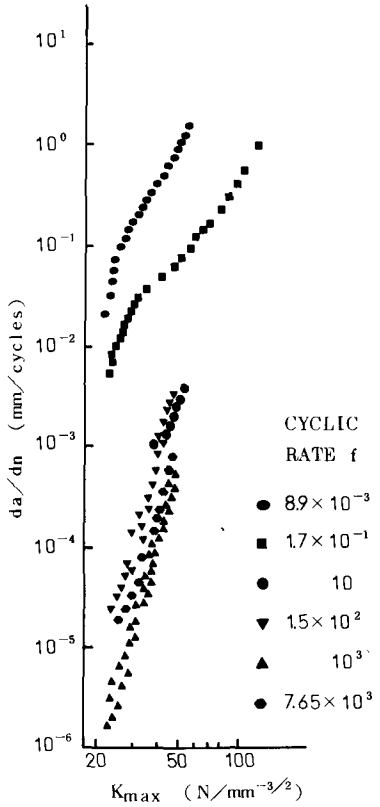


FIG. 11—*Relation between rate of crack propagation rate,* da/dn, *stress intensity factor,* $K_{max}$, *and cyclic rate,* f.

ample, typical fractographs of a corrosion-fatigued specimen at the stress level, $\sigma_N$ = 245 N/mm$^2$, will be shown for the various cyclic rate, as follows.

At the cyclic rate $f$ = 0 rpm, that is, at static loading, typical $f$ features of fracture surface of SCC are shown as a continuous photograph from the notch root to the crack length $a \simeq 0.8$ mm in Fig. 12. No differences were observed in the features from notch root to the center of the specimen. In the figure, the fan-like pattern and the step pattern along the fracture direction are shown and the transgranular fracture was subjected to the fracture surface. These facts were the same results as in previous works [5].

At the cyclic rate $f$ = 0.165 rpm, the fractographic features of a corrosion-fatigued specimen were as follows: similar features to the static SCC were observed from the notch root to the crack length $a \simeq 2.3$ mm as shown in Fig. 13($a$), for example. On the region of the crack length longer than 2.3 mm, intergranular fracture surface was observed as shown in Fig. 13($b$). In these regions, fan-like patterns were partly observed on one grain site.

At the cyclic rate $f$ = 1.5 rpm, the fractographic features had three types of features. Fan-like patterns were observed from the notch root to the crack length $a \simeq 1.2$ mm, as shown in Fig. 14($a$). On the region of crack length, $a$ = 1.2 to 2.0 mm, striations were observed, as shown in Fig. 14($b$).

At the cyclic rate $f$ = 10 rpm, the fractographic features were almost similar to that at $f$ = 1.5 rpm. The transition points were $a \simeq 1.6$ mm from fan-like pattern to striations, and $a \simeq 2.8$ mm from striations to rock candies. Typical striations, partly observed rock candy and dimple pattern, are shown in Fig. 15($a$), ($b$), and ($c$), respectively.

At the cyclic rate $f$ = 150 rpm, the fractographic features were as follows: on the near region of notch root, transgranular fracture surface accompanied with fan-like pattern and ill-defined striations were observed, as shown in Fig. 16($a$). On the region of the crack length $a \simeq 0.9$ to 2.4 mm, well defined striations were observed, as shown in Fig. 16($b$). The dimple patterns were observed on the crack longer than 2.4 mm.

At the cyclic rate $f$ = $10^3$ rpm, the fractographic features were almost similar to the features at $f$ = 150 rpm. On the near region of notch root, transgranular fracture surface accompanied with fan-like pattern and ill-defined striations were observed as shown in Fig. 17($a$). On the region of the crack length $a \simeq 0.7$ to 2.1 mm, well defined striations were observed in Fig. 17($b$) and at final stage, a dimple pattern was observed, as shown in Fig. 17($c$).

The facts just mentioned are summarized as follows: ($a$) at static SCC, transgranular fracture with a fan-like pattern was subjective, ($b$) at lower cyclic rate, a simple transition phenomenon from transgranular fracture to intergranular fracture was observed, ($c$) at medium cyclic rate, two transition phenomena, that is, from fan-like pattern to striations and from striations to rock candies were observed, and ($d$) at higher cyclic rate, tran-

FIG. 12—*Electron micrograph of the fracture surface of SCC at* $\sigma_N = 245\ N/mm^2$ *(scale mark indicates 0.05 mm).*

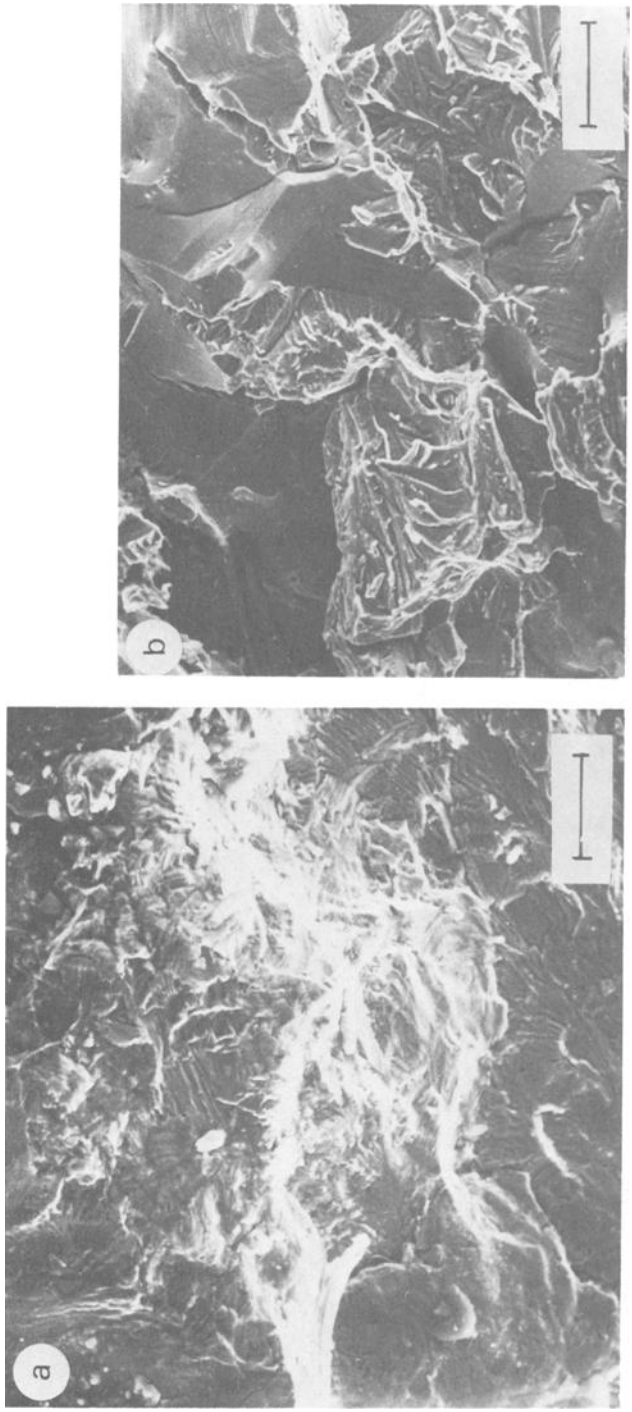


FIG. 13—*Electron micrograph of the fracture surface of corrosion fatigue at* $\sigma_N = 245\ N/mm^2$ *and* $f = 0.156$ *rpm (scale mark indicates 0.05 mm).* (a) $a \simeq 0.6$ *mm and* (b) $a \simeq 2.9$ *mm.*

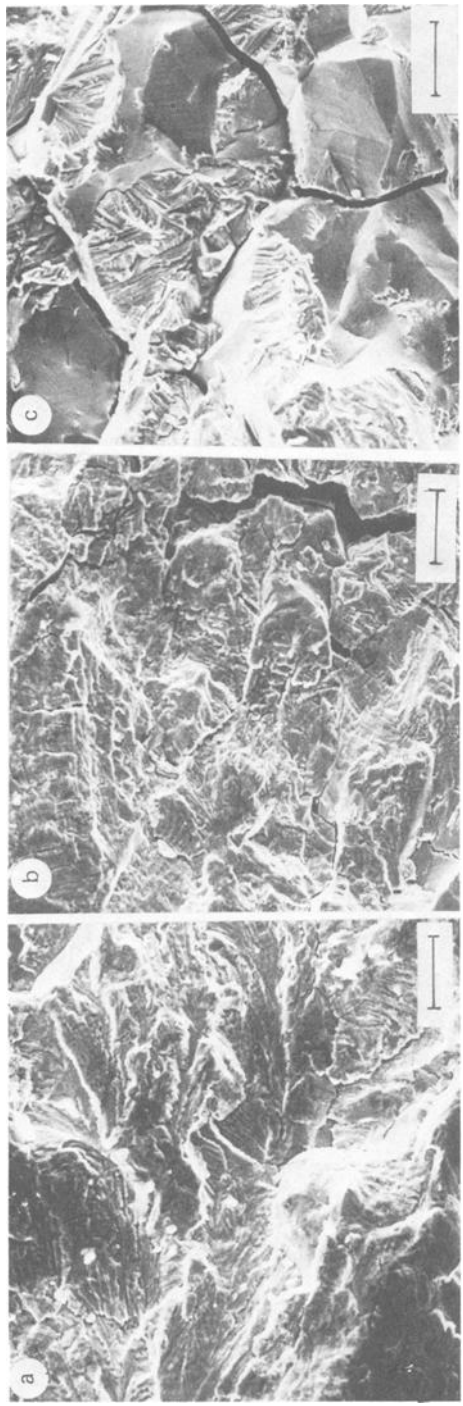


FIG. 14—*Electron micrograph of the fracture surface of corrosion fatigue at* $\sigma_N$ = 245 $N/mm^2$ *and* f = 1.5 *rpm (scale mark indicates 0.05 mm). (a)* a ≃ 0.9 *mm, (b)* a ≃ 1.8 *mm, and (c)* a ≃ 2.9 *mm.*


FIG. 15—*Electron micrograph of the fracture surface of corrosion fatigue at* $\sigma_N$ = 245 $N/mm^2$ *and 10 rpm (scale mark indicates 0.05 mm). (a) 1.8 mm* < a < *2.5 mm, (b)* a ≃ *3.1 mm, and (c)* a ≃ *3.7 mm.*

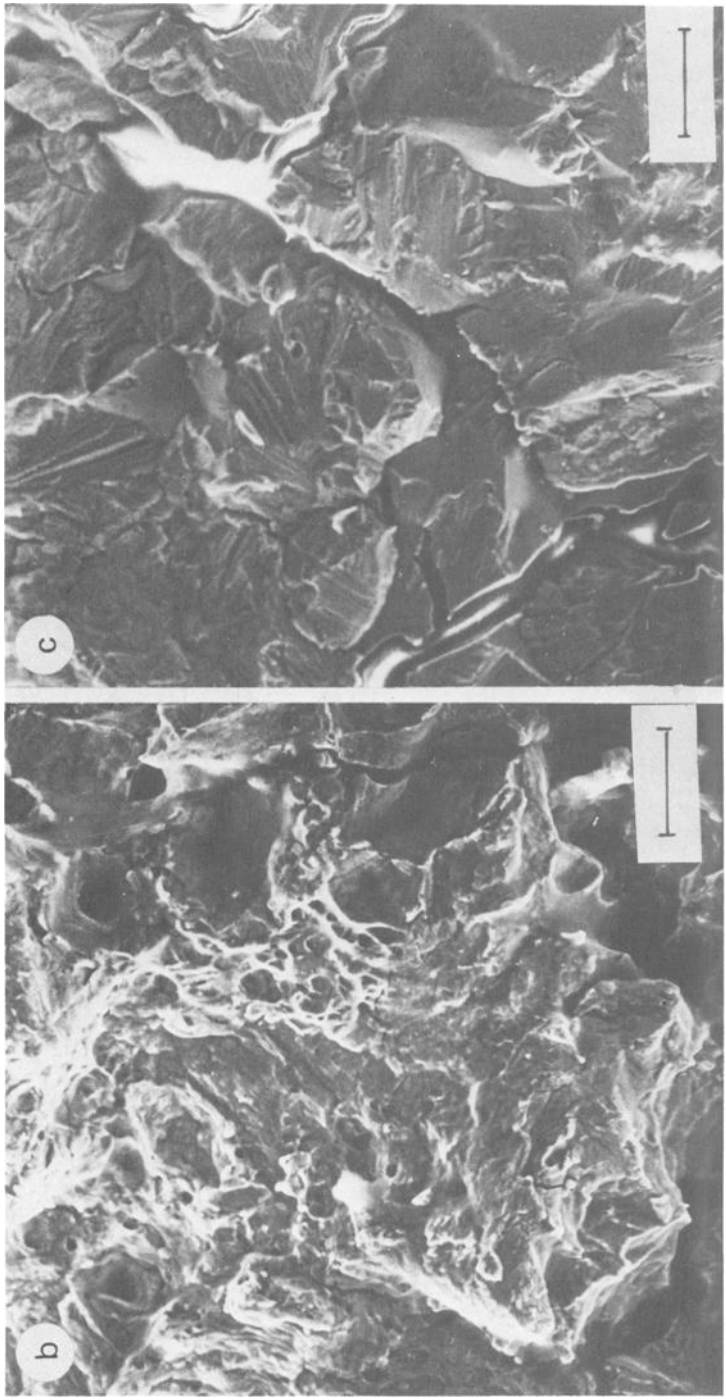


FIG. 15—*Continued.*

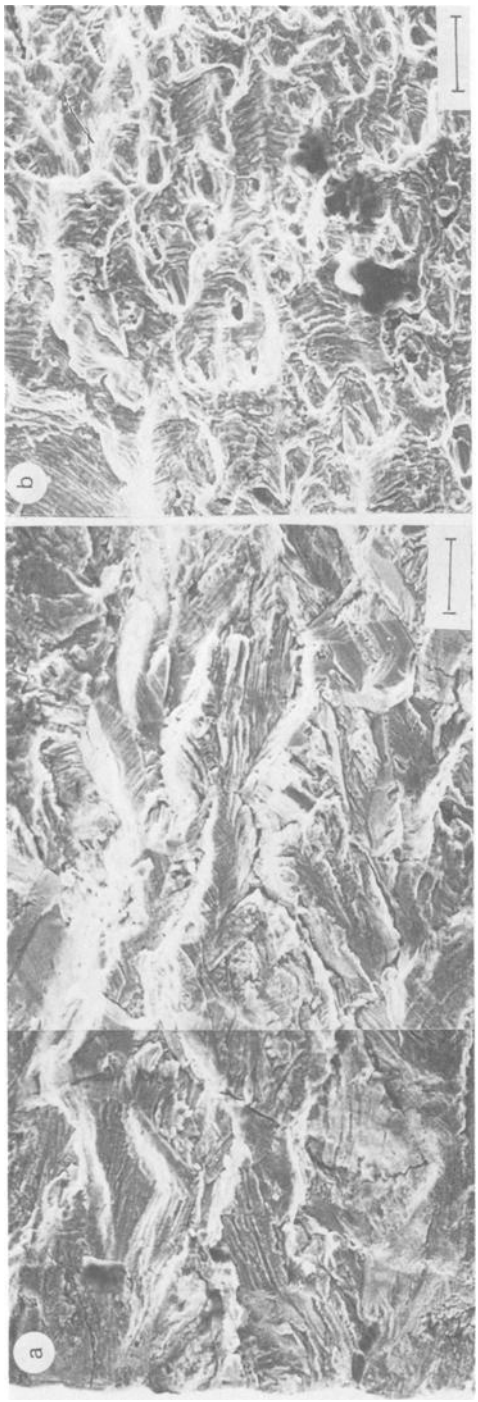


FIG. 16—*Electron micrograph of the fracture surface of corrosion fatigue at* N = 245 $N/mm^2$ *and* f = 150 *rpm (scale mark indicates 0.05 mm). (a)* 0 *mm* < a < 0.56 *mm, and* (b) a ≅ 2.1 *mm.*

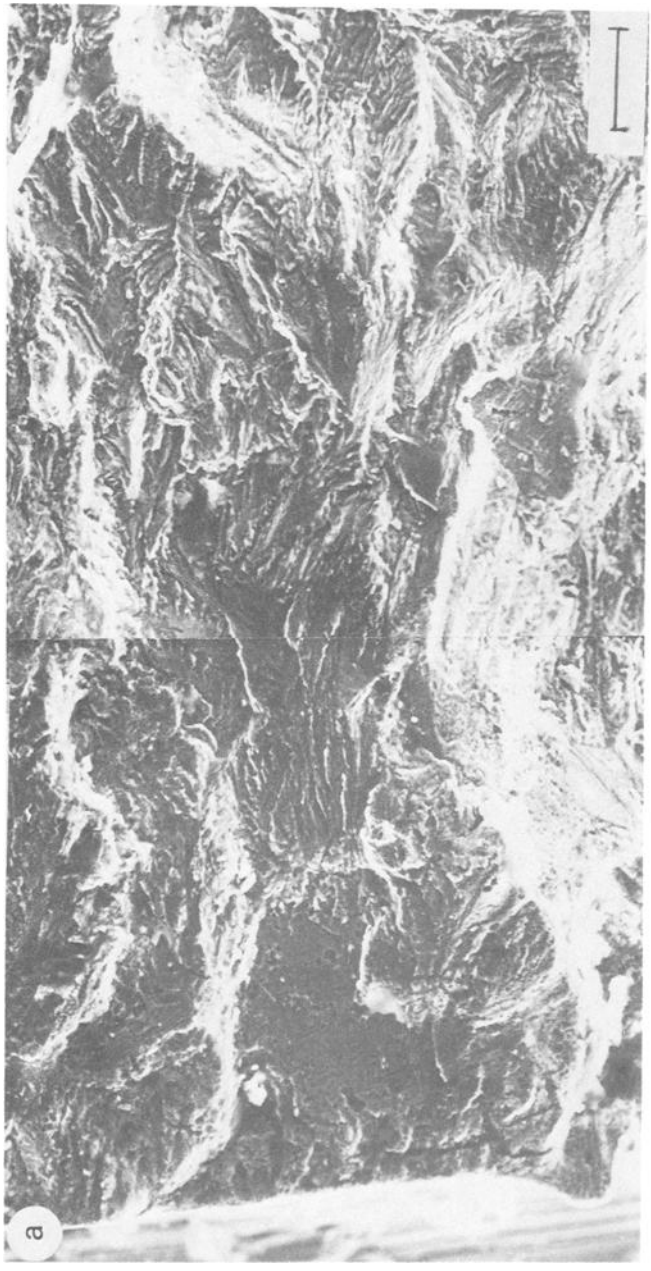
a

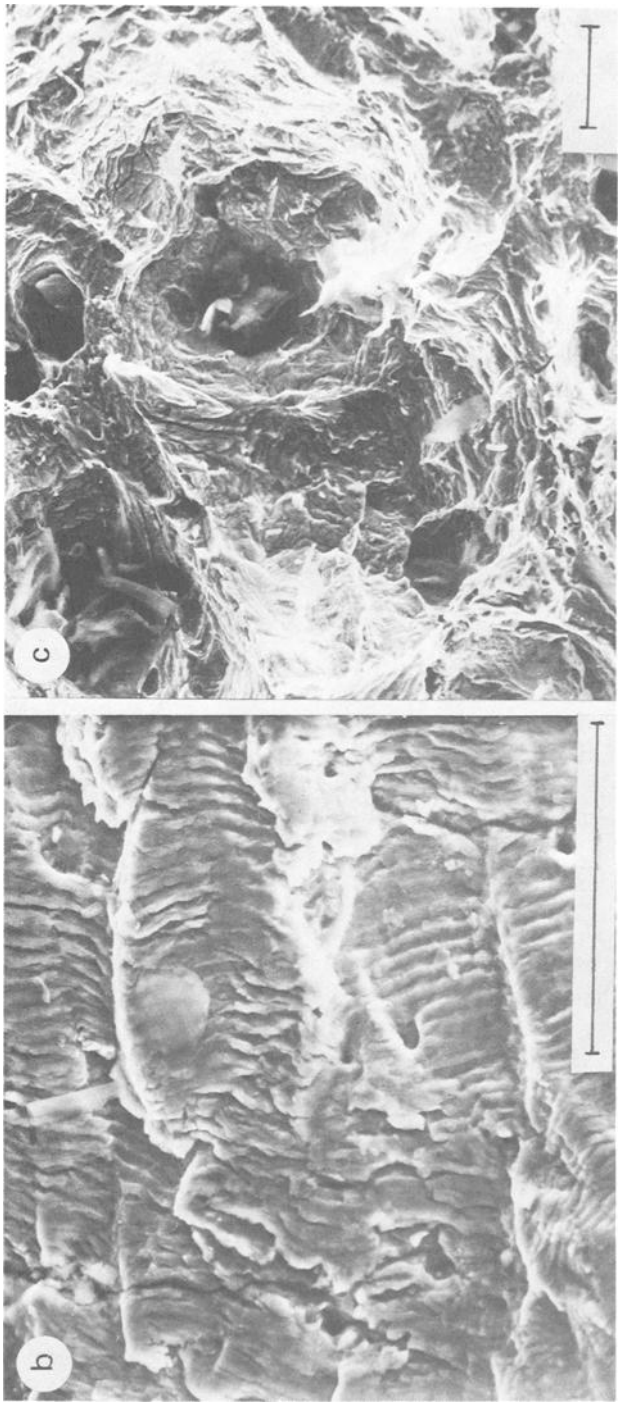


FIG. 17—*Electron micrograph of the fracture surface of corrosion fatigue at* $\sigma_N = 245\ N/mm^2$ *and* $f = 10^3$ *rpm (scale mark indicates 0.05 mm). (a)* $0\ mm < a < 0.6\ mm$, *(b)* $a \simeq 2.0\ mm$, *and (c)* $a \simeq 2.7\ mm$.

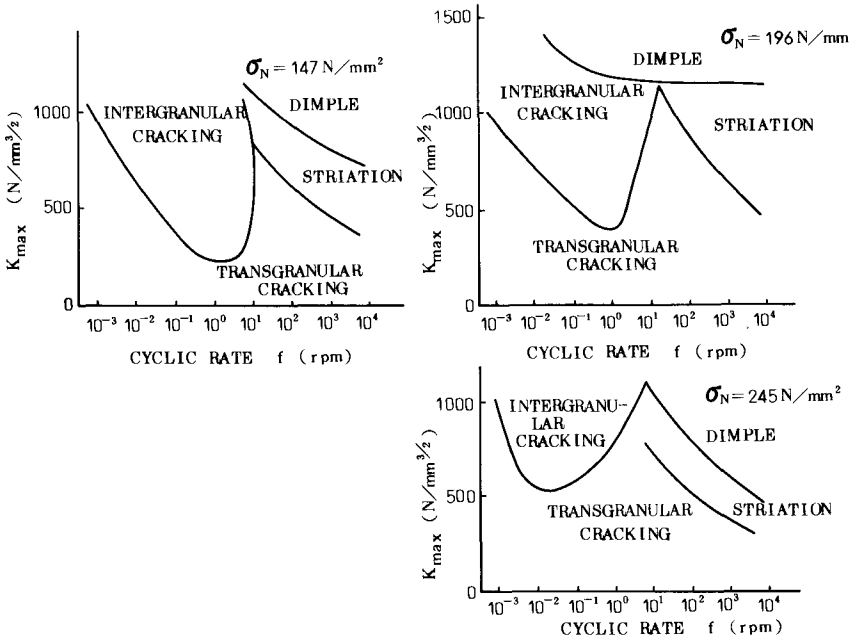


FIG. 18—*Effect of cyclic rate and* $K_{max}$ *on the fractographic feature.*

sition phenomena from transgranular fracture accompanied with fan-like pattern and ill-defined striations to well defined striations were observed and finally dimple pattern was observed. The summary just mentioned is shown in Fig. 18 for the stress level, $\sigma_N$ = 145, 196, and 245 N/mm².

## Conclusion

Corrosion-fatigue tests of Type 304 stainless steel were conducted at various cyclic rates between 0 and $10^4$ rpm in boiling 42 percent $MgCl_2$ solution in rotating bending. As a result, the following conclusions were obtained: (*a*) the cyclic rate affects the failure life at cyclic rates less than $10^3$ rpm; (*b*) the rate of crack propagation, *da/dn*, is proportional to the maximum stress intensity factor $K_{max}$, that is, $da/dn = C K_{max}^m$, where $C$ and $m$ depend on the cyclic rate; and (*c*) the fracture surfaces at higher cyclic rate and static loading were mostly the transgranular type, but the intergranular type was observed partly on the fracture surfaces at lower cyclic rate. Intergranular-type fracture surface was observed more frequently at 1 rpm.

*Acknowledgments*

Authors express their thanks to H. Terasaki for his experimental assistance throughout this work.

## References

[1] Logan, H. L., *The Stress Corrosion of Metals,* Wiley, New York, 1966.
[2] Beachem, C. D. and Brown, B. F. in *Stress Corrosion Testing, ASTM STP 425,* American Society for Testing and Materials, 1966, p. 31.
[3] Wei, R. P. and Landes, J. D., *Materials Research and Standards,* Vol. 9, No. 7, 1969, p. 25.
[4] Sih, G., *Handbook of Stress Intensity Factors,* Lehigh University, Bethlehem, Pa., 1973.
[5] Nielsen, N. A., *Journal of Materials,* Vol. 5, 1970, p. 794.

*Yoshihiko Mukai,[1] Masaki Watanabe,[1] and Masato Murata[1]*

# Fractographic Observation of Stress-Corrosion Cracking of AISI 304 Stainless Steel in Boiling 42 Percent Magnesium-Chloride Solution

**REFERENCE:** Mukai, Yoshihiko, Watanabe, Masaki, and Murata, Masato, "**Fractographic Observation of Stress-Corrosion Cracking of AISI 304 Stainless Steel in Boiling 42 Percent Magnesium-Chloride Solution,**" *Fractography in Failure Analysis, ASTM STP 645,* B. M. Strauss and W. H. Cullen, Jr., Eds., American Society for Testing and Materials, 1978, pp. 164-175.

**ABSTRACT:** The fracture surface of AISI 304 stainless steel in stress corrosion cracking (SCC) in boiling 42 percent magnesium-chloride ($MgCl_2$) solution was investigated fractographically by scanning electron microscopy. To determine the orientation of fracture surface, etch pits were formed on fracture surface by the electroetching method in 1 *N* sulfuric acid ($H_2SO_4$) + 100 mg/litre ammonium thiocyanate ($NH_4SCN$) solution. It was made clear from morphology of etch pit that fracture surface in SCC was almost everywhere on the {100} plane, namely, the path of the crack was determined by crystal orientation and direction of stress. In addition, a striation-like pattern was often found by careful observation on the flat surface.

**KEY WORDS:** fractography, orientation, fan-shaped pattern, step, tear ridge, striations, etch pit, facet, corrosion tunnel, stress intensity factor

Several fractographic studies have been made on stress corrosion cracking (SCC) of austenitic stainless steels by scanning electron microscopy [*1*].[2] These observations have revealed some characteristic fracture surface, namely, in transgranular SCC the fracture surface was characterized by fine parallel pleat patterns. Scully et al mentioned these patterns as traces of corrosion tunnels [*1,2*] and called them fan-shaped patterns. However, the mechanism of forming fan-shaped patterns was not clarified in detail.

Then, in this research, the mechanism of forming these fracture surface features was investigated crystallographically by means of fractographic observations with a scanning electron microscope.

[1] Doctor and professor, Faculty of Engineering; doctor and professor, Welding Research Institute; and Research associate, Faculty of Engineering; respectively, Osaka University, Osaka 565, Japan.

[2] The italic numbers in brackets refer to the list of references appended to this paper.

## Materials and Procedures

The studies were carried out on AISI 304 stainless steel, with a composition as listed in Table 1. The steel was solution treated at 1100°C (2012°F) for 60 min. A bending-type testing machine was used, and the SCC tests were made in magnesium-chloride ($MgCl_2$) aqueous solution, boiling at 143°C (289°F).

Observations of fracture surfaces were made using a scanning electron microscope. Fracture pieces were rinsed in water after removal from the test environment, dried with methanol, and stored in desiccators.

To obtain a correlation between crystal orientation and fracture mode, etch pits were formed on the fracture surfaces by an electroetching method as follows.

The specimens were electroetched at −0.15 V in 1 *N* sulfuric acid ($H_2SO_4$) + 100 mg/litre ammonium thiocyanate ($NH_4SCN$) solution at 40°C (104°F). When the potential was established to −0.15 V against a saturated calomel electrode, pits were formed with {111} planes [*3*] as shown in Fig. 1. The resulting morphology of pits formed on {100}, {110}, and {111} planes are shown in Fig. 2.

TABLE 1—*Chemical composition of used material.*

| Material | Chemical Composition, weight % | | | | | | |
|---|---|---|---|---|---|---|---|
| | C | Si | Mn | P | S | Cr | Ni |
| AISI 304 | 0.076 | 0.85 | 1.15 | 0.020 | 0.012 | 18.35 | 9.2 |

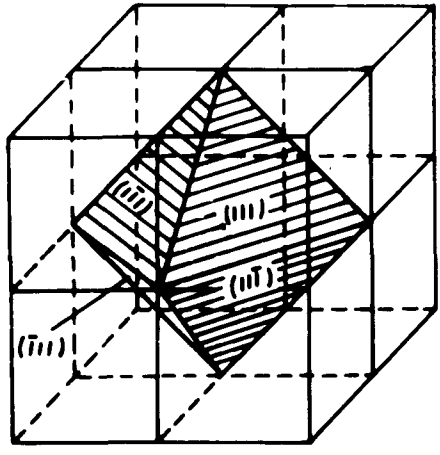


FIG. 1—*Octahedron consisting of {111} planes.*

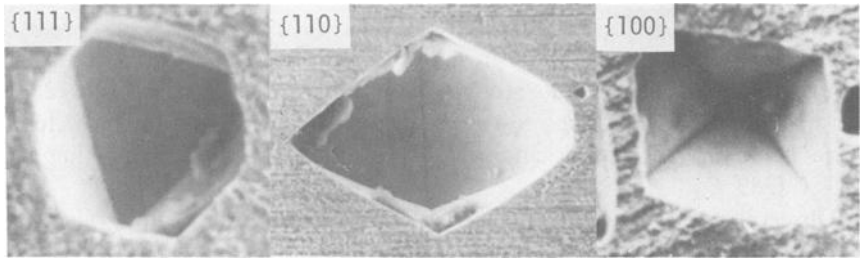


FIG. 2—*Typical etch pits.*

## Results and Discussion

### *Fan-Shaped Patterns*

The fracture mode of AISI 304 stainless steel in SCC was mainly transgranular fracture. The fracture surface consisted of many facets and was characterized by fan-shaped patterns as shown in Fig. 3.

Fan-shaped patterns were observed by tilting the specimen about 40 deg in the scanning electron microscope (example shown in Fig. 4). It was made clear that the fan-shaped pattern was formed with tear ridges and SCC steps.

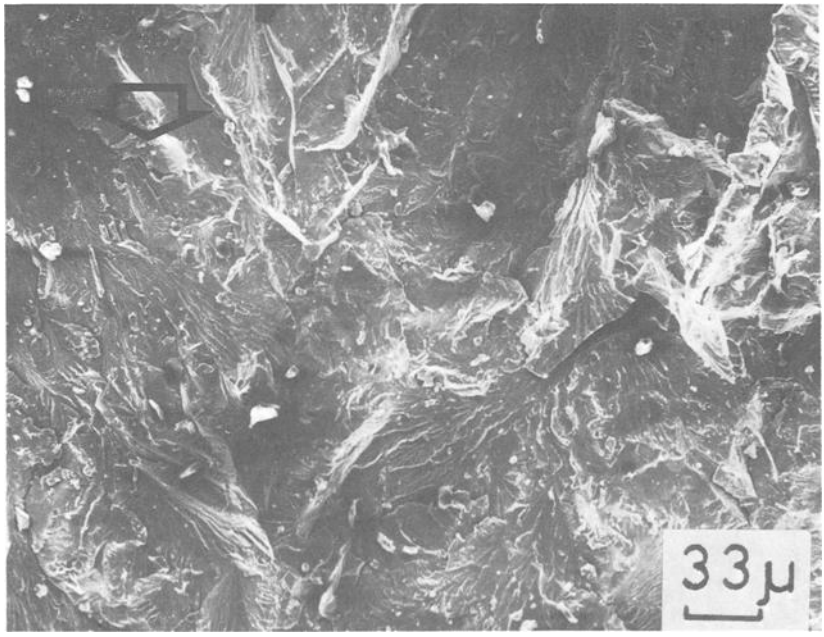


FIG. 3—*Fracture surface of SCC of AISI 304 stainless steel in boiling 42 percent* $MgCl_2$ *solution.*

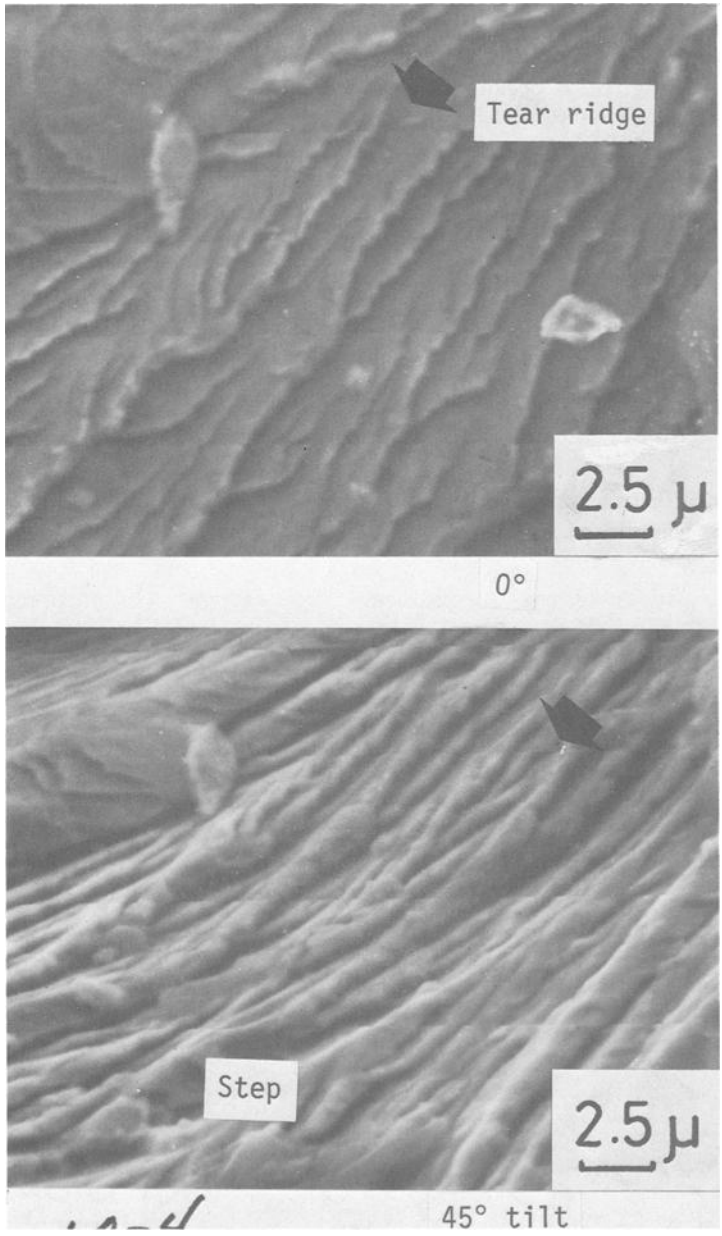


FIG. 4—*Fan-shaped pattern.*

The orientation relation between the direction of fan features and crack growth direction was studied. To show the situation clearly at crack tips in SCC, striation marks were put on the fracture surface by intermittently applying fatigue loads to the specimen in the middle of the SCC test, causing the fan-shaped patterns to be interrupted intermittently by fatigue striations (Fig. 5). It became clear that the direction of crack growth coincided with the direction of the fan, as sketched in Fig. 6.

Figure 6 also shows the frequency distribution of angles between fan and macroscopic crack growth direction. It shows that macroscopic crack growth direction corresponds statistically with the direction of the fans, although microscopic crack growth directions vary. The crack initiation point and crack growth direction may be determined by studying the directions of fans.

In addition, diameters of facets in fracture surfaces were in the range of 120 to 150 $\mu$m (Fig. 7), corresponding with the crystal grain size.

### *Orientation of Crystals in Fracture Surfaces*

Several theories have been proposed concerning crystallographic orientations of fracture paths in SCC. The {100} theory [*3,4*], {110} theory [*5*],

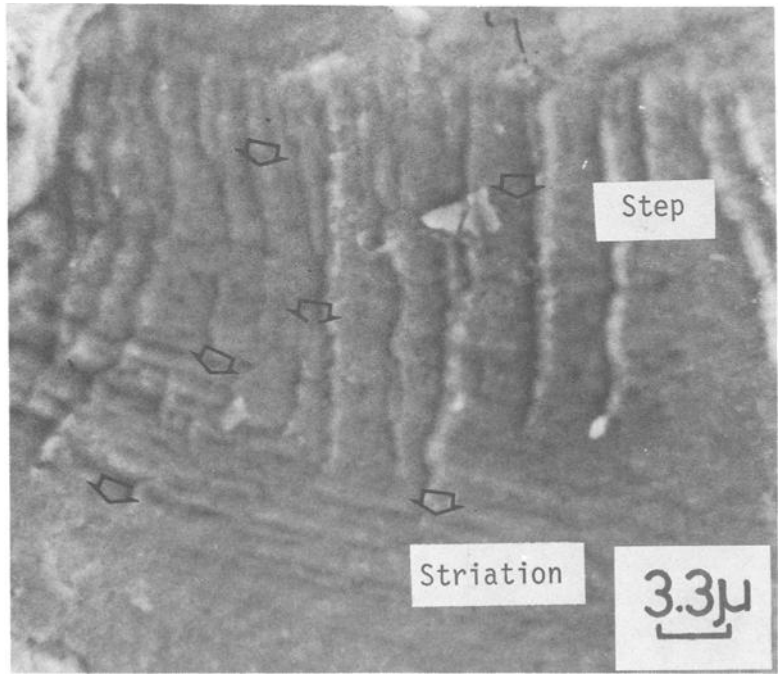


FIG. 5—*Relation between striations of fatigue and SCC steps.*

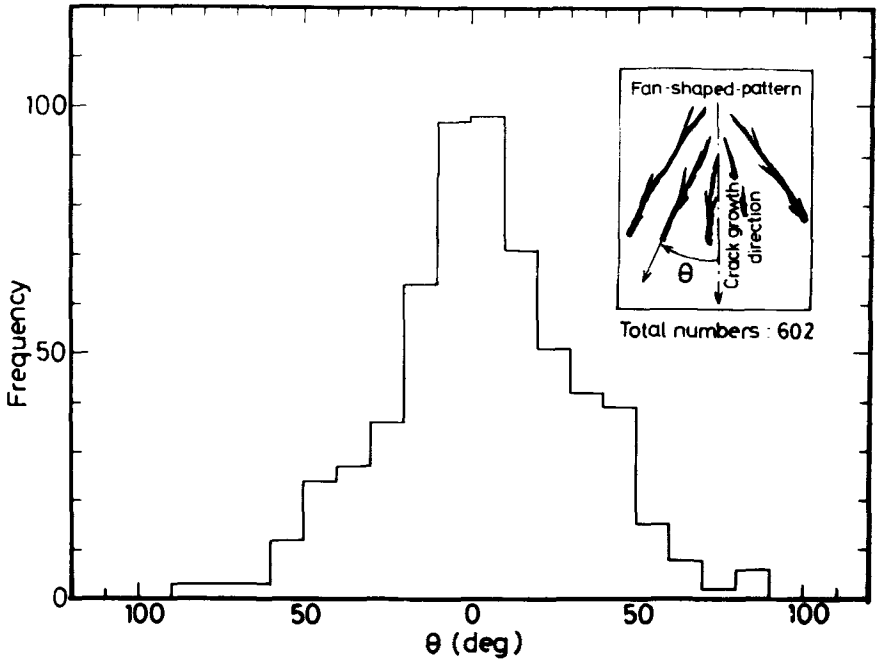


FIG. 6—*Frequency distribution angle between fan and macroscopic crack growth direction.*

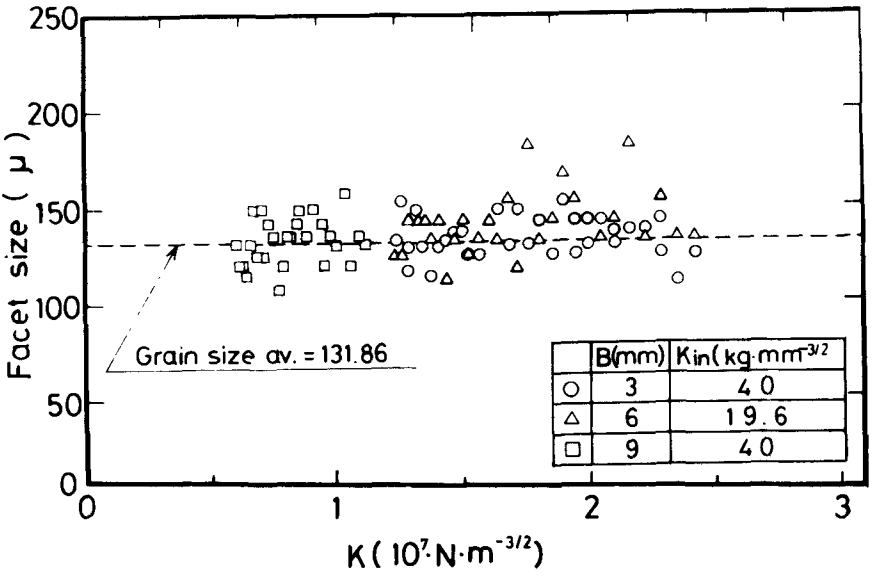


FIG. 7—*Relation between facet size and* K *value.* B = *thickness of specimens and* $K_{in}$ = *initial stress intensity factor.*

{111} theory [6, 7], and others about crystallographic orientations of fracture surfaces scarcely have been proven until now.

The crystallographic orientations of fracture surfaces in SCC were investigated by forming etch pits on fracture surfaces. Figure 8 shows the morphology of pits on a fracture surface. It became clear that the fracture planes were {100} planes almost everywhere, and the crack growth direction was <110> by studying the relation between morphology of pits and directions of fans. Fracture planes were parallel to the {100} planes even across twin and grain boundaries.

The mechanism of forming fan-shaped patterns is illustrated in Fig. 9(*a*) and (*b*).

When the maximum principal stress acts vertically to a {100} plane, the crack surface shows a flat plane. When the crack crosses a twin boundary, the {100} plane is tilted and the resulting crack surface contains considerable steps. Occasionally, secondary cracks are formed at steps. The step planes are perpendicular to a {100} plane, because they are formed along the {100} plane, too.

Consequently, the step plane becomes a part of the crack growth plane. Occasionally, tear ridges were found on step surfaces formed by shear stresses acting on their planes.

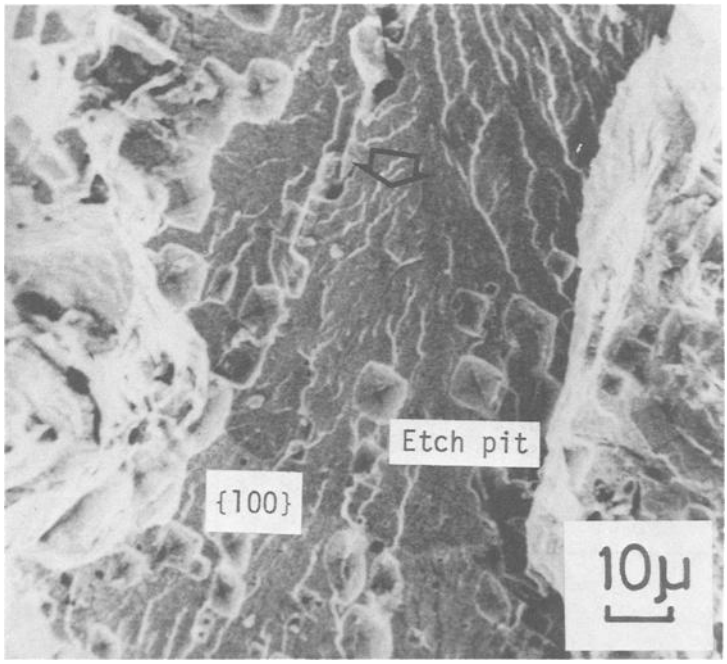


FIG. 8—*Morphology of etch pits on fracture surface of SCC.*

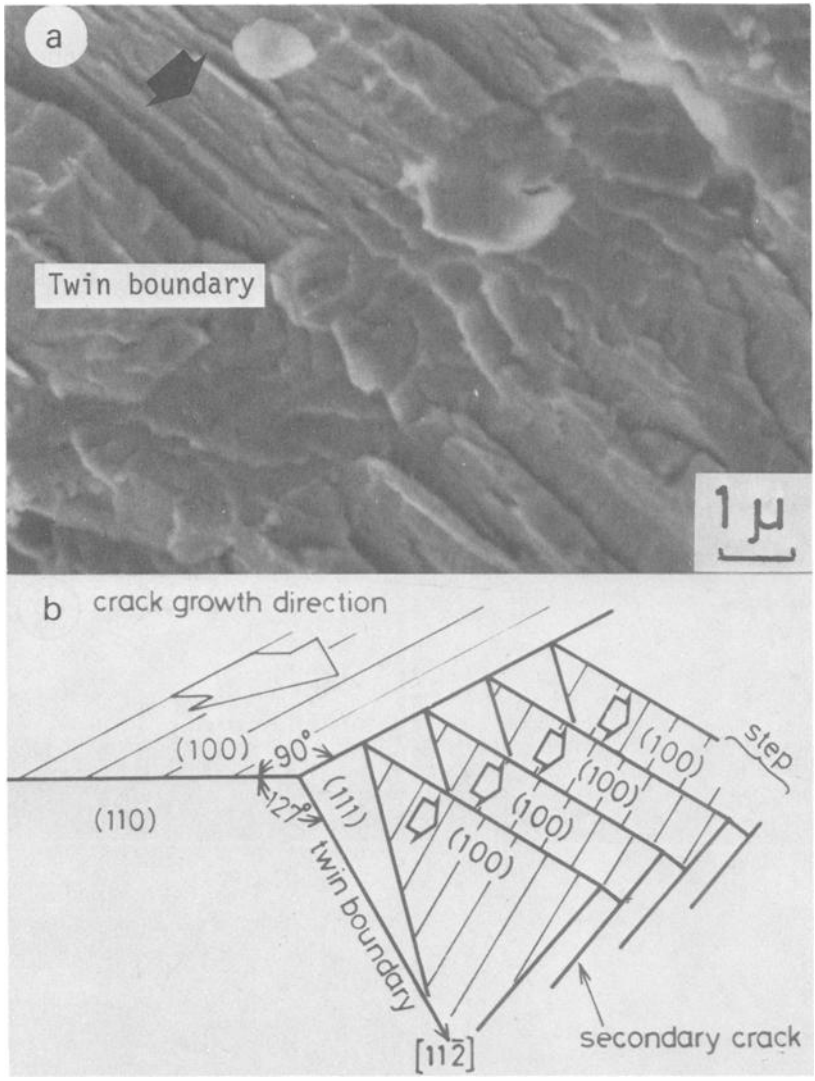


FIG. 9—(a) *Fractograph of fracture surface at twin boundary, and* (b) *schematic view of crack growth on twin boundary.*

Fan-shaped patterns are not traces of corrosion tunnels, but consist of flat facets containing fine steps and a few tear ridges. Fracture surfaces were parallel to {100} planes. From these experimental results, the mechanism of SCC can not be explained solely by a corrosion process. It is necessary to consider mutual effects of both corrosion processes and mechanical fracture processes to understand the mechanisms of SCC.

*Striation-Like Pattern*

Striation-like patterns were found almost everywhere to be perpendicular to the directions of the fans. Figure 10 shows matching striation-like patterns and their stereo pairs. Figure 11 illustrates the schematic view of a cross section of the striation-like pattern constructed from observations of Fig. 10 and shows how the striation-like pattern found in SCC at static loading matched convex and concave surfaces.

The effects of stress intensity factors, $K$, on forming striation-like patterns were investigated, as shown in Fig. 12. It is clear that intervals of striation-like patterns did not depend on stress intensity.

Figure 13 shows the relation between the morphology of pits and striation-like patterns, and Fig. 14 illustrates the schematic view of Fig. 13.

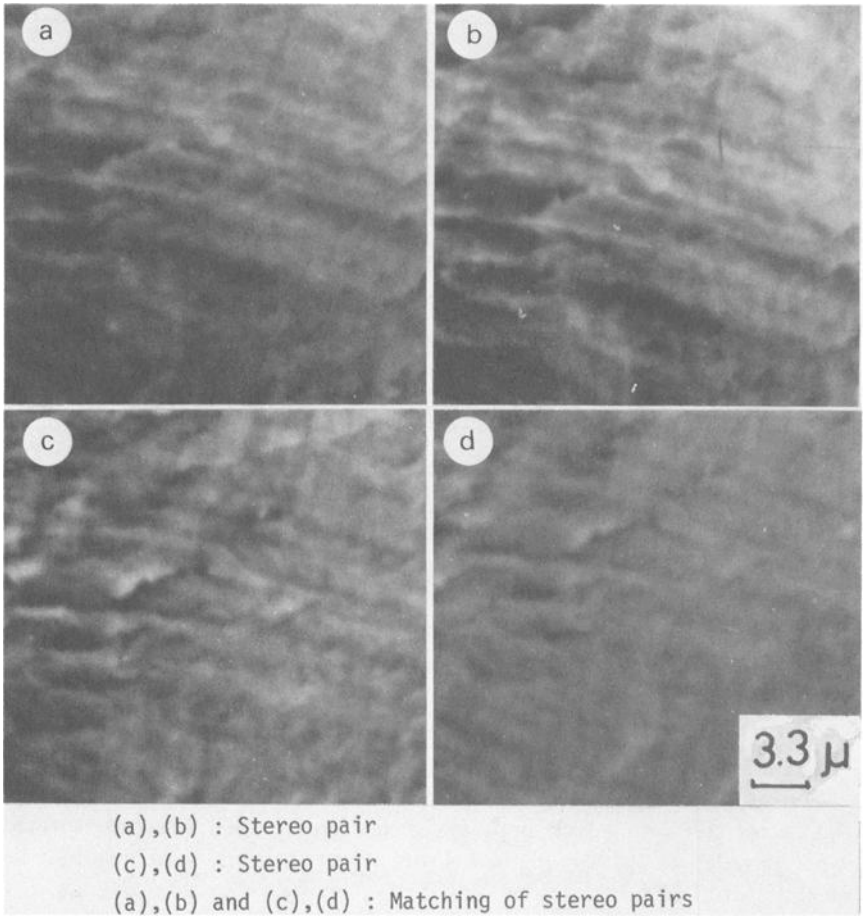


FIG. 10—*Matching stereo pairs of a striation-like pattern.*

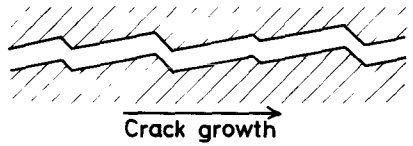


FIG. 11—*Schematic view of section of a striation-like pattern.*

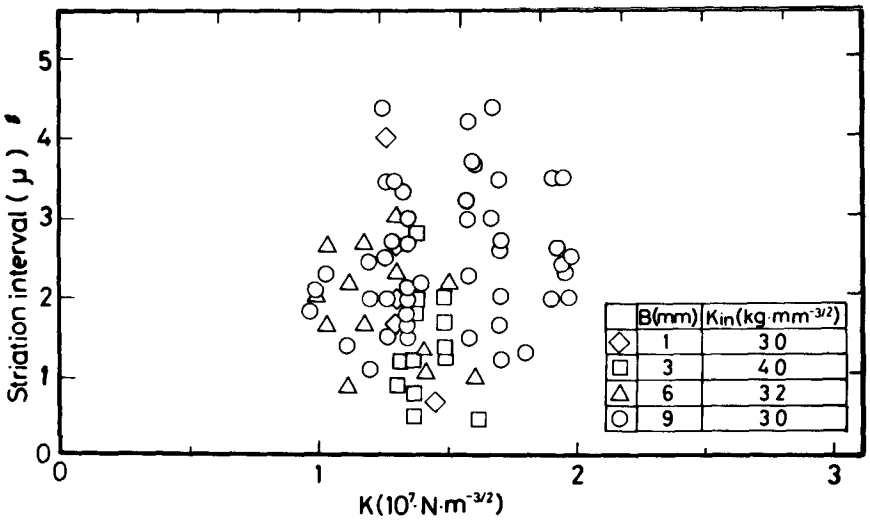


FIG. 12—*Relation between the stress intensity factor and intervals of striation-like patterns.* B = *thickness of specimens and* $K_{in}$ = *initial stress intensity factor.*

From these observations, the characteristics of striation-like pattern in SCC are as follows.

1. Intervals of striation-like patterns did not depend on stress intensity.
2. The direction of stripes in striation-like patterns was < 110 > which was perpendicular to crack growth directions.
3. Striation-like patterns were found locally.

Consequently, striation-like patterns were found when the maximum principal stress activated slip along the most favorable slip planes and slip directions in the crystals.

## Conclusion

A fractographic study was made on AISI 304 stainless steel fractured by SCC. The results are summarized as follows.

1. The direction of fans in fan-shaped patterns coincided with crack growth directions.
2. Average diameters of facets were almost the same as average diameters of the crystals.

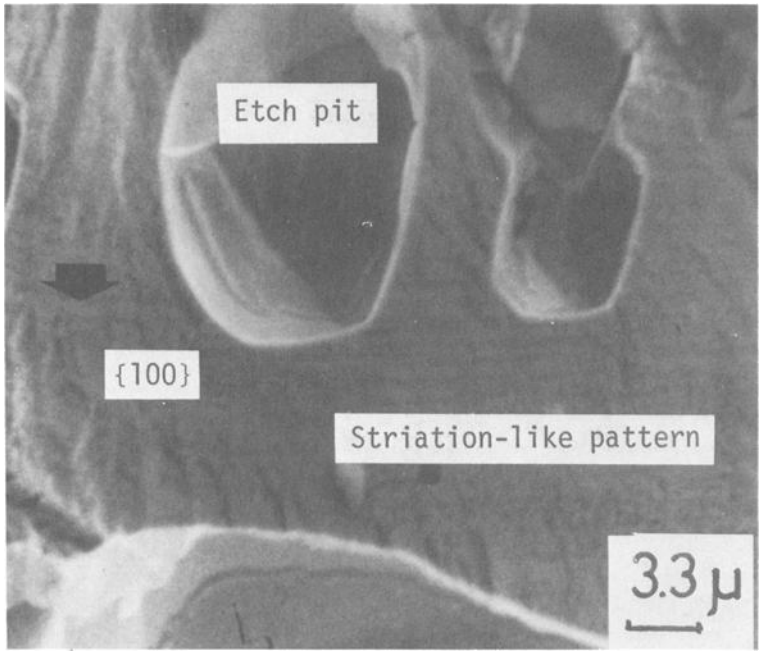


FIG. 13—*Relation between morphology of pits and a striation-like pattern.*

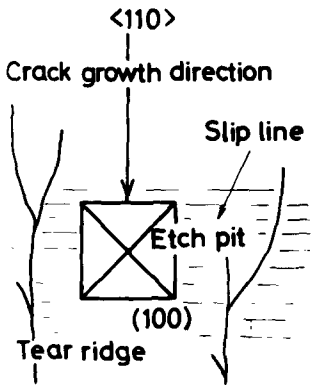


FIG. 14—*Relation between slip lines and orientation of crystal grain.*

3. Fracture surfaces were almost everywhere oriented on the {100} plane, and crack growth directions were < 110 > .

4. Striation-like patterns that were found locally on fracture surfaces were fine slip lines formed perpendicular to directions of crack growth.

*Acknowledgments*

We acknowledge the cooperation of G. Tsujii, a student at Osaka University, who was helped to stimulate progress.

## References

[1] Harston, J. D. and Scully, J. C., *Corrosion,* Vol. 25, 1969, p. 493.
[2] Harston, J. D. and Scully, J. C., *Corrosion,* Vol. 26, 1970, p. 387.
[3] Otani, N., Aihara, K., and Takamoto, S., *Journal of the Japan Institute of Metals,* Vol. 33, 1969, p. 432.
[4] Denhard, E. E., Jr., Masters thesis, Johns Hopkins University, 1957.
[5] Bakish, R. and Robertson, W. R., *Acta Metallurgica,* Vol. 4, 1956.
[6] Pickering, H. W. and Swann, P. R., *Corrosion,* Vol. 19, 1963, p. 373t.
[7] Nielsen, N. A., *Corrosion,* Vol. 20, 1964, p. 104t.

*M. D. Bhandarkar*[1] *and W. B. Lisagor*[2]

# Metallurgical Characterization of the Fracture of Aluminum Alloys

**REFERENCE:** Bhandarkar, M. D. and Lisagor, W. B., **"Metallurgical Characterization of the Fracture of Aluminum Alloys,"** *Fractography in Failure Analysis, ASTM STP 645,* B. M. Strauss and W. H. Cullen, Jr., Eds., American Society for Testing and Materials, 1978, pp. 176–209.

**ABSTRACT:** A systematic investigation was conducted to examine the fracture behavior of the structural aluminum alloys 2024, 6061, 7075, and 7178 (in selected heat treatments) tested under several controlled conditions. The investigation included both time independent (tensile, shear, and precracked notch-bend) fractures and time dependent (fatigue and stress corrosion) fractures. Specimens were obtained from both sheet and plate material and tested in longitudinal and transverse orientations. Strain rate effects on fracture morphology were examined in tension and shear tests. Fatigue fracture studies included an examination of the influence of minimum-to-maximum-load ratio on fracture morphology. Second-phase particles observed on fracture surfaces and metallographically prepared sections and corrosion products associated with stress corrosion fractures were analyzed chemically using scanning electron microscopy and energy-dispersive X-ray analysis. Fracture morphology was related to the microstructural features, the testing conditions, and the form of commercial product. The characteristic and distinguishing fracture features were reported for the different alloys. The information obtained from the systematic and controlled studies described here should prove useful in the analysis of service failures that often occur under complex service conditions.

**KEY WORDS:** fractures (materials), tensile properties, shear stress, bending, fatigue (materials), stress corrosion, fractography, microstructure, aluminum alloys

Fractographic analysis of microscopic fracture processes has assumed increasing importance in studies of material failures occurring in service. The several different types of load-related failures that occur in structural aluminum alloys can be grouped under two broad categories, namely, those that occur under monotonic (static tensile, shear, and flexural) loading and those that occur in a time dependent fashion (resulting from cyclic stresses or sustained loads in the presence of a corrosive environment, or both). Several investigations have been conducted in the past to

[1] Senior metallurgist, Anamet Laboratories, Inc., Berkeley, Calif. 94710.
[2] Materials research engineer, NASA Langley Research Center, Hampton, Va. 23665.

study the fracture behavior of aluminum alloys under both monotonic and discretely changing load conditions. Attempts have been made to relate fracture behavior to microstructure and testing conditions [*1–28*].[3] However, most investigations of this type have been performed as a supplement to a broader program with fracture conditions selected or obtained for reasons other than fractographic analysis. As a result, the information available generally is not developed systematically with respect to the variables contributing to the fracture phenomenon. In addition, documentation is needed of results that can be obtained from the now widely used techniques of scanning electron microscopy and energy-dispersive X-ray analysis.

The problems just cited pose difficulties in analyzing service failures because component failures often occur under complex loading and environmental conditions. Fracture analysis of such failures requires a detailed understanding of fracture appearance resulting from each of these conditions and how their interaction influences the fracture surface appearance of the failed component.

A recent effort which should aid in the solution of these problems involved the documentation of tensile, fatigue, stress rupture, thermal fatigue, and stress-corrosion fracture morphologies of some aluminum and titanium alloys, steels, and superalloys [*29*]. The present investigation was conducted to examine in detail the microstructure and fracture morphology of selected aluminum alloys tested under several controlled conditions with extensive use of the scanning electron microscope and associated X-ray chemical analysis. The influence of test variables, microstructure, and alloy product form on fracture morphology are presented, and the applicability of the results to failure analysis is discussed.

## Experimental Procedure

### *Materials*

The investigation included aluminum alloys 2024, 6061, 7075, and 7178 in sheet and plate forms. The alloys were selected because of their widespread use in aerospace structures. Sheets were 1 mm thick and plates were 25.4 mm thick. Chemical compositions of the alloys are listed in Table 1.

### *Specimens and Test Procedures*

Tension tests were conducted using 12.7-mm-diameter round specimens machined from plate material, and sheet specimens 12.7 mm wide in accordance with ASTM Tension Testing of Metallic Materials (E 8–69).

[3]The italic numbers in brackets refer to the list of references appended to this paper.

TABLE 1—*Chemical compositions of alloys.*

| Alloy | Compositions, Weight Percent | | | | | | | | | |
|---|---|---|---|---|---|---|---|---|---|---|
| | Cu | Mg | Zn | Si | Fe | Cr | Mn | Ti | Others | Al |
| 2024 | 3.8 to 4.9 | 1.2 to 1.8 | 0.25[a] | 0.50 | 0.50 | 0.10 | 0.30 to 0.90 | ... | 0.15 | remainder |
| 6061 | 0.15 to 0.40 | 0.8 to 1.2 | 0.25 | 0.4 to 0.8 | 0.70 | 0.15 to 0.35 | 0.15 | 0.15 | 0.15 | remainder |
| 7075 | 1.2 to 2.0 | 2.1 to 2.9 | 5.1 to 6.1 | 0.50 | 0.7 | 0.18 to 0.40 | 0.30 | 0.20 | 0.15 | remainder |
| 7178 | 1.6 to 2.4 | 2.4 to 3.1 | 6.3 to 7.3 | 0.50 | 0.7 | 0.18 to 0.40 | 0.30 | 0.20 | 0.15 | remainder |

[a] Single compositions represent the maximum amounts allowed.

Strain rate conditions included: (*a*) 0.00008/s to failure, (*b*) 0.025/s to failure, and (*c*) 0.00008/s to yielding followed by 0.0008/s until failure. Shear tests were performed at crosshead displacement rates of 0.04 and 1.27 mm/s using thin sheet specimens [*30*] as shown in Fig. 1(*a*). All tension and shear tests were performed using both longitudinal and long transverse specimens. Three-point bend tests were performed on specimens machined from plates of each alloy and were tested with the plane of the crack normal to both longitudinal and transverse directions with propagation in the short transverse direction (Fig. 1(*b*)). Fatigue tests were conducted using longitudinal and transverse sheet specimens containing a centrally machined (electrical discharge machining) slot as shown in Fig. 1(*c*). Tests were conducted in room temperature air at minimum-to-maximum-load ratios ($R$ values) of 0.05 (at nominal maximum stresses of 51, 64, and 255 MPa), 0.8 (at nominal maximum stress of 255 MPa), and $-1$ (at nominal maximum stresses of 102 and 126 MPa). Stress-corrosion tests were performed using C-ring specimens stressed to 75 to 95 percent of yield strength and tested in accordance with ASTM Recommended Practice for Alternate Immersion Stress Corrosion Testing in 3.5% Sodium Chloride Solution (G 44-75) except that specimens were exposed until fracture occurred. Details of specimen dimensions and orientations with respect to the rolling direction are shown in Fig. 1(*d*).

### *Metallurgical and Fractographic Analysis*

Microstructure and fracture surface morphology were characterized using the optical microscope and the scanning electron microscope. Second-phase particles that were observed on fracture surfaces and metallographically polished sections of the alloys were analyzed using the scanning electron microscope and energy-dispersive X-ray chemical analysis (EDAX) [*31*]. Conventional metallographic procedures were used for microstructural analysis and specimens were etched with a reagent (0.5 percent hydrofluoric, 2.5 percent nitric, 1.5 percent hydrochloric acids, balance water).

## Results

### *Mechanical Property Determinations*

Tensile and shear properties of sheet material and tensile and fracture toughness properties of plate material are shown in Table 2. Stress intensity factors ($K_I$) at failure were calculated using the $K$ expression in ASTM Test for Plane-Strain Fracture Testing of Metallic Materials (E 399-74). The tensile values are indicative of typical values obtained from conventional commercially produced product form [*32*]. Effects of specimen orientation were also typical and an order of magnitude difference in strain rate had

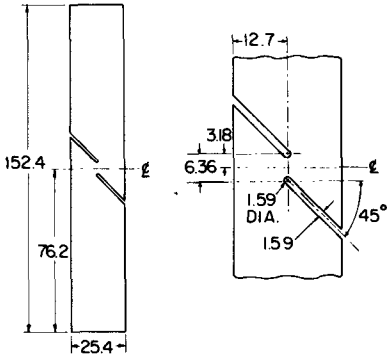


(a) SHEAR SPECIMEN (SHEET)

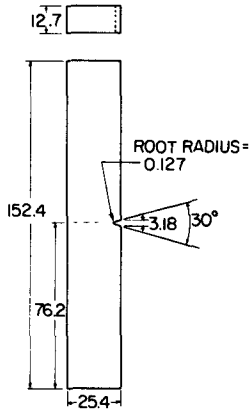


(b) NOTCH-BEND SPECIMEN (PLATE)

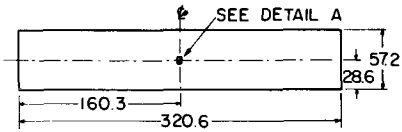


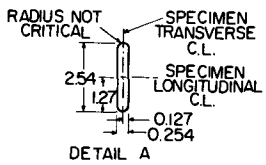


(c) SHEET FATIGUE SPECIMEN

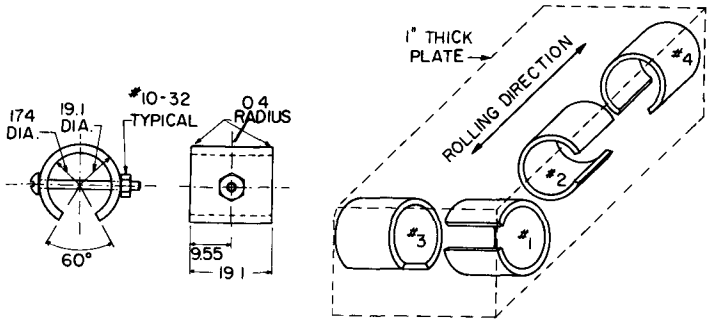


(d) STRESS CORROSION SPECIMEN (PLATE)

DIMENSIONS IN MM

**FIG. 1—*Specimen dimensions and orientations.***

little effect on tensile behavior. However, variation in crosshead displacement rate (and hence, load rate) had a substantial effect on shear strength of all alloys with higher load rates causing 25 to 55 percent lower shear strengths. These differences and their effect on fractographic appearance will be discussed under fracture morphology of sheet shear specimens.

*Microstructures of Alloys*

The characterization of microstructure (including grain structure, second-phase particle distribution, and X-ray chemical analysis) was used to relate the effects of these microstructural variables on fracture morphology where possible.

Figure 2 shows optical and scanning electron microscope photomicrographs of 2024-T351 plate and visual displays of the X-ray displays of three distinct second-phase particles identified on the polished sections. These results are indicative of the type of information obtained for all alloys in both plate and sheet form. The photomicrographs reveal the elongated grain structure and second-phase particle distribution. The X-ray displays reveal the relative intensities of the elements present in the specific particles. These data must be corrected for matrix contribution caused by penetration of the electron beam beyond the particle and into the matrix, which causes portions of the display to result from the irradiated matrix.

After matrix corrections and comparison with identified particles in the literature [*31,33,34*], Particles A and C in Figs. 2(*b*) and (*c*) were identified as copper aluminide ($CuAl_2$) and a metal aluminide of the form ($MAl_6$) with copper, iron, and manganese in substitution (Cu, Fe, Mn) $Al_6$. In addition to finding particles previously identified by other investigators, all alloy plates and sheets were found to contain complex particles not reported previously. The stoichiometry of these particles could not be determined, but identification was positive based on constant elemental intensity ratios obtained on several particles. Table 3 lists particles identified in each alloy plate or sheet, whether or not it has been reported previously, and the fracture surfaces on which it was found. Particles for which stoichiometry could not be identified are shown with all element symbols contained within the parentheses.

The presence of second-phase particles and their condition (whether they were cleaved or fragmented) can indicate their contribution to the final fracture process. The absence of fractured second-phase particles, the presence of voids adjacent to particles that are not fractured, and the presence of unbroken particles in relief on fracture surfaces suggest particle-matrix separation only, with little plastic flow around particles. Also, the presence or absence of fractured particles suggested magnitudes of loading in shear and fatigue tests, discussed in later sections.

The microstructure of all plates were similar with regard to grain struc-

TABLE 2—*Properties of alloys investigated.*

| Alloy and Federal Specification | Product Form | Orientation | Yield Strength, 0.2% Offset, MPa | Ultimate Strength, MPa | Elongation, % in 5 cm | Fracture Toughness, MPa · $m^{1/2}$ | Ultimate Shear Strength, MPa |
|---|---|---|---|---|---|---|---|
| 2024-T351 | plate | L | 423 | 501 | 20 | 40 | ... |
| QQ-A-250/4d | | T | 370 | 484 | 18 | 36 | ... |
| 2024-T3 | sheet | L | 362 | 500 | 24 | ... | 356[a]<br>199[b] |
| QQ-A-250/4d | | T | 314 | 476 | 27 | ... | 357[a]<br>207[b] |
| 6061-T4 | plate | L | 205 | 256 | 26 | ... | ... |
| QQ-A-250/11d | | T | 201 | 277 | 22 | 33 | ... |
| 6061-T4 | sheet | L | 180 | 281 | 27 | ... | 217[a]<br>167[b] |
| QQ-A-250/11d | | T | 170 | 276 | 30 | ... | 216[a]<br>170[b] |
| 6061-T651 | plate | L | 305 | 318 | 22 | 44 | ... |
| QQ-A-250/11d | | T | 303 | 328 | 16 | 44 | ... |
| 6061-T6 | sheet | L | 301 | 331 | 22 | ... | 235[a]<br>174[b] |

| | | | | | | | |
|---|---|---|---|---|---|---|---|
| QQ-A-250/11d | | T | 285 | 325 | 16 | ... | 239[a]<br>185[b] |
| 7075-T651 | plate | L | 557 | 594 | 12 | 41 | ... |
| QQ-A-250/12d | | T | 539 | 595 | 13 | 36[c] | ... |
| 7075-T6 | sheet | L | 519 | 567 | 23 | ... | 401[a]<br>178[b] |
| QQ-A-250/12d | | T | 588 | 663 | 17 | ... | 405[a]<br>186[b] |
| 7178-T651 | plate | L | 589 | 636 | 11 | 29[c] | ... |
| QQ-A-250/14d | | T | 564 | 619 | 11 | 23[c] | ... |
| 7178-T6 | sheet | L | 568 | 617 | 19 | ... | 424[a]<br>210[b] |
| QQ-A-250/14d | | T | 550 | 636 | 19 | ... | 443[a]<br>203[b] |

NOTE—Aluminum Alloy, Plate and Sheet (QQ-A-250/4d)
Aluminum Alloy, Plate and Sheet (QQ-A-250/11d)
Aluminum Alloy, Plate and Sheet, Alclad (QQ-A-250/12d)
Aluminum Alloy, Sheet and Plate (QQ-A-250/14d)

[a] Tested at crosshead speed of 2.54 mm/min.

[b] Tested at crosshead speed of 76.2 mm/min.

[c] Meets ASTM Test E 399-74 validity criteria for valid $K_{Ic}$.

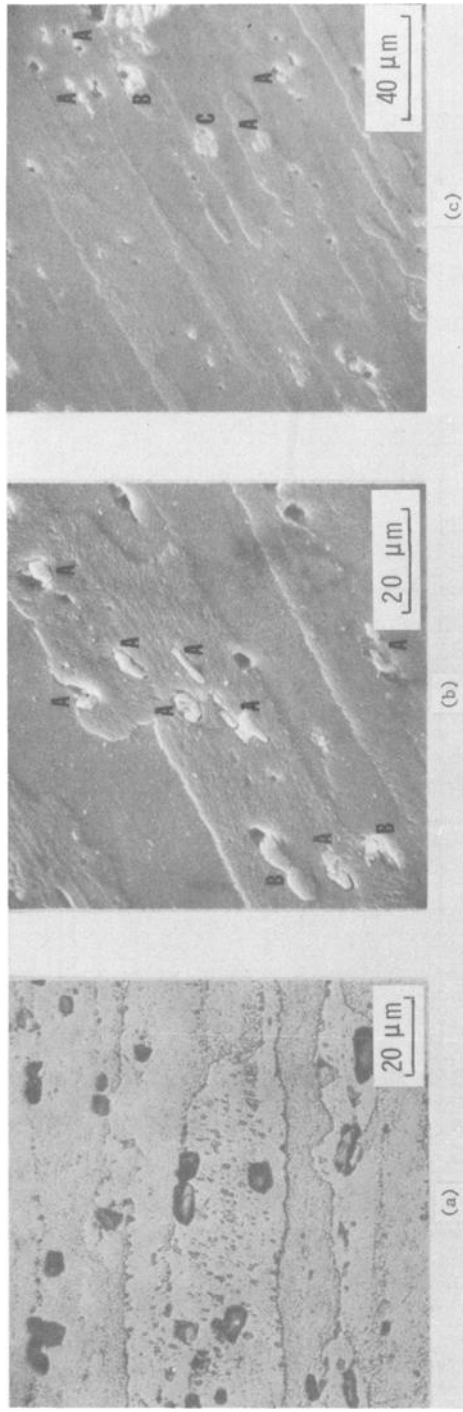
20 µm
(a)
A
A
A
A
A
B
A
B
B
20 µm
(b)
A
A
B
C
A
A
40 µm
(c)

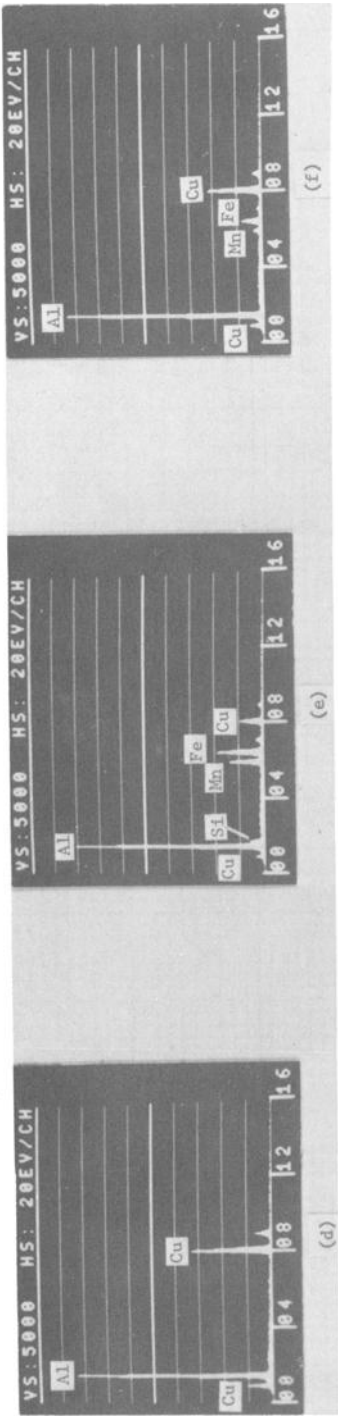


*FIG. 2—Optical micrograph* (a) *and scanning electron micrographs* (b) *and* (c) *of a plate specimen of 2024-T351. The EDAX pattern from second phase particles A, B, and C are shown in* (d), (e), *and* (f), *respectively.*

TABLE 3—*Second-phase particle identification in aluminum alloy fracture surfaces.*

| Alloy | Product Form | Particles Identified by Energy Dispersive X-ray Analysis | Previously Identified in Alloy | Fracture Surfaces on Which Identified |
|---|---|---|---|---|
| 2024-T351 | plate | $CuAl_2$ | yes | tensile, notch bend |
| | | (Cu, Fe, Mn) $Al_6$ | yes | tensile, notch bend |
| | | (Cu, Fe, Mn, Si, Al) | no | tensile, notch bend |
| 2024-T3 | sheet | $CuAl_2$ | yes | tensile, shear, fatigue |
| | | (Cu, Fe, Mn) $Al_6$ | yes | tensile, fatigue |
| | | (Cu, Fe, Mn, Si, Al) | no | tensile, shear, fatigue |
| 6061-T4, 6061-T651 | plate | $Mg_2Si$ | yes | tensile, notch bend |
| | | Si | yes | tensile, notch bend |
| | | (Fe, Si, Cr, Mn, Al) | no | tensile, notch bend |
| 6061-T4, 6061-T6 | sheet | (Fe, Cr, Mn, Al) | no | tensile, shear, fatigue |
| 7075-T651 | plate | (Fe, Cu, Cr, Zn, Mn, Al) | no | notch bend, tensile |
| | | (Cu, Fe, Zn, Cr, Mn, Al) | no | tensile, notch bend |
| | | (Fe, Cr, Si, Mn, Al) | no | notch bend |
| | | $Mg_2Si$ | yes | tensile, notch bend |
| | | $CuMgAl_2$ | yes | notch bend |
| | | (Mg,Si,Zn,Cu,Al) | no | notch bend |
| 7075-T6 | sheet | $FeAl_3$ | yes | tensile, shear, fatigue |
| | | $Cu_3ZnAl_3$ | yes | tensile |
| | | (Fe,Cr,Mn,Cu,Si,Al) | no | shear, fatigue |
| | | $Mg_2Si$ | yes | fatigue |
| | | $CuMgAl_2$ | yes | tensile, fatigue |
| 7178-T651 | plate | $CuAl_2$ | yes | tensile, notch bend |
| | | $CuMgAl_2$ | yes | tensile, notch bend |
| | | (Fe,Cu,Zn,Cr,Mn,Al) | no | tensile, notch bend |
| 7178-T6 | sheet | $FeAl_3$ | yes | tensile, fatigue |
| | | $Mg_2Si$ | yes | fatigue |
| | | (Cu,Zn,Mg,Al) | no | tensile |
| | | (Cu,Fe,Zn,Cr,Mn,Al) | no | shear, fatigue |

ture and second-phase distribution; however, more banding of small second-phase particles was observed in 7075 and 7178 plates. In general, second-phase distribution in sheet materials was more random with little or no banding or segregation. Some of the particles identified by X-ray analysis are of the type which contribute to the precipitation strengthening process during heat treatment. However, when present in large sizes (Fig. 2(*b*) and (*c*)), they are probably the result of incomplete dissolution during solution treating. The materials, however, were still within mechanical property tolerances required by the specifications listed in Table 2.

*Fracture Morphology of Alloys*

*Plate Tension Specimens*—The fracture morphology in plate tension specimens is illustrated by the scanning electron fractographs of Fig. 3. Strain rate variations within the range examined and specimen orientation did not affect fracture morphology.

The dimpled rupture shown in Fig. 3 was the predominant failure mode in alloys 2024-T351, 6061-T4, and 6061-T651. The large dimples contained cleaved or shattered second-phase particles. Dimples on fracture surfaces of 6061-T4 and 6061-T651 tension specimens were more equiaxed and exhibited an increasing degree of size regularity. Nonuniform dimple sizes and irregular dimple shapes were common in alloy 2024-T351 as illustrated in Fig. 4. Areas with fine dimples, nucleated possibly at aging precipitates or dispersoids, or both, are marked A in the figure.

Plate tensile fracture of 7075-T651 and 7178-T651 exhibited a predominance of relatively smooth and flat facets (Figs. 3(*d*) and (*e*), and Fig. 5(*a*)), which, on high magnification examination, revealed shallow, submicron-size dimples (Fig. 5(*b*)). The areas between smooth facets exhibited ductile tearing and pockets containing cracked second-phase particles. The smooth appearance of the facets and their approximate 45-deg orientation to the applied load suggested that the facets were stretched regions formed by extensive tearing along glide planes. Optical microscopy of sections intersecting the fracture surfaces indicated that the facets were formed by transgranular fracture. The fine shear dimples observed on the smooth surfaces were of the proper approximate size range to have been nucleated by strengthening precipitates or dispersoids, or both.

*Sheet Tension Specimens*—Dimpled rupture was the prime failure mode in sheet tension specimens of all the alloys of the present investigation, as is evident from the scanning electron fractographs in Fig. 6. Strain rates within the range examined and specimen orientations did not affect fracture morphology.

Generally, all specimens contained equiaxed dimples in local fracture areas normal to the applied load and elongated dimples resulting from combined shear and normal stresses in fracture areas oblique with respect to

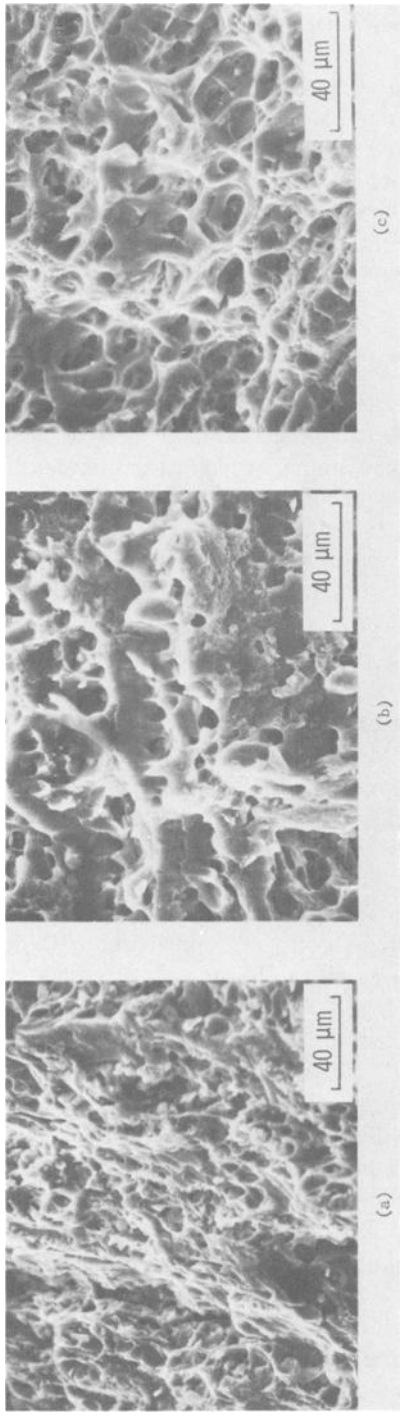
40 µm
(c)
40 µm
(b)
40 µm
(a)

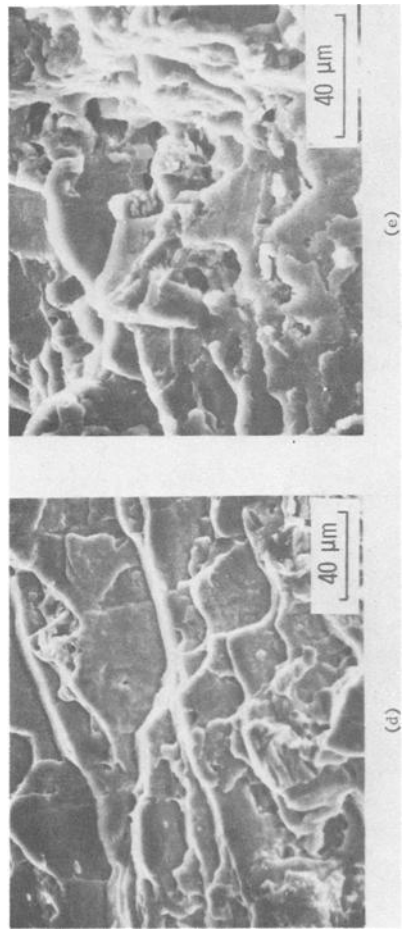


FIG. 3—*Scanning electron fractographs of tensile plate specimens of aluminum alloys:* (a) *2024-T351,* (b) *6061-T4,* (c) *6061-T651,* (d) *7075-T651, and* (e) *7178-T651.*

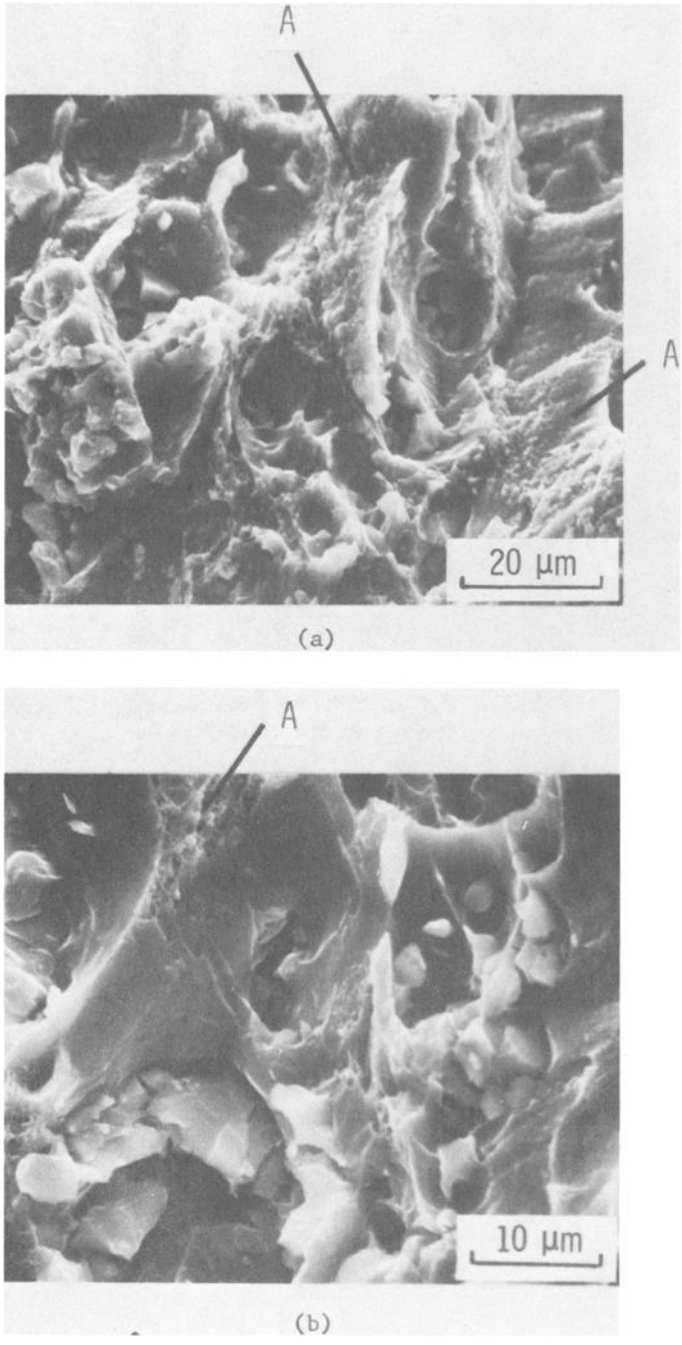


FIG. 4—*Scanning electron fractographs of tensile plate specimens of 2024-T351.*

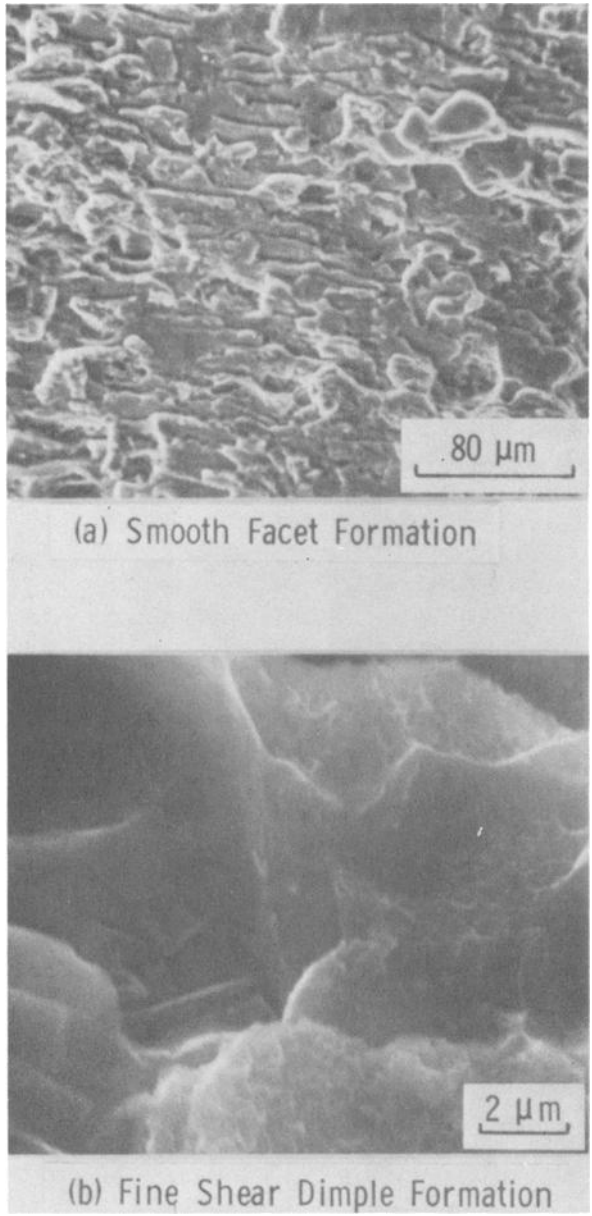


FIG. 5—*Scanning electron fractographs of a tensile plate specimen of 7178-T651.*

the applied load. Regions that failed under a predominantly shear stress exhibited fracture features similar to those in shear test specimens as would be expected. Sheet tensile fracture morphology was essentially similar in the different alloys. In general, a finer, more uniform dimple size was ob-

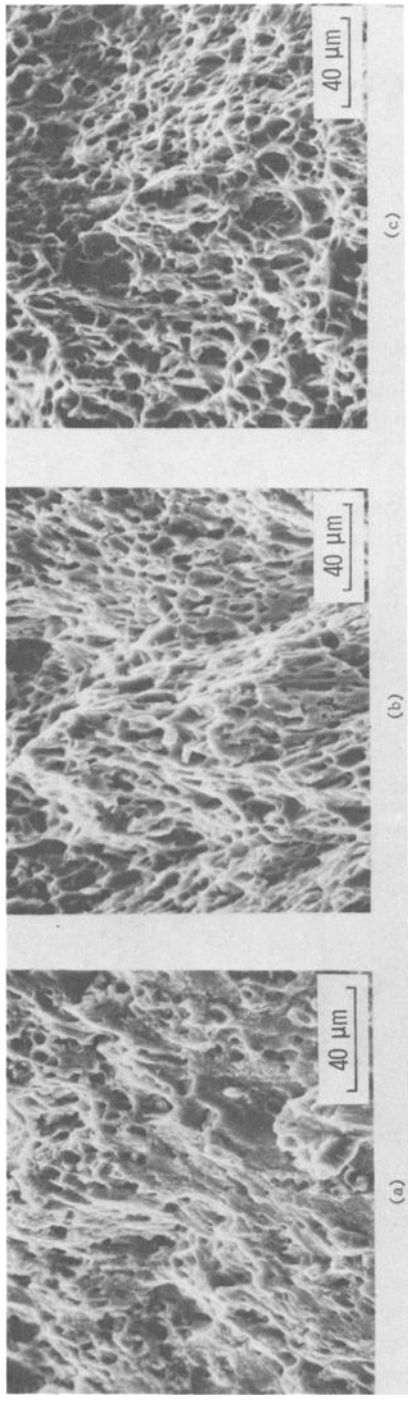
40 µm
(c)
40 µm
(b)
40 µm
(a)

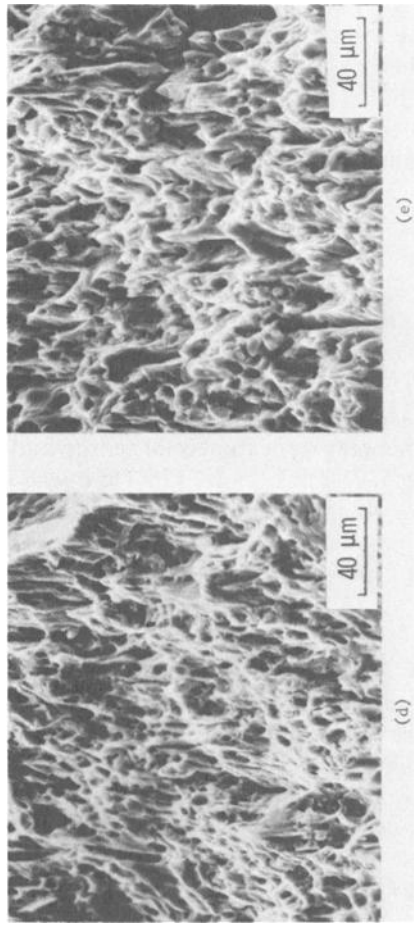


FIG. 6—*Scanning electron fractographs of sheet tension specimens of aluminum alloys,* (a) *2024-T3,* (b) *6061-T4,* (c) *6061-T6,* (d) *7075-T6, and* (e) *7178-T6.*

served compared to plate material, and less second-phase particles were present on the fracture surfaces of sheet specimens.

*Sheet Shear Specimens*—Sheet shear fractures were essentially similar for all the alloys tested at the crosshead displacement rate of 0.04 mm/s in the present investigation. Macroscopically, the fractures were smooth. Microscopic appearances were characterized by large shallow elongated dimples and smooth areas, as illustrated by the scanning electron fractographs in Fig. 7. Examination of the smooth areas at higher magnification revealed fine, shallow dimple formation, possibly nucleated by strengthening precipitates or dispersoids, or both (Fig. 8). When the crosshead displacement rate was changed to 1.27 mm/s, the shear ultimate strengths were lowered by 42 to 56 percent in alloys 2024-T3, 7075-T6 and 7178-T6, and by 21 to 26 percent in alloys 6061-T4 and 6061-T6 (see Table 2). The shear fracture morphology was not affected in the 6061 material, but the faster strain rate produced fractures in alloys 2024-T3, 7075-T6, and 7178-T6 which were rougher and contained more cracked particles than slow strain rate shear fractures (Fig. 9). Specimen orientation with respect to the rolling direction did not influence either shear fracture morphology or shear ultimate strength in the sheet alloys investigated.

*Notch-Bend Specimens*—The microscopic fracture morphology of notch-bend specimens of alloys was essentially similar to the plate tensile fractures. The major difference between appearances of tensile and notch-bend fractures occurred in alloys 7075-T651 and 7178-T651 where secondary cracks and deep grooves were observed only in notch-bend specimens (Fig. 10). Smooth facet formation was more regular (presumably due to controlled crack propagation) in notch-bend specimens than in plate tension specimens.

*Sheet Fatigue Specimens*—The results described herein characterizing fatigue fracture morphology are limited to that area of fracture surface which was produced by fatigue crack growth. The areas associated with the fast fracture portion of failure were similar to sheet tension specimens with more tendency to be planar.

At $R = 0.05$ and nominal maximum stresses of 51 and 64 MPa, fatigue fractures exhibited relatively smooth areas separated by ductile tear ridges and voids formed by particle matrix separation as illustrated in Fig. 11 (voids identified by A). Void formation and tearing were more dominant in 2024-T3, 6061-T4, and 6061-T6 (Fig. 11(*a*), (*b*), and (*c*)) than in 7075-T6 and 7178-T6 (Fig. 11(*d*) and (*e*)). The latter two alloys exhibited a predominance of relatively smooth areas containing poorly defined striations and slip band markings that were not, in most instances, clearly distinguishable from each other (see areas near B in Fig. 11). The rare occurrence of cleaved particles in voids, the presence of unbroken particles adjacent to some voids and in relief on the fracture surfaces suggested that dimples were nucleated mostly by particle-matrix interface failure at

maximum stress values in this range (unbroken particles are illustrated at C in Fig. 11). Specimens tested at $R = 0.05$ and a nominal maximum stress of 255 MPa exhibited greater proportions of void formation and ductile tearing than in fatigue fractures of specimens tested at the lower maximum stresses. Particle cracking also was observed at the higher maximum stress value. These results are consistent with the findings of other investigations [*6,12,18,20*].

Fatigue fractures of specimens tested at $R = 0.8$ and nominal maximum stress of 255 MPa were similar to high maximum stress, low $R$ value fractures and they also exhibited particle cracking. Striations were observed even less under these stress conditions. Specimens tested under fully reversed loading were similar in fracture morphology to constant amplitude tension-tension specimens, except for some contact damage resulting in local areas of surface smearing.

Scanning electron microscope fracture morphology normally associated with fatigue failure is most often characterized by identification of striations. In sheet materials, ductile tear ridges are a far more prominent characteristic on the fracture surface. Striations are often difficult to distinguish from slip band formation and are often poorly defined. The reporting of striations as the prominent fracture feature in fatigue failure of thin gage materials is often misleading.

*Stress-Corrosion Specimens*—The prominent fracture surface characteristic associated with stress-corrosion specimens is corrosion leaf formation which is illustrated in Fig. 12 by the scanning electron microscope fractographs of a 2024-T351 specimen tested in the short transverse direction (orientation 1, Fig. 1). Corrosion leaves result from intergranular cracking along grain boundaries parallel to and nearby the primary crack front. The intergranular cracking is revealed more clearly in Fig. 13 by the optical micrograph of a section approximately normal to the fracture surface. Intergranular stress corrosion cracking (SCC) of this type is commonly encountered in aluminum alloys [*3,13,16,22*]. The degree of leaf formation is affected by alloy susceptibility and orientation. It may also be related to magnitude of stress.

On a microscopic scale, relatively smooth intergranular facets were predominant on stress-corrosion fractures. The fracture surfaces were coated with corrosion products which could be classified in three general categories including nonadherent particle debris, adherent dried mud-flat crack patterns, and adherent continuous coating. Loosely adherent corrosion debris visible in Fig. 12(*a*) was removed upon extended ultrasonic cleaning of the specimen, as shown in Fig. 12(*b*).

Typical higher magnification appearance of intergranular facets and corrosion products are illustrated in Fig. 14 by the scanning electron fractographs of a 7178-T651 alloy specimen tested in the short transverse direction (orientation 1, Fig. 1). The fractograph in Fig. 14(*b*), obtained by

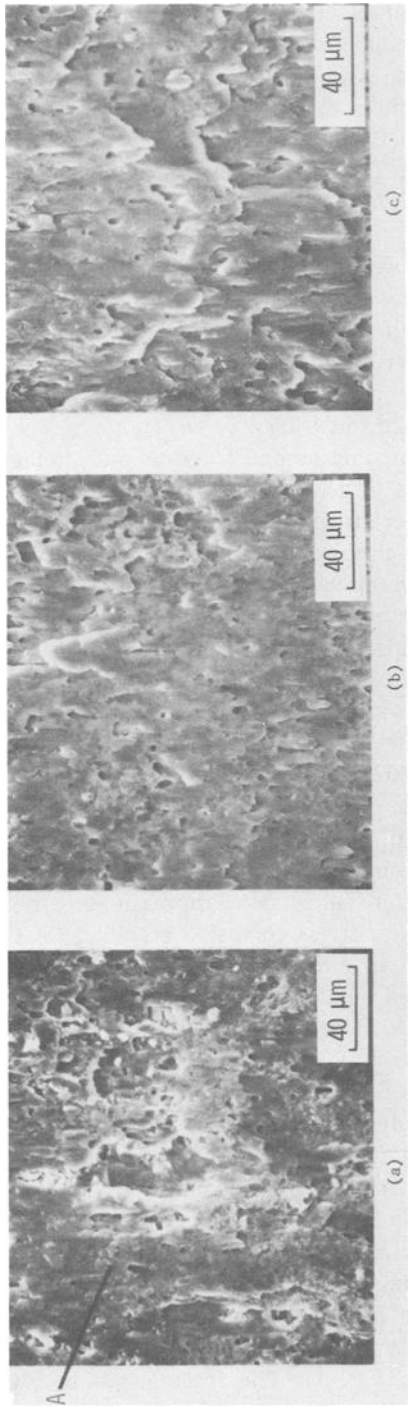
40 μm
(c)
40 μm
(b)
40 μm
(a)
A

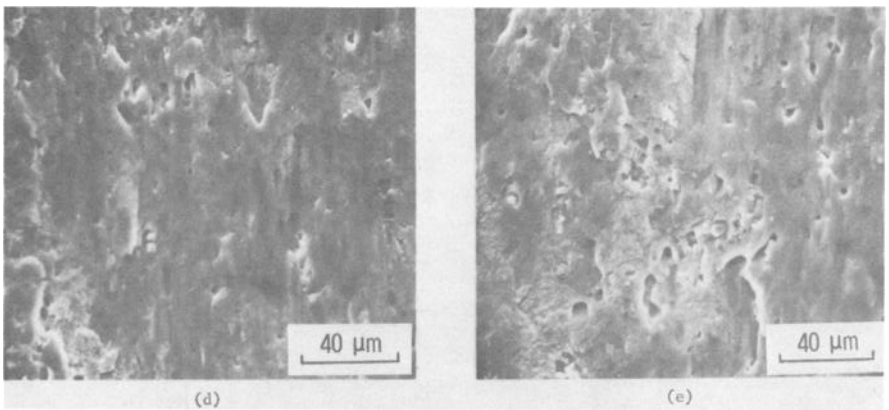


FIG. 7—*Scanning electron fractographs of sheet shear specimens, tested at the crosshead separation rate of 2.54 mm/min, of aluminum alloys*: (a) *2024-T3*, (b) *6061-T4*, (c) *6061-T6*, (d) *7075-T6, and* (e) *7178-T6*.

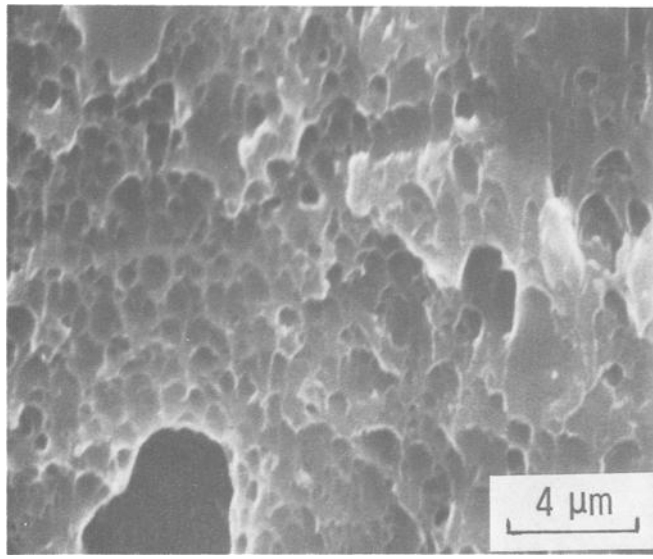


FIG. 8—*Scanning electron fractograph of a 2024-T3 sheet shear specimen, tested at the crosshead separation rate of 2.54 mm/min.*

magnifying the area near A in Fig. 14(*a*), illustrates the dried mud-flat patterns in the corrosion product. The fractograph in Fig. 14(*c*), obtained by magnifying the area B in Fig. 14(*a*), illustrates the smooth corrosion product coating with faint dried mud-flat cracks in some areas. X-ray chemical analysis indicated the loosely adherent particulate debris contains chlorides, probably aluminum and sodium chloride salt deposits from the alternate wet-dry cycles. Neither cracked nor smooth deposits contained chlorides suggesting they were hydrated or oxide products of aluminum. X-ray patterns obtained on both smooth and cracked corrosion products were similar. Cracked products could be the result of excessive thickening of smooth products and subsequent cracking during the drying process.

## Discussion

### *Interrelationships of Fracture Variables*

*Alloy Composition and Microstructure*—Alloy composition had a limited effect on fracture morphology as compared with other test variables. The fracture appearances seemed to group into two categories with the 2000 and 6000 series alloys exhibiting similarity and the two 7000 series alloys appearing similar. The observed appearance of the two groups in plate product form (dimpled structure versus ductile tear ridge formation)

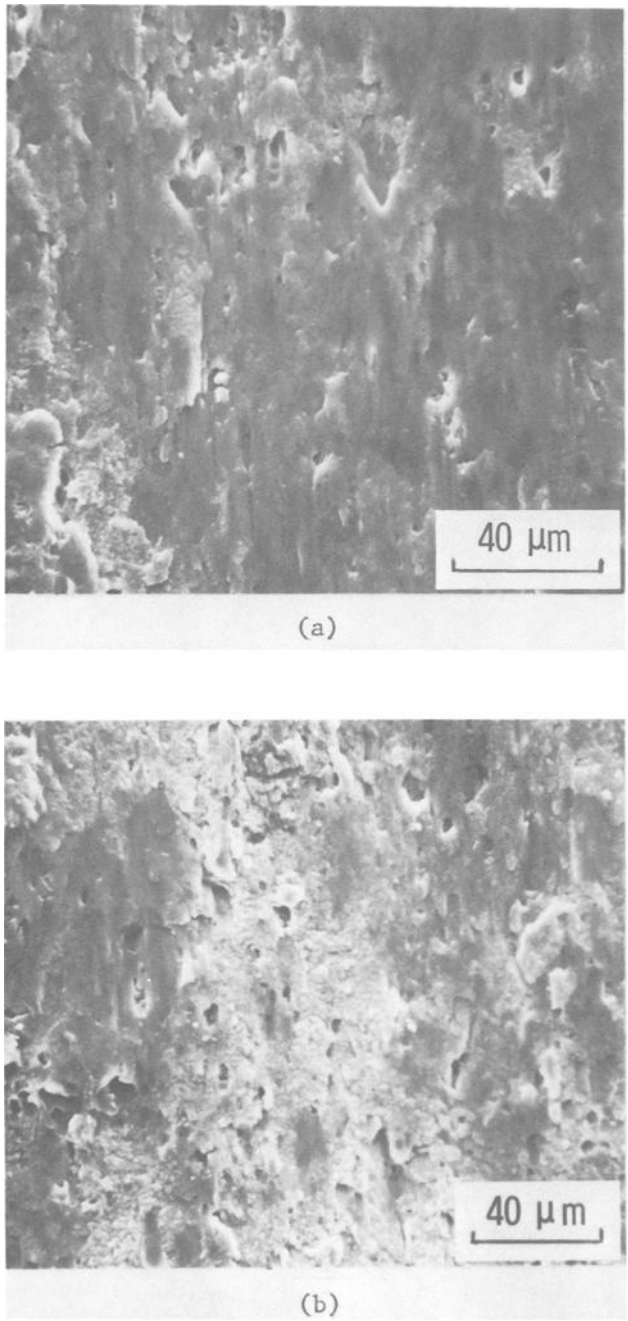


FIG. 9—*Scanning electron fractographs of 7075-T6 sheet shear specimens tested at crosshead separation rates of* (a) *2.54 mm/min and* (b) *76.2 mm/min.*

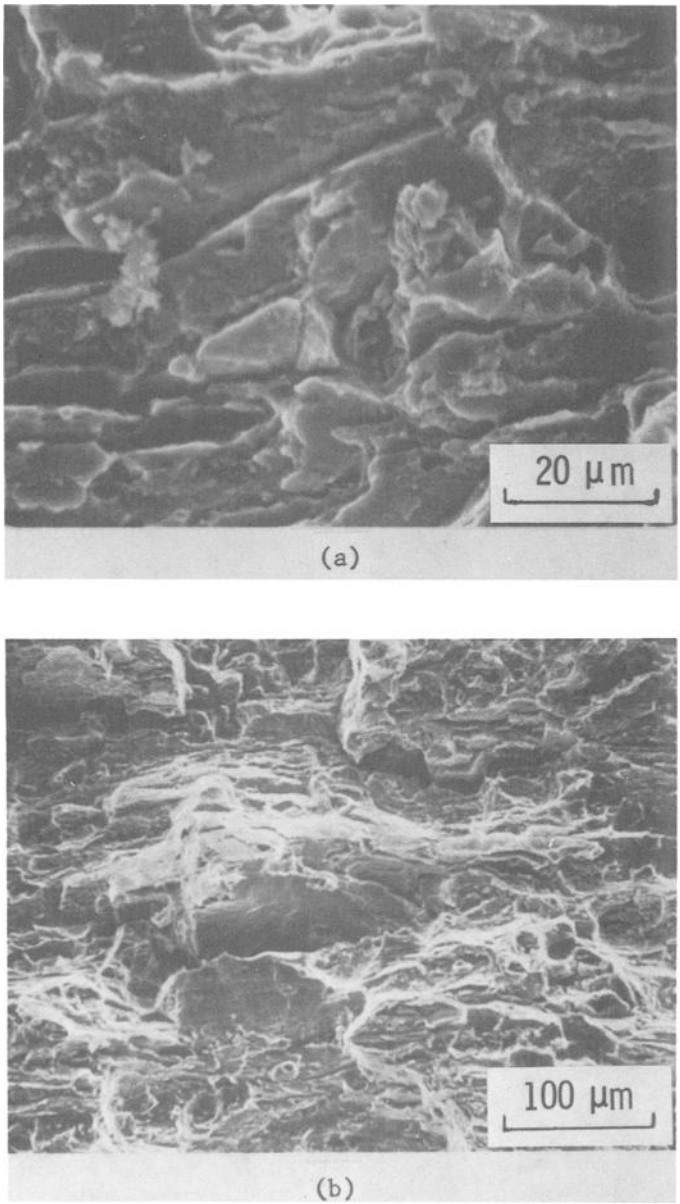


FIG. 10—*Scanning electron fractographs of a 7075-T651 notch-bend specimen.*

appears to be the result of both generic alloy composition differences and the effect of microstructure (banding, segregation). This grouping also followed for the sheet fatigue specimens, but it generally did not follow for shear or stress-corrosion specimens.

Large second-phase particle distribution also contributed to fracture appearance in plate tension and notch-bend specimens and sheet fatigue specimens. Dimple size and uniformity in 6061 alloy was attributed to the dense, homogeneous distribution of intermediate size (0.2 to 1 $\mu$m) particles. The extremely heterogeneous distribution of particles in 7000 series alloys contributed to the ductile tear ridge fracture appearance in plate specimens and smoother appearance (lower local ductility) of sheet fatigue specimen fracture surfaces.

Fracture morphology was not affected significantly by alloy composition and microstructure in sheet tension or stress-corrosion specimens, but increased surface roughness and particle cracking was observed on sheet shear specimens at higher strain rates.

*Product Form and Load Conditions*—Finer, more uniform dimple formation was observed in sheet tension specimens which was attributed to less elastic constraint imposed near microvoid nucleation sites and the general absence of large second phase particles (larger than 8 $\mu$m) in all sheet specimens. Larger particles in plate product contributed to a greater degree in the final fracture process.

Specimen orientation had little or no observable effect on fracture appearance, but strain rate changes affected the shear strengths of all the alloys examined and the fracture surface appearance of the 2024 and 7000 series alloys tested in shear. In sheet fatigue specimens fracture feature variations were more associated with the maximum tensile load experienced than with the load excursion (varying $R$ value). This difference was manifested by presence or absence of voids caused by particle-matrix interface failure and particle cracking, both of which occurred mostly at high maximum tensile stress levels.

Variation in stress level and crack growth direction may also be deduced from observations of fractures produced by SCC. Fracture surfaces which have been formed by a rapidly growing crack may contain less corrosion leaf formation. This would indicate that higher stress levels associated with crack growth direction could be deduced from the manner in which the corrosion leaves peel from the surface.

### *Application to Failure Analysis*

An attempt was made in the present investigation to characterize, in several high strength aluminum alloys, variables influencing fracture surface morphology. Several of the aspects that are summarized here are discussed in greater detail elsewhere [*31*]. The principal objective of the present paper was to identify the main features of fracture morphology of the alloys as influenced by the variables related to alloy and product form, microstructure, and testing conditions, and to highlight some points that are of importance in failure analysis. The ultimate goal of the study was to

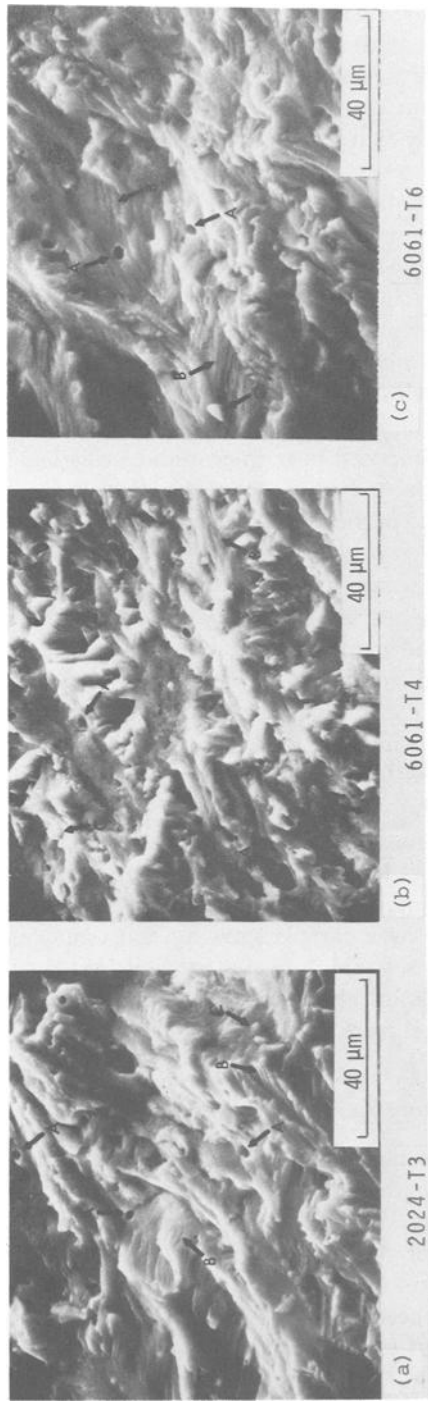
40 µm
(a) 2024-T3
40 µm
(b) 6061-T4
40 µm
(c) 6061-T6

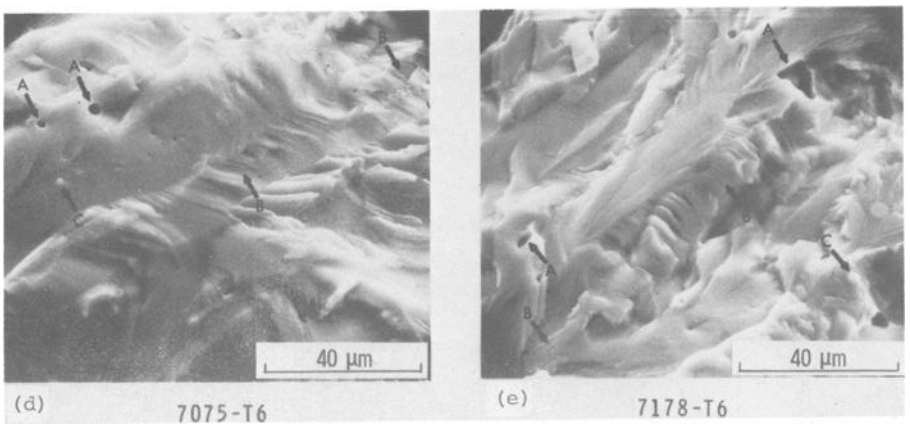


FIG. 11—*Scanning electron fractographs of sheet fatigue specimens at* R = *0.05*: (a) *2024-T3,* (b) *6061-T4,* (c) *6061-T6,* (d) *7075-T6, and* (e) *7178-T6. Nominal maximum stress was 64 MPa for 2024-T3 and 51 MPa for others.*

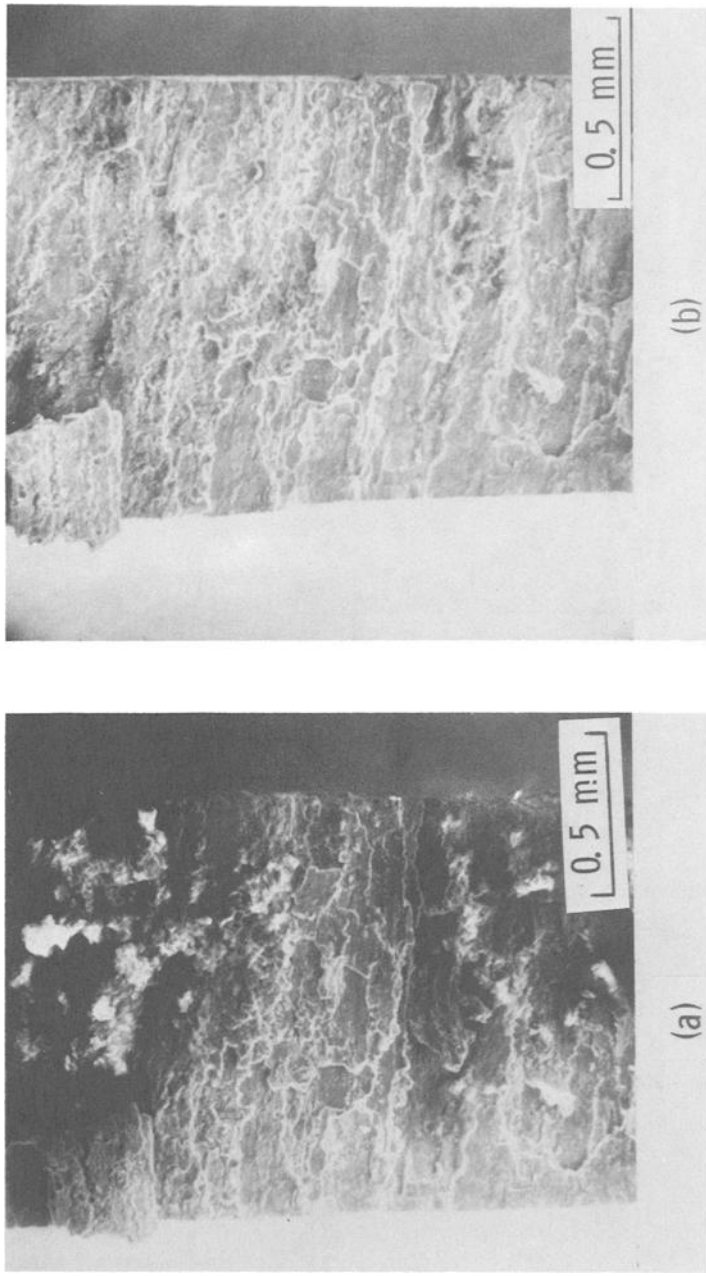


FIG. 12—*Scanning electron fractographs of a 2024-T351 stress-corrosion specimen tested in the short transverse direction:* (a) *after limited ultrasonic cleaning and* (b) *after extensive ultrasonic cleaning.*

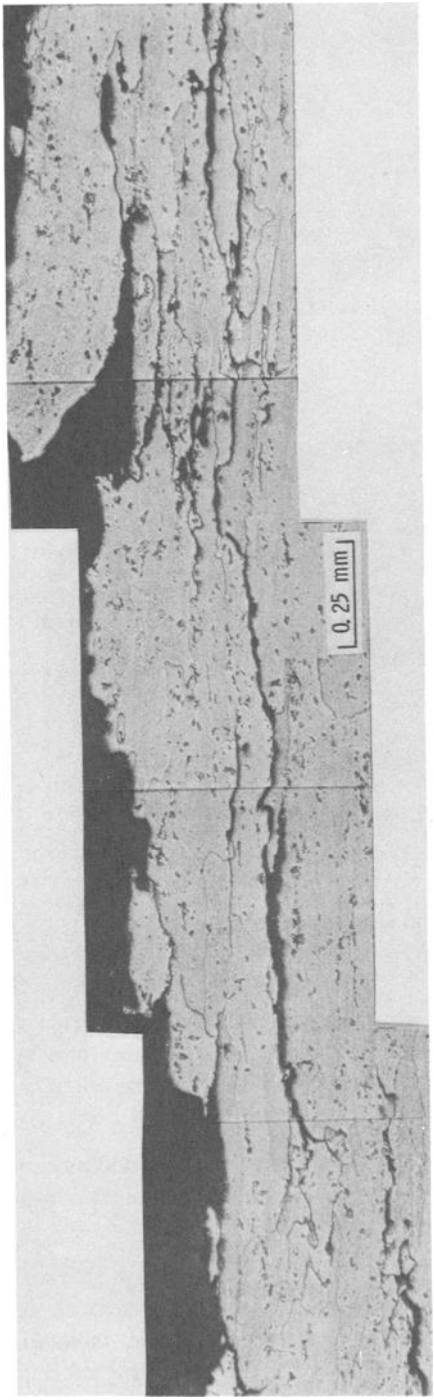


FIG. 13—*Optical micrograph of a section approximately normal to the fracture surface of a 2024-T351 stress corrosion specimen tested in orientation 3 (Fig. 1(d)).*

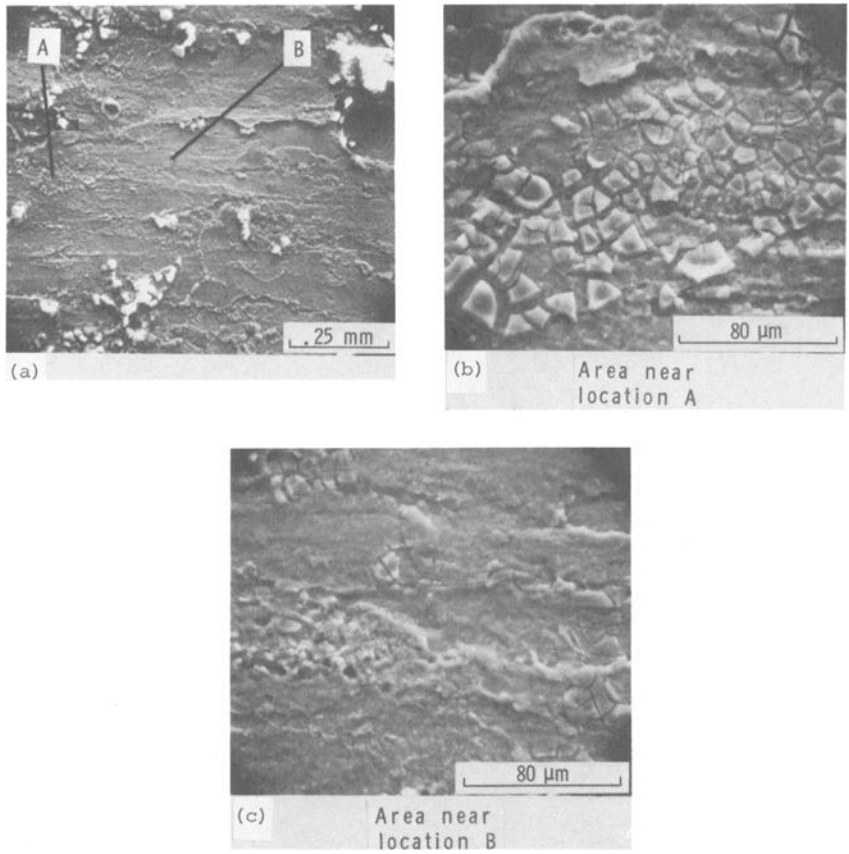


FIG. 14—*Stress corrosion fracture of a 7178-T651 specimen tested in the short transverse direction*: (a) *scanning electron fractograph,* (b) *higher magnification of area near A in* (a), (c) *higher magnification of area near B in* (a).

provide quantitative information which could be used to describe more accurately service failure conditions by analyzing the appearance of the failed component. Typical questions which arise when a service failure is experienced are as follows.

1. Can material quality be identified or excluded as cause of failure?
2. Can fatigue, stress-corrosion, embrittlement, or other service-related environments be identified as cause of failure?

Failure analysis methodology using microscopic, fractographic analysis has not progressed much beyond attempts to answer these basic questions. Most handbook information deals with specific, isolated examples which do not provide general guidelines for use in failure analysis work. Although the present investigation fell short of providing quantitative information re-

lating fracture variables, it did identify some important additional considerations which may have some general utility in advancing failure analysis methodology by fractography in aluminum alloys and providing direction for future work.

Fracture surface appearance of failures which occurred under macroscopically ductile conditions showed limited microscopic ductility associated with tear ridge formation. The random orientation or specific directionality of tear ridges could be used to indicate whether random crack nucleation and growth or specific crack propagation direction had occurred (for example, 7075 and 7178 plate tensile and notch-bend behavior).

In thinner gage materials, well defined striations were not the principle indicator of fatigue damage. Distribution of voids and cracked second-phase constitutents provided indications of load magnitude in fatigue or shear fracture related failures. Strain rate affected both shear ultimate strength and fracture surface morphology.

Observations of fracture surface appearance of failures which occurred by stress-corrosion cracking provided indications of direction of crack growth (for example, degree and orientation of corrosion leaf formation). Fracture surfaces which experienced chemical reaction with environment or exposure to contaminants were examined microscopically and by energy dispersive X-ray analysis both before and after cleaning. This was necessary to separate deposits which resulted from the fracture process from those which occurred as a result of handling after failure.

These observations were identified from considerations of general trends in the present program. Additional work, perhaps using automated analysis techniques, will be necessary to determine if such observations can be further quantified. Such information would be invaluable in furthering effective failure analysis by fractography.

*Acknowledgments*

The research leading to the publication of this report was performed during the tenure of M. D. Bhandarkar as a National Research Council Resident Research Associate at NASA Langley Research Center, Hampton, Va. The authors acknowledge Alberta Saunders, Materials Division, NASA Langley Research Center for considerable assistance in the experimental phase of the program. Appreciation is extended to Anamet Laboratories, Berkeley, Calif., where M. D. Bhandarkar is currently employed, for encouragement in the completion and presentation of the report.

## References

[1] Forsyth, P. J. E. and Ryder, D. A., *Metallurgica*, Vol. 63, 1961, pp. 117-124.
[2] Jacoby, G., *Experimental Mechanics*, Vol. 5, No. 3, 1965, pp. 1-18.

[3] Sprowls, D. O. and Brown, R. H., *Proceedings,* Conference on Fundamental Aspects of Stress Corrosion Cracking, The Ohio State University, 11-15 Sept. 1967, pp. 466-512.
[4] Jacobs, A. J., *Proceedings,* Conference on Fundamental Aspects of Stress Corrosion Cracking, The Ohio State University, 11-15 Sept. 1967, pp. 530-560.
[5] Hunter, M. S. and McMillan, J. C. in *Electron Fractography, ASTM STP 436,* American Society for Testing and Materials, 1968, pp. 196-211.
[6] Broek, D. in *Fracture 1969,* Chapman and Hall, London, 1969, pp. 754-764.
[7] Unwin, P. N. T. and Smith, G. C., *Journal of the Institute of Metals,* Vol. 97, 1969, pp. 299-310.
[8] Singh, S. N. and Flemings, M. C., *Transactions,* Metallurgical Society of American Institute of Mining, Metallurgical and Petroleum Engineers, Vol. 245, 1969, pp. 1811-1819.
[9] Tanaka, J. P., Pampillo, C. A., and Low, J. R., Jr. in *Review of Developments in Plane Strain Fracture Toughness Testing, ASTM STP 463,* W. F. Brown, Jr., Ed., American Society for Testing and Materials, 1970, pp. 191-215.
[10] Wei, R. P., *Engineering Fracture Mechanics,* Vol. 1, 1970, pp. 633-651.
[11] Kirmcin, I., *Metallurgical Transactions,* Vol. 2, 1971, pp. 1761-1770.
[12] Kershaw, J. and Liu, H. W., *International Journal of Fracture Mechanics,* Vol. 7, 1971, pp. 269-276.
[13] Hartman, A., Lievers, J. W., and van der Vet, W. J., "Study of the Growth of Stress Corrosion Cracks in the Aluminum Alloy 7075, Part I: Investigation on the Corrosive Medium," Report No. NLR TR 71090U, National Aerospace Laboratory, The Netherlands, 1971.
[14] Low, J. R., Jr., Van Stone, R. H., and Merchant, R. H., "An Investigation of Plastic Fracture in Aluminum Alloys," NASA Report CR-131100, National Aeronautics and Space Administration, 1972.
[15] Peel, C. J., Wilson, R. N., and Forsyth, P. J. E., *Metal Science Journal,* Vol. 6, 1972, pp. 102-106.
[16] Speidel, M. O. and Hyatt, M. V. in *Advances in Corrosion Science and Technology,* Vol. 2, Plenum Press, New York, 1972, pp. 115-335.
[17] Broek, D., *Engineering Fracture Mechanics,* Vol. 5, 1973, pp. 55-66.
[18] Broek, D., "Some Contributions of Electron Fractography to the Theory of Fracture," Report No. NLR TR 72029U, National Aerospace Laboratory, The Netherlands, 1973.
[19] Jones, D. L. and Liebowitz, H., *Engineering Fracture Mechanics,* Vol. 5, 1973, pp. 397-402.
[20] El-Sondani, S. M. and Pelloux, R. M., *Metallurgical Transactions.* Vol. 4, 1973, pp. 519-531.
[21] Hahn, C. T. and Simon, R., *Engineering Fracture Mechanics,* Vol. 5, 1973, pp. 523-540.
[22] Geschwind, G. and Adler, P. N., *Corrosion/73,* The International Corrosion Forum Devoted Exclusively to the Protection and Performance of Materials, Anaheim, Calif., 19-23 March 1973.
[23] *Metals Handbook,* Vol. 9, American Society for Metals, 1974.
[24] Rosenfield, A. R., Price, C. W., Martin, C. J., Thompson, D. S., and Zinkham, R. E., "Research on Synthesis of High Strength Aluminum Alloys, Part I, The Relation Between Precipitate Microstructure and Mechanical Properties in Aluminum Alloys," Technical Report AFML-TR-74-129, Part I, Air Force Materials Laboratory, Dayton, Ohio, 1974.
[25] Van Stone, R. H., Merchant, R. H., and Low, J. R., Jr. in *Fatigue and Fracture Toughness—Cryogenic Behavior, ASTM STP 556,* American Society for Testing and Materials, pp. 93-124, 1974.
[26] Wood, W. E. and Gerberich, W. W., *Metallurgical Transactions,* Vol. 5, 1974, pp. 1285-1294.
[27] Hahn, G. T. and Rosenfield, A. R., *Metallurgical Transactions A,* Vol. 6A, 1975, pp. 653-670.
[28] Nageswararao, M., Gerold, V., and Kralik, G., *Journal of Materials Science,* Vol. 10, 1975, pp. 515-524.
[29] Pittinato, G. F., Kerlin, V., Phillips, A., and Russo, M. A., *SEM/TEM Fractography Handbook,* Technical Report AFML-TR-75-159, Air Force Materials Laboratory, Dayton, Ohio, 1975.
[30] Aerospace Industries Association, Standard Test Procedure ARTC 13-5-1.

[31] Bhandarkar, M. D. and Lisagor, W. B., "Metallurgical Characterization of the Fracture of Several High Strength Aluminum Alloys," NASA TP-1086, National Aeronautics and Space Administration, Langley Research Center, Hampton, Va., 1977.
[32] *Metals Handbook,* Vol. 1, American Society for Metals, 1961.
[33] *Aluminum, Vol. I, Properties, Physical Metallurgy and Phase Diagrams,* K. R. Van Horn, Ed., American Society for Metals, 1967.
[34] *Metals Handbook,* Vol. 7, American Society for Metals, 1972.

# Fatigue

*P. R. Abelkis*[1]

# Use of Microfractography in the Study of Fatigue Crack Propagation under Spectrum Loading

**REFERENCE:** Abelkis, P. R., **"Use of Microfractography in the Study of Fatigue Crack Propagation under Spectrum Loading,"** *Fractography in Failure Analysis, ASTM STP 645,* B. M. Strauss and W. H. Cullen, Jr., Eds., American Society for Testing and Materials, 1978, pp. 213-234.

**ABSTRACT:** Use of electron microscope fractography in the study of fatigue crack propagation under spectrum loadings is based on the evaluation of 7075-T651 aluminum alloy specimens from an experimental program. Microscopically established crack propagation data by striation spacing measurements are shown to provide cycle-to-cycle evidence of crack propagation behavior under spectrum loading that normally cannot be established under macroscopic observation. Crack propagation rate retardation and acceleration is illustrated through fractographic striation measurements. Contribution and interaction of various loads of a transport wing loads spectrum are illustrated fractographically from the test program.

**KEY WORDS:** fractography, electron microscopes, spectrum loading, aluminum alloys, crack propagation, fatigue (materials)

## Nomenclature

| | |
|---|---|
| $a$ | Half crack length (hole not included) |
| $a_f$ | Total (final) crack length |
| $\Delta a/\Delta N$ | Rate of fatigue crack growth per cycle (also $da/dN$) |
| $\Delta a/\Delta F$ | Rate of fatigue crack growth per flight |
| FbF | Flight-by-flight |
| GAG | Ground-air-ground |
| $K$ | Stress intensity factor |
| $n$ | Number of cycles |
| $N_{a_f}$ | Life corresponding to $a_f$ as determined by striation counting from fractographs |
| $N_f$ | Total (final) test life |

[1] Senior engineer/scientist, Douglas Aircraft Company, McDonnell Douglas Corporation, Long Beach, Calif. 90846.

$R$ Stress ratio, $S_{min}/S_{max}$ or $K_{min}/K_{max}$
$S$ Stress
$S_{m_f}$ Flight mean stress
$S_{m_g}$ Ground mean stress
SEM Scanning electron microscope
TEM Transmission electron microscope
$t$ Sheet thickness
$\mu$m micrometre, $10^{-6}$ m or $3.937 \times 10^{-5}$ in.

This paper deals with the study of fatigue failure process through the use of electron microscope fractography. The emphasis is on the crack propagation stage under fatigue spectrum loading.

The fatigue failure process can be divided into two stages: (*a*) crack nucleation stage during which the load-carrying capacity of the structure experiences no appreciable reduction, and (*b*) crack propagation stage during which the load-carrying capacity is gradually reduced as a function of the crack length and fracture toughness of the material.

Complete failure will occur in either stage when the applied load exceeds the load-carrying capacity at that time. The length of Stage 1 depends on the initial fatigue quality of the material and structure. The length can be diminished substantially if the material in its basic form, or through manufacturing, contains flaws which act as strength reducers relative to standard material allowables or which initiate cracking in a short time. The length of Stage 2 depends on the material and structure basic crack propagation properties and the fatigue loadings and environment in which it operates. To design safe and economical structures, both stages of the failure process must be understood. Safety in the second stage is enhanced by thoroughness and frequency of inspections.

Crack propagation is a measurable quantity. This quantity can be determined on the macroscopic level by observing the crack propagation on the side of a specimen, or it can be established on the microscopic level by studying the fracture surface through the use of the electron microscope. The advantage of the latter method is that it provides cycle-by-cycle evidence, in the form of striations, of crack propagation behavior that normally cannot be established from macroscopic observations. This paper illustrates the use of the electron microscope in establishing the crack propagation rates of specimens subjected to a spectrum loading.

## Fracture Surface and Striations

The fracture surface is a fingerprint, or a record, of the loading experienced by the specimen or test structure in service. Figure 1 shows sample test and service fatigue fracture surfaces. Certain features of the loading are visible on the macroscopic scale. This is particularly true at longer crack

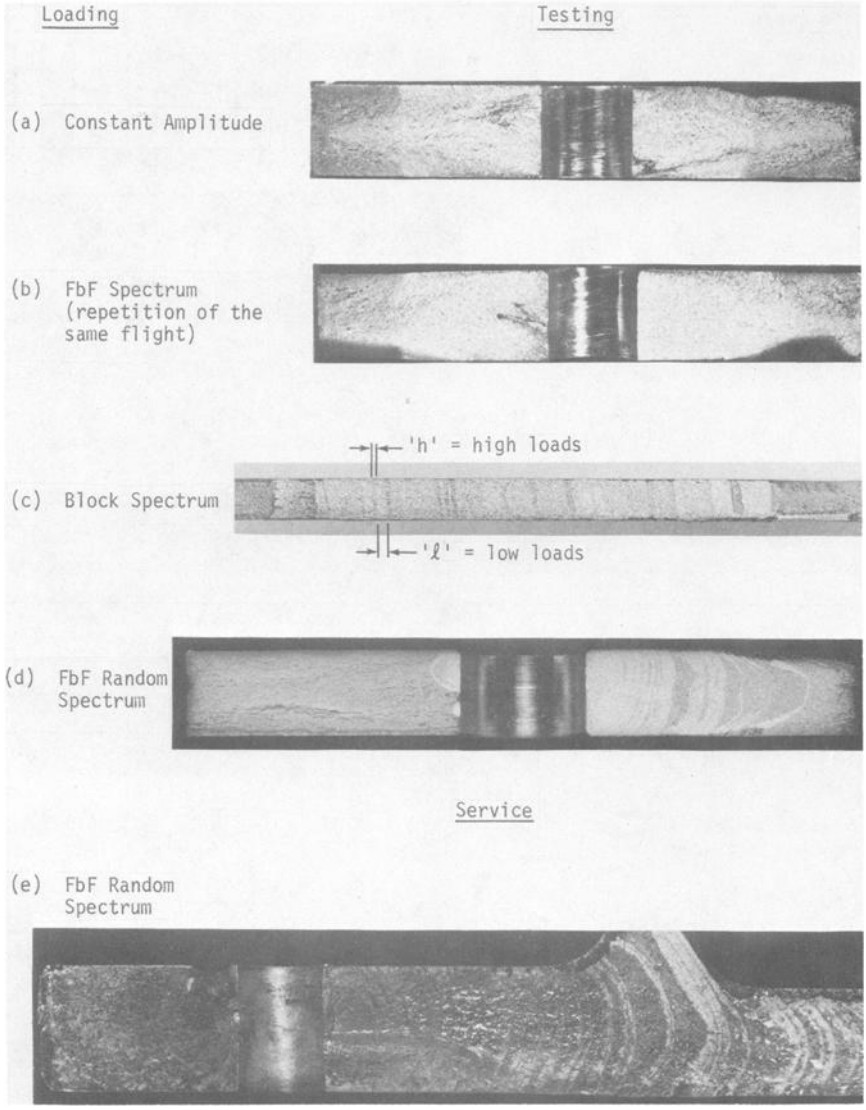


FIG. 1—*Sample test and service fatigue fracture surfaces—aluminum alloys.*

lengths. Larger loads in the spectrum produce a rougher surface which appears darker, while lower loads produce a smoother and brighter surface. Various such features are visible in Fig. 1. A block of higher load cycles is represented by the dark band "h" in Specimen (c) while the following block of lower load cycles is the brighter band "ℓ". In Specimens (d) and (e) at

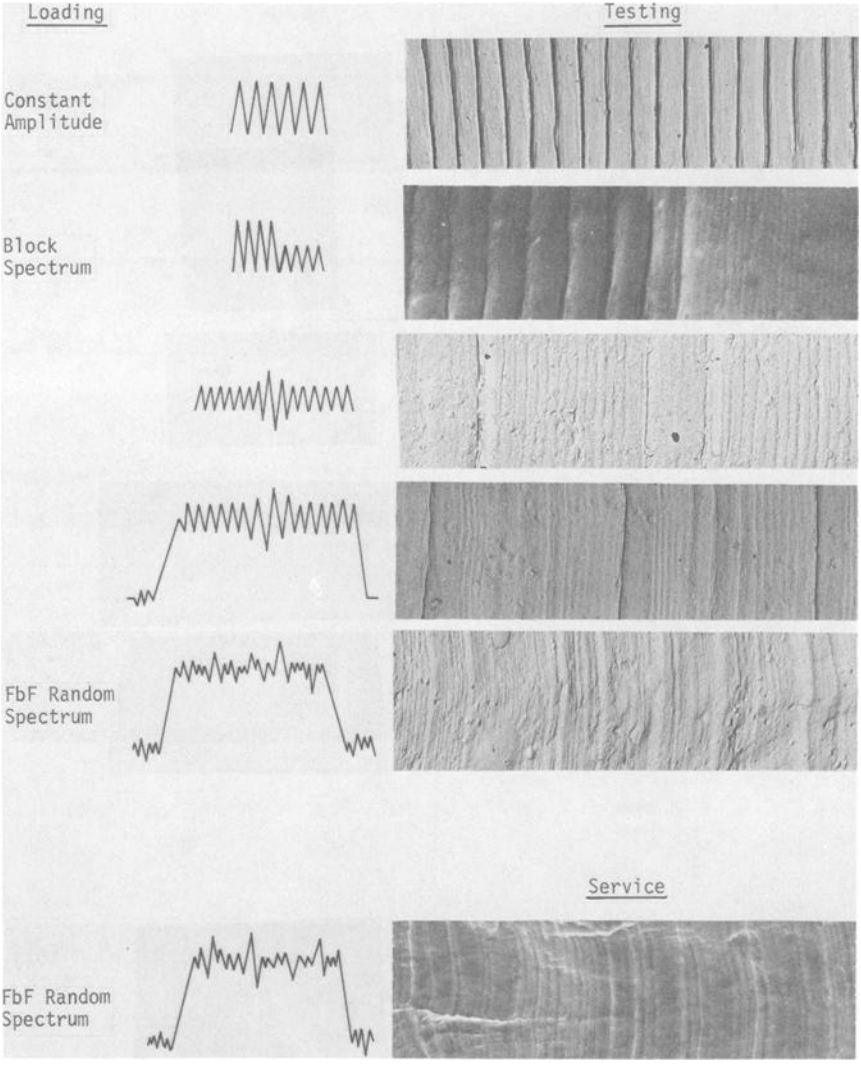


FIG. 2—*Examples of striation markings under various loading conditions—aluminum alloys.*

longer crack lengths, the darker bands are due to single high loads. Thus, limited knowledge can be obtained from such macroscopic observations about the loading spectrum and, if the load's spectrum and sequence are known, about the crack propagation rate. However, detail information about cycle-by-cycle crack propagation rates and load interaction effects can be obtained on the microscopic level through striation counting and

measurement of spacings between striations. In this context, striations are considered to represent successive positions of the crack front. Examples of striation markings, under various loading sequences, are illustrated in Fig. 2.

To obtain crack propagation data from fractographs, one must be able to recognize and relate striations to known loading cycles. The problem is rather straightforward for constant amplitude loading. However, it becomes a complex and difficult problem for spectrum loadings. Interpretation of the striations in this study was based on the following observations and findings [*1,2*].[2]

1. Crack advances only due to increasing tension loading. However, striation profiles and appearance depend on loading and unloading portions of the cycle.

2. Crack propagation can occur only during that portion of the loading cycle in which the crack is fully open at the crack tip.

3. Crack closure may occur before the minimum load is reached.

4. A cycle may not produce a striation and crack advance, because (*a*) previous loading has completely retarded (stopped) cracking, or (*b*) loading is below the threshold value for propagating cracks.

5. A striation may not be visible in a fractograph, because (*a*) it has been obliterated because of fracture surface damage, mechanical or chemical, or (*b*) the angle at which electron microscopy was performed did not reveal the striation.

6. Crack propagation rates from microfractographs are established by measuring the distance between striations and knowing the crack length at that point. The spacing between striations of the same loading in one fractograph or adjacent fractographs may vary much more than the called for change in crack length. This could be due to a number of factors. On the microscopic level, cracks propagate on many planes and in many directions. What is seen on the side of the specimen is the net propagation of the total crack front which exhibits less scatter. Also, locally the crack may be retarded by inclusions, or the fracture surface, as viewed by the electron microscope, may not be perpendicular to the electron beam, and the resulting fractograph will not represent the true dimension. To establish the true dimension, the replicate or the specimen should be rotated in the electron microscope to produce the largest spacing between striations. An example of such striation spacing variation for constant amplitude (CA) loading is given in Fig. 3. Because of such variations, the measurements are (*a*) made in the direction of the general crack front propagation, (*b*) averaged over a number of cycles, and (*c*) made along a somewhat straight line, usually in the middle of the specimen. From this it follows that to establish valid crack propagation rates by striation measurements, one

[2] The italic numbers in brackets refer to the list of references appended to this paper.

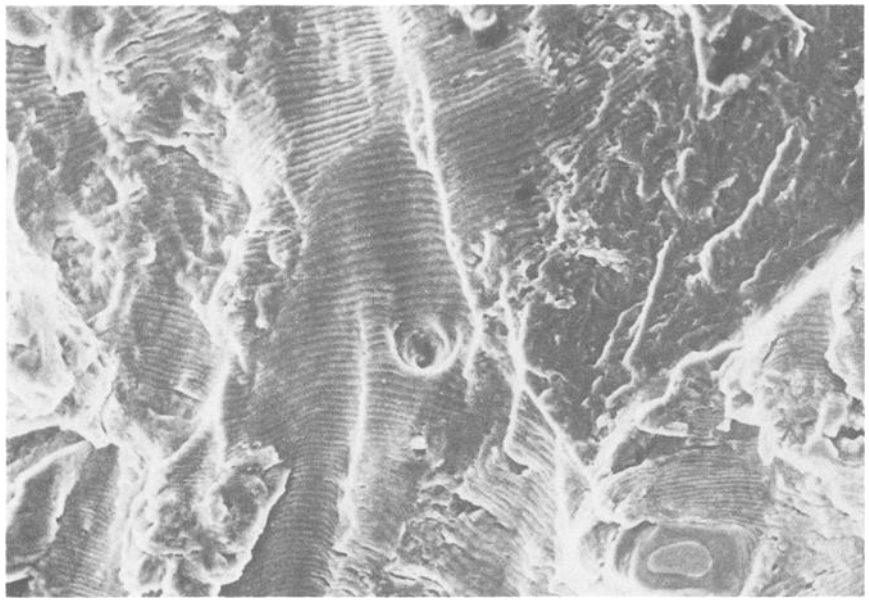

FIG. 3—*Striation spacing variation within one fractograph—constant amplitude loading.*

must obtain data over a reasonably long crack length and cannot depend on the rate established from one fractograph.

## Experimental Program

Unless otherwise noted, the fractography work reported herein was done on a center-hole notched 7075-T651 bare sheet specimen, 6.35 mm (0.25 in.) thick, 38.1 mm (1.5 in.) wide, with a 6.36 mm (0.250 in.) diameter hole. Fatigue cracks were initiated from the hole and the crack length $a$ is taken from the edge of the hole. The program consisted of testing 81 specimens under constant amplitude and spectrum loadings. Fractography work was done on 25 of these specimens. A summary of the loadings on these specimens is presented in Table 1. Total test lives and crack lengths are given in Table 2. Specimens identified as second group specimens were made and tested a year later than the first group. Because of a difference in hole preparation (drilled versus drilled and reamed for the second group), the test lives of the second group specimens were approximately twice as long as those of the first group for the same type of loadings. However, crack propagation rates were about the same, indicating that the difference in hole preparation influenced only the length of crack initiation stage.

The loadings on the specimens were derived from a loads spectrum typical of a short-medium range jet aircraft. The stresses represent the wing

**TABLE 1—*Test loadings.***

Spectrum Loadings:

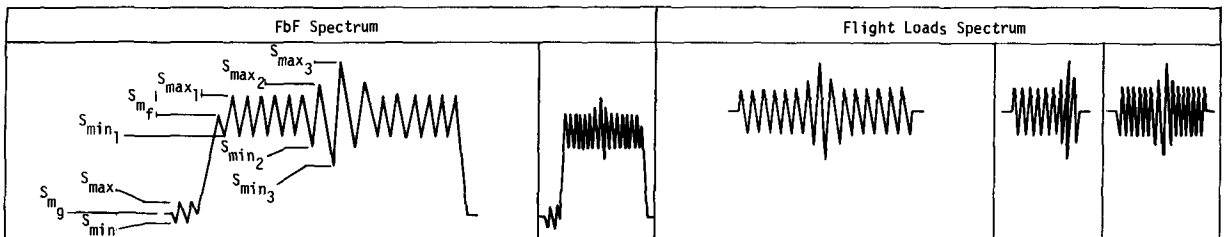


| Specimen | 111,112,113 | 122,123 | 133 | 141 | 163* | 211,212 | 221,222 | 242* | 251* | X211,X212 |
|---|---|---|---|---|---|---|---|---|---|---|
| $S_{m_g}$ | -34.5 (-5.0) | → | → | → | -34.5 (-5.0) | | | | | |
| $S_{max}$ | -21.4 (-3.1) | → | → | -13.8 (-2.0) | -21.4 (-3.1) | | | | | |
| $S_{min}$ | -47.6 (-6.9) | → | → | -55.2 (-8.0) | -47.6 (-6.9) | | | | | |
| $S_{m_f}$ | 86.2 (12.5) | → | → | → | 72.4 (10.5) | 86.2 (12.5) | → | 72.4 (10.5) | → | 86.2 (12.5) |
| $S_{max_1}$ | 111.0 (16.1) | → | → | → | 93.1 (13.5) | 111.0 (16.1) | → | 93.1 (13.5) | → | 111.0 (16.1) |
| $S_{min_1}$ | 61.4 (8.9) | → | → | → | 51.7 (7.5) | 61.4 (8.9) | → | 51.7 (7.5) | → | 61.4 (8.9) |
| $S_{max_2}$ | 120.0 (17.4) | → | → | → | 100.7 (14.6) | 120.0 (17.4) | → | 100.7 (14.6) | → | 120.0 (17.4) |
| $S_{min_2}$ | 52.4 (7.6) | → | → | → | 44.1 (6.4) | 52.4 (7.6) | → | 44.1 (6.4) | → | 52.4 (7.6) |
| $S_{max_3}$ | 166.2 (24.1) | 139.3 (20.2) | 124.1 (18.0) | 139.3 (20.2) | 139.3 (20.2) | 166.2 (24.1) | 139.3 (20.2) | 139.3 (20.2) | → | 166.2 (24.1) |
| $S_{min_3}$ | 6.2 (0.9) | 33.1 (4.8) | 48.3 (7.0) | 33.1 (4.8) | 4.8 (0.7) | 6.2 (0.9) | 4.8 (0.7) | 4.8 (0.7) | → | 6.2 (0.9) |

Constant Amplitude Loadings:

| | Specimen | $S_m$ | $S_{max}$ | $S_{min}$ | R |
|---|---|---|---|---|---|
| Flight Loads Cycles | X311,X313 | 86.2 (12.5) | 166.2 (24.1) | 6.2 (0.9) | 0.036 |
| | 311-2,312-2* | 86.2 (12.5) | 166.2 (24.1) | 6.2 (0.9) | 0.036 |
| | 333 | 86.2 (12.5) | 124.1 (18.0) | 48.3 (7.0) | 0.39 |
| GAG Cycles | X411 | 59.3 (8.6) | 166.2 (24.1) | -47.6 (-6.9) | -0.29 |
| | 423-1* | 46.2 (6.7) | 139.3 (20.2) | -47.6 (-6.9) | -0.34 |
| | 433 | 38.6 (5.6) | 124.1 (18.0) | -47.6 (-6.9) | -0.38 |
| | 452 | 26.2 (3.8) | 86.2 (12.5) | -34.5 (-5.0) | -0.4 |

Stresses shown are test section gross area stresses, MN/m2 (KSI). (Net/Gross) Area Stress = 1.20

*Second group specimens.

TABLE 2—*Test lives and crack propagation.*

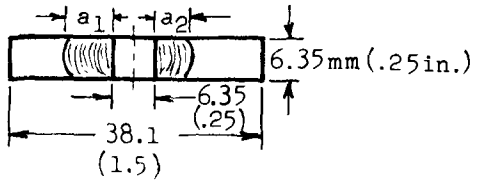


| Specimen | $N_f$[a] | $a_f$ mm (in.) | $N_{af}$ | $N_{af}/N_f$ | $N_{\Delta a}$[b] |
|---|---|---|---|---|---|
| 111 | 11 030 | 8.64 (0.340) | 6 436 | 0.58 | 3 140 |
| 112 | 8 568 | 5.72 (0.225) | 4 568 | 0.53 | 2 835 |
| 113 | 13 533 | 9.53 (0.375) | 12 514 | 0.93 | 5 697 |
| 122 | 17,067 | 11.10 (0.437) | 7 404 | 0.43 | 4 129 |
| 123 | 14 750 | 8.81 (0.347) | 8 821 | 0.60 | 5 919 |
| 133 | 22 340 | 12.70 (0.50) | 9 067 | 0.41 | 4 626 |
| 141 | 15 049 | 10.74 (0.423) | 6 883 | 0.46 | 4 487 |
| 163 | 66 546 | 10.13 (0.399) | 6 936 | 0.10 | 3 635 |
| 211 | 21 178 | 10.67 (0.42) | 10 867 | 0.51 | 4 726 |
| 212 | 14 921 | 7.47 (0.294) | 6 787 | 0.46 | 3 919 |
| X212 | 16 566 | 9.70 (0.382) | 8 216 | 0.50 | 4 475 |
| 221 | 16 194 | 12.78 (0.503) | 8 737 | 0.54 | 4 136 |
| 222 | 36 101 | 13.44 (0.529) | 9 785 | 0.27 | 5 777 |
| 242 | 35 083[c] | ... | ... | ... | ... |
| 251 | 41 612[c] | ... | ... | ... | ... |
| X311 | 25 680 | 7.11 (0.280) | 11 261 | 0.44 | 8 402 |
| X313 | 31 893 | 7.62 (0.30) | 15 533 | 0.49 | 9 498 |
| 311-2 | 55 018 | 9.86 (0.388) | 18 755 | 0.34 | 14 352 |
| 312-2 | 75 087 | 6.99 (0.275) | 11 947 | 0.16 | 10 429 |
| 333 | 214 824 | 14.66 (0.577) | 61 062 | 0.28 | 31 711 |
| X411 | 24 854 | 5.08 (0.20) | 11 020 | 0.44 | 6 258 |
| 423-1 | 78 925 | 7.39 (0.291) | 20 488 | 0.26 | 14 361 |
| 433 | 45 390 | 6.86 (0.27) | 14 348 | 0.32 | 9 741 |
| 452 | 474 514 | 13.72 (0.54) | 54 321 | 0.12 | 39 953 |

[a] Flights for spectrum loadings, cycles for constant amplitude loadings.
[b] $\Delta a \approx 0.30$ to 5.08 mm (0.012 to 0.20 in.).
[c] Grip end failures.

lower surface outboard of the landing gear. The objective of the experimental program was to subject the specimens to a flight-by-flight (FbF) spectrum loading and then to individual components of this spectrum, in order to evaluate their independent contributions to fatigue damage and crack propagation. In this manner, all loadings were divided into four types, using the first digit of the specimen number for identification:

1. FbF spectra
2. Flight loads spectra
3. Flight loads constant amplitude (CA) loadings
4. Ground-air-ground (GAG) CA loadings, which represent the transition from the compression ground loads to the tension flight loads

### Crack Propagation Rates under Constant Amplitude Loading

The simplest fatigue cyclic loading is constant amplitude. It is a loading with constant mean and amplitude (Fig. 2). The crack propagation rates under CA loading usually are presented as

$$da/dN \text{ versus } \Delta K \text{ for a given } R$$

where

$\Delta K = K_{max} - K_{min}$,
$= $ stress intensity factor range,
$K = (\sigma\sqrt{\pi a}) \cdot \lambda = $ stress intensity factor,
$\sigma = $ applied gross area stress,
$a = $ crack length, and
$\lambda = $ correction factor for the effect of hole, width, stiffener, etc.

These data usually are obtained by measuring the crack propagation on the side of a specimen during a test. Use of electron microscope fractography to obtain these data by striation spacing measurements is too tedious, time-consuming, and less accurate due to large scatter. Only for special studies, such as checking the rates at short crack lengths, at multiple crack nucleation sites, or in the interior of the specimen where the crack is not visible on the surface, is use of fractography justified. An example of *da/dN* data obtained in this manner is shown in Fig. 4. The scatter in such data is quite obvious here although the data does follow generally expected *da/dN* data trends as indicated by the Forman [*3*] equation. Also, it should be noted that negative $R$ rates are not the same as $R = 0$ rates.

### Crack Propagation Rates under Spectrum Loadings and Load Interaction Effects

The simplest spectrum loading is a two-load-level block spectrum, Fig. 5. Fractographic analysis shown here was done on a 7075-T651 bare sheet

| a | mm | in. |
|---|---|---|
| $\Delta K$ | $(MN/m^{3/2}) \times 10^3$ | $psi\sqrt{in.}$ |
| $K_c$ | 45,320 | 41,200 |
| n | 2.48 | 2.48 |
| C | $2.19 \times 10^{-10}$ | $9.94 \times 10^{-12}$ |

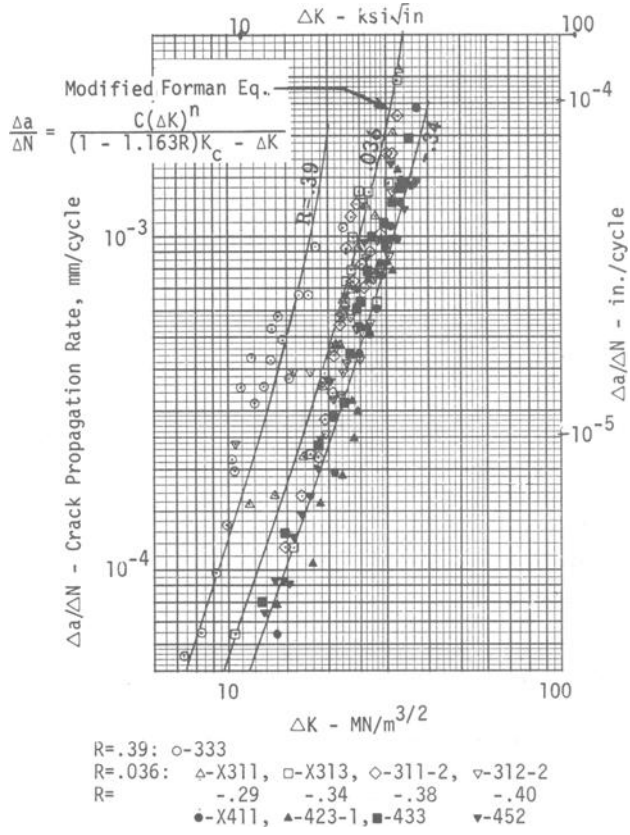


FIG. 4—*7075-T651 crack propagation rates, constant amplitude loading,* $\Delta K = K_{max} - K_{min}$.

center crack, $t$ = 6.35 mm (0.25 in.), 304.8 mm (12 in.) wide specimen. This is an example of studying load interaction effects in the simplest form: transition from high to low and from low to high load and what effect it has on crack propagation rate. The number of cycles chosen for each block, on the basis of plastic zone size due to the high load, were such as to produce, at the end of each block, a crack propagation rate approaching that of CA loading. Microfractographs were obtained at load transition points and at midpoint of the low loading blocks. The data show

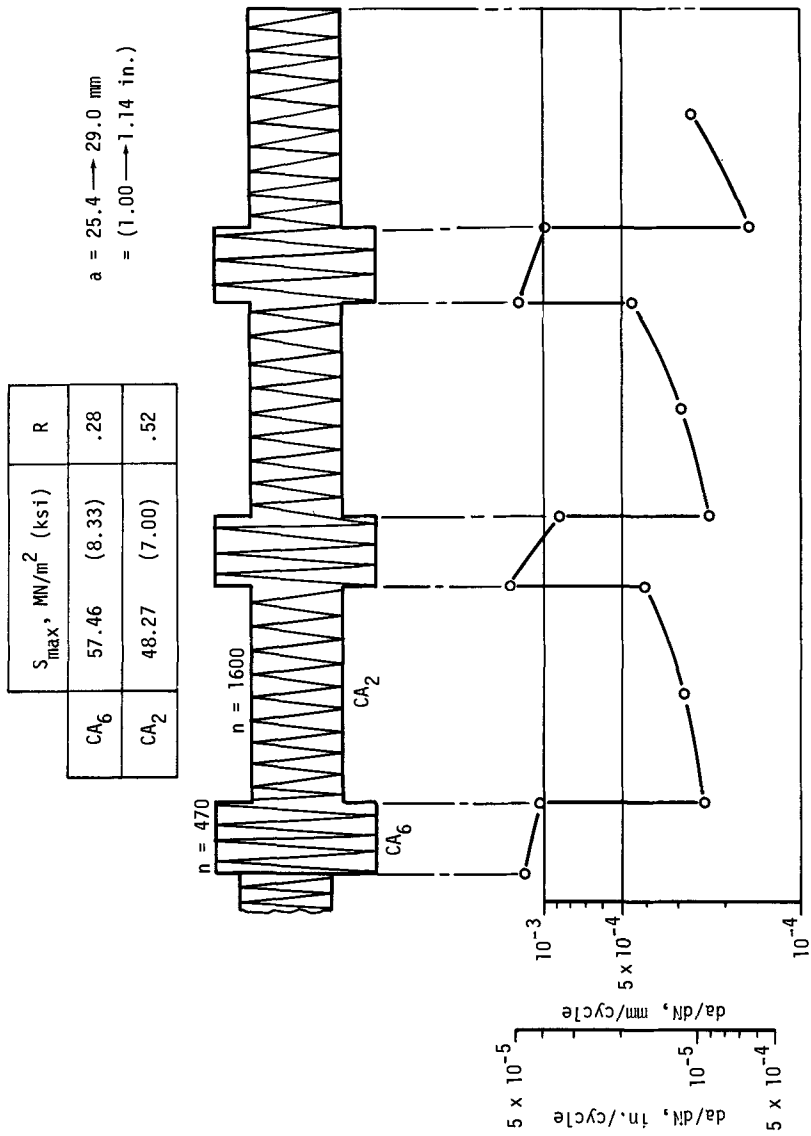


FIG. 5—*Loading interaction effects in crack propagation, 7075-T651, fractography results.*

the well known [*1,2*] crack retardation effect of high load on the following lower load crack propagation rate, although this sometimes is considered not to occur at such a low overload ratio as 1.2 in this case. The data also show that the crack propagation rate at higher load after the transition from the lower load is accelerated when compared to the *da/dN* data at the end of the block. This example shows that retardation and acceleration phenomena in simple spectrum loading crack propagation can be defined through microfractography, although care must be exercised in distinguishing between scatter in crack propagation rates as established by striation spacing measurements and real load interaction effects.

Next, more complicated spectrum loadings of the type shown in Table 1 are considered. Fractographs shown in Fig. 6 illustrate the striation spacings and patterns at various crack lengths for a typical FbF spectrum loading. Figures 7 and 8 illustrate the correlation between striations and individual loading cycles in the spectra. The following observations can be made about the interpretation of these fractographs.

1. Striation groups representing individual flights were identified for all loadings and specimens.

2. Striations of individual cycles within a flight can be identified only at longer crack lengths. At shorter crack lengths, identification is possible only of the major loadings, such as the GAG cycle and the peak flight load. Close to crack initiation, a complete flight appears as one striation. Striations representing one flight can be identified at crack lengths as short as 0.076 to 0.152 mm (0.003 to 0.006 in.).

3. Best striation identification is possible for spectra with the lower flight peak loads. Identification of all individual striations becomes more difficult for the spectra with the higher peak loads, in particular, the striations due to the highest load cycles. Difficulties also are encountered in trying to identify the separation of the GAG cycle striation from the following flight low load cycle striations, as well as the beginning of the low load cycle striations after the flight peak loads. In general, the flight low load striations are clearer after the GAG cycle than after the peak loads.

4. Significant markings (deep valleys or high peaks) are associated with the GAG and the peak flight load cycles. Since these markings seem to precede these cycles, they appear to be caused by the large unloadings preceding these cycles. These markings remain dominant in the fractographs at shorter cracks while the striations of the lesser cycles become indistinguishable.

5. Crack propagation, as measured by striations, is primarily due to the increasing load between reversals, although the striation profile and to a certain extent the striation width are influenced by previous loadings and the following unloading.

Crack propagation rates for these types of spectra loadings, as established by striation spacing measurements, are given in Figs. 9 and 10. The rates

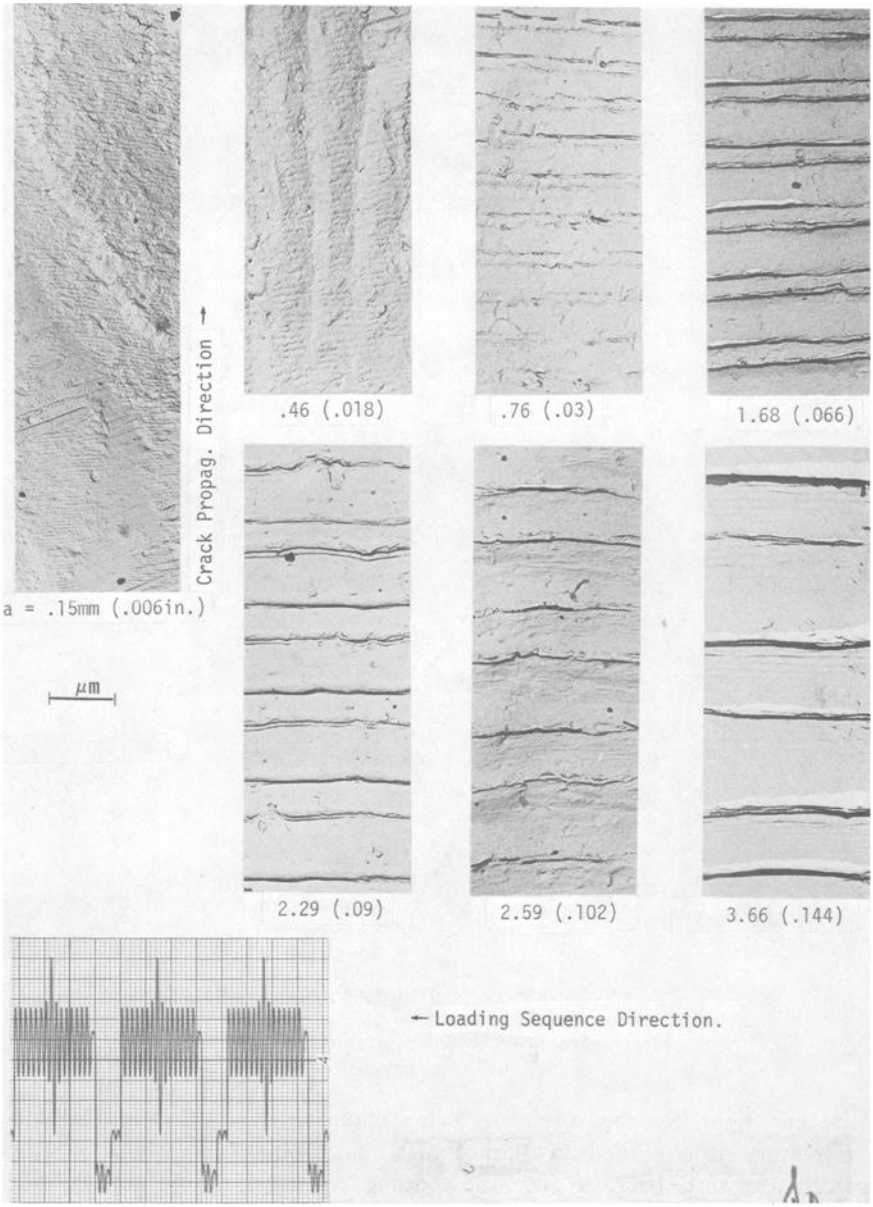


FIG. 6—*FbF spectrum loading, specimen 113 fractographs.*

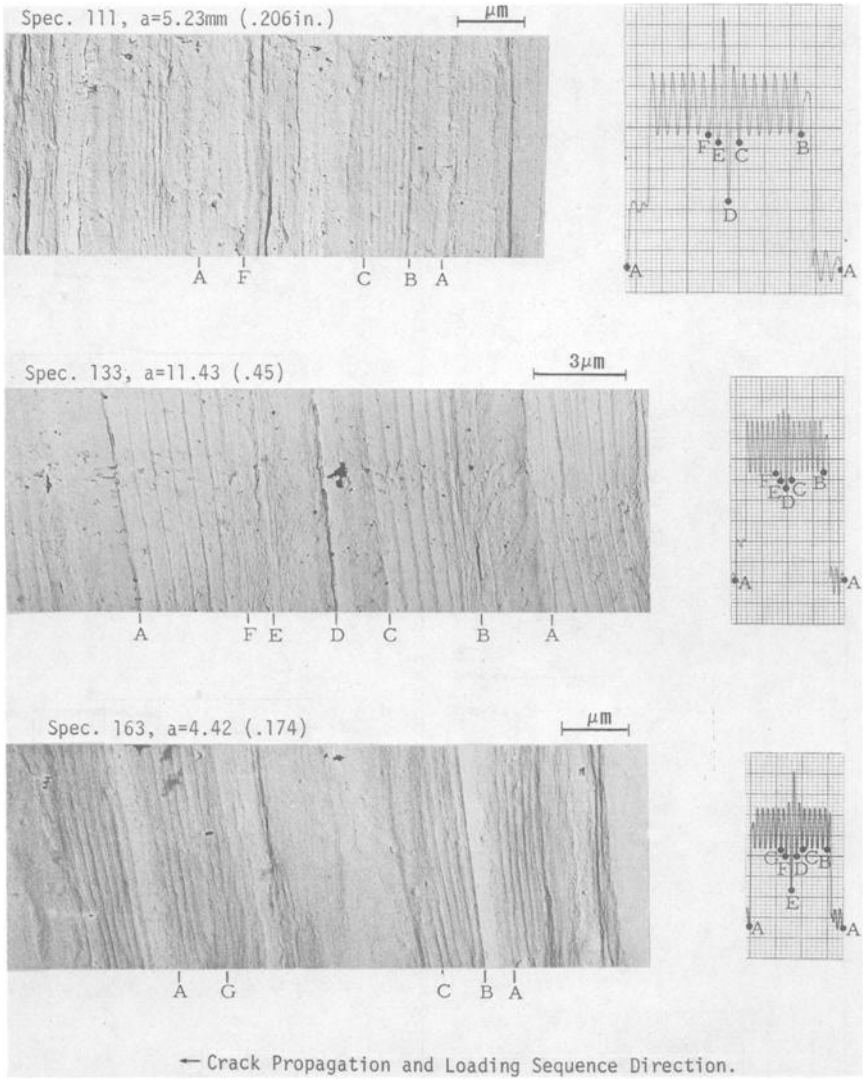


FIG. 7—*Striation—loading correlation, FbF Spectra.*

are per flight, the measurements being made for a group of cycles which represent a flight. Identification of striation groupings as a flight is rather straightforward here because the loading consisted of the repetition of exactly the same flight (Figs. 7 and 8). The identification is first accomplished at longer crack lengths and then chronologically the groupings can be traced to shorter crack lengths (Fig. 6). Several observations and interpretations can be made about these rates.

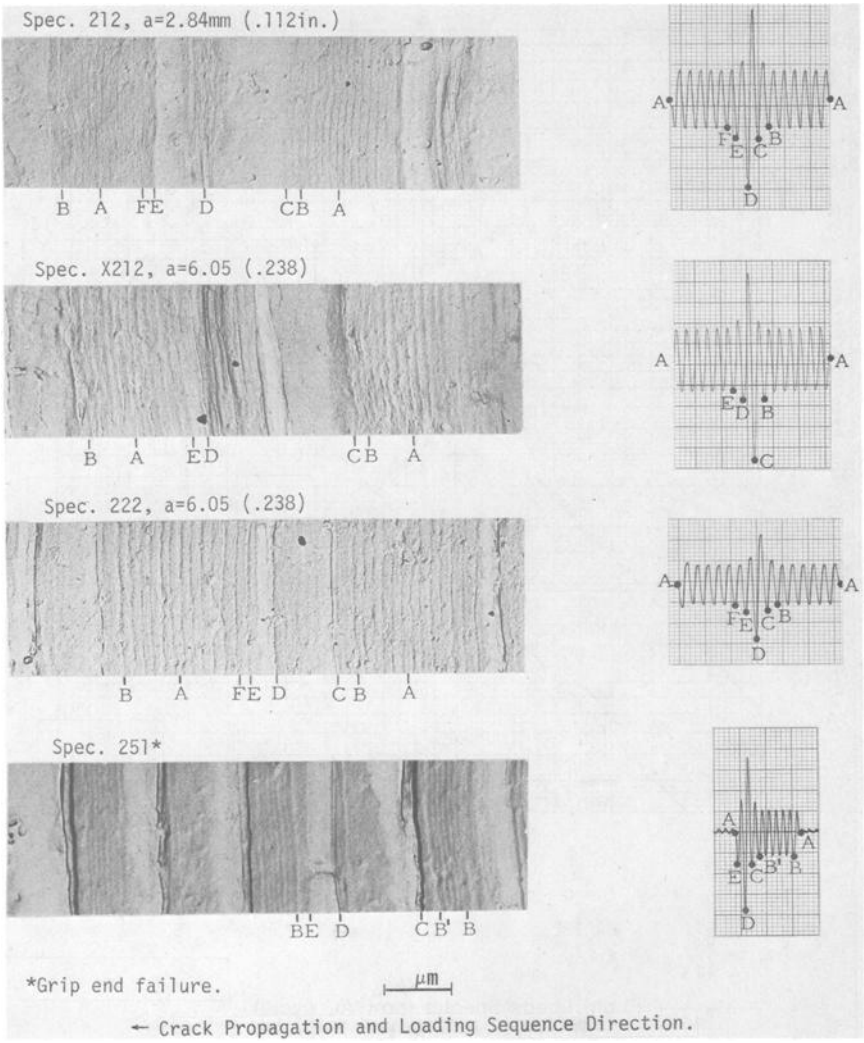


FIG. 8—*Striation—loading correlation, flight loads spectra.*

1. Crack propagation rates were approximately the same for spectra run in opposite directions with respect to loading sequence. Compare rates of Specimens 211 and 212 against Specimen X212 (Fig. 10 and Table 2). Similar results have been observed by other investigators [*4*].

2. There appear to be no significant trends in the crack propagation rates with respect to the flight peak load when observing the data in Figs. 9 and 10. All rates fall within the same general scatter band. However, a more detailed analysis of the data, such as in Table 2, shows a tendency

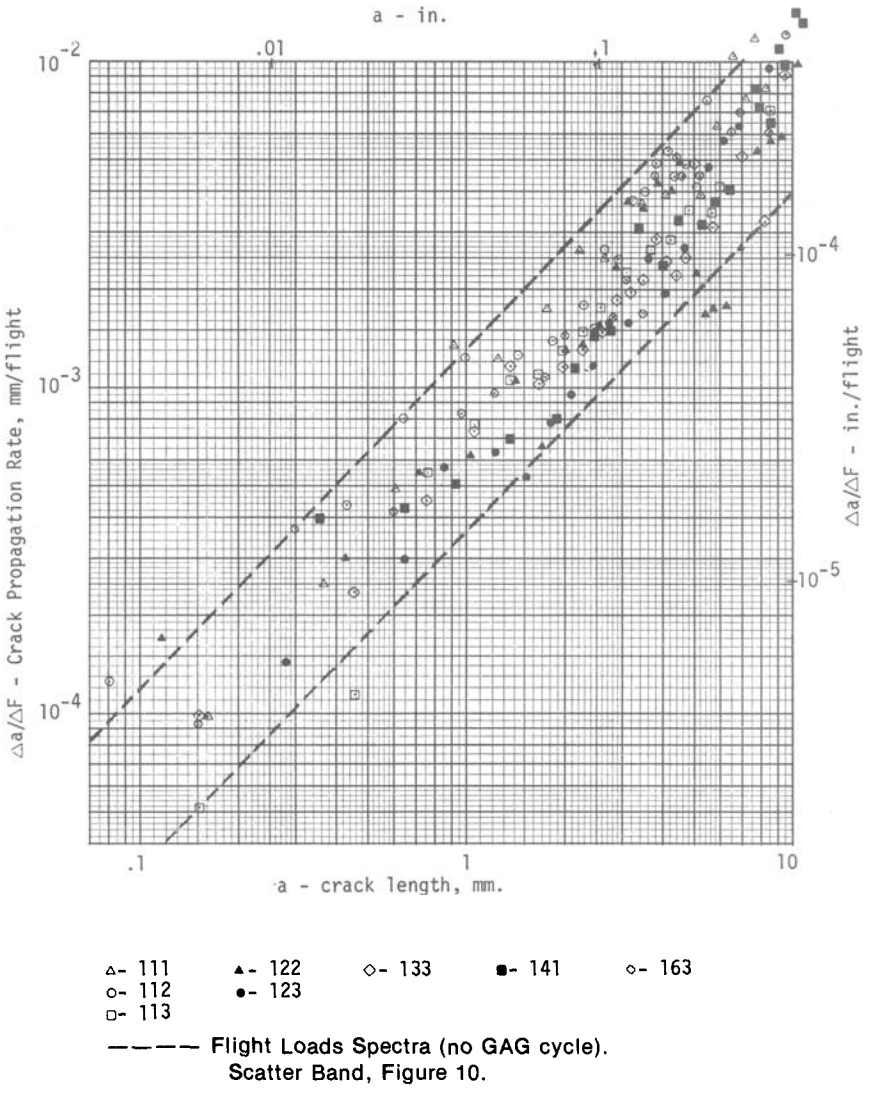


FIG. 9—*Crack propagation rates, FbF spectra.*

for the rate to increase as the flight peak load increases. In general, the small differences in the rates are probably due to the fact that as the crack propagation rate due to peak load itself increases, the rate of the lower loads decreases due to the increasing retardation, with the two rate changes in opposite directions tending to offset each other.

3. Within the general scatter, the crack propagation rates per flight with or without the GAG cycle appear to be the same when comparing the rates

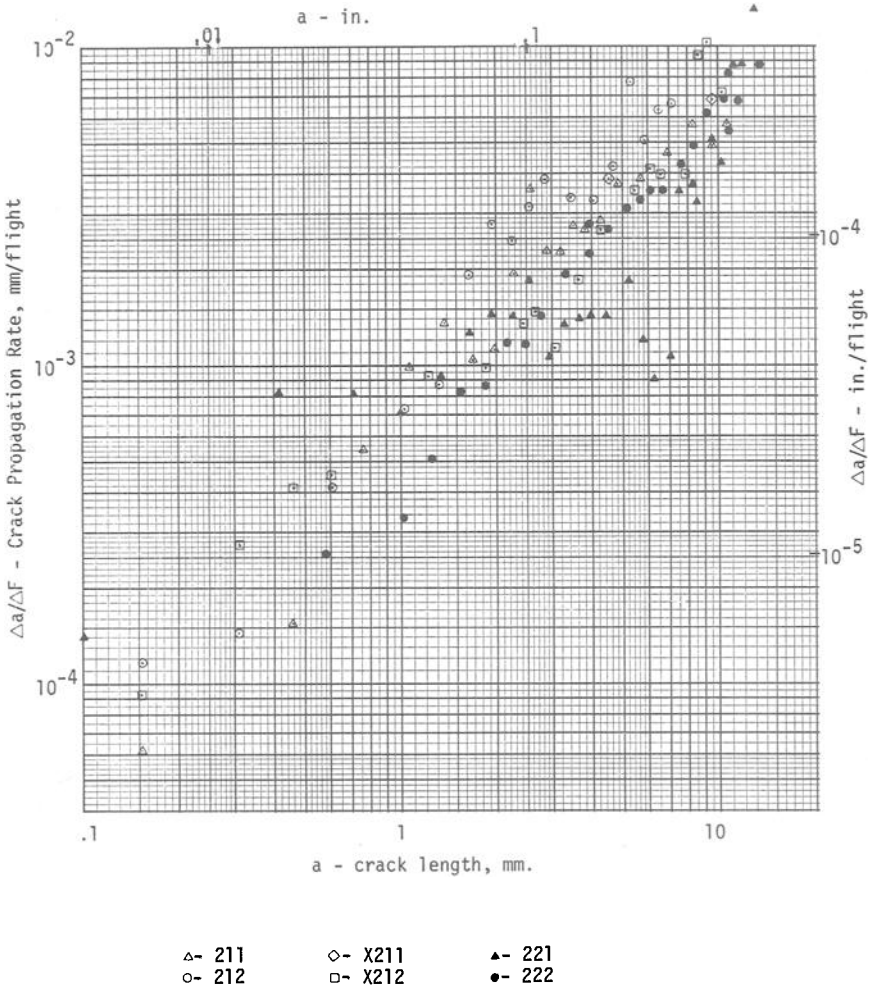


FIG. 10—*Crack propagation rates, flight loads spectra.*

between Figs. 9 and 10. However, a more detailed analysis of the data, such as in Table 2, indicates some tendency for the loading with the GAG cycle (FbF) to have a higher rate. This is to be expected when considering the fact that the GAG cycle contributes to the rate increase directly by being an additional cycle and indirectly by perhaps increasing the crack propagation rate of subsequent low load cycles.

More detailed analysis of individual striation spacings within a flight provides information on contribution of the different types of loading cycles to the crack propagation, as well as on possible loads interaction effects. The contribution of individual cycles or groups of cycles to the total crack

propagation, as percentage of total, is given in Table 3. Clear identification of individual striations was possible only at longer crack lengths, and these percentages are typical only of crack lengths beyond $a$ = 2.54 mm (0.10 in.). The following observations can be made about these percentages.

1. Crack propagation due to the GAG cycle in the FbF spectra is small, anywhere from 7 to 24 percent, depending on crack length and the spectrum. Note that the percentage is lower for the spectrum (Loading 16) with the lower flight mean. This is a much lower percentage than has been attributed to this cycle in fatigue damage calculations in the past, where the contribution has been claimed to be as high as 80 or 90 percent.

2. The flight low load cycles, which represent the majority of cycles in the spectra, produce between 30 and 58 percent of the crack propagation in the FbF spectra and less than 52 percent in the flight loads spectra. There is a tendency for the percentage to increase as the peak load decreases because of the combined effect of the smaller crack propagation due to the peak loads and the smaller retardation on the lower load rates. The lower percentages for Loadings 16 and 25 are due to lower loads and fewer cycles, respectively. Also, it is interesting to note that whereas these lowest loads are below the fatigue limit for crack initiation, they do

TABLE 3—*Contribution of individual cycles in spectrum loading to crack propagation.*

FbF Spectra:

| | GAG Cycle A to B[a] | | Low Loads B to C | | Intermediate and High Loads C to F | | Low Loads F to A | |
|---|---|---|---|---|---|---|---|---|
| Loading | *n* | % | *n* | % | *n* | % | *n* | % |
| 11 | 1 | 10 to 23 | 6 | 16 to 26 | 3 | 40 to 50 | 6 | 16 to 21 |
| 12 | 1 | 13 to 24 | 6 | 20 to 29 | 3 | 31 to 46 | 6 | 17 to 24 |
| 13 | 1 | 14 to 23 | 6 | 19 to 28 | 3 | 31 to 39 | 6 | 21 to 30 |
| 14 | 1 | 13 to 15 | 6 | 22 to 26 | 3 | 38 to 40 | 6 | 22 to 24 |
| 16 | 1 | 7 to 10 | 5 | 15 to 18 | 4 | 57 to 63 | 6 | 15 to 16 |

Flight Loads Spectra:

| | Low Loads F to A to B[b] | | Intermediate and High Loads B to F | |
|---|---|---|---|---|
| Loading | *n* | % | *n* | % |
| 21 | 11 | 29 to 46 | 4 | 54 to 71 |
| X21 | 12 | 36 to 48 | 3 | 52 to 64 |
| 22 | 11 | 37 to 52 | 4 | 48 to 63 |
| 24 | 11 | 32 to 35 | 4 | 65 to 68 |
| 25 | 5 | 18 to 27 | 4 | 73 to 82 |

[a] See Fig. 7 for cycle identification.
[b] See Fig. 8 for cycle identification.

produce crack propagation even with retardation present. This is an example of the differences that exist between crack initiation and crack propagation failure models.

3. The three or four intermediate and high load flight cycles produce the major portion of the crack propagation. The percentage increases with the increase of the peak load and its relative magnitude to the lower loads.

Finally, load interaction effects were studied by comparing individual cycle rates from spectrum loading fractographs to the CA loading rates, shown in Fig. 11. The $\Delta K$ is based on the increasing load between successive loading reversals and for negative $R$ loadings $\Delta K = K_{max} - K_{min}$ includes compression. Data in Fig. 11 show the following.

1. The crack propagation rate due to flight low loads (cycles defined by $S_{min_1}$ and $S_{max_1}$ in Table 1) is retarded by high loads. The retardation is greater in the flight loads spectra than in the FbF spectrum. Possible explanation is that the GAG cycle, which includes compression, accelerates the rate, or, in effect, reduces the retardation due to the high loads. Similar rate acceleration due to compression overloads has been observed by others [5]. Also, in the FbF spectra, the rate of the low loads tends to be higher after the GAG cycles than after the peak load, further indicating the acceleration effect of the GAG cycle.

2. The rate of the GAG cycle (defined by $S_{min}$ and $S_{mf}$ or $S_{min}$ and $S_{max_1}$ in Table 1) shows some acceleration tendencies. This could be partly due to the difficulty in clearly defining the striations for this cycle.

The effect of load interaction on the rates of intermediate and peak load cycles (defined by $S_{min_2}$ and $S_{max_2}$, $S_{min_1}$ and $S_{max_2}$ or $S_{min_2}$ and $S_{max_1}$, and $S_{min_3}$ and $S_{max_3}$ or $S_{min_2}$ and $S_{max_3}$ in Table 1) is more difficult to ascertain because of difficulties in separating striation spacing for these cycles. Peak load retardation effects on the rate of intermediate cycles were found to be similar to the flight low loads just discussed. An example of the difference in the rate of the intermediate loading cycle before and after the peak load is illustrated clearly in Fig. 7, Specimen 133, CD and EF loadings. Rates of the peak load cycles were the most difficult to establish but appeared to be unaffected by load interactions. However, a more detailed analysis should be performed before a firm conclusion is reached on this point.

## Crack Initiation and Propagation Lives

Because of possible differences in crack initiation and crack propagation failure mechanisms and analysis methods, it becomes important to separate the crack initiation and crack propagation lives. For this reason, crack propagation test lives, as determined by striation counting from fractographs, are presented in Table 2. With the exception of one specimen (113), crack propagation lives of most specimens represent between 40 and 60 percent of the total test lives. This percentage decreases

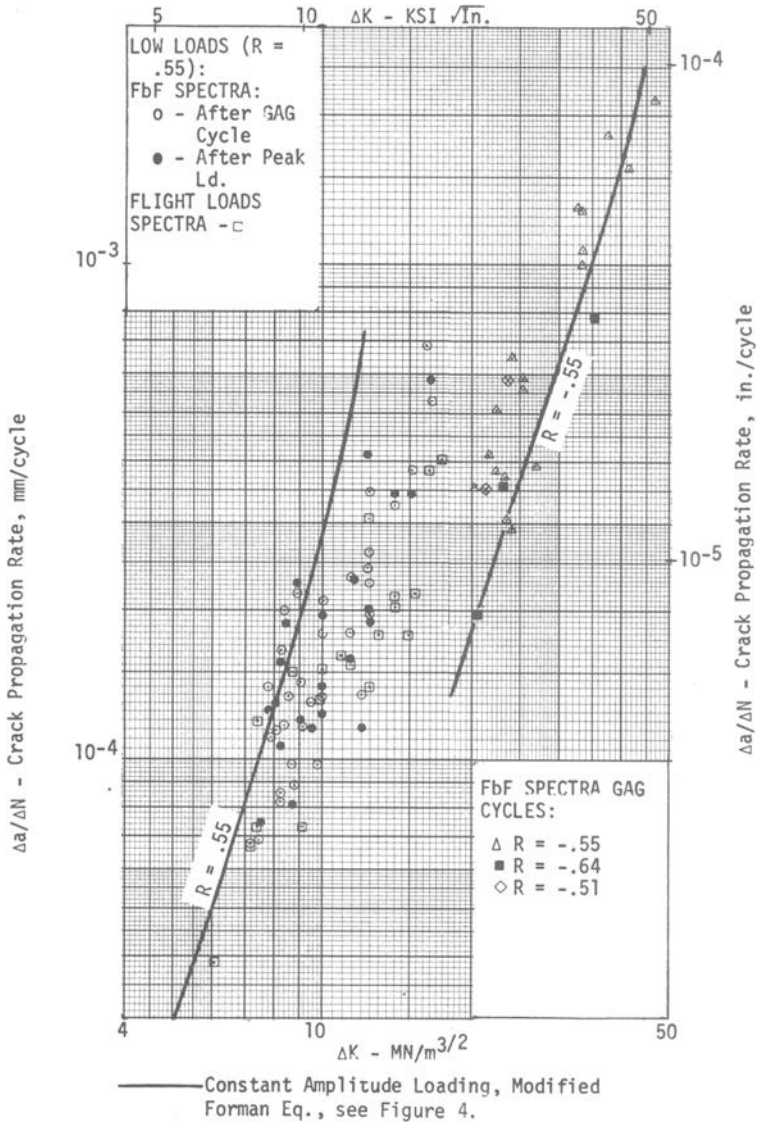


FIG. 11—*Comparison of crack propagation rates between constant amplitude and spectrum individual loadings.*

as the total life increases. Most of the crack propagation life is consumed in the initial crack propagation stages where it is most difficult to establish the rate by striation counting. Up to 50 percent of the crack propagation life may be consumed in propagating to 0.30-mm (0.012-in.) crack length, although a more typical value was about 30 percent, with a low of 5 per-

cent for the long life, low loading Specimen 452. The length of the crack propagation life of a specimen depends on the type of initial notch, loading, and specimen geometry, and the ability to find and measure striation spacings at very short cracks.

Another aspect of crack initiation that must be mentioned here is the location of crack nucleation sites. Usually it is assumed that cracks initiate at the "corners" of a hole. In this program, most of the cracks started inside the hole, as illustrated in Fig. 12, with a high degree of correlation between crack nucleation sites and the predominant hole machining tool marks inside the hole.

## Service Cracking Interpretation

Service cracking fracture surface fractographic analysis is performed mainly to identify cracking origin, mode of cracking, and to establish crack propagation rates. In the preceding discussion it was seen that crack propagation rates under spectrum loadings can be established from fractographs if the loading and sequence are known. However, attempts in establishing crack propagation rates from service cracked fracture surfaces have not been very successful unless the loading happened to be constant amplitude or a particular repetitive feature of the spectrum loading was known and could be identified in the fractograph.

## Conclusions

Electron microscope fractography is a useful tool in the study of fatigue crack propagation failure process under a known loading sequence. Crack

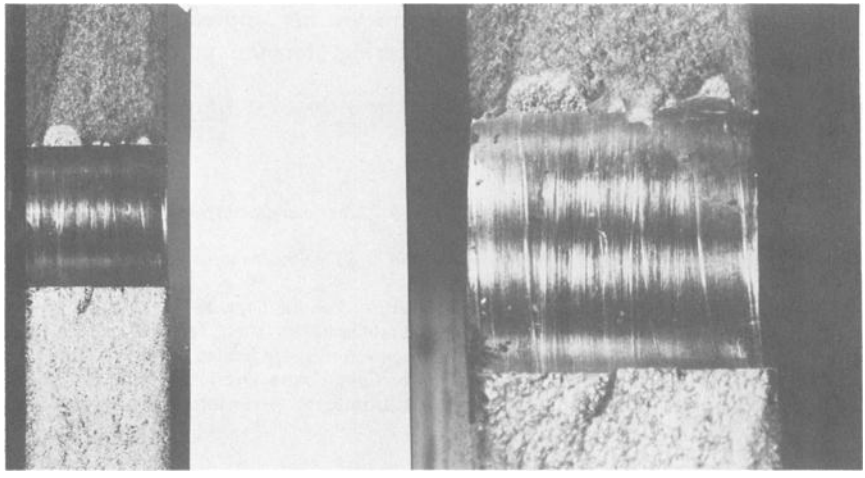

FIG. 12—*Crack nucleation sites in the notch hole, Specimen 313.*

propagation rates and loads interaction effects under spectrum loadings can be determined by measurement of striation spacings. Use of this method has produced the following findings and confirmations of the fatigue crack propagation failure process.

1. Under spectrum loading of small notched fatigue specimens, up to 50 percent of the total test life is consumed in crack propagation that can be defined by striations in a microfractograph.
2. Retardation and acceleration of cracking rates under spectrum loadings due to loads interaction were identified.
3. Striations are associated with the increasing load between successive load reversals. Also, striations and crack propagation rates appear to be influenced by the unloading portion of the cycle.
4. Crack propagation rates established by striation measurements exhibit large scatter.
5. Crack propagation rates under constant amplitude negative $R$ loading, as established by striation measurements, are not represented by $R = 0$ loading rates.
6. In the context of a transport wing lower surface loads spectrum evaluated in this paper, the GAG cycle was found to be not the most significant contribution to crack propagation, representing only from 7 to 24 percent of the total.

*Acknowledgment*

This paper summarizes work performed at the Douglas Aircraft Company in the Structures Engineering subdivision under the sponsorship of the Independent Research and Development (IRAD) Program of the McDonnell Douglas Corporation.

The author acknowledges and expresses his appreciation to D. L. Brown, Materials and Process Engineering, for the preparation of the fractographs.

## References

[1] *Fatigue Crack Propagation, ASTM STP 415,* American Society for Testing and Materials, 1967.
[2] *Damage Tolerance in Aircraft Structures, ASTM STP 486,* American Society for Testing and Materials, 1971.
[3] Forman, R. G. et al, *Journal of Basic Engineering,* Vol. 89, Sept. 1967.
[4] Schijve, J. et al, "Crack Propagation in Aluminum Alloy Sheet Materials under Flight Simulation Loading," NRL-TR 67117U, National Aerospace Laboratory NRL, Dec. 1968.
[5] Hsu, T. M. and Lassiter, L. W., "Effects of Compressive Overloads on Fatigue Crack Growth," AIAA Paper 74-365, American Institute of Aeronautics and Astronautics, April 1974.

*Daniel Eylon*[1] *and W. R. Kerr*[2]

# Fractographic and Metallographic Morphology of Fatigue Initiation Sites

**REFERENCE:** Eylon, Daniel and Kerr, W. R., **"Fractographic and Metallographic Morphology of Fatigue Initiation Sites,"** *Fractography in Failure Analysis, ASTM STP 645,* B. M. Strauss and W. H. Cullen, Jr., Eds., American Society for Testing and Materials, 1978, pp. 235-248.

**ABSTRACT:** An approach for analyzing fatigue failures by investigating the underlying microstructure of the fatigue crack origin sites is presented. A precision sectioning technique, developed by the authors, makes it possible to slice fatigue specimens through the crack initiation sites thus permitting concurrent fractographic and metallographic examination. This failure analysis was found useful in determining the reason for low fatigue lives of titanium alloy powder compacts; nonmetallic inclusions were found to be the prime source for early fatigue initiation. In superalloy powder compacts, residual porosity was related to the fatigue crack origins. In $\beta$-processed or cast titanium alloy products, the shear of large colonies of transformed $\alpha$-platelets and fracture along grain boundary $\alpha$ were identified as the main initiation mechanisms. The identification and the elimination of the metallurgical crack initiating features has the potential for improving the fatigue life and reducing the scatter of the fatigue results, since the largest proportion of fatigue life is spent in crack initiation.

**KEY WORDS:** fractography, fractures (materials), fatigue (materials), fatigue life, crack initiation, crack nucleation, titanium, titanium powder, titanium castings, titanium microstructure, heat resistant alloys, superalloy powder, nonmetallic inclusions, precision sectioning

In recent years a great deal of research effort has been directed towards investigation of fatigue crack growth behavior of different metals and alloys. Yet, when the whole scope of the fatigue behavior of metallic systems is examined, one cannot escape the conclusion that in most cases the majority of the fatigue life of a component or a specimen is spent in initiating a crack rather than propagating it. In many commercial alloys and processed products, this portion of fatigue life will be limited by the existence of macro- and microimperfections in the structure. The identification and

[1]Department of Materials Science and Metallurgical Engineering, University of Cincinnati, Cincinnati, Ohio 45221.

[2]Metals and Ceramics Division, Air Force Materials Laboratory, Wright-Patterson Air Force Base, Ohio 45433.

investigation of fatigue fracture origins and the determination of their metallurgical nature and source can lead to improved processing of materials, hence to components with higher fatigue life. A procedure for examination of fatigue initiation sites that has the potential of providing accurate identification of the fracture origin will be presented here.

In certain fatigue life tests of flat, thin, notched specimens, it is possible to detect the appearance of the initial crack in the course of the test run. Figure 1(*a*) is a replot of high cycle, axially loaded, notch fatigue test results for Ti-6Al-4V [*1*][3] tested at different maximum stress levels. The percent of the fatigue life spent in initiating a 0.5-mm crack ($N_i/N_t \times 100$) is plotted against the total number of cycles to failure, $N_t$ where $N_i$ is the number of cycles to 0.5-mm crack initiation. It can be seen that in the $10^4$ cycle region about 85 percent of the fatigue life is spent initiating the crack, and in the $10^6$ cycle region about 99 percent is spent in initiation. This plot demonstrates the role of fatigue crack initiation in determining the majority of the total fatigue life. Thus, any microstructural imperfection that may cause an early crack initiation will severely reduce the fatigue life. Gell and Leverant [*2*] showed that in directionally solidified Mar-M200 fatigue tested at room temperature, the fatigue life can be decreased sharply with an increase of the size of the fatigue initiating microstructural defects, namely pores and MC carbides. Figure 1(*b*) is a $N_i/N_t \times 100$ versus $N_t$ replot of high temperature, low cycle, fatigue test results of Ti-11 alloy [*3*] (6Al-2Sn-1.5Zr-1Mo-0.35Bi-0.1Si). In this work, the high temperature test procedure limited the determination of the initial crack length to 0.75 mm. All data points were obtained at the same stress level, and the results indicate a wide scatter band between $10^4$ to $10^5$ cycles. It can be seen that while the longest life specimens spent almost 90 percent of the fatigue life in initiating an 0.75-mm crack, the shortest life specimen spent only 25 percent in initiation. This plot demonstrates the major role of fatigue crack initiation in determining the scatter of fatigue results.

## Current Methods of Crack Initiation Location

The present fractographic methods, utilizing optical and scanning electron microscope (SEM) equipment, permit, in most cases, the identification of the origin of a fatigue failure on the fracture surface. However, in order to identify the metallurgical reason for this initiation, it is necessary to examine the underlying microstructure. The authors were able to perform this type of examination using a precision sectioning technique discussed in detail elsewhere [*4*]. The precision sectioning provides separate or combined metallographic and fractographic images of the initiation site. Thus it is possible to have a microstructural, chemical, and fractographic evaluation of the site as will be explained later in detail. Another section-

[3] The italic numbers in brackets refer to the list of references appended to this paper.

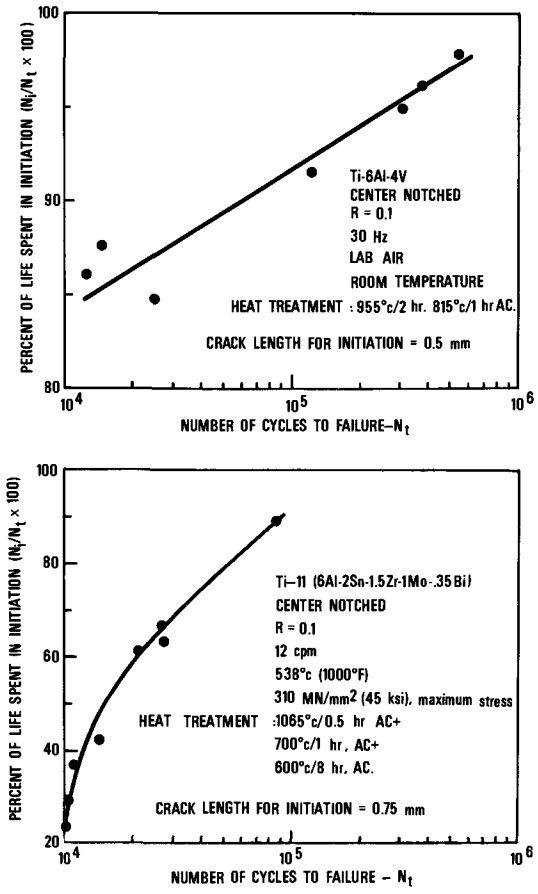


FIG. 1—*Percent of total fatigue life spent in initiating* (a) *0.5-mm crack in Ti-6Al-4V at room temperature and different stress levels, and* (b) *0.75-mm crack in Ti-11 at 538°C and at a constant stress level.*

ing method [5] provides a combined fractographic-metallographic image at an angle of 120 deg to the fracture surface but lacks the precision required to cut through a small fatigue initiation site and is limited in use to a rather random sectioning through a fracture surface. Other methods that provide fractographic-metallographic images [6, 7] use a stop-off lacquer to protect a specific area on the fracture surface while its surroundings are removed by electropolishing. These methods also do not have the accuracy of the precision sectioning technique, and some inclusions in the initiation site may be polished out preferentially and therefore would not be available for microchemical analysis. Furthermore, the angle between the fracture plane and the electropolished face cannot be determined accurately,

making it difficult to measure the angle between the tensile axis and the observed shear planes in fatigue crack initiation locations.

### Precision Sectioning Procedure and Results

Microstructural imperfections which may initiate fatigue cracks are located best by testing smooth cylindrical specimens with rather long gage lengths to allow relatively large gage volumes to be tested. Axial tension-tension loading which preserves the fracture surface is preferred. Obtaining subsurface, microstructural related origins requires that surface initiation be minimized; this involves ensuring a good surface finish, free of scratches and machining marks, and good alignment of test equipment to prevent bending stresses.

Often it is possible to identify the defect causing the crack initiation merely by examining the fracture surface. Figure 2(*a*) shows the fracture surface of a $\beta$-III titanium alloy (11.5Mo-6Zr-4.5Sn) powder compact, smooth, fatigue specimen. The processing and heat treatment conditions of this and other alloys discussed are listed in Table 1. The average room temperature, high cycle fatigue life of the powder compacts (at 827 $MN/m^2$ peak load and stress ratio $R = 0.1$) were found to be more than two orders of magnitude shorter than that for the wrought product, while other properties like tensile strength and fracture toughness remained the same [*8*]. The SEM image of the fracture surface indicates subsurface initiation in Location A. A higher magnification image (Fig. 2(*b*)) shows an inclusion lying close to the fracture surface; X-ray scan analysis identified it as being silicon dioxide ($SiO_2$).

In other cases, the source of the crack initiation is located well under the fracture surface. Such an instance is shown in Fig. 3(*a*) (same material and test conditions as in Fig. 2(*a*)). The precision sectioning method [*4*] involves identifying the fracture origin in the SEM, cutting close to the origin on a plane perpendicular to the fracture surface, measuring the distance from the cut face to the origin, and grinding off this distance in a standard, plastic mold, metallographic technique. After the specimen is polished to the exact location (Line B in Fig. 3(*a*)) it is possible to obtain a micrograph of the underlying microstructure, showing details that will help in the interpretation of the fatigue failure. The SEM image in Fig. 3(*b*) is a modification of this method in which the mount material has been dissolved carefully to make it possible to obtain the fracture surface at the origin and the underlying microstructural features in the same SEM picture. The $SiO_2$ particle that was not visible on the fracture surface can be seen at this stage. It is also seen that the fracture has originated as a shear type fracture on Plane D which lies close to 45 deg to the fatigue tensile axis which is the vertical direction of the photograph. Unlike Fig. 2(*b*), the sectioned plane image (Fig. 3(*b*)) can provide more information about the shape and

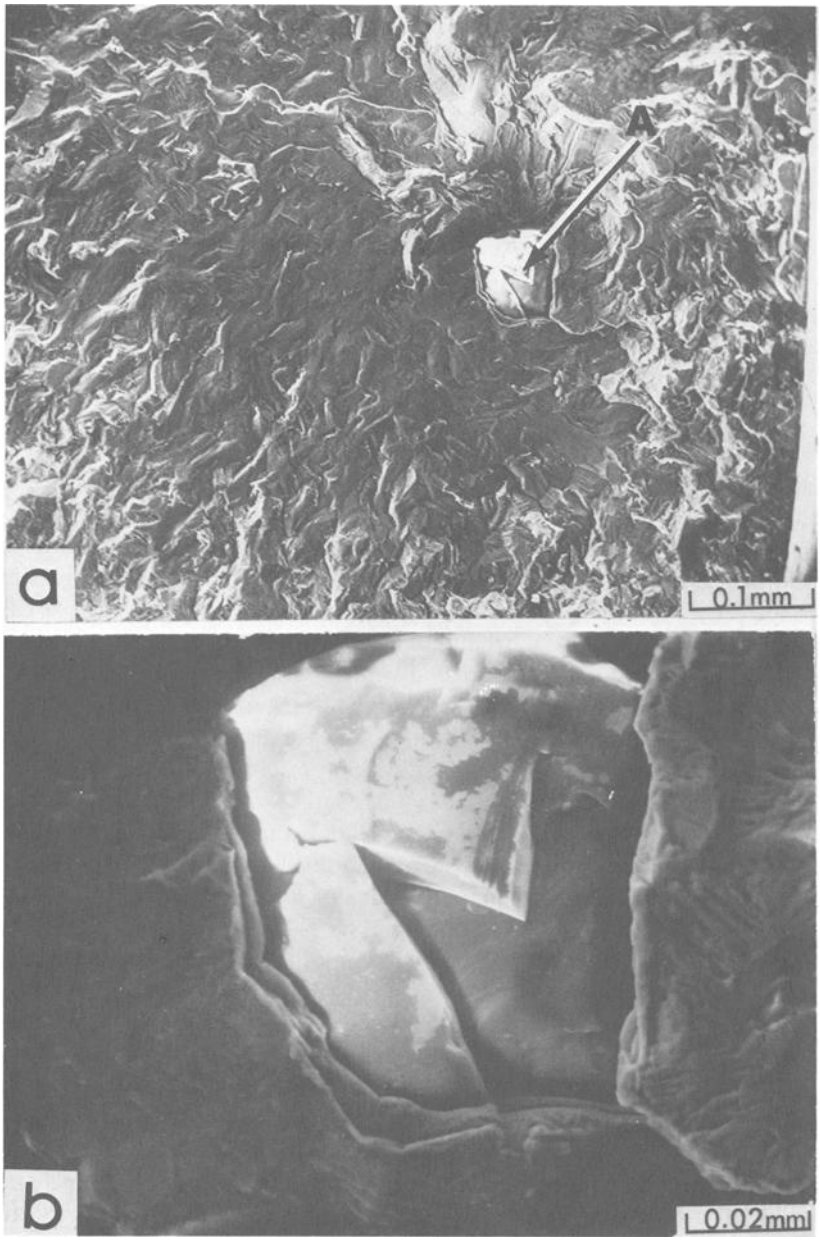


FIG. 2—(a) *SEM image of a subsurface fatigue failure origin, at A, of a β-III powder compact specimen, and* (b) *a $SiO_2$ inclusion at the origin site.*

TABLE 1—*Processing and heat treatment conditions for the alloys discussed.*

| β-III Powder Compacts | Ti-17 | Ti-6Al-4V Cast |
|---|---|---|
| extrusion (10:1) at 788°C<br>760°C/½ h, WQ +<br>482°C/8 h, AC | 845°C/4 h, AC +<br>800°C/4 h, WQ +<br>635°C/8 h, AC | hot isostatically pressed<br>(HIP) at 900°C/100 MN/m$^2$/2 h |

| IMI-685 | AF-115 |
|---|---|
| forged at 1050°C<br>1050°C/½ h, OQ +<br>850°C/8 h, AC | HIP 1190°C/100 MN/m$^2$<br>forged at 1150°C<br>1190°C/4 h AC +<br>760°C/16 h AC |

NOTE—AC = air cooled,
WQ = water quenched, and
OQ = oil quenched.

size of the inclusion as well as how it interacts with the microstructure and how the first crack was initiated. Previous precision sectioning work on Ti6Al-6V-2Sn [*4*] powder showed that, in certain cases, diffusion of α or β stabilizing elements from the inclusion will change the neighboring microstructure by stabilizing either the α-phase or the β-phase. In those cases where the α-phase was stabilized by the existence of oxygen in the inclusion, cracks initiated within the embrittled α-phase rather than in the inclusion.

The same fatigue failure analysis was tried and found successful in superalloy powder compacts of an advanced nickel base superalloy, AF-115. These compacts showed subsurface initiation origins when hourglass specimens were fatigue tested at 760°C (1400°F), $R = -1$ and maximum stress = 620 MN/m$^2$ (90 ksi). Figure 4 is a section through a fatigue specimen at the initiation site. It can be seen that the fatigue crack was initiated from an area containing clusters of unhealed pores (marked A) and large unsolutioned γ′ particles (marked B). The two curved fracture segments (marked A′) may be the lower part of the pores which initiated the crack.

In many cases, the subsurface fatigue origins will result from certain microstructural features rather than from inclusions, pores, or other defects. Figure 5(*a*) shows the microstructure of a Ti-17 (5Al-2Sn-2Zr-4Mo-4Cr) titanium alloy forged at 1065°C (1950°F). This is 200°F above the β-transus temperature and resulted in an acicular transformed β microstructure. This material was subsequently heat treated as indicated in Table 1. The micrograph shows a *colony* of α platelets, all oriented in the same direction as at A, as well as longer and wider continuous *grain boundary* α film (GBα) which outlines prior β grain boundaries as at B and B′. The flat cleavage-like facet, C, in the center of Fig. 5(*b*) is the subsurface fatigue initiation site on an hourglass specimen tested at 1034 MN/m$^2$ (150 ksi), $R = 0.1$ at room temperature. This specimen had lower fatigue life than

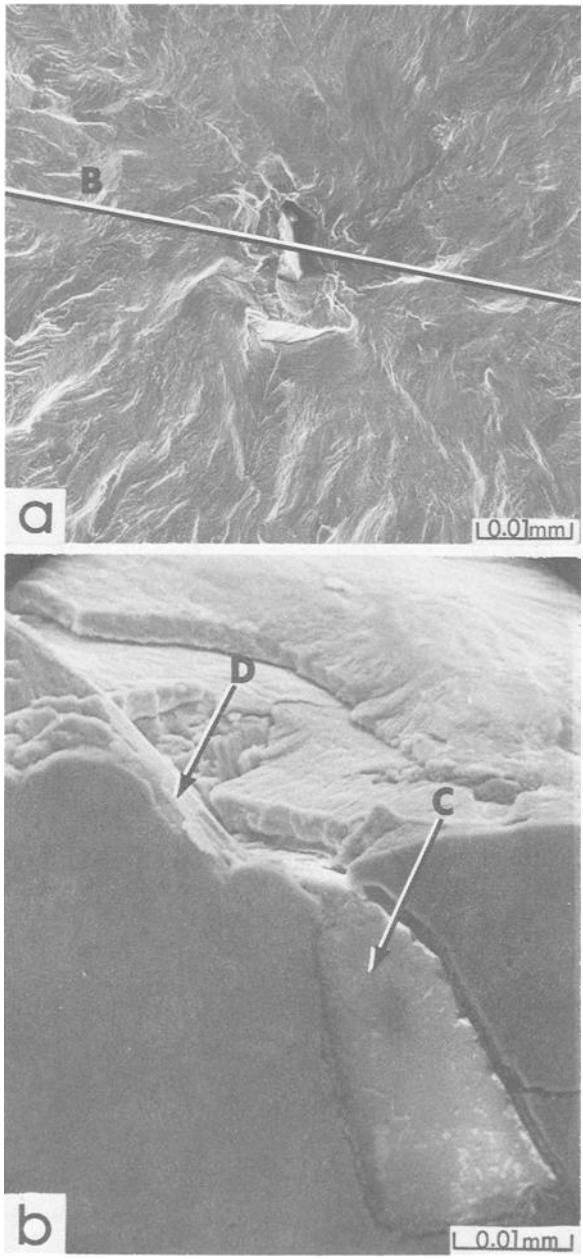


FIG. 3—(a) *SEM image of a subsurface fatigue fracture origin of a β-III powder compact specimen. Using the precision sectioning technique, the fracture surface was sectioned along line B.* (b) *SEM combined image of the sectioned plane and the fracture surface showing an $SiO_2$ inclusion (C) located under A. The fatigue crack initiated on shear plane D.*

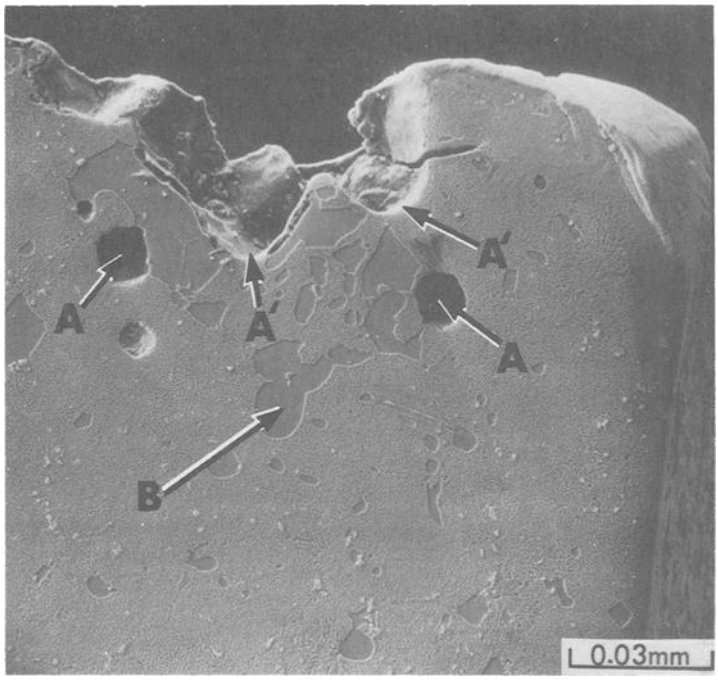


FIG. 4—*SEM image of fatigue crack initiation site in a powder compact of nickel base superalloy AF 115 showing cluster of pores at A and unsolutioned* $\gamma'$ *at B. The crack was initiated at A'.*

specimens forged within the $\alpha + \beta$ temperature range. Figure 5(*c*) is a low magnification SEM picture of the section along line D in Fig. 5(*b*); E marks the location of the crack initiation. Figure 5(*d*) is the light microscope image of the metallographically polished and etched area under the initiation site E. This clearly shows that the fatigue initiated at planar GB$\alpha$ similar to that at B' in Fig. 5(*a*). This GB$\alpha$ is oriented close to 45 deg to the major tensile axis (the vertical direction of the picture) and thus promoted a slip related fracture on the long $\alpha/\beta$ interface which was oriented in a direction close to the maximum shear stress. Figure 6(*a*) is the SEM image of the same location as in Fig. 5(*d*), after the mount material was dissolved carefully. This picture gives the combined view of the fracture surface and underlying microstructure of the initiation site at higher magnification. Since the GB$\alpha$ forms during slow cooling from above the $\beta$ transus temperature, it may be possible to eliminate it with fast cooling from the forging press and thus improve the room temperature high cycle fatigue life. The same type of GB$\alpha$ fatigue crack initiation was found associated with large colony structure in Ti-6Al-4V castings (Table 1) fatigue tested at room temperature at 413 MN/m$^2$ (60 ksi) maximum stress, $R = 0.1$.

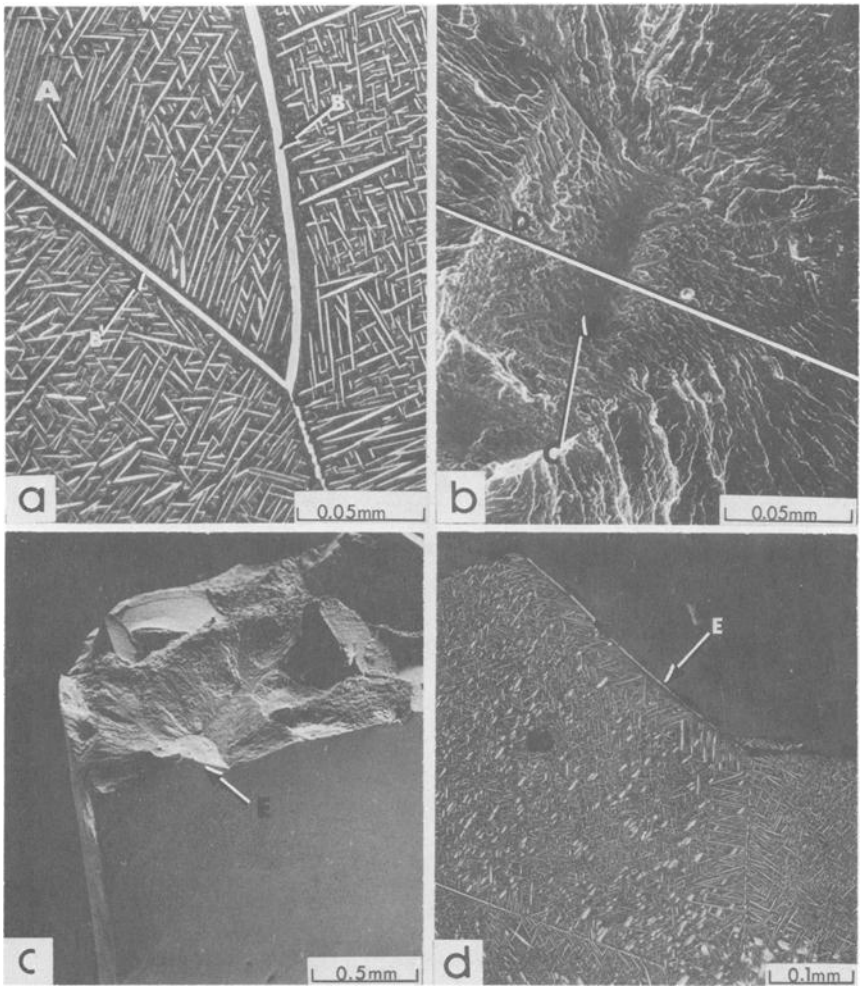


FIG. 5—(a) *Ti-17 fatigue specimen with acicular microstructure showing colonies of transformed α platelets at A and grain boundary α at B and B'.* (b) *Flat fracture initiation site at C was sectioned on line D.* (c) *Low magnification SEM image shows the initiation site at E.* (d) *Underlying microstructure showing fatigue crack initiation along the GBα phase.*

Figure 6(*b*) clearly shows the shear type fracture origin (A) at the $\alpha/\beta$ interface (B) of a planar GB$\alpha$ (C) inclined about 45 deg to the major tensile axis.

The large colonies of $\alpha$ platelets (D in Fig. 6(*b*)) are also typical of as-cast microstructure of Ti-6Al-4V alloy and relate to another type of microstructure-related fatigue crack initiation. This is shown in Fig. 7(*a*) for the test conditions just described. This type of fatigue initiation is associated with the formation of shear bands across the colonies of similarly oriented

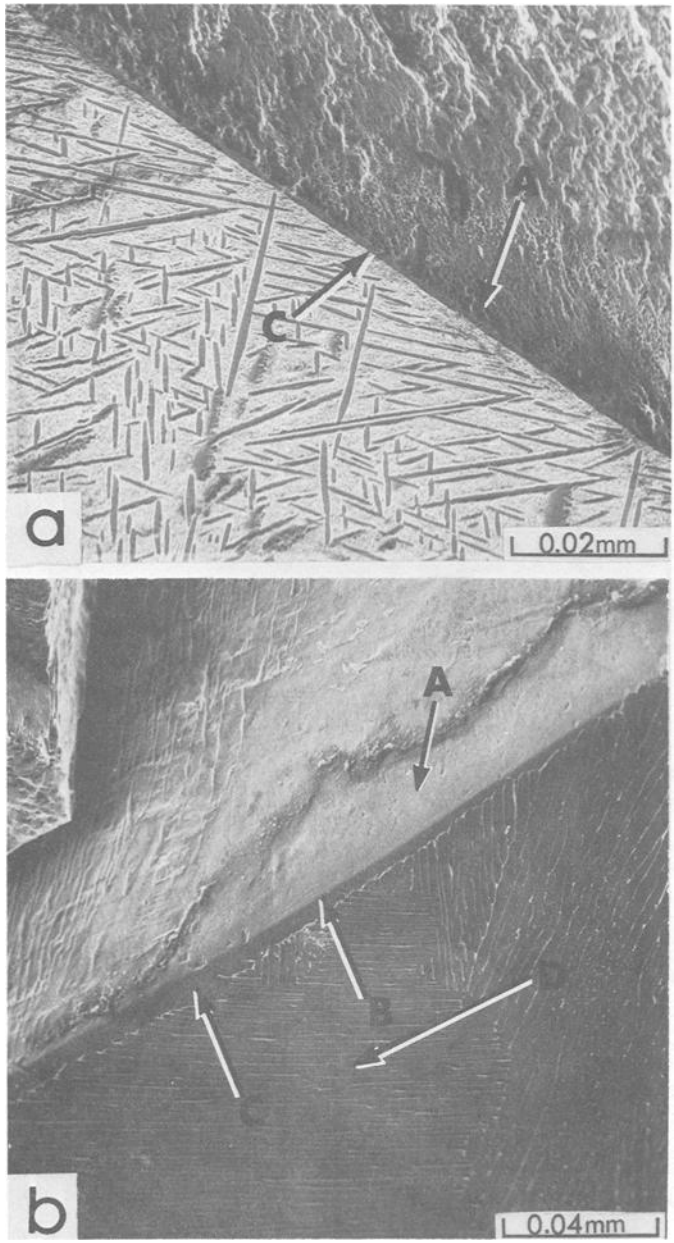


FIG. 6—(a) *High magnification SEM combined image of the fracture initiation site at A along the GBα at C and the underlying microstructure of the specimen shown in Fig. 5.* (b) *GBα fatigue initiation, at A, along the α/β interphase boundary (B) of the GBα (C) in the large colony (D) microstructure of cast Ti-6Al-4V.*

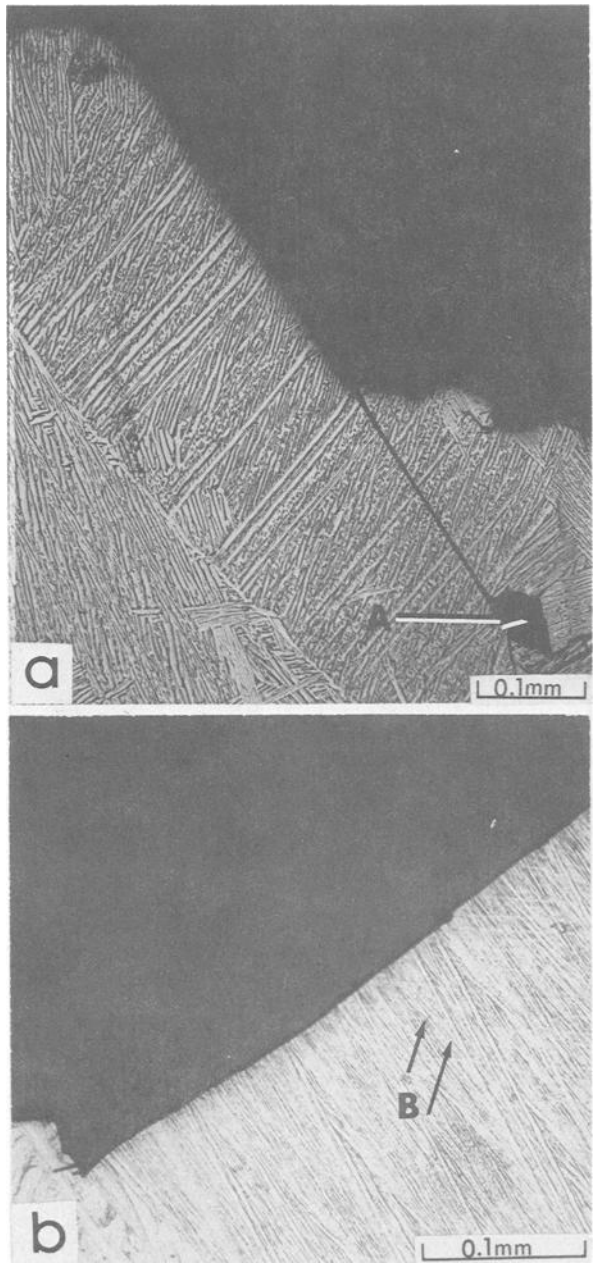


FIG. 7—(a) *Trans-colony fatigue shear initiation in cast Ti-6Al-4V originated in pore A.* (b) *Trans-colony shear initiation in IMI 685 titanium alloy showing slip traces in B.*

$\alpha$ platelets. In the case of Ti-11 [*3*] and IMI-685 [*9*] (6Al-5Zr-0.5Mo-0.25Si) alloys, the trans-colony shear fracture was found to dominate both initiation and the propagation stages of the fatigue failure. In Fig. 7(*a*), the trans-colony fracture may have originated from the small unhealed casting pore (A). Also in this case, the shear type fracture propagated in a direction close to 45 deg to the tensile axis. Figure 7(*b*) shows a similar trans-colony shear fatigue initiation for IMI-685 titanium alloy (Table 1). Traces of another slip system can be seen across the colony at B. Fatigue crack initiations of this nature were associated with a fatigue life debit [*9*] only when a 5-min hold time was applied at the maximum stress position of the fatigue cycle.

## Discussion

To demonstrate the range of usefulness and the generality of the precision sectioning fatigue crack initiation analyses, a variety of fatigue failures in wrought and cast titanium alloy material and powder compacts of titanium and nickel base superalloys were presented in the previous sections. Since surface fatigue crack initiation may be connected to surface conditions like machining marks, corrosion, and contamination, subsurface fatigue origins were examined. It was the authors' experience that most fatigue specimens with subsurface fracture origins yielded unambiguous answers on the nature of these origins. On the other hand, it was very difficult to identify the fatigue initiation mechanism in surface initiated failures.

The subsurface fracture origins can be divided into two groups: (*a*) origins related to defects such as pores and inclusions, and (*b*) origins related to microstructural features. Using this analysis technique, it is possible to distinguish between these two types.

The first group was frequently found in castings and powder compacts. The most common fatigue initiating defect in titanium castings is porosity. In powder compacts, fatigue cracks may initiate from a larger variety of defects. They may be metallic or nonmetallic inclusions, high interstitial brittle phases, or powder compaction porosity. In most cases, the identification of the fatigue-failure causing defect can lead to improved processing that will eliminate these defects. The porosity can be reduced or eliminated by better casting or powder handling and compaction techniques. Identifying the chemical composition of the metallic and nonmetallic inclusions may often permit their elimination at the source of contamination. In the case of titanium alloy powder compacts, heat treated to maximum tensile strength [*10*], a very low content of nonmetallic inclusions (volume fraction less than 1-ppm $SiO_2$) was sufficient to initiate an early fatigue failure. Since the smooth fatigue life is so sensitive to these inclusions and since it is practically impossible to trace them by chemical analysis, smooth fatigue testing

and precision sectioning of the initiation site was found to be the only effective method for detection and identification.

Fatigue origins relating to microstructural features were found in powder, wrought, and cast materials. If low fatigue life is attributed to this type of fatigue initiation, thermomechanical or heat treatment of the alloy may be modified sometimes to eliminate the initiation related microstructural features. The elimination of the grain boundary $\alpha$ in the Ti-17 alloy (Fig. 5(*a*)) by fast cooling from the $\beta$-phase is a good example.

All of the discussed types of fatigue initiations can lead to a low fatigue life or to a wide scatter of the fatigue test results. Since the initiation of the first small crack in fatigue often constitutes the majority of the fatigue life of a component or specimen, the improvement of the material and processing to make it more fatigue-initiation resistant has the potential of increasing the fatigue strength and reducing the fatigue life scatter.

## Conclusions

1. The majority of the fatigue life often is spent in initiating the first crack.
2. Defects in the material and some microstructural features can promote early crack initiation and thus early fatigue failure.
3. The precision sectioning analysis permits a complete characterization of the fatigue failure origin.
4. Using this technique, the fatigue initiation sources in wrought, cast, and powder compact titanium and nickel base alloys were successfully analyzed and identified.
5. The identification of the fatigue initiation sources may enable one to eliminate them from the final product and thus has the potential of increasing the fatigue strength and reducing scatter in fatigue life.

*Acknowledgments*

The authors gratefully acknowledge the assistance of W. A. Houston, University of Cincinnati, and A. Kiefer and D. Kirk, Monsanto Research Corporation, for the precision sectioning and the metallography, and M. B. Strope and A. G. Jackson, Systems Research Laboratory, for the fractography. Also, we would like to acknowledge N. Birla and J. M. Hyzak for providing some of the test material.

## References

[*1*] Eylon, D. and Pierce, C. M., *Metallurgical Transactions A*, Vol. 7A, 1976, pp. 111-120.
[*2*] Gell, M. and Leverant, G. R. in *Fatigue at Elevated Temperatures, ASTM STP 520*, American Society for Testing and Materials, 1973, pp. 37-67.
[*3*] Eylon, D., Hall, J. A., Pierce, C. M., and Ruckle, D. L., *Metallurgical Transactions A*, Vol. 7A, 1976, pp. 1817-1876.

[4] Kerr, W. R., Eylon, D., and Hall, J. A., *Metallurgical Transactions A*, Vol. 7A, 1976, pp. 1477-1480.
[5] Sasaki, G. and Yokota, M. T., *Metallography*, Vol. 8, 1975, pp. 265-268.
[6] Shechtman, D., *Metallurgical Transactions A*, Vol. 7A, 1976, pp. 151-152.
[7] Chesnutt, J. C. and Spurling, T. A., *Metallurgical Transactions A*, Vol. 8A, 1977, pp. 216-218.
[8] Birla, N., DePierre, V., and Adair, A. M., Technical Report AFML-TR-76-8a, Air Force Materials Laboratory, June 1976.
[9] Eylon, D. and Hall, J. A., *Metallurgical Transactions A*, Vol. 8A, 1977, pp. 981-990.
[10] Eylon, D. and Birla, N., *Metallurgical Transactions A*, Vol. 8A, 1977, pp. 367-369.

*L. D. Kramer*[1]

# Fractographic Analysis of Low Cycle Fatigue Specimens from a Failed Steam Turbine Rotor

**REFERENCE:** Kramer, L. D., **"Fractographic Analysis of Low Cycle Fatigue Specimens from a Failed Steam Turbine Rotor,"** *Fractography in Failure Analysis, ASTM STP 645,* B. M. Strauss and W. H. Cullen, Jr., Eds., American Society for Testing and Materials, 1978, pp. 249–274.

**ABSTRACT:** Because the TVA Gallatin Number 2 steam turbine rotor burst resulted from creep-low cycle fatigue interaction, the present study was undertaken to establish the effect of strain range, increasing hold times, and degree of segregation in the intermediate temperature range corresponding to Gallatin origin conditions. Manganese-sulfide (MnS) inclusions were found to be preferential initiation sites independent of hold-time duration, surface oxide spiking, and most strain ranges, but no significant decrease in specimen cyclic lives was observed to occur with variable MnS concentrations corresponding to different locations in the rotor. Fractographic simulation of the Gallatin origin was obtained by imposing a 23-h hold time on bore segregated material at 427°C and a 2.98 percent strain range. Periphery material or decreasing hold times to a 4-h cycle caused a change from intergranular to transgranular fracture at 427°C. When selected hold-time tests were interrupted at less than 20 percent of expected cyclic life, early cracking was observed with the largest MnS linkup distance occurring in bore segregated material.

**KEY WORDS:** fractography, chromium-molybdenum-vanadium, creep-low cycle fatigue, rotors, turbines, inclusions, life (durability), separation, hold time, linkup, topography, oxide spikes

As a result of the 19 June 1974 steam turbine rotor burst in the TVA Gallatin Number Two unit, an investigation was initiated at the Westinghouse Steam Turbine Division to explain the failure. The subsequent analyses [*1-3*][2] developed the following conclusions.

1. The initiating flaws were not gross manufacturing defects (that is, hydrogen bursts, unconsolidated porosity, etc.) although the forging contained positive alloy and manganese sulfide (MnS) inclusion segregation throughout the near bore origin metal volume. Because the origin was internal to

[1] Fellow materials engineer, Westinghouse Steam Turbine Division, Lester, Pa. 19113.
[2] The italic numbers in brackets refer to the list of references appended to this paper.

the forging, external failure mechanisms such as stress corrosion cracking were eliminated.

2. The origin location contained significant microstructural intergranular creep damage associated with this near bore positive alloy and MnS inclusion segregation. Elsewhere, in the rotor, this damage or microstructure was not observed.

3. All mechanical properties testing, including creep methods, did not show significant decreases. With the exception of the 23-h hold time 427°C strain controlled low cycle fatigue test of bore material, no other mechanical specimen fractographically simulated the failed rotor. This result was particularly surprising in that creep specimens of near origin material had been tested over a reasonable range of Larson-Miller parameters with temperatures as high as 593°C and times in excess of 10 000 h. These specimens contained a similar microstructure to the initiating flaw, yet all creep failures were by microvoid coalescence (that is, no intergranular cracking) [*4*].

4. Using both the life fraction creep analysis as well as universal slopes low cycle fatigue analysis, failure of the rotor could not be calculated on a mechanical stress analysis basis. Only when a frequency modified Coffin-Manson approach was utilized could the initiation of cracks (as defined by Manson to be empirically 2 to 6 $\times$ $10^{-4}$ mm in length) be calculated using the TVA Gallatin cyclic conditions and the direct measurement of origin fracture plane inclusion sizes and distances [*3,5*].

5. The initiation step leading to the critical flaw size for brittle bursting of the rotor was concluded to result from plastic fatigue cycling of the near bore MnS inclusions at service temperature with the steady state loading of the turbine imposing the long hold times needed for creep damage. Since the bore material is constrained by the surrounding rotor, this superimposed hysteresis loop seen by the MnS inclusions is always positive (that is, the only way to approach a symmetric hysteresis is to cool the periphery relative to the bore in such a manner that the compressive thermal stress exceeds the applied tangential stresses—an impossible condition in practice).

Because a large number of high temperature steam turbine rotors of this 1950's generic class of chromium-molybdenum-vanadium (Cr-Mo-V) air-melted material are in service throughout the world, the Electric Power Research Institute (EPRI) funded a research program (RP-502) to develop calculation methods for predicting remaining rotor life given ultrasonic data verification by dissection of actual rotors, unit operating history, and rotor mechanical properties. This latter effort resulted in additional low cycle fatigue testing of the Gallatin rotor to understand further the effect of ingot segregation, cycling rate, hold time, and temperature on the initial mechanism to reach the critical flaw size for bursting [*4,6*]. Accordingly, the EPRI test results, along with the earlier fatigue tests, are significant because of the lack of literature information on strain range and hold times

at temperatures less than 483°C where creep interaction effects are assumed to be negligible. Conversely, higher temperature data exist for the current ASTM Specification for Vacuum-Treated Carbon and Alloy Steel Forgings for Turbine Rotors and Shafts (A 470-74), Class 8 grade [*7-10*] or similar foreign grades [*11-13*] due to the wide applicability of this alloy to steam turbine rotors, disks, bolts, and cylinders. Unfortunately, all such tests correspond to steam inlet design parameters which are presumed to be "worst case" creep-fatigue interaction conditions.

Since large turbine rotors are known to contain significant heterogeneities, [*14-16*] turbine manufacturers often sample axial core bars and periphery prolongation rings to check these variations as a condition of purchasing production forgings. Conventional tension, stress rupture, Charpy V-notch impact, and bend specimens often are required for these acceptance tests; however, with one exception, low cycle fatigue testing [*17*] has not been used to understand the role of segregation. The following paper is a summation of both fatigue data from the Westinghouse failure investigation and the later EPRI program. Together, the combined data are presented to compare the effect of strain range, increasing hold times, and degree of segregation in the intermediate temperature range corresponding to the Gallatin origin conditions. Hopefully, a fractographic simulation of the origin topography would result since the frequency modified low cycle fatigue analytical model predicted a creep-fatigue interaction. The other conventional mechanical test methods (namely, tension, Charpy V-notch, $K_{Ic}$, fatigue crack growth, and creep testing) obtained either cleavage, microvoid, or striated fracture morphologies.

## Experimental Procedure

All low cycle fatigue specimens were removed from the rotor in a tangential direction. The axial position of the specimens correspond as close as possible to the origin location denoted in Fig. 7 of Ref *2*. All specimens were removed within 50 mm of the actual bore or periphery surfaces depending on the degree of segregation to be studied. Due to the random nature of the segregate banding as determined by macroetching, no reproducible method was found to assure a full segregate band would exist completely through the specimen gage diameter. For this reason, specimens probably did not contain on a random basis the degree of through-section segregation that was available in the rotor itself. A typical bulk chemistry for the origin bore material is presented in Table 1. While this area was observed previously [*2*] to be segregated macroscopically, the analysis is within the applicable specification of the 1950s material.

The specimen geometry was a threaded plain bar axial push-pull design with a 7.6-mm reduced section diameter and a 16.5-mm gage length. All testing was done by closed-loop strain control. In each case, the extensom-

TABLE 1—*Chemical analysis of TVA Gallatin No. 2 IP-LP rotor material.*

| Element | ASTM Method A 470-74, Class 8 | Bore Material Chemistry of Gallatin 2 Adjacent Origin |
|---|---|---|
| C | 0.25 to 0.35 | 0.34 |
| Mn | 1.00 max | 0.97 |
| P | 0.015 max | 0.016[a] |
| S | 0.018 max | 0.019[a] |
| Si | 0.15 to 0.35 | 0.27 |
| Ni | 0.75 max | 0.07 |
| Cr | 0.90 to 1.50 | 1.10 |
| Mo | 1.00 to 1.50 | 1.43 |
| V | 0.20 to 0.30 | 0.25 |

[a] Met 1950s grade requirements. ASTM Method A 470-74, Class 8 values represent improvements in subsequent steel making requirements.

eter was a linear variable differential transformer (LVDT) located external to the surrounding electric resistant furnace. Temperature control of ±2°C along the specimen gage length was maintained over the test duration. Most continuous cycle testing utilized an asymmetric triangular waveform from zero to maximum strain and back to zero. When required, hold times were imposed at the maximum strain point. The reasons for this particular waveform have been outlined previously [*3*], with Fig. 1 indicating the specifics of both fatigue cycles. For comparison, a few symmetric loop tests also have been conducted. A complete summary of test conditions are detailed in Tables 2 and 3. All testing was done in air with no attempt to separate environment as a test parameter. Subsequent data will show that the external environment did not affect specimen initiation sites.

Upon the termination of cycling, each specimen was inspected visually under a ×60 optical binocular microscope to determine further areas of interest such as initiation sites, secondary cracking in the gage length, etc. Significant areas were documented optically and viewed by scanning electron microscopy (SEM). If oxidation of the specimen during the test duration was particularly bad, the specimen was cleaned electrolytically by a current reversing technique and was reinspected by SEM. For tests which were terminated prior to the advent of gross cracking (that is, early life specimens), the surface condition of the gage length was cleaned directly to reveal exterior cracking and oxide spiking both optically and by SEM. All significant specimens then were sectioned by conventional metallographic techniques and etched using sodium tridecyl benzene sulfonate (STBS). Grip ends of several fatigue bars including the 23-h hold time specimens were sectioned after testing to assure that no preexisting flaws from the forging manufacturing process were present in the relatively unstressed ends. No flaws were found.

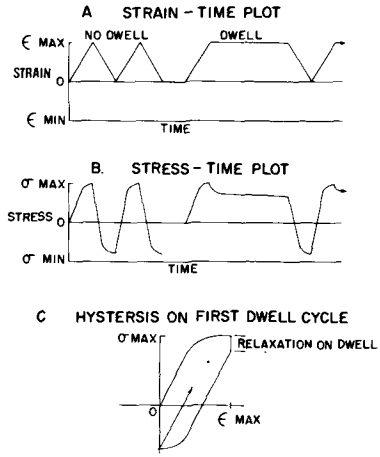


FIG. 1—*Schematic diagrams for both continuous cycling and hold-time tests showing the strain pattern imposed on the specimen, the resultant stress profile, and a typical initial hold-time hysteresis loop.*

## Results and Discussion

### *Low Cycle Fatigue Test Life Data*

All low cycle fatigue life plots are presented in Figs. 2 and 3. Figure 2 is a summation of all continuous cycle results utilizing temperature, cycling rate, and location of specimen material as the appropriate test variables. The significant observations in these data are the tightness of the scatter and the intensitivity of the material to test temperature up to 427°C. This observation is particularly surprising since the 110°C data fall within the higher temperature scatterband. Ordinarily, a material which follows "universal slopes" behavior would have a longer life presumably due to higher tensile ductility at lower temperatures. Furthermore, the 110°C points and possibly the 371°C points in Fig. 2 show a preference for shorter periphery fatigue lives; however, the few data points are grouped so closely that they may not represent a sufficient statistical difference. On the other hand, both the universal slopes deviation and this latter observation may be explainable on the basis of differential ductilities of the banded and unbanded areas within the specimen gage lengths since gross microstructural differences that effect ductility (for example, grain size, amount of ferrite, etc.) were observed elsewhere [*2*].

Figure 3 is the same format for all hold-time points with three temperatures (371, 427, and 482°C), duration of hold time, and specimen location as the test variables. For comparison, the Fig. 2 continuous cycling scatterband is superimposed over the hold-time data. Three additional early life specimens which were terminated at 20 percent or less of the respective test

TABLE 2—*Summary of continuous cycle testing conducted on Gallatin No. 2 intermediate pressure end material.*

| Specimen Location | Test Temperature, °C | Cycle Rate, cpm | Total Strain Range, % | Life to Failure, $N_f$ | Comments |
|---|---|---|---|---|---|
| Bore | 110 | 1 | 2.25 | 206 | ... |
| Bore | 110 | 1 | 1.12 | 1080 | ... |
| Bore | 110 | 1 | 0.63 | 5827 | ... |
| Periphery | 110 | 1 | 2.29 | 145 | ... |
| Periphery | 110 | 1 | 1.13 | 692 | ... |
| Periphery | 110 | 1 | 0.64 | 3964 | ... |
| Bore | 371 | 1 | 4.80 | 23 | ... |
| Bore | 371 | 1 | 2.10 | 319 | ... |
| Bore | 371 | 1 | 1.00 | 1015 | ...[a] |
| Bore | 371 | 1 | 0.72 | 2473 | ... |
| Periphery | 371 | 1 | 4.80 | 3 | ... |
| Periphery | 371 | 1 | 2.10 | 162 | ... |
| Periphery | 371 | 1 | 1.00 | 669 | ...[a] |
| Periphery | 371 | 1 | 0.72 | 1617 | |
| Bore | 427 | 1 | 4.30 | 41 | Figs. 6, 7, and 8 |
| Bore | 427 | 1 | 1.90 | 335 | |
| Bore | 427 | 1 | 0.95 | 1475 | ...[a] |
| Bore | 427 | 1 | 0.60 | 3285 | Figs. 4 and 5 |
| Periphery | 427 | 1 | 3.05 | 73 | ... |
| Periphery | 427 | 1 | 1.43 | 340 | ... |
| Periphery | 427 | 1 | 0.75 | 1239 | ...[a] |
| Periphery | 427 | 1 | 0.56 | 2359 | ... |
| Bore | 427 | 100 | 1.83 | 205 | ... |
| Bore | 427 | 100 | 0.81 | 1545 | ... |
| Bore | 427 | 100 | 0.48 | 6080 | ...[a] |
| Bore | 427 | 100 | 0.33 | 40876 | ... |

[a] Symmetric loop tests.

condition failure lifes are shown as triangular points. Two significant points are evident from these observations of Fig. 3. First, with the exception of a single 4-h hold-time point, the hold-time data do not show a significant decrease in life over the continuous cycling data. Thus, any creep damage introduced in the hold time in the temperature range of 371 to 482°C did not appreciably shorten the fatigue life. Secondly, within the hold-time scatterband, distinct trends in the data are not obvious, probably because specimen-to-specimen microstructural heterogeneities have a competitive effect on fatigue initiation and growth with test temperature and hold-time duration. Details of selected microstructures will be discussed later.

### *Effect of Strain Range (Continuous Cycling) on Fracture Mode*

For brevity, since the continuous cycling tests showed the same basic fractographic features irrespective of temperature, location of material,

TABLE 3—*Summary of hold-time testing conducted on Gallatin No. 2 intermediate pressure end material.*

| Specimen Location | Test Temperature, °C | Total Cycle Time, h | Hold Time, h | Total Up and Down Ramp Time, h | Total Strain Range, % | Life to Failure, $N_f$ | Comments |
|---|---|---|---|---|---|---|---|
| Periphery | 371 | 1 | 59/60 | 1/60 | 1.82 | 192 | |
| Periphery | 371 | 1 | 59/60 | 1/60 | 1.00 | 2337 | |
| Bore | 427 | 1 | 59/60 | 1/60 | 3.23 | 106 | Figs. 9 and 10 |
| Bore | 427 | 1 | 59/60 | 1/60 | 1.91 | 304 | |
| Periphery | 427 | 1 | 59/60 | 1/60 | 1.74 | (60) | 20% $N_f$, Fig. 16 |
| Bore | 427 | 1 | 59/60 | 1/60 | 0.78 | 1800 | |
| Bore | 427 | 4 | 3 59/50 | 1/60 | 2.85 | 69 | Figs. 11 and 12 |
| Bore | 427 | 4 | 3 59/60 | 1/60 | 1.59 | 145 | |
| Bore | 427 | 24 | 23 | 1 | 2.98 | 76 | Figs. 13 and 14 |
| Bore | 427 | 24 | 23 | 1 | 2.98 | (12) | 16% $N_f$, Fig. 15 |
| Periphery | 427 | 24 | 23 | 1 | 2.98 | (7) | 9% $N_f$, Fig. 17 |
| Periphery | 482 | 1 | 59/60 | 1/60 | 1.30 | 712 | |
| Periphery | 482 | 1 | 59/60 | 1/60 | 2.90 | 97 | |

[a] Parentheses denote initiation specimen terminated for destructive cut up.

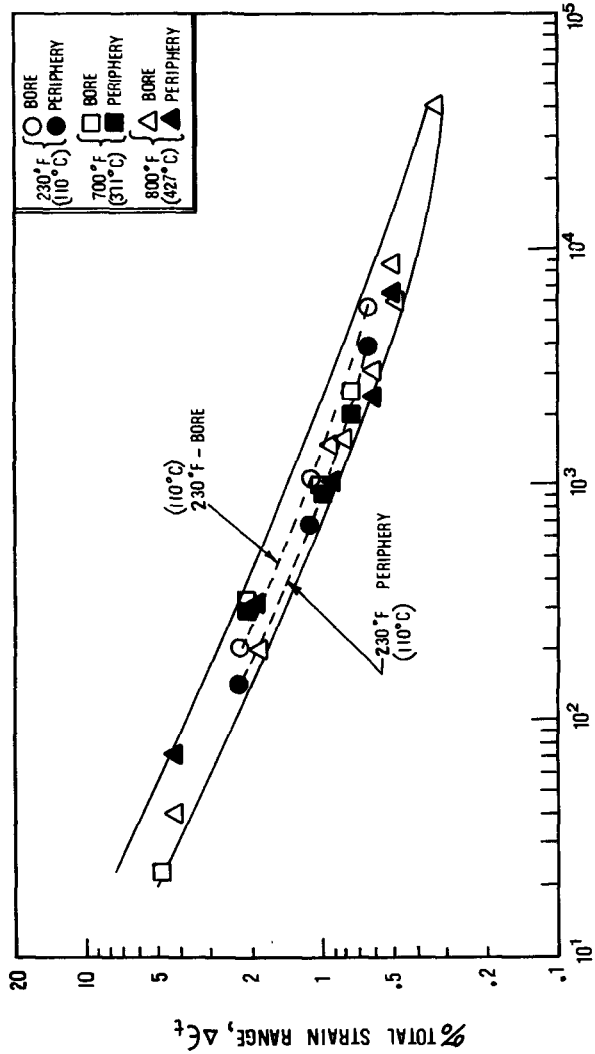


FIG. 2—*A summary of all continuous cycling axial fatigue results.*

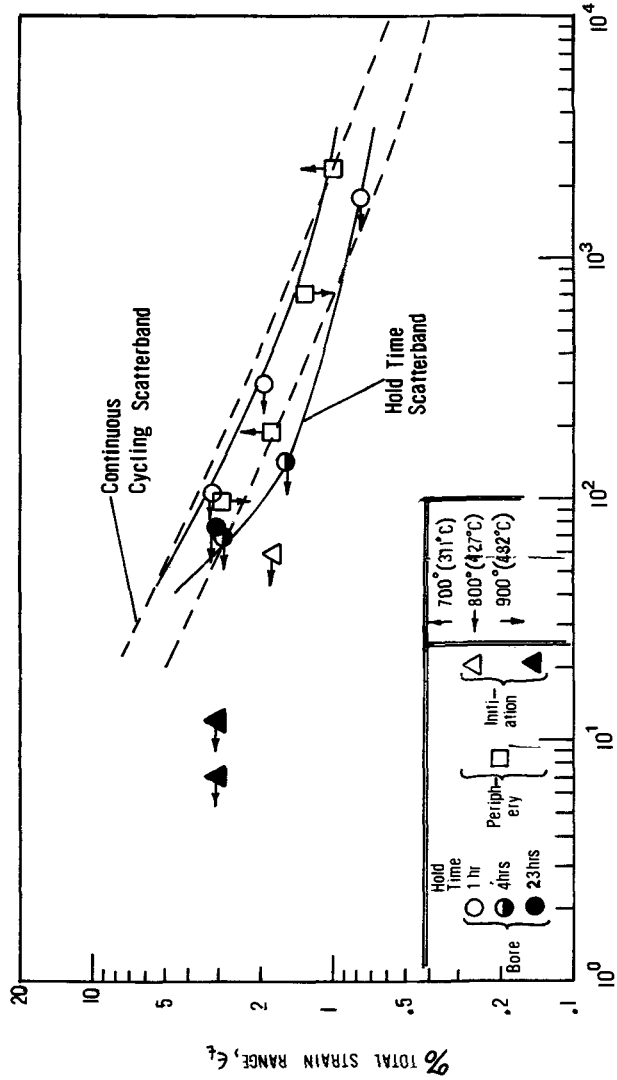


FIG. 3—*A summary of all hold-time axial fatigue results with superposition of the continuous cycling scatterband.*

and cycling rate, only the bore specimens which bracket the minimum and maximum strain ranges at 427°C will be discussed. The fractography of the lowest strain range ($\epsilon_t$ = 0.5 percent, $N_f$ = 7500 cycles) 427°C bore specimen is shown in Fig. 4. Surface initiation occurred around 90 percent of the gage circumference (as visually observed at ×60); however, subsurface initiation just adjacent to the surface (Area P) as well as internal initiation (Area Q) both occurred at MnS inclusions. All initiation sites were rubbed mechanically during the reversed ramp loading to zero strain, but propagation topography was highly striated. Surface oxide spiking was not observed. A metallographic section (Fig. 5) along the subsurface inclusion in Area P revealed transgranular initiation with a slight amount of branching at the crack tip. Similar behavior was observed at secondary cracks along the gage length below the main fracture.

By comparison, the maximum strain range ($\epsilon_t$ = 4.3 percent, $N_f$ = 41 cycles) 427°C bore specimen solely initiated internally at MnS stringers.

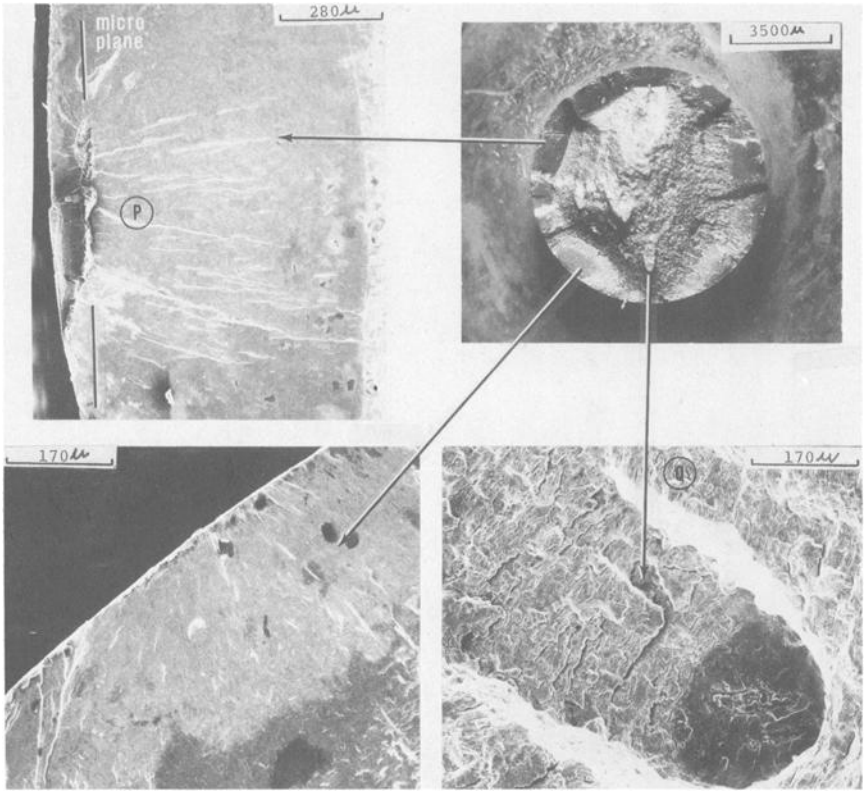


FIG. 4—*Topography of the minimum strain range (0.6 percent) bore 427°C continuous cycling specimen fracture showing internal MnS inclusions (Area Q) near surface MnS inclusions (Area P), and zero defect surface locations which were all initiation sites.*

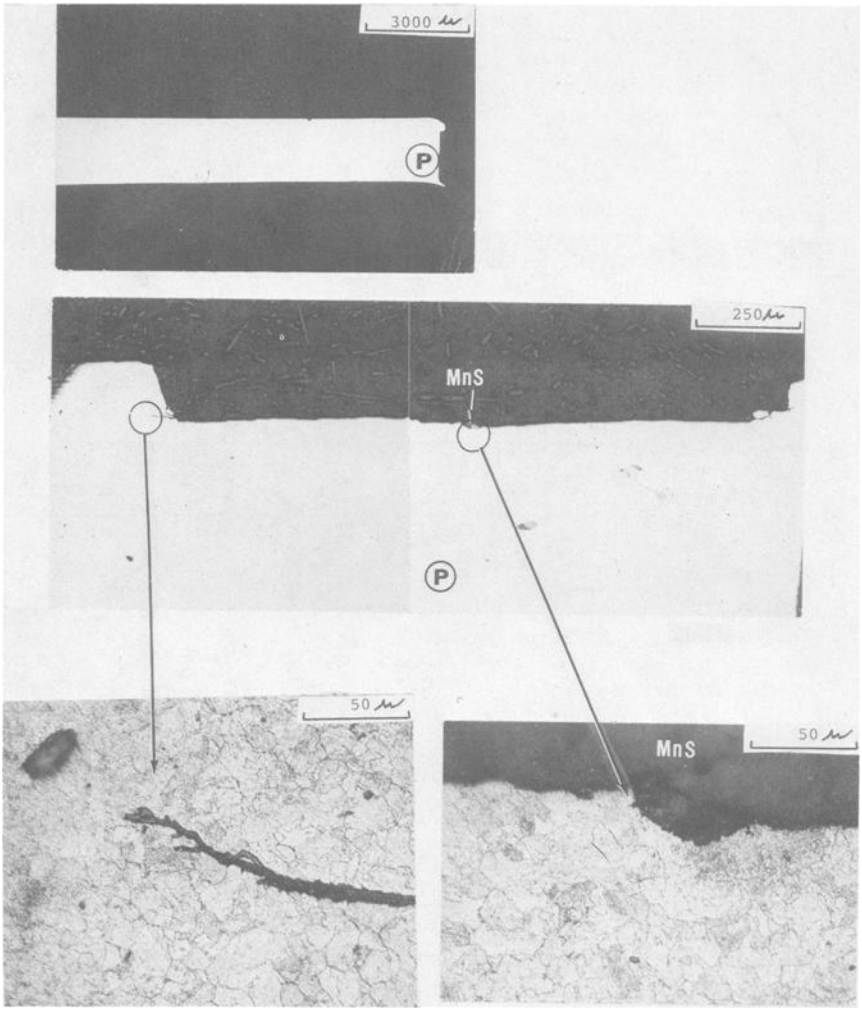


FIG. 5—*Selected metallography through Area P in Fig. 4. Sodium tridecyl benzene sulfonate (STBS) for etched microsections.*

Figure 6 denotes the multiple level fracture surface with each level corresponding to a MnS concentration. Since these inclusions were known to be concentrated in inverse "V" segregation [*2*], it is not surprising that parallel macroplanes are observed at each cluster concentration. Area Y in Fig. 6 is a typical example of this behavior. SEM fractography indicates that each major inclusion or cluster of minor inclusions has a small patch of transgranular fatigue initiate from each discrete inclusion on a plane exactly normal to the applied stress axis. Once growth proceeds sufficiently to link

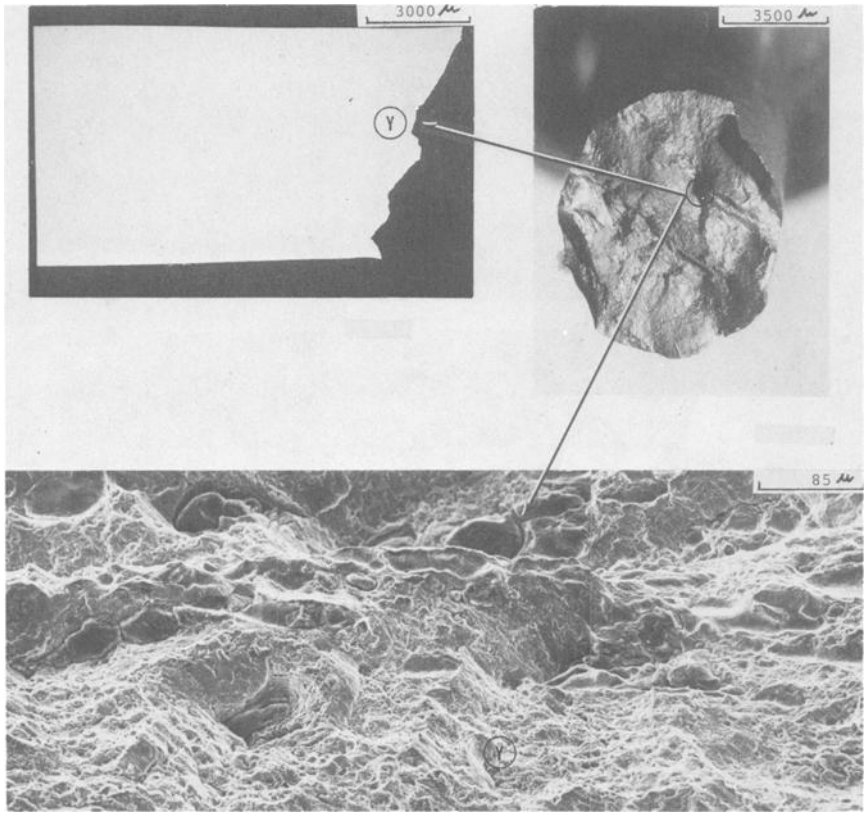


FIG. 6—*Topography of the maximum strain range (4.3 percent) bore 427°C continuous cycling specimen fracture showing planar transgranular linkup of MnS inclusions internal to the gage diameter (for example, at Area Y). Macroscopic observation of the specimen fracture readily shows parallel MnS concentrations corresponding to Area Y.*

up adjacent stringers, shearing occurs between these planar fatigue cracks. As expected, a relatively small fraction of final topography is fatigue with the bulk being shear dimples. The surface of the gage length was perforated with oxide spikes (Fig. 7); however, this phenomenon was not observed to affect either initiation location nor propagation direction. Metallography revealed transgranular main fracture propagation; however, secondary cracking was significantly more branched than at lower strain ranges (Fig. 8).

### *Effect of Hold Time (Constant Strain Range)*

In order to compare the effect of increasing hold time at approximately constant strain range, three near bore specimens were run at 427°C to failure. The initial hold-time test was a 1-h cycle to a strain range of 3.2

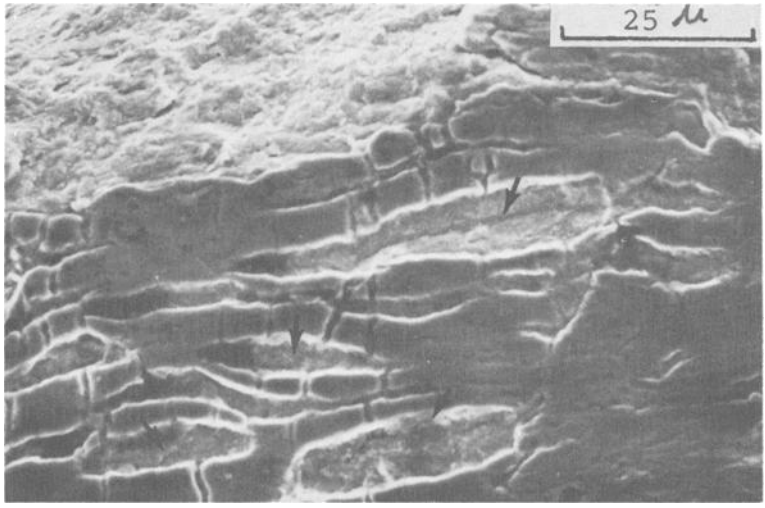


FIG. 7—*Oxide spiking (arrows) on the gage section surface of Fig. 6.*

percent ($N_f$ = 106 cycles). Longer hold-time cycles of 4 h ($N_f$ = 71 cycles) and 23 h ($N_f$ = 76 cycles) were tested at a total strain range of 2.85 and 2.98 percent, respectively. Details of the cycle ramp rates and hold times are given in Table 3.

The 1-h cycle hold-time specimen cross section is presented in Fig. 9 and appears to have similar planar shearing as observed in the previous example (Area K). Unfortunatley, the fracture topography was grossly obliterated by oxidation due to fracture surface exposure during the test. The gage section was penetrated uniformly with oxide spikes to 1.2 mm depth (Area B). Metallography revealed transgranular cracking with various degrees of branching (Fig. 10). Where MnS inclusions were present, transgranular cracks originated from these defects (Area S).

Detailed fractography of the 4-h cycle hold-time specimen is presented in Figs. 11 and 12. This specimen has definite internal initiation at discrete MnS inclusions (Areas U and J), transgranular striated fatigue linkup at these inclusions, shearing between fatigue planes, and a preponderance of surface spiking (Area Z) not associated with any subsurface initiation sites. Metallography revealed all cracking to be branched but transgranular.

The 23-h hold-time specimen as-received condition is detailed in Fig. 13. The primary fracture surface must have been open to the air for at least 20 cycles during testing, and the topography was oxidized by the furnace atmosphere. This estimate is based on the observations of 5 percent load drop in the stable hysteresis loop at cycle 47 as well as noticeable stable loop shape deformation at cycle 56 (failure occurred at cycle 76). Careful observation after electrolytic cleaning did reveal an intergranular remnant

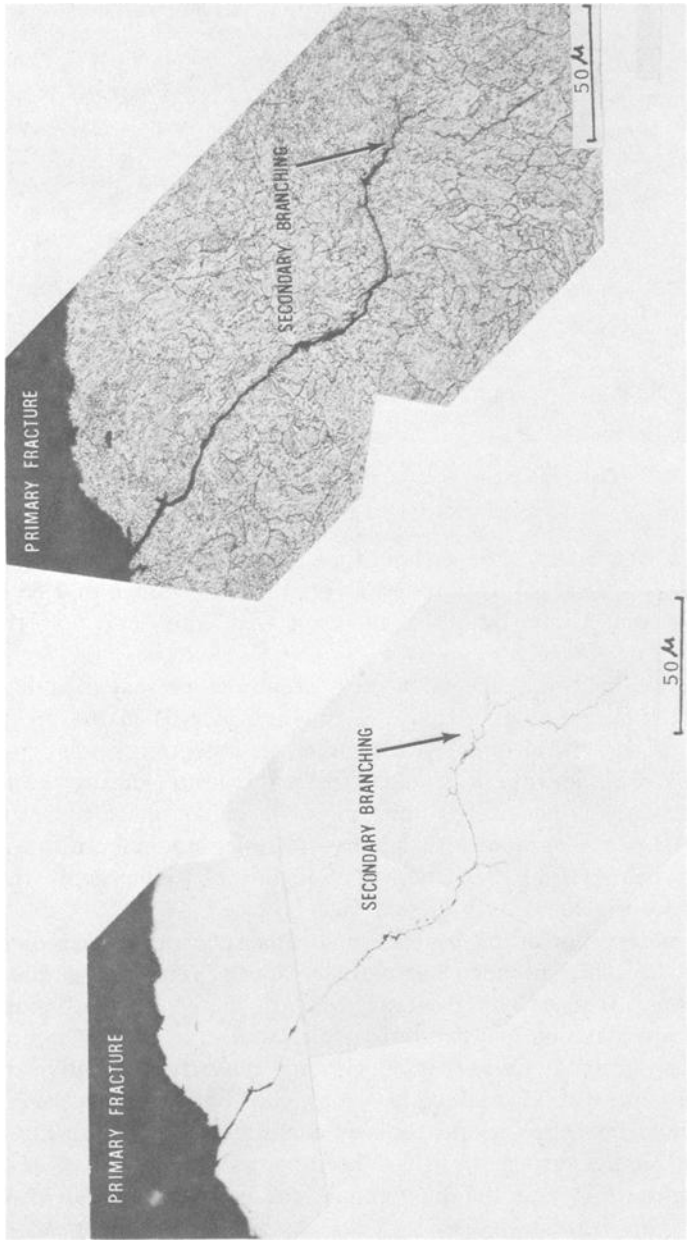


FIG. 8—*Branched transgranular secondary cracking off the primary fracture in Fig. 7. STBS etchant.*

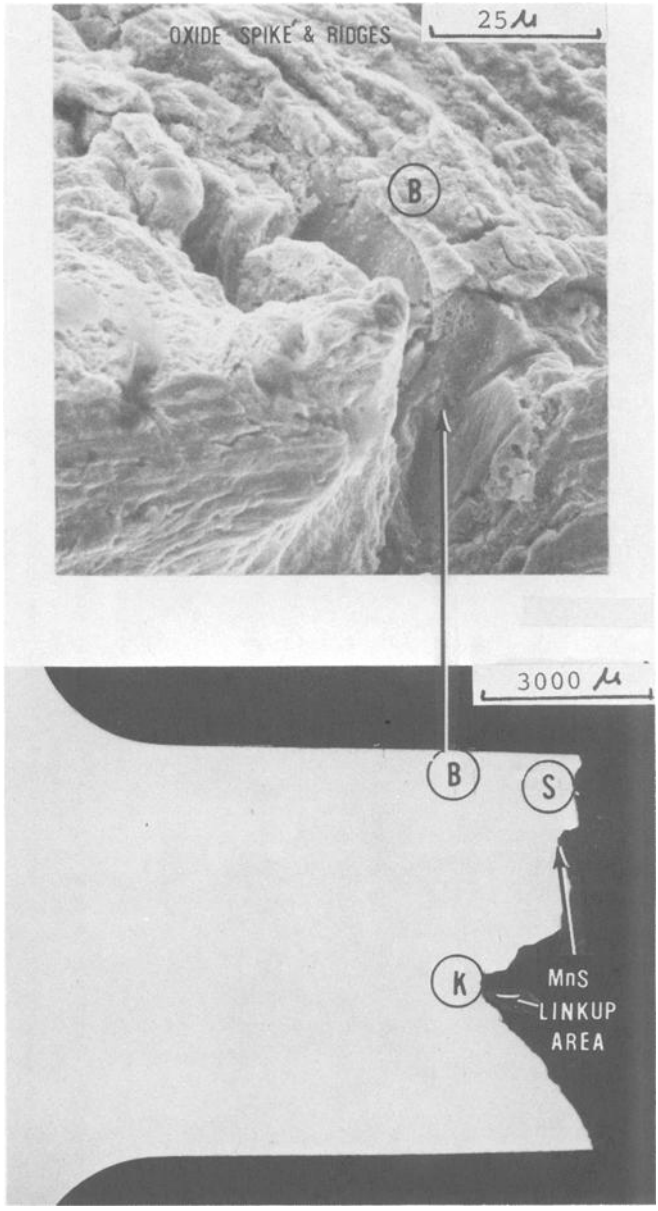


FIG. 9—*Internal initiation (Areas K and S) at MnS inclusions and oxide spiking (Area B) in the bore 1-h cycle hold-time specimen tested to failure at 427°C and a total strain range of 3.23 percent.*

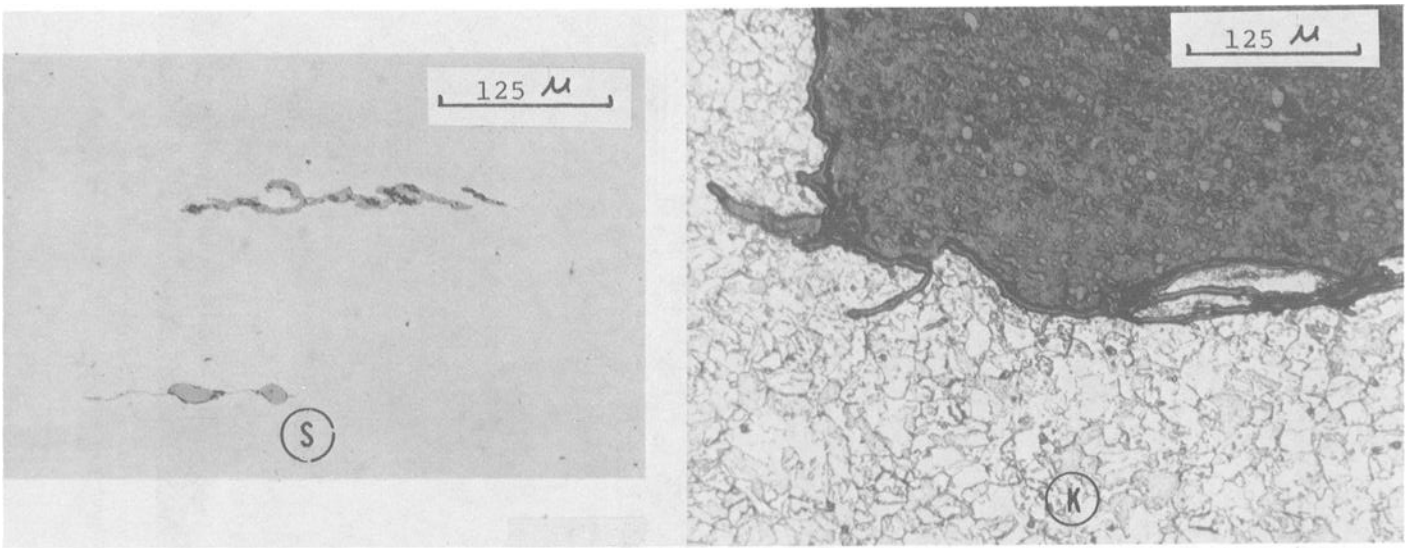


FIG. 10—*Selected metallography of Areas K and S in Fig. 9 showing transgranular cracking in each case. Area K had been observed previously to have a high local MnS concentration. However, due to the degree of fracture surface oxidation, the subsequent electrolytic cleaning method also removed most of the MnS inclusions entrained in the oxide. Thus, no MnS inclusions remain in the microsection. STBS etchant.*

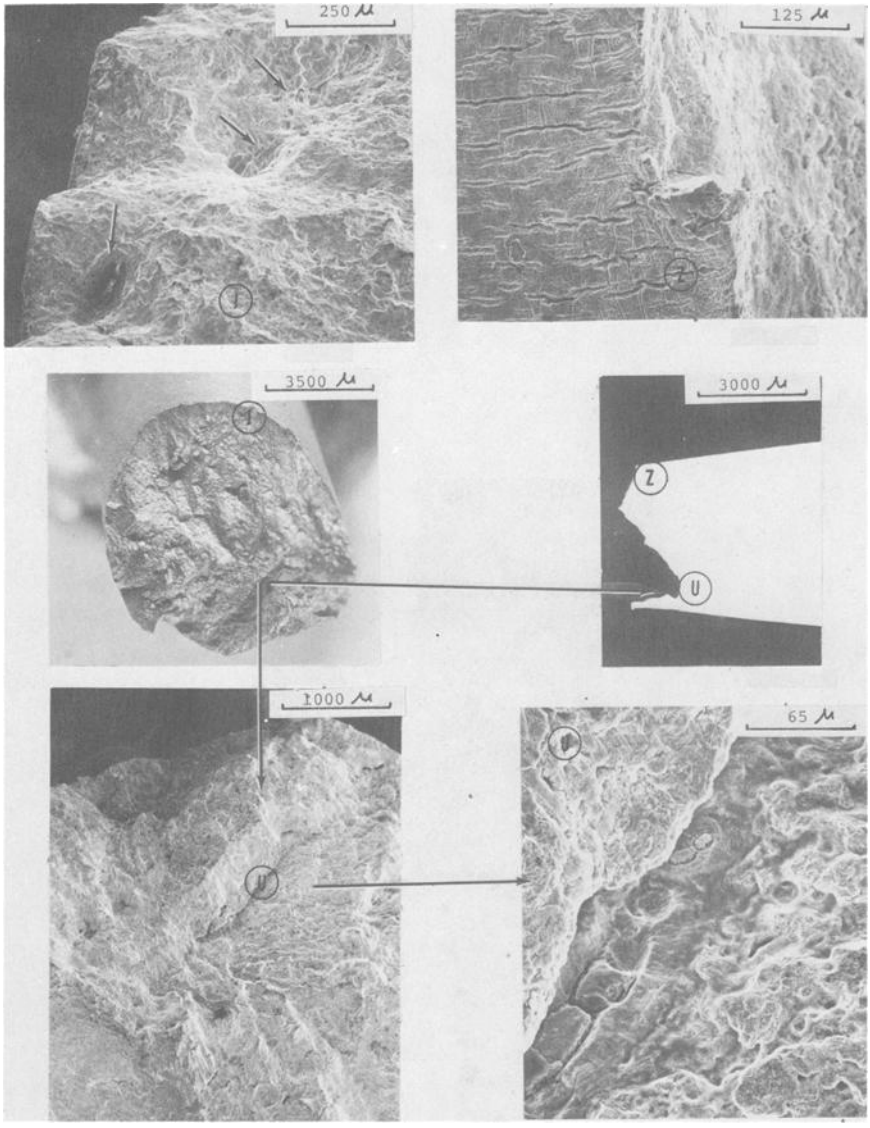


FIG. 11—*Internal initiation (Areas J and U) at MnS inclusions in the bore 4-h cycle hold-time specimen tested to failure at 427°C and a total strain range of 2.85 percent. Transgranular linkup of inclusions is obvious despite numerous oxide spikes (Area Z).*

when viewed as a stereo pair. An axial metallographic section (Fig. 14) through this specimen gage section revealed numerous intergranular secondary cracks (Area F, Cracks 1, 2, and 3) below the primary plane of fracture. Each crack corresponded exactly to a dark etching band of positive segregation in a similar manner to cracking at the Gallatin No. 2 origin

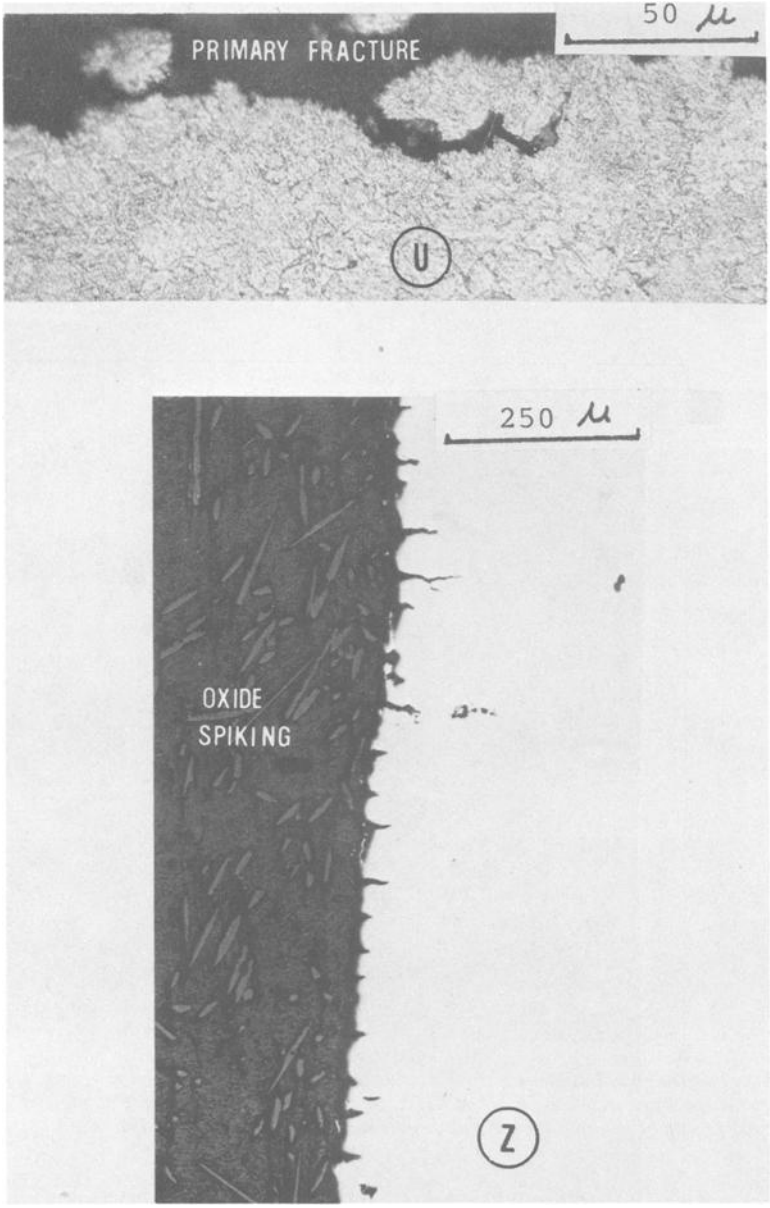


FIG. 12—*Selected metallograph of fatigue propagation (Area U) and oxide spiking (Area Z). STBS etchant is used where etched.*

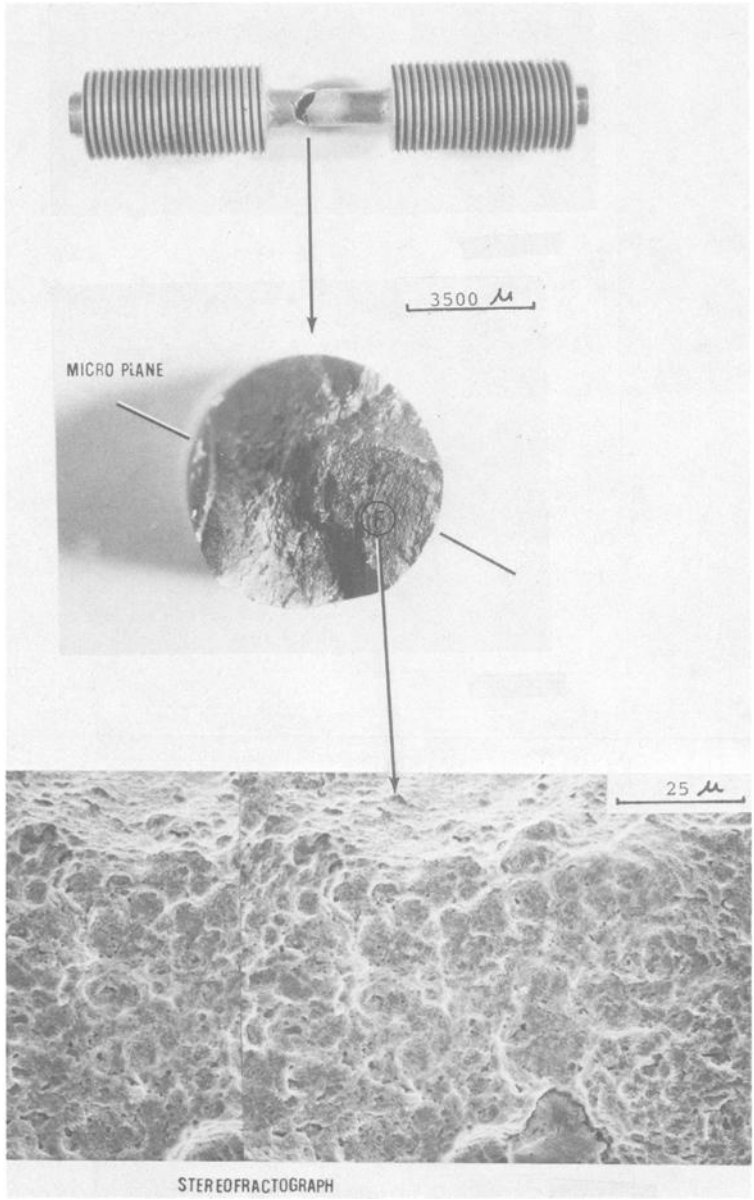


FIG. 13—*As-received condition of the bore 24-h cycle hold-time specimen tested to failure at 427°C and a total strain range of 2.98 percent. Even though the fracture had been oxidized severely during testing, a stereo pair shows a distinct remnant of intergranularity.*

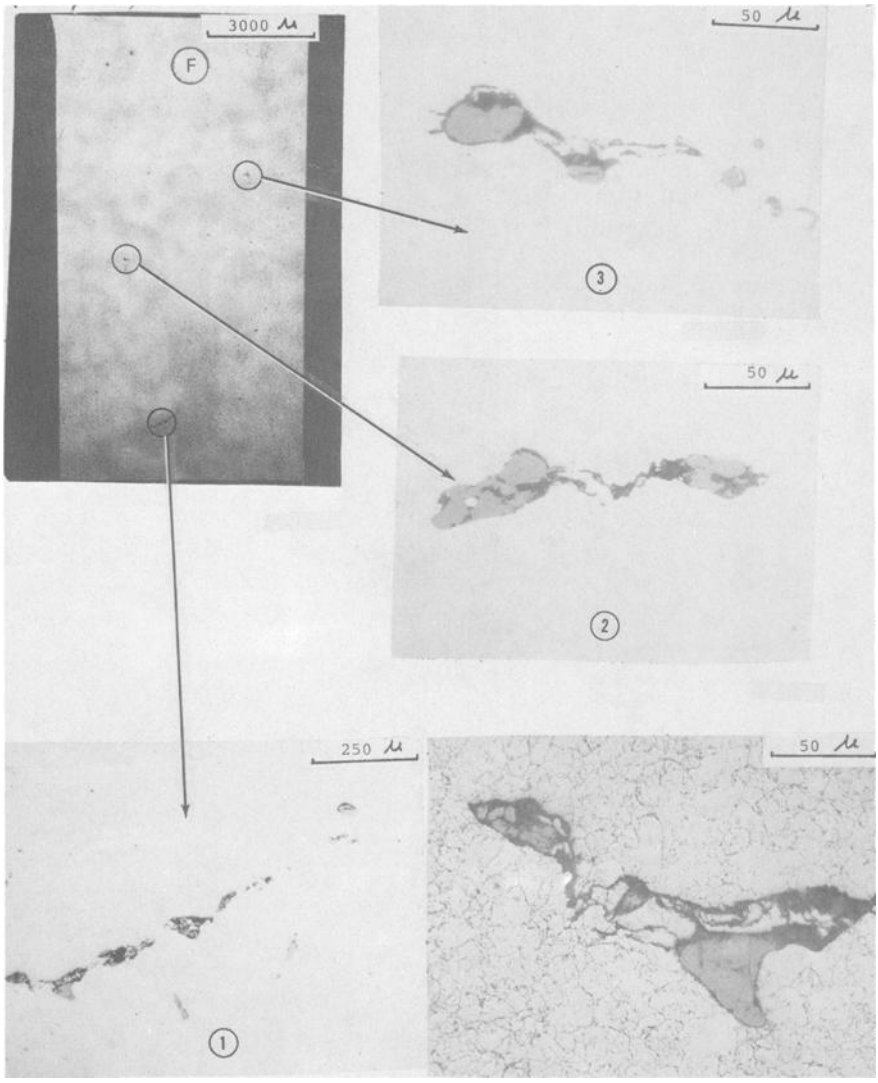


FIG. 14—*Selected metallography of Fig. 13 showing greater inclusion linkup distances associated with the darker etching, highly segregated Area F (Location 1 compared to Locations 2 and 3) Crack morphology was intergranular. STBS etchant is used where etched.*

[2]. The more intense etching banded areas had closer spaced *MnS* inclusions and thereby longer linkup distances. This statement is corroborated by comparing Locations 1, 2, and 3 in Fig. 14. Detailed metallography of Location 1 (Fig. 14) shows the same inclusion decohesion and branched intergranular cracking observed in Gallatin. This behavior was also reproducible in the 12-cycle early-life specimen which exhibited up to 1.2 ×

$10^{-4}$ mm branched intergranular linkup between inclusions internal to the gage section (Fig. 15).

*Effect of Material Location (Hold-Time Tests)*

Since continuous cycling tests showed no difference in either initiation or propagation topography with radial location (that is, variable segregation), early-life hold-time specimens were sectioned to verify cracking morphology differences with specimen location. Figures 16 and 17 are periphery mate-

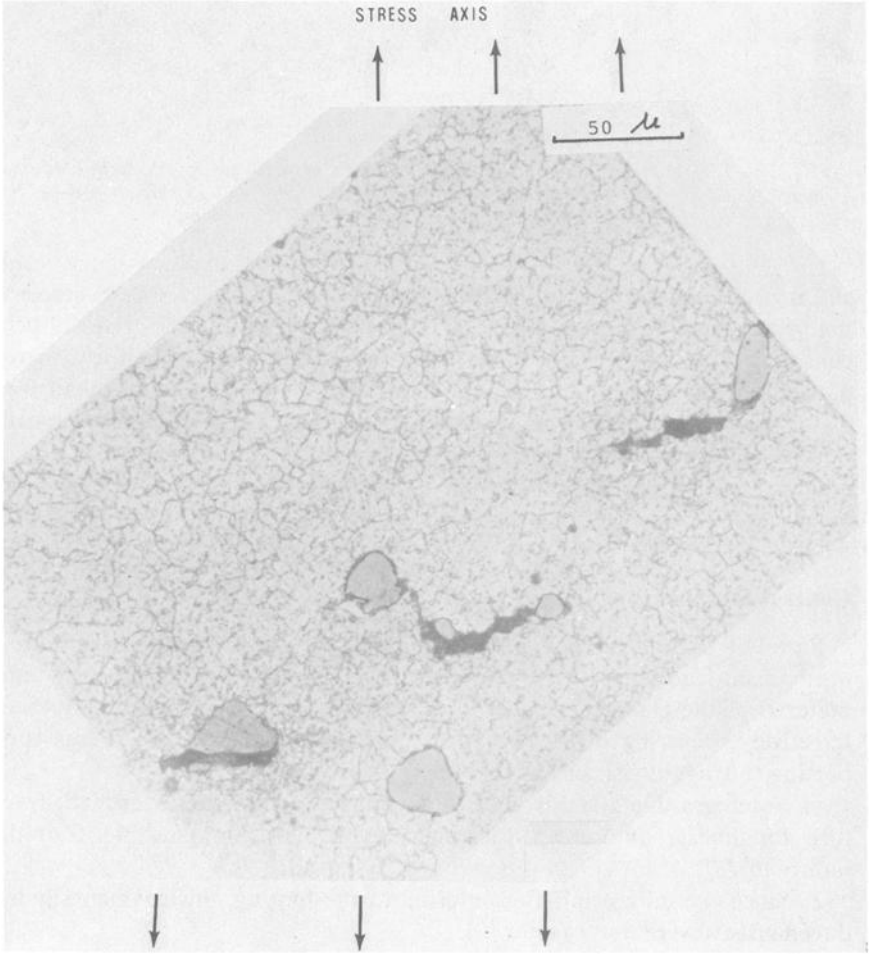


FIG. 15—*Similar intergranular initiation between MnS inclusions in another bore 24-h cycle hold-time specimen tested at 427°C and a total strain range of 2.98 percent. Testing was terminated upon reaching 12 strain cycles (16 percent of life). STBS etchant.*

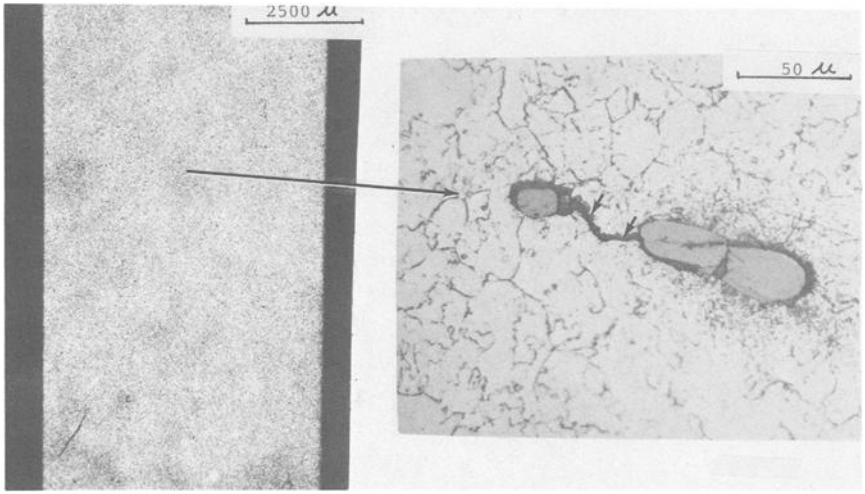


FIG. 16—*Transgranular initiation at MnS inclusions in a periphery 1-h cycle hold-time specimen tested to 60 strain cycles (20 percent of life) at a range of 1.75 percent and 427°C. Little segregation is observed at this position in the forging. STBS etchant.*

rial microsections of 1-h ($\epsilon_t$ = 1.74 percent) and 23-h ($\epsilon_t$ = 2.98 percent) hold-time specimens after 60 cycles (20 percent of $N_f$) and 7 cycles (9 percent of $N_f$), respectively. In both cases, the structure was much less segregated than the corresponding bore specimens; hence, the MnS mean free distance was larger than previously noted. Slight inclusion-matrix decohesion occurred as well as transgranular linkup between a few adjacent inclusions. No simulation of the Gallatin crack morphology was observed.

## General Comments

Based on the preceding experiments as well as earlier work, the *initiation* mechanism leading to the development of elliptical flaws in the near bore material of the Gallatin is most likely a creep-low cycle fatigue interaction selectively occurring in bore segregate banded microstructure. Items supporting this hypothesis are as follows.

1. Fractographic analysis of tension, impact, fatigue crack growth, fracture toughness, and creep specimens could not simulate the Gallatin failure [*6,18*].

2. Since the failure initiated internal to the forging, environmentally induced effects were not a factor [*2*].

3. Based on a review of known forging quality defects, additional metallography of selected macroetched rotor sections, nondestructive inspection of the original failed rotor fragments, metallography of the specimens (in-

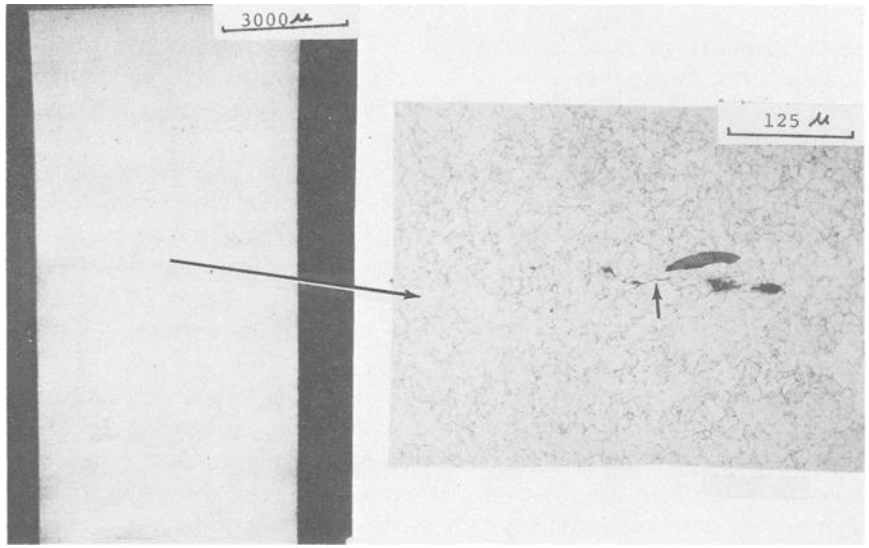


FIG. 17—*Transgranular initiation at MnS inclusions in a periphery 24-h cycle hold-time specimen tested to 7 cycles (9 percent of life) at a range of 2.98 percent and 427°C. Again, little segregation is observed at this position in the forging. STBS etchant.*

cluding the fatigue bar grip ends), and the appearance of the initiating flaws themselves, no original manufacturing flaw existed in the rotor prior to entering service with the exception of the alloy segregation and MnS concentrations.

4. The imposition of a 23-h hold-time strain controlled fatigue cycle was able to simulate the intergranular linkup between MnS inclusions in the same bore microstructure as observed in the Gallatin rotor. No other fatigue parameters resulted in a fractographic simulation. Furthermore, when the bore material test was stopped at 16 percent of cyclic life, similar linkup already had occurred when adjacent inclusions were of the same interparticle distances as noted at the Gallatin origin (2 to 6 $\times$ $10^{-4}$ mm). The degree of segregation and concentration of inclusions were probably less than the actual origin location due to the random amounts of segregation in each specimen. The presence of significant intergranular linkup at 16 percent of cyclic life in the fatigue specimen thereby implies that areas at least as heavily segregated in the actual rotor could undergo similar early initiation. In other words, the presence of a fairly continuous planar concentration of MnS inclusions with this 2 to 6 $\times$ $10^{-4}$ mm interparticle spacing when linked up by a creep-fatigue interaction would be expected to result in the critical flaw size for bursting (that is, the actual 5.5 by 0.25-in. elliptical flaw). The 16 percent early life test was not intended to define the exact cycle at which initiation occurred but rather to demonstrate that crack linkup is extremely early in specimen life. Furthermore, the degree

of creep relaxation (that is, hold-time duration) to produce intergranular linkup is not known; however, 23 h is a convenient value probably representing a realistic minimum value seen by many fossil steam turbines in actual service.

5. Given these long hold times in fatigue, the location of material (namely, the microstructure) has a significant effect on MnS inclusion linkup frequency and fracture path. Since the periphery material (Fig. 16) was less segregated, the MnS interparticle distance was greater thereby decreasing the possibility of linkup. Furthermore, the unbanded periphery material was found to be unlike the bore microstructure which was highly duplexed in the bands [*2,6*].

Although the preceding points support the creep-fatigue mechanism of linkup between MnS inclusions of 2 to 6 $\times$ $10^{-4}$ mm interparticle spacings, two items are not resolved by these experiments. First, on a fatigue life basis ($N_f$), the hold-time loops are essentially no more damaging (that is, shorter life) than the continuous cycle over the same strain ranges. Secondly, when reviewing the bore hold-time data alone, the 4-h hold times appear more damaging than either the 23 or 1-h holds. For both cases, comparisons with the same higher temperature data of Leven [*8*] for the same class of alloy but with a homogeneous microstructure definitely imply increasing hold times to be consequently more damaging than continuous cycling. Accordingly, testing at lower temperatures such as 427°C, one would expect the same trend but with a lesser magnitude in damage with increasing hold times. The difference between the expected and actual behaviors is obviously the heterogeneity of the Gallatin bore microstructure; hence, the variable volume fraction of segregates present on a specimen-to-specimen basis probably masks any real effect at hold time in the 371 to 483°C range. Early in the Gallatin failure analysis, the banded-nonbanded volume fraction was investigated using television quantitative metallographic techniques; however, due to the diffuse boundary of interdendritic segregation, no consistent workable method of defining segregate volume fraction was obtained [*18*].

## Conclusions

1. MnS inclusions preferentially act as internal crack initial sites for both bore and periphery material at most test conditions; however, these respective differences in inclusion concentrations had no significant effect on actual specimen cyclic life. Only at very low strain ranges during the continuous cycling tests were both surface and MnS initiations sites observed.

2. At high strain ranges and long exposures, surface oxide spiking does not seem to affect preferential MnS initiation.

3. Fractographic simulation of the Gallatin No. 2 rotor burst origin can

be obtained provided that long hold times (that is, at least 23 h) are imposed on an asymmetric strain controlled loop ($\epsilon_t$ = 2.98 percent) at 427°C in near bore segregated material. Removal of near bore segregation or long hold times forced the topography to become transgranular (that is, not typical of the actual failure topography).

4. Hold-time tests run to failure at 427°C did show essentially the same fatigue life as observed in the continuous cycling tests; however, when three selected specimens were terminated within 20 percent of the expected failure life, early subsurface initiation at inclusions had occurred. The greatest extent of planar MnS linkup occurred in the 23-h hold-time specimen from bore material which had a $1.2 \times 10^{-4}$ mm intergranular crack after 16 percent of expected life.

*Acknowledgments*

The author would like to thank the Westinghouse Steam Turbine Division and the Electric Power Research Institute for permission to publish these data. In particular, the advice and comments of B. B. Seth are gratefully appreciated. Metallurgical analyses were conducted by D. Hamilton, T. Calabrese, and J. M. Shinefield. T. Fabis of the Westinghouse Research and Development Laboratories conducted the low cycle fatigue testing. This work was sponsored under EPRI Contract RP 502, Dr. F. Gelhaus, program manager.

## References

[1] Hammond, J. C. and Schmerling, J. M., "Investigation of the Tennessee Valley Authority, Gallatin Unit No. 2 Turbine Rotor Burst," Presentation before the 38th Annual Meeting of the American Power Conference, Chicago, Ill., 21 April 1976.

[2] Kramer, L. D. and Randolph, D. D. in the *1976 ASME-MPC Symposium on Creep-Fatigue Interaction*, R. M. Curran, Ed., American Society of Mechanical Engineers, New York, 1976, pp. 1-24.

[3] Weisz, D. A. in *1976 ASME-MPC Symposium on Creep-Fatigue Interaction*, R. M. Curran, Ed., American Society of Mechanical Engineers, New York, 1976, pp. 25-40.

[4] Kramer, L. D. et al, "Reliability of Steam Turbine Rotors-2nd Semi Annual Report," EPRI Contract No. RP502-4, Electric Power Research Institute, 19 April 1977.

[5] Manson, S. S., *Experimental Mechanics*, Vol. 7, No. 5, May 1965, pp. 193-226.

[6] Kramer, L. D. et al, "Reliability of Steam Turbine Rotors—1st Semi Annual Report," EPRI Contract No. RP502-4, Electric Power Research Institute, July 1976.

[7] Krempl, E. and Walker, C. D. in *Fatigue at High Temperature, ASTM STP 459*, American Society for Testing and Materials, 1969, pp. 75-99.

[8] Leven, M. M., *Experimental Mechanics*, Vol. 13, No. 9, Sept. 1973, pp. 353-372.

[9] Curran, R. M. and Wundt, B. in *Reports of Current Work on Behavior of Materials at Elevated Temperatures*, A. O. Schaefer, Ed., American Society of Mechanical Engineers, New York, 1974.

[10] Curran, R. M. and Wundt, B. in *1976 ASME-MPC Symposium on Creep-Fatigue Interaction*, R. M. Curran, Ed., American Society of Mechanical Engineers New York, 1976, pp. 203-283.

[11] Hill, G. J., in *Thermal and High Strain Fatigue*, Institute of Metals, London, 1967, pp. 312-327.

[*12*] Coles, A. et al in *Thermal and High Strain Fatigue*, Institute of Metals, London, 1967, pp. 270–294.
[*13*] Coles, A. and Chitty, A. in *Thermal and High Strain Fatigue*, Institute of Metals, London, pp. 328–345.
[*14*] Smith, H. C. et al, "The Nature and Source of Nonmetallic Inclusions in Large Forgings," Presentation to the 1977 Annual Meeting of the International Forgemasters Conference, Kyoto, 23–28 Oct. 1977.
[*15*] Ferdinandez, S., "Influence of 'A' Segregations on the Mechanical Properties of Forgings Obtained from Vacuum Poured Ingots," Sixth International Forgemasters Meeting, Cherry Hill, N.J., 1972.
]*16*] Snow, R. B., "Source of Inclusions in Forging Ingots," Sixth International Forgemasters Meeting, Cherry Hill, N.J., 1972.
[*17*] Watanabe, J. et al, "A Study of Crack Initiation in Rotating Parts," Presentation to the 2nd International Conference on Mechanical Behavior of Materials, Boston, 16–20 Aug. 1976.
[*18*] Kramer, L. D., Unpublished data.

*A. Joshi*[1]

# Role of Interface Chemistry in Failure of Materials

**REFERENCE:** Joshi, A., **"Role of Interface Chemistry in Failure of Materials,"** *Fractography in Failure Analysis, ASTM STP 645,* B. M. Strauss and W. H. Cullen, Jr., Eds., American Society for Testing and Materials, 1978, pp. 275-293.

**ABSTRACT:** Properties of many materials are influenced strongly by small compositional changes that occur at interfaces such as phase and grain boundaries. Knowledge of the elements involved and whether they are segregated or present in a second phase provides a better understanding of the failure mechanism. In many instances of grain boundary failures, the chemistry provides the most comprehensive and useful information. Examples of such studies discussed here include temper embrittlement and other forms of impurity-induced low temperature embrittlement, weld-metal embrittlement, grain boundary corrosion, and intergranular stress corrosion cracking. Failures at phase boundaries and other more macroscopic interfaces such as encountered in fiber/metal matrix composites, interparticle interfaces in powder metallurgy materials and bonded (thermal compression, solder, or diffusion bonded) interfaces also can be understood by close examination of chemistry of these interfaces.

In many of these examples, the zone of segregation at boundaries is very small, only a few angstroms, the same as the boundary width. The interface chemistry has been studied successfully in a scanning Auger microprobe by Auger electron spectroscopic analysis of grain boundary fracture surfaces obtained inside the vacuum system.

**KEY WORDS:** fractography, Auger electrons, spectroscopy, embrittlement, fractures, (materials) grain boundaries, corrosion, stress corrosion, weld metal, composite material, hydrogen embrittlement

Properties of many polycrystalline materials are influenced strongly by the presence of solid-solid interfaces such as the phase and grain boundaries. These interfaces, like surfaces (solid-vapor interfaces), are high energy regions having an atomic structure different from that of the bulk. Further, they often act as a source or sink for atomic defects and are preferred sites for solid state reactions, such as phase transformations and precipitation. The kinetics of the processes involving grain boundaries also are different, resulting in accelerated diffusion, growth of phases, etc. The structural difference between the grain boundaries and bulk is the basic reason for

[1] Assistant director, Analytical Laboratory, Physical Electronics Industries, Inc., Eden Prairie, Minn. 55343.

these differences and also leads to localized variations in composition of alloys due to equilibrium as well as nonequilibrium processes of segregation.

The differences in interface chemistry and bulk chemistry can be significant. In extreme cases, the interfaces may be occupied completely by a layer of foreign atoms whose concentration in the bulk is in the parts per million range. Such differences can arise due to segregation during heat treatment or thermomechanical treatments, diffusion from surfaces, or due to vacancy drag in certain quenched materials. The compositional changes, even if they are small, can influence significantly many material properties, such as mechanical strength, corrosion, and stress corrosion behaviors. Knowledge of the elements involved and whether they are segregated or present in a second phase provides better understanding of the failure mechanism.

The unambiguous detection of segregated species has been difficult for quite sometime. The chemical etching, neutron activation, and electron probe techniques only rarely have been successful in detection. In most techniques, the difficulty arises primarily due to inadequate resolution or low detection sensitivity. The advances in surface analysis techniques, in particular Auger electron spectroscopy (AES), now make it possible to detect segregation levels as low as 0.1 atomic percent of most elements present to within a monolayer at interfaces. At present, AES is the most widely used technique for interface chemical studies and the purpose of this article is to review some of the understanding provided by this technique in relating interface chemistry to material properties.

## Auger Electron Spectroscopy to Study Interface Chemistry

The high surface sensitivity of the AES techniques is used in obtaining interface chemistry. The examination of interface chemistry is facilitated by fracturing the material in such a manner that the interfaces are made into surfaces. Thus, in many instances of grain boundary embrittlement, the fracture surfaces are the prior grain boundaries and analysis of such surfaces represents grain boundary chemistry. The analysis of boundaries in materials that do not fail by grain boundary fracture is difficult, and techniques are being developed to facilitate studies in such materials as well.

The principles and techniques of AES have been described in detail elsewhere [*1*][2] and will not be repeated here. An Auger spectrum represents the composition of the top 5 to 20 Å of the surface and is presented most commonly as the derivative of the electron energy distribution, $dN(E)/dE$, as a function of kinetic energy, $E$. Elements present are simply identified from the energy positions at which peaks occur in the Auger spectrum. Since the peak-to-peak heights are generally proportional to the atomic

[2] The italic numbers in brackets refer to the list of references appended to this paper.

concentration [2], quantitative calculations simply can be made by utilizing the elemental sensitivity factors [3,4]. In order to minimize the contamination of the fracture surface from the atmosphere, the fractures are often performed within the vacuum system. While in some cases, externally fractured and field fractured surfaces have been examined with fair success, fracture within the high vacuum system is required in most cases. Ultra-high vacuum systems providing pressure in the $10^{-10}$ torr range having oil-free pumping devices are found to be extremely satisfactory.

The Auger spectra also contain a wealth of chemical binding information, which is usually derived from the peak shifts and peak shape changes. Many metals, such as aluminum, silicon, magnesium, vanadium, tantalum, niobium, iron, titanium as well as non-metals such as boron, phosphorus, sulfur, and chlorine can be distinguished in their oxide forms from their elemental forms. Carbon exhibits peak shape changes that are distinctly different for carbide from carbonate [5], graphite, diamond, and carbon monoxide [6]. Figure 1, from the work of Haas et al [6], depicts some of these differences. The micrograph shown in Fig. 2 is a secondary electron image obtained from a polished nodular cast iron using a scanning Auger microprobe. The carbon peak shape obtained from the nodule (Fig. 2) is typical of that of graphite while the spectrum obtained from the pearlite region (Fig. 3) suggests the presence of both carbide and graphite. In

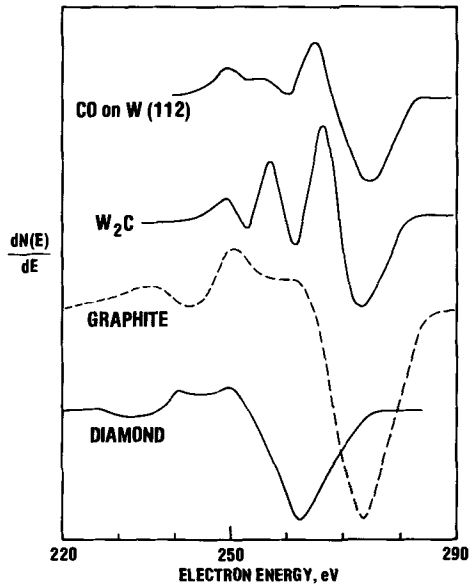


FIG. 1—*Spectra of the carbon KLL Auger transitions for carbon monoxide (CO) on tungsten (112), tungsten carbide ($W_2C$), graphite, and diamond (after Haas et al* [6]).

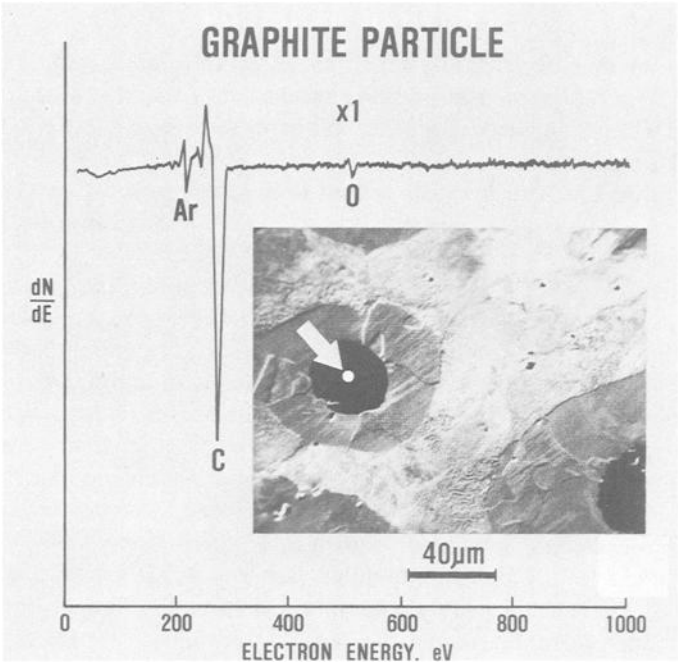


FIG. 2—*Auger spectrum from the graphite nodule. Spectrum was obtained after sputter cleaning the polished surface with argon ions.*

addition to obtaining the point spectra from selected regions of the surface, modern instruments also permit selected element Auger imaging. Figure 4 shows the Auger elemental images of carbon and iron from the polished cast iron surface discussed in Fig. 3. Auger imaging of this nature at the fracture surfaces provides information on uniformity of grain boundary segregation and on occurrence of second phases.

Depth distribution of elements is accomplished by Auger analysis in conjunction with ion sputtering. Presently available multiplexing units permit simultanoous display of approximate atomic concentrations as a function of deptn. The example in Fig. 5 shows that iron oxides rather than chromium oxides form on the surface upon oxidizing a Type 304 stainless steel at 500°C in air, an observation contrary to the common expectation of chromium oxide formation. Combining the ion sputtering techniques with the capability of Auger imaging amounts to what may be closest to a three-dimensional analysis in practical materials.

## Material Failure Studies

Changes in interface chemistry often can explain material failure problems associated with interfaces. The properties that are quite often in-

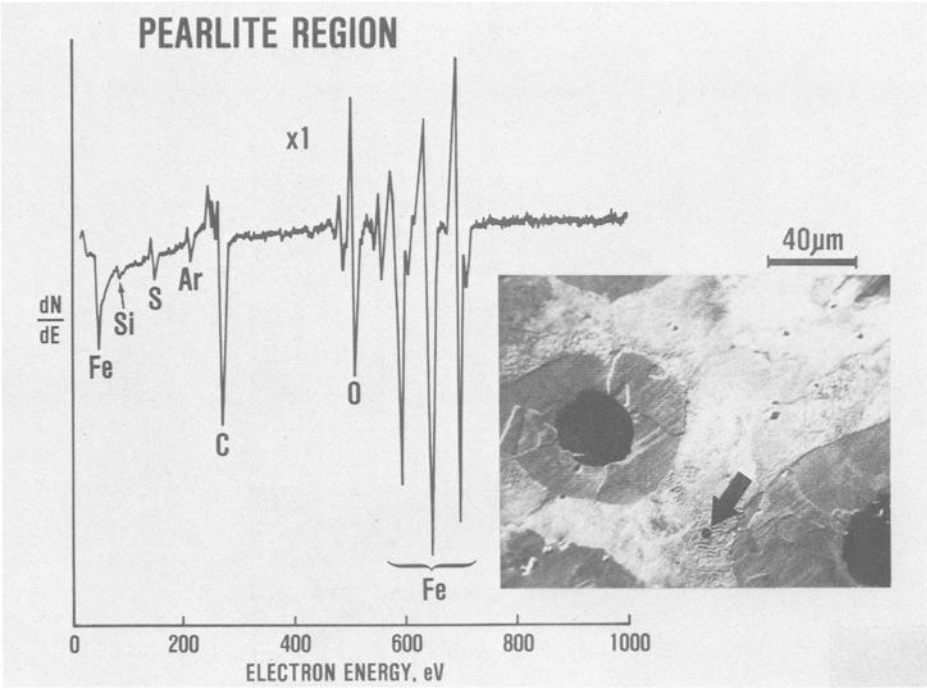


FIG. 3—*Auger spectrum from the pearlite region.*

fluenced are corrosion, stress corrosion cracking, hydrogen embrittlement behavior, and mechanical properties that encompass low and high temperature embrittlement and fatigue. AES studies have made it possible to correlate chemistry to material failure and properties, and some are discussed in the following paragraphs.

### *Low Temperature Embrittlement*

Low temperature embrittlement is a widely investigated phenomenon. One particular case of extensive investigation has been the failure in tempered steels. The problem commonly known as temper embrittlement occurs in alloy steels when tempered in the range of 350 to 525°C or slowly cooled through this range of temperature and is characterized by a drastic increase in the ductile to brittle transition temperature. The embrittlement is reversible and completely eliminated when the steel is heated to about 600°C for a few minutes. Auger examination [*7-11*] of freshly fractured surfaces of temper embrittled steels has shown the presence of elements such as phosphorus, tin, and antimony which have long been suspected. Figure 6 shows the Auger spectrum obtained from an antimony doped (bulk concentration 280 ppm) experimental 3340 steel, showing grain boundary en-

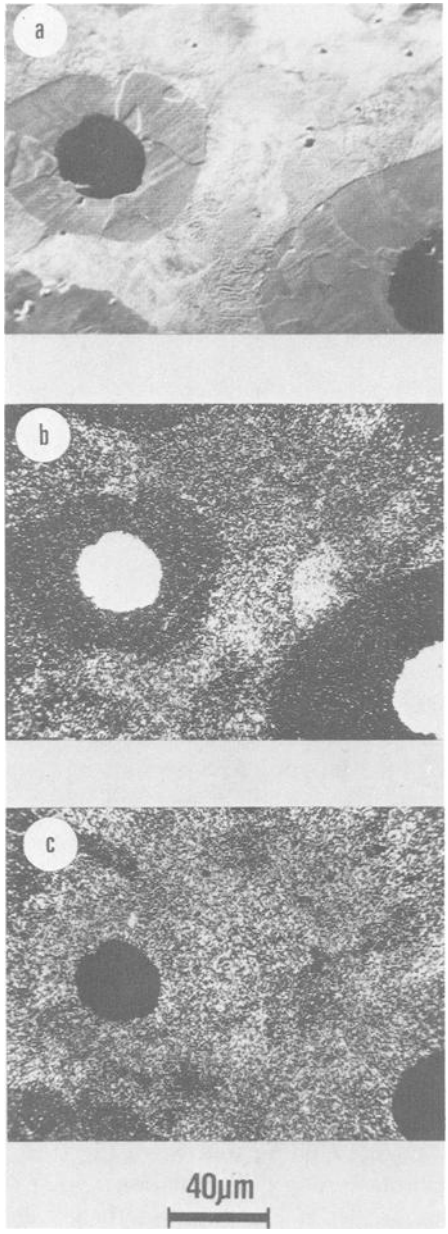


FIG. 4—(a) *Secondary electron,* (b) *carbon Auger, and* (c) *iron Auger images of the polished cast iron surface.*

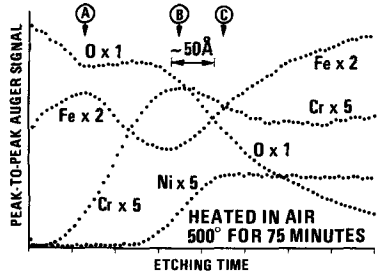


FIG. 5—*Depth-composition profile for Type 304 stainless steel showing the* (A) *iron oxide,* (B) *chromium rich oxide, and* (C) *oxide/steel interface regions.*

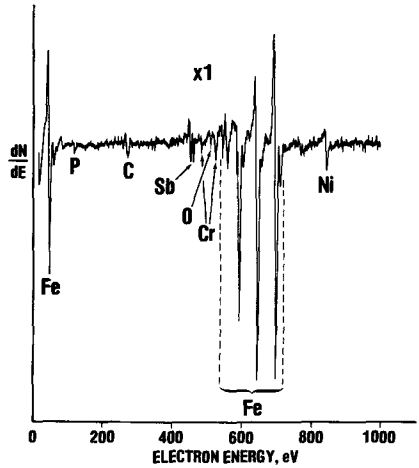


FIG. 6—*Auger spectrum obtained from the intergranular fracture surface of a 3340 steel.*

richment of not only antimony (~4 atomic percent) but also chromium, nickel, and carbon. The carbon peak shape clearly suggests its occurrence in the form of a carbide. Detailed studies [*7*] of this alloy system (Fig. 7) also showed that the shift in the transition temperature could be directly correlated to the antimony segregation. The results (Fig. 8) also demonstrate clearly that grain boundary segregation of antimony, nickel, and chromium is increased with increasing bulk antimony concentration suggesting that metalloid-metal (for example, antimony-nickel) interactions predominate leading to segregation. The extent of segregation at the boundary of the metalloid impurities has been studied in conjunction with ion sputtering. Figure 9 shows the summary of such studies [*11*] in many ferrous systems. In all these cases, metalloid segregation occurred in a very narrow region of less than 5 Å at the grain boundary. While these observations are consistent with the equilibrium models of segregation, presence of a nickel en-

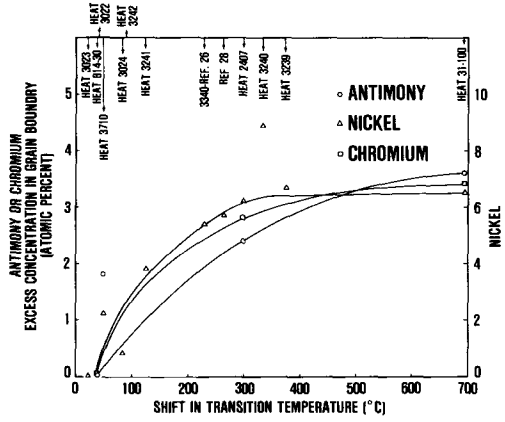


FIG. 7—*Shift in transition temperature related to segregation in alloy steels (after Joshi and Stein* [7]).

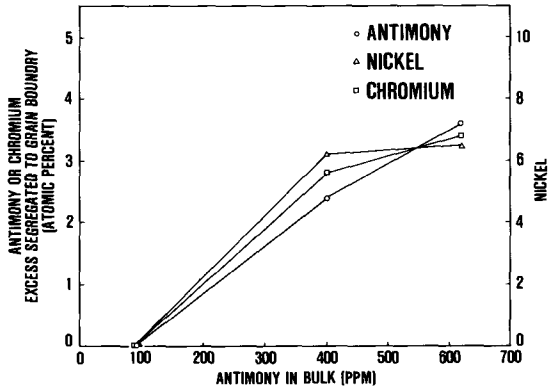


FIG. 8—*Segregation of nickel, chromium, and antimony to grain boundaries in nickel-chromium-carbon steels versus antimony bulk concentration (after Joshi and Stein* [7]).

riched region to greater depths near the boundary suggests predominance of nonequilibrium forces in segregation of this element. Other studies have also shown that elements such as sulfur [*12*], tellurium [*13*], manganese [*14*], and silicon [*14*] segregate to grain boundaries and thereby influence the low temperature mechanical behavior. Precipitation of titanium carbides and segregation of boron in maraging steels [*15*] also is shown to enhance intergranular embrittlement.

Low temperature embrittlement and failures have been investigated in many nonferrous systems. AES studies clearly correlated deterioration in mechanical properties due to segregation of bismuth [*16*] and sulfur in copper, phosphorus [*17*] in tungsten and sulfur [*18*] in nickel alloys.

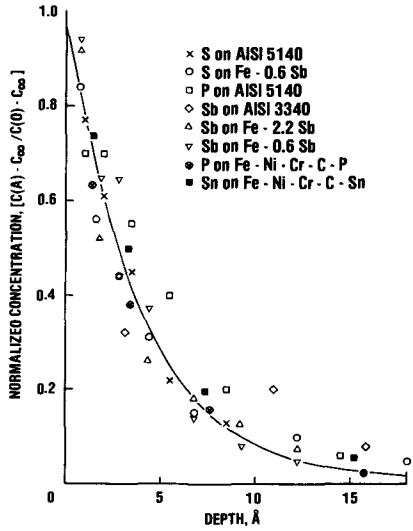


FIG. 9—*Normalized concentration of segregated solute on fracture surface versus average amount removed by ion sputtering (after Marcus et al* [11]).

Many of these studies were performed on specimens that failed primarily in the intergranular mode upon fracture. The development of the scanning Auger instruments makes it possible now to examine specimens that only partially fail in the intergranular mode. Since the scanning Auger microprobe (SAM) systems [*19*] combine scanning electron fractography with Auger analysis, the areas of interest can be selected and complete analysis performed from the selected intergranular portions. Auger elemental imaging is also extremely helpful in doing the analysis. Figure 10 shows the results of a study performed on a 2.25Cr-1Mo commercial plate steel that failed primarily by cleavage. Prior to the fracture within the vacuum system, the specimen received a 955°C (1750°F) austenitization followed by a quench, a 6 h 695°C (1280°F) plus 10 h 665°C (1225°F) temper, and a 10 000 h 480°C (900°F) embrittlement. The elemental imaging clearly shows enrichment of phosphorus, molybdenum, carbon, and chromium in the intergranular portions of the fracture surface. Spectra obtained from the cleavage and in the high phosphorus regions (Fig. 11) clearly show the differences between the bulk and grain boundary chemistry. The data also strongly support the hypothesis that phosphorus segregation occurring at the molybdenum and chromium carbide rich phases present at the prior austenite grain boundaries causes intergranular weakness.

Embrittlement of weld metals and the heat affected zones (HAZ) of the weld have been investigated in few alloy systems. The grain boundary fractures that occur at the welds and HAZs appear to be some form of impurity induced embrittlement. Figure 12 shows an example of a 2.25Cr-1Mo

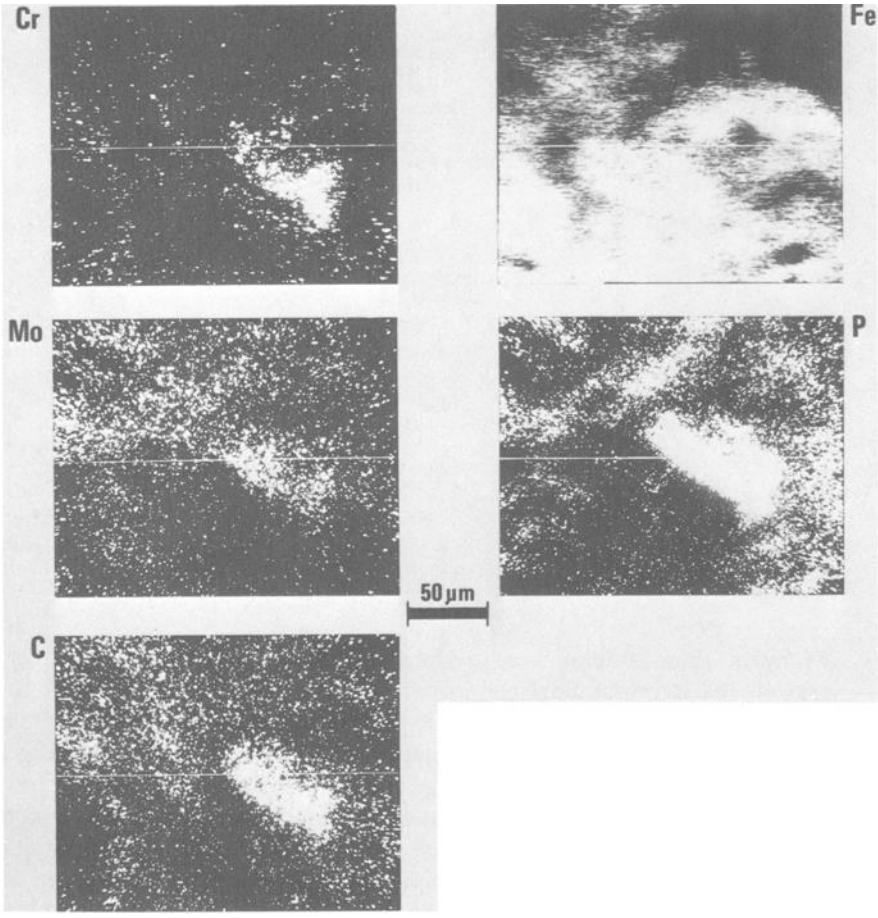


FIG. 10—*Auger elemental images of chromium, molybdenum, carbon, and phosphorus obtained from the fracture surface of an embrittled 2.25Cr-1Mo steel.*

submerged arc weld metal failed along grain boundaries and characterized by phosphorus and tin enrichment to the interfaces which are also rich in chromium and molybdenum carbides. Small amounts of tin and nitrogen also were detected.

Impurity elements segregated at the grain boundaries can further enhance embrittlement in presence of hydrogen. The metalloid impurities are believed to be acting as hydrogen recombination poisons thereby keeping hydrogen in an atomic state and accelerating its diffusion along the grain boundaries, where the metalloid elements are segregated. The experiments performed on nickel [*20*] suggest that tin and antimony act as such recombination poisons. These and other studies suggest that impurity elements

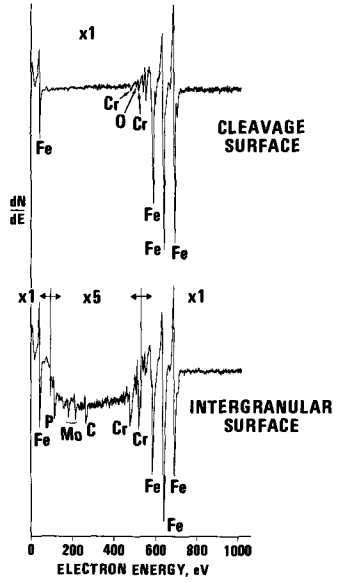


FIG. 11—*Auger spectra from cleavage and intergranular fracture surfaces of 2.25Cr-1Mo steel.*

may play an important role in several other incidences where hydrogen alone was believed to be the cause for intergranular failures.

The information presented here suggests that impurity elements were detected in all events of intergranular embrittlement. The only exceptions noted were in quenched steels [*7,21*] where there might only be small or undetected segregation or that the fracture may be influenced strongly by the internal stresses resulting from the quench.

### *High Temperature Embrittlement*

High temperature embrittlement is complicated by the fact that diffusion of alloying elements and impurities could occur under high temperature and stress conditions. Studies performed on Type 304 stainless steels [*22*] clearly indicated that high temperature and stress accentuate segregation of impurity elements such as sulfur and phosphorus to grain boundaries. Direct evidence for the grain boundary segregation of sulfur, bismuth, tellurium, and lead has been shown by Auger spectroscopy in super alloys that were stressed at elevated temperatures [*23*].

### *Interphase Embrittlement*

Many materials, whether conventional alloy systems or composite ma-

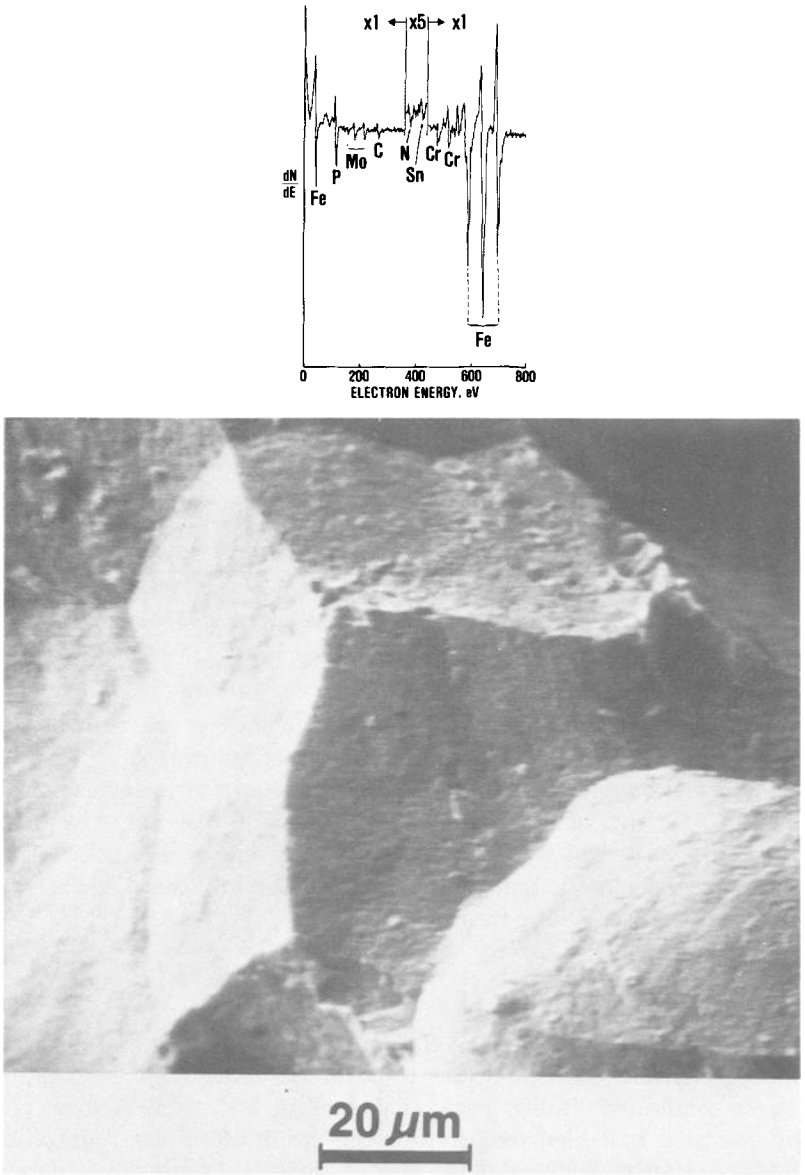


FIG. 12—*Fracture surface and Auger spectrum from it depicting grain boundary composition of 2.25Cr-1Mo submerged arc weld metal.*

terials, can fail along phase boundaries. Analysis of such interfaces by Auger spectroscopy is no different from examining the grain boundaries. Figure 13 shows the fracture obtained within the vacuum system of an aluminum/carbon composite material. The decohesion of the matrix and

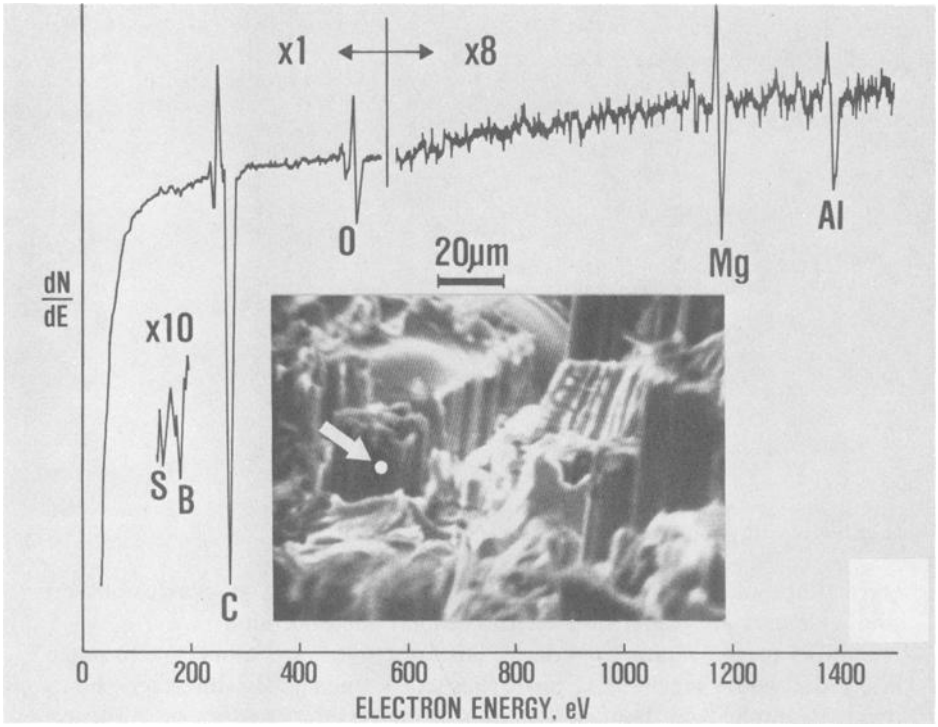


FIG. 13—*Auger spectrum showing the interface chemistry of the aluminum/carbon fiber composite material.*

carbon fibers was studied by AES analysis of the freshly opened interface. The Auger spectrum in Fig. 13 clearly indicates the enrichment of magnesium and oxygen at this interface. The magnesium Auger fine structure (plasmon loss peaks), characteristic of its chemical environment, is suggestive of existence of magnesium oxide at this interface. The magnesium-oxide layer was believed to be the reason for poor adhesion between the carbon fiber and the aluminum matrix. An examination of the process variables suggested that segregation of magnesium occurs from the aluminum during processing.

Embrittlement in powder metallurgical materials can be even more complex as it can be influenced strongly by the surface chemistry of starting materials and powder preparation techniques as well as the processing variables. The example of a careful study [*24*] performed on powder metallurgy compacts showed that several elements such as sulfur, oxygen, chlorine, and carbon predominate at the original particle interfaces. The study also indicated that oxygen and not sulfur or chlorine or carbon has the damaging effects on the strength properties or density of the compacts examined. Figure 14 shows such a correlation and clearly indicates that

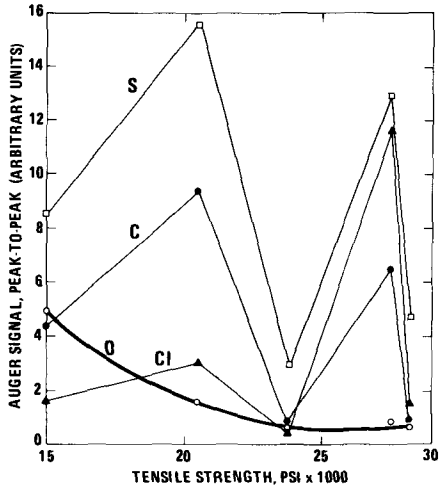


FIG. 14—*Variation of sulfur, chlorine, and carbon at the fracture surface of powder metallurgy iron versus tensile strength (after Joshi et al* [24]).

correlations of this sort are important before arriving at conclusions on what elements are responsible for the property deterioration.

Similar to the phase boundaries just discussed are other macroscopic interfaces whose mechanical properties are influenced by interface chemistry. Examples are bonded (thermal compression, solder, or diffusion bonded) interfaces, platings, and other thick and thin coatings. In several of these cases, AES studies have shown that interface chemistry plays an important role on adhesion at surfaces. A brief review on adhesion studies may be found in Ref *1*.

### *Intergranular Corrosion and Stress Corrosion Cracking*

Second phase precipitation and solute segregation at grain boundaries can significantly change the intergranular corrosion, stress corrosion cracking (SCC), and liquid metal penetration properties of the material. Some of the early work done on understanding the intergranular corrosion properties of stainless steels and recent studies on intergranular SCC properties will be discussed in the following paragraphs.

Intergranular corrosion of Type 304 (austenitic) stainless steels sensitized in the 450 to 900°C (842 to 1652°F) range has been attributed widely to the chromium depletion resulting from formation of grain boundary carbides. Several corrosive environments, generally highly oxidizing in nature such as nitric acid ($HNO_3$) solutions, are found in which intergranular corrosion of stainless steels occurs in solution treated condition with no detectable carbides at grain boundaries. Solute segregation at grain boundaries that was undetected by the transmission electron microscopy and other

techniques was believed to be responsible for corrosion in these solutions. In a careful study [*25*] the corrosion susceptibilities of Type 304 stainless steel in Strauss and Huey solutions as a function of heat treatment were conducted and related to the grain boundary compositions obtained by Auger spectroscopy. The results shown in Table 1 clearly suggest that sulfur segregating in nonsensitized stainless steels permits intergranular attack in nitric-dichromate ($HNO_3$-$K_2Cr_2O_7$) solutions while chromium depletion and not sulfur segregation is responsible for corrosion in sulfuric acid-copper sulfate ($H_2SO_4$-$CuSO_4$) solutions. The evidence for chromium depletion also was obtained in this study and is shown in Fig. 15. The results obtained from other examined steels also suggest that nitrogen, phosphorus, and silicon may play a role in deteriorating the corrosion properties in nitric-dichromate solutions.

Stress corrosion behaviors in which the cracking occurs along grain boundaries have been correlated with grain boundary chemistry obtained by AES analysis of *in-situ* fracture surfaces. Sulfide stress cracking (SCC) of commercial high strength steels [*26*] and 7075 aluminum alloys [*27*] to be discussed here are particularly interesting since hydrogen is believed to be the predominant factor in determining the cracking behavior in these materials. The SSC study correlated the boundary chemistry of selected high strength steels with the minimum stress at failure in hydrogen-sulfide solutions at room temperature. The studies indicate that either phosphorus present at grain boundaries or sulfur and manganese, precipitated in a thin film of (iron, manganese) sulfur, degrade the SSC properties of these materials. Correlation of average grain boundary sulfur concentration to the minimum stress at failure is shown in Fig. 16 and demonstrates the role of sulfur in SSC.

The stress corrosion experiments [*27*] on 7075 aluminum alloy were conducted in 3.5 percent neutral sodium-chloride solutions. The specimens for the tests were prepared by solution treating at various high temperatures for 1 h, water quenched, and aged for 24 h at 120°C (250°F). Auger data from the fracture surfaces were obtained within a vacuum system on specimens that were similarly treated. The effect of heat treatment on the relative amounts of magnesium, zinc, copper, silicon, and iron in the grain boundaries was of most significance. In otherwise similarly treated alloys, solute enrichment was found to increase with the solution treatment temperature and could be correlated extremely well with the stress corrosion crack plateau velocities. This result, as in the SSC studies just discussed, clearly suggests that there may be other important variables besides hydrogen to account for the observed properties. Solute or impurity segregation is one such variable shown to play an important role in hydrogen-assisted cracking behavior. Auger spectroscopy, by providing direct analysis of grain boundary composition, allows this variable to be related to the corrosion and SCC properties of materials.

TABLE 1—*Auger spectroscopic analysis of Type 304 stainless steel fracture surfaces.*

| Treatment | C/Fe | Si/Fe | S/Fe | Cr/Fe | Ni/Fe | Corrosion Rate, mg/cm$^2$ h | |
|---|---|---|---|---|---|---|---|
| | | | | | | Boiling Nitric-Dichromate[a] Solution | Modified Strauss Test[b] |
| 2 h, 1050°C, WQ[c] | 0.0128 | ND[d] | 1.230 | 0.664 | 0.102 | 2.25 | negligible |
| 2 h, 1050°C, WQ + 2 h, 850°C, WQ | 0.177 | 0.066 | 0.588 | 0.515 | 0.111 | 0.84 | 0.016 |
| 2 h, 1050°C, WQ + 2 h, 650°C, WQ | 0.011 | 0.111 | 0.920 | 0.525 | 0.109 | 2.93 | negligible |
| 2 h, 1050°C, WQ + 2 h, 600°C, WQ | 0.0645 | ND | 0.881 | 0.548 | 0.103 | 2.64 | negligible |
| 2 h, 1050°C, WQ + 3 days, 650°C, WQ | 0.283 | ND | 0.850 | 0.459 | 0.119 | 0.87 | 0.447 |

[a] Weight loss rate determined at the end of 14-h corrosion test in nitric-dichromate solutions.
[b] Weight loss rate determined from a 60-h corrosion test.
[c] WQ = water quenched.
[d] ND = none detected.

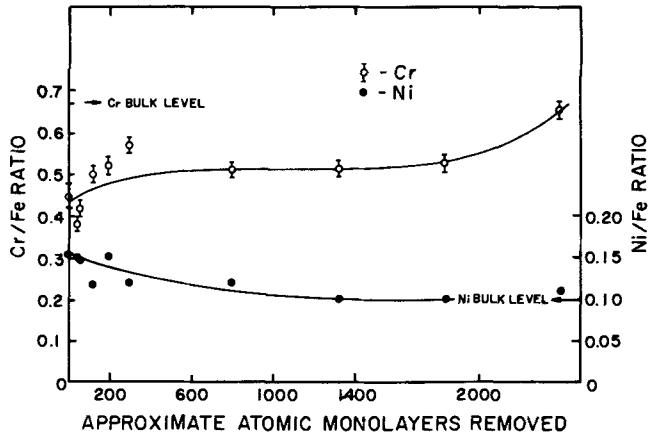


FIG. 15—*Concentration profiles of chromium and nickel as a function of distance from fracture surface of a Type 304 stainless steel sensitized by heating at 600°C for 2 h (after Joshi and Stein* [25]).

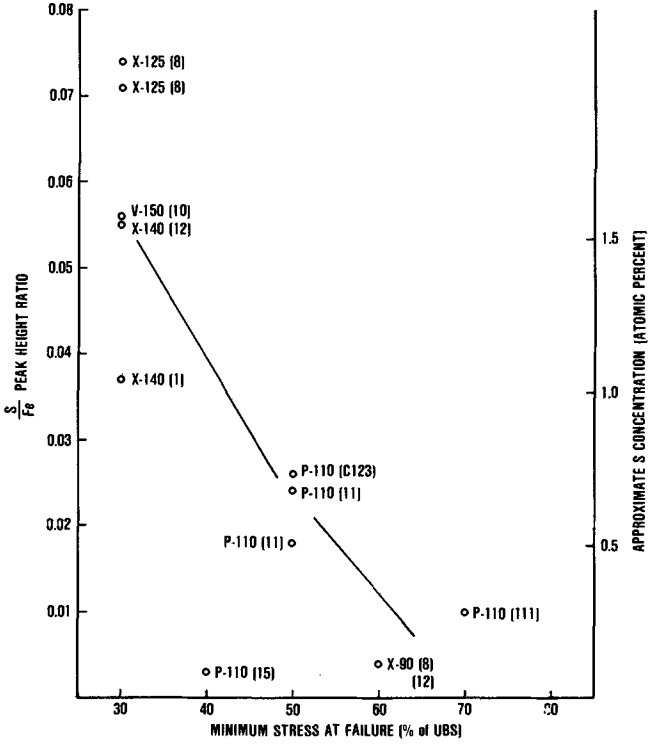


FIG. 16—*Sulfur content of the predominantly intergranular fracture surface as a function of minimum stress at failure in hydrogen sulfide solutions* [26].

While these studies are attempts to relate fracture surface composition to corrosion and stress corrosion properties, there also have been attempts involving direct examination of SCC failed specimens as well as *in-situ* SCC experiments inside the Auger system, with some success. The analyses in most practical cases are hampered by the massive corrosion products or films that form on the surfaces that need to be analyzed.

## Summary

Recent advances in the technique of Auger electron spectroscopy have made it possible to evaluate the role of interface chemistry in failure of materials. In many of the systems studied, impurity or solute segregation occurring in a narrow region at grain boundaries has been found to deteriorate the mechanical properties at room and elevated temperatures as well as the corrosion and stress corrosion properties. The segregants either decrease the fracture surface energy of the material or lower the plastic strain energy associated with fracture or both, thereby weakening the interfaces. The studies also have shown that solute-hydrogen interactions predominate in some alloy systems thereby possibly accelerating the penetration of hydrogen along grain boundaries and finally resulting in hydrogen assisted cracking.

## *Acknowledgments*

The author expresses his sincere appreciation to C. T. Hovland for obtaining several spectra and electron micrographs presented in the article and to G. E. Riach and L. E. Davis for critically reviewing the manuscript.

## References

[1] Joshi, A., Davis, L. E., and Palmberg, P. W. in *Methods of Surface Analysis*, Elsevier, New York, 1975, p. 159.
[2] Weber, R. E. and Johnson, A. L., *Journal of Applied Physics*, Vol. 10, 1969, p. 314.
[3] Davis, L. E., MacDonald, N. C., Palmberg, P. W., Riach, G. E., and Weber, R. E., *Handbook of Auger Electron Spectroscopy*, 2nd ed., Physical Electronics Industries, Eden Prairie, 1976.
[4] Davis, L. E. and Joshi, A. in *Surface Analysis Techniques for Metallurgical Applications, ASTM STP 596*, American Society for Testing and Materials, 1976, p. 52.
[5] Joshi, A. and Davis, L. E., unpublished research.
[6] Haas, T. W., Grant, J. T., and Dooley, G. J. in *Adsorption-Desorption Phenomena*, Academic Press, New York, 1972, p. 359.
[7] Joshi, A. and Stein, D. F. in *Temper Embrittlement of Alloy Steels, ASTM STP 499*, American Society for Testing and Materials, 1972, p. 59.
[8] Stein, D. F., Joshi, A., and LaForce, R. P., *Metallurgical Transactions Quarterly*, Vol. 62, 1969, p. 776.
[9] Marcus, H. L. and Palmberg, P. W., *Transactions*, American Institute of Mining, Metallurgical and Petroleum Engineers, Vol. 245, 1969, p. 1164.

[10] Viswanathan, R., *Metallurgical Transactions*, Vol. 2, 1971, p. 809.
[11] Marcus, H. L., Hackett, L. H., and Palmberg, P. W. in *Temper Embrittlement of Alloy Steels, ASTM STP 499,* American Society for Testing and Materials, 1972, p. 90.
[12] Ramasubramanian, P. V. and Stein, D. F., *Metallurgical Transactions,* Vol. 3, 1972, p. 2939.
[13] Rellick, J. R., McMahon, C. J., Jr., Marcus, H. L., and Palmberg, P. W., *Metallurgical Transactions,* Vol. 2, 1971, p. 1492.
[14] Joshi, A., Stein, D. F., and Palmberg, P. W., *Metallurgical Transactions,* Vol. 6A, 1975, p. 2160.
[15] Johnson, W. C. and Stein, D. F., *Metallurgical Transactions,* Vol. 5, 1974, p. 549.
[16] Joshi, A. and Stein, D. F., *Journal of the Institute for Metals,* Vol. 99, 1971, p. 178.
[17] Joshi, A. and Stein, D. F., *Metallurgical Transactions,* Vol. 1, 1970, p. 2543.
[18] Johnson, W. C., Doherty, J. E., Kear, B. H., and Gramei, A. F., *Scripta Metallurgia,* Vol. 8, 1974, p. 971.
[19] MacDonald, N. C., Riach, G. E., and Gerlach, R. L., *Research and Development,* Vol. 27, 1976, p. 42.
[20] Latanision, R. M. and Opperhauser, H., *Metallurgical Transactions,* Vol. 5, 1974, p. 483.
[21] Schulz, B. J. and McMahon, C. J., Jr. in *Temper Embrittlement of Alloy Steels, ASTM STP 499,* American Society for Testing and Materials, 1972, p. 104.
[22] Joshi, A. and Gurinsky, D. H., presented at the 6th Annual Spring Meeting of the American Institute of Mining, Metallurgical, and Petroleum Engineers, Pittsburgh, 22 May 1974.
[23] Walsh, J. M. and Anderson, N. P. in *Surface Analysis Techniques for Metallurgical Applications, ASTM STP 596,* American Society for Testing and Materials, 1976, p. 58; *Superalloys: Metallurgy and Manufacture,* Proceedings of the Third International Symposium, 12-15 Sept. 1976, Seven Springs, Pa., Claitors, Baton Rouge, 1976.
[24] Joshi, A., Wildermuth, J., and Stein, D. F., *International Journal of Powder Metallurgy,* Vol. 11, 1975, p. 137.
[25] Joshi, A. and Stein, D. F., *Corrosion,* Vol. 28, 1972, p. 321.
[26] Joshi, A., presented at Corrosion/77 Conference, 14-18 March 1977, San Francisco, Calif.
[27] Joshi, A., Shastry, C. R., and Levy, M., unpublished research.

# Stress and Nonmetals

*M. C. Coleman*[1]

# Examination of Fracture in a Pressure Vessel under Creep Conditions

**REFERENCE:** Coleman, M.C., **"Examination of Fracture in a Pressure Vessel under Creep Conditions,"** *Fractography in Failure Analysis, ASTM STP 645,* B. M. Strauss and W. H. Cullen, Jr., Eds., American Society for Testing and Materials, 1978, pp. 297-311.

**ABSTRACT:** The relevance of creep crack growth data obtained from uniaxial laboratory experiments to the assessment of defects in plants is being investigated in a pressure vessel research program involving full size half-percent chromium-molybdenum-vanadium components containing machined defects. The first vessel in this program contained external circumferential notches in a large pipe and was tested at 565°C and 62.5 $MN/m^2$ steam pressure, during which time crack growth and deformation in the vessel were monitored. Final failure occurred in an explosive manner after 1583 h. This paper concentrates on the fractographic and metallographic aspects of the failure analysis.

Examination of the vessel revealed three fracture modes across the failed ligament. Intergranular creep fracture occurred immediately ahead of the machined notch, followed by 45-deg ductile shear involving extensive deformation and finally low ductility shear fracture causing fast failure. These observations are interpreted primarily in terms of the mechanisms involved, with some consideration given to the mechanics of the fracture. The intergranular creep fracture mode is considered typical of that associated with plant failures and the significance of this in defect assessment is mentioned. The transfer to ductile shear is discussed in terms of the formation of void sheets, and net section yielding is related to uniaxial tensile data. The change in mode to fast shear fracture, attributed to gross overloading, produced an explosive failure.

The main implication of the failure analysis is that defects in this material can be assessed using mechanics describing intergranular creep fracture. Even so, it is demonstrated that in a nominally ductile situation final failure can be rapid and catastrophic.

**KEY WORDS:** fractography, metallography, fractures (materials), pressure vessels, steels, elevated temperature, creep properties, voids, crack propagation, plastic deformation, shear properties

In recent years the increased application of nondestructive testing (NDT) techniques to steam generating plants in the Central Electricity Generating Board has revealed a high incidence of crack-like defects, particularly in welded components [*1*].[2] These defects are usually in the weld metal and

[1] Research officer, Central Electricity Generating Board, Research Department, Marchwood Engineering Laboratories, Marchwood, Southampton, Hampshire, SO4 4ZB, England.

[2] The italic numbers in brackets refer to the list of references appended to this paper.

heat affected zone (HAZ) and may arise from the welding process or, more usually, during heat treatment or early in the service life of the vessel. In plants operating at high temperatures, growth of these defects can occur by creep, and it is important to be able to assess the significance of any defects in terms of the integrity of the plant.

The assessment route generally used for chromium-molybdenum-vanadium (CrMoV) materials is based on correlations between creep crack growth rate and the linear elastic stress intensity factor [*2–4*]. However, since creep is a time dependent process, the linear elastic approach should not be strictly applicable and, indeed, a number of alternative models based on net section stress [*4*], crack opening displacement [*5*], and reference stress [*6*] have been suggested as being more appropriate to describe creep crack growth. In all cases, the mechanics of the models and the mechanisms of cracking to which they apply are based on observations made in relatively small uniaxial laboratory tests. It is important therefore to examine their validity in large components so they may be used with confidence to assess defects in full size plants.

Accordingly, a program has been initiated to study crack growth in pressure vessels under conditions directly relevant to steam generating plants, an essential part of the work being the metallurgical aspects of the mechanisms of failure. This paper considers the first experiment on a circumferentially notched pressure vessel fabricated in 1/2CrMoV material and deals specifically with the fractographic and metallographic analyses of crack growth and failure. The features observed are described in detail, and the mechanisms of fracture are related to certain aspects of the mechanics of crack growth, details of which are reported elsewhere [*7*].

## Experimental Procedure and Results

### *Pressure Vessel Design and Testing*

A relatively simple pressure vessel based on a main steam pipe containing external circumferentially machined notches was selected for the experiment. The pipe dimensions were 350-mm outside diameter, 60-mm wall; the defect orientation corresponded to the circumferential mode often observed in plant as weld HAZ cracking. It was necessary to give careful consideration to the shell and notch design [*7*] since the hoop stress would be greater than the axial stress and could lead to failure by an axial split rather than by crack propagation. The final vessel and notch dimensions are shown in Fig. 1; only the complete circumferential notches are considered here.

The vessel was constructed in 1/2CrMoV steel normalized at 970°C and tempered for 4 h at 690°C. The microstructure consisted of ferrite, with a grain size of 70 $\mu$m, containing alloy carbides, about 5 percent bainite and elongated silicate-type inclusions distributed in an axial direction along the

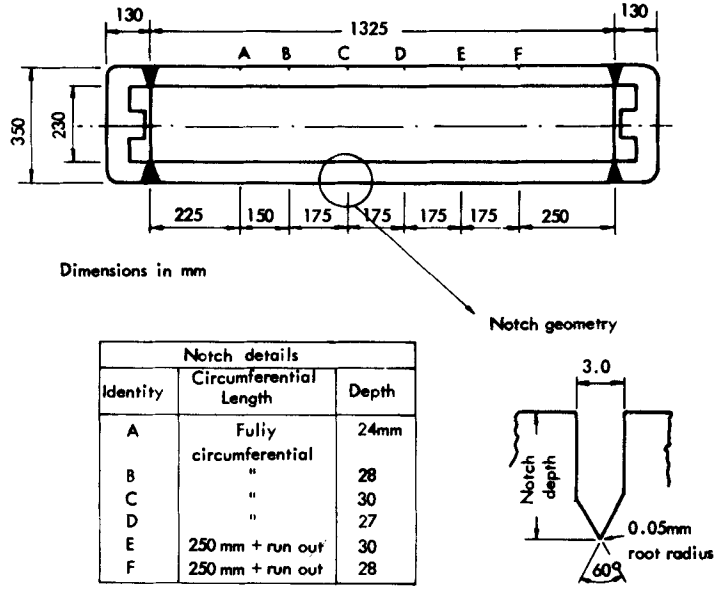


| Notch details | | |
|---|---|---|
| Identity | Circumferential Length | Depth |
| A | Fully circumferential | 24mm |
| B | " | 28 |
| C | " | 30 |
| D | " | 27 |
| E | 250 mm + run out | 30 |
| F | 250 mm + run out | 28 |

FIG. 1—*Details of the circumferentially notched pressure vessel.*

pipe, parallel to the original hot working direction. Testing took place in a purpose-built pressure vessel testing facility [*8*]. The vessel was positioned vertically in a bell furnace, in which the temperature was maintained at 565 ± 5°C, and was internally pressurized using steam at 62.5 MN/m$^2$. This produced a mean diameter hoop stress of 150 MN/m$^2$ and a maximum axial stress of 106 MN/m$^2$ on the ligament ahead of the 30 mm-deep notch. At this notch, crack growth was monitored continuously using the potential drop technique [*9*]. Activity in this region was also followed using an acoustic emission coincidence counting technique. In addition, capacitance strain gages were used to monitor displacement across the 28-mm-deep notch. The NDT inspections were carried out at ambient temperature to measure crack growth at the notches and, on these occasions, measurements also were made on the shell and notches across specific locations to determine the creep strains and displacements that occurred during each test period.

### *Observations During Pressure Testing*

At the first inspection, after 290 h, no crack growth was found at any of the notches. The first indication of growth came from the 30-mm notch after about 700 h when the potential drop and acoustic emission monitoring techniques recorded increased voltages and stress wave emissions, respectively. An inspection at 1192 h confirmed these indications and showed that

growth had started at all the notches. Crack growth data continued to be generated during the test and was substantiated by further NDT inspections at 1361 and 1577 h. The ultrasonic inspection also showed that crack growth was asymmetrical at the 30-mm notch and, although for much of the test there was less than 2-mm difference, at the final inspection the average minimum and maximum crack depths were 35 and 38 mm, respectively. This was also accompanied by an increase in the notch edge opening displacement on the side of maximum crack depth, indicating that bulging was taking place in the vessel as cracking extended from the root of the machined notch, as shown in Fig. 2. Failure finally occurred in an explosive manner after 1583 h with the vessel fracturing across the ligament ahead of the 30-mm notch.

*Failure Examination*

After failure, an extensive metallurgical examination was made on the fracture faces. A macroscopic examination was carried out to categorize the different modes of fracture, and the areas of each were determined using a quantitative television microscope (QTM). Several fractographic and metallographic specimens were taken from the fracture faces and were prepared for examination using conventional techniques. The microstruc-

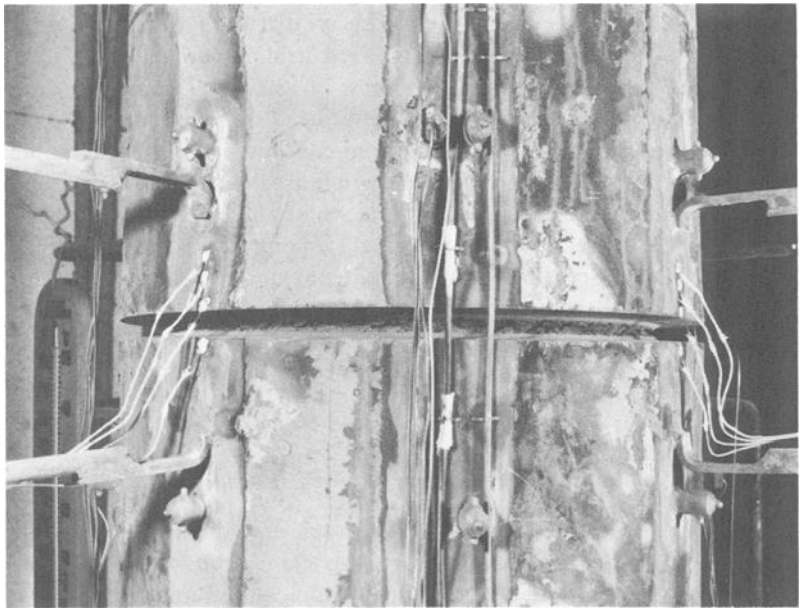

FIG. 2—*Bulging displacement and crack growth apparent at 30-mm-deep notch after 1361 h at 565°C and 62.5 MN/m$^2$ internal pressure.*

tural and topographical features of each mode were studied then in detail using optical and scanning electron microscopes (SEM).

In addition, specimens were taken from a number of positions around each of the other three fully circumferential notches for comparison with those from the fractured ligament. Other sections from the failed vessel were used to determine the values of strain in the bore regions ahead of each notch by using a surface roughness measuring instrument to determine the spacing of the markings on the machined surfaces. The variation in spacing of the machine markings even before testing was such that this technique was only capable of detecting strains in excess of 3 percent.

As can be seen in Fig. 1, the vessel also contained two-part circumferential notches. However, this portion was salvaged complete from the failure and was fabricated into a separate vessel which is currently under test.

### *Examination Results*

The general appearance of the fracture surface is shown in Fig. 3 and schematically, in Fig. 4. The numbers 1 to 8, which relate to the positions where strain measurements were made at inspections during the test, were used throughout the failure examination as reference positions.

Three distinct regions were apparent between the root of the 30-mm-deep notch and the bore of the vessel.

*Region I*—This was a region of oxidized crack growth, coplanar with the notch, extending in from the root, all around the circumference, and varying in depth from about 7 mm at Position 2 to 12 mm at Position 6 as shown in Fig. 4.

*Region II*—The fracture between Position 4 increasing to 8 inclined at a 45-deg angle and had a rough oxidized surface to within a few millimetres of the bore in most places. Between Positions 5 and 6 where bulging was a maximum, as indicated in Fig. 4, this type of fracture was continuous to the bore.

*Region III*—Over the remainder of the failed ligament, the fracture also followed a 45-deg angle but was smooth and less darkened by oxidation. This type of fracture was particularly noticeable between Positions 8 through 1 to 4, where the surface also contained striation type markings as can be seen between Positions 8 and 1 in Fig. 3.

From the distribution of the three fracture regions in Fig. 4, it can be seen that there is a rough line of symmetry about the diameter through Positions 2 to 6. From this representation, the proportion of each region was determined using a QTM. Region I, oxidized crack growth extending from the notch, represented 39 percent of the failed ligament, Region II, the rough 45-deg fracture, 17 percent, with Region III, the smooth 45-deg fracture, accounting for the remaining 44 percent. The symmetry of fracture

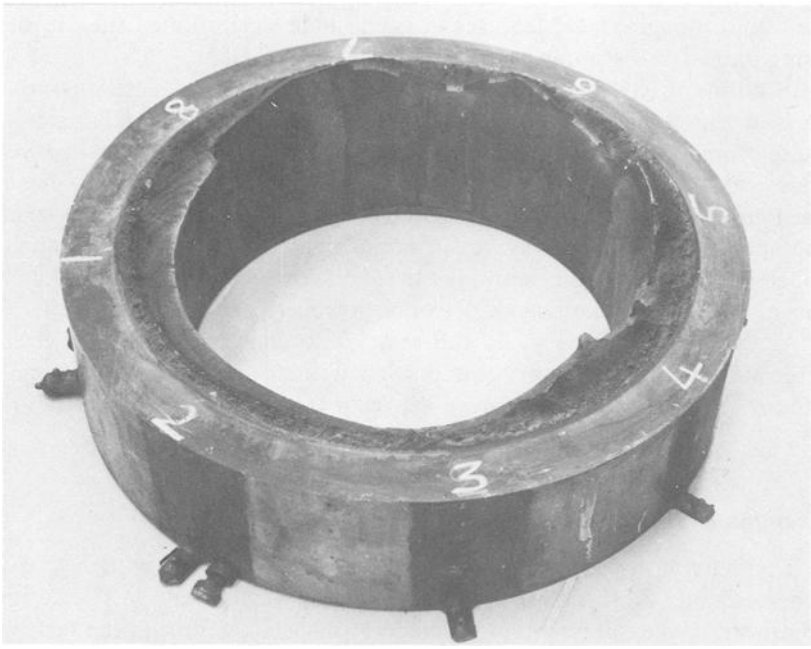


FIG. 3—*General appearance of the failed ligament surface.* ×*1/4.*

also was reflected in the symmetry of deformation observed at the bore of the vessel. Between Positions 4 and 8, the bore had a necked-down appearance, this effect being particularly marked between Positions 5 and 6, the region of maximum bulging. In contrast, immediately opposite this area and adjacent to Region III, bore deformation was not apparent.

### *Fractography and Metallography*

Fractographic examination of Region I confirmed that where bulging occurred, between Positions 4 and 8, the surface was covered completely with oxide up to where Region II started and showed that on the opposite side of the vessel the last millimetre or so before Region III was clear of oxide. In this area, grain boundary cavitation and intergranular cracking typical of creep fracture were observed, Fig. 5. Metallographic sections revealed cavities on grain boundaries linking to give short cracks and side branching of the main crack, as shown in Fig. 6. Between Positions 4 and 8, the creep crack reached a maximum depth of 12.5 mm and creep damage was confined to a strip 5 mm to either side of the main crack. Between Positions 8 through 1 to 4, the creep fracture extended generally to 7 mm, reaching 10 mm in one region, and the damaged material was confined to within 3 mm of the main crack.

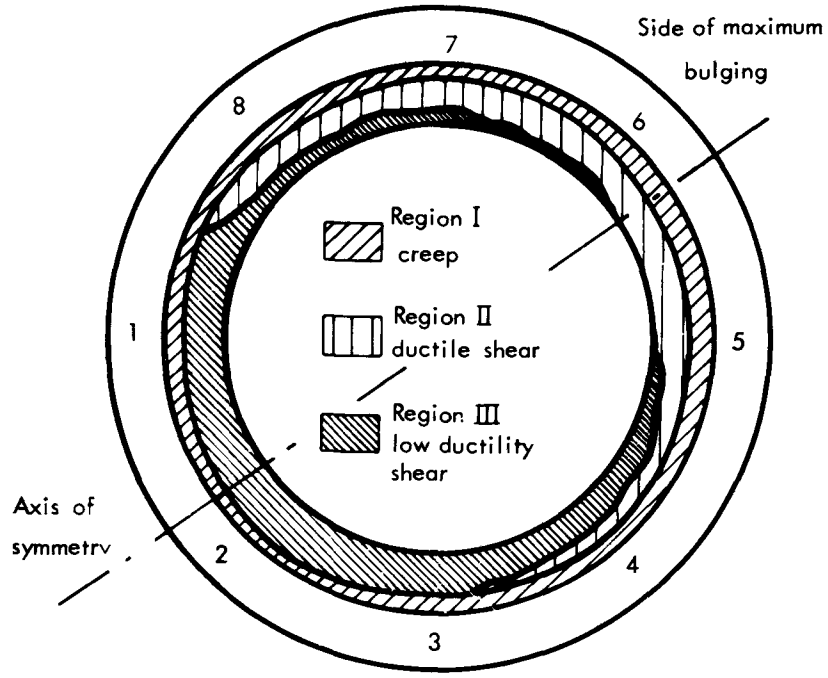


FIG. 4—*Schematic representation of the three regions of fracture across the failed ligament ahead of the 30-mm-deep notch.* ×*1/4.*

Regions II and III, both 45-deg fractures, exhibited considerable contrast in their fractographic and metallographic features. Region II, on the side of the vessel where bulging occurred, was a ductile shear fracture showing clear evidence of deformation with deep elongated dimples throughout the fracture surface. This is shown in Fig. 7 and is very similar to the appearance of a highly ductile high temperature tension test fracture surface. The microstructure in this area was heavily deformed, parallel to the longitudinal axis of the vessel, and it was apparent that crack propagation occurred in a ductile manner by necking down and linking between the many elongated voids, as shown in Fig. 8. At about Position 5, the ductile shear fracture extended fully to the bore and deformation was still apparent in the bore of the vessel some 30 mm below the fracture tip.

Region III, on the side of the vessel between Positions 8 through 1 to 4 where bulging was not apparent, was a remarkably featureless low ductility shear fracture, as shown in Fig. 9. The fracture surface in general was very flat and contained smooth areas free of detail as well as many shallow dimples that in most cases were less than 10 $\mu$m in diameter. The striations on the fracture surface appeared as simple steps, and no fractographic features were observed to account for this phenomenon. The metallographic

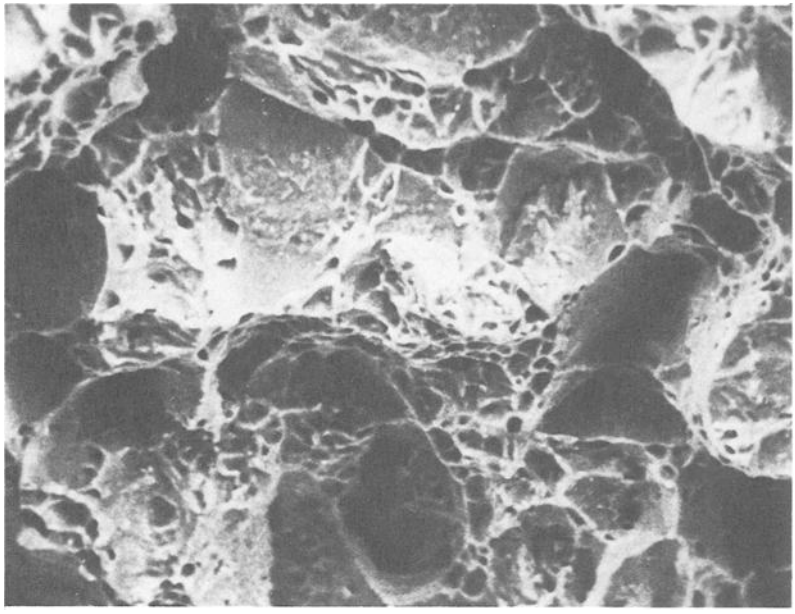

FIG. 5—*SEM showing the intergranular creep fracture region immediately ahead of the 30-mm-deep notch.* ×*300.*

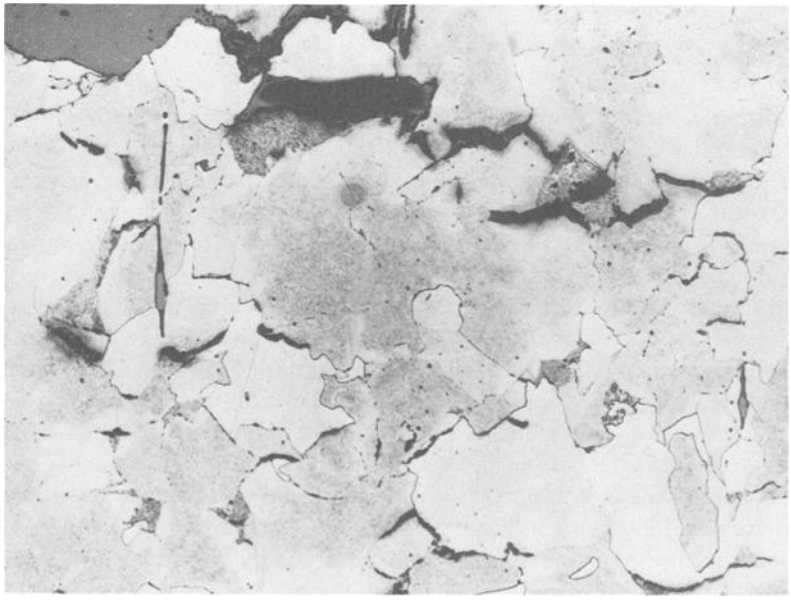

FIG. 6—*Optical micrograph showing the grain boundary cavitation and cracking associated with the intergranular creep fracture.* ×*200.*

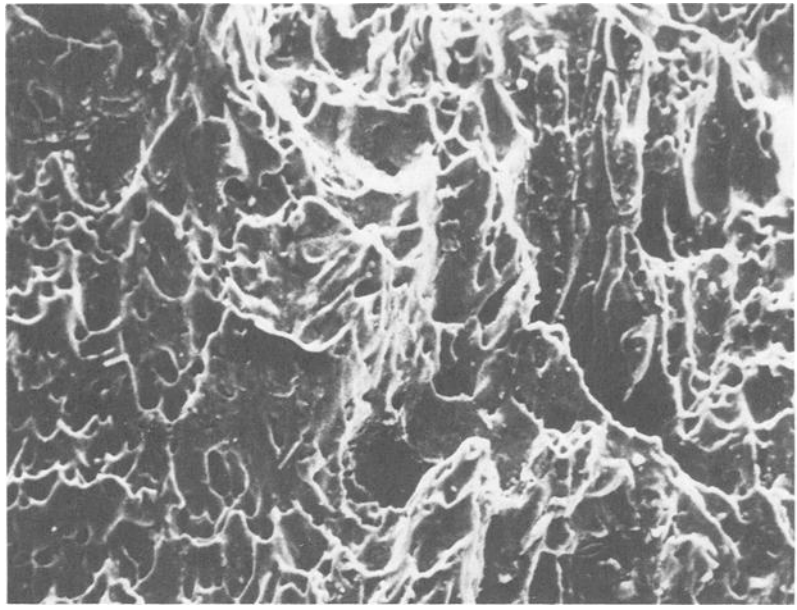

FIG. 7—*SEM showing the 45-deg ductile shear fracture surface.* ×*300.*

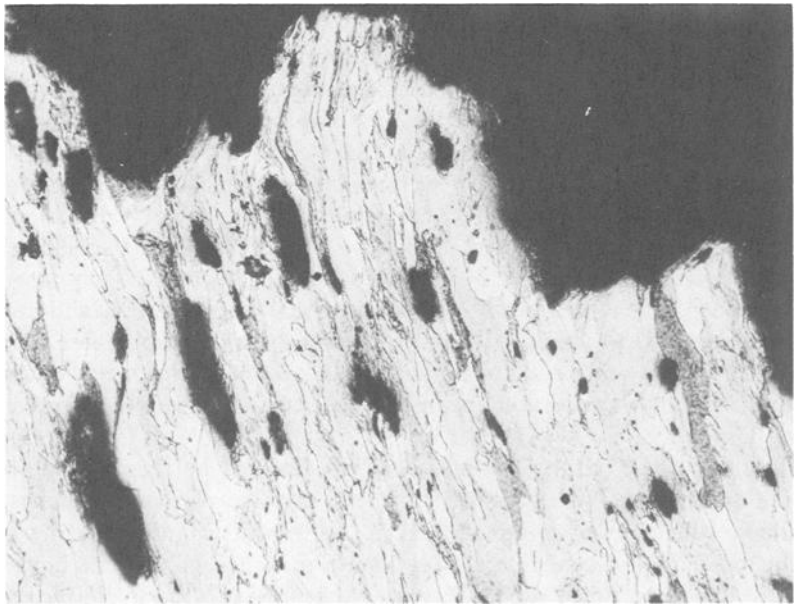

FIG. 8—*Optical micrograph showing the heavily deformed microstructure and voids associated with the 45-deg ductile shear fracture.* ×*200.*

FIG. 9—*SEM showing the smooth 45-deg low ductility shear fracture surface.* ×*300.*

examination revealed a limited amount of deformation immediately adjacent to the fracture surface and to a much lesser extent in a layer about 300 μm thick, where deformation appeared as slip bands across the ferrite grains, as shown in Fig. 10. Apart from this, the remainder of the material in the ligament appeared as in the as-received condition.

Metallographic examination of sections through the three circumferential notches that did not fracture completely revealed intergranular creep fracture similar to that shown in Fig. 6. The extent of the cracking increased from 2 mm for the 24-mm-deep notch to about 3.5 mm for the 28-mm-deep notch, and in all cases grain boundary cavitation and cracking was confined to within 3 mm of the crack path and tip. There was no evidence of any other mode of fracture and, outside the creep cracking regions, the parent material appeared to be unchanged from the as-received condition.

Finally, surface roughness measurements detected no strain in the bore of the vessel ahead of the three unfractured circumferential notches. A similar result also was obtained from measurements made up to the edge of the low ductility shear fracture, at about Position 2. In contrast however, on the side of the ductile shear fracture, at Position 5, the strain increased from 0 to 4 to 8 percent at distances of 75, 50, and 25 mm from the fracture tip, reaching 28 percent strain at the fracture edge.

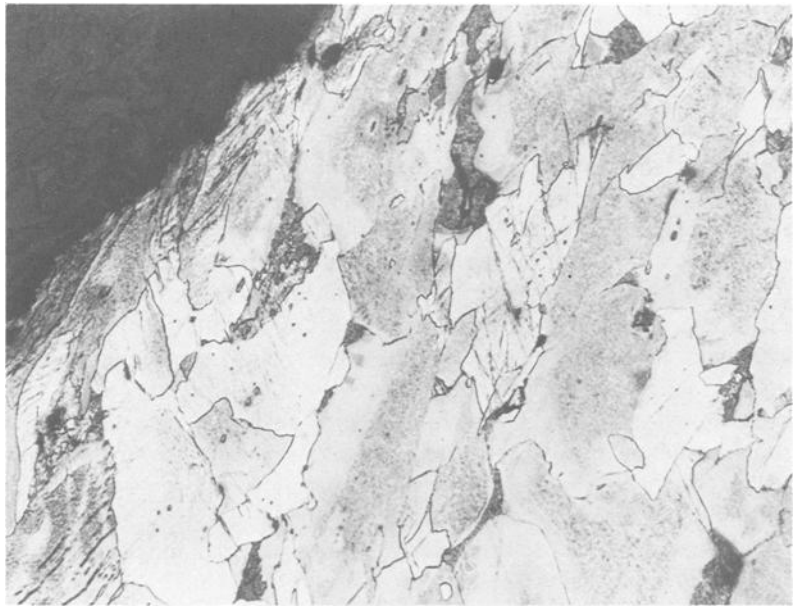

FIG. 10—*Optical micrograph showing the limited deformation closely associated with the 45-deg low ductility shear fracture.* ×*200.*

## Discussion

The fractographic and metallographic analyses of the failure revealed that Region I consisted of grain boundary cavitation and intergranular cracking. This was also the only mode observed ahead of the three notches that did not fail. This is typical of intergranular creep fracture and indicates that the pressure vessel experiment has produced the features generally associated with high temperature plant failures, albeit in a normalized and tempered material.

The extent of the damage associated with the creep fracture can be used to assess the stress conditions controlling the failure process. In an elastic situation the plastic zone radius at the root of a notch can be determined from the models of Irwin [*10*] and Dugdale [*11*]. For the 30-mm notch in the pressure vessel, these models predict a radius of approximately 2 mm, the exact value depending on the yield stress. Hence there will be a stress distribution ahead of the notch decaying from the yield stress, about 230 $MN/m^2$, at the edge of the plastic zone to the net section stress in the ligament, 106 $MN/m^2$. Consequently, creep damage would be expected to occur over at least a radius of 2 mm even if the controlling parameter was the crack tip stress alone. In the present work, the radius of creep damage

ranges from 5 mm at the 30-mm notch to about 3 mm at the other notches. This indicates that creep damage has occurred even outside the notch root plastic zone, as would be expected from the level of the stress distribution, but nevertheless is closely confined to this notch root region. Furthermore, it confirms that even though the pressure vessel was constructed in a ductile material crack growth and failure has not occurred simply by plastic collapse of the ligament.

The creep fracture extended to a depth between 37 and 42.5 mm from measurements at failure, while the NDT assessment at the inspection prior to failure indicated depths from 35 to 38 mm. Bearing in mind the accuracy of ultrasonic measurements, ± 2 mm, and the fact that some creep crack growth most probably occurred in the short test period immediately prior to failure these results are in good agreement. Consequently, the data generated throughout the life of the vessel, which have been reported separately to show a relationship between crack growth rate and reference stress [*7*], relate specifically to crack propagation occurring by intergranular creep.

The mode of fracture in Region II was ductile shear. In the reviews of the mechanisms of ductile or plastic fracture, based mainly on room temperature laboratory tests, Rosenfield [*12*] and Sullivan [*13*] show that the dominant factors are the formation of microvoids and the concentration of shear in sharply defined bands. In general, a uniaxial test gives a region of microvoid coalescence in the center of the specimen while a void-sheet mechanism [*14,15*] results in shear bands of deformation forming at the crack tip. Growth occurs initially in a direction macroscopically normal to the tensile axis, transferring to 45-deg shear as a free surface is approached. In a similar manner, it appears that in the present failure the latter stages of creep crack growth, although remaining normal to the axial stress in the vessel, occurred while shear deformation was taking place in the ligament ahead of the crack tip. This would account for the gross bulging observed on the vessel between Positions 4 and 8 towards the end of testing when intergranular creep cracking was still occurring. In addition, the heavy oxide layer observed at the limit of the creep fracture between Positions 4 and 8 may be attributed to easy ingress of the atmosphere resulting from shear deformation in the ligament displacing the cracked surfaces. Finally, the creep mode of fracture transferred to fully ductile shear. It is known that shear separation can be rapid [*16*], which is consistent with the earlier deduction that shear occurred late in the vessel life.

In terms of the mechanics involved, a model proposed by McClintock [*17*], based on uniaxial data, indicated that the transfer from homogenous flow, analogous to the creep fracture mode, to localized shear occurs simply when the loads for each mechanism are equal. The model however related largely to idealized situations where the size and distribution of microvoids are readily determined. In the present work, the size and distribution of microvoids is not regular but, nevertheless, all combinations have been

analyzed. The McClintock model predicts that even where creep fracture is observed, the load for shear fracture is always less than that for homogenous flow, and in many cases is negative. Clearly, therefore, it has not been possible to account for the transfer from creep to ductile shear fracture on the basis of this model.

The mechanics of the final stage of ductile shear, however, can be discussed quantitatively from the results of the present work. The QTM measurements show that at the end of ductile shear only 44 percent of the original ligament was remaining. At an internal pressure of 62.5 $MN/m^2$ and assuming uniform loading, the stress on the remaining ligament would be about 245 $MN/m^2$ which is some 5 percent greater than the mean 0.2 percent proof stress for the material [*18*]. In addition, the mean strain for failure in these materials is 30 percent at 565°C, and the maximum bore strain measurement of 28 percent clearly indicates that this region has necked down fully in a tensile fashion to fracture in a ductile shear mode.

As the experiment progressed, it was anticipated that a leak situation would finally arise due to the asymmetry of crack growth, but in fact a rapid explosive failure occurred by shear involving little deformation. However, it is apparent that the remaining ligament was stressed above the proof stress and the material would be in a condition for plastic collapse. In addition, if a leak occurred, and little evidence was found for this, the leak rate did not depressurize the vessel sufficiently to reduce the ligament stress below that for plastic collapse before the low ductility shear fracture had fully propagated. From previous work [*16*] it is clear that coalescence of microvoids in the void sheet can be catastrophic. Thus, the difference in the extent of deformation associated with the ductile shear in Region II and the low ductility shear in Region III is almost certainly a reflection of the high plastic strain rate in the latter which led to high velocity crack propagation around the remaining ligament and explosive failure.

In summary, failure of the pressure vessel occurred across the ligament ahead of the 30-mm-deep notch and involved three fracture mechanisms in sequence. Initially creep fracture occurred ahead of the notch tip with damage closely confined to the crack plane. This extended asymmetrically and, on the side where bulging was most apparent, reached a depth of 42.5 mm before transferring to ductile shear fracture. This mechanism produced gross deformation and ductile crack extension through to the bore on one side of the vessel. At this instant, the remaining ligament was subjected to a stress of yield magnitude, and the final failure occurred by rapid crack growth involving a low ductility shear fracture running around the ligament. It is clear from the striation markings on Region III and the axis of symmetry across the failure surface that the crack ran out in both directions from the position where ductile shear reached the bore and that the two accelerating crack fronts met at the opposite side of the vessel when total separation resulted.

## Concluding Remarks

The main implication of the failure analysis is that defects in normalized and tempered 1/2CrMoV material now can be assessed using mechanics known to describe the intergranular creep fracture mechanism. In addition, it is clear that even in ductile materials operating under nominally ductile conditions, rapid and catastrophic failure can occur. However, in operating plants, while intergranular creep fracture is the expected mode of crack propagation, neither the shear modes nor catastrophic failure are likely to occur. They have only arisen in this work because an extremely large defect of axisymmetric geometry was allowed to remain in a vessel subjected to nominally tensile loading.

Future work in this area is intended to examine the more usual plant problems of defect growth in weld metals and HAZs. In this respect, the present work is considered to provide a sound basis for future pressure vessel failure analyses.

### *Acknowledgments*

The author would like to thank his colleagues for their interest and valuable discussion of this work. The work was carried out at Marchwood Engineering Laboratories of the Central Electricity Generating Board and is published by permission of the Director.

## References

[*1*] Toft, L. H. and Yeldham, D. E., "Welding Research Related to Power Plant," Proceedings of an International Conference, Central Electricity Generating Board, London 1972, pp. 5–19.

[*2*] Siverns, M. J. and Price, A. T., *Nature*, Vol. 228, No. 5273, 1970, pp. 760–761.

[*3*] Siverns, M. J. and Price, A. T., *International Journal of Fracture Mechanics*, Vol. 9, No. 2, 1973, pp. 199–207.

[*4*] Neate, G. J. and Siverns, M. J., "Creep and Fatigue in Elevated Temperature Applications," Proceedings of an International Conference, Paper No. C234, Institution of Mechanical Engineers, London, 1973.

[*5*] Haigh, J. R., PhD thesis, Council for National Academic Awards, London, 1973.

[*6*] Williams, J. A. and Price, A.T., *Journal of Engineering Materials and Technology*, 1975, pp. 214–222.

[*7*] Coleman, M. C., Price, A. T., and Williams, J. A., *Fracture*, Vol. 2, 1977, pp. 649–662.

[*8*] Eaton, N. F. and Rowley, T., "Experimental Evaluation of Creep Behavior of Welded Vessels," International Institute of Welding Colloquium, Toronto, 1972.

[*9*] Coleman, M. C., Fidler, R., and Williams, J. A. in *Detection and Measurement of Cracks*, The Welding Institute, Cambridge, 1976, pp. 40–44.

[*10*] Irwin, G. R., *Metals Engineering Quarterly*, Vol. 3, 1963, p. 24.

[*11*] Dugdale, D. S., *Journal of the Mechanics and Physics of Solids*, Vol. 8, 1960, p. 100.

[*12*] Rosenfield, A. R., *Metallurgical Reviews*, Vol. 13, No. 121, 1968, pp. 29–48.

[*13*] Sullivan, C. P., "A Review of Some Microstructural Aspects of Fracture in Crystalline Materials," Bulletin No. 122, Welding Research Council, New York, 1967.

[*14*] Rogers, H. C., *Transactions*, Metallurgical Society of the American Institute of Mining, Metallurgical, and Petroleum Engineers, 1960, Vol. 218, pp. 498–506.

[15] Cox, T. B. and Low, J. R., *Metallurgical Transactions,* Vol. 5, 1974, pp. 1457-1470.
[16] Bluhm, J. I. and Morrissey, R. J., *Fracture*, Proceedings of the First International Conference, The Japanese Society for Strength and Fracture of Materials, Vol. 2, 1966, pp. 1739-1780.
[17] McClintock, F. A. in *Ductility,* American Society for Metals, Metals Park, Ohio, pp. 255-277.
[18] Johnson, R. F., May, M. J., Truman, R. J., and Mickleraith, J., "High-Temperature Properties of Steels," Proceedings of a Conference, ISI Publication No. 97, The Iron and Steel Institute, 1967, pp. 229-263.

*R. F. McCartney*[1] *and J. V. Pellegrino*[1]

# Strength, Toughness, and Flaw Tolerance of 25.4-mm (1-in.) Alloy Steel Lifting Chain*

**REFERENCE:** McCartney, R. F. and Pellegrino, J. V., **"Strength, Toughness, and Flaw Tolerance of 25.4-mm (1-in.) Alloy Steel Lifting Chain,"** *Fractography in Failure Analysis, ASTM STP 645,* B. M. Strauss and W. H. Cullen, Jr., Eds., American Society for Testing and Materials, 1978, pp. 312-334.

**ABSTRACT:** The interrelationship of strength, toughness, and flaw tolerance of 25.4-mm (1-in.) alloy steel lifting chain procured from five chain manufacturers has been investigated. Both International Standards Organization (ISO) Grade 63 and Grade 80 chains were tested. The susceptibility of these chains to sudden fracture in service in the presence of flaws is of interest to producers and users, and it was anticipated that the results would be helpful in arriving at a recommended upper limit of strength consistent with safety, inspection, and economic considerations.

Small round-bar tension-test and Charpy impact-test specimens were machined from each chain to characterize the materials. Fracture-mechanics calculations of critical flaw sizes then were conducted by using a Charpy-$K_{Ic}$ correlation. The results showed that the Grade 80 chain, having a Rockwell C hardness (HRC) of 40, is susceptible to brittle fracture in the presence of small flaws. Tension tests on specimens from chain samples containing machined flaws 2.54 mm (0.1 in.) deep confirmed the calculations. Grade 80 chain containing the machined flaw fractured at less than half the load required to break unnotched chain; however, Grade 63 chain, having a HRC of 33, was virtually unaffected by the presence of a 2.54-mm (0.1-in.) deep flaw.

**KEY WORDS:** steel chain, mechanical properties, fractures (materials), toughness, notch sensitivity, fractography

The present investigation was conducted to indicate the interrelationships of strength, toughness, and flaw tolerance of 25.4-mm (1-in.) alloy-steel lifting chains procured from five chain manufacturers. The susceptibility of these chains to sudden fracture in service in the presence of flaws is of interest to producers and users, and it was anticipated that the results would be generally helpful in arriving at a recommended upper limit of strength consistent with safety, inspection, and economic considerations.

*Original experimental data were measured in U.S. customary units.

[1] Associate research consultant and project analyst, respectively, United States Steel Corporation, Research Laboratory, Monroeville, Pa. 15146.

The chain manufacturing process consists of forming the link, electrical-resistance welding, normalizing, quenching (in water), and tempering. Usually only one weld is present on a side of the link; however, at least one manufacturer welds both sides of the link in their process. Tempering at about 480°C (900°F) results in the strength level required for International Standards Organization (ISO) Grade 63 chain, and tempering at about 345°C (650°F) results in the higher strength of ISO Grade 80 chain. A material tensile strength of 1035 MPa (150 ksi) and hardness level of 33 according to Rockwell hardness, C scale (HRC), are characteristic of Grade 63, and tensile strength in the range 1240 to 1380 MPa and (180 to 200 ksi) and hardness of 40 HRC are typical for Grade 80 chain. The present paper includes a characterization of chain materials, a description of full-size chain tests, the application of fracture mechanics to calculate flaw tolerance at various nominal stress levels, and a description of notched-chain tests on Grade 63 and Grade 80 chain.

## Materials and Experimental Work

The chemical compositions of the various chain samples included in this investigation are shown in Table 1. Tension and standard-size Charpy V-notch impact tests were conducted on specimens machined from chain links as shown in Fig. 1. On chain links with two welds, base metal properties were determined on specimens where the gage section was offset from the weld. Hardness profiles across the diameter of the links were determined at 1.6-mm (1/16-in.) intervals, and full-size cross sections of the links were examined metallographically. In addition, full-size chain tension tests (5 links) were conducted on Grade 80 and Grade 63 chains. The chain coded 401 was not included in the full-size tests because of insufficient material, and the specimen coded 420 could not be tested because the 19-mm (3/4-in.) chain furnished did not fit the testing fixtures.

The susceptibility of these chains to sudden fracture in service in the presence of flaws was determined by employing an empirically developed correlation of Charpy test results and $K_{Ic}$ values[2] and then using the $K_{Ic}$ values to calculate critical crack sizes for given stress levels through fracture-mechanics equations. Full-size tests were conducted on additional Grade 63 and Grade 80 chains to determine the effects of notches machined into chain links on the breaking loads.

## Results and Discussion

### *Characterization of Chain Materials*

It is apparent from the mechanical compositions described in Table 1

[2] Barsom, J. M. and Rolfe, S. T. in *Impact Testing of Metals, ASTM STP 466,* American Society for Testing and Materials, 1970, p. 281.

TABLE 1—*Chemical composition of chains investigated, percent.*

| Probable AISI Steel Grade | Specimen Code | C | Mn | P | S | Si | Cu | Ni | Cr | Mo | V | Ti | Al | N | B |
|---|---|---|---|---|---|---|---|---|---|---|---|---|---|---|---|
| 8620 | 400 | 0.22 | 0.86 | 0.013 | 0.024 | 0.35 | 0.21 | 0.46 | 0.60 | 0.21 | 0.010 | 0.002 | 0.028 | 0.006 | 0.0001 |
| 8630 | 401 | 0.31 | 0.82 | 0.005 | 0.031 | 0.25 | 0.18 | 0.50 | 0.57 | 0.16 | 0.008 | 0.003 | 0.016 | 0.006 | 0.0001 |
| 8630 | 402 | 0.30 | 0.77 | 0.010 | 0.030 | 0.27 | 0.27 | 0.48 | 0.57 | 0.16 | 0.008 | 0.003 | 0.048 | 0.008 | 0.0001 |
| 86B20 | 403 | 0.18 | 0.81 | 0.006 | 0.020 | 0.14 | 0.13 | 0.48 | 0.54 | 0.15 | 0.009 | 0.026 | 0.036 | 0.008 | 0.0008[a] |
| 94B17 | 420 | 0.18 | 0.90 | 0.039 | 0.034 | 0.25 | 0.03 | 0.39 | 0.46 | 0.10 | 0.009 | 0.025 | 0.072 | 0.006 | 0.0008[a] |
| 8620 | 444 | 0.23 | 1.07 | 0.018 | 0.035 | 0.28 | 0.21 | 0.43 | 0.58 | 0.20 | 0.007 | 0.001 | 0.035 | 0.006 | 0.0001 |
| 8620 | 450 | 0.22 | 1.07 | 0.018 | 0.029 | 0.24 | 0.25 | 0.42 | 0.65 | 0.20 | 0.008 | 0.002 | 0.030 | 0.006 | 0.0001 |
| 8620 | 166 | 0.22 | 1.06 | 0.020 | 0.033 | 0.27 | 0.22 | 0.41 | 0.58 | 0.20 | 0.009 | 0.002 | 0.048 | 0.006 | 0.0001 |
| 8620 | 167 | 0.23 | 1.08 | 0.018 | 0.035 | 0.27 | 0.23 | 0.42 | 0.58 | 0.20 | 0.008 | 0.002 | 0.037 | 0.006 | 0.0001 |
| 8620 | | 0.18 | 0.70 | 0.040 | 0.040 | 0.20 | | 0.40 | 0.40 | 0.15 | | | | | |
| Specification | | 0.23 | 0.90 | max | max | 0.35 | | 0.70 | 0.60 | 0.20 | | | | | |
| 8630 | | 0.28 | 0.70 | 0.040 | 0.040 | 0.20 | | 0.40 | 0.40 | 0.15 | | | | | |
| Specification | | 0.33 | 0.90 | max | max | 0.35 | | 0.70 | 0.60 | 0.20 | | | | | |
| 94B17 | | 0.15 | 0.75 | 0.040 | 0.040 | 0.20 | | 0.30 | 0.30 | 0.08 | | | | | |
| Specification | | 0.20 | 0.100 | max | max | 0.35 | | 0.60 | 0.50 | 0.15 | | | | | |

[a] Boron steels, minimum 0.0005 percent boron content.

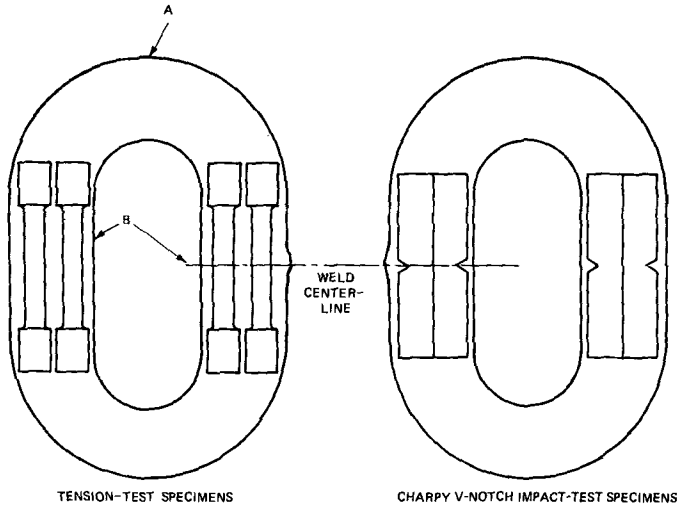


FIG. 1—*Layout showing location of specimens.*

that various grades of steel are used by the different manufacturers. AISI 8620, 86B20, 8630, and 94B17 were among those used.

The results of round-bar tension tests on specimens machined from the chain links are shown in Table 2. Specimens across the welds exhibited essentially the same yield strength and tensile strength as the base metal, but the elongation and reduction of area across the welds were lower, as expected. Similarly, the Charpy V-notch impact-test energies were substantially lower in the weld than in the remainder of the link, Table 3 and Fig. 2. In general, the notch toughness of the welds and of the base metal was substantially higher for the Grade 63 chain than for the Grade 80 chain. The behavior is consistent with the expected effects of the tempering treatments.

The hardness surveys across the links are summarized in Table 4. Maximum, minimum, and average values are shown, but hardness measurements were made every 1.6 mm (1/16 in.) across the link diameter. The hardness survey and an accompanying metallographic examination of the full cross section indicate that the chains had been properly heat treated before the other mechanical tests were conducted on the chains.

### *Full-Size Chain Tests*

An elastic stress analysis[3] of an open chain link indicates that the maximum tensile fiber stress occurs on the outer surface at the ends of the link

[3] Goodenough, G. A. and Moore, L. E., "Strength of Chain Links," Bulletin 18, Engineering Experimental Station, University of Illinois, 1907.

TABLE 2—*Results of tension tests*[a] *on specimens machined from chain links.*

| Specimen Code | Chain Size (Diameter, in.) and Grade | Specimen Location | Yield Strength (0.2% Offset), ksi | Tensile Strength, % | Elongation in 1 in., % | Reduction of Area, % |
|---|---|---|---|---|---|---|
| 400 | 1, 63 | base metal | 147.0 | 157.2 | 18.0 | 65.1 |
| | | weld | 145.9 | 154.9 | 10.0 | 39.7 |
| 401 | 1, 80 | base metal | 191.4 | 210.2 | 13.5 | 56.2 |
| | | weld | 188.6 | 210.8 | 10.5 | 44.9 |
| 402 | 1, 80 | base metal | 189.8 | 205.3 | 14.0 | 53.7 |
| | | weld | 184.2 | 200.3 | 3.5 | 13.0 |
| 403 | 1, 80 | base metal | 164.0 | 178.6 | 14.0 | 63.4 |
| | | weld | 164.0 | 175.8 | 4.0 | 17.6 |
| 420 | ¾[b] | base metal | 141.6 | 162.9 | 16.0 | 63.7 |
| | | weld | 139.6 | 158.6 | 14.0 | 22.6 |
| 450 | 1, 80 | base metal | 161.2 | 180.6 | 14.0 | 61.0 |
| | | weld | 149.7 | 164.2 | 8.0 | 43.0 |

*Conversion Factors*—
1 in. = 25.4 mm, and
1 ksi = 6.895 MPa.

[a] 0.252-in.-diameter specimen.

[b] Not tension tested as chain, therefore grade unknown.

TABLE 3—*Results of Charpy V-notch impact tests on specimens machined from chain links.*

| Specimen Code | Chain Size (Diameter, in.) and Grade | Specimen Location | 0°F Energy Absorbed, ft · lb | 0°F Shear, % | 72°F Energy Absorbed, ft · lb | 72°F Shear, % |
|---|---|---|---|---|---|---|
| 400 | 1, 63 | base metal | 78 to 78 | 100 to 100 | 80 to 88 | 100 to 100 |
| | | weld | 19 to 54 | 20 to 100 | 57 to 80 | 100 to 100 |
| 401 | 1, 80 | base metal | 16 to 17 | 15 to 15 | 18 to 21 | 35 to 40 |
| | | weld | 7 to 7 | 10 to 10 | 9 to 14 | 25 to 35 |
| 402 | 1, 80 | base metal | 15 to 15 | 15 to 15 | 17 to 17 | 30 to 30 |
| | | weld | 5 to 5 | 10 to 10 | 5 to 7 | 5 to 5 |
| 403 | 1, 80 | base metal | 12 to 19 | 15 to 15 | 43 to 45 | 60 to 60 |
| | | weld | 11 to 12 | 15 to 15 | 15 to 19 | 35 to 40 |
| 420 | ¼[a] | base metal | 20 to 21 | 15 to 15 | 26 to 37 | 35 to 50 |
| | | weld | 15 to 21 | 15 to 20 | 19 to 26 | 60 to 70 |
| 450 | 1, 80 | base metal | 15 to 15 | 5 to 5 | 20 to 22 | 20 to 20 |
| | | weld | 8 to 12 | 5 to 5 | 11 to 15 | 20 to 20 |

*Conversion Factors*—
1 in. = 25.4 mm,
1 ft · lb = 1.36 J, and
°C = 5/9 (°F − 32).

[a] Not tension tested as chain; therefore grade unknown.

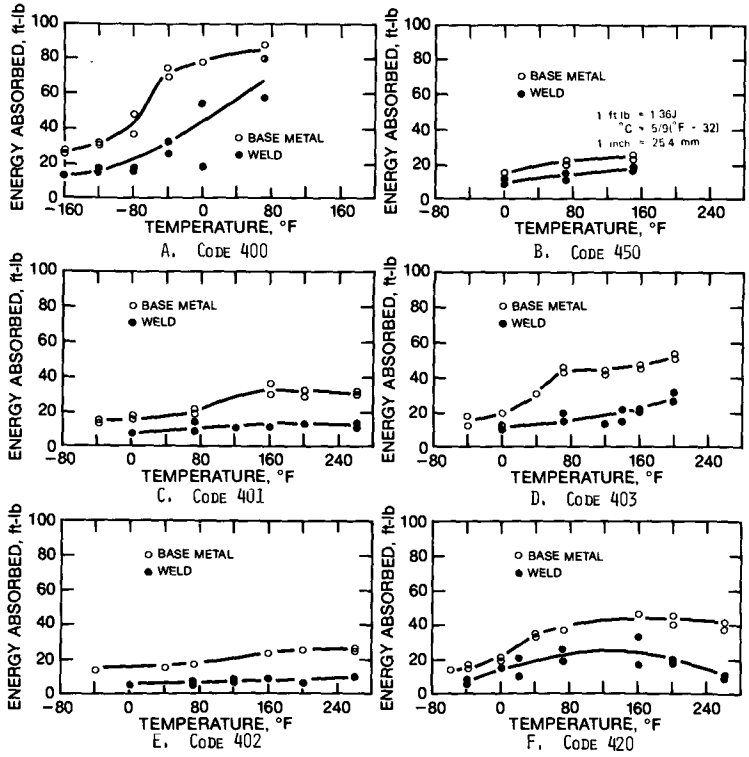


FIG. 2—*Energy absorbed in Charpy tests of chains investigated.*

TABLE 4—*Hardness determinations on cross sections of chain links.*

| Specimen Code | Chain Size (Diameter, in.) and Grade | HRC | | | Weld Centerline[a] |
|---|---|---|---|---|---|
| | | Maximum | Minimum | Average | |
| 400 | 1, 63 | 34.3 | 32.5 | 33.5 | 28.1 |
| 401 | 1, 80 | 43.5 | 40.5 | 42.5 | 45.3 |
| 402 | 1, 80 | 42.5 | 40.2 | 41.9 | 43.9 |
| 403 | 1, 80 | 40.3 | 38.5 | 39.4 | 33.7 |
| 420 | ¼[b] | 41.5 | 40.0 | 40.7 | 31.8 |
| 450 | 1, 80 | 41.0 | 34.8 | 37.9 | 32.4 |
| 166A | 1, 80 | 42.3 | 35.4 | 39.4 | ... |
| 166B | 1, 80 | 42.5 | 37.0 | 39.9 | ... |
| 167A | 1, 63 | 34.5 | 31.5 | 34.0 | ... |
| 167B | 1, 63 | 34.8 | 30.2 | 34.0 | ... |

*Conversion Factor*—
1 in. = 25.4 mm.

[a] Hardness converted from diamond pyramid hardness (DPH).

[b] Not tested as chain, therefore grade unknown.

at Position A in Fig. 1, where the stress equals $2\ P/A$ (where $P$ is the load, and $A$ is the cross-sectional area of the link). The locations of next highest tensile stress are Positions B, where the stress equals $1.8\ P/A$. The weld is located at Position B also, and sudden fracture of chain in service is reportedly usually observed at this location.

In the full-size chain tension tests, the load-displacement curves departed from linearity when the stress at Position A reached the yield strength of the material. These loads are listed in Tables 5 and 6 under the column heading, Yield Load. For example, if the yield load of 396 kN (89 kips) for the specimens coded 400 is substituted into the expression for the stress at Position A, $2\ P/A$, the tensile stress at Position A is calculated to be 1015 MPa (147.4 ksi), in good agreement with the yield strength 1013 MPa (147.0 ksi) Table 2, measured on the round-bar tension-test specimen.

The minimum breaking load specified for 25.4-mm (1-in.) chain of Grade 63 is 639 kN (143.6 kips), and the minimum proof test load is 365 kN (82 kips). Specified breaking and proof-test loads for 25.4-mm (1-in.) chain of Grade 80 are 812 and 464 kN (182.4 and 104.2 kips), re-

TABLE 5—*Results of full-size chain tension tests.*

| Specimen Code | Chain Size (Diameter, in.) and Grade | Yield Load, kips | Maximum Load, kips | Elongation % |
|---|---|---|---|---|
| 400 | 1, 63 | 89 | 175.0 | 18.3 |
| 401 | 1, 80 | ... | ... | ... |
| 402 | 1, 80 | 137 | 204.0 | 15.2 |
| 403 | 1, 80 | 105 | 186.0 | 18.0 |
| 420 | ¾[a] | ... | ... | ... |
| 166A | 1, 80 | 107 | 169.5[b] | 8.0 |
| 444 | 1, 80 | 107 | 213.5 | 16.1 |
| 167A | 1, 63 | 86 | 160.5 | 15.8 |

[a] Not tested as chain, therefore grade unknown.
[b] Broke in weld.

TABLE 6—*Results of full-size notched-chain tension tests.*

| Specimen Code | Chain Size (Diameter, in.) and Grade | Yield Load, kips | Maximum Load, kips | Elongation % |
|---|---|---|---|---|
| 166B[a] | 1, 80 | ... | 91.0 | ... |
| 167B[a] | 1, 63 | 77 | 157.0 | ... |

*Conversion Factors—*
1 in. = 25.4 mm, and
1 kip = 4.45 kN.
[a] Notch 0.006 in. wide by 0.100 in. deep machined in center link of test length.

spectively. The working-load limit for both chains is 50 percent of the proof load, resulting in a safety factor of 3.5.

Two unnotched specimens of Grade 63 chain, coded 400 and 167A, broke at loads of 779 and 714 kN (175 and 160.5 kips), respectively (Table 5), well above the specified minimum of 639 kN (143.6 kips). Both fractures were ductile and occurred when the links necked and then sheared, Figs. 3 and 4.

Three unnotched specimens of Grade 80 chain, coded 402, 403, and 444, broke at loads of 908, 828, and 948 kN (204, 186, and 213 kips), respectively, all in excess of the specified minimum of 812 kN (182.4 kips). All three fractures were ductile shear, Figs. 5, 6, and 7. A fourth unnotched Grade 80 specimen, coded 166A, broke in the weld at a load of 752 kN (169 kips), below the specified minimum, Fig. 8. This weld fracture originated at a subsurface weld imperfection, Area B, Fig. 9(*a*), and then propagated in a brittle manner, Area C, Fig. 9(*a*). The inclusions present in the fracture origin in Fig. 9(*b*) were identified using energy dispersive X-ray analysis as manganese silicate and manganese sulfide. The fracture mode in Area B was primarily dimpled rupture. Figure 9(*c*) shows that the fracture propagated primarily by a cleavage fracture mode. During the electrical-resistance welding of the chain link, the two surfaces being welded together are upset-forged. The resulting plastic flow tends to orient the fibrous inclusions more parallel to the weld surface. As a result, the mechanical properties across the weld would be similar to through thickness rather than longitudinal properties of the bar from which the chain links were made.

### *Notch Sensitivity of Chains*[4]

In order to appraise the susceptibility of chains to sudden fracture in the presence of flaws, fracture-mechanics calculations were made to relate stress, toughness, and flaw size, Table 7. The flaw size required to cause catastrophic fracture at a given stress level is called the critical flaw size. Nominal stress levels of 690, 1035, and 1240 MPa (100, 150, and 180 ksi) were assumed to approximate, respectively, (*a*) a working stress frequently reached, (*b*) the yield strength of Grade 63, and (*c*) the yield strength of Grade 80 chain. Two levels of toughness were assumed: (*a*) a Charpy V-notch impact test energy of 5 J (4 ft·lb) which corresponds to about the lowest toughness measured in any of the chain tested; this toughness correlates empirically with a critical stress intensity ($K_{Ic}$) of 27.5 MPa/$\sqrt{m}$ (25 ksi$\sqrt{in.}$), and (*b*) a Charpy energy level of 22 J (16 ft ·lb) which corresponds to the average toughness measured in the Grade 80 chain tested at −17.8°C (0°F); this toughness correlates with a $K_{Ic}$ of 55 MPa/$\sqrt{m}$ (50 ksi$\sqrt{in.}$). A

[4] For the reader wishing more background in fracture mechanics, refer to Rolfe, S. T. and Barsom, J. M., *Fracture and Fatigue Control in Structures: Application of Fracture Mechanics,* Prentice-Hall Inc., 1976.

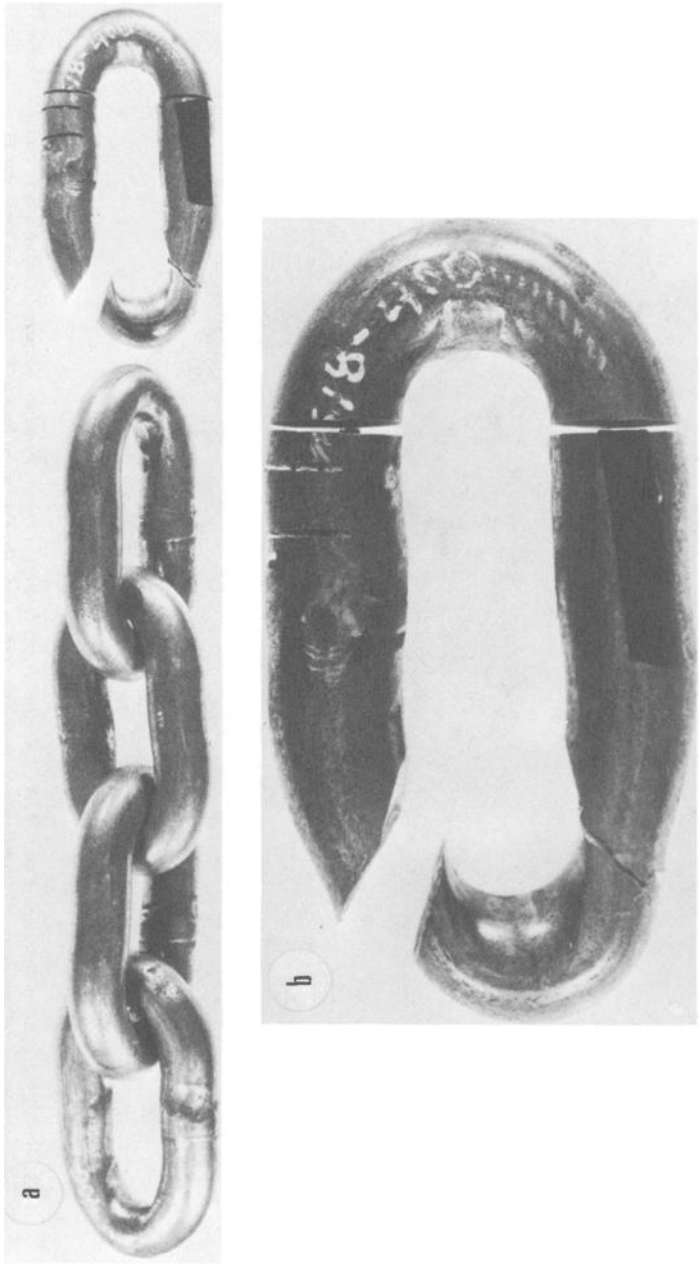


FIG. 3—*Photographs of specimen Code 400 25.4-mm (1-in.) Grade 63 chain. Fracture occurred through base metal with evidence of prefracture deformation.* (a) *Five-link full-size chain test,* ×*0.3.* (b) *Fractured link in full-size chain test,* ×*0.75.*

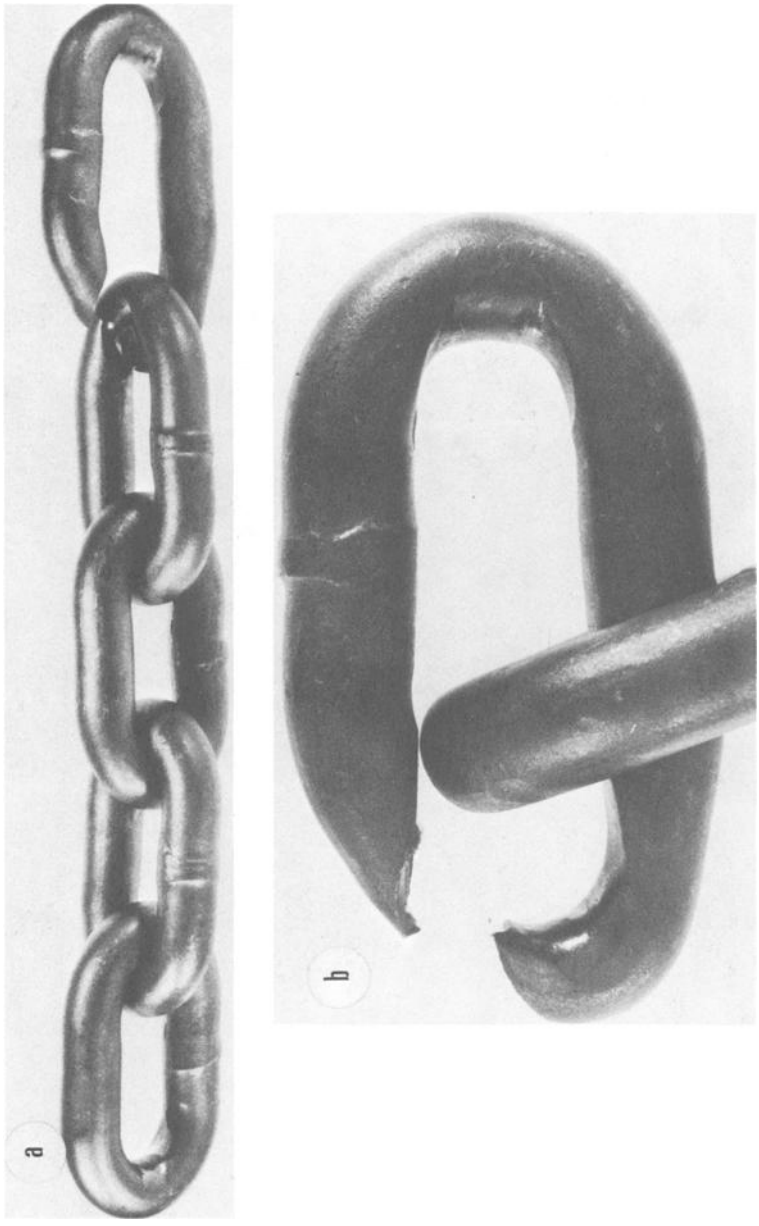


FIG. 4—*Photographs of specimen Code 167A 25.4-mm (1-in.) Grade 63 chain. Fracture occurred through base metal with evidence of prefracture deformation.* (a) *Five-link full-size chain test,* ×*0.3.* (b) *Fractured link in full-size chain test,* ×*0.75.*

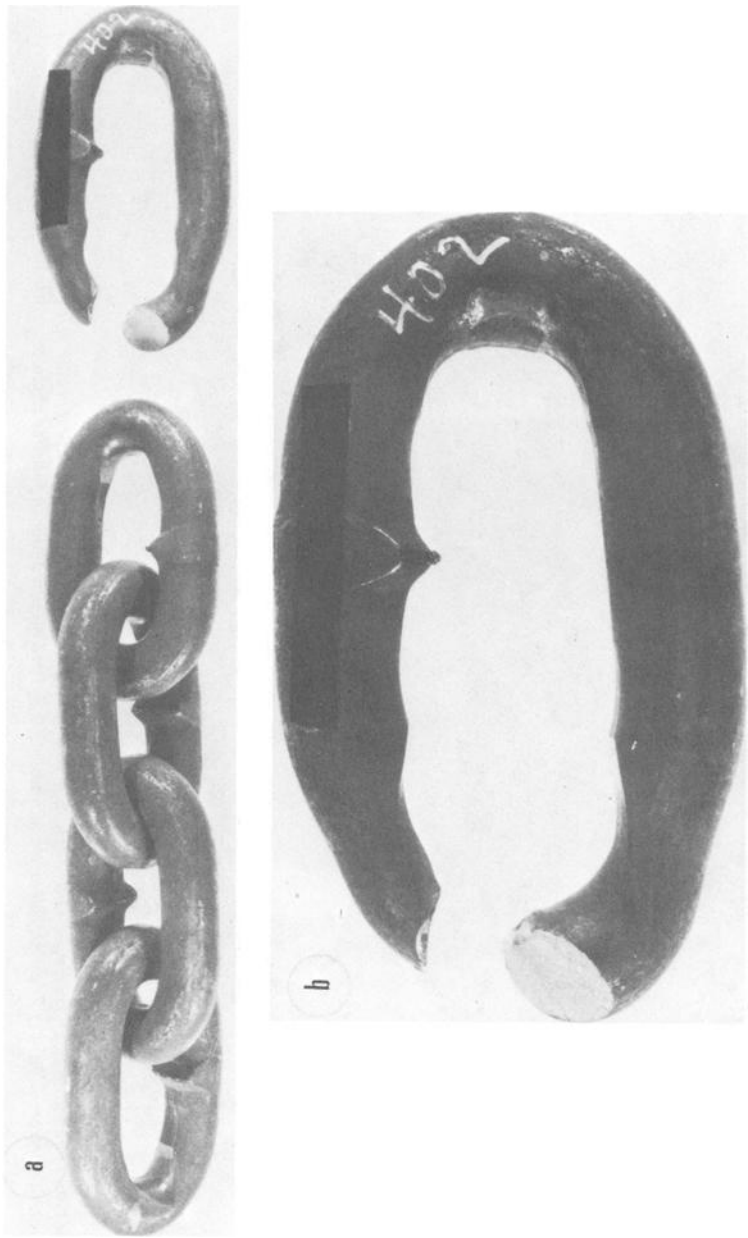


FIG. 5—*Photographs of specimen Code 402 25.4-mm (1-in.) Grade 80 chain. Fracture occurred through base metal with evidence of prefracture deformation.* (a) *Five-link full-size chain test,* ×0.3. (b) *Fractured link in full-size chain test,* ×0.75.

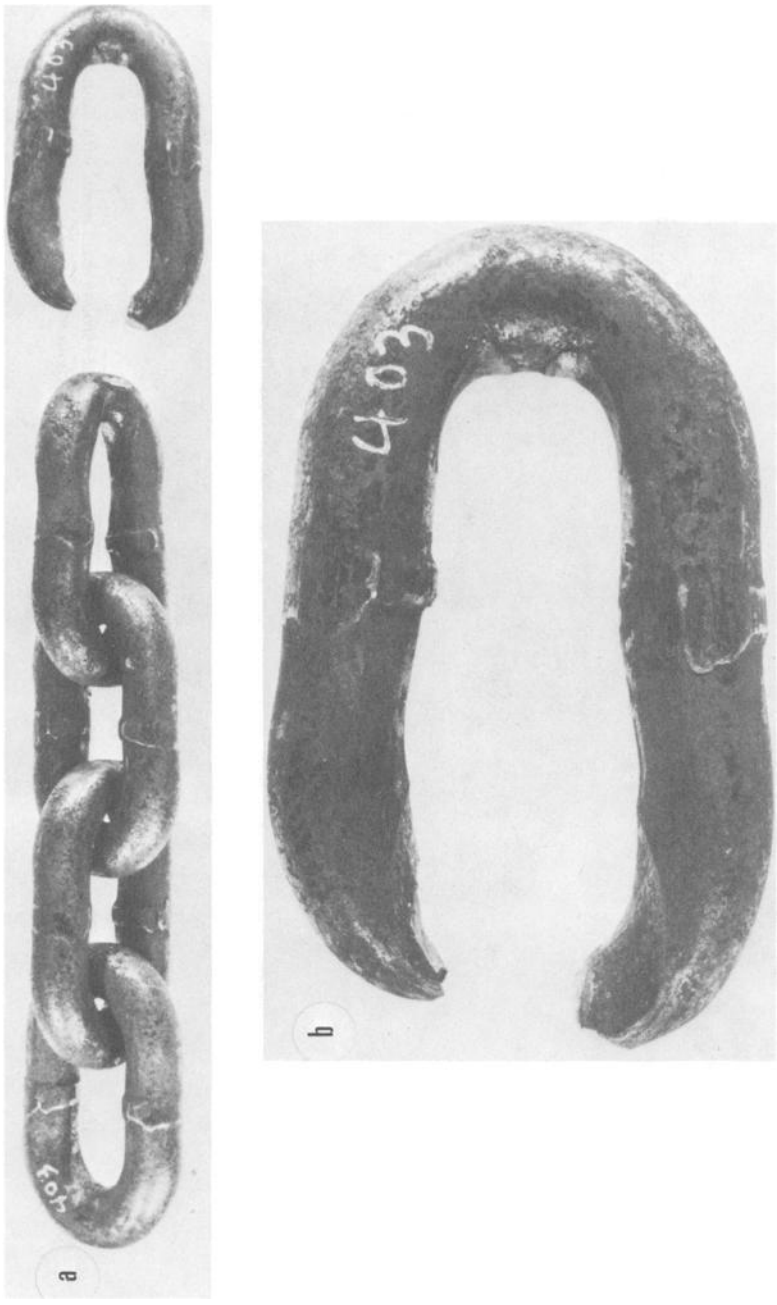


FIG. 6—*Photographs of specimen Code 403 25.4-mm* (1-in.) *Grade 80 chain. Fracture occurred through base metal with evidence of prefracture deformation.* (a) *Five-link full-size chain test,* ×0.3. (b) *Fractured link in full-size chain test,* ×0.75.

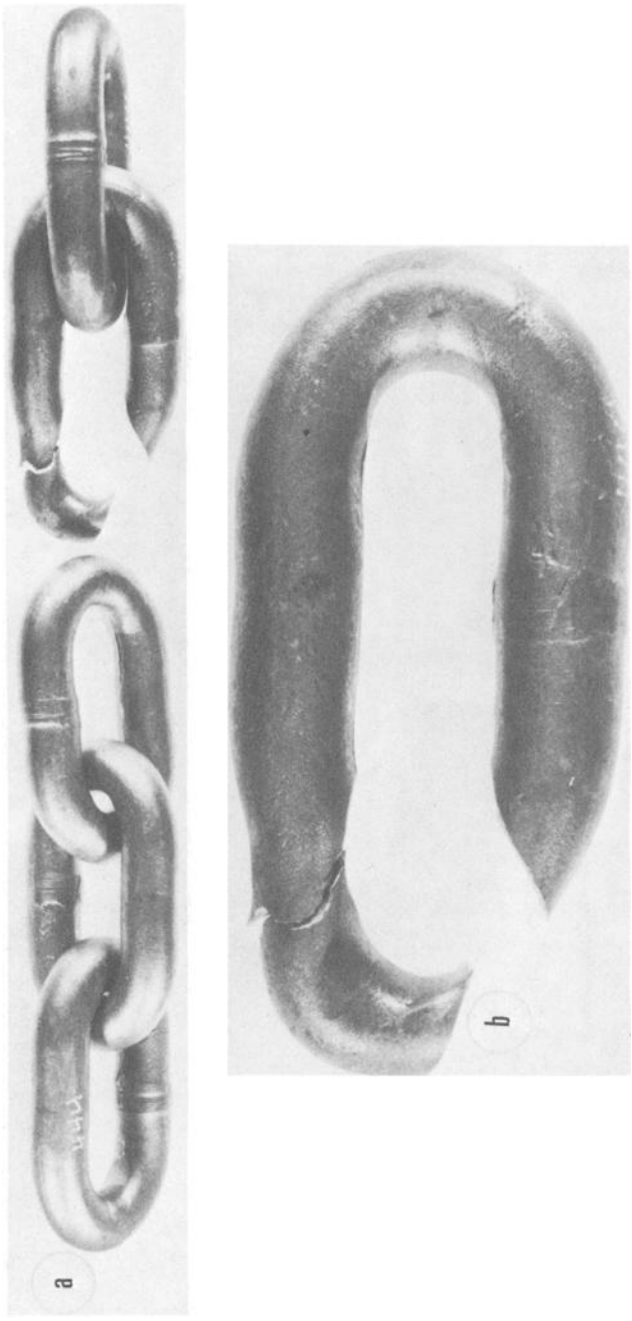


FIG. 7—*Photographs of specimen Code 444 25.4-mm (1-in.) Grade 80 chain. Fracture occurred through base metal with evidence of prefracture deformation.* (a) *Five-link full-size chain test,* ×0.3. (b) *Fractured link in full-size chain test,* ×0.75.

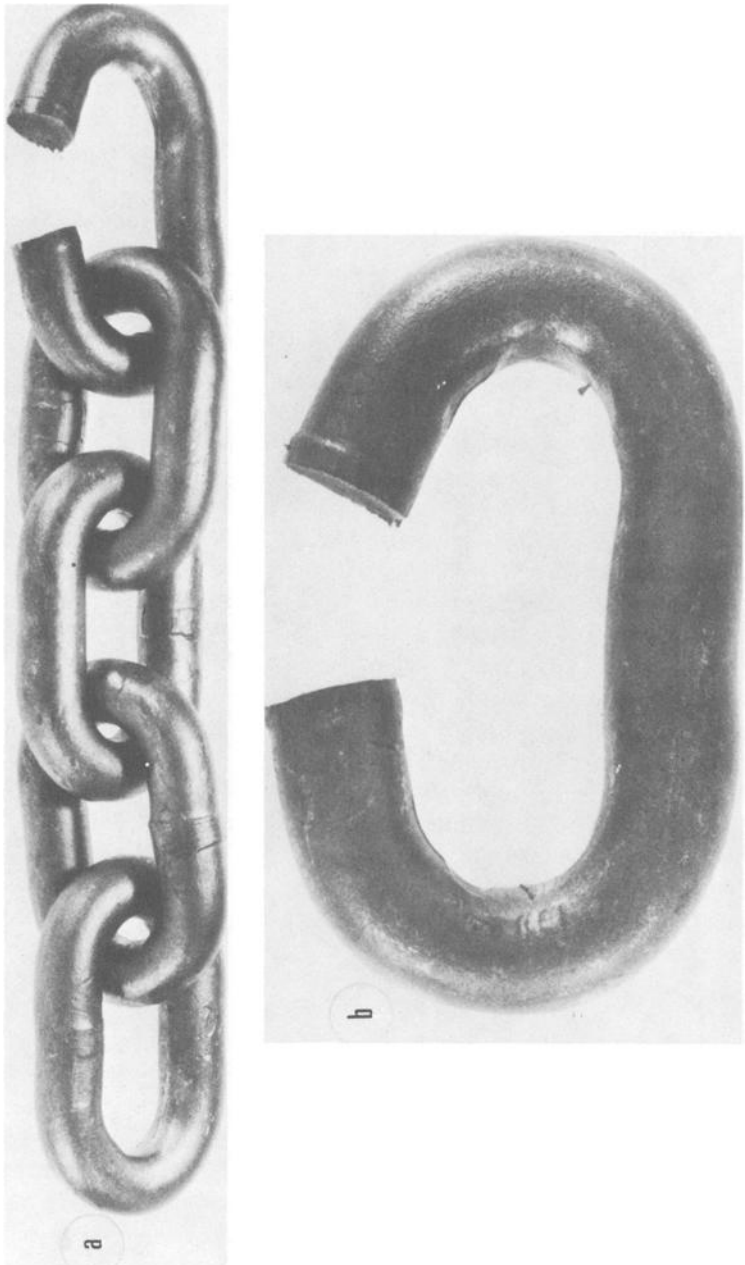


FIG. 8—*Photographs of specimen Code 166A 25.4-mm (1-in.) Grade 80 chain. Fracture occurred through the weld with little evidence of prefracture deformation.* (a) *Five-link full-size chain test,* ×0.3. (b) *Fractured link in full-size chain test,* ×0.75.

crack geometry in which the crack length on the surface was four times the crack depth was assumed, and the fracture-mechanics surface flaw equation, $K_{Ic} = 1.1\sigma\sqrt{\pi a/Q}$, was used to calculate critical flaw depths. ($Q$ is a crack geometry factor with a value of 1.2 when $\sigma/\sigma ys = 1$ and the crack length = 4 times the crack depth.) For example, for an assumed nominal stress level ($\sigma$) of 1035 MPa (150 ksi) and $K_{Ic}$ 27 MPa/$\sqrt{m}$ (25 ksi $\sqrt{in.}$), the critical flaw depth ($a_c$) is 0.23 mm (0.009 in.). Susceptibility to sudden fracture in service under yield-stress loading in the presence of flaws of a few mils in depth is obviously undesirable. If the $K_{Ic}$ is 55 MPa/$\sqrt{m}$ (50 ksi$\sqrt{in.}$), the critical flaw size is only 0.89 mm (0.035 in.) for the same nominal stress level of 1035 MPa (150 ksi). The opposite extreme—that is, the high level of toughness exhibited by the Code 400 Grade 63 Chain (82 J (60 ft·lb) in the weld)—indicates totally ductile behavior because a flaw size approaching the chain diameter could be tolerated and failure could occur only by overloading. For example, the Charpy V-notch impact test energy of 82 J (60 ft · lb) correlates empirically with a critical stress intensity ($K_{Ic}$) of 218 MPa/$\sqrt{m}$ (198 ksi$\sqrt{in.}$). At the yield stress level of 1035 MPa (150 ksi) exhibited by the Code 400 Grade 63 chain, the calculated critical flaw depth ($a_c$) is 14.2 mm (0.56 in.), more than half the diameter of the chain. Clearly, ductile behavior is assured in this chain.

In order to demonstrate the effect of flaws on the breaking strength of chains, specimens of both Grades 63 and Grade 80 chains were notched at Position A in Fig. 1 by using a 0.15-mm-thick (0.006-in.) milling cutter. Position A was selected for the notch because (*a*) the elastic stress analysis at that point was known, and (*b*) it was not possible to place the milling cutter at Position B. A slot 0.15 by 2.54 by 10.9 mm (0.006 by 0.10 by 0.43 in.) in Grade 63 chain had a negligible effect on breaking strength; the unnotched chain (Code 167A) exhibited a breaking strength of 714 kN (160.5 kips), Table 5, and the notched chain (Code 167B) broke at 699 kN (157.0 kips) Table 6 and Fig. 10. In contrast, the unnotched Grade 80 chain (Code 444) broke at a load of 950 kN (213.5 kips), Table 5, and the notched chain (Code 166B), Fig. 11, broke at 405 kN (91.0 kips), Table 6. This degradation of breaking strength of the Grade 80 chain in the presence of an artifical notch 2.54 mm (0.1 in.) in depth was predictable from the fracture-mechanics calculations. In fact, a back-calculation using (*a*) a 405-kN (91.0-kips) load, (*b*) a level of toughness associated with energy absorption at 27 J (20 ft · lb) in the Charpy test (the same toughness measured at room temperature in the Grade 80 chain), and (*c*) an estimated decrease in tensile fiber stress of 20 percent due to the bending stress gradient with depth, resulted in a calculated critical flaw depth of 1.78 mm (0.07 in.) The machined flaw, which is not as sharp or as effective in producing failure as a natural crack of the same depth, therefore caused the fracture to occur as predicted.

It is recognized that the experiment just described, in which the machined

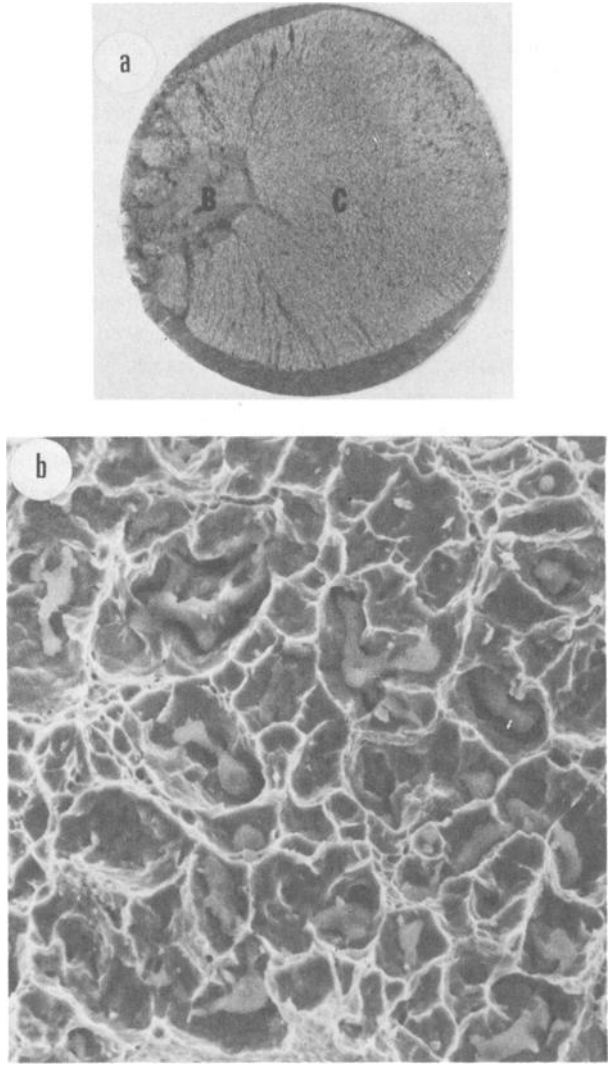


FIG. 9—*Specimen Code 166A 25.4-mm (1-in.) Grade 80 chain. Fracture origin (B) exhibits large inclusions and dimple rupture, and the fracture propagated (C) in a cleavage mode.* (a) *Fracture surface of weld failure of broken link in full-size chain test,* ×2. (b) *Scanning electron fractograph of fracture origin on broken link in full-size chain test,* ×1500. (c) *Scanning electron fractograph of propagating fracture on broken link in full-size chain test,* ×1500.

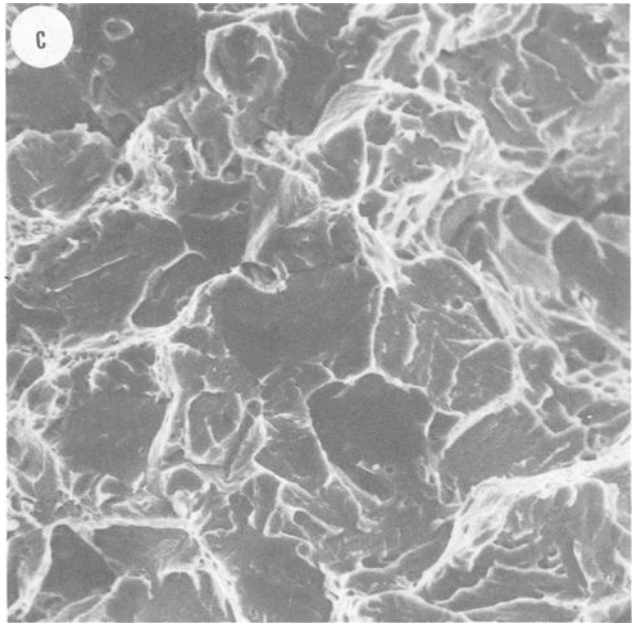


FIG. 9—*Continued.*

notches are located at Position A, is only a demonstration of the reduction in load-carrying capacity of chain in the presence of a notch of arbitrary size in the body of the most probable origin of a fracture. Furthermore, the fracture toughness of the weld is the lowest of any location in the chain link, so a weld flaw becomes critical and propagates at a lower stress level than if a flaw of the same size were located elsewhere in the link. Therefore,

TABLE 7—*Fracture-mechanics calculations of critical flaw sizes.*

| Nominal Stress Level, $\sigma$, ksi | Critical Flaw Depth, $a_c$, in. | |
|---|---|---|
| | For Charpy V-Notch = 4 ft · lb or $K_{Ic}$ = 25 ksi $\sqrt{\text{in.}}$ | For Charpy V-Notch = 16 ft · lb or $K_{Ic}$ = 50 ksi $\sqrt{\text{in.}}$ |
| 100 | 0.020 | 0.080 |
| 150 | 0.009 | 0.035 |
| 180 | 0.006 | 0.025 |

*Conversion Factors—*
1 in. = 25.4 mm,
1 ksi = 6.895 MPa,
1 ksi $\sqrt{\text{in.}}$ = 1.1 MPa/$\sqrt{\text{m}}$, and
1 ft · lb = 1.36 J.

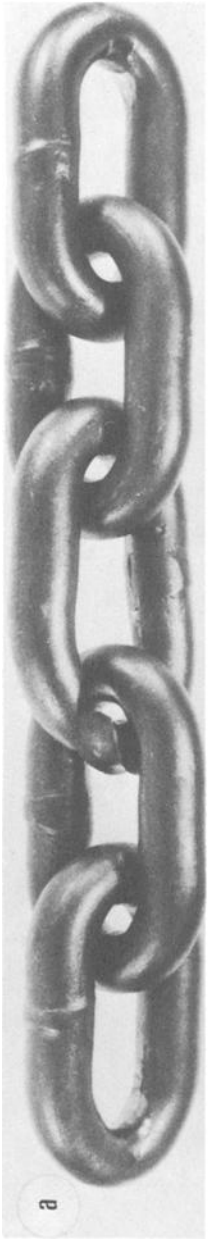
a

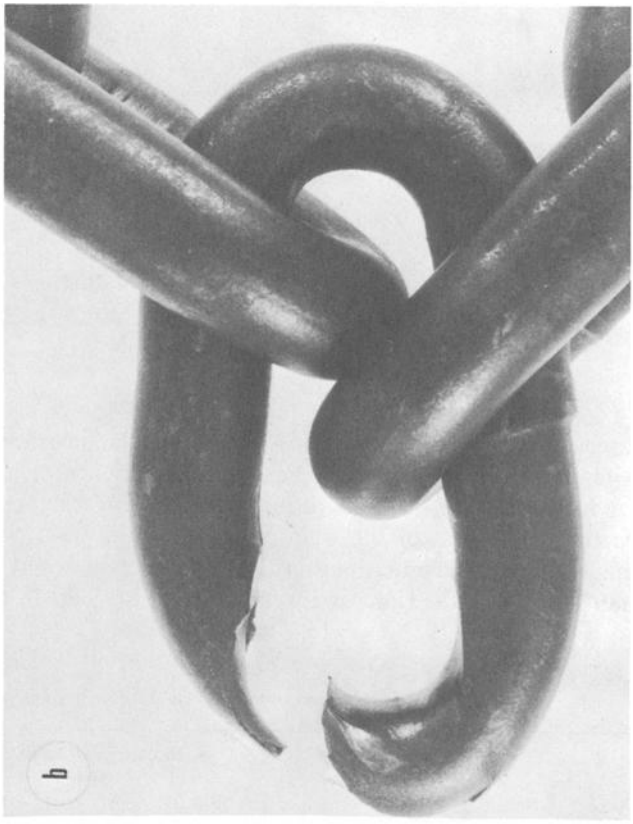
b

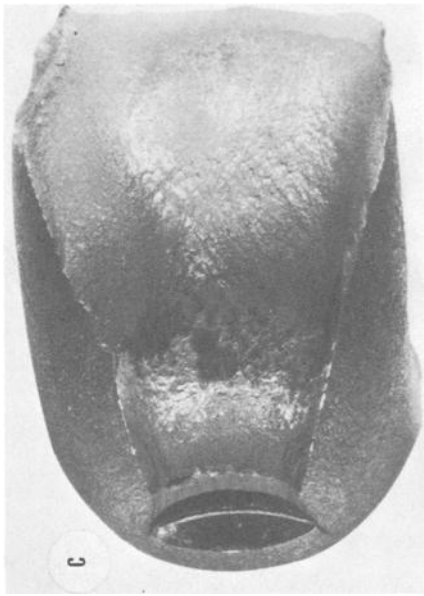

FIG. 10—*Photographs of specimen Code 167B 25.4-mm (1-in.) Grade 63 chain. Fracture occurred through the machined notch with evidence of prefracture deformation.* (a) *Five-link full-size chain test,* ×*0.3.* (b) *Fractured link in full-size chain test,* ×*0.75.* (c) *Fractured surface showing machined flaw and ductile shear fracture,* ×*2.0.*

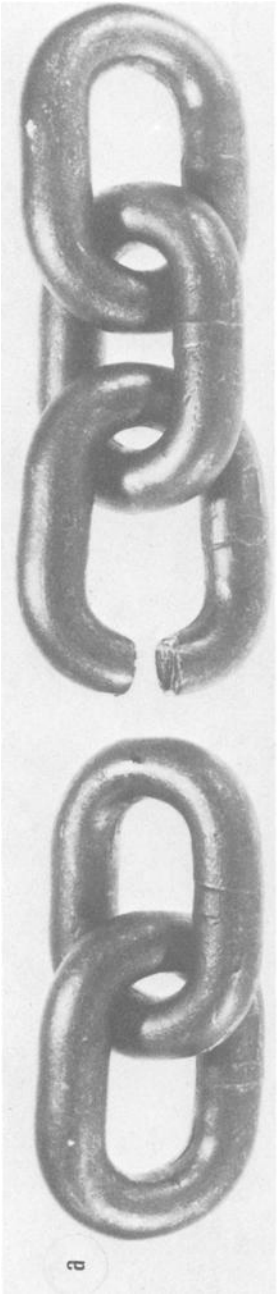
a


b

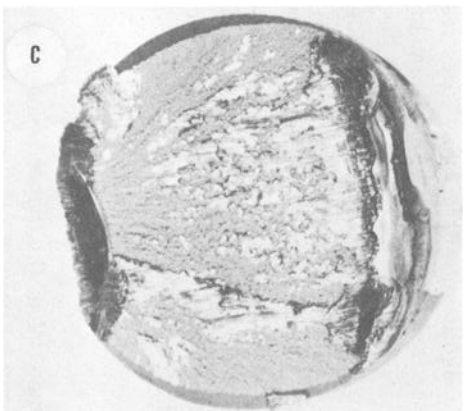


FIG. 11—*Photographs of specimen Code 166B 25.4-mm (1-in.) Grade 80 chain. Fracture occurred through the machined notch with little evidence of prefracture deformation.* (a) *Five-link full-size chain test, ×0.3.* (b) *Fractured link in full-size chain test, ×0.75.* (c) *Fractured surface showing machined flaw and brittle (cleavage) fracture, ×2.0.*

the toughness of the weld material appears to be the parameter that governs the susceptibility of chain to brittle fracture in service.

## Summary

The present investigation was conducted to examine the interrelationships of strength, toughness, and flaw tolerance of 25.4 mm (1-in.) alloy steel lifting chain procured from five chain manufacturers. Small round-bar tension-test and Charpy V-notch impact-test specimens were machined from each chain to characterize the materials. Then an empirically developed Charpy-$K_{Ic}$ correlation was employed, and fracture-mechanics calculations of critical flaw size were carried out. The results showed that Grade 80 chain, exhibiting a hardness of 40 HRC and relatively low toughness, is susceptible to brittle fracture in the presence of small flaws. In contrast, the high level of toughness for Grade 63 chain, exhibiting a hardness of 33 HRC, can tolerate significantly larger flaw sizes resulting in a chain failure when the tensile stresses in the remaining ligament exceed the yield stress.

Tension tests on specimens from chain samples containing machined notches 2.54 mm (0.1 in.) deep confirmed the calculations. Grade 80 chain containing the machined notch fractured at less than half the load required to break unnotched chain; however, Grade 63 chain was virtually unaffected by the presence of an 2.54 mm (0.1 in.) deep notch. The amount of degradation of the breaking strength of the Grade 80 chain containing the flaw was in agreement with fracture-mechanics calculations.

### *Authors' Note*

It is understood that the material in this paper is intended for general information only and should not be used in relation to any specific application without independent examination and verification of its applicability and suitability by professionally qualified personnel. Those making use thereof or relying thereon assume all risk and liability arising from such use or reliance.

*H. Takada,[1] K. Kaneko,[1] T. Inoue,[1] and S. Kinoshita[1]*

# Effect of the Amount and Shape of Inclusions on the Directionality of Ductility in Carbon-Manganese Steels

**REFERENCE:** Takada, H., Kaneko, K., Inoue, T., and Kinoshita, S., "**Effect of the Amount and Shape of Inclusions on the Directionality of Ductility in Carbon-Manganese Steels,**" *Fractography in Failure Analysis, ASTM STP 645*, B. M. Strauss and W. H. Cullen, Jr., Eds., American Society for Testing and Materials, 1978, pp. 335-350.

**ABSTRACT:** The present work has been made to elucidate the quantitative effects of the amount and shape of inclusions in carbon-manganese steel plates on the tensile and impact ductilities in connection with test directions.

The influence of rolling conditions on ductility can be expressed as a function of the shape parameter of the inclusions in terms of the aspect ratio of elliptical manganese sulfide on the polished surface.

Tensile and impact ductilities in transverse and through-thickness directions were improved by rare earth metal (REM) additions to such an extent that the ductilities of REM-treated steel specimens were nearly the same as those of the REM-free steel specimens, although the inclusion content of the former was as much as two or three times more than that of the latter.

Efforts were made to express ductility in one parameter regardless of the inclusion shape and test directions, and it was found that the ductility was closely related to an inclusion area fraction on the ductile fracture surface.

**KEY WORDS:** fractography, steels, ductility, inclusions, directionality

It is well known that impact and tensile ductilities of steel plates are decreased to a greater extent by the presence of nonmetallic inclusions acting as nucleation sites of void in ductile fracture [*1,2*],[2] so that efforts are made in production of clean steel by steel makers. Moreover, during the hot rolling of aluminum-killed steel, the manganese-sulfide (MnS) inclusion deforms and the elongated inclusion reduces the ductility not only in the through-thickness direction but also in the transverse direction [*3,4*].

In recent years, since the importance of the through-thickness ductility

[1]Chief researcher, research metallurgist, research metallurgist, and senior researcher, respectively, Department of Physical Metallurgy, Central Research Laboratory, Kobe Steel, Ltd., Kobe, Japan.

[2]The italic numbers in brackets refer to the list of references appended to this paper.

has been emphasized in fabricating large and complex constructions, the additions of rare earth metal (REM) or zirconium have been studied intensively to prevent the harmful effects of elongated inclusions [*5,6*]. For instance, these alloying elements have been utilized in lamellar-tearing-resistant steel.

The MnS inclusion is known to deform to a larger extent at a lower rather than higher rolling temperature [*7*], and the influence of the volume fraction and shape of the elongated inclusions on ductility have been studied extensively [*1,4,8,9*]. However, no attempt has been made to introduce a parameter expressing the ductility, regardless of test directions and inclusion variables.

The present study is intended first to obtain the quantitative relationship between the ductility of rolled plates and the shape of inclusions which would be affected by rolling temperatures and rolling reduction ratios.

Secondly, we have attempted to express the ductility of rolled plates in all directions as a function of one parameter irrespective of the test directions, rolling conditions, or volume fraction of inclusions and, moreover, to know how the ductilities are affected by the addition of REM as a sulfide-shape control agent.

## Procedure

The specimens used in this study were from heats with base compositions of 0.15C-1.5Mn. The sulfur and REM contents and the general chemical composition are given in Table 1.

Specimens A and B were obtained as slabs of commercial grade, and Specimens C and D were 90-kg ingots from laboratory heats. Specimen blanks from the slabs and the laboratory ingots were hot-rolled at high (~1250°C) and low (~900°C) austenite temperatures at various rolling reduction ratios. In order to keep the rolling temperatures as constant as possible, specimens were reheated to the rolling temperature every two or three rolling passes. Rolling temperatures were estimated to range from 1100 to 1250°C for high temperature rolling and from 780 to 900°C in the case of low temperature rolling.

TABLE 1—*Chemical composition of steel (weight percent).*

| Specimen | C | Si | Mn | P | S | Al | Ce | La |
|---|---|---|---|---|---|---|---|---|
| A | 0.13 | 0.24 | 1.34 | 0.009 | 0.017 | 0.027 | ... | ... |
| B | 0.15 | 0.37 | 1.35 | 0.018 | 0.008 | 0.032 | 0.007 | 0.005 |
| C | 0.15 | 0.41 | 1.52 | 0.012 | 0.009 | 0.036 | 0.006 | 0.006 |
| D | 0.14 | 0.45 | 1.64 | 0.012 | 0.024 | 0.044 | 0.061 | 0.008 |

Tensile and Charpy impact ductilities of the rolled plates were measured in the longitudinal and transverse directions after normalization at 920°C. Since the rolled plates were too thin to be tested directly in the through-thickness direction, dummy materials were friction-welded to each side of the rolled surface, and then Charpy and tension specimens were machined after normalization at 920°C.

In Specimen A, which had no inclusion shape-control elements, some elongated MnS and aluminum oxide ($Al_2O_3$) inclusions were observed on the polished surface, while nondeformed sulfide and oxisulfide of REM and some $Al_2O_3$ predominated in REM-treated steel (Specimens B, C, and D).

Major axis (a) and minor axis (b) of each elliptical inclusion in rolled plates were measured on the microphotographs taken at ×400 or ×1000 of the polished surface parallel to the rolling direction. The minimum detectable inclusion size for the measurements was about 0.5 μm. For the inclined inclusions, the projection lengths were measured as shown in Fig. 1. The measurements were carried out on more than 50 inclusions out of approximately 10 fields. The value of log (a/b) was calculated for each inclusion and the mean value was defined as the inclusion shape parameter of the rolled plate.

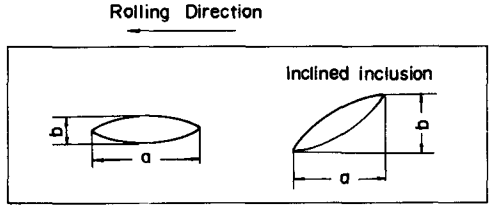


FIG. 1—*Measurement of inclusion shape parameter.*

After Charpy and tension tests, the ductile fracture surfaces of each rolled plate of REM-free and REM-treated steels were examined with a scanning electron microscope (SEM).

Since an inclusion acts as an origin of ductile fracture, a certain correlation was expected between the amount of inclusion existing on the ductile fracture and the ductility of the steel. Therefore, area fractions of sulfide and alumina inclusions on the fracture surface were measured using a quantitative television microscope (Quantimet 720) on the photographs of S-Kα and Al-Kα specific X-ray images at ×400 on one side of the fracture surface of the broken Charpy and tension test specimens. The measured areas were a total of 0.18 $mm^2$ of the fracture surfaces.

## Experimental Results

### *Influence of Rolling Conditions*

Tensile ductility (reduction of area) of each direction in Specimen A (REM-free steel) is illustrated against the rolling reduction ratio in Fig. 2. The reduction of area in the longitudinal direction remained almost unchanged with variations in rolling conditions, but in the transverse and the through-thickness directions, the values decreased not only with increasing rolling reduction ratio but also with decreasing rolling temperature. The Charpy shelf energy changed in a similar fashion as did the reduction of area with the rolling reduction ratio and rolling temperature, as shown in Fig. 3. A significant feature was that the tensile and impact ductilities decreased systematically, corresponding to the variation of inclusion shape affected by the temperature and rolling reduction ratio.

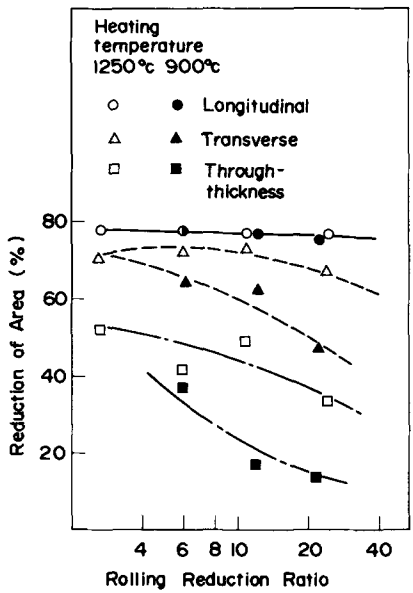


FIG. 2—*Effects of rolling reduction ratio and temperature on reduction of area.*

On the other hand, the reduction of area of REM-treated Specimen B is shown against the rolling reduction ratio in Fig. 4. These results suggest that the influence of rolling conditions on the ductility of the REM-treated steel is much smaller than is the case with the REM-free steel. This is in good agreement with previous investigations [*6, 9*].

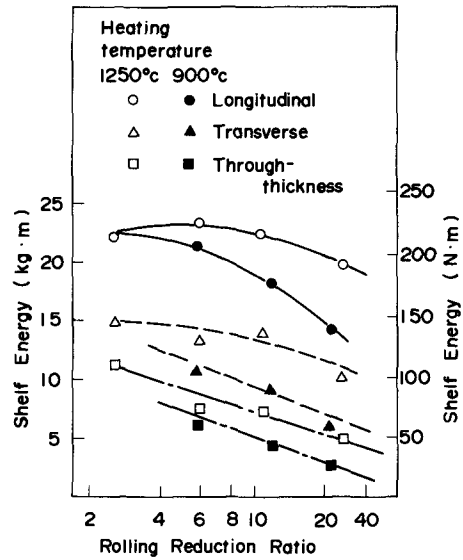


FIG. 3—*Effects of rolling reduction ratio and temperature on Charpy shelf energy in Specimen A.*

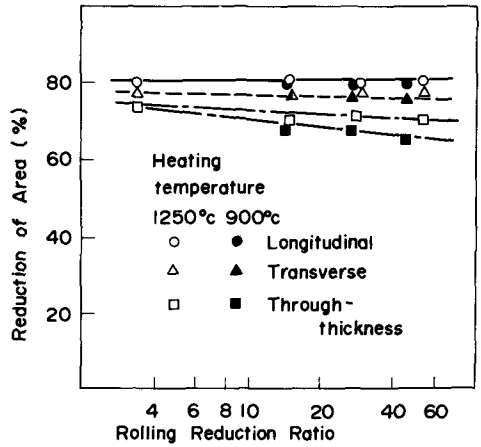


FIG. 4—*Effects of rolling reduction ratio and temperature on reduction of area in REM-treated Specimen B.*

## *Effect of Inclusion Shape Parameter*

The results just mentioned in Specimen A suggest that the ductility in each direction depended primarily upon the shape of MnS which deformed under various rolling conditions.

The reduction of area was plotted against the inclusion shape parameter, log (a/b), in Specimen A rolled at high or low temperature and is shown in Fig. 5. In the longitudinal direction, the effect of shape parameter on the tensile ductility was small, but the ductility of the transverse and through-thickness directions decreased in proportion to the increasing log (a/b). When the value of log (a/b) exceeded approximately 1.8, the relation in the through-thickness direction deviated from the linearity.

The Charpy shelf energies of each direction also were affected by inclusion shape and, as shown in Fig. 6, these decreased with increasing log (a/b).

It was observed that the ductility decreased as the rolling reduction ratio increased or as rolling temperature dropped, and this effect is ascribed to the inclusion shape change as shown in Figs. 5 and 6.

### *Influence of Volume Fraction of Inclusion*

Although the influence of the inclusion shape on the ductility of rolled steels was important, total volume fraction of inclusions had a similar effect. Volume fraction of inclusion was regarded as the same value as the inclusion area fraction on the polished surface.

Figure 7 shows the relationship between Charpy shelf energy and inclusion volume fraction of REM-free specimens on plate rolled to a reduction ratio of 12 at low temperature and on some commercially rolled plates which had similar chemical compositions and inclusion shape parameters of log (a/b) of about 1.8.

Figure 8 shows the similar relation in REM-treated Specimen B rolled to reduction ratio of 16, Specimens C and D rolled to reduction ratio 9 at

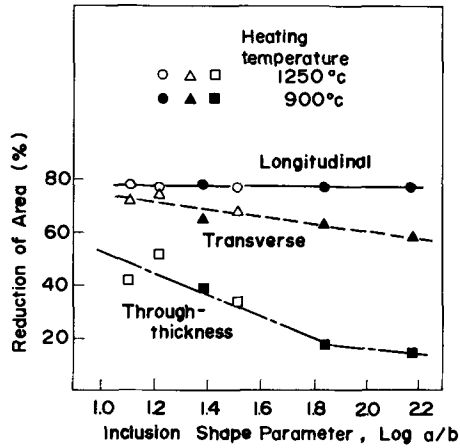


FIG. 5—*Dependence of reduction of area in each direction upon inclusion shape parameter in Specimen A.*

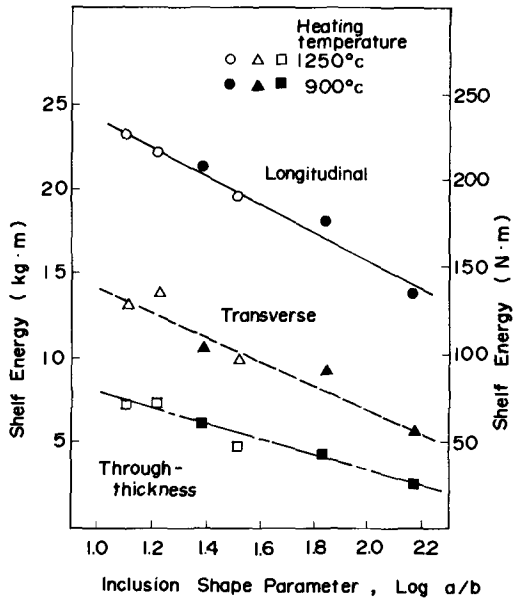


FIG. 6—*Dependence of Charpy shelf energy upon inclusion shape parameter in Specimen A.*

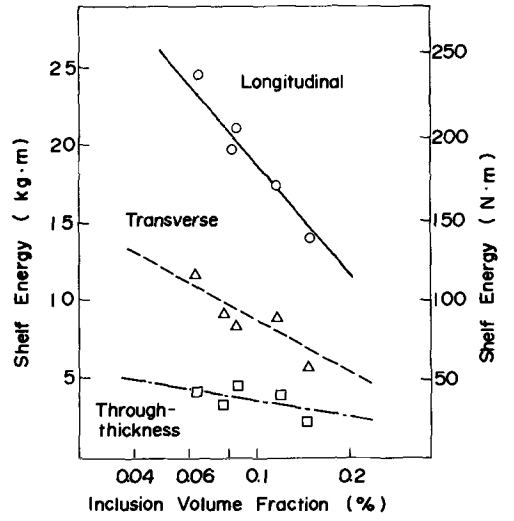


FIG. 7—*Influence of inclusion volume fraction on Charpy shelf energy in REM-free steels.*

low temperature, and some commercially rolled plates having similar chemical compositions.

These figures indicated that the impact ductility of each direction in REM-treated steel was higher than that in REM-free specimens when com-

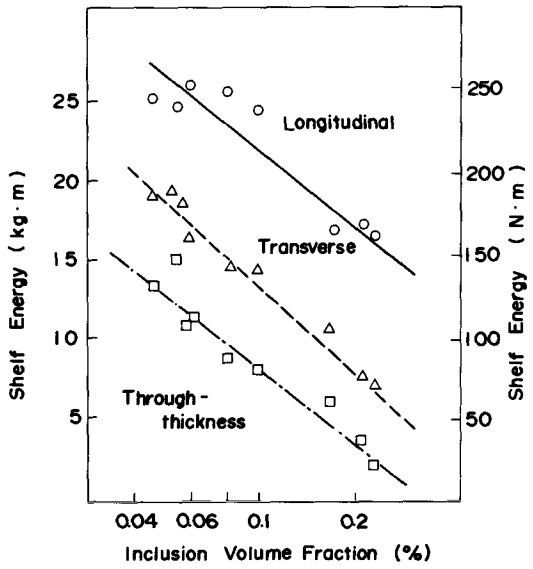


FIG. 8—*Influence of inclusion volume fraction on Charpy self energy in REM-treated steels.*

pared having the same amount of inclusions. Figure 9 shows the influence of the volume fraction of inclusions on the reduction of area of through-thickness direction in both kinds of steel. It also can be seen that the REM addition resulted in the formation of nondeformed inclusions and rendered a larger tensile ductility than REM-free specimens. The Charpy shelf energy and reduction of area of REM-treated steels fell almost on the same level as those of REM-free steels, even though the former contained two or three times as many inclusions as that of the latter.

### *Influence of Inclusion Area Fraction on the Ductile Fracture Surface*

Figure 10 shows the fracture surface of the Charpy specimen in the longitudinal direction in Specimen A rolled to the reduction ratio of 23 at 1100 to 1250°C. The MnS inclusions were found at the bottom of large dimples. The fracture surface of the transverse direction of the same specimen is shown in Fig. 11, and MnS also can be seen lying at the bottom of large elongated dimples. Both fracture surfaces were composed mainly of large dimples with small dimples around them. Figure 12 shows the fracture surface of the through-thickness direction in Specimen A rolled to the reduction ratio of 12 at 780 to 900°C. It can be seen that MnS inclusions are plate-like and also lie parallel to the fracture surface. The photographic features of the fracture surface and appearance of MnS inclusions on it in Specimen A varied significantly with test directions, while in a REM-

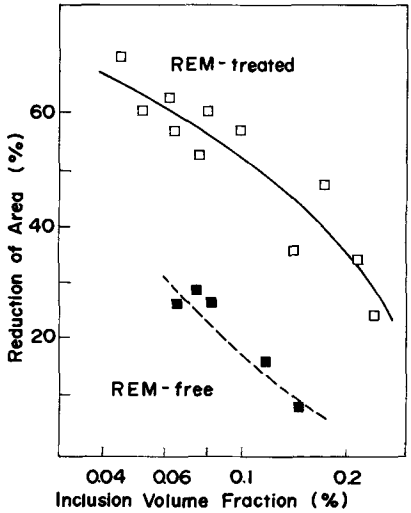


FIG. 9—*Influence of inclusion volume fraction on reduction of area of through-thickness direction in REM-treated and REM-free steels.*

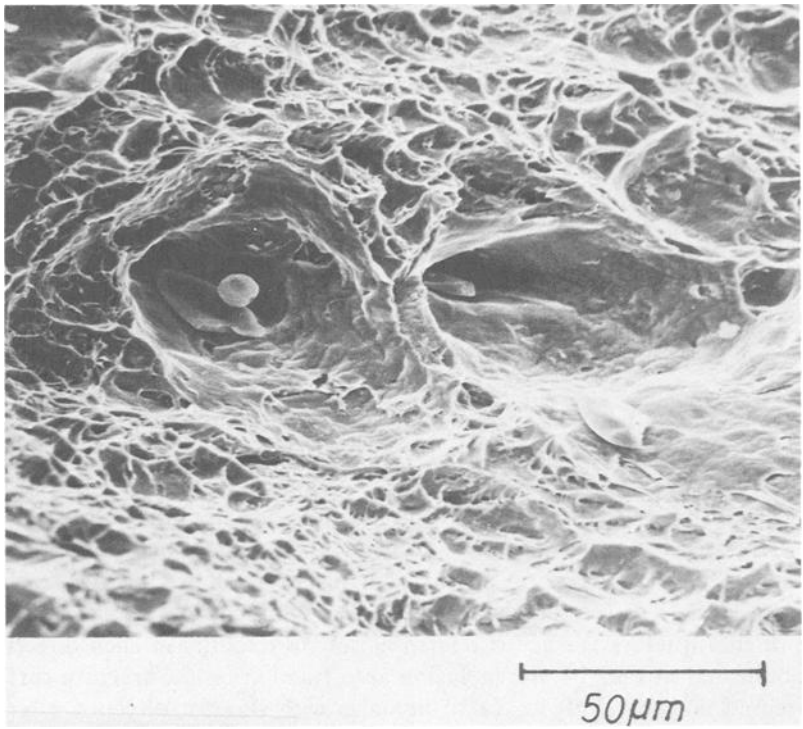


FIG.10—*Fracture surface of longitudinal Charpy specimen in Specimen A rolled to reduction ratio of 23 to 1250°C.*

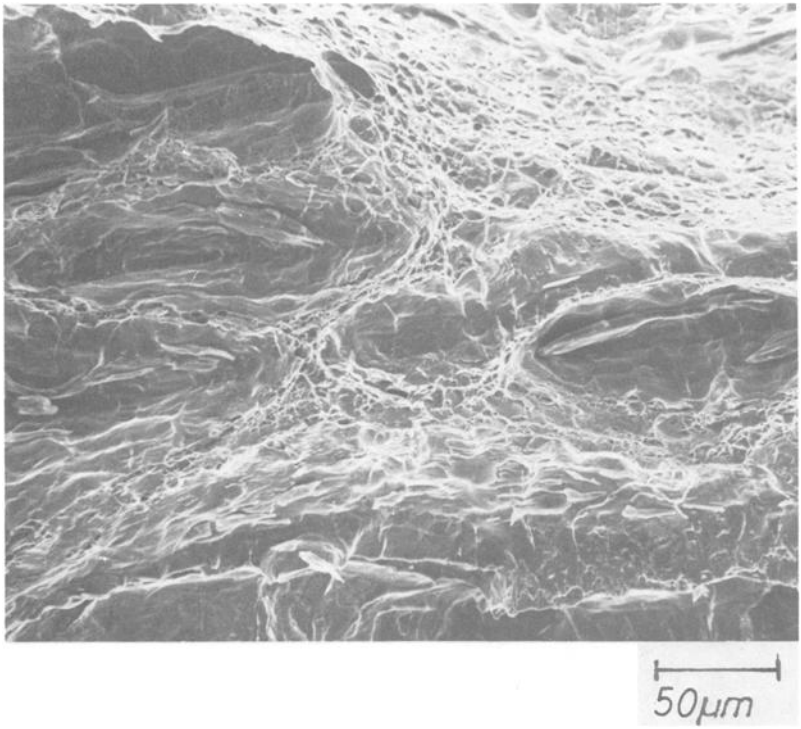


FIG.11—*Fracture surface of transverse Charpy specimen in Specimen A rolled to reduction ratio of 23 at 1250°C.*

treated specimen, globular or cluster-type inclusions predominated as shown in Fig. 13. This figure shows the fracture surface of the through-thickness direction of commercial steel (0.11C-1.4Mn-0.005S-0.02Ce), and no significant difference was found in the features of inclusions with regard to the test directions.

As mentioned previously, tensile and impact ductilities were found to be expressible as a function of the inclusion shape parameter log (a/b) but they still could not be expressed except with reference to test directions.

Several previous investigations had pointed out that the anisotropy of ductility was due primarily to the presence of elongated inclusions [*10,11*]. Since the inclusions, acting as nuclei of fracture, appear on the fracture surface [*1,4*], it is reasonable to expect that the inclusion area fraction on the ductile fracture surface is related closely to ductility in each direction. As indicated in Fig. 14, the inclusion area fraction on the fracture surface increased not only with log (a/b) but also with the test direction altering from longitudinal to transverse and transverse to through-thickness. It should be noticed that this trend is very closely related to ductility.

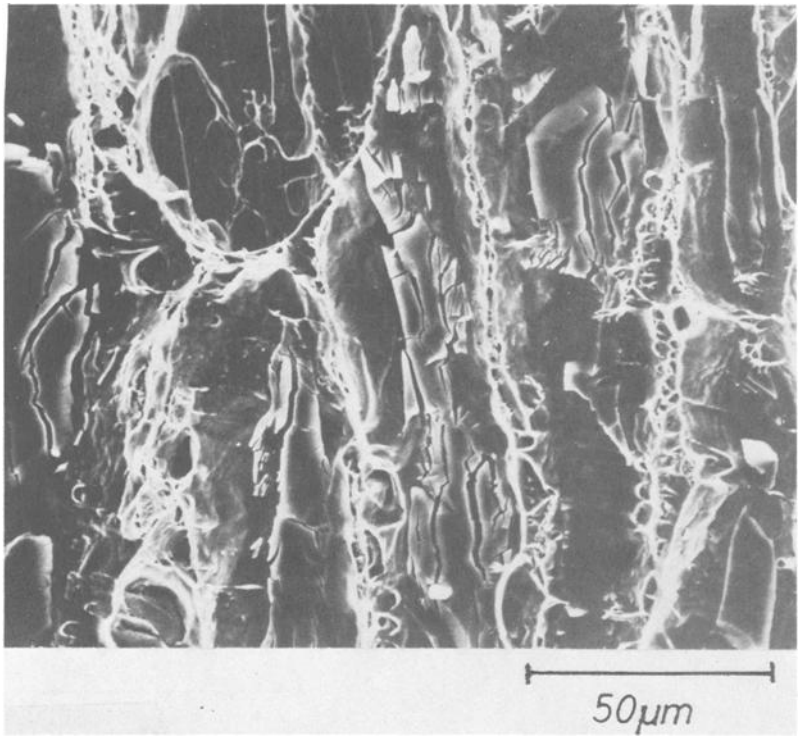


FIG.12—*Fracture surface of through-thickness Charpy specimen in Specimen A rolled to reduction ratio of 12 at 900°C.*

Charpy shelf energy and tensile fracture strain $\epsilon_f$ are plotted against the log of the inclusion area fraction on the fracture surface and are shown in Figs. 15 and 16, respectively. Here tensile fracture strain $\epsilon_f$ is related to the reduction of area $\rho$ by the equation $\epsilon_f = \ln 1/(1 - \rho)$. The results of REM-treated steel and other commercial steel plates with different sulfur contents are also plotted in both figures.

As can be seen in Figs. 15 and 16, it is noteworthy that the ductilities of all steel specimens show the same relationship to inclusion area fraction on the fracture surface. This relationship is independent of any factors such as rolling conditions, sulfur contents, REM additions, or test directions, which control the shape and volume fraction of inclusions. This relationship will be discussed later. It also is seen in these figures that the ductilities increase with the decrease of inclusion area fraction on the fracture surface. However, the ductilities deviated from the linear relation and leveled off as the inclusion area fraction on the fracture surface decreased to zero. This can probably be attributed to the fact that ductility came to be governed primarily by other second-phase particles as the amount of inclusions

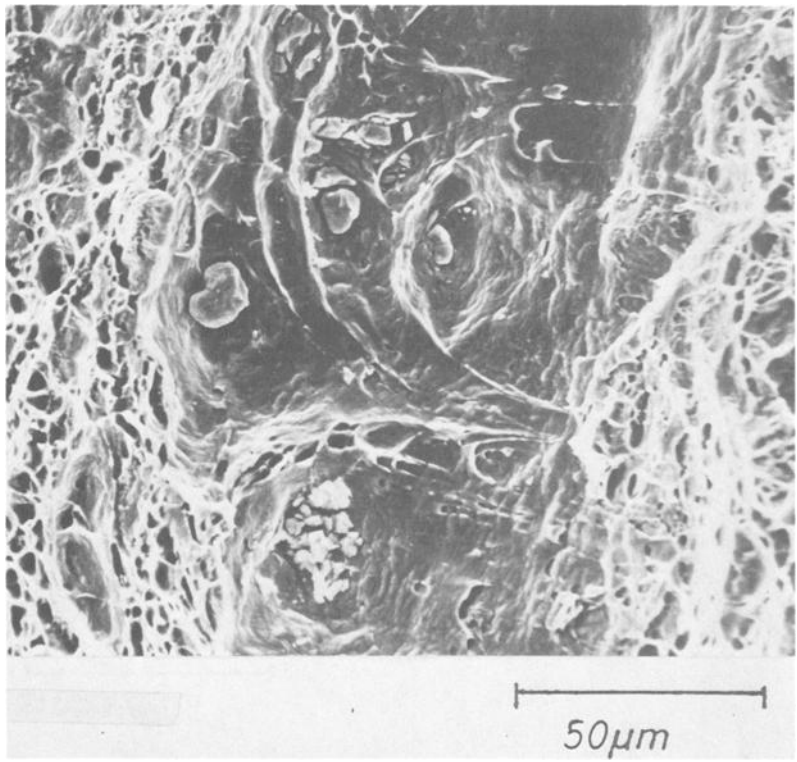


FIG.13—*Fracture surface of through-thickness Charpy specimen in commercial REM-treated steel plate.*

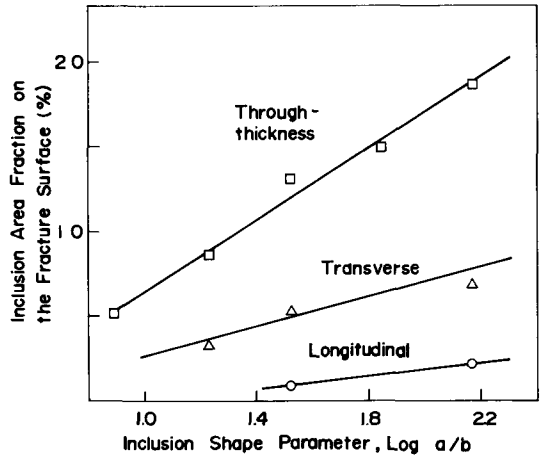


FIG.14—*Inclusion area fraction existing on the Charpy fracture surface as a function of inclusion shape parameter.*

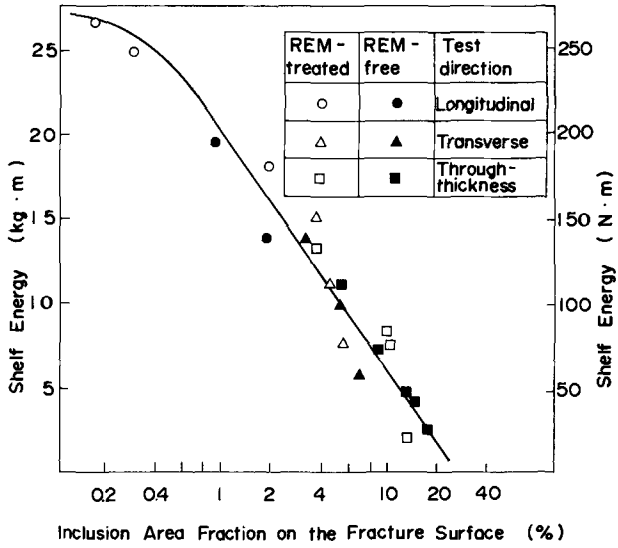


FIG. 15—*Relationship between Charpy shelf energy and the logarithm of inclusion area fraction on the fracture surface.*

became extremely small. The fracture strain approached $\epsilon_f = 1.64$, which corresponds to the fracture strain of a ferrite-pearlite structure of 0.15C steel [*12*].

## Discussion

The results described in this paper indicate that there exists a definite relation between ductilities and inclusion area fraction on the ductile fracture surface regardless of test directions, rolling conditions, or the amount and shape of inclusions of the specimens.

It is generally known that there is an approximate equation between true stress ($\sigma$) and true strain ($\epsilon$)

$$\sigma = k\,\epsilon^n \tag{1}$$

where $k$ and $n$ are material constants of the specimen.

Assuming Eq 1 is satisfied until the fracture occurs, then the equation is rewritten as

$$\sigma_f = k\,\epsilon_f^n \tag{2}$$

where $\sigma_f$ is the true fracture stress corrected by the Bridgman method and $\epsilon_f$ is the true fracture strain. Suppose the effect of the inclusion is sufficiently small, $\sigma_f$ would be equal to the fracture stress of the matrix, $\sigma_m$, and $\epsilon_f$ to the fracture strain of the matrix, $\epsilon_m$, then Eq 1 is rewritten as

$$\sigma_m = k \epsilon_m^n \tag{3}$$

As the inclusion area fraction on the fracture surface increases, the fracture stress of the matrix increases according to the equation

$$\sigma_m = \sigma_f \ (1 - 2f_a) \tag{4}$$

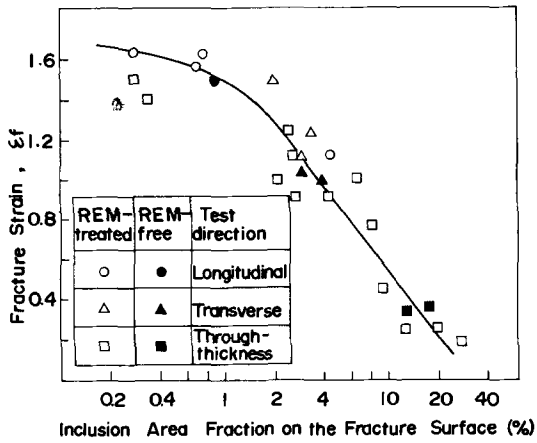


FIG.16—*Relationship between tensile fracture strain and the logarithm of inclusion area fraction on the fracture surface.*

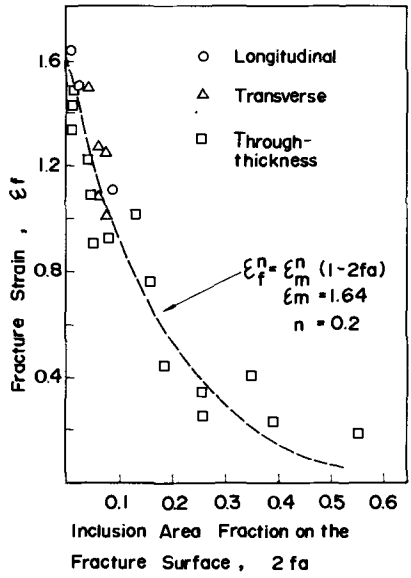


FIG.17—*Calculated and experimental relationships between strain to fracture and inclusion area fraction existing on the fracture surface.*

where $f_a$ is the inclusion area fraction on one of the fracture surfaces out of a pair of broken specimens. The relation between $\epsilon_f$ and $\epsilon_m$ is obtained from Eqs 2, 3, and 4 and is given by

$$\epsilon_f{}^n = \epsilon_m{}^n(1 - 2f_a) \tag{5}$$

Since $\epsilon_m$ is the fracture strain of the matrix, it will be independent of the variables relating to inclusions and is expected to be a fracture strain at an extremely low $f_a$, being regarded as $\epsilon_m = 1.64$ from Fig. 16. Equation 5 predicts the ductility as a function of $f_a$. Figure 17 shows the calculated result, letting the strain hardening exponent $n$ be equal to 0.2. This is in good agreement with experimental values.

## Conclusion

Impact and tensile ductilities were measured in longitudinal, transverse, and through-thickness directions of rolled steel specimens of two groups. In the first group, the shape of inclusion varied with rolling conditions, and in the second group the inclusion shape was controlled by the addition of REM.

The ductilities varied to a larger extent with the variables governing the shape and amount of inclusions such as rolling conditions, sulfur contents, and the addition of REM. However, it was indicated that the ductilities were expressed by one unique parameter, the inclusion area fraction on the fracture surface, regardless not only of inclusion variables but also of the test directions. Moreover, this parameter would be more useful for estimating the ductilities of materials containing second-phase particles if we could predict it in a nondestructive way. For this reason, further investigations are under way to achieve the expression of the parameter as a function of shape parameter and volume fraction of inclusions.

## References

[1] Gurland, J. and Plateau, J., *Transactions*, American Society for Metals, Vol. 56, 1963, pp. 442-454.
[2] Ashby, M. F., *Philosophical Magazine*, Vol. 14, 1966, pp. 1157-1178.
[3] Vogels, H. A., Dahl, W., Hengstenberg, H., and Brüning, F., *Archiv für das Eisenhüttenwesen*, Vol. 33, 1962, pp. 649-659.
[4] Baker, T. J. and Charles, J. A., "Effect of Second-Phase Particles on the Mechanical Properties of Steel," The Iron and Steel Institute, 1971, pp. 79-87.
[5] Luyckx, L., Bell, J. R., McLean, A., and Korchynsky, M., *Metallurgical Transactions*, Vol. 1, 1970, pp. 3341-3350.
[6] Croll, J. E. and Macdonald, J. K., *The Journal of Australian Institute of Metals*, Vol. 19, 1974, pp. 161-167.
[7] Maunder, P. J. H. and Charles, J. A., *Journal of The Iron and Steel Institute*, Vol. 206, 1968, pp. 705-715.
[8] Thomason, P. F., *Journal of the Institute of Metals*, Vol. 96, 1968, pp. 360-365.

[9] Bernard, G., Grumbach, M., and Moliexe, F., *Metals Technology*, Vol. 2, 1975, pp. 512-521.
[10] Morrison, W. B., *Metals Technology*, Vol. 2, 1975, pp. 33-41.
[11] Grange, R. A., *Metallurgical Transactions*, Vol. 2, 1971, pp. 417-426.
[12] Inoue, T. and Kinoshita, S., *Transactions of the Iron and Steel Institute of Japan*, Vol. 17, 1977, pp. 245-251.

*G. E. Hicho[1] and C. M. Gilmore[2]*

# Comparison of the Threshold Stress Intensities and Fracture Characteristics for Temper Embrittled and Deembrittled 2¼Cr-1Mo Steel in a Hydrogen Charging Environment

**REFERENCE:** Hicho, G. E. and Gilmore, C. M., **"Comparison of the Threshold Stress Intensities and Fracture Characteristics for Temper Embrittled and Deembrittled 2¼Cr-1Mo Steel in a Hydrogen Charging Environment,** *Fractography in Failure Analysis, ASTM STP 645,* B. M. Strauss and W. H. Cullen, Jr., Eds., American Society for Testing and Materials, 1978, pp. 351-362.

**ABSTRACT:** Fracture toughness tests and fractographic examinations were conducted on temper embrittled and deembrittled 2¼Cr-1Mo steel using double cantilever-beam specimens. The tests were conducted in an aqueous/acetic acid solution containing hydrogen sulfide ($H_2S$). The threshold stress intensity of the temper embrittled specimen tested in the $H_2S$ environment was lower than that of the deembrittled specimens tested in a similar environment. For the purpose of comparing fracture appearances, temper embrittled and deembrittled specimens were fractured in air.

The fracture appearances of the temper embrittled and the deembrittled specimens tested in the $H_2S$ environment and the temper embrittled specimen fractured in air were predominantly intergranular. The fracture appearance of the deembrittled specimen fractured in air exhibited a transgranular ductile mode of failure. These results indicate that the embrittling effects due to temper embrittlement and to the $H_2S$ environment act cooperatively in reducing the threshold stress intensity of 2¼Cr-1Mo steel.

**KEY WORDS:** steels, temper embrittlement, hydrogen embrittlement, fracture properties, fractography

One of the more important metallurgical problems occurring in the petrochemical industry concerns the effects of a hydrogen sulfide ($H_2S$) environment on the fracture toughness of 2¼Cr-1Mo steel. This steel is often used in gas-well tubings and petrochemical units because of its resistance to hydrogen attack, especially at high temperatures. However, ex-

[1] Metallurgist, National Bureau of Standards, Washington, D.C. 20234.
[2] Associate professor, George Washington University, Washington, D.C. 20006.

posure of this steel to $H_2S$ from "sour" gas may promote hydrogen-assisted stress corrosion cracking (HASCC) which leads to a reduction in the ability of the steel to resist crack growth.

The HASCC effects have been studied on numerous alloys. An examination of some of the fundamental theories of stress corrosion cracking was presented elsewhere [*1*].[3]

In addition to the problem of HASCC, temper embrittlement sometimes results from prolonged exposure to high temperatures. Temper embrittlement has been studied extensively and has been discussed in an interpretive review by McMahon [*2*]. Temper embrittlement occurs when certain alloy steels are heated or cooled within a particular temperature range. This results in the segregation of the elements phosphorus, arsenic, antimony, and tin to the prior austenitic grain boundaries [*3-7*] allowing grain boundary failure to occur more readily. These elements have also been known to promote HASCC in steel [*8*].

Investigations of the effects of a combination of temper embrittlement and hydrogen embrittlement on various materials have been published. Cabral et al [*9*] have presented results describing the effects of the segregation of impurities on hydrogen-induced cracking in high strength steel. Their results showed that the threshold stress for tempered nickel-chromium steel tested in a sulfuric acid ($H_2SO_4$) solution was reduced when the steel was aged at 773 K (932°F).

Yoshino and McMahon [*10*] performed experiments on 5 percent nickel-chromium-molybdenum-vanadium (NiCrMoV) steel in the embrittled and nonembrittled condition in a $H_2SO_4$ environment and observed a reduction in the $K$ threshold of the embrittled material. They attributed their results to the presence of grain boundary impurities. These impurities were said to reduce the grain boundary cohesion, thus allowing grain boundary fracture to occur more readily.

Viswanathan et al [*11*], in their work on 4340 steel, determined that temper embrittlement caused a reduction in the $K_{Ic}$ as well as the $K_{Iscc}$ in $H_2S$. Their results showed that phosphorus had the most significant effect on $K_{Iscc}$ and $K_{Ic}$. In addition, they stated that for low strength steels, impurity segregation caused weakening of the grain boundaries and subsequently reduced the $K_{Iscc}$.

McMahon et al [*12*] have shown recently that as the grain boundary concentration of embrittling impurities increases, the intergranular cohesive strength and the threshold stress intensity for hydrogen-induced cracking decreases. These results indicate that the threshold stress intensity is reduced by a combination of these phenomena.

This investigation uses fracture mechanics to show that the threshold stress intensity, $K_{th}$, for 2¼Cr-1Mo steel double cantilever beam (DCB)

[3] The italic numbers in brackets refer to the list of references appended to this paper.

specimens temper embrittled and tested in an aqueous $H_2S$ environment, was lower than the $K_{th}$ for the same steel deembrittled and tested in a similar $H_2S$ environment. It was believed that these are the first results of this type of 2¼Cr-1Mo steel.

Fractographic results are presented which show the fracture appearance for the test and specimen conditions described. In addition, fracture toughness and fractographic results are presented for temper embrittled and deembrittled specimens tested in air.

## Experimental Procedure

The test methods and procedures followed in this investigation were those recommended by Heady [*13*].

The steel used in this investigation was temper embrittled by subjecting it to a temperature range of 616 to 727 K (650 to 850°F) for 10 000 h and subsequently characterized by the determination of the chemical composition, tensile properties, and impact properties.

For comparison purposes, it was necessary to deembrittle a portion of the as-received material. This was accomplished by subjecting the steel to 866 K (1100°F) for 75 min and quenching it in room-temperature water.

Fracture toughness tests were conducted on the wedge-loaded DCB specimens. A drawing of the DCB specimen is shown in Fig. 1. To avoid the problem of side cracking, the specimens were machined from the plate so that their orientation corresponded to the S-T orientation as described in ASTM Test for Plane-Strain Fracture Toughness of Metallic Materials (E 399-74).

The specimen thickness used in this investigation was 9.5 mm (0.375 in.), and this thickness did meet the size criteria established for plane strain conditions as stated in ASTM Test E 399-74. The size criteria and its relation to HASCC is now discussed.

According to ASTM Test E 399-74, the primary criteria for plane strain conditions is that $B$, the specimen thickness, determined by the following equation be satisfied

$$B \geq 2.5 \left( \frac{K_{Ic}}{\sigma_{ys}} \right)^2 \tag{1}$$

This equation was not developed to apply to environmentally induced fracture, and its applicability is open to question [*14*]. For example, in a discussion of stress corrosion test methods, Parkins [*15*] states that when very ductile materials are tested and plane strain conditions are to be followed, a very thick specimen is required. Since most corrosion failures

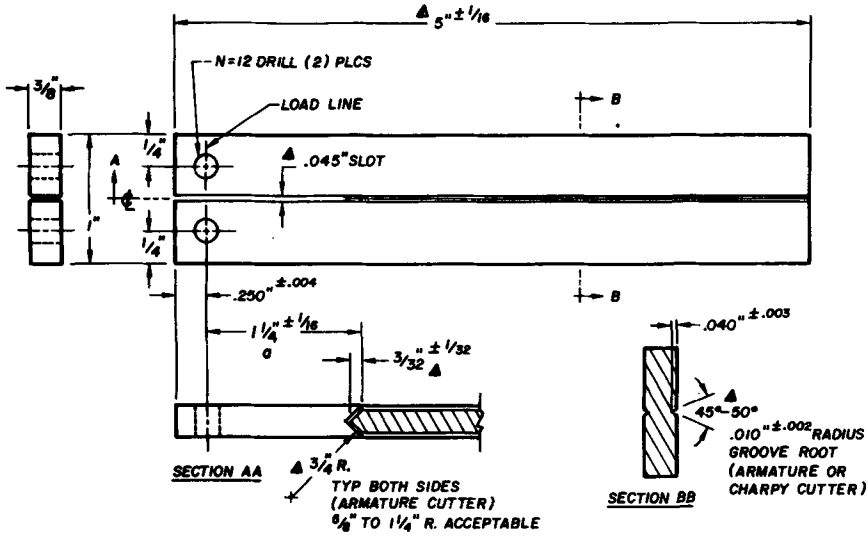


FIG. 1—*The DCB specimen.*

occur in very ductile material in thin sections, it is implied that the fracture mechanics criteria as to specimen size is not applicable. On the other hand, Brown [*16*] suggests that fracture mechanics could be used in stress corrosion work, "as a means of referencing stress in a body containing a crack in a manner applicable to various geometries." It appears that using fracture mechanics to determine the threshold stress intensity due to a corrosive environment is acceptable.

Precracking of the DCB specimens was accomplished by inserting a wedge into a specimen that was cooled previously in liquid nitrogen. The wedge was tapped and the specimen was observed for pop in. Care was taken so that the displacement created during precracking did not exceed the displacement necessary to obtain the initial $K$ value.

Once a crack was observed in the specimen, the crack length was measured to the nearest 0.25 mm (0.01 in.) using a microscope accurate to 0.0025 mm (0.0001 in.). Each crack length was measured three times on each side of the specimen. The average of these six measurements was taken as the initial crack length.

Preliminary test results of Interrante and Hicho [*17*] served as a basis for determining the initial $K$ value to which specimens were to be loaded in this investigation. Their work revealed that for 2¼Cr-1Mo steel (HRC 20) loaded to an initial $K$ of about 110 MPa $\sqrt{m}$ (100 ksi $\sqrt{in.}$), the $K_{th}$ due to the $H_2S$ environment was 33 MPa $\sqrt{m}$ (30 ksi $\sqrt{in.}$). As a result of that work, the initial stress intensities were set at the values listed in Table 1.

Additional preliminary work showed that the incubation period for crack initiation was about 3 to 5 h and that crack growth had terminated after five days.

TABLE 1—*Fracture and fractographic test results. Specimens 2, 7, and 8 were wedge-loaded DCB specimens. Specimens 10 and 11 were loaded as single-edge notch specimens.*

| | | | Test Condition | | Initial $K$ | | $K_{th}$ | | |
|---|---|---|---|---|---|---|---|---|---|
| Specimen | Deem-brittled | Temper Embrittled | $H_2S$ | Air | MPa$\sqrt{m}$ | ksi$\sqrt{in.}$ | MPa | ksi$\sqrt{in.}$ | Fracture Appearance |
| 10 | | X | | X | 129 | 117 | ... | ... | intergranular |
| 11 | X | | | X | 204 | 186 | ... | ... | ductile |
| 2 | | X | X | | 66 | 60 | 53 | 48 | intergranular |
| 7 | X | | X | | 96 | 87 | 77 | 70 | intergranular |
| 8 | X | | X | | 112 | 102 | 82 | 75 | intergranular |

After loading to the initial $K$ value, the deembrittled specimens were placed in a test environment consisting of distilled water containing ½ weight percent glacial acetic acid saturated with $H_2S$ at one atmosphere. The environment was charged each day with $H_2S$ for 5 min. After five days, the specimens were removed from the environment. Crack growth was measured on each specimen and the $K_{th}$ calculated. From the $K_{th}$ results for the deembrittled specimens, the temper embrittled specimen was loaded to 66 MPa $\sqrt{m}$ (60 ksi $\sqrt{in.}$) and placed in the test environment for five days.

For comparison of fracture appearance, deembrittled and temper embrittled specimens were tested in air. The specimens were precracked according to the previously described method, then placed in a tensile machine for loading as one would load a single-edge notch specimen. The load necessary to obtain crack instability was obtained and the stress intensity factor was calculated using the equation for single edged notch specimens [*18*].

Fractographic examinations were conducted on all of the specimens using a scanning electron microscope (SEM). The surfaces were cleaned in flowing hydrogen gas prior to examination [*17*] to remove a corrosion product which formed on the specimens subjected to the $H_2S$ environment.

## Results and Discussion

Table 1 shows the results of the fracture toughness tests and subsequent fracture appearances. The results show that the temper embrittled specimens tested in the $H_2S$ environment and in air had lower threshold stress intensities than the deembrittled specimens tested in the $H_2S$ environment.

Figure 2 shows a macrograph representative of the fracture surface of

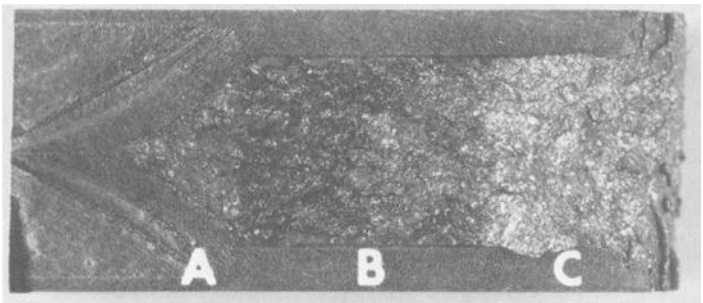


FIG. 2—*Macrograph of Specimen 2 showing three distinct areas of crack growth: Area A, the precrack region; Area B, crack growth due to the test environment; and Area C, crack growth due to the specimen being pulled apart at liquid $N_2$ temperature (X6).*

a specimen. Three areas of crack growth are evident: Area A, the precrack region; B, crack growth due to the $H_2S$ environment; and C, crack growth due to being pulled apart at liquid $N_2$ temperature.

Figure 3(*a*) and (*b*) are SEM fractographs (Area B) of the temper embrittled and deembrittled specimens tested in the $H_2S$ environment. The fracture appearance of both specimens was intergranular.

Figure 4(*a*) and (*b*) are SEM fractographs of the temper embrittled and deembrittled specimens tested in air. The fracture appearance of the temper embrittled specimen was intergranular whereas the fracture appearance of the deembrittled specimen was transgranular ductile.

Based primarily on the fracture appearances of the specimens, in particular the absence of shear lips, it was concluded that plane strain conditions existed. Final crack measurements revealed that growth exceeded the plastic zone size [*19*] established for plane strain conditions. These results indicated that the $K_{th}$ values obtained in this investigation are valid.

The results of the chemical analyses, Table 2, shows the weight percentages of the temper embrittling elements arsenic, antimony, tin, and phosphorus. The weight percentages of these elements usually are reported in parts per million for normal steels, but they were found to be abnormally high in this steel. It was concluded that the segregation of these elements to the prior austenitic grain boundaries and the exposure to 616 to 727 K (650 to 850°F) for 10 000 h produced the temper embrittlement observed in the steel. It was also concluded that temper embrittlement was the primary cause of the intergranular fracture observed in the fractographs.

A measure of the extent of temper embrittlement is revealed in the Charpy impact test results. Impact test results for the temper embrittled and deembrittled material are shown in Fig. 5. The results clearly showed that the temper embrittled material (intergranular fracture) absorbed less energy at a given temperature than the deembrittled material.

Table 3 shows the tensile results for the temper embrittled material. Viswanathan et al [*11*] have shown that for a 4340 steel at the yield strength of approximately 1150 MPa (167 000 psi), the segregation impurities produce a weakening of the grain boundaries with a reduction in the $K_{Iscc}$. The yield strength of the material used in this investigation was 421.5 MPa (62 000 psi). It was concluded from a comparison of these yield strengths that grain boundary weakening should also be expected to occur in the material used in this investigation.

In addition to the temper embrittlement, the $H_2S$ environment is also considered to be a promoter of intergranular fracture.

The $H_2S$ environment, in conjunction with temper embrittlement, produced conditions that favored intergranular failure. This strong tendency for intergranular failure subsequently led to a reduction in the $K_{th}$ *of* 2¼Cr-1Mo steel.

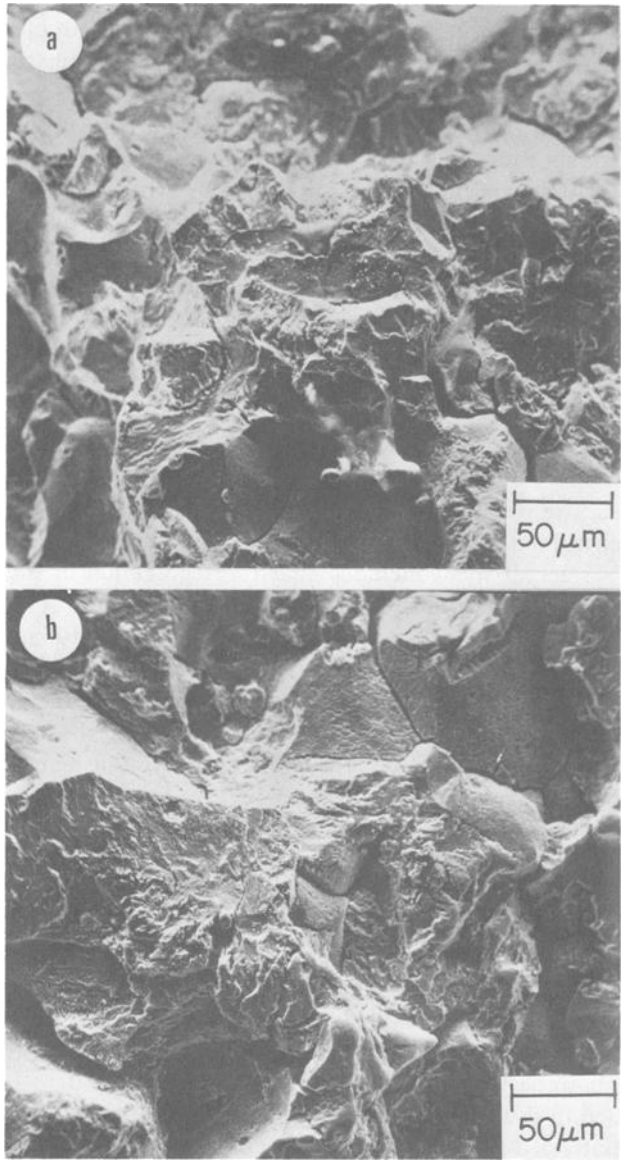


FIG. 3—*SEM fractographs of the temper embrittled Specimen 2,* (a), *and the deembrittled Specimen 8,* (b) *taken in the crack growth Region B shown in Fig. 2. Both specimens were tested in the $H_2S$ environment. Fractures were primarily intergranular.*

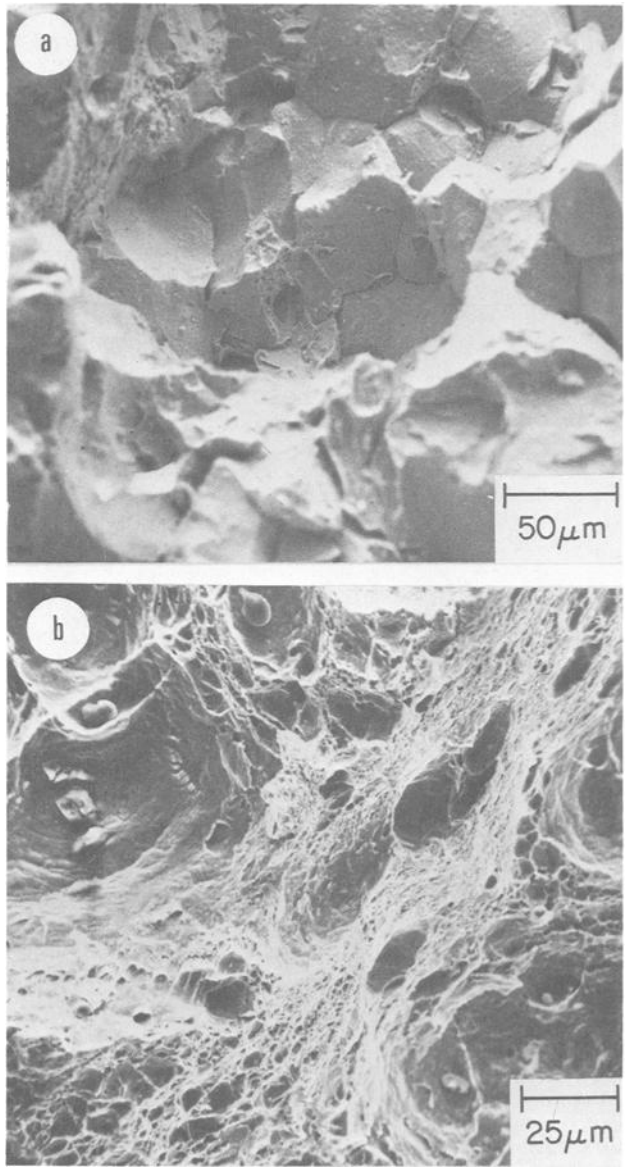


FIG. 4—*SEM fractographs of the temper embrittled Specimen 10,* (a) *and the deembrittled Specimen 11,* (b). *Both specimens were tested in air. Fracture of* (a) *was primarily intergranular whereas* (b) *was transgranular ductile.*

TABLE 2—*Chemical composition of the as-received, temper embrittled 2¼Cr-1Mo plate (weight percent).*

| | |
|---|---|
| C | 0.14 |
| Mn | 0.65 |
| P | 0.018 |
| S | 0.006 |
| Si | 0.27 |
| Cr | 2.32 |
| Ni | 0.20 |
| Mo | 1.05 |
| Cu | 0.20 |
| As | 0.016 |
| Sn | 0.026 |
| Sb | 0.0044 |

TABLE 3—*Room temperature tension tests results for the temper embrittled 2¼Cr-1Mo plate.*

| | Specimen Orientation | |
|---|---|---|
| | Longitudinal | Transverse |
| Ultimate tensile strength | 599.8 MPa (87 000 psi) | 586.1 MPa (85 000 psi) |
| Yield strength, 0.2% offset | 421.5 MPa (62 000 psi) | 420.6 MPa (61 000 psi) |
| Elongation, 5.08 cm (2 in.) | 30% | 29% |
| Reduction of area | 71% | 68% |

## Conclusions

Experimental results have shown that subjecting temper embrittled 2¼Cr-1Mo steel to a $H_2S$ environment reduces the threshold stress intensity. These results indicate that temper embrittlement and a $H_2S$ environment act cooperatively in promoting intergranular fracture of 2¼Cr-1Mo steel.

### *Acknowledgments*

The authors wish to thank D. Truax of the Standard Oil Company of California for the test material used in this investigation. The chemical, tensile, and impact data on the test material also were supplied by Truax.

The authors wish to acknowledge the following members of the Mechanical Properties Section of the National Bureau of Standards for their efforts: C. G. Interrante, J. G. Early, D. E. Harne, L. C. Smith, C. H. Brady, and

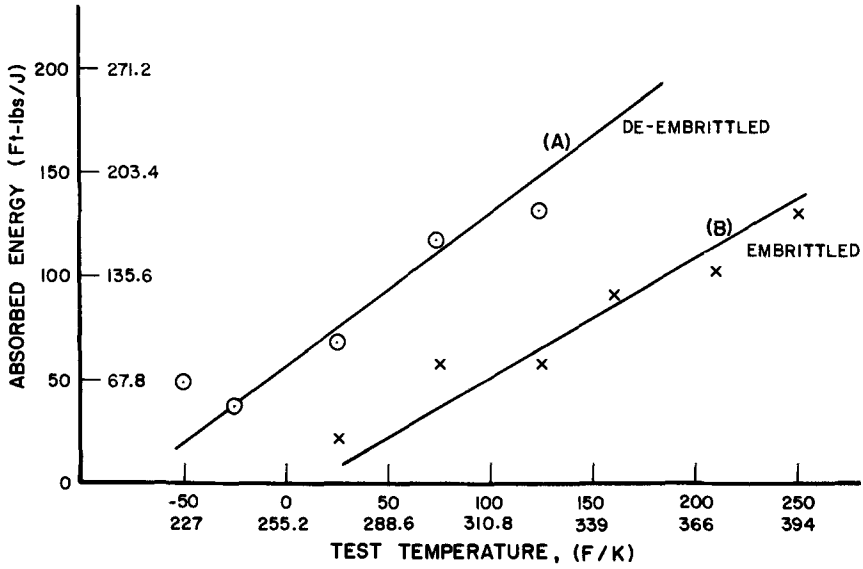


FIG. 5—*Charpy V-notch impact test results for the temper embrittled and deembrittled test material.*

L. E. Ketron, who aided in the preparation of the photographs and graphs used in this paper.

## References

[1] *The Theory of Stress Corrosion Cracking In Alloys,* J. C. Scully, Ed., North Atlantic Treaty Organization, Scientific Affairs Division, Brussels, 1971.

[2] McMahon, C. J., Jr. in *Temper Embrittlement in Steel, ASTM STP 407,* American Society for Testing and Materials, 1968, pp. 127-167.

[3] Steven, W. and Balajiva, K., *Journal of the Iron and Steel Institute,* Vol. 193, 1959, pp. 141-147.

[4] Marcus, H. L. and Palmberg, P. W., *Transactions,* Metallurgical Society of the American Institute of Mining, Metallurgical, and Petroleum Engineers, Vol. 245, 1960, pp. 1664-1666.

[5] Palmberg, P. W. and Marcus, H. L., *Transactions,* American Society for Metals, Vol. 62, 1969, pp. 1016-1018.

[6] Stein, D. F., Joshi, A., and Laforce, R. P., *Transactions,* American Society for Metals, Vol. 62, 1969, pp. 776-783.

[7] Low, J. R., Jr., Stein, D. F., Turkalo, A. M., and Laforce, R. P., *Transactions,* Metallurgical Society of the American Institute of Mining, Metallurgical, and Petroleum Engineers, Vol. 242, 1968, pp. 14-24.

[8] McCright, R. D. and Staehle, R. W., International Conference on Stress Corrosion Cracking and Hydrogen Embrittlement of Iron Base Alloys, Firming, France, 1973.

[9] Cabral, U. Q., Hache, A., and Constant, A., *Computed Rendus Acad of Sci,* Vol. 260T, 1965, p. 6887.

[10] Yoshino, K. and McMahon, C. J., Jr., *Metallurgical Transactions,* Vol. 5, 1974, p. 363.

[11] Viswanathan, R. and Hudak, S. J. in *Effect of Hydrogen on the Behavior of Materials,* American Institute of Mining, Metallurgical, and Petroleum Engineers, 1975, pp. 262-272.

[12] McMahon, C. J., Jr., Briant, C. L., and Banerji, S. K., *Fracture 1977*, Vol. 1, IC4F, Waterloo, Canada, 1977, pp. 363-373.
[13] Heady, R. B., "Sulfide Corrosive Cracking in Gas and Oil Wells. XIV," Technical Progress Report BRC-Corp 5-74-B, Shell Oil Company, Houston, Tex.
[14] Novak, S., *Engineering Fracture Mechanics*, Vol. 5, 1973, pp. 727-763.
[15] Parkins, R. N. in *The Theory of Stress Corrosion Cracking In Alloys*, 1971, pp. 449-468.
[16] Brown, B. F. in *Stress Corrosion Cracking of Metals—A State of the Art, ASTM STP 518*, American Society for Testing and Materials, 1971, pp. 3-15.
[17] Interrante, C. G. and Hicho, G. E. in *Stress Corrosion—New Approaches, ASTM STP 610*, American Society for Testing and Materials, 1976, pp. 349-365.
[18] Tada, H., Paris, P. C., and Irwin, G. R. in *The Stress of Analysis of Cracks Handbook*, Del Research, 1973, p. 216.
[19] Irwin, G. R., *Engineering Fracture Mechanics*, Vol. 1, No. 2, 1968, pp. 241-255.

*J. J. Mecholsky,[1] S. W. Freiman,[1] and R. W. Rice[1]*

# Fractographic Analysis of Ceramics

**REFERENCE:** Mecholsky, J. J., Freiman, S. W., and Rice, R. W., **"Fractographic Analysis of Ceramics,"** *Fractography in Failure Analysis, ASTM STP 645,* B. M. Strauss and W. H. Cullen, Jr., Eds., American Society for Testing and Materials, 1978, pp. 363-379.

**ABSTRACT:** The development of fracture surface observations into a quantitative tool for analysis of brittle fracture is reviewed. The effect of temperature, strain rate, and residual stresses on the "mirror constant," $A$, is discussed through recent experimental results, as well as new analysis of established literature. The current theories of mirror formation in glasses, glass ceramics, single crystals, and polycrystalline ceramics are compared to the results of a number of investigators. The relationship of the mirror constant to fracture toughness, that is, $K_{Ic}$, is discussed. Methods to incorporate the effects of grain size and internal stress on fracture are demonstrated. Finally, application of fracture surface analysis to scientific and applied problems are enumerated.

**KEY WORDS:** fractography, fracture surface analysis, ceramics, fractures (materials), brittle materials, mechanical properties

Since at least the 1920s, characteristic fracture features have been observed on glass [*1,2*][2], single crystals [*3*], natural polycrystalline materials like basalt [*4,5*], and intermetallic fibers [*6*]. In addition, Wallner [*7*] noted characteristic lines formed on the "mirror" surface of glass from the intersection of the primary stress front with the stress front generated from a secondary flaw. From these early observations of characteristic features, relationships between these features and the fracture stress in brittle materials was noted, in particular by Shand [*8*], Terao [*9*], and Smekal [*10*]. It was also shown [*8*] that these "Wallner lines" can be used to calculate the velocity of the crack front. These characteristic features have been shown to be related to the fracture origin [*11,12*], velocity of crack propagation [*13*], and critical stress intensity [*14,15*] and strain intensity [*16*] at fracture. These relationships are used to analyze the fracture of brittle material. This paper will review the current state of understanding of fracture sur-

[1] Research ceramic engineer, supervisory research engineer, and supervisory research ceramic engineer, respectively, Naval Research Laboratory, Washington, D.C. 20375.

[2] The italic numbers in brackets refer to the list of references appended to this paper.

face analysis and will discuss the important applications of this technique to brittle failure.

## Fracture Surface Analysis

Fracture in brittle materials occurs from defects like machining or mechanically produced cracks, pores, and inclusions. Although actual defects are not necessarily regular in shape, they usually can be idealized by semielliptical flaws in the manner prescribed by Randall [*17*]. For surface flaws that are perpendicular to the applied stress, one can relate the size of the original defect, $c$, to the failure stress, $\sigma$, through fracture mechanics equations[3] similar to those used for metals

$$\sigma \sqrt{c} = \frac{\Phi K_{Ic}}{\sqrt{1.2\pi}} \tag{1}$$

where $K_{Ic}$ is the critical stress intensity factor, and $\Phi$ is an elliptical integral of the second kind which accounts for the geometry of the crack.

Specifically, flaws due to machining have been characterized and shown to agree well with Eq 1 to predict failure of brittle materials [*18*]. Pores, either singly or in groups, act as the source of failure and can be analyzed according to Eq 1 as long as the relationship of the pores to the local microstructure is taken into consideration [*19*]. Likewise, inclusions [*20*] and grain boundary grooves [*21*] can be treated as fracture-initiating flaws in such a way that Eq 1 can be utilized.

While observation of the fracture-initiating flaw is important to analysis, in many cases flaws are nonplanar, too small, do not have clear boundaries, or a chip has come out that includes the flaw, so that one cannot estimate the flaw size. The real power of fracture surface analysis is in utilizing the fracture boundaries that form outside the flaw to describe fracture behavior, regardless of the flaw shape and any difficulties in identifying the fracture origin. Four definitive regions of fracture, surrounding fracture-initiating flaws, have been observed in brittle materials [*22,23*] (Fig. 1). The first region, generally smooth and commonly known as a mirror, is bounded by another region of small radial ridges, known as mist, which in turn is bounded by an even rougher area, known as hackle, which in turn is bounded by macroscopic crack branching. The distances from the fracture initiating flaw to these boundaries, that is, $r_i$, $r_o$, $r_{cb}$, have been shown experimentally to be related to the fracture stress, $\sigma$

$$\sigma r^{1/2} = \text{constant} = A \tag{2}$$

[3] This expression neglects the corrections for a back-face free surface and plastic flow at the crack tip as given in Ref *17* because, for most cases, these are not applicable for ceramics. Also, failure generally occurs at or near the surface.

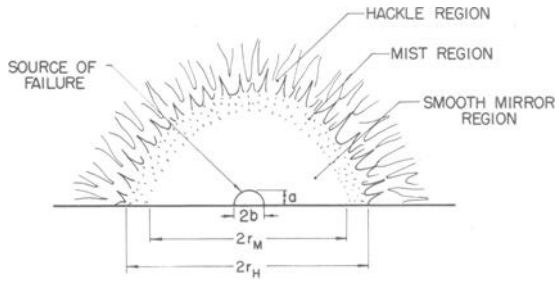


FIG. 1—*Schematic of the shape and general appearance of fracture mirror and related features on typical brittle fracture surface.*

These radii are commonly referred to as mirrors in brittle materials, so that the distinction is made between inner (mirror-mist) and outer (mist-hackle) mirror boundaries with their corresponding "mirror constant," $A$. It also should be indicated that in many instances the specimen size is too small to contain all of these boundaries so only some of the features are seen.

In order to understand this relationship, it is necessary to examine the fracture process, at least qualitatively. When a flaw begins to propagate as a sharp crack, its velocity increases with increasing crack length until it nears the terminal velocity for that material, approximately 0.6 of the shear wave velocity. Since the strain energy associated with the lengthening crack plus its kinetic energy can no longer be used to increase its velocity, other processes commence. These processes lead to the four definitive regions surrounding the fracture origin (Fig. 1). These regions are observed as long as the specimen size is large enough to accommodate the features, since the crack basically propagates as though it were in an infinite body regardless of specimen size. The first feature formed is a bright, shiny region; in glass, it is known as the fracture mirror. As the terminal velocity is approached, nucleation in the vicinity of the crack tip of microcracks (mist) occurs which are energetically unable to propagate over large distances. As the crack propagates further, enough energy becomes available so that the secondary cracks now can propagate over longer distances, leading to hackle. In all materials, when the crack becomes large enough, macroscopic crack branching occurs, although this phenomena is not always observed because the specimen is too small or there is propagation into a compressive region. The attempts to explain crack branching quantitatively will be discussed later. At this point we will show the results of the experimentally observed fracture mirror.

Micrographs of representative fracture surfaces of glass-ceramic, fine-grain polycrystalline and single-crystal ceramics, and glass, showing the areas of fracture initiation, are presented in Figs. 2 and 3. In comparing Figs. 1, 2, and 3, one can see the similarity of most brittle materials. In

many ceramics, there is an identifiable region surrounding the failure origin that reflects light better than regions further from the origin and usually is bounded by small flakelike particles (mist). The beginning of hackle is clearly evident on these micrographs, as it is on most other ceramics examined, and closely resembles that observed on glasses.

While there is some evidence of mist formation, this feature is not always discernible in polycrystalline ceramics, especially in large grain or highly porous materials. In large grain ceramics, many of the fracture steps left from transgranular failure on the easy cleavage plane or on grains of limited misorientation focus onto the fracture origin thus making identification of the source of failure easier. Cleavage or fracture steps as well as hackle markings also appear on the fracture surfaces of single crystals

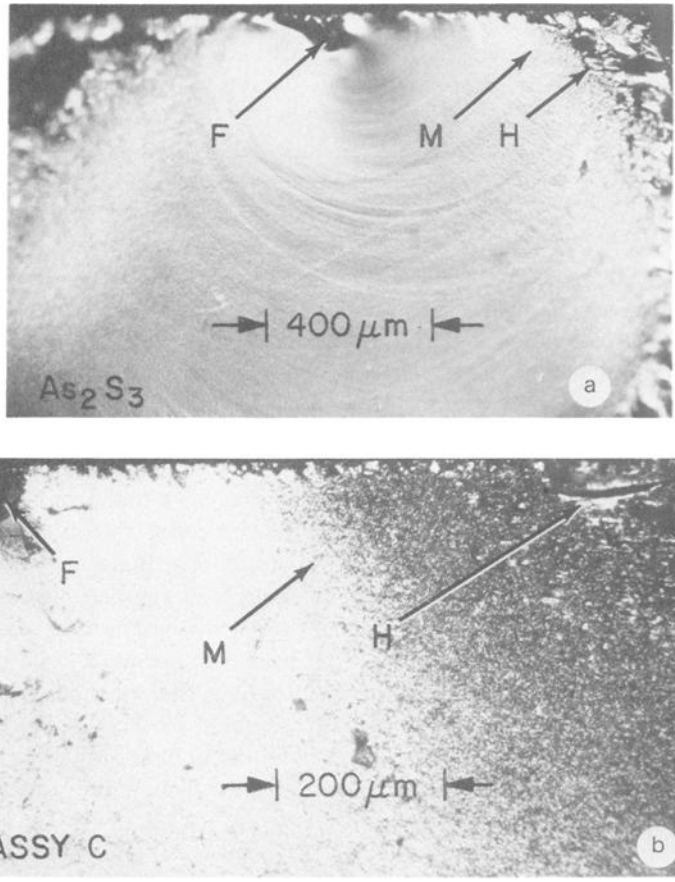


FIG. 2—*Optical photographs of fracture surfaces of* (a) *arsenic trisulfide* ($As_2S_3$), *and* (b) *glass carbon showing source of failure* (*F*), *mist* (*M*), *and hackle* (*H*) *regions. The fracture surface of* $As_2S_3$ *is similar to those of silicate glasses, whereas in glassy carbon the separation of mist and hackle is greater.*

depending on the orientation of crack propagation. However, in single crystals, the occurrence of mist and hackle depends on the fracture plane and the direction of propagation on this plane [*22*].

In glasses, the energy needed to initiate or propagate a secondary crack is isotropic so the formation of mist is expected to occur at an energy near that required to form hackle, as is observed experimentally. In polycrystalline ceramics, however, secondary cracks can be nucleated on cleavage planes within grains or along grain boundaries at an energy near that of single crystals, and hence much less than that required to propagate the primary crack through the polycrystalline microstructure, leading to much earlier formation of mist. For these secondary cracks to extend to form hackle means that more energy must be supplied to the fracture process. In polycrystalline ceramics, this energy comes from the greater extension of cracks away from the inner (mirror-mist) boundary leading to larger ratios of hackle to mist radii [*15*]. However, even with individual differences, the features on the fracture surfaces of glasses, polycrystalline, and single crystal ceramics generally obey Eq 2.

Logarithmic plots of flexural strength versus the outer mirror radii are presented in Figs. 4 and 5 to demonstrate the difference in mirror constant for several representative materials. The curves are the best fit straight lines of slope $-0.5$. The use of this slope is based on the assumption that Eq 1 is valid for these materials. In fact, in many cases, the best linear least squares fit had a slope of $-0.5$. Extended data for glasses and ceramics were given in previous papers [*12,15*]. Strength mirror size curves for ADP [*24*], hot pressed alumina [*25*], sapphire [*15,26*], silicon nitride [*23*], and AlSiMag 614 [*23*] are also given in the literature. There are, however, external factors than can also influence the mirror constant. These are discussed in the following sections.

### *Effect of Temperature*

Both Shinkai [*27*] and Mecholsky [*28*] found that the mirror constant in glass was higher at $-150\,^{\circ}C$ than at $20\,^{\circ}C$. Mecholsky [*28*] also found that not only was the mirror constant higher at $-150\,^{\circ}C$ but also that the inner mirror to flaw size ratio was much smaller (6:1 compared to 13:1), a value commonly observed in polycrystalline ceramics. This decrease indicates that this temperature decrease produces more than just an increase in fracture toughness. The limited research in this area and at elevated temperature [*29*] indicates that much more research is needed in the area of fracture surface analysis at low and high temperatures.

### *Effect of Residual Stresses*

In a study of the effect of tempering on strength, Kerper and Scuderi [*30*] found the mirror size-modulus of rupture relationship to be independent

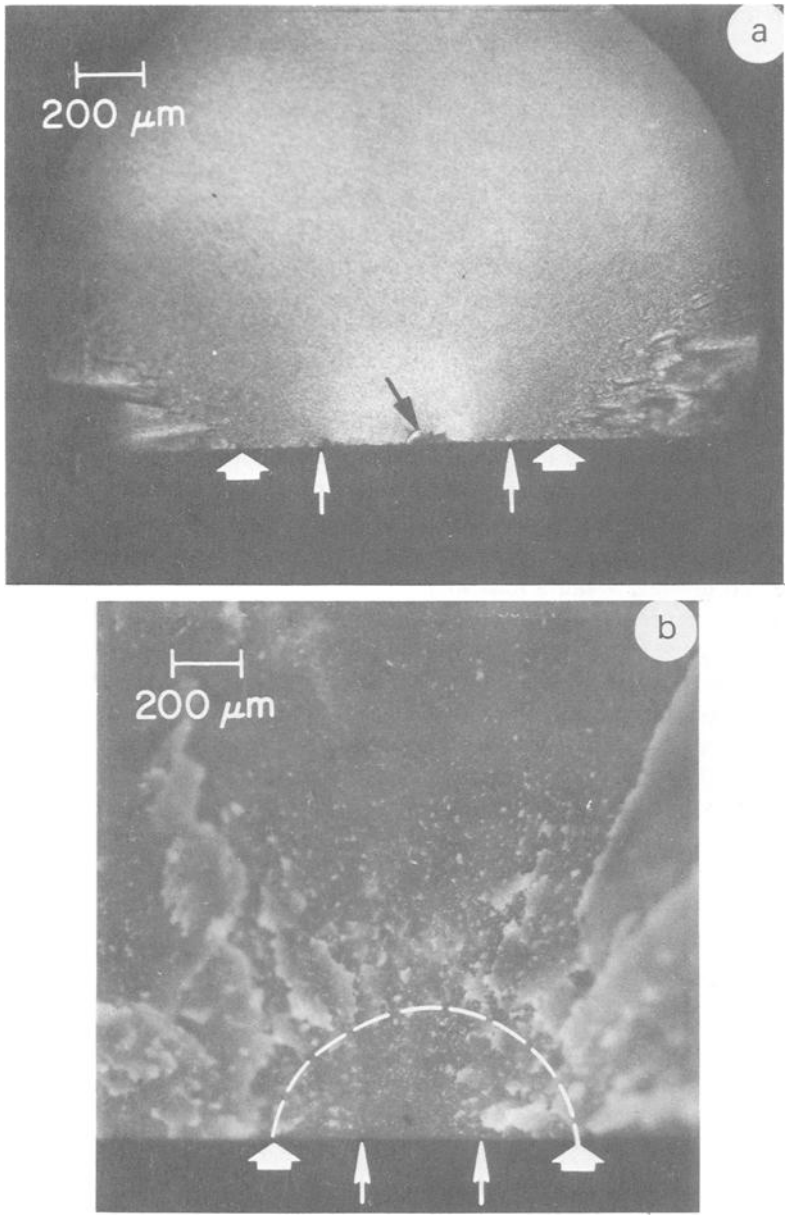


FIG. 3—*Optical fractographs of* (a) *baria-silica* ($3BaO \cdot 5SiO_2$) *glass ceramic,* (b) *hot-pressured silicone nitride* ($Si_3N_4$), *and* (c) *single crystal ammonium diphosphate* (*ADP*). *Broad arrows indicate outer mirror demarcations; thin arrows in* (a) *and* (b) *indicate inner mirror boundaries; thin arrows in* (c) *may be outer mirror boundary with no inner mirror* (*mirror-mist*) *boundary present. Black arrows indicate machined flaws which acted as the source of failure. The failure origin in* (b) *is an inclusion* (*black dot approximately in the center of the broad arrows*). *The dashed line is just inside the outline of the outer mirror.*

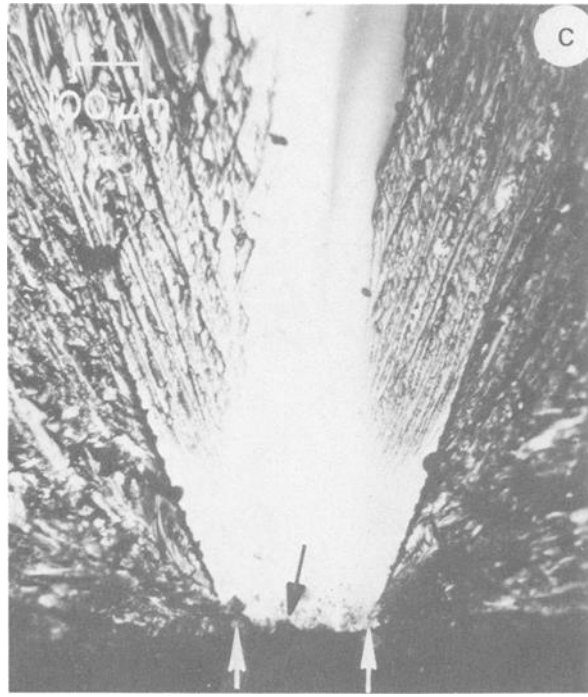


FIG. 3—*Continued.*

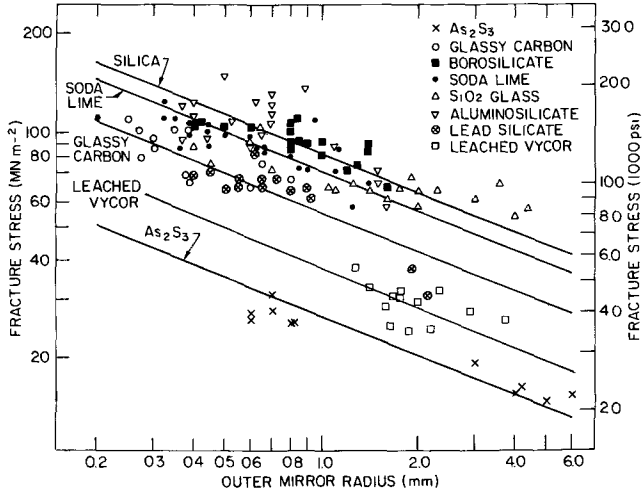


FIG. 4—*Fracture stress versus outer (mist-hackle) mirror radius of silicate and nonoxide glasses. Solid lines represent slope of* $-0.5$ [12].

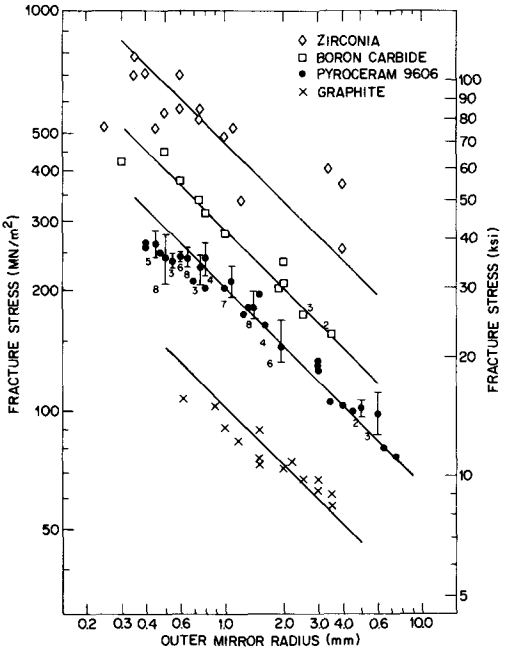


FIG. 5—*Fracture stress as a function of outer mirror (mist-hackle) radius for representative polycrystalline ceramics. Solid lines are least squares fit of slope* $-0.5$ *(*$10^3$ *psi = 1 ksi) (1 ksi = 6.9 MPa)* [15].

of location of fracture origin for new glass. For semitempered and tempered glass, they found that the slope of the logarithmic plot of $\sigma$ versus $r^{1/2}$ did not equal 0.5 as predicted by Eq 2. However, there are two approaches to plotting these data: (*a*) plot the data on a log-log plot and use regression analysis to determine the slope or (*b*) assume Eq 2 holds and attribute deviations in the intercept to extrinsic variations such as residual stress [*23,31*]. For example, if unlike Kerper and Scuderi [*30*] who followed the first approach, one assumes that Eq 2 is valid and plot $\sigma$ versus $r^{1/2}$ for these data (Fig. 6), a residual stress of approximately 70 MPa is predicted in their tempered glass as might be expected.

### *Effect of Strain Rate*

Although the values of fracture stress are changed with rate of loading, the mirror constant should be relatively insentitive to this parameter.[4] Kirchner [*31*] used fracture mirrors to study impact of various glasses and

[4] Although the average fracture stress increases with an increase in the rate of loading, the distance to the mirror boundaries would correspondingly decrease, thereby not changing the value of the mirror constant.

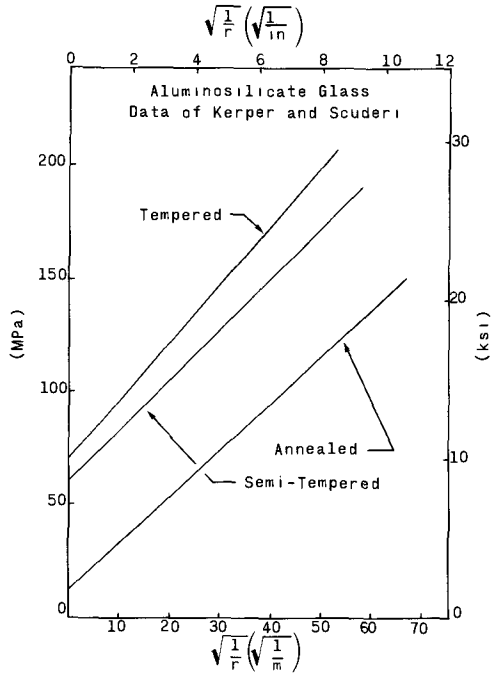


FIG. 6—*The data of Ref* 30 *replotted assuming Eq 2 is valid. This gives an estimate of the residual stress present for each heat treatment.*

polycrystalline ceramics both at room and elevated temperatures. He made the assumption that the relationship in Eq 2 is valid for different rates of loading, which recently has been substantiated for glasses by Bradt et al [*32*]. More recently, Kirchner [*33*] has shown that even impact loading producing Hertzian cone fractures lead to fracture mirrors which can be used in the analysis of brittle fracture for dynamic loading. Pohanka et al [*24*] have shown that mirror formation from dynamic stresses in piezoelectric ceramics produced by voltage application give rise to mirror constants that agree with those observed for the normal fracture (Fig. 7).

## Criteria for Formation of Fracture Features

Many attempts have been made to try to explain the formation of mist, hackle, and crack branching. These phenomena can basically be represented by three approaches; crack branching occurs: (*a*) at a characteristic or critical velocity [*34*]; (*b*) at particular strain intensity [*16*] or stress intensity [*15,35,35*] values; or (*c*) when the strain energy release rate exceeds that required for propagating planar cracks [*37-42*].

Most of the velocity flaw size relations are of the form

$$v^2 \alpha \left(1 - \frac{c}{r}\right) \tag{3}$$

where $v$ is the velocity of the crack of length, $r$, and $c$ is the critical flaw size. Because $c/r$ at branching is small compared to 1, however, large changes in $c/r$ make only small changes in velocity, so that estimates of ratios of (mist-hackle) radius to flaw size from velocity data are subject to large inaccuracies. It is unclear at this time whether the three criteria are different or whether they really result in the same predictions of fracture mirror formation and boundaries. That is, Bansal [*42*] and Abdel-Latif et al [*40*] have related the mirror constant to the critical stress intensity factor, including a kinetic energy term similar to the approach of Johnson and Holloway [*14*] through the energy balance approach suggested by Roberts and Wells [*38*].

Regardless of the criteria which govern the formation of mist and hackle, Eq 2 is still valid and can be used in fracture surface analysis. Fracture mechanics expressions (Eq 1) can be combined with fracture surface analysis (Eq 2) to explain quantitatively the mirror boundaries [*15*]. The mirror constant has been shown to be related to the critical stress intensity factor, the fracture stress, and the mirror to flaw size ratio

$$A = \sigma r^{1/2} = \frac{\Phi K_{1c}}{\sqrt{1.2\pi}\left(\frac{c}{r}\right)^{1/2}} \tag{4}$$

This relationship states that the mirror constant is proportional to the critical stress intensity factor at failure.[5] These results are compared to actual measurements of mirror constants in Table 1. In fact, qualitatively comparing all these results implies that the velocity is constant for a given $c/r$ ratio. In the velocity formulations, however, numerical predictions of mirror constants from these equations are not in general agreement with actual observations (Table 1), but there are some parameters in the equations that are difficult to determine, so one can understand if accurate predictions are not possible. The formulation which includes the mirror to flaw size ratio [*15*] agrees well with this observation. This implies that the distance to the fracture mirror boundaries most likely includes any kinetic energy effects on crack propagation. In addition, these equations suggest that the velocity, strain energy release rate, and strain intensity criteria are really different expressions of the same phenomenon. It is clear, however, from the fact that boundaries do not occur in certain directions in single

[5] This is the same form of the equation with slight modifications as given by the strain intensity proponents. Since the velocity is related to the ($c/r$) ratio, this form is also the same as the energy balance proponents as well as the constant velocity proponents for formation of crack branching, Table 1.

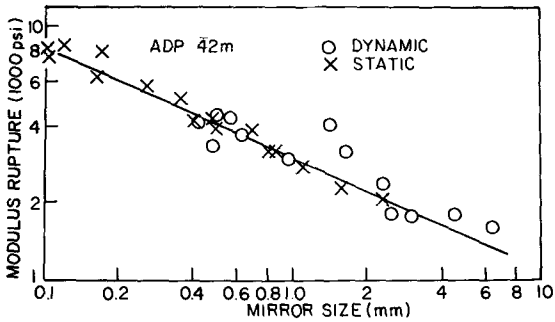


FIG. 7—*Static and dynamic fracture stress versus mirror size for ADP single crystal. The static strength was measured on several sizes of 45-deg z-cut ADP bars in three-point flexure. The dynamic strength was measured by driving the bars piezoelectrically in a free-free longitudinal mode until failure occurred* [24].

crystals [22] that all of these are necessary but not sufficient conditions for boundary formation.

If we plot available data as $A$ versus $K_{Ic}$ (Fig. 8) as suggested by Eq 4 with certain exceptions discussed later, the data are seen to fall within a band centered on a mirror to flaw size ratio of 13 to 1 (for semicircular flaws). There is no evidence to suggest that the points falling either above or below this trend represent failure of a particular type, for example, machine flaws, pores, large grains, etc. This trend implies that the ratio of outer mirror size to flaw size is a constant in glasses and ceramics independent of crystal structure (but not direction in crystals), composition, or microstructure. The data in Fig. 8 would tend to suggest that Eq 4 is valid for a wide range of ceramics and that if the mirror size can be measured on the fracture surface and $K_{Ic}$ is also known, an estimate of the flaw size can be obtained for that specimen. The validity of this approach has been shown for many glasses, polycrystalline ceramics, and single crystal ceramics as well as glass ceramics [15]

The lithia-silica glass ceramics are notable exceptions to the relationship in Fig. 8. The deviation of these data would predict that their mirror to flaw size ratio would be about 8 to 1, when in reality, measurement of the mirror to flaw size ratio gives a number around 13 to 1 [43]. The difference has been explained by the presence of microcracking at the top of the primary crack front which would be an energy-absorbing process in this material, analogous to the plastic zone in metals. The existence of microcracking in lithia-silica glass ceramics is well established [44,45]. In fact, the amount of deviation to the right of the curve provides a measure of the amount of microcracking that is occurring in the material, that is, at the given mirror constant the intersection with the line in Fig. 8 would give the critical stress intensity factor for a lithia-silica glass ceramic without microcracking.

TABLE 1—*Comparison of criteria for crack branching.*[a]

| Author(s) | $(A/K_{Ic})$ Formulation | $(A/K_{Ic})$ (boundary) | $(A/K_{Ic})$ Measured |
|---|---|---|---|
| Johnson and Holloway [*14*] | $\left[\frac{4}{2\pi - \frac{k\rho v^2}{E}}\right]^{1/2}$ | (mirror-mist)<br>(mist-hackle)<br>1.2 (branching) | 2.5<br>2.7 |
| Congelton and Petch [*13*] | $\sqrt{\frac{2}{\pi}}$ | 0.8 (branching) | 1.4 |
| Abdel-Latif, Bradt, and Tressler [*40*][b] | $\left[\frac{2}{3\left(1 - \frac{k\rho v^2}{E}\right)}\right]^{1/2}$ | 1.8 (mirror-mist) | 2.3 |
| Bansal [*42*] | $\left[\frac{2\pi}{8 - \frac{3k\rho v^2}{2E}}\right]^{1/2}$ | 1.6 (mirror-mist) | 2.3 |
| Mecholsky, Freiman, and Rice [*15*] | $\left[\frac{1.25}{2\left(\frac{c}{r}\right)}\right]^{1/2}$ | 2.8 (mirror-mist)<br>3.2 (mist-hackle) | 2.7<br>3.1 |

NOTE—$v$ = 1500 m/s,
$\rho$ = 2.5 g/cm$^2$, and
$k$ = 44.

[a] Soda-lime glass.

[b] Tensile case; since $k$ = 44 or $v$ = 1500 m/s cannot be used because the term in parenthesis becomes negative; $k$ = 22 and $v$ = 1000 m/s were used as suggested in the reference.

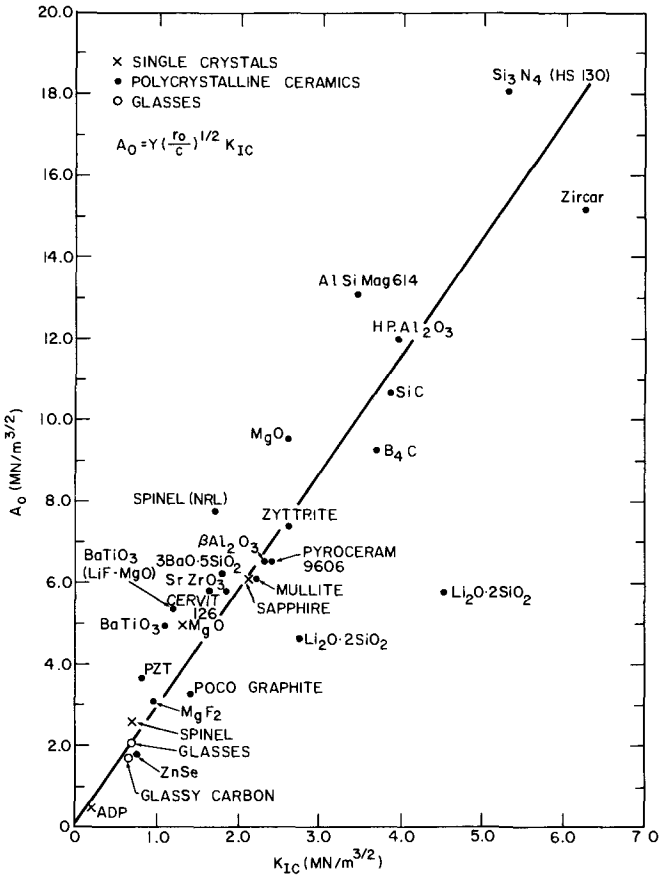


FIG. 8—*Outer mirror (mist-hackle) contant,* $A_o$, *as a function of the critical stress intensity,* $K_{Ic}$, *for ceramic materials* [15].

Other materials also have been shown to exhibit microcracking [*46*] (for example, Poco graphite [*47*], zirconia [*48*], alumina-zirconia [*49*], silicon nitride, some aluminas, and many other noncubic ceramics). Modifications of Eq 2 must be made to account for the effect of microcracking in any analysis.

Another factor that must be considered is that when the fracture initiating flaw is of the order of the size of the local microstructure, single crystal rather than polycrystalline fracture mechanics applies. That is, the calculations predicting either strength or flaw size demonstrate that a value of $\gamma_e$ approaching that of a single crystal is appropriate for materials in which flaws are contained in one or two grains [*50,51*]. Because of the large size of the crack compared to the microstructure, the stress intensity of the mirror boundary as represented by the mirror constant, $A$,

is a measure of the average fracture toughness of the material. It should not be surprising then that this value cannot be used to predict failure conditions for the local properties in the materials where the flaw size is smaller than the large grains; Eqs 1 and 4 must be modified by including the single crystal rather than the polycrystalline $K_{Ic}$ [*51*].

Also, if internal stress is present due to either thermal expansion anisotropy in noncubic ceramics such as beryllium oxide (BeO) and alumina or as a result of phase transformations, Eq 1 must be modified to account for this stress [*52*]

$$\sigma_a + \langle \sigma_i \rangle = \frac{\Phi K_{Ic}}{1.12\sqrt{\pi c}} \tag{5}$$

where $\langle \sigma_i \rangle$ is the effective internal stress acting on the flaw. Since even a small flaw may encompass several grains, there will be some averaging of the stresses around its perimeter. Hence, the value of $\langle \sigma_i \rangle$ will depend on the ratio of the flaw size to the grain size. $\langle \sigma_i \rangle$ would be expected to approach zero as the flaw size increases, namely, as the perimeter of the flaw averages more and more of the tensile and compressive components of the internal stress in the body. Studies [*53*] have corroborated the hypothesis that $\langle \sigma_i \rangle$ decreases from a value approaching the theoretical limit in the material for very small flaws, to zero for large flaws.

### Application of Fracture Surface Analysis

Observation of characteristic markings from fracture surfaces can be used not only in the study of basic phenomena of crack propagation but also as an aid in determining the effects of various mechanical phenomena: polishing, grinding, impact, and processing. Several examples are given here to demonstrate the usefulness of fracture surface analysis.

Mecholsky et al [*18*] used the relationship between fracture mirror and flaw sizes to study the effect of machining on the shape of the fracture initiating flaws in the fracture of soda lime glass. From this study it was shown that mirror size measurements followed Eq 2 even when the fracture-initiating flaw was out of the plane of fracture or a very complicated type flaw, thus demonstrating the power of fracture mirror measurements over local measurements at the crack tip. In addition, they showed that fracture energy, and thus $K_{Ic}$, was independent of flaw geometry. They further observed that the area of the flaw divided by the square of the outer mirror radius was a constant in agreement with the subsequent prediction of Bansal [*54*]. In addition, the use of fracture surface analysis explained differences of strength produced by grinding in two different directions. These studies have been extended to polycrystalline ceramics

and single crystals and to polishing of ceramics. Since polishing is commonly a random process of fine grinding, a failure occurs from the worst case, generally an elongated flaw, $a/b \approx 0.5$ in both glasses and polycrystalline ceramics. The case for single crystals is complicated by elastic anisotropy, but the study of fracture surface analysis has provided a tool to investigate the effect of anisotropy on flaws produced by grinding, and, hence, on fracture.

Another example is in the field of high strength optical fibers. In drum-to-drum proof testing of optical fibers, there are numerous breaks. It cannot always be determined whether the breaks occur when full tension is on the fiber or before it. By use of fracture surface analysis, one can determine not only the strength at failure but also the source of failure. For example, by observing the fracture surface Mecholsky et al [*55*] determined that two fibers which were thought to be proof tested at 1379 MPa (200 000 psi) failed at much lower strength, around 345 MPa (50 000 psi), because of a crack and a dust particle which were fused to the fiber surface, respectively. The latter, most likely, occurred during the drawing process, causing a sharp flaw upon cooling. These fibers obviously failed before they reached the full stress on the drum. Without fracture surface analysis, one would have suspected that these two fibers reached the 1379-MPa (200 000-psi) level. An important result that came from another study of optical fibers by Maurer et al [*56*] was that the mirror constant for fiber rods is the same for that as silica bars tested in three-point bending, thus extending the strength-mirror size relationship for glasses.

Although they will not be discussed in detail here, there are a number of other applications of fracture surface analysis to ceramics. These include the analysis of stresses during impact [*31*], failure stress predictions due to thermal shock [*29*], and analysis of failures of piezoelectric components which occur during voltage application [*25,57*].

## Summary

Fracture in ceramic materials results in fracture surface features known as mirror, mist, and hackle. The formation of mist and hackle, which represent different stages of secondary crack formation, occurs due to the excess energy of the moving crack over what is needed to propagate it. The boundaries of the mist and hackle regions have been shown to be related quantitatively to the stress at fracture as well as to the critical flaw size in the material. It was demonstrated that the so called mirror constant, $A$, can be thought of as a measure of the stress intensity factor at the mist and hackle boundaries. The ratio of $A$ to the critical stress intensity factor for fracture, $K_{Ic}$, is a constant for a wide range of ceramic materials. In any quantitative analysis of fracture of polycrystalline ceramics, however, one

must take into account any internal or residual stresses in the body as well as consider the ratio of the critical flaw size to the size of microstructural features. Finally, a number of applications of fracture surface analysis were discussed.

## References


[1] Preston, F. W., *Journal of the American Ceramic Society*, Vol. 14, 1931.
[2] Preston, F. W., *Journal of the Society of Glass Technology*, Vol. 10, 1926, pp. 234–269.
[3] Zaffee, C. A. and Wardon, C. O., *Acta Crystallographica*, Vol. 2, Part 6, 1949, pp. 377–382.
[4] Iddings, J. P., *American Journal of Science*, Vol. 31, 1886, p. 321.
[5] Preston, F. W., *Proceedings of the Royal Society, B*, 1930.
[6] Davies, G. J. and Broom, N. D., *The Philosophical Magazine*, 1972.
[7] Wallner, H., *Zeitschrift fur Physik*, Vol. 114, 1939, pp. 368–378; *Ceramic Abstracts*, Vol. 19, No. 6, 1940, p. 137.
[8] Shand, E. B., *Journal of the American Ceramic Society*, Vol. 37, No. 12, 1954, pp. 559–572.
[9] Terao, N., *Journal of Physics, Proceedings of the Physical Society, Japan*, Vol. 8, 1953, pp. 545–549.
[10] Smekal, A., *Journal of the Society of Glass Technology*, Vol. 20, 1936.
[11] Krohn, D. A. and Hasselman, D. P. H., *Journal of the American Ceramic Society*, Vol. 54, No. 8, 1971, p. 411.
[12] Mecholsky, J. J., Rice, R. W., and Freiman, S. W., *Journal of the American Ceramic Society*, Vol. 57, 1974, p. 440.
[13] Congelton, J. and Petch, N. J., *The Philosophical Magazine*, Vol. 16, 1967, p. 749.
[14] Johnson, J. W. and Holloway, D. C., *The Philosophical Magazine*, Vol. 14, 1966, p. 731.
[15] Mecholsky, J. J., Freiman, S. W., and Rice, R. W., *Journal of Material Science*, Vol. 11, 1976, pp. 1310–1319.
[16] Kirchner, H. P., "Criteria for Fracture Mirror Boundary Formation in Ceramics," Proceedings of ICM-II, Boston, Mass., 1976.
[17] Randall, P. N. in *Plain Strain Crack Toughness Testing of High-Strength Metallic Materials, ASTM STP 410*, W. F. Brown, Jr. and J. E. Srawley, Eds., 1966, pp. 88–126.
[18] Mecholsky, J. J., Freiman, S. W., and Rice, R. W., *Journal of the American Ceramic Society*, Vol. 60, No. 3–4, 1977, pp. 114–117.
[19] Evans, A. G. and Tappin, G., *Proceedings of the British Ceramic Society*, Vol. 20, 1972, p. 275.
[20] Baratta, F. I., Driscoll, G. W., and Katz, R. N. in *Ceramics for High Performance Applications*, Proceedings of the 2nd Army Materials Technology Conference, Hyannis, Mass., Nov. 1973.
[21] Coble, R. L., *Journal of the American Ceramic Society*, Vol. 54, 1971, p. 59.
[22] Rice, R. W., *Surface and Interfaces of Glass and Ceramics*, Frechette, Lacourse, and Burdick, Eds., Plenum, New York, 1972.
[23] Kirchner, H. P. and Gruver, R. M. in *Proceedings of Symposium on Fracture Mechanics of Ceramics*, Bradt, Hasselman, and Lange, Eds., Plenum, New York, Vol. 1, 1973, pp. 309–321.
[24] Pohanka, R. C., Smith, P. L., and Pasternak, J., "Report of NRL Progress," U.S. Naval Research Laboratory, Jan. 1975, p. 21.
[25] Kirchner, H. P. and Gruver, R. M., *The Philosophical Magazine*, Vol. 27, 1973, p. 1433.
[26] Becher, P. F., U.S. Naval Research Laboratory, private communication.
[27] Shinkai, N., *Japanese Journal of Applied Physics*, Vol. 14, No. 1, 1975, pp. 147–148.
[28] Mecholsky, J. J., U.S. Naval Research Laboratory, unpublished data.
[29] Kirchner, H. P., Gruver, R. M., and Sotter, W. A., Ceramic Finishing Company Report No. 2, 1974.
[30] Kerper, M. J. and Scuderi, T. G., *Journal of the American Ceramic Society*, Vol. 44, No. 12, 1965, pp. 953–955.

[31] Kirchner, H. P. and Sotter, W. A., Ceramic Finishing Company Report No. 1, 1974.
[32] Bradt, R. C., Pennsylvania State University, private communications.
[33] Kirchner, H. P. and Gruver, R. M., Ceramic Finishing Company Report No. 5, Jan. 1977.
[34] Yoffee, E. H., *The Philosophical Magazine*, Vol. 42, 1951, p. 739.
[35] Clarke, A. B. J. and Irwin, G. R., *Experimental Mechanics*, Vol. 23, 1966, pp. 321-330.
[36] Petch, N. J. in *Fracture*, H. Liebowitz, Ed., Academic Press, Vol. 1, 1968, pp. 351-393.
[37] Mott, N. F., *Engineering*, Vol. 165, 1948.
[38] Roberts, D. K. and Wells, A. A., *Engineering*, Vol. 178, 1954, p. 1820.
[39] Berry, J. P., *Journal of Mechanics and Physics of Solids*, Vol. 8, 1969, pp. 194-216.
[40] Abdel-Latif, A. I. A., Tressler, R. E., and Bradt, R. C., *International Journal of Fracture Mechanics*, to be published, 1977.
[41] *Dynamic Crack Propagation*, G. C. Sih, Ed., Nordoff, 1973.
[42] Bansal, G. K., *The Philosophical Magazine*, to be published.
[43] Mecholsky, J. J. and Freiman, S. W. "Fracture Surface Analysis of Glass Ceramics," Proceedings of Eleventh International Congress on Glass, Prague, Czechoslovakia, July 1977.
[44] Sahoo, M., Rao, A. S., and Nadeau, J. S., Technical Report, Center for Materials Research, University of British Columbia, 1972.
[45] Freiman, S. W. and Hench, L. L., *Journal of the American Ceramic Society*, Vol. 55, 1972, p. 86.
[46] Wu, C. Cm., Rice, R. W., Freiman, S. W., and Mecholsky, J. J., submitted to the *Journal of Material Science*, 1977.
[47] Meyer, R. W., Zimmer, J., and Almon, M. C., Report No. ATR74 (7408) 2, Aerospace Corp. March 1974.
[48] Green, D. J., Nicholson, P. S., and Embory, J. D., *Journal of the American Ceramic Society*, Vol. 56, 1973, p. 619.
[49] Claussen, N., *Journal of the American Ceramic Society*, Vol. 59, No. 1-2, 1976, pp. 49-51.
[50] Rice, R. W. in *Proceedings of Symposium on Fracture Mechanics of Ceramics*, Pennsylvania State University, July 1973.
[51] Freiman, S. W., Mecholsky, J. J., Rice, R. W., and Wurst, J. C., *Journal of the American Ceramic Society*, Vol. 58, 1975, p. 406.
[52] Pohanka, R. C., Rice, R. W., and Walker, B. E., *Journal of the American Ceramic Society*, Vol. 59, 1976, p. 71.
[53] Pohanka, R. C., Freiman, S. W., and Bender, B. A., *Journal of the American Ceramic Society*, Vol. 61, 1978, pp. 1-2.
[54] Bansal, G. K., *Journal of the American Ceramic Society*, Vol. 59, No. 1-2, 1976, pp. 87-88.
[55] Mecholsky, J. J., Freiman, S. W., and Morey, S. M., *Bulletin of the American Ceramic Society*, accepted for publication, Dec. 1977.
[56] Maurer, R. C., Miller, R. A., Smith, D. D. and Trondeen, J. C., ONR Contract N00014-73-C-0293, Corning Glass Works Technical Report, March 1974.
[57] Pohanka, R. C., Rice, R. W., Pasternak, J., Smith, P. L., and Walker, B. E., *Proceedings of Workshop on Sonar Transducer Materials*, Smith and Pohanka, Eds., U.S. Naval Research Laboratory, Nov. 1976.

# Summary

# Summary

This symposium volume is divided into four areas: techniques, environmental effects, fatigue, and stress and nonmetals.

In the techniques section, the common approach was to develop a set of reference fractographs of cracks with known histories for comparison to the fractographs from service failures. Steele and Lentz utilized both microscopy and fractography to characterize cleavage, ductile rupture, intergranular separation, and hydrogen embrittlement in low carbon steel and then compared the resulting fractographs to those characterizing failures in drawn cup walls, and quenched and tempered plate. Young and Kumar simulated the manufacturing environment which caused hydrogen embrittlement of 9Ni-4Co-0.20C steel to produce the same intergranular fracture found in a service failure of the aft-fuselage structure of the B-1 aircraft.

Meyn presents examples of a wide range of materials and components which had failed and the techniques employed to identify the fracture mode. The techniques used consist of the entire range of resolution from the unaided eye to the transmission electron microscope.

Madeyski and Albertin are more general in their suggested techniques. They discuss the unconventional technique of looking at electrically conductive replicas in the scanning electron microscope and compensating for mirror image effects by electronically reversing the image. They also have gotten good correlation in relating striation spacing in fatigue failures to macroscopic $da(\Delta K)/dN$ by means of the Bates-Clark relation and present a practical example.

Papers on environmental effects deal primarily with hydrogen embrittlement phenomena, corrosion fatigue, and stress-corrosion cracking. Gangloff and Wei examined the mechanism of hydrogen-induced cracking in 18Ni maraging steels and conclude that the crack path depends mainly on temperature. At low temperatures, intergranular cracking proceeded along prior austenite grain boundaries, and as the temperature increased the cracks became transgranular and propagated along the lath martensite boundaries. This was in complete agreement with the results presented by Kikuta et al, who made the same observations in other steels. Both papers agreed that the hydrogen-assisted cracking mechanism can be characterized by the role of microstructural sites participating in hydrogen diffusion resulting in the embrittlement process.

Lee et al discuss two similar failures in Ti-8Al-1Mo-1V gas turbine fan blades. Both failures had initiated by stress corrosion cracking: one at high temperature, the other at ambient. The remainder of the subcritical crack growth in both failures was found to be fatigue at ambient temperature. Laboratory controlled hot salt stress corrosion tests provided the basis for comparison with the service failures.

Corrosion fatigue was also examined by Hioki and Mukai. Their work was on Type 304 stainless steel in boiling 42 percent magnesium chloride. They utilized a parametric approach in determining the service life of this material in this environment. They conclude that the cyclic rate affects fatigue life at rates less than $10^3$ cycles per minute (cpm), that the rate of crack propagation is proportional to the maximum stress intensity factor, and that the fractography, at higher cyclic rates and static loading, is transgranular, and at lower cyclic rates, such as 1 cpm, intergranular.

Mukai et al examined the same material in the same hostile environment under constant load and found that the orientation of the fracture surface was in the (100) plane. They also contend that striation-like markings appeared in the flat regions. This normally would not be expected in nonfatigue service.

There are several interesting approaches to examining fatigue failures and their causes. Bhandarkar and Lisagor examined stress corrosion cracking and fatigue as well as time independent fracture processes on four aluminum alloys. What resulted is a systematic compilation of fractographic features which serve as a basis for examining failures in these and similar aluminum alloys.

Abelkis also studied fatigue in aluminum but concentrated on correlating crack propagation under spectrum loading with fracture morphologies. Excellent correlation between changes in loading schemes and striation spacing are demonstrated. Eylon and Kerr analyzed fatigue failures by investigating the microstructure of the origin sites using a precision sectioning technique. This technique was extremely useful in determining that nonmetallic inclusions were fatigue initiation sites in titanium alloy powder compacts. In superalloy compacts, porosity was related to fatigue initiation.

Kramer found manganese-sulfide (MnS) inclusions to be the cause of a fatigue failure in a steam turbine rotor. His analysis included an exhaustive study of alternative mechanisms before concluding that it was a fatigue failure, while Takada et al examined the effect of quantity and shape of MnS inclusions on ductility of carbon-manganese (C-Mn) steel plates. They determined that ductility was related to the inclusion area fraction on a ductile fracture surface.

Joshi discussed, in general terms, the application of surface analysis methods such as electron spectroscopy for chemical analysis (ESCA) and Auger electron analysis in the determination of temper embrittlement, grain boundary corrosion, and intergranular stress-corrosion cracking. The

ability to analyze several monolayers of a surface without the masking effects of the bulk metal has already proved to be a powerful addition to fractographic studies.

The effects of stress on material behavior were examined by various methods. Most authors employed both microscopy and fracture mechanics. Hicho and Gilmore found in comparing deembrittled and embrittled 2¼Cr-1Mo steels that the fracture morphology of the deembrittled specimen was transgranular, while temper embrittlement resulted in an intergranular failure. Stress corrosion cracking tests showed that these embrittling effects result in a marked lowering of the threshold stress intensity.

Creep mechanisms in pressure vessels were discussed by Coleman. He observed that intergranular separation initiated at a notch in the vessel wall by means of classical grain boundary cavitation. This initiating mechanism was followed by two shear mechanisms, one relatively ductile and one with low ductility.

McCartney and Pellegrino investigated the relationship of strength, toughness, and flaw tolerances in steel-lifting chains by means of fracture mechanics. Their studies showed that higher strength chains were more notch sensitive and were susceptible to brittle failure if they contained flaws 1 in. deep.

Perhaps the newest area discussed at the symposium was the Mecholsky et al paper on the fractographic analysis of ceramics. The introduction of the concept of mirror constant and its relationship to fracture toughness was discussed as well as the current theories of mirror formation. Several examples of typical ceramic failures and their important features are discussed. We will look forward to additional work in this area in the future.

*B. M. Strauss*
Gulf Research and Development Company, Pittsburgh, Pa. 15230, editor

*W. H. Cullen, Jr.*
U.S. Naval Research Laboratory, Washington, D.C. 20375, editor

# Index